inventions

Special Issue Reprint

Innovative Research and Applications in Hydrodynamics and Flow Control

Edited by
Peng Du, Haibao Hu and Xiaopeng Chen

mdpi.com/journal/inventions

MDPI

Innovative Research and Applications in Hydrodynamics and Flow Control

Innovative Research and Applications in Hydrodynamics and Flow Control

Guest Editors

Peng Du
Haibao Hu
Xiaopeng Chen

MDPI

Basel • Beijing • Wuhan • Barcelona • Belgrade • Novi Sad • Cluj • Manchester

Guest Editors

Peng Du
School of Marine Science and Technology
Northwestern Polytechnical University
Xi'an
China

Haibao Hu
School of Marine Science and Technology
Northwestern Polytechnical University
Xi'an
China

Xiaopeng Chen
School of Marine Science and Technology
Northwestern Polytechnical University
Xi'an
China

Editorial Office
MDPI AG
Grosspeteranlage 5
4052 Basel, Switzerland

This is a reprint of the Special Issue, published open access by the journal *Inventions* (ISSN 2411-5134), freely accessible at: https://www.mdpi.com/journal/inventions/special_issues/0IQ90E0EKX.

For citation purposes, cite each article independently as indicated on the article page online and as indicated below:

Lastname, A.A.; Lastname, B.B. Article Title. *Journal Name* **Year**, *Volume Number*, Page Range.

ISBN 978-3-7258-8793-4 (Hbk)
ISBN 978-3-7258-8794-1 (PDF)
https://doi.org/10.3390/books978-3-7258-8794-1

© 2026 by the authors. Articles in this reprint are Open Access and distributed under the Creative Commons Attribution (CC BY) license. The reprint as a whole is distributed by MDPI under the terms and conditions of the Creative Commons Attribution-NonCommercial-NoDerivs (CC BY-NC-ND) license (https://creativecommons.org/licenses/by-nc-nd/4.0/).

Contents

About the Editors . . . . . **vii**

Preface . . . . . **ix**

Peng Du, Haibao Hu and Xiaopeng Chen
Innovative Research and Applications in Hydrodynamics and Flow Control
Reprinted from: *Inventions* **2024**, *9*, 99, https://doi.org/10.3390/inventions9050099 . . . . . **1**

Carlos Mauricio Ruiz-Díaz, Erwing Eduardo Perilla-Plata and Octavio Andrés González-Estrada
Two-Phase Flow Pattern Identification in Vertical Pipes Using Transformer Neural Networks
Reprinted from: *Inventions* **2024**, *9*, 15, https://doi.org/10.3390/inventions9010015 . . . . . **4**

Ilya Olegovich Starodumov, Sergey Yurievich Sokolov, Pavel Vladimirovich Mikushin, Margarita Alexandrovna Nikishina, Timofey Vitalievich Mityashin, Ksenia Yevgenievna Makhaeva, et al.
Computer Vision Algorithm for Characterization of a Turbulent Gas–Liquid Jet
Reprinted from: *Inventions* **2024**, *9*, 9, https://doi.org/10.3390/inventions9010009 . . . . . **19**

Hai An, Po Yang, Hanyu Zhang and Xinquan Liu
Numerical Study of the Influence of the Type of Gas on Drag Reduction by Microbubble Injection
Reprinted from: *Inventions* **2024**, *9*, 7, https://doi.org/10.3390/inventions9010007 . . . . . **39**

Real J. KC, Trevor C. Wilson, Aaron S. Alexander, Jamey D. Jacob, Nicholas A. Lucido and Brian R. Elbing
Evaluation of a Serrated Edge to Mitigate the Adverse Effects of a Backward-Facing Step on an Airfoil
Reprinted from: *Inventions* **2023**, *8*, 160, https://doi.org/10.3390/inventions8060160 . . . . . **59**

Amalia Moutsopoulou, Markos Petousis, Nectarios Vidakis, Georgios E. Stavroulakis and Anastasios Pouliezos
Applications of the Order Reduction Optimization of the H-Infinity Controller in Smart Structures
Reprinted from: *Inventions* **2023**, *8*, 150, https://doi.org/10.3390/inventions8060150 . . . . . **75**

Alexey Savitskii, Dmitriy Sharaborin, Leonid Chikishev and Vladimir Dulin
Flow Instability Control in a Model Swirl-Stabilized Combustor with Central Jet Injection
Reprinted from: *Inventions* **2023**, *8*, 148, https://doi.org/10.3390/inventions8060148 . . . . . **94**

Mansour Al Qubeissi and Scott Daniel Beard
A Hydro-Powered Climate-Neutral Pump: Full Cycle Simulation and Performance Evaluation
Reprinted from: *Inventions* **2023**, *8*, 147, https://doi.org/10.3390/inventions8060147 . . . . . **113**

Anning Yi, Chen Wang, Lei Wang and Xinli Wang
A Wide Operating Range Ejector with Part Nested Nozzles for PEMFC Hydrogen Recirculation System
Reprinted from: *Inventions* **2023**, *8*, 133, https://doi.org/10.3390/inventions8060133 . . . . . **139**

Rui Han, Jiayi Chen and Taikun Guo
A Modified Phase-Transition Model for Multi-Oscillations of Spark-Generated Bubbles
Reprinted from: *Inventions* **2023**, *8*, 131, https://doi.org/10.3390/inventions8050131 . . . . . **158**

Ilya Starodumov, Sergey Sokolov, Ksenia Makhaeva, Pavel Mikushin, Olga Dinislamova and Felix Blyakhman
Obtaining Vortex Formation in Blood Flow by Particle Tracking: Echo-PV Methods and Computer Simulation
Reprinted from: *Inventions* **2023**, *8*, 124, https://doi.org/10.3390/inventions8050124 . . . . . **173**

Likang Wang and Rui Huo
Effect of Support Stiffness Nonlinearity on the Low-Frequency Vibro-Acoustic Characteristics for a Mechanical Equipment—Floating Raft—Underwater Cylindrical Shell Coupled System
Reprinted from: *Inventions* **2023**, *8*, 118, https://doi.org/10.3390/inventions8050118 . . . . . **187**

Victor Shcherba and Irina Bulgakova
Mathematical Model of the Working Processes of the Gas Cap of a Piston Pump Installed in the Discharge Line
Reprinted from: *Inventions* **2023**, *8*, 95, https://doi.org/10.3390/inventions8040095 . . . . . **211**

Ilya V. Myachin and Leonid O. Kononov
Mixer Design and Flow Rate as Critical Variables in Flow Chemistry Affecting the Outcome of a Chemical Reaction: A Review
Reprinted from: *Inventions* **2023**, *8*, 128, https://doi.org/10.3390/inventions8050128 . . . . . **229**

About the Editors

Peng Du

Peng Du is currently a professor and doctoral supervisor at the School of Marine Science and Technology, Northwestern Polytechnical University. He also serves as the deputy director of the Shaanxi Provincial Key Laboratory. Prof. Peng Du's research focuses on the environmental hydrodynamics of marine structures. He has published over 80 journal papers, applied for more than 40 invention patents, and registered over 30 software copyrights. He serves as an editorial board member for the *Journal of Hydrodynamics* and *Chinese Journal of Ship Research*, as a young editorial board member for *Engineering Reports* and *Marine Engineering*, and as a reviewer for more than 30 journals. He has been invited to give plenary/keynote speeches at numerous academic conferences and has led several national and provincial-level projects.

Haibao Hu

Haibao Hu is a professor and doctoral supervisor at the School of Marine Science and Technology, Northwestern Polytechnical University. He is a national leading talent and a recipient of the Shaanxi Provincial Distinguished Youth Award. He serves as the director of the Shaanxi Key Laboratory of Marine Engineering Hydrodynamics and Underwater Power Technology. He has long been dedicated to the overall design of underwater vehicles, complex hydrodynamics, and research and engineering applications of underwater drag reduction and energy-saving technologies. He has published more than 110 academic papers in journals such as *Science Advances*, *Journal of Fluid Mechanics*, *Physics of Fluids*, and *Ocean Engineering*.

Xiaopeng Chen

Xiaopeng Chen is a Professor at the School of Marine Science and Technology, Northwestern Polytechnical University. His research focuses on multiphase flow, bubble dynamics, the lattice Boltzmann method, and computational fluid mechanics. He has conducted extensive research on bubble dynamics and multiphase flow applications in ocean engineering. He has served as a Guest Editor for multiple special issues related to hydrodynamics and CFD.

Preface

This Reprint presents published papers from the Special Issue "Innovative Research and Applications in Hydrodynamics and Flow Control" in *Inventions* (MDPI). Hydrodynamics and flow control lie at the core of critical engineering fields, including marine vehicles, underwater systems, energy equipment, aerospace propulsion, and environmental engineering. In recent years, rapid developments in computational methods, experimental fluid mechanics, intelligent algorithms, and multiphase dynamics have driven continuous breakthroughs in flow control efficiency, drag reduction, flow stability, and hydrodynamic performance optimization.

This Special Issue aimed to gather frontier research that bridges fundamental fluid mechanics and industrial applications. It welcomed original research articles, numerical studies, experimental investigations, and review papers covering ship and underwater vehicle design, shape optimization, CFD methods, active and passive flow control, multiphase and bubble dynamics, fluid–structure interaction, and machine learning for fluid systems.

Following rigorous peer review, a series of high-quality papers were selected and included in this Reprint. These works demonstrate diverse methodologies and valuable engineering insights: from two-phase flow identification and turbulent jet characterization to microbubble drag reduction, flow instability control, hydrodynamic optimization of smart structures, ejector design, bubble dynamics modeling, and low-frequency vibration–acoustic characteristics of coupled systems. Together, they represent the current state of the art in hydrodynamics and flow control innovation.

We sincerely thank all authors for their high-quality contributions, the reviewers for their professional and rigorous comments, and the editorial office of *Inventions* for efficient support. We hope this Reprint will promote academic exchange, inspire further research, and support technological advances in hydrodynamics and flow control worldwide.

Peng Du, Haibao Hu, and Xiaopeng Chen
Guest Editors

inventions

MDPI

Editorial

Innovative Research and Applications in Hydrodynamics and Flow Control

Peng Du *, Haibao Hu and Xiaopeng Chen

School of Marine Science and Technology, Northwestern Polytechnical University, Xi'an 710072, China
* Correspondence: dupeng@nwpu.edu.cn

This work aims to collect cutting-edge developments in the area of hydrodynamics and flow control, including both fundamental and engineering research. Hydrodynamics is of great importance in many fields including ships, marine engineering, energy, etc. It influences the kinetics and kinematics of ships, underwater vehicles, and marine structures. Flow control techniques can manipulate hydrodynamics and lead to benefits such as energy-saving capabilities, high performance, etc. The following topics are covered: the design of ships, underwater vehicles, and marine structuresß; shape optimization of marine vehicles; experimental fluid mechanics of marine structures; computational methods for fluids; applications of CFD (Computational Fluid Dynamics) methods; flow control techniques; fluid mechanics; and machine learning methods for fluids. Thirteen works have been collected, comprising one review article and twelve research articles.

The review article focuses on chemical reactions (contribution 1), which comprise an important area in flow chemistry. This work aims to solve the problem of mixer design in order to realize the purpose of reaction controls, especially for those experiments that are difficult to explain. These data were identified and rational explanations were proposed, based on a supramer approach.

The jet phenomenon is commonly seen when a stream of fluid is projected into a surrounding medium. A computer vision algorithm for the parameter determination of a two-phase jet flow was proposed (contribution 2). The mass exchange can thus be evaluated in real time. This approach is useful for the real-time control of a multi-phase jet. Central jet injection was utilized as a flow control strategy in a model swirl-stabilized combustor (contribution 3). It was found that the asymmetric hydrodynamics mode is suppressed, while the symmetrical one becomes dominant.

A pump can convert electrical energy into hydraulic energy by moving fluids using mechanical action. A mathematical model to predict the working processes of the piston pump cap was established (contribution 4), taking into account the phase transition process and gas solubility. It was found that increasing the pipeline length and the revolution of the crankshaft were necessary to decrease the feed irregularity. A study of a multistorey hydro-pump was presented (contribution 5), which promoted further understanding of its physical properties in order to strengthen its performance. It was found that a small chamber diameter and a high supply head resulted in high pressure.

Several fundamental fluid mechanics problems were also investigated in several of the collected works. A modified phase-transition model was proposed (contribution 6) for the study of the multi-oscillation of bubbles. The transition of the phase exhibited a strong influence on bubbles during this process. An approximation of the thermal boundary layer was implemented into the Rayleigh–Plesset equation and rigorous validation was conducted, using experimental data. Finally, the condensation rate and its dependence on phase transition and the air were investigated. The adverse effect of backward step on airfoil was studied to evaluate the performance of the airfoil (contribution 7). A three-dimensional low-profile serrated pattern was used to weaken the adverse effect.

The machine learning approach is currently a popular approach in the field of fluid mechanics, and an emerging approach in intelligent fluid mechanics. A transformer neural network was used for two-phase flow pattern identification in vertical pipes (contribution 8). Various configurations were proposed and tested to discern the one with the most accurate predictions. Order reduction optimization was used for smart structures' vibration suppression (contribution 9). A directive of the controller was set, with the allowance of a lower order.

Several other works with various engineering backgrounds were also included. Echo-PV (particle velocimetry) methods and computer simulation were conducted to obtain information about vortex formation in blood flow (contribution 10). Microbubble injection was utilized to investigate the effect of gas on the drag reduction effect (contribution 11). The influence of support stiffness nonlinearity on vibro-acoustic properties was studied (contribution 12). Finally, a part-nested four-nozzle ejector was presented (contribution 13), which aimed to strengthen hydrogen recycling efficiency by limiting the flow in the nozzle.

In conclusion, this Special Issue collects 13 works, comprising innovative research and applications in hydrodynamics and flow control. These works are promising for relevant fundamental research and engineering purposes.

Author Contributions: Conceptualization, P.D.; resources, P.D., H.H. and X.C.; writing—original draft preparation, P.D.; writing—review and editing, P.D.; supervision, P.D. All authors have read and agreed to the published version of the manuscript.

Funding: This research was supported by the National Natural Science Foundation of China (Grant Nos. 52201380, 52471344), the Fundamental Research Funds for the Central Universities (D5000230080), and the Innovation Capability Support Program of Shaanxi (Program No. 2024RS-CXTD-15).

Acknowledgments: The authors wish to thank all contributors to this Special Issue.

Conflicts of Interest: The authors declare no conflicts of interest.

List of Contributions:

1. Myachin, I.V.; Kononov, L.O. Mixer design and flow rate as critical variables in flow chemistry affecting the outcome of a chemical reaction: A review. *Inventions* **2023**, *8*, 128. https://doi.org/10.3390/inventions8050128.
2. Starodumov. I.; Sokolov, S.; Mikushin, P.; Nikishina, M.; Mityashin, T.; Makhaeva, K.; Blyakhman, F.; Chernushkin, D.; Nizovtseva, I. Computer Vision Algorithm for Characterization of a Turbulent Gas–Liquid Jet. *Inventions* **2024**, *9*, 9. https://doi.org/10.3390/inventions9010009.
3. Savitskii, A.; Sharaborin, D.; Chikishev, L.; Dulin, V. Flow Instability Control in a Model Swirl-Stabilized Combustor with Central Jet Injection. *Inventions* **2023**, *8*, 148. https://doi.org/10.3390/inventions8060148.
4. Shcherba, V.; Bulgakova, I. Mathematical Model of the Working Processes of the Gas Cap of a Piston Pump Installed in the Discharge Line. *Inventions* **2023**, *8*, 95. https://doi.org/10.3390/inventions8040095.
5. Al Qubeissi, M.; Beard, S.D. A Hydro-Powered Climate-Neutral Pump: Full Cycle Simulation and Performance Evaluation. *Inventions* **2023**, *8*, 147. https://doi.org/10.3390/inventions8060147.
6. Han, R.; Chen, J.; Guo, T. A Modified Phase-Transition Model for Multi-Oscillations of Spark-Generated Bubbles. *Inventions* **2023**, *8*, 131. https://doi.org/10.3390/inventions8050131.
7. KC, R.J.; Wilson, T.C.; Alexander, A.S.; Jacob, J.D.; Lucido, N.A.; Elbing, B.R. Evaluation of a Serrated Edge to Mitigate the Adverse Effects of a Backward-Facing Step on an Airfoil. *Inventions* **2023**, *8*, 160. https://doi.org/10.3390/inventions8060160.
8. Ruiz-Díaz, C.M.; Perilla-Plata, E.E.; González-Estrada, O.A. Two-Phase Flow Pattern Identification in Vertical Pipes Using Transformer Neural Networks. *Inventions* **2024**, *9*, 15. https://doi.org/10.3390/inventions9010015.
9. Moutsopoulou, A.; Petousis, M.; Vidakis, N.; Stavroulakis, G.E.; Pouliezos, A. Applications of the Order Reduction Optimization of the H-Infinity Controller in Smart Structures. *Inventions* **2023**, *8*, 150. https://doi.org/10.3390/inventions8060150.

10. Starodumov, I.; Sokolov, S.; Makhaeva, K.; Mikushin, P.; Dinislamova, O.; Blyakhman, F. Obtaining Vortex Formation in Blood Flow by Particle Tracking: Echo-PV Methods and Computer Simulation. *Inventions* **2023**, *8*, 124. https://doi.org/10.3390/inventions8050124.
11. An, H.; Yang, P.; Zhang, H; Liu, X. Numerical Study of the Influence of the Type of Gas on Drag Reduction by Microbubble Injection. *Inventions* **2024**, *9*, 7. https://doi.org/10.3390/inventions9010007.
12. Wang, L.; Huo, R. Effect of Support Stiffness Nonlinearity on the Low-Frequency Vibro-Acoustic Characteristics for a Mechanical Equipment—Floating Raft—Underwater Cylindrical Shell Coupled System. *Inventions* **2023**, *8*, 118. https://doi.org/10.3390/inventions8050118.
13. Yi, A.; Wang, C.; Wang L; Wang, X. A Wide Operating Range Ejector with Part Nested Nozzles for PEMFC Hydrogen Recirculation System. *Inventions* **2023**, *8*, 133. https://doi.org/10.3390/inventions8060133.

Disclaimer/Publisher's Note: The statements, opinions and data contained in all publications are solely those of the individual author(s) and contributor(s) and not of MDPI and/or the editor(s). MDPI and/or the editor(s) disclaim responsibility for any injury to people or property resulting from any ideas, methods, instructions or products referred to in the content.

inventions

MDPI

Article

Two-Phase Flow Pattern Identification in Vertical Pipes Using Transformer Neural Networks

Carlos Mauricio Ruiz-Díaz [1], Erwing Eduardo Perilla-Plata [2] and Octavio Andrés González-Estrada [2,*]

[1] Industrial Multiphase Flow Laboratory (LEMI), São Carlos School of Engineering, University of São Paulo, São Carlos 13563-120, Brazil; carlosruiz978@usp.br
[2] Research Group in Energy and Environment (GIEMA), Universidad Industrial de Santander, Santander, Bucaramanga 680002, Colombia; plataperillaodraude@gmail.com
* Correspondence: agonzale@uis.edu.co

Abstract: The oil and gas industry consistently embraces innovative technologies due to the significant expenses associated with hydrocarbon transportation, pipeline corrosion issues, and the necessity to gain a deeper understanding of two-phase flow characteristics. These solutions involve the implementation of predictive models utilizing neural networks. In this research paper, a comprehensive database comprising 4864 data points, encompassing information pertaining to oil–water two-phase flow properties within vertical pipelines, was meticulously curated. Subsequently, an encoder-only type transformer neural network (TNN) was employed to identify two-phase flow patterns. Various configurations for the TNN model were proposed, involving parameter adjustments such as the number of attention heads, activation function, dropout rate, and learning rate, with the aim of selecting the configuration yielding optimal outcomes. Following the training of the network, predictions were generated using a reserved dataset, thus facilitating the creation of flow maps depicting the patterns anticipated by the model. The developed TNN model successfully predicted 9 out of the 10 flow patterns present in the database, achieving a peak accuracy of 53.07%. Furthermore, the various predicted flow patterns exhibited an average precision of 63.21% and an average accuracy of 86.51%.

Keywords: transformer neural network; two-phase flow; flow pattern identification; machine learning; fluid transport

1. Introduction

The transportation of multiphase flows is a commonplace practice in today's industrial landscape. These flows typically consist of two or more phases and may include various physical states, such as liquid, solid, or gaseous components. Multiphase flows find applications across diverse industrial sectors, including agriculture, food production, pharmaceuticals, and oil extraction, among others. To categorize multiphase flows effectively, they are classified based on the specific phases involved. Three-phase flows, for instance, encompass gas, oil, and solid substances. However, the primary focus of study within multiphase flows often centers on two-phase flows, which can manifest as gas–liquid, gas–solid, liquid–solid, or liquid–liquid configurations [1,2]. The subcategory of two-phase liquid–liquid flows is particularly relevant in the oil and gas industry. It pertains to the production of crude oil from water and oil mixtures within pipelines. These mixtures are then transported to processing facilities or refineries for further treatment and refinement [3–5].

An essential aspect of multiphase flows is their internal geometric configuration or flow pattern. This configuration arises from the interactions between the different substances involved and is contingent on various factors, including the flow rates of these substances, the diameter of the pipe, and the transport properties unique to each of the flows [1]. A crucial variable in determining the type of flow pattern within a pipe is its

inclination. This is due to the fact that the flow patterns observed in horizontal pipes differ from those encountered in vertical pipes [6]. Investigating the behavior of two-phase flow patterns in pipelines is of utmost importance, particularly in addressing challenges like the reduction of pumping costs associated with the extraction of heavy crude oils, which often possess viscosities exceeding 10,000 cP [7], given that these make up a third of the world's hydrocarbon reserves [8]. Furthermore, the oil industry faces a significant challenge related to pipeline corrosion, both internally and externally. Studies have estimated that around 80% of pipeline failures in the oil transportation sector are attributed to internal corrosion. These corrosion-related failures result in substantial maintenance costs. Therefore, it becomes imperative to accurately determine the flow pattern within the pipeline as a means to mitigate these corrosion-related failures and reduce maintenance expenses [9].

Furthermore, in reference [10], predictive models are explored for calculating the volumetric fraction of a horizontal two-phase water–oil flow using an artificial neural network. The results indicate a mean absolute percentage error (MAPE) of 3.01% and a coefficient of determination of 0. Additionally, in reference [11], it is mentioned that utilizing Computational Fluid Dynamics (CFD) predictions of a two-phase flow with STAR-CCM+ software (Version 8.06) enables precise control of the corrosion risk in pipelines. Moreover, simulation has yielded significant contributions to gas lift processes based on the two-fluid model [12], as well as the capture and recovery of CO_2 with the formation of gas combustion hydrates in both frozen and unfrozen sediments [13]. Furthermore, it enables the development of two-dimensional models to simulate asphaltene deposition in wells and pipelines [14] and optimization in determining the minimum miscibility pressure between CO_2 and petroleum using hybrid methods [15]. Additionally, thanks to the progress brought about by the fourth industrial revolution (Industry 4.0), benefits have been implemented in various fields with the assistance of artificial intelligence (AI), which has the potential to process vast amounts of data [16]. The scope of application of this learning technique extends to various industrial sectors, as is the case with the oil and gas sector. Therefore, innovative methods are required to replace the old monitoring methods in hydrocarbon transport, where the presence of multiphase flows in different combinations of liquids, gases, and solids is recorded. Consequently, the simulation of processes involving multiphase flows has allowed for the generation of solutions to various engineering problems through modeling. This extends to a wide range of applications that ensure the proper flow of hydrocarbons inside pipelines [17–20].

The extensive domain of machine learning has generated various alternatives to address complex problems associated with data recognition and classification [20]. Among the implemented techniques is the Transformer Neural Network (TNN), a neural network originally created for translating long strings of text [21]. It has also demonstrated high performance in multilingual models [22]. Additionally, leveraging the BERT architecture, derived from the original TNN, it has been applied in a variety of applications, such as text analysis for text classification [23] or emotion classification [24]. Tasks traditionally handled by convolutional neural networks, such as image detection and classification, have been adapted to TNN in a model known as the Visual Transformer [25]. Moreover, in DNA research, TNN-based models have been developed for genome sequence identification [26,27], as well as protein sequence profile prediction [28]. Furthermore, this technique has been implemented in engineering for wind energy prediction [29,30]. Additionally, a fundamental aspect of using neural networks is the allocation of 80% of the database for model training, 10% for testing, and 10% for validation [31].

Given the increasing implementation of AI in the petrochemical industry for controlling multiphase fluid-related processes, this study develops an intelligent model based on a TNN capable of predicting flow patterns within vertical pipelines with liquid–liquid two-phase flow of oil and water. First, the most suitable transformer-type neural network for the desired application is selected. Then, the data structure related to the water/oil two-phase flow is developed using available information from various sources. The database is filtered and divided, ensuring that the training dataset contains the minimum and max-

imum values of each parameter used in the model's inputs. Different configurations of the Transformer Neural Network are implemented to select the most suitable one based on the error and accuracy of each trained model. Finally, the most relevant conclusions are presented.

2. Materials and Methods

The architecture of the original TNN is based on the encoder–decoder, as depicted in Figure 1. This architecture is widely used for tasks such as machine translation, where a sequence of words is translated from one language to another. This architecture consists of two components: the encoder, which converts a sequence of input tokens into a sequence of embedding vectors, and the decoder, which iteratively uses the hidden state of the encoder to generate an output sequence of tokens, one token at a time.

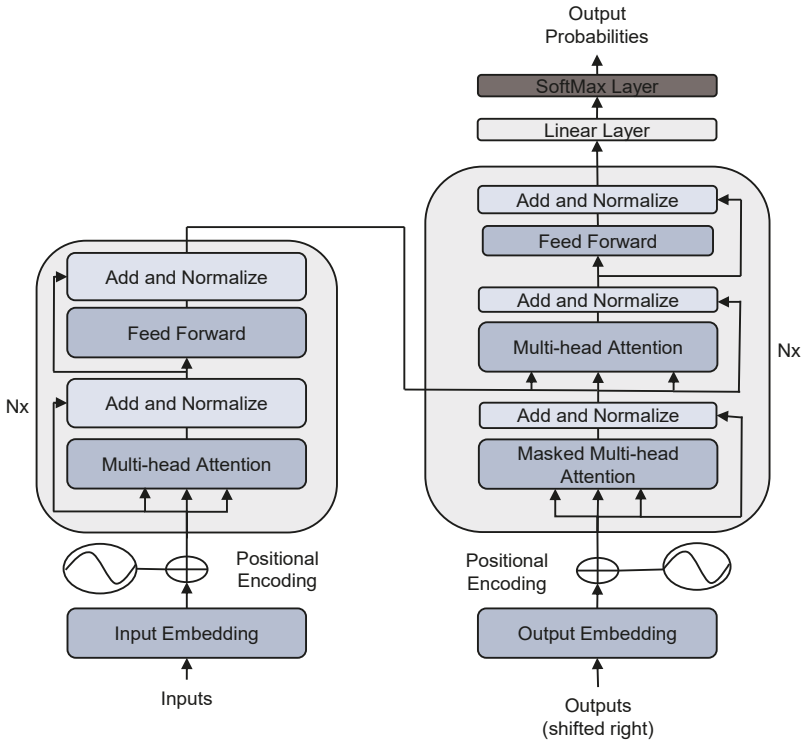


Figure 1. A comprehensive overview of the neural network structure for two-phase flow pattern identification in vertical pipelines using a transformer encoder–decoder architecture.

2.1. Types of Transformers

The architecture of the transformer was initially designed for sequence-to-sequence tasks like machine translation, but it was soon adapted with independent encoders and decoders, resulting in three different types of transformers [32]:

- Encoder-only: This model can convert an input sequence of text into a numerical representation suitable for tasks such as text classification or named entity recognition. The representation calculated for a given token in this architecture depends on bidirectional attention, meaning it relies on both the left and right context of the token.
- Decoder-only: This type of model is capable of automatically completing a sequence by iteratively predicting the most probable next word. In this case, the model relies on causal or autoregressive attention, meaning that the representation calculated for a token in this architecture depends solely on the left context.
- Encoder–decoder: these are used to model complex mappings from one sequence of text to another, making them suitable for tasks such as machine translation and summarization.

For this work, the encoder-only model is used. Therefore, the structure of the encoder block is explained in detail below. The structure of the encoder block is shown in Figure 2.

A sequence of embeddings enters this block and is processed through the following layers: a multi-head self-attention layer and a feed-forward layer.

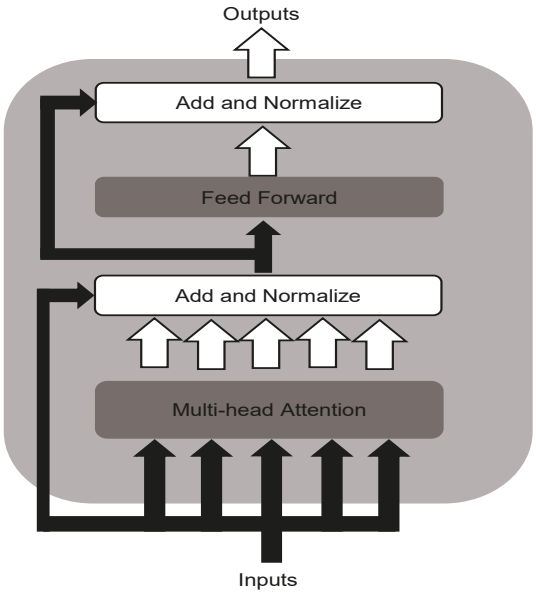


Figure 2. Structural components and workflow of the neural network encoder.

Self-attention is a mechanism that allows neural networks to assign a different amount of attention, meaning a different weight value, to each element of a sequence. Therefore, the main idea of self-attention is to use the entire sequence to calculate a weighted average for each embedding. One way to formulate this is that given a sequence of tokens $X_1, \ldots, X_n$, self-attention produces a sequence of new embeddings $X_1', \ldots, X_n'$, where each X_i' is a linear combination of all the X_j, as shown in Equation (1):

$$X_i' = \sum_{j=1}^{n} w_{ji} x_j \tag{1}$$

where the coefficient w_{ji} is the attention weight and is normalized in such a way that $\Sigma_j w_{ji} = 1$.

The self-attention process involves three vectors: Q, queries, K, *keys* y, and V, *values*, which are derived by multiplying each input entry by weight matrices W (trained during training). A dot product is computed between the vector Q and the vector K. The result is then divided by the square root of the dimension size of the original input vectors (d_k), normalized using the *SoftMax* operation, and multiplied by the vector V. For computational efficiency, the information is treated in the matrix form. Equation (2) represents the attention process.

$$Attention(Q, K, V) = Z = SoftMax\left(\frac{Q * K^T}{\sqrt{d_k}}\right) * V \tag{2}$$

2.2. Data Structure

A database was structured based on experimental data already available in the literature related to two-phase flow consisting of water and oil in vertical pipelines. A total of 4864 data points were collected from 18 different authors, as detailed in Table 1, which provides comprehensive information regarding the data from each author. The table indicates the pipe diameter (D) used in the experiments, the viscosity (μ_o) and density (ρ_o) of the oil used, the number of flow patterns identified, and the quantity of extracted data.

Table 1. General information of the database for two-phase water and oil flow in vertical pipes: a comprehensive overview of key data parameters and characteristics.

Reference	D [m]	μ_o [Pa·s]	ρ_o [kg]/m^3	Number of Flow Patterns	Data
[33]	0.0284	0.488	925	3	392
[34]	0.1064	0.00188	800	6	49
[35]	0.02	0.011	856	3	101
[36]	0.05	0.02	850	5	126
[37]	0.04	0.035	860	4	92
[38]	0.0263	0.0201	851	2	15
[39]	0.02	0.125	801	4	175
[40]	0.127	0.001	801	2	9
[41]	0.027	0.02	801	4	109
[42]	0.0254	0.001	792	4	55
[43]	0.0254	0.001	792	5	32
[44]	0.01	0.287	1823	3	1421
[45]	0.026	0.0011	793	5	90
[46]	0.03	0.03	856	4	252
[47]	0.0284	0.5	930	1	92
[48]	0.03	0.044	860	4	98
[49]	0.02	0.09732	857	7	1699
[50]	0.04	0.0041	824	1	57

Based on the schemes developed in each study, a total of 9 distinct flow patterns were identified, characterized by variations in the continuous phase, either aqueous (w) or oily (o). These patterns include very fine dispersed droplets (VFDs) o/w (265 cases) and w/o (204 cases), drops (D) o/w (947 cases) and w/o (1292 cases), slug (S) o/w (459 cases) and w/o (656 cases), churn (21 cases) o/w and (126 cases) w/o, annular (Core flow) with 480 cases, and the transition region (TF) with 314 cases. Figure 3 provides a graphical representation illustrating the behavior of the most prominent flow patterns.

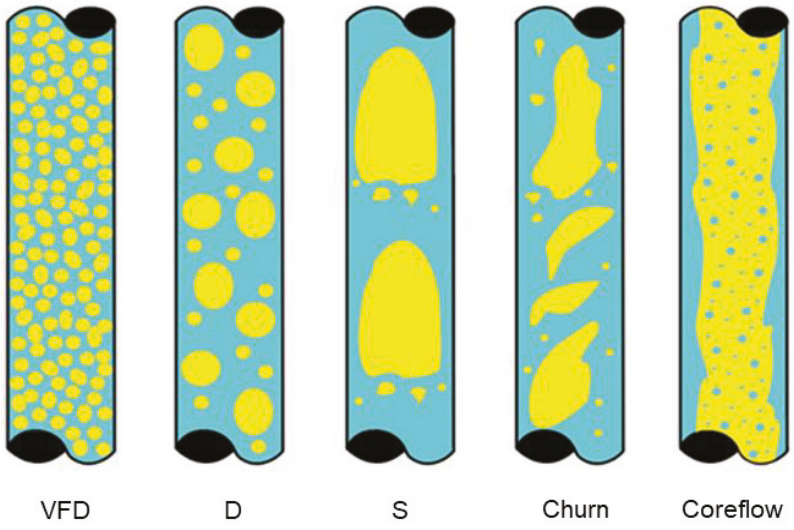


Figure 3. Two-phase flow patterns in vertical pipes: a comprehensive visualization of fluid dynamics and transition phenomena.

In general, when the presence of variation from one flow pattern to another is evident, it can be defined as a transition intermediate flow (TF). On the other hand, the studied database has information related to the surface velocities of the fluids involved and their mixture, the volume fraction of water and oil, the diameter of the implemented pipe, the viscosity of the oil, and the type of flow patterns developed.

2.3. Transformer Neural Network Model

The structure of the implemented model consists of the encoder implemented in TNN and a SoftMax layer at the model's output. The input vector X is composed of the superficial velocities of the fluids (oil and water), their sum, the in situ volumetric fraction (holdup) of both fluids, the viscosity of the oil, and the diameter of the circular cross-section pipe, as shown in Equation (3).

$$X = \begin{Bmatrix} J_o \\ J_w \\ J_{o+w} \\ \varepsilon_o \\ \varepsilon_w \\ D \\ \mu_o \end{Bmatrix} \tag{3}$$

The selected optimizer for training is Adam, as it integrates the characteristics of two methodologies: one is the gradient descent algorithm with momentum, and the other is the RMSP (Root Mean Square Propagation) algorithm. Gradient descent with momentum is used to accelerate the gradient descent algorithm by considering the exponentially weighted average of gradients, meaning that using averages makes the algorithm converge towards minima at a faster rate. This method is defined in Equations (4) and (5).

$$\omega_{t+1} = \omega_t - \alpha m_t \tag{4}$$

where

$$m_t = \beta m_{t-1} + (1-\beta)\left[\frac{\delta L}{\delta \omega_t}\right] \tag{5}$$

were m_t is the aggregated gradients at the current time step t, initially set to 0. Additionally, m_{t-1} represents the aggregated gradients at time step $t-1$, ω_t is the weight at time step t, ω_{t+1} is the weight at time step $t+1$, α is the learning rate at time step t. Furthermore, δL is the derivative of the loss function, $\delta \omega_t$ is the derivative of weights at time step t, and $\beta = 0.9$ is the moving average parameter.

The Root Mean Square Propagation (RMSP), instead of accumulating squared gradients, uses exponential moving averages. It is defined as follows in Equation (6).

$$\omega_{t+1} = \omega_t - \frac{\alpha}{(v_t + \varepsilon)^{\frac{1}{2}}}\left[\frac{\delta L}{\delta \omega_t}\right] \tag{6}$$

where

$$v_t = \beta v_{t-1} + (1-\beta)\left[\frac{\delta L}{\delta \omega_t}\right]^2 \tag{7}$$

where v_t is the sum of past squared gradients, i.e., sum$(\delta L/\delta \omega_{t-1})$. Initially, $v_t = 0$. $\varepsilon = 10^{-8}$ is a small positive constant to prevent division by zero when $v_t \longrightarrow 0$, and $\alpha = 0.001$ is the learning rate parameter.

Therefore, Adam controls the gradient descent speed, making it possible to reach the global minimum with small steps and steps large enough to overcome local minima along the way, thus achieving efficiency. In this case, Equation (8) is used.

$$m_t = \beta_1 m_{t-1} + (1-\beta_1)\left[\frac{\delta L}{\delta \omega_t}\right]; \quad v_t = \beta_2 v_{t-1} + (1-\beta_2)\left[\frac{\delta L}{\delta \omega_t}\right]^2 \tag{8}$$

where $\beta_1 = 0.9$ and, $\beta_2 = 0.999$ are the decay rates for the gradient averages in the two previous methods.

Given that m_t and v_t are initialized as 0 according to the previous methods, they tend to be biased towards 0 because β_1 and $\beta_2 \approx 1$. Adam solves this problem by computing bias-corrected m_t and v_t. This is carried out to have control over the weights while reaching

the global minimum and to avoid high oscillations when approaching it, meaning it adapts to gradient descent with each iteration. The equations used are (9) and (10):

$$\widehat{m_t} = \frac{m_t}{1-{\beta_1}^t};\ \widehat{v_t} = \frac{v_t}{1-{\beta_2}^t} \tag{9}$$

therefore

$$\omega_{t+1} = \omega_t - \widehat{m_t}\left(\frac{\alpha}{\sqrt{\widehat{v_t}}+\varepsilon}\right) \tag{10}$$

The loss function implemented in the training of the developed model is the Binary Cross entropy function, which is typically used in binary classification problems but can also be applied to problems where the variables to predict take values between 0 and 1. This function is defined in Equation (11):

$$\mathcal{L}_{BCE} = -\frac{1}{n}\sum_{j=1}^{n}\sum_{i=1}^{c}[y_i \log \widehat{y_i} + (1-y_i)\log(1-\widehat{y_i})] \tag{11}$$

where y_i is the actual class to be predicted, $\widehat{y_i}$ is the predicted probability for the class, c is the number of classes, and n is the number of examples.

Variations were performed using 4 different activation functions, among which we have the *ReLU* function, which transforms input values by zeroing out the negative values and leaving the positive ones unchanged. It is defined as Equation (12).

$$ReLu(x) = \max(0, x) = \begin{cases} 0 \text{ for } x < 0 \\ x \text{ for } x \geq 0 \end{cases} \tag{12}$$

The second activation function is the sigmoid function, which is used in models where it is necessary to predict probabilities as an outcome, as it takes a range of values between 0 and 1. Its definition is shown in Equation (13).

$$Sigmoid(x) = \frac{1}{1+e^{-x}} \tag{13}$$

Also, the hyperbolic tangent function was implemented, which is similar in continuity to the sigmoid function but has outputs in a range from -1 to 1, and it is defined in Equation (14):

$$Tanh(x) = \frac{e^x - e^{-x}}{e^x + e^{-x}} \tag{14}$$

Finally, the GeLU activation function was used, as defined in Equation (15), which adds nonlinearity by multiplying a stochastic sigmoid function by the input, resembling the *ReLU* function.

$$GeLU(x) = \frac{1}{2}\,x\left[1 + \operatorname{erf}\left(\frac{x}{\sqrt{2}}\right)\right] \tag{15}$$

Firstly, the learning rate (LR) was varied with the following values: 0.005, 0.001, and 0.0005. The dropout layer was considered with values of 0.1, 0.3, and 0.5. The attention heads in the multi-head-attention layer were set to 1, 2, and 4, and a single encoder was implemented. The embedding dimension was 32, and the feed-forward layer dimension was 32 as well. For each particular simulation, 55 epochs were considered during the neural network training process, and a batch size of 2800 was used. To compare the performance of different configurations, accuracy was evaluated as the number of correct predictions divided by the total number of data points for each phase.

Furthermore, a confusion matrix was generated for the models selected based on their performance, from which precision and accuracy were extracted for each of the flow patterns. It is necessary to calculate the values of true positives (TP), true negatives (TN),

false positives (FP), and false negatives (FN) first. Precision is defined in Equation (16), and accuracy is defined in Equation (17).

$$Precision = \frac{\text{VP}}{\text{VP} + \text{FP}} \tag{16}$$

$$Accuracy = \frac{\text{VP} + \text{VN}}{\text{VP} + \text{FN} + \text{FP} + \text{VN}} \tag{17}$$

3. Results

Tests were conducted with 110 different parameter configurations, from which eight models were selected based on configurations that exhibited minimal overfitting during the training phase while identifying the highest number of flow patterns in the validation phase. Table 2 presents the results obtained during the TNN training with various parameter variations. The table displays the precisions achieved by each model in different phases (training, testing, and validation).

Table 2. Precision results for the training, testing, and validation phases for different models.

Parameters	Model 1	Model 2	Model 3	Model 4	Model 5	Model 6	Model 7	Model 8
Activation function	sigmoid	ReLU	sigmoid	ReLU	sigmoid	Tanh	Gelu	ReLU
N° attention heads	2	4	4	4	1	2	2	2
Dropout	0.3	0.5	0.5	0.1	0.1	0.3	0.3	0.1
Learning rate	0.001	0.001	0.001	0.0005	0.001	0.001	0.001	0.001
Training accuracy (%)	99.92	99.54	99.49	99.38	99.97	99.61	99.72	99.97
Test accuracy (%)	52.25	51.23	51.43	51.64	55.53	52.87	49.80	54.10
Validation accuracy (%)	51.04	48.98	49.18	52.87	52.25	50.00	48.98	53.07

Conducting a detailed analysis of the accuracy achieved by the models developed using the Transformer Neural Network, it was possible to identify the best results during the training and testing phases, which correspond to models 1, 5, and 8. These models were selected because their accuracy exceeds 99.9% during the training phase and 52% during the testing phase.

Figure 4 displays the precision curves generated during the training phase for the three selected models. It can be observed that models 5 and 8 tend to reach their maximum value close to one in the epoch range between epochs 46 and 55.

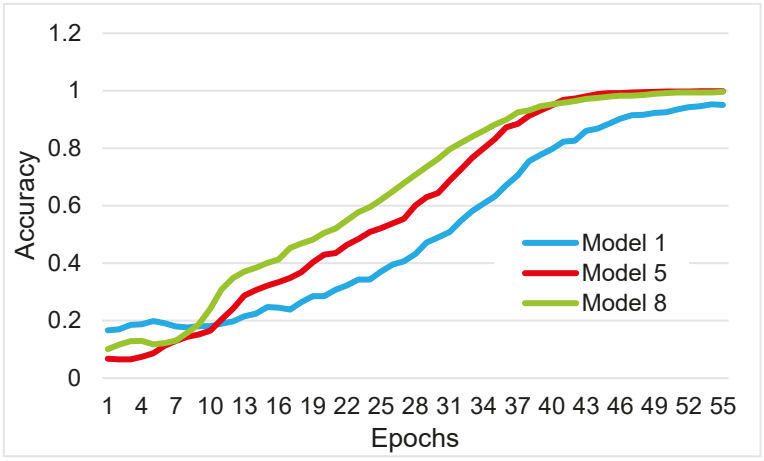


Figure 4. Precision behavior during the training phase.

Additionally, it is possible to identify that the curve generated by model 8 shows a growing trend when iterated with a smaller number of epochs compared to model 5. This is because its values, until reaching maximum precision, always remain lower than the

curve of model 8. This behavior is generated by the optimized structure created for model 8. In this case, the internal mathematical process of the TNN accelerates by implementing the ReLU activation function, which does not activate all layers simultaneously, combined with a dropout of 0.1 and two attention heads.

On the other hand, the precision curve generated by model 1 shows a slower increasing trend, which required a greater number of epochs beyond 55 to reach values close to unity. This demonstrates that despite achieving a precision of 99.92%, it is not the most efficient model. This is because the sigmoid function exhibits slow growth when the gradient descent approaches zero, delaying the learning of the model in question.

In Figure 5, the precision curves generated during the testing phase are presented. It is observed that model 5 achieves higher precision from epoch number 40 onwards, which is the same epoch when the precision curves of models 1 and 8 have already stabilized at their maximum values of 52.25% and 54.10%, respectively. Additionally, the curve generated by model 5 exhibits gradual growth, lower than the curves presented by models 1 and 8. Despite having better precision in the testing phase, model 1 consumes more computational resources as it requires a greater number of epochs to stabilize at its maximum value, which is not efficient when considering that models 1 and 8 only require 31 epochs to reach this point.

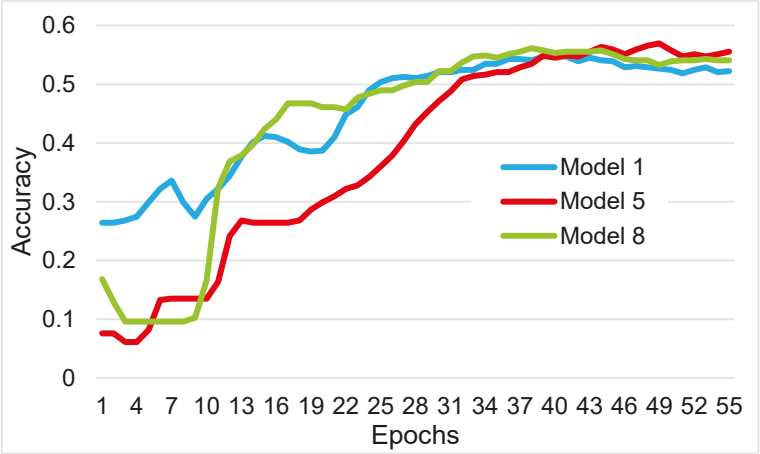


Figure 5. Accuracy behavior during the testing phase.

For the selected models, confusion matrices were constructed to analyze the behavior of predictions for each of the flow patterns. In the confusion matrix, the true positives (TPs) for each category are observed, meaning the number of data points that were correctly predicted for a specific flow pattern. Likewise, other correctly predicted patterns will be true negatives (TNs), i.e., the other values on the main diagonal. False positives (FPs) are those that the model believes it is predicting correctly; these values correspond to the column of the predicted flow pattern. False negatives (FNs) are values corresponding to the row of the true flow pattern. These confusion matrices can be seen in Figure 6a–c. For example, for model 1, taking the D w/o pattern as a reference, TP = 99, adding the other values on the main diagonal results in TN = 150, summing the other values in the D w/o column gives FP = 104, and summing the other values in the D o/w row results in FN = 31.

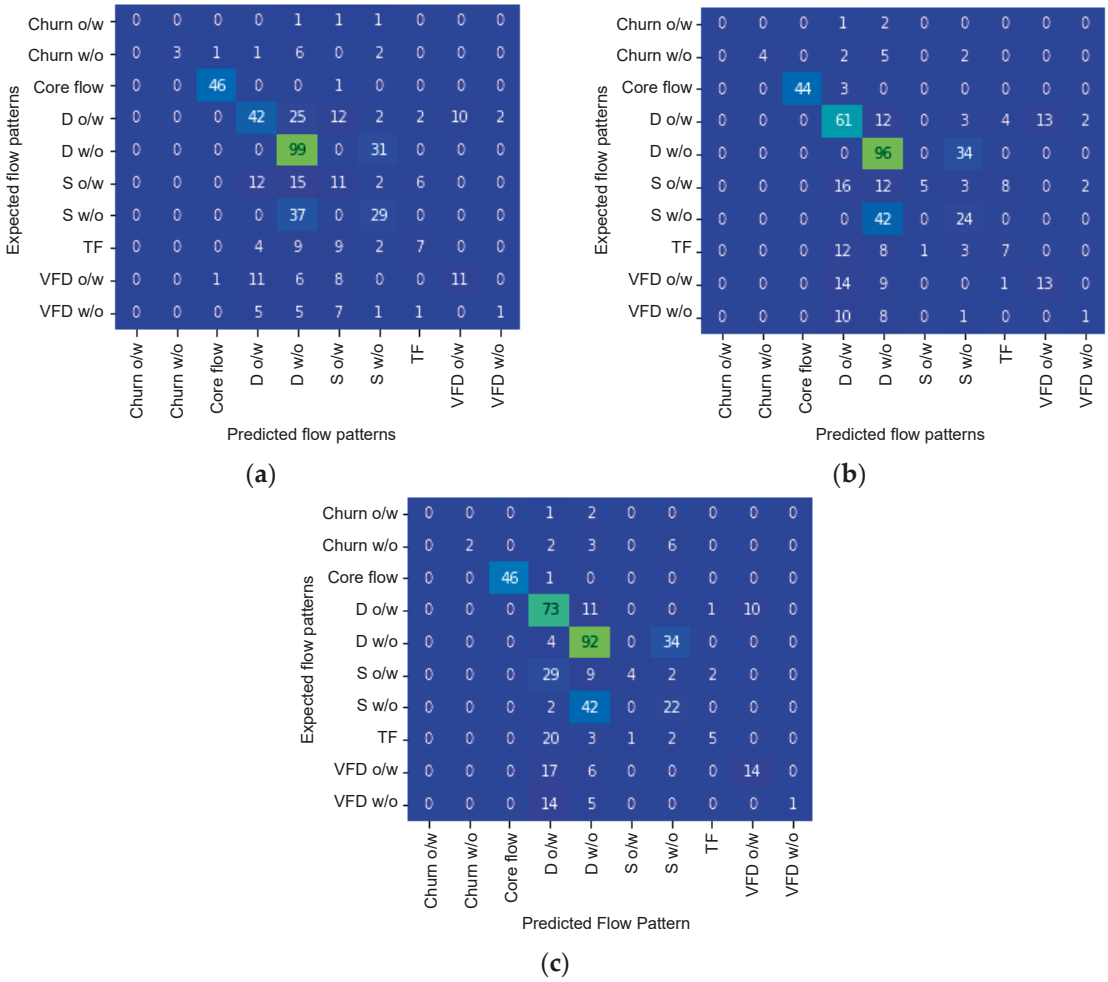


Figure 6. Confusion matrix for: (**a**) model 1, (**b**) model 5, and (**c**) model 8.

Table 3 displays the precision and accuracy values by flow type for the three selected models, obtained by applying Equations (16) and (17). According to Table 3, it can be observed that the best performance corresponds to model 8, with an average precision of 63.21% and an accuracy of 86.51%.

Table 3. Precision and accuracy results by flow type according to the predictions made by the models.

	Model 1		**Model 5**		**Model 8**	
	Precision [%]	**Accuracy [%]**	**Precision [%]**	**Accuracy [%]**	**Precision [%]**	**Accuracy [%]**
Churn o/w	0.00	98.81	0.00	98.84	0.00	98.85
Churn w/o	100.00	96.14	100.00	96.59	100.00	95.93
Core flow	95.83	98.81	100.00	98.84	100.00	99.62
D o/w	56.00	74.33	51.26	73.49	44.79	70.00
D w/o	48.77	64.84	49.48	65.89	53.18	68.52
S o/w	22.45	77.33	83.33	85.86	80.00	85.76
S w/o	41.43	76.15	34.29	74.34	33.33	74.64
TF	43.75	88.30	35.00	87.33	62.50	89.93
VFD o/w	52.38	87.37	50.00	87.33	58.33	88.70
VFD w/o	33.33	92.25	20.00	91.76	100.00	93.17
Average	49.39	85.43	52.34	86.03	63.21	86.51

Figure 7 presents the flow map structured from the gathered information, using the superficial velocities of oil and water as references. In this map, you can identify the different regions where the 10 flow patterns listed initially appear.

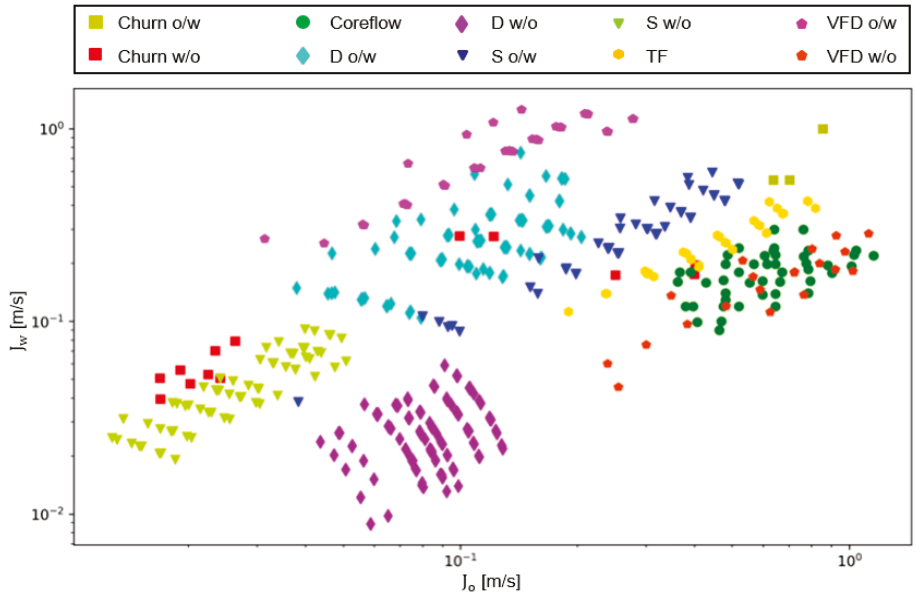


Figure 7. Flow map structured with the information collected from the literature for all authors.

In Figure 8, the predicted flow map by model 8 is presented. It is possible to observe that the selected model can predict 9 out of the 10 types of flow patterns shown in Figure 7. However, model 8 fails to predict the churn o/w flow pattern correctly. This is because in the used database, it is the flow pattern with the fewest occurrences (21), and only 15 of these are used for training when considering the defined percentage segmentation. This generates a significant data imbalance when compared to the D o/w pattern with 1196 data points, for example. The map in Figure 8 shows clusterization similar to the reference data, with some overlap in certain areas, except for the churn o/w flow pattern, which is absent in the predictions of model 8.

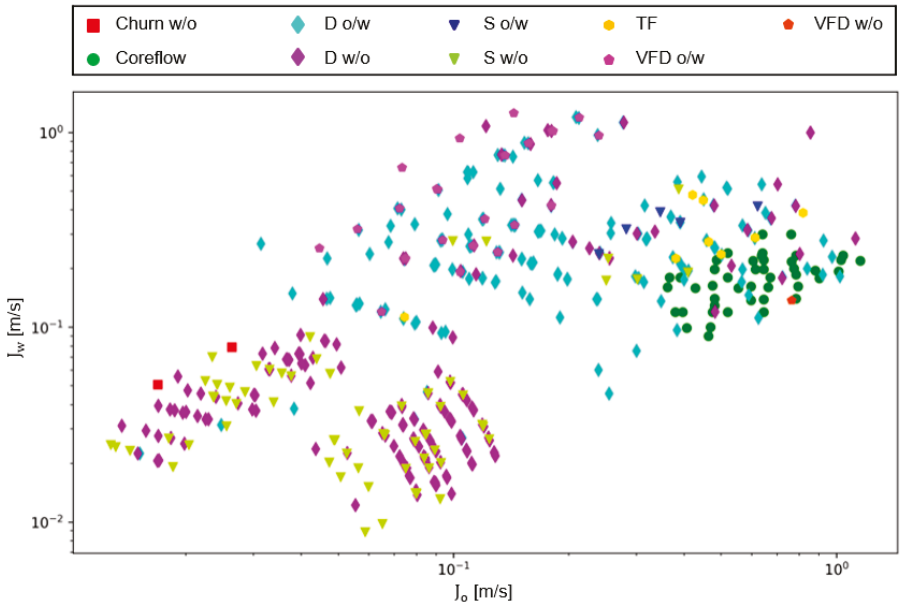


Figure 8. Flow map structured from the results obtained by model 8.

4. Conclusions

A database of two-phase flow patterns was structured based on information reported in the literature by various authors, comprising a total of 4864 experiments. This database includes seven parameters related to multiphase flows and identifies 10 different flow patterns.

A Transformer Neural Network was developed using Python to predict two-phase flow patterns, achieving a training accuracy of 99.97% and a validation accuracy of 53.07% for model 8. This model successfully predicted 9 out of the 10 flow patterns used in the training phase with an average precision of 63.21% and an average accuracy of 86.51%. This indicates that the Transformer Neural Network can predict different flow patterns with high accuracy and reasonable precision. It is worth noting that the TNN does not require excessive computational resources for training, as it achieves near-perfect accuracy during this phase with a substantial batch size and a small number of epochs, making it an efficient neural network.

Flow maps were constructed using both reference data and the predictive model, revealing a striking resemblance between the map generated from predicted data and the one generated from experimental data. Additionally, data clustering and transition zones between flow patterns were clearly evident.

The best prediction results from the models were achieved with sigmoid and ReLU activation functions, using a learning rate of 0.001. Regarding the number of attention heads, good results were observed with either one or two heads. Additionally, it is worth mentioning that a dropout rate of 0.1 or 0.3 is sufficient.

The study underscores the effectiveness of the Transformer Neural Network (TNN) model in identifying two-phase flow patterns in vertical pipelines, not reported before, and highlights its potential applications in the oil and gas industry. The TNN model's precision in recognizing flow patterns suggests opportunities for optimizing hydrocarbon transportation processes, leading to increased operational efficiency and reduced costs. Moreover, its implementation in monitoring systems could aid in the early detection of flow patterns contributing to pipeline corrosion, enhancing facility integrity management. In oil and gas production, understanding flow patterns using the TNN model could improve production efficiency by allowing real-time adjustments in extraction and processing. Furthermore, the TNN model could be incorporated into ongoing monitoring systems to formulate predictive maintenance strategies, anticipating possible concerns related to equipment wear.

As further work, it is recommended to create a database with a larger amount of data, ensuring a balanced representation of data points for each flow pattern implemented. This will improve the TNN model, mitigating the risk of biasing predictions toward the flow pattern with the highest data volume during the training phase.

Author Contributions: Conceptualization, C.M.R.-D., E.E.P.-P. and O.A.G.-E.; Data curation, C.M.R.-D.; Formal analysis, E.E.P.-P. and O.A.G.-E.; Funding acquisition, O.A.G.-E.; Investigation, E.E.P.-P. and O.A.G.-E.; Methodology, C.M.R.-D. and O.A.G.-E.; Project administration, O.A.G.-E.; Supervision, O.A.G.-E.; Validation, C.M.R.-D. and O.A.G.-E.; Writing—original draft, E.E.P.-P.; Writing—review and editing, C.M.R.-D. and O.A.G.-E. All authors have read and agreed to the published version of the manuscript.

Funding: This work was supported by Universidad Industrial de Santander (grant number VIE-3714). We acknowledge the support of the Industrial Multiphase Flow Laboratory (LEMI) of the Sao Carlos School of Engineering, University of Sao Paulo.

Data Availability Statement: The raw data supporting the conclusions of this article will be made available by the authors on request.

Conflicts of Interest: The authors declare no conflict of interest. The authors declare that they have no known competing financial interests or personal relationships that could have appeared to influence the work reported in this paper.

References

1. Rosa, E.S. *Escoamento Multifásico Isotérmico: Modelos de Multifluidos e de Mistura*; Bookman: Porto Alegre, Brasil, 2012; ISBN 9788540700703.
2. Hernández-Cely, M.M.; Ruiz-Díaz, C. Estudio de los fluidos aceite-agua a través del sensor basado en la permitividad eléctrica del patrón de fluido. *Rev. UIS Ing.* **2020**, *19*, 177–186. [CrossRef]
3. Santos, D.S.; Faia, P.M.; Garcia, F.A.P.; Rasteiro, M.G. Oil/water stratified flow in a horizontal pipe: Simulated and experimental studies using EIT. *J. Pet. Sci. Eng.* **2019**, *174*, 1179–1193. [CrossRef]
4. Liu, H.; Duan, J.; Li, J.; Gu, K.; Lin, K.; Wang, J.; Yan, H.; Guan, L.; Li, C. Numerical quasi-three dimensional modeling of stratified oil-water flow in horizontal circular pipe. *Ocean Eng.* **2022**, *251*, 111172. [CrossRef]
5. Obaseki, M.; Elijah, P.T.; Alfred, P.B. Development of model to eliminate sand trapping in horizontal fluid pipelines. *J. King Saud Univ.-Eng. Sci.* **2022**, *34*, 425–434. [CrossRef]
6. Gomez, C.; Ruiz, D.; Cely, M. Specialist system in flow pattern identification using artificial neural Networks. *J. Appl. Eng. Sci.* **2023**, *21*, 285–299. [CrossRef]
7. Bazon, P.B.; Castro-Bolivar, J.E.; Ruiz-Diaz, C.M.; Hernández-Cely, M.M.; Rodriguez, O.M.H. Hybrid machine learning model applied to phase inversion prediction in liquid-liquid pipe flow. *Multiph. Sci. Technol.* **2023**, *35*, 35–53. [CrossRef]
8. de Almeida Coelho, N.M.; Taqueda, M.E.S.; Souza, N.M.O.; de Paiva, J.L.; Santos, A.R.; Lia, L.R.B.; de Moraes, M.S.; de Moraes Júnior, D. Energy savings on heavy oil transportation through core annular flow pattern: An experimental approach. *Int. J. Multiph. Flow* **2020**, *122*, 103127. [CrossRef]
9. Sánchez, E.; Romero, C.; Zeppieri, S.; González-Mendizabal, D. Estudio experimental sobre patrones de flujo líquido-líquido en tuberias verticales. In *Proceedings of the 8° Congreso Iberoamericano de Ingeniería Mecánica*; Universidad Pontificia del Peru: Cusco, Mexico, 2007.
10. Ruiz-Díaz, C.; Hernández-Cely, M.M.; González-Estrada, O.A. Modelo predictivo para el cálculo de la fracción volumétrica de un flujo bifásico agua- aceite en la horizontal utilizando una red neuronal artificial. *Rev. UIS Ing.* **2022**, *21*, 155–164. [CrossRef]
11. Sanguino, V. Modelamiento en CFD de Flujo Bifásico (Aceite-Agua) en una Tubería Vertical. Bachelor's Thesis, Universidad de los Andes, Bogotá, Colombia, 2014.
12. Vasheghani Farahani, M.; Jahanpeyma, Y.; Taghikhani, V. Dynamic Modeling and Numerical Simulation of Gas Lift Performance in Deviated Oil Well Using the Two-Fluid Model. In Proceedings of the 80th EAGE Conference and Exhibition 2018, Copenhagen, Denmark, 11–14 June 2018; European Association of Geoscientists & Engineers: Utrecht, The Netherlands, 2018. [CrossRef]
13. Hassanpouryouzband, A.; Yang, J.; Tohidi, B.; Chuvilin, E.; Istomin, V.; Bukhanov, B. Geological CO_2 Capture and Storage with Flue Gas Hydrate Formation in Frozen and Unfrozen Sediments: Method Development, Real Time-Scale Kinetic Characteristics, Efficiency, and Clathrate Structural Transition. *ACS Sustain. Chem. Eng.* **2019**, *7*, 5338–5345. [CrossRef]
14. Hassanpouryouzband, A.; Joonaki, E.; Taghikhani, V.; Bozorgmehry Boozarjomehry, R.; Chapoy, A.; Tohidi, B. New Two-Dimensional Particle-Scale Model To Simulate Asphaltene Deposition in Wellbores and Pipelines. *Energy Fuels* **2018**, *32*, 2661–2672. [CrossRef]
15. Norouzi, S.; Nazari, M.; VasheghaniFarahani, M. A Novel Hybrid Particle Swarm Optimization-Simulated Annealing Approach for CO_2-Oil Minimum Miscibility Pressure (MMP) Prediction. In Proceedings of the 81st EAGE Conference and Exhibition 2019, London, UK, 3–6 June 2019; European Association of Geoscientists & Engineers: Utrecht, The Netherlands, 2019; pp. 1–5. [CrossRef]
16. Sossa, J. El papel de la inteligencia artificial en la Industria 4.0. In *Inteligencia Artificial y Datos Masivos en Archivos Digitales Sonoros y Audiovisuales*; Rodríguez Reséndiz, P.O., Ed.; Univ. Nacional Autónoma de México: Mexico City, Mexico, 2020.
17. Valle Tamayo, G.A.; Romero Consuegra, F.; Cabarcas Simancas, M.E. Predicción de flujo multifásico en sistemas de recolección de crudo: Descripción de requerimientos. *Rev. Fuentes Reventón Energético* **2017**, *15*, 87–99. [CrossRef]
18. Ruiz-Diaz, C.M.; Hernández-Cely, M.M.; González-Estrada, O.A. A Predictive Model for the Identification of the Volume Fraction in Two-Phase Flow. *Cienc. Desarro.* **2021**, *12*, 49–55.
19. Jahanandish, I.; Salimifard, B.; Jalalifar, H. Predicting bottomhole pressure in vertical multiphase flowing wells using artificial neural networks. *J. Pet. Sci. Eng.* **2011**, *75*, 336–342. [CrossRef]
20. Semeraro, F.; Griffiths, A.; Cangelosi, A. Human–robot collaboration and machine learning: A systematic review of recent research. *Robot. Comput. Integr. Manuf.* **2022**, *79*, 102432. [CrossRef]
21. Vaswani, A.; Shazeer, N.; Parmar, N.; Uszkoreit, J.; Jones, L.; Gomez, A.N.; Kaiser, L.; Polosukhin, I. Attention is All you Need. In Proceedings of the Advances in Neural Information Processing Systems 30: Annual Conference on Neural Information Processing Systems 2017, Long Beach, CA, USA, 4–9 December 2017; Guyon, I., von Luxburg, U., Bengio, S., Wallach, H.M., Fergus, R., Vishwanathan, S.V.N., Garnett, R., Eds.; Curran Associates, Inc.: Red Hook, NY, USA, 2017; pp. 5998–6008.
22. Lakew, S.M.; Cettolo, M.; Federico, M. A comparison of transformer and recurrent neural networks on multilingual neural machine translation. In Proceedings of the COLING 2018—27th International Conference on Computational Linguistics, Santa Fe, NM, USA, 20–26 August 2018; pp. 641–652.

23. Brown, T.B.; Mann, B.; Ryder, N.; Subbiah, M.; Kaplan, J.; Dhariwal, P.; Neelakantan, A.; Shyam, P.; Sastry, G.; Askell, A.; et al. Language models are few-shot learners. *Adv. Neural Inf. Process. Syst.* **2020**, *2020*, 1154–1156.
24. Safi Samghabadi, N.; Patwa, P.; Pykl, S.; Mukherjee, P.; Das, A.; Solorio, T. Aggression and Misogyny Detection using BERT: A Multi-Task Approach. In *Proceedings of the Second Workshop on Trolling, Aggression and Cyberbullying*; European Language Resources Association (ELRA): Marseille, France, 2020; pp. 126–131.
25. Meng, L.; Li, H.; Chen, B.-C.; Lan, S.; Wu, Z.; Jiang, Y.-G.; Lim, S.-N. AdaViT: Adaptive Vision Transformers for Efficient Image Recognition. In Proceedings of the IEEE/CVF Conference on Computer Vision and Pattern Recognition (CVPR), Nashville, TN, USA, 20–25 June 2021; pp. 12309–12318.
26. Le, N.Q.K.; Ho, Q.T. Deep transformers and convolutional neural network in identifying DNA N6-methyladenine sites in cross-species genomes. *Methods* **2022**, *204*, 199–206. [CrossRef] [PubMed]
27. Sharma, A.; Jain, P.; Mahgoub, A.; Zhou, Z.; Mahadik, K.; Chaterji, S. Lerna: Transformer architectures for configuring error correction tools for short- and long-read genome sequencing. *BMC Bioinform.* **2022**, *23*, 25. [CrossRef]
28. Behjati, A.; Zare-Mirakabad, F.; Arab, S.S.; Nowzari-Dalini, A. Protein sequence profile prediction using ProtAlbert transformer. *Comput. Biol. Chem.* **2022**, *99*, 107717. [CrossRef]
29. Qu, K.; Si, G.; Shan, Z.; Kong, X.G.; Yang, X. Short-term forecasting for multiple wind farms based on transformer model. *Energy Rep.* **2022**, *8*, 483–490. [CrossRef]
30. Wang, L.; He, Y.; Li, L.; Liu, X.; Zhao, Y. A novel approach to ultra-short-term multi-step wind power predictions based on encoder–decoder architecture in natural language processing. *J. Clean. Prod.* **2022**, *354*, 131723. [CrossRef]
31. Gomaa, I.; Gowida, A.; Elkatatny, S.; Abdulraheem, A. The prediction of wellhead pressure for multiphase flow of vertical wells using artificial neural networks. *J. Geosci.* **2021**, *14*, 1–10. [CrossRef]
32. Tunstall, L.; Von Werra, L.; Wolf, T. *Natural Language Processing with Transformers: Building Language Applications with Hugging Face*; O'Reilly: Sebastopol, CA, USA, 2022; ISBN 978-1-098-10324-8.
33. Bannwart, A.C.; Rodriguez, O.M.H.; de Carvalho, C.H.M.; Wang, I.S.; Vara, R.M.O. Flow Patterns in Heavy Crude Oil-Water Flow. *J. Energy Resour. Technol.* **2004**, *126*, 184–189. [CrossRef]
34. Abduvayt, P.; Manabe, R.; Watanabe, T.; Arihara, N. Analisis of Oil-Water Flow Tests in Horizontal, Hilly-Terrain, and Vertical Pipes. In *Proceedings of the SPE Annual Technical Conference and Exhibition*; Society of Petroleum Engineers: London, UK, 2004; pp. 1335–1347. [CrossRef]
35. Du, M.; Jin, N.-D.; Gao, Z.-K.; Wang, Z.-Y.; Zhai, L.-S. Flow pattern and water holdup measurements of vertical upward oil–water two-phase flow in small diameter pipes. *Int. J. Multiph. Flow* **2012**, *41*, 91–105. [CrossRef]
36. Flores, J.; Chen, X.; Brill, J. Characterization of Oil-Water Flow Patterns in Vertical and Deviated Wells. In *Proceedings of the SPE Annual Technical Conference and Exhibition*; Society of Petroleum Engineers: London, UK, 1997; Volume 1, pp. 55–64. [CrossRef]
37. Ganat, T.; Ridha, S.; Hairir, M.; Arisa, J.; Gholami, R. Experimental investigation of high-viscosity oil–water flow in vertical pipes: Flow patterns and pressure gradient. *J. Pet. Explor. Prod. Technol.* **2019**, *9*, 2911–2918. [CrossRef]
38. Govier, G.W.; Sullivan, G.A.; Wood, R.K. The upward vertical flow of oil-water mixtures. *Can. J. Chem. Eng.* **1961**, *39*, 67–75. [CrossRef]
39. Han, Y.F.; Jin, N.D.; Zhai, L.S.; Zhang, H.X.; Ren, Y.Y. Flow pattern and holdup phenomena of low velocity oil-water flows in a vertical upward small diameter pipe. *J. Pet. Sci. Eng.* **2017**, *159*, 387–408. [CrossRef]
40. Hasan, A.R.; Kabir, C.S. A New Model for Two-Phase Oil/Water Flow: Production Log Interpretation nd Tubular Calculations. *SPE Prod. Eng.* **1990**, *5*, 193–199. [CrossRef]
41. Hasan, A.R.; Kabir, C.S. A simplified model for oil/water flow in vertical and deviated wellbores. *SPE Prod. Facil.* **1999**, *14*, 56–62. [CrossRef]
42. Jana, A.K.; Das, G.; Das, P.K. Flow regime identification of two-phase liquid–liquid upflow through vertical pipe. *Chem. Eng. Sci.* **2006**, *61*, 1500–1515. [CrossRef]
43. Jana, A.K.; Ghoshal, P.; Das, G.; Das, P.K. An Analysis of Pressure Drop and Holdup for Liquid-Liquid Upflow through Vertical Pipes. *Chem. Eng. Technol.* **2007**, *30*, 920–925. [CrossRef]
44. Guo, J.; Yang, Y.; Zhang, S.; Zhang, D.; Cao, C.; Ren, B.; Liu, L.; Xing, Y.; Xiong, R. Heavy oil-water flow patterns in a small diameter vertical pipe under high temperature/pressure conditions. *J. Pet. Sci. Eng.* **2018**, *171*, 1350–1365. [CrossRef]
45. Mazza, R.A.; Suguimoto, F.K. Experimental investigations of kerosene-water two-phase flow in vertical pipe. *J. Pet. Sci. Eng.* **2020**, *184*, 106580. [CrossRef]
46. Mydlarz-Gabryk, K.; Pietrzak, M.; Troniewski, L. Study on oil–water two-phase upflow in vertical pipes. *J. Pet. Sci. Eng.* **2014**, *117*, 28–36. [CrossRef]
47. Rodriguez, O.M.H.; Bannwart, A.C. Experimental study on interfacial waves in vertical core flow. *J. Pet. Sci. Eng.* **2006**, *54*, 140–148. [CrossRef]
48. Xu, J.; Li, D.; Guo, J.; Wu, Y. Investigations of phase inversion and frictional pressure gradients in upward and downward oil–water flow in vertical pipes. *Int. J. Multiph. Flow* **2010**, *36*, 930–939. [CrossRef]

49. Yang, Y.; Guo, J.; Ren, B.; Zhang, S.; Xiong, R.; Zhang, D.; Cao, C.; Liao, Z.; Zhang, S.; Fu, S. Oil-Water flow patterns, holdups and frictional pressure gradients in a vertical pipe under high temperature/pressure conditions. *Exp. Therm. Fluid Sci.* **2019**, *100*, 271–291. [CrossRef]
50. Zhao, D.; Guo, L.; Hu, X.; Zhang, X.; Wang, X. Experimental study on local characteristics of oil-water dispersed flow in a vertical pipe. *Int. J. Multiph. Flow* **2006**, *32*, 1254–1268. [CrossRef]

Disclaimer/Publisher's Note: The statements, opinions and data contained in all publications are solely those of the individual author(s) and contributor(s) and not of MDPI and/or the editor(s). MDPI and/or the editor(s) disclaim responsibility for any injury to people or property resulting from any ideas, methods, instructions or products referred to in the content.

inventions

MDPI

Article

Computer Vision Algorithm for Characterization of a Turbulent Gas–Liquid Jet

Ilya Starodumov [1], Sergey Sokolov [1,2], Pavel Mikushin [1], Margarita Nikishina [1], Timofey Mityashin [1], Ksenia Makhaeva [1], Felix Blyakhman [1,2], Dmitrii Chernushkin [3] and Irina Nizovtseva [1,*]

[1] Laboratory of Multiphase Physical and Biological Media Modeling, Ural Federal University, Ekaterinburg 620000, Russia; sergey.sokolov@urfu.ru (S.S.)
[2] Department of Biomedical Physics and Engineering, Ural State Medical University, Ekaterinburg 620028, Russia
[3] NPO Biosintez Ltd., Moscow 109390, Russia
* Correspondence: nizovtseva.irina@gmail.com

Abstract: A computer vision algorithm to determine the parameters of a two-phase turbulent jet of a water-gas mixture traveling at a velocity in the range of 5–10 m/s was developed in order to evaluate the hydrodynamic efficiency of mass exchange apparatuses in real time, as well as to predict the gas exchange rate. The algorithm is based on threshold segmentation, the active contours method, the regression of principal components method, and the comparison of feature overlays, which allows the stable determination of jet boundaries and is a more efficient method when working with low-quality data than traditional implementations of the Canny method. Based on high-speed video recordings of jets, the proposed algorithm allows the calculation of key characteristics of jets: the velocity, angle of incidence, structural density, etc. Both the algorithm's description and a test application based on video recordings of a real jet created on an experimental prototype of a jet bioreactor are discussed. The results are compared with computational fluid dynamics modeling and theoretical predictions, and good agreement is demonstrated. The presented algorithm itself represents the basis for a real-time control system for aerator operation in jet bioreactors, as well as being used in laboratory jet stream installations for the accumulation of big data on the structure and dynamic properties of jets.

Keywords: gas–liquid flows; jet stream; computer vision; edge detection; algorithms; image processing

1. Introduction

Intense fluid jetting is a key technical element in a number of industrial devices, e.g., grinding [1–3], cutting [4,5], etc. The detailed characterization of multiphase gas–liquid flows is critical in metallurgical processes, the design of efficient air and ground devices, combustion devices in aircraft and aerospace systems, and engines in transportation and marine engines, as well as when developing new technologies leading to technological advances [6–9]. The system's jet parameters determine the characteristics of the device and its efficiency and also provide relevant information for industrial biotechnology due to the increased demand for efficient technological solutions in the field. Devices and apparatuses are important components when jets play the role of a kinetic mixer [10,11], providing intensive mass exchange in the volume of the liquid.

Jet stream bioreactors [12,13] represent a type of machine with the recirculation of the liquid and gas phases caused by generated multiscale gas–liquid jets with a high volume content of gas bubbles. The behavior of the jet can be characterized as a high-turbulence physical process, frequently leading to technical problems related to flow control, analyzing its parameters, and further optimizing design elements such as the nozzle and jet pump. There is a liquid core region, the structure of which is affected by interaction with the gas phase, which leads to its significant change, i.e., deformation of the continuous flow.

The interaction of the liquid and gas phases generates a number of physical phenomena, such as the exchange of momentum and energy between the flow phases, a unique structure of flow pulsations, phase transitions, bubble effects, and dissolution processes in the gas phase, which significantly change the characteristics of the heat and mass transfer [14–16]. External forces acting on the jet surface can lead to oscillations and perturbations of the jet boundaries. This oscillation can intensify and eventually lead to the disintegration of the flow into small droplets, or even the flow's complete destruction.

The peculiarity of these devices is that they can combine high jet flow energies and considerable apparatus sizes. The kinetic energy of a jet represents the main source of turbulence and drives the microscale mixing of the liquid and gas phases by turbulent diffusion. This means that high specific costs are associated with the formation of the jet stream. In the case of such a jet having low efficiency, i.e., its significant destruction, the costs become significant.

Therefore, a fundamental physical understanding of jet formation and behavior is an important research and operational challenge.

A number of techniques are known to be applicable to the study of gas–liquid jets due to their wide application in technical and biotechnical problems [17]. Recently, various studies have relied on the computational fluid dynamics (CFD) modeling of hydrodynamic processes in bioreactors [13,18–24]. The mathematical description of multiphase flows is complicated in many aspects due to the peculiarities associated with the mutual influence of continuous and dispersed phases. Therefore, the bubble flow [13,25–27], annular flow [28], and more complex flows [21,23,29] have received a new wave of study. Important mass transfer characteristics of the process are studied in [12,19,23,30]. In addition to characterizing multiphase flows, CFD methods have found application in solving the problem of achieving optimal performance in bioreactors [22]. However, the problem is always associated with the description of multiphase multicomponent flows with developed turbulence, which makes the task of computer simulation computationally complex. Meanwhile, the list of factors affecting the formation of jets is quite significant, and experimental studies and objective monitoring remain valid sources of data on jets' properties.

It has now been shown that, in a number of areas, new deep and machine learning methods, particularly computer vision (CV) methods, outperform previous, state-of-the-art methods [31–33]. These papers often represent general information on new methods or compare them. With recent advances in digitization and big data analytics, digital tools are gradually beginning to be adopted in biotechnology research. Biological, hydrodynamic, and heat and mass transfer processes in bioreactor (fermenter) circuits are key targets for such digital approaches, as these processes are often complicated to analyze [34–37]. The maximum bioreactor efficiency is primarily determined by gas phase transfer through the gas–liquid interface. Therefore, hydrodynamic parameters such as the bubble sizes in the gas–liquid stream significantly influence the flow behavior and determine the overall performance of the fermenter. Machine learning algorithms show advantages in terms of accuracy with respect to bubble sizing [38–40]. Used to capture real-time parameters and support decision making to control and optimize key performance and safety indicators of the biosynthesis process, success stories are increasingly appearing in the scientific and technical literature and reports, where computer vision is proving to be not only one of the most efficient but also one of the most affordable non-destructive methods compared to expensive, invasive methods that require additional, sometimes redundant, equipment with sets of sensors, transducers, detectors, and neural networks, which, in turn, are also attractive tools for a number of their characteristics, such as accuracy and the ability to handle small objects.

Experiments show that the best mixing in jet bioreactors is provided by a coherent jet with the lowest mass loss in the form of detached droplets and the highest vertical velocity. Visually, such a jet is characterized by the smallest opening angle and the absence of edge fluctuations. However, unlike other technical devices, in jet bioreactors, the water jet at the nozzle outlet contains a large amount of gas phase (up to a volume proportion of 1:1 [41]).

Depending on the liquid delivery mode determined by the pump operation, such a flow can be a bubble flow, an annular flow, or a set of many individual jets and droplets. Thus, the CV observation of the shape, structure, and velocity of the jet becomes one of the ways to select the optimal mode of operation of the bioreactor.

The following sections will propose a computer vision algorithm that allows the stable processing of a gas–liquid video obtained from a high-speed camera.

2. Materials and Methods

Various parameters, such as the jet opening angle, contour deviations, and jet velocity, are known to have a significant impact on the breakup length and pattern of liquid jets [42] (see Figure 1).

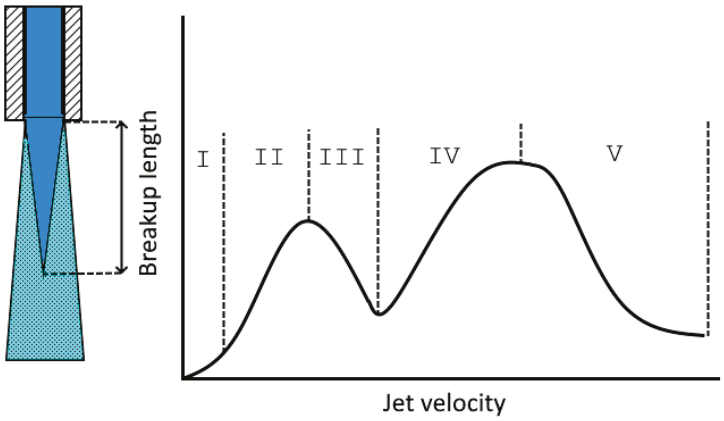


Figure 1. Schematic representation of jet breakup length and its dependence on velocity [42]. The diagram shows jet regimes: I—dripping flow. II—laminar flow. III—transition region. IV—turbulent flow. V—fully developed spray.

The angle and deviations from the line of a liquid jet's contour determine its shape. A jet with a narrow angle and few deviations will have a more streamlined shape, resulting in a longer breakup length. On the other hand, a wider angle and more deviations in the contour can lead to an irregular shape, causing the jet to break up sooner.

The velocity of the liquid jet plays a crucial role in its breakup length and pattern. Higher velocities tend to create thinner, more elongated jets that experience greater aerodynamic instability. This instability might cause the jet to break up earlier and result in a more chaotic breakup pattern. Conversely, lower velocities lead to thicker jets that are relatively more stable and have a longer breakup length. However, as the jet speed increases, both an increase and a decrease in breakup length can occur, depending on the speed range in which the experiments are carried out. In the case of a low speed of turbulent flow, an increase will be observed, and when a certain critical point is reached, the increase will be replaced by a decrease. The conditions at the jet boundary, such as the presence of surrounding gas or a solid surface, can significantly influence the breakup of the liquid jet. For instance, if the jet is fully surrounded by a gas medium, it experiences less resistance and can travel for a longer distance before breaking up. Alternatively, if the jet comes into contact with a solid surface, it may undergo secondary breakup or atomization, leading to a shorter breakup length and a more dispersed pattern.

2.1. Data Parameters and a General Description of the Order of Operations for Algorithms

In order to evaluate the characteristics of the jet and subsequently relate them to the parameters of the apparatus for its production, we have developed algorithms based on computer vision methods. High-speed camera records provide initial data.

Each video after loading is converted into a three-dimensional array of scalars and pixel intensities. Here, indices along one of the axes allow us to work with individual frames. We use the grayscale color model so that the algorithms that we implement do

not depend on the color features of the lighting equipment or the environment. It also allows a reduction in the weight of the data in the array itself, which is very important for the fast execution of algorithms. Next, we normalize the data so that, regardless of the format of the source data, the minimum intensity is 0 and the maximum is 255. After this, to determine the parameters of a gas–liquid jet, we propose the following set of steps:

1. detection of the edge of the jet (gas–liquid boundary) in the form of a set of coordinates of points on this boundary for each frame of the video sequence;
2. determination of the straight line of the best approximation to points on the jet boundary;
3. calculation of the root-mean-square deviation of points on the jet boundary from the straight line of best approximation;
4. calculation of the angle of deviation of the line of the best approximation from the vertical for both the right and left edge of the jet; the difference between these angles is equal to the angular expansion of the jet.

Using computer vision algorithms, it is necessary to take into account the features of specific data sets. In our case, there is heterogeneity in the images, i.e., areas of high and low pixel intensity. The image regions between these irregularities can be used to detect jet boundaries. However, the original image does not have high contrast, and it also contains noise, i.e., the visible boundaries are blurred. This is due to the fact that the flows and environments studied impose physical limitations on the image quality. The selected computer vision methods should be sufficiently resistant to noise and blurring.

The study of the data by plotting pixel intensity distributions (Figure 2) is an important step in choosing the parameters of filters for image processing, as well as the parameters of methods for the detection of jet boundaries.

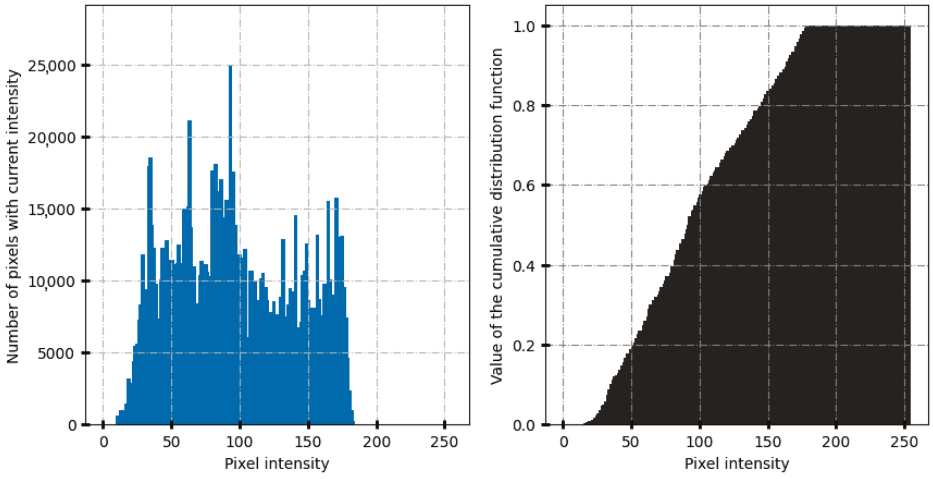


Figure 2. An example of the distribution of intensities in one of the experimental frames. Left panel: distribution of pixel intensities in a frame. The presence of clearly defined peaks indicates the presence of areas of increased and decreased intensity (heterogeneity). Right panel: the cumulative distribution function of the intensity of pixels on the frame. Here, we can see that gray dominates in the frame and starts from a certain threshold value. The corresponding intensities belong to a few bright highlights.

However, the mere presence of heterogeneity is not enough. Of great importance is the relative position of such pixels. In this vein, it is necessary to take into account the characteristic pixel intensity gradients that the images have, since it is the magnitude of this gradient that makes it possible to clearly detect the border. Accordingly, the algorithm used for border detection must be able to work with exactly the range of gradients that we observe. In our case, the boundaries are very blurred; the gradients are small, and, accordingly, purely gradient methods are less preferred. Another limitation is the physical

continuity of the boundary of the gas–liquid jet. The algorithm must be able to construct a continuous boundary, even if the jet boundaries appear steep in the image.

Another feature of our data is the dynamic changes over time (Figure 3). The average brightness intensity of the pixels and their distribution in the frame can vary very significantly as we move from frame to frame. Accordingly, methods applied to such data must be robust to such dynamic changes.

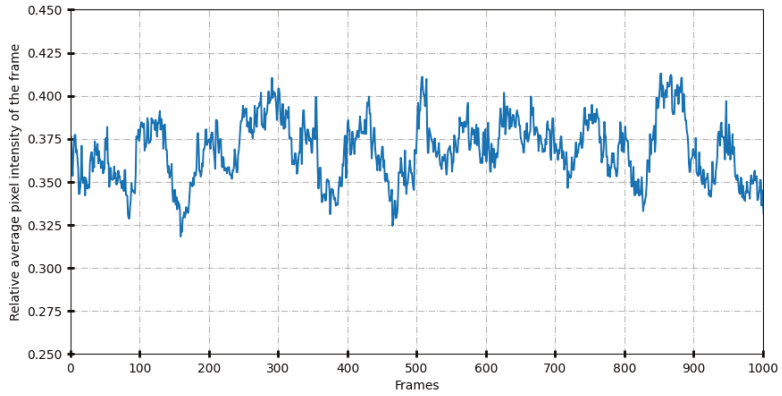


Figure 3. Changing the relative average pixel intensity for each frame of the video. The real physical time is 1 s. Oscillations around some average value with an amplitude of about 30% can be observed. The procedure for the ordinate values' calculation is the division of the total intensity sum by all pixels at a single frame by the maximum intensity and by the horizontal and vertical length of the image in pixels.

The dynamic nature of the data variability (Figure 3) corresponds to the physical causes and hydrodynamic features of the studied gas–liquid system. This must also be taken into account since such variability is also observed in the form of boundary deviations. As the jet stream angle increases, the size of the area corresponding to the jet will increase, which means that the average pixel intensity in the frames will also change.

2.2. Active Contours Method for Jet Edge Detection

A number of publications describe several approaches to determining the jet edge, i.e., the gas–liquid interface [43–46]. All methods are based on gradient methods, primarily on the Canny edge method [47]. However, to find the edges of the jet on our data, these methods produce a lot of side contours. Therefore, it was decided to use the active contour model (ACM) method [48,49] to determine the boundaries of objects on 2D images. In ACM, the object boundary is considered as an elastic line (spline) specified by the coordinates (x, y) of the points on it, and the functional E is minimized [50]:

$$E = \int_0^1 \left[E_{int}\left(v(s)\right) + E_{image}\left(v(s)\right) \right] ds \quad (1)$$

where $v(s) = (x(s),\ y(s))$ is the parametric representation of the contour, and $s \in [0; 1]$ is the contour parameter.

$E_{int}\left(v(s)\right) = \alpha|v_s|^2 + \beta|v_{ss}|^2$ is the internal energy of the spline; v_s and v_{ss} are the first derivative and the second derivative of v with respect to s, respectively.

$E_{image} = -\gamma|\nabla I(x, y)|^2$ is the so-called image energy; α, β, and γ are the parameters of the ACM method. Thus, by minimizing the functional E, it is possible to "pull" the contour to the boundaries with a sharp difference in brightness while, at the same time, avoiding excessively long and crimped contours. If there is a noticeable level of noise and interfering artifacts (for example, splashes) in the image, Gaussian smoothing is first applied to the intensity function $I(x, y)$ before calculating E_{image}. On the first frame of the video sequence, the points of the beginning and end of the lines of the initial approximation

of the jet boundaries are placed, which are then used as initial conditions on all analyzed frames. Moreover, the distance between the upper points of the initial approximation lines is used to obtain the length scale factor (the diameter of the pipe outlet nozzle is known).

Figure 4 shows an example of the application of the ACM method to determine the boundaries of the jet.

Before the analysis of data, it is necessary to align (rotate) the image so that the normal to the plane of the nozzle runs strictly vertically. For a quantitative assessment of such jet parameters as the angle of divergence and fluctuations in the boundary contour, a straight line of best approximation is determined for both edges of the jet. Since the position of the jet in the initial data is close to vertical, the best results for determining the approximating straight line are given by the principal component method (PCA) [50] compared to the least squares method. In the approach that we used, an approximating line was obtained in the form of a sequence of coordinates of its points (x_i, y_i), $i = 1 \ldots n$, where the number of points n was equal to their number on the original contour.

The angle of deviation of the line of best approximation of the edge of the jet from the vertical position α_{edge} was calculated as

$$\alpha_{edge} = \tan^{-1}\left(\frac{x_n - x_1}{y_n - y_1}\right) \quad (2)$$

x_1, x_m, y_1, y_n are, respectively, the x and y coordinates of the first and last points on the line of best approximation of the given edge of the jet (see Figure 4).

The difference between the angles α_{edge} of both the right and left edges of the jet is equal to the angular opening (expansion) of the jet. Further, in this article, this value is called the jet angle.

Next, the root-mean-square deviation of the contour points of the jet edges from the corresponding approximating straight lines is calculated. This parameter characterizes numerically the oscillatory behavior of the jet edges (boundaries).

2.3. Method for Determination of the Flow Velocity in a Jet

An important characteristic of the processes occurring in the bioreactor is the rate of liquid supply to it. Measuring the solution pumping rate with a flow meter is not always possible. Therefore, we have developed an approach to estimate the linear jet flow velocity using computer vision methods. When analyzing the original video recordings, it can be seen that there are structures on the surface of the jet that move, as we assume, at the speed of the jet itself. The "lifetime" of such structures is mainly from 2 to 5 frames of video recording produced at a speed of 1000 frames per second. It is possible to trace the interframe movement of such structures throughout their existence interval and estimate the average displacement during the interframe interval.

Figure 5c in a later section shows an example of two adjacent frames with an estimated offset of a given structure. The flow velocity estimate is calculated according to

$$v_{flow} = \frac{dy}{dt}, \quad (3)$$

where dy is the interframe shift of the selected structure, dt is the time interval between adjacent video frames. This approach will give a suitable estimate of the flow velocity only at high shooting speeds, since the lifetime of isolated structures on the flow surface is, according to our estimates, no more than 5–8 ms (5–8 frames at a shooting rate of 1000 frames per second).

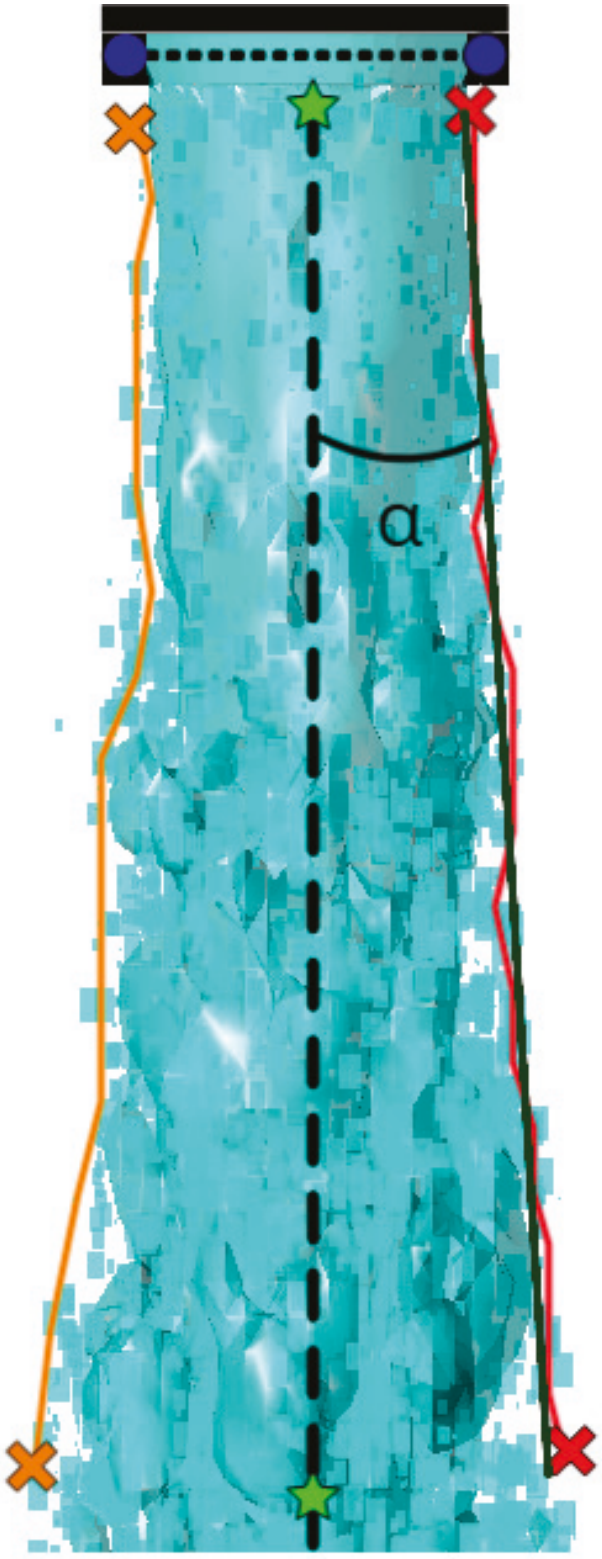


Figure 4. Principal scheme of the jet stream angle calculation method. Blue labels are used for image scaling and calculations in millimeters (the pipe diameter is known). Green labels are used to set the vertical. Orange (for the left border) and red (for the right border) labels define the margin points of the segments, which are further used as an initial approximation for the active contour method. Using the highlighted edge contours, the jet angle is calculated (α from Equation (2)—the angle between the vertical direction and the linear approximation of the edge—black line).

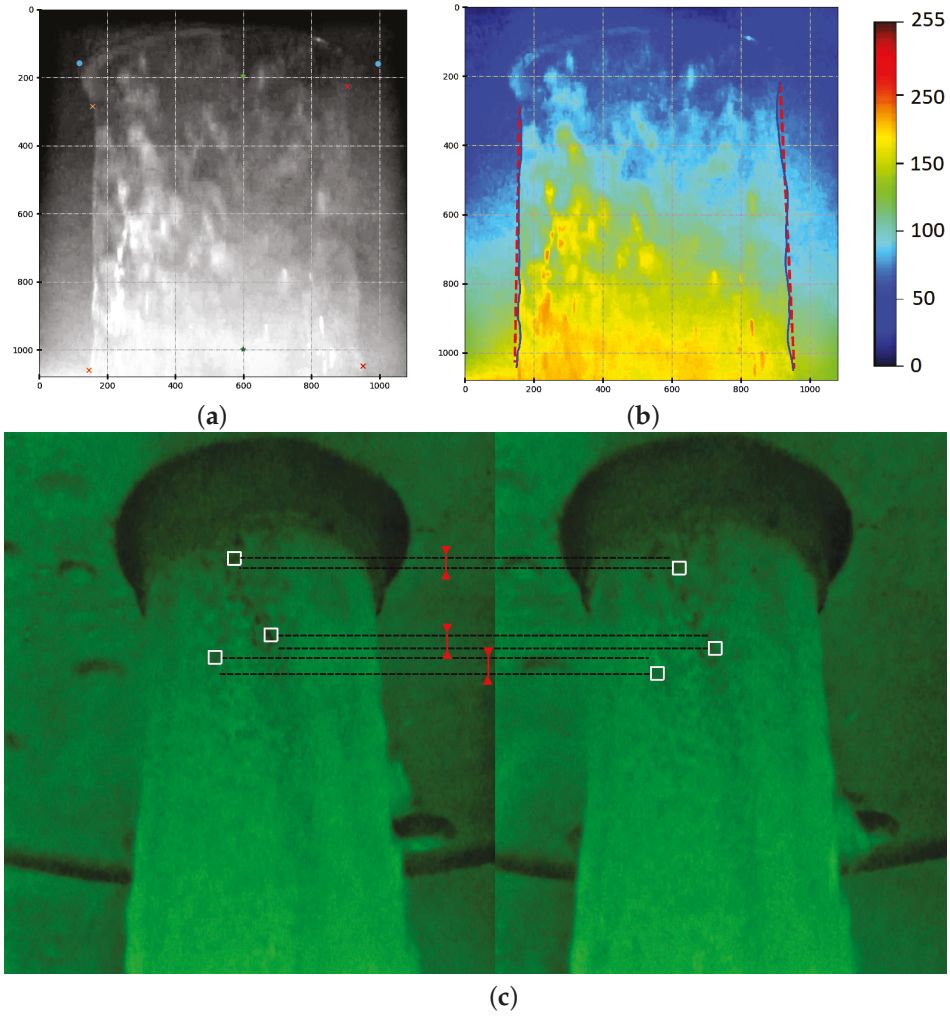


Figure 5. Stages of application of algorithms and results: (**a**) Arrangement of scaling points, vertical, and initial approximation for the left and right borders in accordance with (Figure 4). (**b**) The result of applying the method of active contours in the "jet" color scheme (pixels with low intensity correspond to cold colors; those with high intensity correspond to warm colors). The dark blue continuous curves are those found by the active contours method. The red dotted line is the initial approximation. (**c**) A scheme for calculation of the speed of two adjacent frames. The red labels indicate the distance traveled by the drop.

To improve the accuracy of stream velocity estimation, we propose, firstly, to place at least 10 points on each frame—the centers of the structures, the interframe shift of which will be measured. Secondly, such measurements are made on a relatively large number of frames. The obtained values of the flow rate estimates are subjected to statistical processing. The mean value v and the root-mean-square spread σ_x are calculated. Values that do not fall within the interval $v \pm 2\sigma_v$ are excluded from further analysis. The average value of the remaining values is the estimate of the flow velocity.

To automatically select the centers of the structures whose interframe shift will be evaluated, the following approach is proposed. Preliminarily, Gaussian smoothing of the processed frame of the video sequence is performed in order to reduce the influence of random fluctuations. Next, the image is binarized with a threshold, which is currently set manually. It is necessary to adjust the threshold so that only a few (about 10) individual small areas remain. All the indicated transformations of the image are performed only between the boundaries of the flow found earlier. Figure 6 shows an example of the original frame and that after binarization. To reduce the size of the areas that will be followed further, the erosion procedure was applied to them [47].

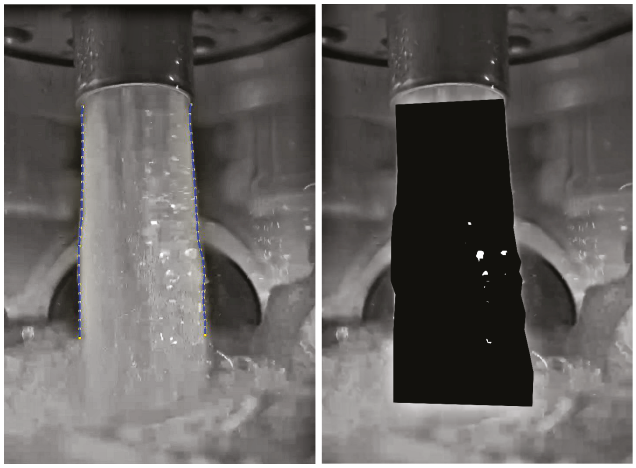


Figure 6. Source frame with recognized jet edges (**left** panel) and binarization after thresholding (**right** panel).

The centers of the found areas are taken as the centers of the structures, the interframe shift of which will be measured to estimate the flow rate. To find the coordinates of the selected structure on the next frame, the method of maximum mutual spatial correlation is used [51,52].

We carried out a visual comparison of the results of manual marking with the results of the algorithm (Figure 7). The resulting differences are practically insoluble visually. Calculating the errors for such algorithms is quite complicated since the boundaries of the jet are not known in advance and the data are obtained experimentally. However, by performing a similar assessment for a synthetic image of a jet, we can estimate the root-mean-square error as 0.07 pixels.

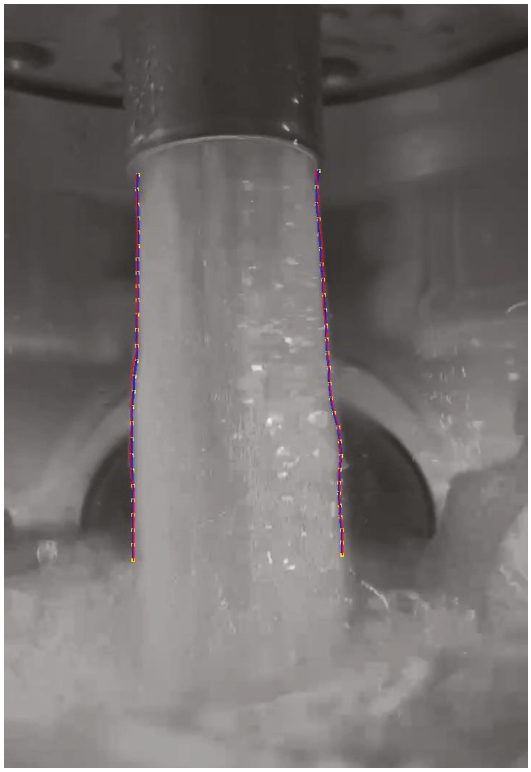


Figure 7. An example of detecting liquid–gas boundaries using the active contour method (blue curve) and manual tracing (red curve).

The algorithm was also compared with a well-known method of determining edges in images, i.e., the Canny edge method [47]. Figure 8 shows an example of the application of the Canny method to a jet image, both synthetic and experimentally obtained. On the synthetic image, the Canny method showed a good result, in contrast to the image obtained experimentally. It can be seen that due to the presence in the real image of a large number of objects and structures with complex boundaries, the Canny edge method, on the one hand, allowed many false detections of edges; on the other hand, there are discontinuities at the detected liquid–gas interface. Finally, it can be concluded that, with no special preprocessing, the algorithms based on the Canny method with respect to image series are unstable.

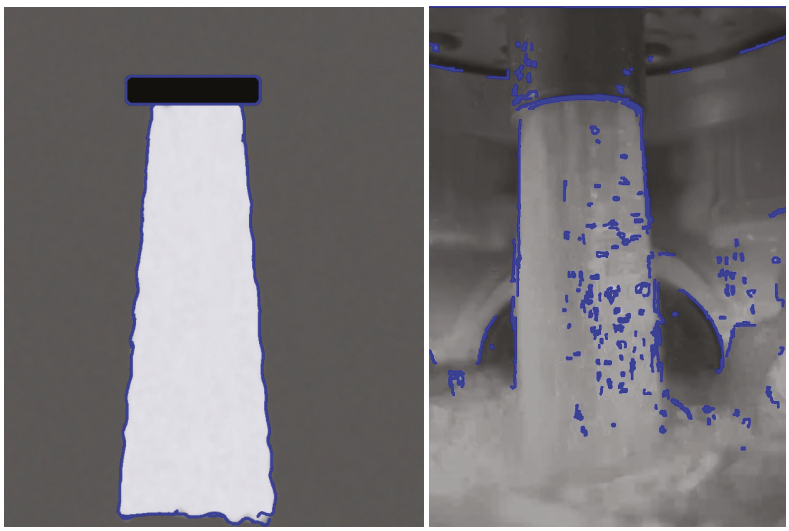


Figure 8. Examples of applying the Canny edge method to synthesized (**left** panel) and experimentally obtained (**right** panel) images of the liquid–gas interface.

Thus, the proposed algorithm for the detection of the liquid–gas interface on experimentally obtained images, being almost completely automatic, is practically not inferior in accuracy to manual tracing.

2.4. Jet Properties at Different Flows: Algorithm Usage

The developed algorithms were tested on the example of data obtained with the experimental setup, which is represented by a jet-stream-type mass exchange apparatus; see Figure 9. Previously, such a setup was used in the study of bubble generation by computer vision methods [38].

The mass exchange apparatus in Figure 9 is a closed hydrodynamic circuit. The mixing and circulation of the liquid are carried out using the circulation pump. Along the flow of the liquid, the pipeline and heat exchanger are located. The aerator mixes the sucked gas and liquid phases and then accelerates the gas–liquid jet and penetrates into the liquid inside the machine body, where the video is taken through the viewing window.

The operating mode of this setup is regulated by the rotation speed of the pump, which in turn depends on the value of the frequency converter. The pump creates a flow of liquid, which is saturated with gas by passing through the aerator and descends through the pipe into the tank, forming a high-turbulence gas–liquid jet. Due to the complex flow kinetics, the characteristics of the jet will be determined by many factors, such as the nozzle shape, gas phase fraction, medium structure, pressure, turbulent energy, etc.

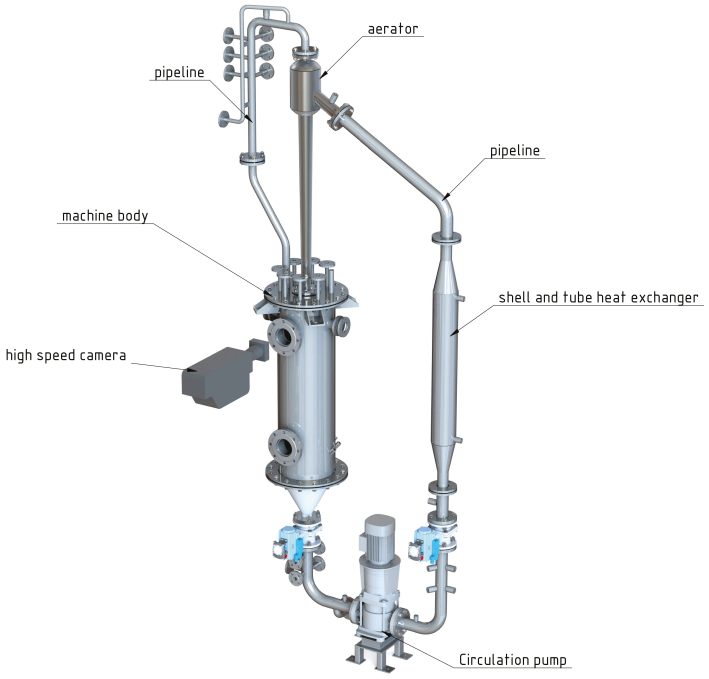


Figure 9. Scheme of the experimental setup.

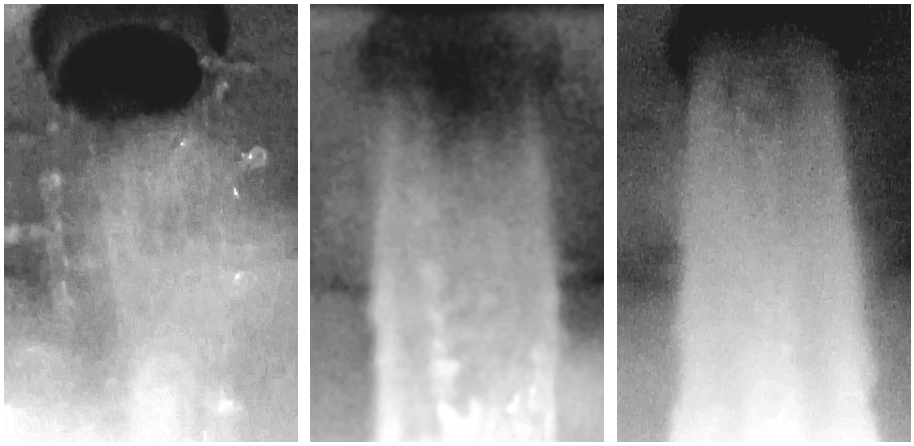
Thus, it is difficult to consider all the physical factors and predict the jet characteristics that affect the convection and, ultimately, mass transfer in the setup machine body (the tank). One solution is to create advanced CFD models, but this method is computationally intensive and needs experimental verification. Therefore, we investigated the task of processing a set of experimental video recordings of a jet flow in the setup at different pump operation modes. Note that the video records were made in a foggy environment inside the tank, caused by the peculiarities of the fluid dynamic currents inside the apparatus. Thus, such data are a good test for the proposed computer vision algorithms.

Table 1 shows the investigated operating modes of the unit and the visually observed structural features of the jet.

Figure 10 shows three types of gas–liquid jet flow structures. The images are presented without processing; the blurring is due to the highly foggy environment inside the tank. All structures are united by the presence of sharp jet boundaries, which form the divergence of the jet. By total jet divergence, we refer to an angle 2α where a is calculated for each edge of the jet, as shown in Figure 4.

Table 1. The description of the observed jet structures on the video data for different setup regimes. By the regime, we consider the value on the frequency converter that controls the pump performance.

Setup Regime, Hz	Jet Structure	Comment
20	Split	The water flow is insufficient to fill the entire nozzle volume. The jet is discontinuous and represented by split streams.
25	Split	Similar to the regime of 20 Hz.
30	Ring (annular)	The fluid flow is uninterrupted along the nozzle walls, but there is not enough fluid to fill the entire nozzle cross-section. A ring current is observed.
35	Uniform	The liquid flow fills the nozzle completely, and the jet appears to be continuous, in which the liquid and gas fractions are uniformly distributed.
40	Uniform	Similar to the regime of 35 Hz.
45	Uniform	Similar to the regime of 35 Hz.
50	Uniform	Similar to the regime of 35 Hz.



(**a**) (**b**) (**c**)

Figure 10. Examples of the different jet structures observed on various regimes (see Table 1). (**a**) Split, (**b**) Ring, (**c**) Uniform.

Figure 5 shows the steps of applying the algorithm to calculate the characteristic velocity of a gas–liquid jet. Figure 5a schematically represents the necessary labels that will be used in constructing the contours in the active contours method. Figure 5b shows the continuous curves for one gas–liquid jet flow structure, which characterizes the contours from which the jet angle will be calculated. Figure 5c shows schematically the velocity calculation for two consecutive frames using the threshold segmentation method. The threshold segmentation method identifies specific areas corresponding to highlights in two adjacent frames. Next, the vertical shift in pixels is calculated for each selected segment. Then, the displacement value is converted into a physical distance by scaling at the extreme points of the pipe (fixed diameter). In order to calculate the segment speeds, the resulting distance in millimeters is divided by the time between two successive frames. Averaging the obtained velocities makes it possible to calculate the characteristic velocity of the gas–liquid jet under the assumption that the velocity of the glare along the vertical axis is approximately equal to the velocity of the flow.

All videos discussed in this paper were captured by a Sony ZV-1 (Sony Corp., Beijing, China) high-speed (1000 frames per second) video recorder. The deviation of the jet contours illustrates the pulsation of internal flows and their properties. For the best possible convection of the medium in the tank, the jet must be continuous, forming a single mass body, and have downward directed velocities at all points in the volume. This means that the effective jet must have the lowest edge deviation. At the same time, to increase convection, the jet must have the maximum momentum, which refers to the largest vertical velocity component. For the 20–50 Hz regimes (see Table 1) of the investigated jet stream setup, the liquid and gas phase fluxes were measured in experiments earlier. The measured curves are presented in Figure 11.

The volumetric fluid flow rate was measured as a function of the pump capacity and is a smooth curve. The gas volume flow rate provided by the free suction of the aerator was measured by anemometry and represents a significantly non-linear curve. An important characteristic of the aerator is the ejection coefficient, which is the ratio of the volumetric gas flow rate to the liquid flow rate. In Figure 11, one can see that the ejection coefficient of the aerator of the experimental setup varies non-monotonically, which indicates a change in the gas content and in the structure of the gas–liquid flow in the jet. Thus, the jet characteristics are difficult to predict due to the complex nonlinear relationship between the ejection process and pump performance and cannot be reliably interpolated or extrapolated.

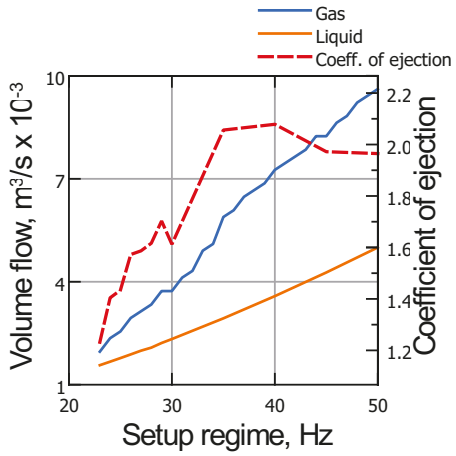


Figure 11. Experimentally measured liquid and gas phase flow rates for 20–50 Hz regimes of the investigated jet stream setup.

3. Results and Discussion

In this section, we analyze the results of applying the presented algorithm to the jet videos obtained using the experimental setup considering different modes of pump operation (which is equivalent to changing the input mechanical energy, since all the energy in the setup is inputted only by the rotating pump blades). For simplicity, we will denote the pump modes by the frequency of the electric current due to its linearly related quantities.

For each mode of the setup (20 Hz, 25 Hz, 30 Hz, 35 Hz, 40 Hz, 45 Hz, 50 Hz), frame-by-frame measurements of the jet angle, edge divergence, and flow rate parameters were performed. For this purpose, video recordings with a length of 1000 frames (1 s of physical time) were selected. Figures 12–15 represent the results of these studies. Table 1 summarizes the qualitative characteristics of the jet structure observed visually.

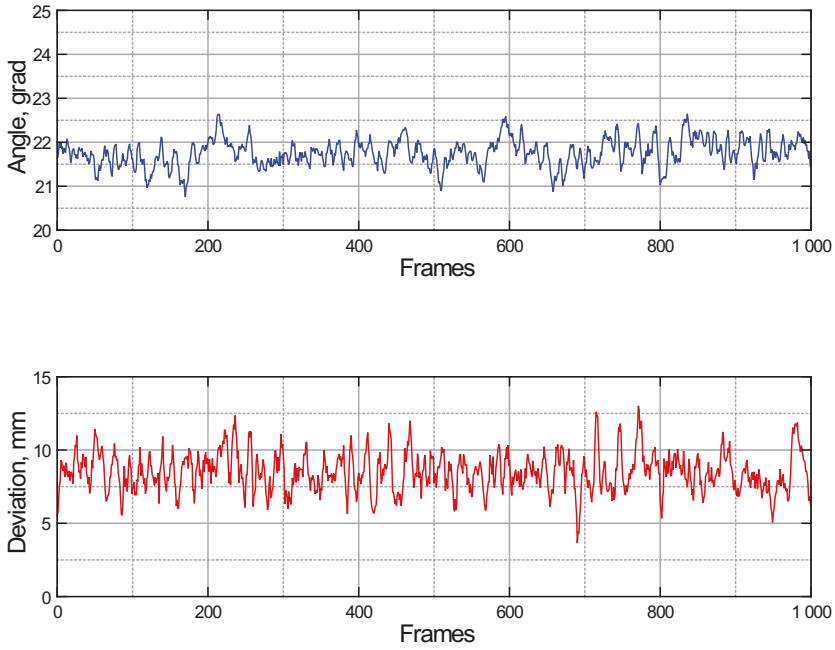


Figure 12. Results of video frame-by-frame processing for the setup regime 20 Hz: the jet angle (**upper** panel) and mean deviation of the jet edges (**lower** panel).

Note that in the 20 Hz mode, the jet with a discontinuous split flow structure (Figure 10a) has a large angle (up to 23 degrees) and average deviation (about 9 mm). From the physical

point of view, this is explained by the low energy and flow density (because the pump fluid supply is minimal compared to other modes), as well as the fact that the fluid is not sufficient, not only to fill the entire nozzle but also to form a film flow. As a result, individual jets fly out of the nozzle and then disintegrate into droplets and fly in different directions. Such a jet does not provide the penetration of the water column in the bioreactor tank, which means that mixing and mass transfer are at a very low level.

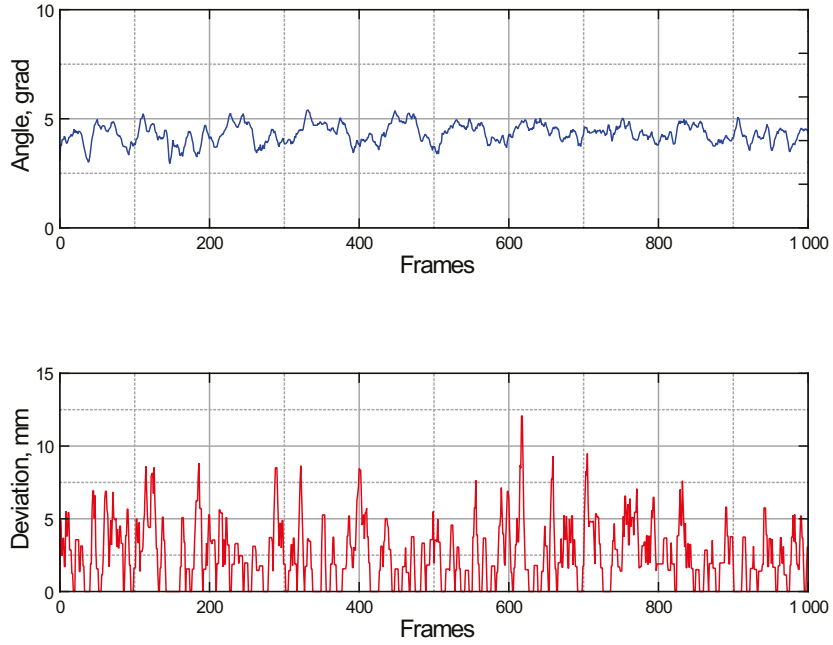


Figure 13. Results of video frame-by-frame processing for the setup regime 30 Hz: the jet angle (**upper** panel) and mean deviation of the jet edges (**lower** panel).

In the 30 Hz mode, a jet with continuous boundaries is formed at the nozzle outlet. Visually, it can be seen that the boundaries of the jet are quite thin, and, in the center of the flow, there is a solid gas phase. This type of flow is usually called a ring flow. In this case, the angle is decreased by almost five times compared to the 20 Hz mode, to about 5 degrees, while the mean edges' deviation is decreased by about two times to 4–5 mm. These observations are attributed to an increase in the fluid flow, which is sufficient to form a continuous ring. The fluid ceases to disintegrate into droplets and is no longer dispersed, as was observed in the case of the 20 Hz mode.

The bulk of the gas moves in the center of the jet separately from the liquid boundary layer, in the structure of which there are few bubbles, and therefore the structure is almost homogeneous. This reduces the deviation of the jet boundaries. In terms of efficiency, such a jet has a good penetration capacity at relatively low pump speeds, but the low gas content makes the jet inefficient in terms of mass transfer: gas does not enter the unit tank in bubble form, and the contact area of the liquid and gas phases as a result is low.

In the 40 Hz setup mode, a continuous gas–liquid jet is observed. The pulsations of the bubble phase cause local turbulence and oscillations of the jet, which can be seen by the increase in the boundary deviation up to 15 mm. At the same time, the jet has a small angle (about 5 degrees), which means that the velocities in the flow have a predominantly vertical direction. Such a jet has a large penetration force while providing not only mixing but also high mass transfer rates.

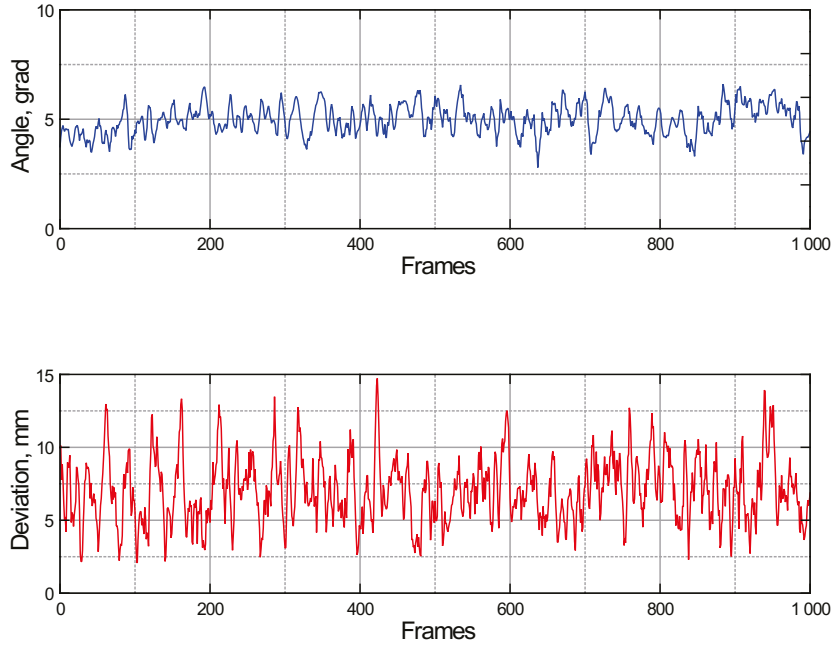


Figure 14. Results of video frame-by-frame processing for the setup regime 40 Hz: the jet angle (**upper** panel) and mean deviation of the jet edges (**lower** panel).

Increasing the pump rpm after the 40 Hz mode led to the formation of a column of bubbly medium above the nozzle (see Figure 15). Thus, a pressure gradient was formed at the nozzle outlet: the compressed mixture of gas and liquid flies out of the nozzle and sharply decompresses, which leads to an increase in the jet angle up to 12 degrees and the growth of the boundary deviation up to 15 mm. Such a jet has a high momentum and penetration force, but, because of the large angle, the vertical velocity component may be equivalent to a jet in the 40 Hz mode, which would reduce the specific mixing efficiency per unit of energy expended.

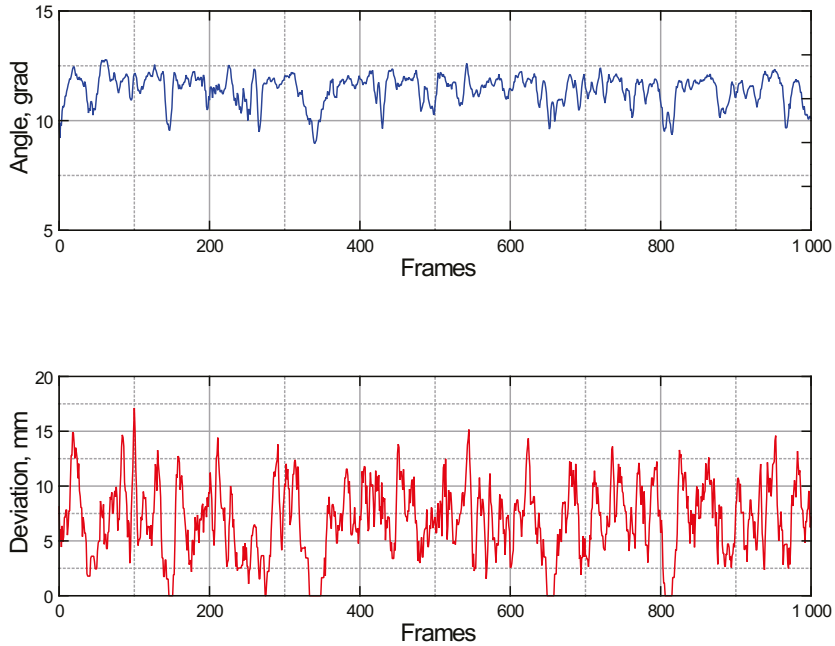
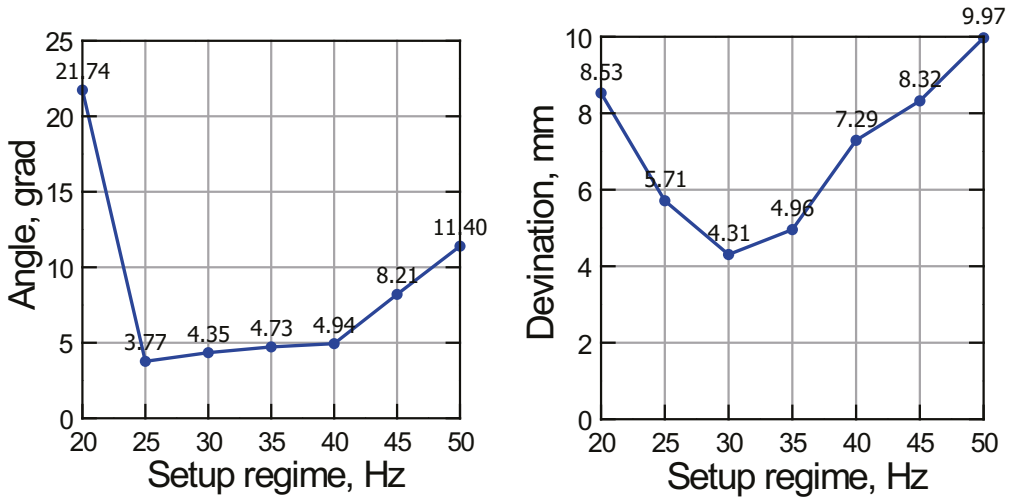


Figure 15. Results of video frame-by-frame processing for the setup regime 50 Hz: the jet angle (**upper** panel) and mean deviation of the jet edges (**lower** panel).

In Figure 16, the average angle and edge deviation for different setup regimes are presented. Note the tendency of a decreasing angle and deviation when passing from low-intensity and fluid flow modes, for which split jet flows are observed, to modes corresponding to continuous flows (from 30 Hz). Further, there is a build-up of gas content in the liquid flow, which leads to pulsations and a growth in deviation. When a certain critical mode is reached (in our case, it is 40 Hz), a significant pressure gradient appears at the nozzle outlet, as a result of which the jet is decompressed and its angle increases rapidly along with the deviation.



(**a**) (**b**)

Figure 16. (**a**) Average jet angle and (**b**) average edge deviation for different setup operation regimes.

In Figure 17a, the average jet velocities measured with the proposed CV algorithm for each of the installation modes are presented (blue line). Note that for the 20–25 Hz modes with a split jet, the velocity values will be affected by the resistance of the gas phase to individual droplets. Therefore, it is expected that despite the growth in the liquid flow rate, the jet velocity grows slowly. As soon as the jet flow passes to the ring or continuous state (from 30 Hz), the velocity begins to grow almost linearly with the increase in liquid flow as the carrying phase. In the 40–50 Hz regimes, there is a decrease in the aerator ejection coefficient (Figure 11), which is an indication of insufficient gas phase inflow due to the design limitations of the aerator. At the same time, significant pressure and velocity pulsations may occur in the jet, which lead to an increase in the jet angle and deviation of the edge contour. In general, the jet velocity can be predicted from the balance of the liquid Q_{liq} and gas Q_{gas} flow rates. Since these flow rates are measured directly (see Figure 11), the velocity can be approximated as $\frac{Q_{gas}+Q_{liq}}{A_{nozzle}}$, where A_{nozzle} is the nozzle cross-sectional area. This estimation is averaged over time and space and does not take into account the local influence of the wall roughness, bubble size, and structure on the hydraulic resistance of the flow. It also does not take into account the slip velocities between the bubbles and the fluid. Earlier, in work [13], it was shown that in a relevant bubble descent flow, the slip velocity can reach 10% of the liquid phase velocity. However, this is a good, physically reasonable approach for the verification of the computer vision method. Comparing the jet velocity from CV measurements and the predicted velocity based on the conservation principle (blue and orange curves in Figure 11), one can see a difference not exceeding 15%.

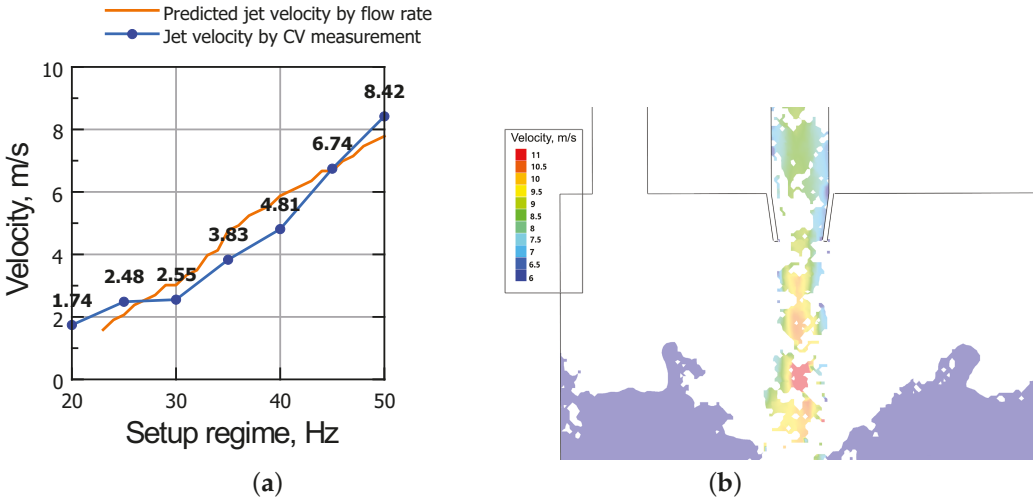


Figure 17. (**a**) Average jet velocity for different setup operation regimes, by CV measurement and predicted from flow rate balance, versus (**b**) results of CFD simulation of the velocity field in the lengthwise cross-section of the jet at the setup regime of 50 Hz.

Earlier, CFD simulations using the FlowVision software [53] of the jet flow in the unit were performed for the 50 Hz mode and showed liquid flow velocities from 8.5 m/s at the edges of the jet to 11 m/s in the center of the jet (see Figure 17b). Taking into account such a convex velocity profile, and the fact that the proposed computer vision method works only with the jet surface, we note the good correspondence of the obtained velocity measurement results with the results of CFD simulations.

These conclusions can be considered as verification of the developed algorithm.

Using the represented methodology, we were able to determine the optimal operating mode of the experimental setup in terms of maximizing the specific impulse per unit volume of the gas–liquid jet. This mode corresponds to the minimum jet angle and edge deviation and maximum flow velocity. In the case of industrial fermenters, the comparison of CV measurements and averaged predictions of gas and liquid flow rates at the aerator inlet allows the localization of anomalous modes of jet formation (e.g., due to design defects in the aerator or equipment wear during operation). The flexibility of the methodology that we propose is limited by the possibilities of verification. For each new jet stream apparatus, it is necessary to calibrate the computer vision method in order to obtain adequate results.

4. Conclusions

The methods of threshold segmentation, active contours, the regression of principal components, and the comparison of feature overlays made it possible to implement a scheme for the calculation of the jet stream angles, edge deviations, and velocities of gas–liquid jets for various video data and operating modes of the experimental setup.

The comparison of experimental data and modeling with computer vision calculations showed that the velocity estimates were close and the differences did not exceed 15%. Moreover, the CV measurements were consistent with third-party CFD calculations. At the same time, edge detection was found to be quite accurate and stable even with noisy data and a rough initial approximation in the form of a segment for all frames of one video recording. The comparison of the proposed algorithm with the results of partitioning using the classical Canny method yielded an RMS error of no more than 0.07 pixels. At the same time, the Canny method loses robustness when jet droplets break away and therefore requires resource-intensive image preprocessing. The proposed algorithm does not demonstrate this problem.

Test CV measurements have shown that the real jet in the apparatus may have asymmetric angles for the left and right boundaries. In addition, the environment inside the apparatus (foggy with high light scattering) leads to noise in the original data images. The

robustness of the proposed algorithm allows us to handle such data while maintaining sufficient accuracy.

The presented algorithms for the evaluation of jet characteristics by computer vision methods based on high-speed video records currently have a number of limitations. First, the efficiency of the algorithms (in terms of accuracy and stability) depends on the quality of the original image. The presence of splashes, blur, low or uneven image contrast, and the excessive illumination of certain areas affects the accuracy of the final result. This leads to the need to carefully choose the video shooting point, the type of lighting (front or back), and its intensity. Image preprocessing methods also require further research. In particular, it is obvious that for the automatic selection of structures whose interframe shift is estimated in the flow velocity measurement algorithm, it is necessary to use an adaptive threshold during binarization, as well as histogram intensity equalization algorithms in the jet image region.

In addition, it was found that the jet structure, which depends on the gas content, local velocities, and bubble sizes, as well as aerator operation features, can significantly affect the flow velocity profile in the jet. When a flow core with significantly higher velocities is formed in the center of the jet rather than near the walls, the CV algorithm can significantly underestimate the velocity values compared to the average cross-sectional velocity value.

The absence of a dependency on hardware and software and the great potential for the optimization of the program code make it possible to use the proposed method "in real time", directly during experiments and in industrial processes.

Author Contributions: Conceptualization, I.S. and P.M.; methodology, F.B., S.S., P.M., I.S. and T.M.; software, P.M., S.S. and M.N.; formal analysis, I.S. and P.M.; investigation, I.S., P.M., T.M. and K.M.; resources, F.B. and I.D.; data curation, T.M. and P.M.; writing—original draft preparation, I.S., S.S. and P.M.; writing—review and editing, I.S., I.N., P.M., S.S. and K.M.; visualization, P.M., I.S. and K.M.; supervision, F.B. and I.S.; project administration, I.S., D.C. and F.B.; funding acquisition, I.S., F.B., D.C. and I.N. All authors have read and agreed to the published version of the manuscript.

Funding: The research funding from the Ministry of Science and Higher Education of the Russian Federation (Ural Federal University Program of Development within the Priority-2030 Program) is gratefully acknowledged.

Data Availability Statement: Data are contained within the article.

Conflicts of Interest: D.C. is an employee of NPO Biosintez Ltd. Other authors declare no conflict of interest.

References

1. Geilert, P.; Heinzel, C.; Wagner, A. Grinding Fluid Jet Characteristics and Their Effect on a Gear Profile Grinding Process. *Inventions* **2017**, *2*, 27. [CrossRef]
2. Lightstone, M.; Koshy, P.; Tullis, S. High-coherence jets for focused fluid delivery in grinding. *CIRP Ann.* **2021**, *70*, 293–296. [CrossRef]
3. Hatami Farzaneh, O.; Adibi, H.; Rezaei, S.M. Evaluation of the grinding process utilizing an auxiliary compressed air jet on cleaning the grinding wheel surface. *Proc. Inst. Mech. Eng. Part J. Process. Mech. Eng.* **2023**, *237*, 740–752. [CrossRef]
4. Hocheng, H.; Tsai, H.; Chang, K. Water Jet Machining. *Adv. Anal. Nontradit. Mach.* **2013**, 359–401. [CrossRef]
5. Kong, C. Water-jet cutting. *Cirp Encycl. Prod. Eng.* **2014**, 1298–1311.
6. Cumpsty, N.; Heyes, A. *Jet Propulsion*; Cambridge University Press: Cambridge, UK, 2015.
7. Balz, R.; Bernardasci, G.; von Rotz, B.; Sedarsky, D. Influence of nozzle geometry on spray and combustion characteristics related to large two-stroke engine fuel injection systems. *Fuel* **2021**, *294*, 120455. [CrossRef]
8. Batraev, I.; Prokhorov, E.; Ul'yanitskii, V.Y. Acceleration of Dispersed Particles by Gas Detonation Productions in an Expanding Channel. *Combust. Explos. Shock Waves* **2021**, *57*, 588–596. [CrossRef]
9. Chen, W.; Pan, J.; Liu, Y.; Fan, B.; Liu, H.; Otchere, P. Numerical investigation of direct injection stratified charge combustion in a natural gas-diesel rotary engine. *Appl. Energy* **2019**, *233*, 453–467. [CrossRef]
10. Fossett, H. The action of free jets in mixing of fluids. *Trans. Inst. Chem. Eng.* **1951**, *29*, 322–332.
11. Kalaichelvi, P.; Swarnalatha, Y.; Raja, T. Mixing time estimation and analysis in a jet mixer. *Arpn J. Eng. Appl. Sci.* **2007**, *2*, 35–43.

12. Starodumov, I.; Nizovtseva, I.; Lezhnin, S.; Vikharev, S.; Svitich, V.; Mikushin, P.; Alexandrov, D.; Kuznetsov, N.; Chernushkin, D. Measurement of Mass Transfer Intensity in Gasn-Liquid Medium of Bioreactor Circuit Using the Thermometry Method. *Fluids* **2022**, *7*, 366. [CrossRef]
13. Nizovtseva, I.; Starodumov, I.; Schelyaev, A.; Aksenov, A.; Zhluktov, S.; Sazonova, M.; Kashinsky, O.; Timkin, L.; Gasenko, V.; Gorelik, R.; et al. Simulation of two-phase air–liquid flows in a closed bioreactor loop: Numerical modeling, experiments, and verification. *Math. Methods Appl. Sci.* **2022**, *45*, 8216–8229. [CrossRef]
14. Du Cluzeau, A.; Bois, G.; Leoni, N.; Toutant, A. Analysis and modeling of bubble-induced agitation from direct numerical simulation of homogeneous bubbly flows. *Phys. Rev. Fluids* **2022**, *7*, 044604. [CrossRef]
15. Yan, P.; Jin, H.; He, G.; Guo, X.; Ma, L.; Yang, S.; Zhang, R. Numerical simulation of bubble characteristics in bubble columns with different liquid viscosities and surface tensions using a CFD-PBM coupled model. *Chem. Eng. Res. Des.* **2020**, *154*, 47–59. [CrossRef]
16. Hoque, M.M.; Joshi, J.B.; Evans, G.M.; Mitra, S. A critical analysis of turbulence modulation in particulate flow systems: A review of the experimental studies. *Rev. Chem. Eng.* **2023**. [CrossRef]
17. Prasser, H.M.; Häfeli, R. Signal response of wire-mesh sensors to an idealized bubbly flow. *Nucl. Eng. Des.* **2018**, *336*, 3–14. [CrossRef]
18. Guseva, E.M.N.; Safarov, R.; Boudrant, J. An approach to modeling, scaling and optimizing the operation of bioreactors based on computational fluid dynamics. *Int. J. Softw. Prod. Syst.* **2015**, *112*, 249–255.
19. Petersen, L.A.; Villadsen, J.; Jørgensen, S.B.; Gernaey, K.V. Mixing and mass transfer in a pilot scale U-loop bioreactor. *Biotechnol. Bioeng.* **2017**, *114*, 344–354. [CrossRef]
20. Krychowska, A.; Kordas, M.; Konopacki, M.; Grygorcewicz, B.; Musik, D.; Wójcik, K.; Jędrzejczak-Silicka, M.; Rakoczy, R. Mathematical modeling of hydrodynamics in bioreactor by means of CFD-based compartment model. *Processes* **2020**, *8*, 1301. [CrossRef]
21. Yao, Y.; Fringer, O.B.; Criddle, C.S. CFD-accelerated bioreactor optimization: Reducing the hydrodynamic parameter space. *Environ. Sci. Water Res. Technol.* **2022**, *8*, 456–464. [CrossRef]
22. Panunzi, A.; Moroni, M.; Mazzelli, A.; Bravi, M. Industrial Case-Study-Based Computational Fluid Dynamic (CFD) Modeling of Stirred and Aerated Bioreactors. *ACS Omega* **2022**, *7*, 25152–25163. [CrossRef]
23. Ramírez, L.A.; Pérez, E.L.; García Díaz, C.; Camacho Luengas, D.A.; Ratkovich, N.; Reyes, L.H. CFD and Experimental Characterization of a Bioreactor: Analysis via Power Curve, Flow Patterns and k L a. *Processes* **2020**, *8*, 878. [CrossRef]
24. Cappello, V.; Plais, C.; Vial, C.; Augier, F. Scale-up of aerated bioreactors: CFD validation and application to the enzyme production by Trichoderma reesei. *Chem. Eng. Sci.* **2021**, *229*, 116033. [CrossRef]
25. Sato, Y.; Sekoguchi, K. Liquid velocity distribution in two-phase bubble flow. *Int. J. Multiph. Flow* **1975**, *2*, 79–95. [CrossRef]
26. Wang, S.; Lee, S.; Jones, O., Jr.; Lahey, R., Jr. 3-D turbulence structure and phase distribution measurements in bubbly two-phase flows. *Int. J. Multiph. Flow* **1987**, *13*, 327–343. [CrossRef]
27. Ohba, K.; Yuhara, T.; Matsuyama, H. Simultaneous measurements of bubble and liquid velocities in two-phase bubbly flow using laser Doppler velocimeter. *Bull. JSME* **1986**, *29*, 2487–2493. [CrossRef]
28. Xu, Y.; Luo, L.; Yuan, J. CFD simulations to portray the bubble distribution and the hydrodynamics in an annulus sparged air-lift bioreactor. *Can. J. Chem. Eng.* **2011**, *89*, 360–368. [CrossRef]
29. Haringa, C.; Tang, W.; Wang, G.; Deshmukh, A.T.; van Winden, W.A.; Chu, J.; van Gulik, W.M.; Heijnen, J.J.; Mudde, R.F.; Noorman, H.J. Computational fluid dynamics simulation of an industrial P. chrysogenum fermentation with a coupled 9-pool metabolic model: Towards rational scale-down and design optimization. *Chem. Eng. Sci.* **2018**, *175*, 12–24. [CrossRef]
30. Buffo, M.; Corrêa, L.; Esperança, M.; Cruz, A.; Farinas, C.; Badino, A. Influence of dual-impeller type and configuration on oxygen transfer, power consumption, and shear rate in a stirred tank bioreactor. *Biochem. Eng. J.* **2016**, *114*, 130–139. [CrossRef]
31. Voulodimos, A.; Doulamis, N.; Doulamis, A.; Protopapadakis, E. Deep Learning for Computer Vision: A Brief Review. *Comput. Intell. Neurosci.* **2018**, *2018*, 7068349. [CrossRef]
32. O'Mahony, N.; Campbell, S.; Carvalho, A.; Harapanahalli, S.; Hernandez, G.V.; Krpalkova, L.; Riordan, D.; Walsh, J. Deep learning vs. traditional computer vision. In *Advances in Computer Vision: Proceedings of the 2019 Computer Vision Conference (CVC)*; Springer: Berlin/Heidelberg, Germany, 2020; pp. 128–144.
33. Zhu, J.; Pan, L.; Zhao, G. An Improved Near-Field Computer Vision for Jet Trajectory Falling Position Prediction of Intelligent Fire Robot. *Sensors* **2020**, *20*, 7029. [CrossRef]
34. Shafizadeh, A.; Shahbeig, H.; Nadian, M.H.; Mobli, H.; Dowlati, M.; Gupta, V.K.; Peng, W.; Lam, S.S.; Tabatabaei, M.; Aghbashlo, M. Machine learning predicts and optimizes hydrothermal liquefaction of biomass. *Chem. Eng. J.* **2022**, *445*, 136579. : 10.1016/j.cej.2022.136579 [CrossRef]
35. Ignacz, G.; Alqadhi, N.; Szekely, G. Explainable machine learning for unraveling solvent effects in polyimide organic solvent nanofiltration membranes. *Adv. Membr.* **2023**, *3*, 100061. : 10.1016/j.advmem.2023.100061 [CrossRef]
36. Mann, V.; Venkatasubramanian, V. AI-driven hypergraph network of organic chemistry: Network statistics and applications in reaction classification. *React. Chem. Eng.* **2023**, *8*, 619–635. [CrossRef]
37. Yu, S.I.; Rhee, C.; Cho, K.H.; Shin, S.G. Comparison of different machine learning algorithms to estimate liquid level for bioreactor management. *Environ. Eng. Res.* **2023**, *28*, 220037. [CrossRef]

38. Nizovtseva, I.; Palmin, V.; Simkin, I.; Starodumov, I.; Mikushin, P.; Nozik, A.; Hamitov, T.; Ivanov, S.; Vikharev, S.; Zinovev, A.; et al. Assessing the Mass Transfer Coefficient in Jet Bioreactors with Classical Computer Vision Methods and Neural Networks Algorithms. *Algorithms* **2023**, *16*, 125. [CrossRef]
39. Biessey, P.; Bayer, H.; Theßeling, C.; Hilbrands, E.; Grünewald, M. Prediction of bubble sizes in bubble columns with machine learning methods. *Chem. Ing. Tech.* **2021**, *93*, 1968–1975. [CrossRef]
40. Hessenkemper, H.; Starke, S.; Atassi, Y.; Ziegenhein, T.; Lucas, D. Bubble identification from images with machine learning methods. *Int. J. Multiph. Flow* **2022**, *155*, 104169. [CrossRef]
41. Nizovtseva, I.G.; Starodumov, I.O.; Lezhnin, S.I.; Mikushin, P.V.; Zagoruiko, A.N.; Shabadrov, P.A.; Svitich, V.Y.; Vikharev, S.V.; Tatarintsev, V.V.; Nikishina, M.A.; et al. Influence of the gas–liquid non-equilibrium media structure on the mass transfer dynamics in biophysical processes. *Smart Mater. Struct.* **2023**, *33*, 015028. [CrossRef]
42. Bravo, L.; Kweon, C.B. A Review on Liquid Spray Models for Diesel Engine Computational Analysis. In *Army Research Laboratory Technical Report Series, ARL-TR-6932*; Army Research Laboratory: Aberdeen Proving Ground, MD, USA, 2014.
43. Westerweel, J.; Hofmann, T.; Fukushima, C.; Hunt, J. The turbulent/non-turbulent interface at the outer boundary of a self-similar turbulent jet. *Exp. Fluids* **2002**, *33*, 873–878. [CrossRef]
44. Ibarra, E.; Shaffer, F.; Savaş, Ö. On the near-field interfaces of homogeneous and immiscible round turbulent jets. *J. Fluid Mech.* **2020**, *889*, A4. [CrossRef]
45. Carrillo, J.M.; Ortega, P.R.; Castillo, L.G.; García, J.T. Experimental characterization of air entrainment in rectangular free falling jets. *Water* **2020**, *12*, 1773. [CrossRef]
46. Cordova, Y.; Rivera, Y.; Blanco, D.; Berna, C.; Muñoz-Cobo, J.L.; Escrivá, A. Experimental investigation of submerged horizontal air–steam mixture jets into stagnant water. *Wit Trans. Eng. Sci.* **2020**, *128*, 89–101.
47. Shapiro, L.; Stockman, G. *Computer Vision*; Prentice Hall: Hoboken, NJ, USA, 2000; p. 608.
48. Sokolov, S.Y.; Volchkov, S.; Bessonov, I.; Chestukhin, V.; Kurlyandskaya, G.; Blyakhman, F. Estimation of blood flow velocity in coronary arteries based on the movement of radiopaque agent. *Pattern Recognit. Image Anal.* **2019**, *29*, 750–762. [CrossRef]
49. Kass, M.; Witkin, A.; Terzopoulos, D. Snakes: Active contour models. *Int. J. Comput. Vis.* **1988**, *1*, 321–331. [CrossRef]
50. Jolliffe, I.T. A note on the use of principal components in regression. *J. R. Stat. Soc. Ser. Appl. Stat.* **1982**, *31*, 300–303. [CrossRef]
51. Sokolov, S.Y. Improving the accuracy and stability of the speckle tracking technique in processing images obtained in echocardiographic examinations. *Pattern Recognit. Image Anal.* **2013**, *23*, 536–540. [CrossRef]
52. Sokolov, S.; Grinko, A.; Tourovskaia, A.; Reitz, F.; Yakovenko, O.; Pollack, G.; Blyakhman, F. "Minimum average risk" as a new peak-detection algorithm applied to myofibrillar dynamics. *Comput. Methods Programs Biomed.* **2003**, *72*, 21–26. [CrossRef]
53. Aksenov, A.A. Flowvision: Industrial computational fluid dynamics. *Comput. Res. Model.* **2017**, *9*, 5–20. [CrossRef]

Disclaimer/Publisher's Note: The statements, opinions and data contained in all publications are solely those of the individual author(s) and contributor(s) and not of MDPI and/or the editor(s). MDPI and/or the editor(s) disclaim responsibility for any injury to people or property resulting from any ideas, methods, instructions or products referred to in the content.

inventions

MDPI

Article

Numerical Study of the Influence of the Type of Gas on Drag Reduction by Microbubble Injection

Hai An *, Po Yang, Hanyu Zhang and Xinquan Liu

College of Aerospace and Civil Engineering, Harbin Engineering University, Harbin 150001, China
* Correspondence: anhai@hrbeu.edu.cn

Abstract: In this work, a novel numerical method for studying the influence of gas types on drag reduction by microbubble injection is presented. Aimed at the microbubble drag reduction (MBDR) process for different types of gases, the mass transfer velocity of different types of gases in the gas–liquid phase is defined by writing a user-defined function (UDF), which reflected the influence of gas solubility on the drag reduction rate. An Eulerian multiphase flow model and the Realizable $k-\varepsilon$ turbulence model are used for numerical calculation. The population balance model is used to describe the coalescence and breakup phenomena of the microbubble groups. Henry's theorem is used to calculate the equilibrium concentration of the microbubble mixed flow. The interphase mass transfer rate of the microbubble injection process for different types of gases is studied by using permeation theory. The local mass fraction of the mixed flow is solved by the component transport equation. It is found that the larger the solubility of the gas, the lower the efficiency of MBDR. When the volume flow rate of the same type of gas is the same but the injection speed is different, the larger the solubility of the gas is, the greater the difference in the drag reduction ratio.

Keywords: numerical study; type of gas; microbubble drag reduction; interphase mass transfer rate; drag reduction ratio

1. Introduction

Microbubble drag-reduction technology is a new powerful means of ship energy saving and emission reduction. Gas is injected into the boundary layer covering the ship bottom from a series of slots, nozzles, openings, or porous material flush with the surface designed to generate a bubble stream, so the flow downstream of the nozzles or outlets will form a mixture of microbubbles and water to reduce the skin-friction drag of the hull. The buoyancy of the bubbles pushes them towards the bottom of the hull within the turbulent boundary layer, and the ship motion sweeps them aft. Research [1] has been carried out into the effect of injected bubble size and it has been proposed from laboratory tests that relatively small bubble diameter (0.3–0.5 mm) gives the best results. The drag reduction rate of microbubbles is generally about 25% [2], which can effectively reduce the power consumption of the ship's main engine. The surface vehicle can directly use air injection to form microbubbles, while the underwater vehicle can only choose other types of gas injection due to its isolation from the air. Therefore, the study of the influence of gas type on the efficiency of MBDR is of great significance for the reduction in skin friction drag of underwater vehicles.

It is generally believed that the mechanism of MBDR is the change in velocity gradient of the turbulent boundary layer caused by gas injection, which reduces the viscosity and density of local fluid, and thus reduces the turbulent kinetic energy and shear stress between water and wall [3]. Moreover, the type of injected gas is also an important factor in microbubble drag reduction. McCormick [4] reduced the viscous drag of a fully submerged rotating body by producing hydrogen gas on the hull by electrolysis. The experimental results showed that hydrogen microbubbles are very effective in reducing drag. Pal [5]

used flush-mounted hot-film probes to measure the shear stress fluctuations when air and helium were injected into the turbulent boundary layer, respectively. Deutsch and Castano [6] measured the skin friction drag after gas injection into a turbulent boundary layer of a submerged axisymmetric body. It was found that the reduction in skin friction reduction increases with increasing free-stream speed. At high speeds, helium injection is more effective at reducing skin friction than air injection. Fontaine and Deutsch [7] measured the effects of five different gases—air, helium, carbon dioxide, argon, and sulfur hexafluoride—on the microbubble skin friction reduction on an axisymmetric model. It was found that Sulfur hexafluoride is less effective in reducing drag, and helium has a better drag reduction effect than other gases. Deutsch [8] used carbon dioxide as an injection to carry out experiments and studied the influence of surface roughness on microbubble drag reduction. The study took advantage of the solubility of carbon dioxide, which can minimize problems with mean velocity measurements and optical access. Zhu [9] proposed a novel self-adaptive microbubble electrolysis control technique for the problem of stable, high-efficiency flow drag reduction for underwater vehicles. The flow drag reduction performance and mechanisms of microbubble arrays were investigated by experimental and numerical methods. Skudarnov [10] introduced CO_2 gas as a species mass source and used numerical methods to assess the role of mixture density variation of microbubbles on the drag reduction rate. The numerical model proposed in the study only considered the convective diffusion process between injected gas and water and did not consider the interphase mass transfer process between soluble gas CO_2 and water during microbubble injection.

Numerical simulation is an effective method to study the microbubble drag reduction mechanism. For the turbulent motion with a low Reynolds number, more accurate results can be obtained by direct numerical simulation. Mattson and Mahesh [11] presented the results from a one-way coupled, Euler–Lagrange direct numerical simulation of bubbles injected into a turbulent boundary layer. By analyzing the forces on the bubble, it was found that the carrier-fluid acceleration is the main reason for moving the bubbles away from the wall. Pang et al. [12] established the Euler–Lagrange two-way coupling model and carried out a numerical study on MBDR of the flat plate. Direct numerical simulation was used to solve the velocity field of the liquid, and the Newton equation of motion was used to calculate the bubble trajectory. Rawat et al. [13] numerically studied the interaction between a dispersed phase composed of microbubbles and a turbulent boundary layer flow. The Euler–Lagrange approach based on Direct Numerical Simulation of the continuous phase flow equations and a Lagrange tracking for the dispersed phase were used. The feedback effect of dispersed bubbles on the carrying flow was considered in this study. The local and temporal variations of bubble concentration and momentum source terms were considered in the mass and momentum balance equations. Velasco et al. [14] used the Euler–Lagrange approach and the bidirectional coupling direct numerical simulation method to study the interaction between microbubbles and turbulence in vertical upward channel flow.

For the numerical study of the turbulent motion with a high Reynolds number, a suitable turbulence model is usually chosen to solve the governing equation. Aiming at the drag reduction process using microbubbles, it is one of the main research methods to establish the microbubble coalescence and fragmentation models. Mohanarangam et al. [15] studied MBDR of two-dimensional plates using multi-size groups (MUSIG) based on population balance models. The model took into account the interphase drag and focused on the effect of bubble coalesce and breakup on MBDR. Wei [16] used Euler–Euler two-phase flow model to simulate MBDR on a bulk carrier. The model considered the interphase resistance, but ignored the influence of bubble deformation, coalescence and breakup. Pang and Zhang [17] used a mixture multiphase flow model combined with the population balance model to study MBDR of horizontal channel turbulence, and the model described the coalescence and breakup phenomena of the bubble groups. Qin et al. [18] simulated the bubbly flow along the flat plate based on Eulerian–Eulerian

two-fluid modeling combined with a population balance model. Bubble coalescence and breakup were considered and drag and lift were fully modeled based on applicable closure models. Zhang et al. [19] proposed an Euler–Lagrange model that can simulate bubble coalescence and breakup. The bubble-size distribution, the bubble trajectory, and the mechanism of bubble induced turbulence modulation and its relationship with bubble-size distribution were analyzed. For other methods of microbubble drag reduction, Lyu et al. [20] proposed a gas–liquid two-phase flow model based on the mixed-flow model, and numerically simulated the MBDR process of the SUBOFF rotating model. Wang et al. [21] used a two-way coupled Euler–Lagrange approach based on a large eddy simulation to study the MBDR mechanism in a fully developed turbulent boundary layer over a flat-plate. Zhao et al. [22] used an OpenFOAM frame to study the two-phase micro-bubble flow over an axisymmetric body. The numerical models included an Eulerian–Eulerian two-fluid model with closure relationships for the interfacial momentum transfer to capture the interfacial momentum transfer of multiphase flows, and a standard $k-\varepsilon$ model for the continuous phase and one turbulence model inside the OpenFOAM for the dispersed phase. Wang [23] numerically studied MBDR by using a flat-plate model, and compared the relationship between the Eulerian multiphase flow model and the mixed multiphase flow model. The results indicated that the mixed multiphase flow model requires less mesh than the Eulerian multiphase flow model. Eulerian multiphase flow model has high calculation accuracy, but long calculation time and poor convergence. The calculation time of the mixed multiphase flow model is short, the convergence is good, but the error is large.

So far, no similar numerical method for MBDR considering gas solubility has been found in the published literature. In this work, by writing UDF in fluent fluid software, the mass transfer velocity of different types of gases in the gas–liquid phase is defined, and the influence of gas types on MBDR is studied. The types of gases selected are air, carbon dioxide, helium and argon. The Euler multiphase flow model and Realizable $k-\varepsilon$ turbulence model are used to describe the turbulence problems of microbubble drag reduction caused by gas injection on an axisymmetric body. The population balance model is used to describe the coalescence and breakup of bubbles. Henry theorem is used to calculate the equilibrium concentration of the microbubble mixed flow. The mass transfer coefficient is based on the K_{L} model which combines the Higbie permeation theory and the velocity slip model. The local mass fraction of the mixed flow is solved by the convection–diffusion equation. Finally, the drag reduction ratio of microbubble injection for different types of gases is calculated numerically according to some working conditions of the water tunnel experiment, and the influence of the solubility of different types of gas on the drag reduction rate during the process of microbubble injection is analyzed by comparing with the experimental data, and the correctness of the numerical models proposed is verified.

2. Numerical Simulation Scheme and Physical Model

In this section, the numerical simulation scheme and the physical model are proposed based on the partial experimental conditions of the water tunnel experiment conducted by Fontaine and Deutsch [7] in a 12-inch diameter water tunnel at ARL Penn State, in which the influence of the type of gas on the reduction in skin friction resistance by microbubble injection is investigated.

2.1. Establishment of the Water Tunnel Experiment [7] and Numerical Simulation Scheme

The water tunnel experiment was carried out in the cylindrical experimental section of the water tunnel. The experimental model was an axisymmetric vehicle 632 mm long and 89 mm in diameter. The model was held in the center of the cylindrical section by a 200 mm long sting. In the experiment, an isolated cylindrical section with shear members was used as a force balance to measure the skin friction. The balance was 273 mm long with nominal gaps of 0.127 mm and 0.254 mm located at axial distances of 196 and 469 mm from the nose, respectively. The gas was injected by a cylindrical sintered porous plastic section 6.35 mm long and 5.17 mm thick with a nominal pore size of 5 microns. The gas injection

section is 146.5 mm from the nose. The experimental model was installed as shown in Figure 1. All gases in the experiment were supplied from a compressed gas cylinder and the volume flow rate through the injection system was controlled at a nearly constant rate by using a Kates control valve (Kates, model 6BIT-DEJ).

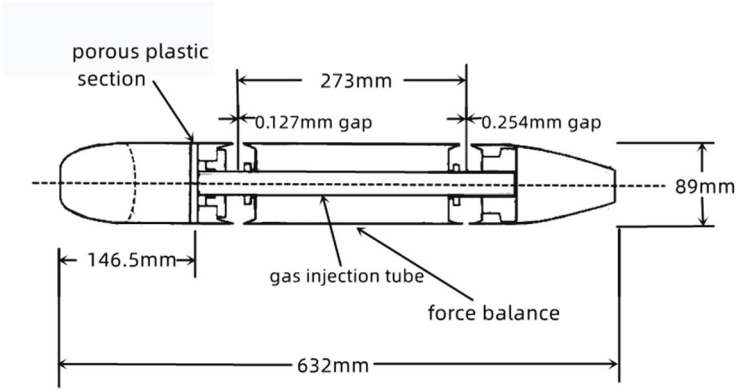


Figure 1. Schematic diagram of the experimental model.

In the numerical simulation scheme, four types of gas with relatively complete experimental data in the water tunnel experiment—air, helium, argon and carbon dioxide—are selected as gas injection sources to obtain a wide range of the solubility values of gas. The chosen experimental parameters consist of a water tunnel pressure set at 15 psi, a free-stream speed maintained at 13.7 m/s, and the gas volume flow rate representing certain conditions within the water tunnel, serving as the basis for numerical simulation. By comparing the numerical results with the experimental data, the difference between the numerical results and the experimental data during the drag reduction process of microbubble injection of different types of gases is analyzed, and the influence of the solubility of gas on drag reduction is found out. It should be emphasized that in the water tunnel experiment in reference [7], gas was injected through the porous plastic section. Since the opening holes ratio of the plastic section (area of gas injection holes/total area of the gas injection section) is not provided, the speed of gas injection cannot be determined. Therefore, the numerical calculation of this study can only ensure that the volume flow rate of gas injection is the same as that of the water tunnel experiment but cannot guarantee that the gas injection speed is the same as that of the experiment. As a result, when the volume flow rate of gas injection is small, the drag reduction ratio in numerical simulation is greatly different from the experimental data due to the influence of gas injection speed and gas solubility.

2.2. Physical Model Description

The physical model of the vehicle used in the numerical study is designed in full accordance with the model size in the water tunnel experiment [7], as shown in Figure 2. The model is a symmetrical rotary body, and the gas injection section is 146.5 mm from the nose of the model. The measuring section of the skin friction drag is 273 mm long and is located at the axial distances of 196 mm and 469 mm from the nose, respectively. The model parameters are shown in Table 1.

Table 1. Model parameter.

Model Length L (mm)	Diameter of the Model D (mm)	Location of Gas Injection L1 (mm)
632	89	146.5

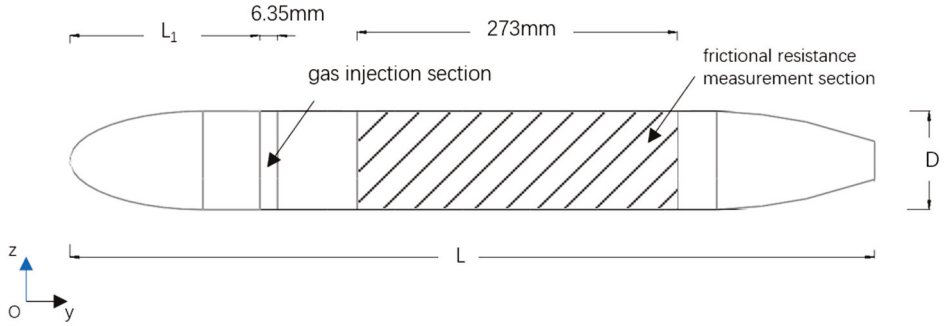


Figure 2. Physical model of the vehicle.

3. Numerical Model Study

3.1. Governing Equations

In this study, the Eulerian multiphase flow model is used to simulate the gas–liquid two-phase flow. Compared with the mass conservation of a single phase, the mass change in one phase in the control body increases the mass transfer phase between the phases. So, the continuity equation of the qth phase is:

$$\frac{\partial}{\partial t}(\alpha_q \rho_q) + \nabla \cdot \left(\alpha_q \rho_q \vec{v}_q\right) = \sum_{p=1}^{n} (\dot{m}_{pq} - \dot{m}_{qp}) + S_q, \tag{1}$$

where α_q represents the gas phase volume fraction of the qth phase, ρ_q represents the density of the qth phase, $\vec{v}_q$ represents the velocity of the qth phase, $\dot{m}_{pq}$ represents the mass transfer from the pth phase to the qth phase, S_q represents source term.

The momentum equation of the qth phase is:

$$\begin{gathered}\frac{\partial}{\partial t}(\alpha_q \rho_q \vec{v}_q) + \nabla \cdot (\alpha_q \rho_q \vec{v}_q \vec{v}_q) = -\alpha_q \nabla p + \nabla \cdot \bar{\bar{\tau}}_q + \alpha_q \rho_q \vec{g} + \sum_{p=1}^{n} (\vec{R}_{pq} + \dot{m}_{pq} \vec{v}_{pq} - \dot{m}_{qp} \vec{v}_{qp}) \\ +(\vec{F}_{d,q} + \vec{F}_{lift,q} + \vec{F}_{vm,q} + F_{vol})\end{gathered}, \tag{2}$$

where $\bar{\bar{\tau}}_q$ is the stress tensor of the qth phase, which can be expressed as:

$$\bar{\bar{\tau}}_q = \alpha_q \mu_q \left(\nabla \vec{v}_q + \nabla \vec{v}_q^T\right) + \alpha_q \left(\lambda_q - \frac{2}{3}\mu_q\right)\left(\nabla \cdot \vec{v}_q\right)\bar{\bar{I}}, \tag{3}$$

where μ_q represents the shear viscosity of the qth phase, λ_q represents the bulk viscosity of the qth phase, $\vec{F}_{d,q}$ represents drag force, $\vec{F}_{lift,q}$ represents lift, $\vec{F}_{vm,q}$ represents virtual mass force, F_{vol} represents surface tension, $\vec{R}_{pq}$ represents the interaction force between phases, $\vec{v}_{pq}$ represents inter-phase velocity.

In Eulerian model, the phases are seen as representing a continuum that runs through each other, so the volume fraction is needed to represent the space occupied by the phases in the control body. The sum of all phase volume fractions is 1, which can be expressed as:

$$\sum_{q=1}^{n} \alpha_q = 1. \tag{4}$$

3.2. Turbulence Model

In this study, the turbulence model is selected as the Realizable $k-\varepsilon$ model [24]. The model can provide a more accurate prediction of the divergence ratio of the plate and cylindrical jets. Among all $k-\varepsilon$ models, this model has a good performance for flow separation and complex secondary flows. The model is suitable for a wide range of flow types, including the rotational uniform shear flow, the free flow (jet and mixed layer), the

cavity flow and the boundary layer flow. The transport equations of turbulent kinetic energy and dissipation rate of the Realizable $k-\varepsilon$ model are:

$$\frac{\partial}{\partial t}(\rho k)+\frac{\partial}{\partial x_j}(\rho k u_j)=\frac{\partial}{\partial x_j}\left[\left(\mu+\frac{\mu_t}{\sigma_k}\right)\frac{\partial k}{\partial x_j}\right]+G_k+G_b-\rho\varepsilon-Y_m+S_k, \tag{5}$$

$$\frac{\partial}{\partial t}(\rho \varepsilon)+\frac{\partial}{\partial x_j}(\rho \varepsilon u_j)=\frac{\partial}{\partial x_j}\left[\left(\mu+\frac{\mu_t}{\sigma_\varepsilon}\right)\frac{\partial \varepsilon}{\partial x_j}\right]+\rho C_1 S\varepsilon-\rho C_2\frac{\varepsilon^2}{k+\sqrt{v\varepsilon}}-C_{1\varepsilon}\frac{\varepsilon}{k}C_{3\varepsilon}G_b+S_\varepsilon, \tag{6}$$

where G_k represents the turbulent kinetic energy caused by the mean velocity gradient, G_b represents the turbulent kinetic energy caused by buoyancy, Y_m represents the influence of turbulent pulsating flow on the total dissipation rate, μ_t represents turbulence viscosity coefficient, $\mu_t=\rho C_\mu\frac{k^2}{\varepsilon}$. σ_k, σ_ε represents the turbulent Prandtl numbers of the turbulent kinetic energy and the dissipation rate, respectively. C_1, C_2, $C_{1\varepsilon}$,$C_{3\varepsilon}$ represents the coefficient, respectively.

3.3. Interphase Force

3.3.1. Drag Force

The drag force $\vec{F}_{d,q}$ is the drag generated when a discrete gas moves relative to a fluid, which is simulated by the Schiller–Naumann interphase drag force model [25] in this study. Assuming the bubble is spherical, the drag coefficient C_d is defined:

$$C_d=\begin{cases}24(1+0.15\mathrm{Re}_g{}^{0.687})/\mathrm{Re}_g & \mathrm{Re}_g\le 1000\\ 0.44\mathrm{Re}_g & \mathrm{Re}_g>1000\end{cases}, \tag{7}$$

where Re_g represents the bubble Reynolds number.

The drag force is calculated as follows:

$$F_{d,q}=\frac{3}{4}C_d\alpha_p\frac{\rho_q}{d_p}(\vec{v}_q-\vec{v}_p)\times(\nabla\times\vec{v}_q), \tag{8}$$

where d_p represents the bubble diameter.

3.3.2. Lift

Lift force $\vec{F}_{lift,q}$ is the force caused by radial and circumferential velocity gradients; the magnitude is related to the relative velocity and the velocity curl of the fluid, and the direction is perpendicular to the relative velocity. In this study, it is assumed that the bubble is formless and has spherical fluid particles. The lift force is calculated as follows [26]:

$$\vec{F}_{lift,q}=C_l\rho_q\alpha_p(\vec{v}_q-\vec{v}_p)\times(\nabla\times\vec{v}_q), \tag{9}$$

where C_l represents the lift coefficient.

In this paper, the Legendar–Magnaudet [27] lift coefficient model is used, which takes into account the momentum transfer between the flow around the particles caused by fluid friction/stress at the fluid interface and the recirculation flow inside the fluid particles. The evolution of lift at low a Reynolds number is different from that at a high Reynolds number, and the expression of lift coefficient is:

$$C_l=\sqrt{(C_{l,lowRe})^2+(C_{l,highRe})^2}, \tag{10}$$

where

$$\begin{cases} C_{l,lowRe} = \frac{6}{\pi^2}(Re_p Sr)^{-0.5}\frac{2.55}{(1+0.2\frac{Re_p}{Sr})^{1.5}}, \\ C_{l,highRe} = \frac{1}{2} \times \frac{1+16Re_p^{-1}}{1+29Re_p^{-1}}, \end{cases} \tag{11}$$

where $Re_p = \frac{\rho_q|\vec{V}_q - \vec{V}_p|d_p}{\mu_q}$, $Re_\omega = \frac{\rho_q|\nabla \times \vec{V}_q|d_p^2}{\mu_p}$, $\beta = 0.5(Re_\omega / Re_p)$, Sr represents the dimensionless shear rate, $Sr = 2\beta \leq 1$.

3.3.3. Virtual Mass Force

In the calculation of multiphase flow, when the bubble accelerates or decelerates in the liquid, the surrounding liquid will be driven by the bubble to accelerate or decelerate, and the interphase force generated is called the virtual mass force. In the study, the virtual mass force $\vec{F}_{vm}$ is taken into account and expressed as:

$$\vec{F}_{vm,q} = C_{\mathrm{vm}}\alpha_p\rho_q \cdot \left(\frac{dqv_q}{dt} - \frac{dqv_p}{dt}\right), \tag{12}$$

where C_{vm} represents the virtual mass force coefficient. According to Magnaudet [28], the virtual mass force coefficient for spherical bubbles is close to 0.5.

3.3.4. Surface Tension

The attraction between molecules in the fluid creates the surface tension. Bubbles in the fluid are acted upon by neighboring molecules. On the surface of the bubble, the combined action of the radiating inward radial component makes the surface of the bubble shrink, thus increasing the pressure on the concave side of the surface. The surface tension can be given in terms of the pressure across the surface, using the divergence theorem, expressed as a volume force. If there are only two phases in a fluid unit, then the surface tension can be expressed as follows:

$$F_{vol} = \sigma_{qp}\frac{\rho\kappa_q\nabla\alpha_q}{\frac{1}{2}(\rho_q + \rho_p)}, \tag{13}$$

where σ_{qp} represents the tension coefficient between the qth phase and the pth phase, ρ represents the average volume density, κ_q representative surface curvature.

3.4. Population Balance Model

In this study, the population balance model is used to describe the coalescence and breakup of bubble groups. The population balance model takes the bubbles as discrete phases on a scale and solves the number density function of each group of bubbles. The smallest size of bubbles does not consider the breakup phenomenon, and the largest size of bubbles does not consider the coalescence phenomenon. For other sizes of bubbles, both coalescence and breakup are considered.

Yeoh et al. [29] proposed a generalized calculation model of population balance equation, which can be expressed as:

$$\frac{\partial n(v, \vec{x}, t)}{\partial t} + \nabla \cdot [\vec{u}_b(v, \vec{x}, t)n(v, \vec{x}, t)] = S(v, \vec{x}, t), \tag{14}$$

where $n(v, \vec{x}, t)$ represents the number density of bubbles, $\vec{u}_b(v, \vec{x}, t)$ representative bubble velocity, $S(v, \vec{x}, t)$ represents the source term of the coalescence and breakup of bubble groups, which can be defined as follows:

$$S(v,\vec{x},t)=\underbrace{\frac{1}{2}\int_0^v n(v-v',\vec{x},t)n(v',\vec{x},t)c(v-v',v')d\vec{\xi}'}_{\text{birth due to coalescence}}-\underbrace{n(v,\vec{x},t)\int_0^\infty n(v',\vec{x},t)c(v,v')dv'}_{\text{death due to coalescence}}+\underbrace{\int_v^\infty \gamma(v')n(v',\vec{x},t)b(v',v)\beta(v,v')dv'}_{\text{birth due to breakup}}-\underbrace{n(v,\vec{x},t)b(v,v')}_{\text{death due to breakup}}, \tag{15}$$

where $c(v,v')$ represents the coalescence rate of bubbles with volumes v and v', $b(v',v)$ represents the breakup rate at which the bubbles of volume v' break into the bubbles of volume v, $\gamma(v')$ represents the number of sub-bubbles of volume v', using binary decomposition, $\gamma(v')=2$. $\beta(v,v')$ represents the probability density function of the bubble of volume v' breaking into the bubble of volume v, which can be expressed as: $\beta(v,v')=\frac{30}{v'}\left(\frac{v}{v'}\right)^2\left(1-\frac{v}{v'}\right)^2$.

3.4.1. Luo Coalescence Model

The coalescence rate of bubbles will depend on coalescence efficiency and coalescence probability. Luo model [30] is adopted in this study, and the bubble coalescence rate can be expressed as:

$$c(v_i,v_j)=\omega(v_i,v_j)P(v_i,v_j), \tag{16}$$

where $\omega(v_i,v_j)$ representative collision frequency, which can be defined as follows:

$$\omega(v_i,v_j)=\frac{\pi}{4}\left({d_i}^2+{d_j}^2\right)n_i n_j\overline{u}_{ij}, \tag{17}$$

where $\overline{u}_{ij}$ represents the collision characteristic velocity of two bubbles with diameters d_i and d_j and densities n_i and n_j, $\overline{u}_{ij}=\left(\overline{u}_i^2+\overline{u}_j^2\right)^{1/2}$, $\overline{u}_i=1.43(\varepsilon d_i)^{1/3}$.

$P_{ag}(v_i,v_j)$ represents the probability that a collision will result in a convergence, and can be expressed as:

$$P=exp\left\{-c_3\frac{\left[\ 0.75\left(1+x_{ij}^2\right)\ \left(1+x_{ij}^3\right)\ \right]^{1/2}}{(\rho_2/\rho_1+0.5)^{1/2}\left(1+x_{ij}\right)^3}We_{ij}^{1/2}\right\}, \tag{18}$$

where c_3 is constant, $x_{ij}=d_i/d_j$, $We_{ij}=\frac{\rho_l d_i(\overline{u}_{ij})^2}{\sigma}$.

3.4.2. Laakkonen Breakup Model

Since the viscosity of a gas is very low compared to a liquid, the viscous stress resisting bubble rupture is thought to be proportional to the viscosity of the liquid surrounding the bubble. Laakkonen [31] proposed the general expression of the bubble breakage rate, which is expressed as:

$$g(V')=C_4\varepsilon^{1/3}erfc\left(\sqrt{C_5\frac{\sigma}{\rho_L\varepsilon^{2/3}d^{5/3}}+C_6\frac{\mu_L}{\sqrt{\rho_L\rho_G}\varepsilon^{2/3}d^{5/3}}}\right), \tag{19}$$

where ε represents the vortex dissipation in liquid phase, μ_L represents the liquid viscosity, $C_4=2.52$, $C_5=0.04$, $C_6=0.01$.

3.5. Interphase Mass Transfer Model

When the temperature and pressure are constant, the gas absorber (solution) is in contact with the gas, and the gas phase is transferred to the liquid phase. Transfer continues until the solute in the liquid phase is saturated and the composition in the liquid phase no

longer increases. At this time, the saturated composition of the gas in the liquid is called the solubility of the gas in the liquid. In the same liquid, the solubility of different gases is very different.

3.5.1. Equilibrium Concentration

The concentration at which the solute reaches equilibrium is called the equilibrium concentration and can be calculated using Henry theorem expressed in the form of the $p_i^* - x_i^*$ relation. It can be expressed as follows:

$$p_i^* = Ex_i^*, \tag{20}$$

where p_i^* represents the equilibrium pressure of the solute in the gas phase, x_i^* represents the molar fraction of the solute at equilibrium in the liquid phase, E representative Henry coefficient.

In this study, the mass transfer direction is determined by calculating the solute equilibrium concentration. When the actual molar fraction x_i of the solute in the liquid phase is less than the molar fraction x_i^* at the equilibrium concentration, it indicates that the solution has not reached the saturated state, and the gas solute in the solution must continue to dissolve, and the direction of mass transfer is from the gas phase to the liquid phase. Conversely, the direction of mass transfer is from the liquid phase to the gas phase.

The Henry coefficients of the four gases in the study at 20 °C are shown in Table 2 [32].

Table 2. Henry coefficients for four gases at 20 °C.

Gases	Henry Coefficient ($m^3 \cdot Pa/mol$)
helium	2.839×10^5
air	1.359×10^5
carbon dioxide	3.09×10^2
argon	7.14×10^3

3.5.2. Convective Mass Transfer

Convective mass transfer refers to the mass transfer process that occurs between the moving fluid and the phase interface. In this study, the mass transfer rate of the convective mass transfer process is defined by the source term S_q, and can be expressed as follows:

$$S_q = K_L \cdot a \cdot (x_q^* - x_q) \cdot M_q, \tag{21}$$

where K_L represents the gas–liquid interface mass transfer coefficient, M_q represents the molar mass of the qth phase, a represents the area of the gas–liquid interface, which can be expressed as [33]:

$$a = 6\phi_G / d, \tag{22}$$

where ϕ_G represents gas content.

Theoretical studies on convective mass transfer have been developed since the last century, including the dual mode theory [34], the permeation theory [35] and the surface renewal theory. On the basis of the three classical theories, some new and improved models are developed. With the development of computers, many mass transfer models combined with CFD have been proposed [36–38]. For mass transfer modeling, the parameters in the theoretical model must be experimentally measurable. Among them, the K_L model, which combines Higbie permeation theory and velocity slip model, is more practical. Therefore, K_L model is chosen to use in this study, can be expressed as:

$$K_{\mathrm{L}} = 2\sqrt{D_L v_S / (\pi d)}, \tag{23}$$

where v_S represents the bubble slip velocity, D_L represents the liquid phase diffusion coefficient.

The diffusion coefficients of the four gases used in the study in water are shown in Table 3 [39].

Table 3. Diffusivity coefficients of four gases in water.

Gases	Diffusivity Coefficient D_L(m^2/s)
helium	4.8×10^{-9}
air	3.23×10^{-9}
carbon dioxide	1.99×10^{-9}
argon	2.5×10^{-9}

3.6. Component Transport Equation

In this study, the component transport equation is used to numerically solve the change in local mass fraction during microbubble injection of different types of gases, and to determine whether a gas dissolved in water reaches saturation. In the component transport model, the local mass fraction of each component is predicted by solving the convective diffusion equation of the qth component. The convective diffusion equation can be expressed as follows:

$$\frac{\partial}{\partial t}(\rho_q Y_q) + \nabla \cdot (\rho_q \vec{v}_q Y_q) = -\nabla \cdot \vec{J}_q + S_q, \tag{24}$$

where Y_q represents the concentration of the qth component in the fluid, $\vec{J}_q$ represents the diffusion flux of the qth component in the fluid, S_q represents the mass transfer rate generated by the qth phase from any source.

For turbulent flow, the diffusion flux $\vec{J}_q$ can be expressed as:

$$\vec{J}_q = -\left(\rho_q D_q + \frac{\mu}{Sc}\right)\nabla Y_q, \tag{25}$$

where Sc represents the turbulence Schmidt number, μ represents the turbulent viscosity, D_q represents the diffusion coefficient of the qth component in the fluid.

3.7. UDF and Calculation Domain

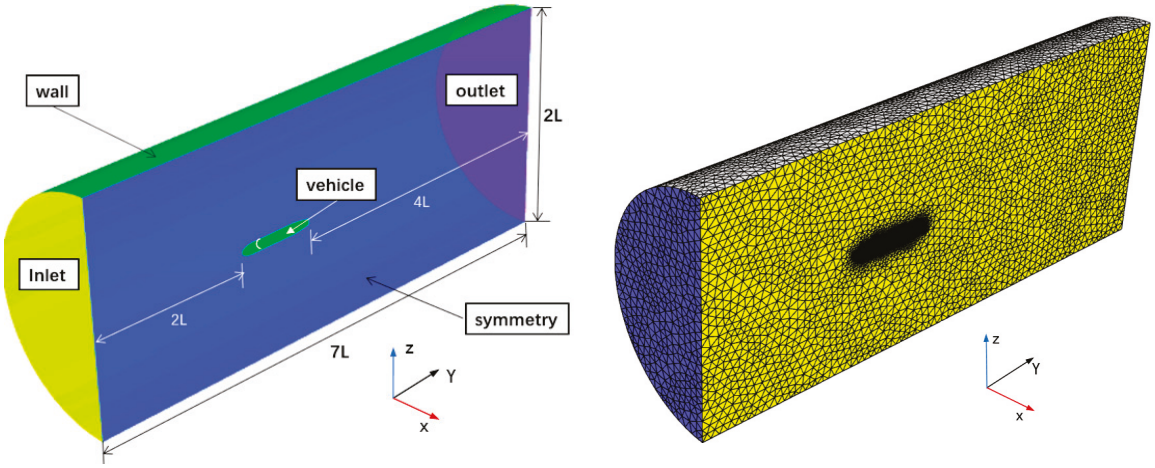
3.7.1. Writing of UDF

In this study, commercial computational fluid dynamics (CFD) software ANSYS Fluent 2023 R1 version is used for numerical simulation. The mass transfer rate is defined as the source term in the software transmission equation by writing UDF. Thus, the mass transfer velocity of different types of gases in the process of microbubble formation is calculated, and the influence of gas type on the drag reduction rate in the process of MBDR is reflected. The writing principle is mainly to calculate the current equilibrium concentration at partial pressure by Henry's theorem and compare it with the current concentration calculated by the component transport model, so as to determine the direction and speed of interphase mass transfer.

3.7.2. Calculation Domain and Boundary Conditions

Due to the fact that the physical model in this study is axisymmetric, a semi cylindrical computational domain is adopted, which can reduce computational time and cost while ensuring the accuracy of the calculation results. Then, the influence of the type of gas on drag reduction is studied. The calculation domain is shown in Figure 3. In Figure 3a, the cross-sectional radius is 2 L and the length is 7 L. The entrance of the computational domain is defined as the velocity inlet, and the outlet of the computational domain as the

pressure outlet. Grid division of the computational domain is shown in Figure 3b. The gas injection section is defined as the velocity inlet, and the injected gas direction is the *X*-axis direction shown in Figure 2. The gas injection holes are the same as the experiment, and the diameter is set to 0.005 mm. The bubble sizes are set to 6 groups, which are 0.005 mm, 0.01 mm, 0.022 mm, 0.046 mm, 0.096 mm and 0.2 mm, respectively. The cross section of a half cylinder is defined as the symmetrical plane, and the rest are walls. The surface of the vehicle is defined as the non-sliding wall, and the rest is the sliding wall. The speed inlet is 2 L away from the nose of the vehicle, and the pressure outlet is 4 L away from the tail of the vehicle. In the initial condition setting of the software, the reference pressure is set to 1 atm. The surface grid of the vehicle is refined by y + = 1, and the annular vents are also refined, as shown in Figure 4. The boundary conditions are set according to the experimental conditions [7], as shown in the Table 4.



(**a**) (**b**)

Figure 3. Computing domain and grid division. They can be listed as: (**a**) Description of the calculation domain of the vehicle; (**b**) description of grid division of the computational domain.

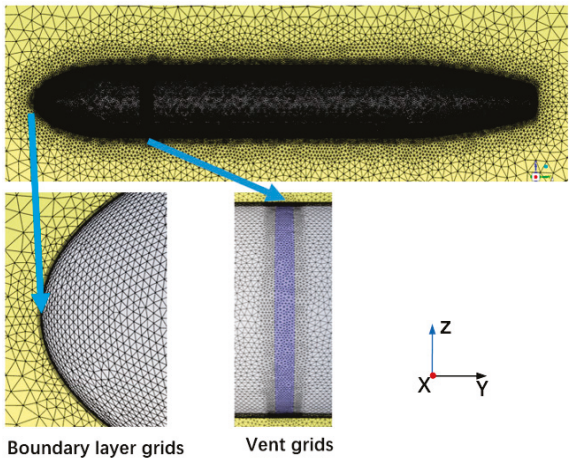


Figure 4. Meshing of the vehicle surface in the calculation domain. The arrows represent detail enlargements.

Table 4. Parameters for the initial boundary conditions.

Parameters	Values
Inlet Velocity	13.7 m/s
Temperature	20 °C
Density of Water	998 kg/m^3
Viscosity of Water	1.003×10^{-3} kg/m
Inlet Pressure (Gauge)	0 Pa
Outlet Pressure (Gauge)	0 Pa
Tunnel Pressure	15 psi, 30 psi

In this study, three sets of computation grids of different sizes (fine grid, medium grid and coarse grid) are generated on the surface of the vehicle for the grid independence analysis. The number of cells in the three grids is 1.2 million, 1.8 million and 3.5 million, respectively. Table 5 shows the comparison of drag reduction rates of the model under different grids. From Table 5, it can be seen that the relative deviation between the coarse and medium grids is 2.26%, and the relative deviation between the medium and fine grids is 0.88%, indicating that the calculation results of the medium and fine grids are basically consistent. Moreover, the drag reduction rates of fine and medium grids are in good agreement with the experimental results. Considering the calculation time and cost, the medium grid is used to simulate the vehicle. In the solver setup, the fully implicit coupled solving algorithm is used to solve the momentum equation and the continuity equation. The non-stationary terms in the numerical model are calculated using a second-order upwind Euler scheme. The convective terms are discretized in a high-resolution format. Based on computational convergence analysis, the simulation time step is 0.1 ms.

Table 5. Grid independence analysis.

Mesh Generation	Grid Size (mm)	Number of Grids (million)	Time Step (ms)	Courant	Drag Reduction Rate (%)
Fine grid	0.8	3.5	0.06	1	83.73
Medium Grid	1.3	1.8	0.10	1	84.61
Coarse grid	2.1	1.2	0.16	1	86.87

4. Result Analyses and Discussion

4.1. Numerical Result Verification

Numerical conditions are based on some experimental conditions [7], as shown in Tables 6 and 7. In working condition 1, injected gases are air, carbon dioxide, helium and argon, and the specific experimental parameters are listed in Table 6. In working condition 2, air, carbon dioxide and helium are used as the injected gases. The specific experimental parameters are listed in Table 7. It should be pointed out that the Henry coefficient here is expressed by the ratio of the equilibrium partial pressure of the gas in an aqueous solution to the mole fraction of the gas, and the smaller the Henry coefficient, the stronger the solution power and the greater the solubility.

Table 6. Parameters of working condition 1.

Gases	Tunnel Pressure (psi)	Free-Stream Speed (m/s)	Gas Volume Flow Rate (m^3/s $\times$ 10^3)
air	15	13.7	1, 2, 3, 4, 5, 6, 7, 8.
carbon dioxide	15	13.7	1.2, 2, 3, 4, 5, 6, 7, 8, 9.
helium	15	13.7	1, 2, 2.7, 3.2, 4, 4.6.
argon	15	13.7	1.8, 3.2, 4, 5.2, 6.2.

Table 7. Parameters of working condition 2.

Gases	Tunnel Pressure (psi)	Free-Stream Speed (m/s)	Gas Volume Flow Rate ($m^3/s \times 10^3$)
air	30	13.7	0.73, 1.5, 2, 3, 4, 5.2, 6.7, 8, 9.1, 12.5.
carbon dioxide	30	13.7	0.88, 2, 3, 3.9, 4.9, 6.5, 8.4, 9.6, 12.
helium	30	13.7	1, 2.2, 3, 3.6, 4.4, 6, 7.7, 9.

In Figures 5 and 6, experimental data and numerical simulation results of the drag reduction ratio (c_f/c_{f0}) and the gas volume flow rate for microbubble injection for different types of gases are presented, respectively, where c_f represents the drag of the vehicle after gas injection to generate microbubbles and c_{f0} represents the drag of the vehicle without gas injection.

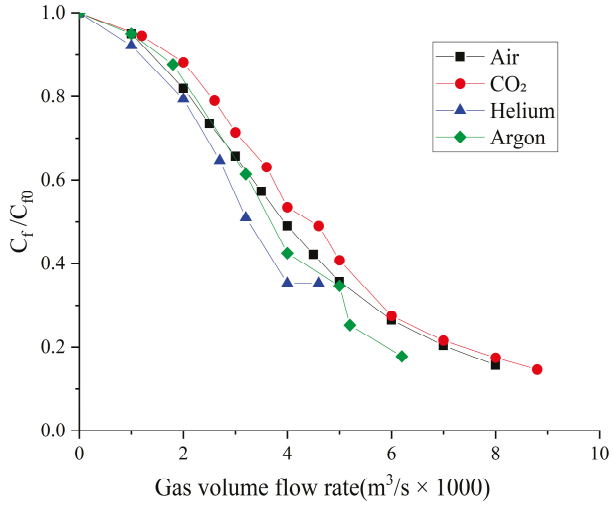


Figure 5. Drag reduction ratio of different types of gas varies with the volume flow rate of injected gas in the experiment. The experimental data described in the figure comes from the water tunnel experiment [7].

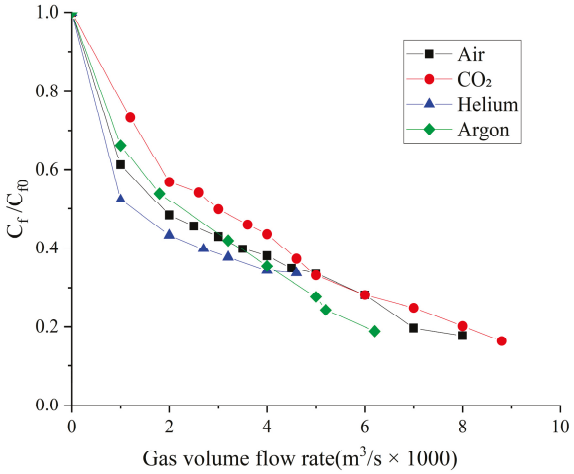


Figure 6. Drag reduction ratio of different types of gas in the numerical simulation varies with the volume flow rate of injected gas.

As can be seen from Figures 5 and 6, the drag reduction ratio of the experimental data and the numerical simulation results are basically consistent with the variation trend of the volume flow rate of gas injection. With the increase in the volume flow rate of gas injection, the drag reduction ratio gradually decreases and then becomes stable. However,

for different types of gases, the speed at which the drag reduction ratio decreases is different. The drag reduction ratio decreases the fastest in the condition of helium injection and the slowest in the condition of carbon dioxide injection. In other words, for the same gas injection flow rate, the drag reduction rate of helium is the largest, and that of carbon dioxide is the smallest. This result is consistent with the experiment, and also corresponds to the smallest solubility of helium in water and the largest solubility of carbon dioxide in water among these gases. Therefore, it can be concluded that the gas with small solubility is more suitable for microbubble drag reduction.

4.2. Influence of the Type of Gas on Drag Reduction by Microbubble Injection

In Figures 7–13, the numerical simulation results and experimental data of drag reduction ratio of different types of gases under the same injection volume flow rate are plotted when the water tunnel pressure is respectively 15 psi and 30 psi (the experimental data described in the Figures came from the water tunnel experiment [7]). By comparing numerical simulation results with experimental data, it can be seen that:

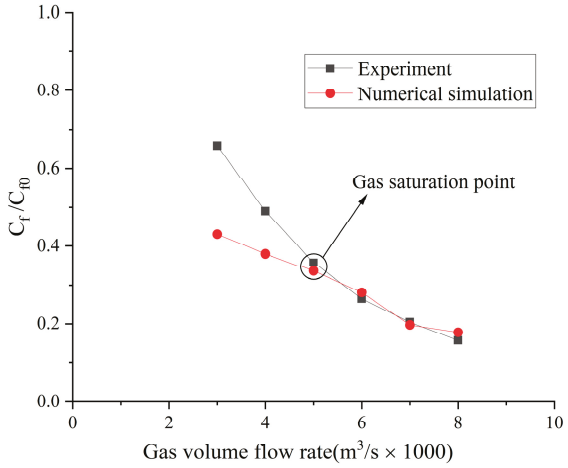


Figure 7. Comparison of numerical results and experimental data of drag reduction ratio during air injection. Tunnel pressure = 15 psi.

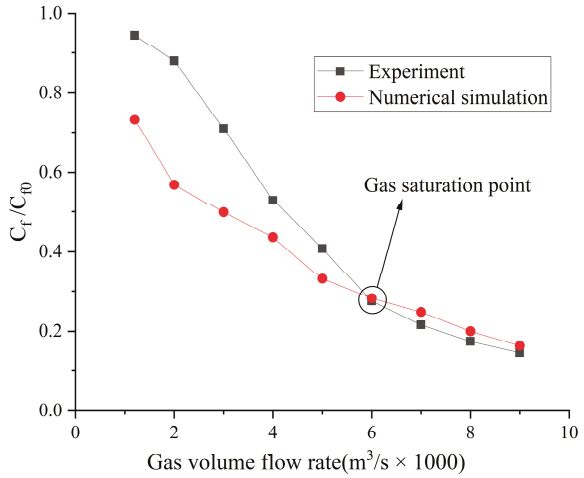


Figure 8. Comparison of numerical results and experimental data of drag reduction ratio during CO_2 injection. Tunnel pressure = 15 psi.

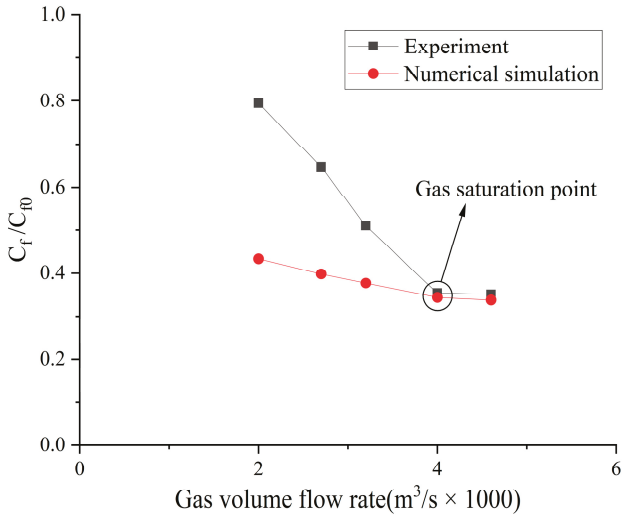


Figure 9. Comparison of numerical results and experimental data of drag reduction ratio during Helium injection. Tunnel pressure = 15 psi.

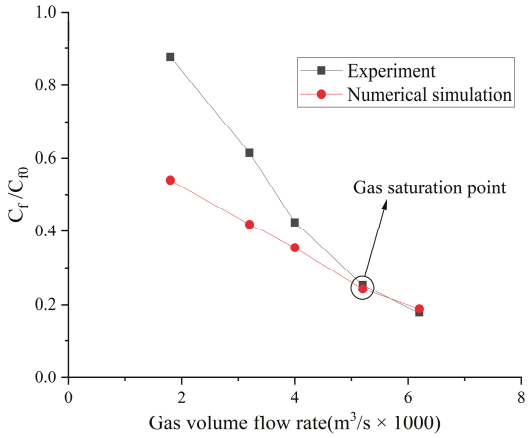


Figure 10. Comparison of numerical results and experimental data of drag reduction ratio during Argon injection. Tunnel pressure = 15 psi.

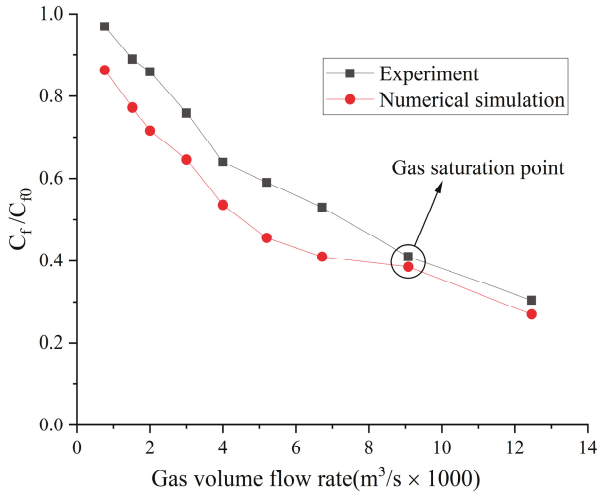


Figure 11. Comparison of numerical results and experimental data of drag reduction ratio during air injection. Tunnel pressure = 30 psi.

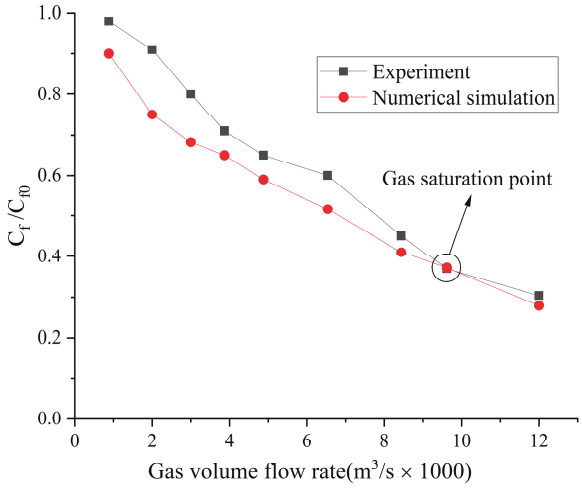


Figure 12. Comparison of numerical results and experimental data of drag reduction ratio during CO_2 injection. Tunnel pressure = 30 psi.

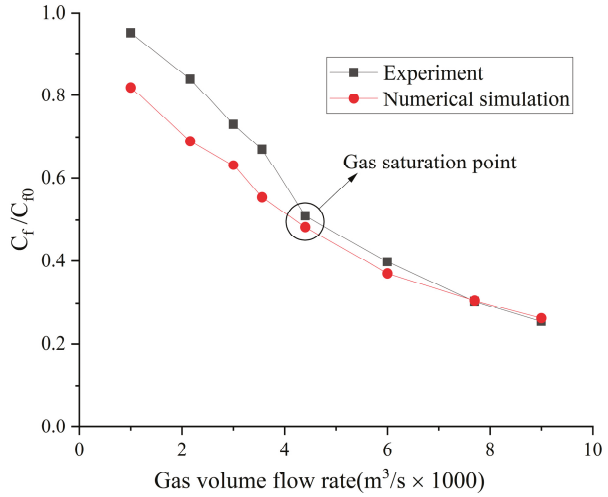


Figure 13. Comparison of numerical results and experimental data of drag reduction ratio during Helium injection. Tunnel pressure = 30 psi.

(1) When the volume flow rate of the gas injection is small, the experimental data of the drag reduction ratio is obviously larger than the numerical simulation results, and for different types of gases, their drag reduction ratio decreases at different rates. This is mainly due to the fact that the opening holes ratio in the numerical simulation is larger than that in the experiment. In the case of the same volume flow rate for gas injection, the gas injection speed of simulation is different from that of the experiment due to the difference of the opening holes rate. According to the microbubble drag reduction mechanism, the drag reduction ratio is mainly affected by the diameters of the microbubbles in the boundary layer, which are determined by the gas injection speed [40], and the gas dissolution in the boundary layer further increases this influence. Finally, there is a big gap between the simulation results and the experimental data of the drag reduction ratio;

(2) With the increase in the volume flow rate of gas injection, when the volume flow rate reaches a certain value, the value of the drag reduction ratio in the experiment is very close to the numerical simulation result, and this close point is marked in the figure, which is defined as the gas saturation point. The existence of the gas saturation point indicates that the gas injection velocity no longer influences the diameters of the microbubbles in the boundary layer. Observing Figures 7–10, it can

be seen that there are gas saturation points for different types of gases, but these points correspond to different volume flow rates. Observing the volume flow rate of the gas saturation point, it can be seen that helium is about 0.004 m^3/s, air and argon are about 0.005 m^3/s, argon is slightly larger than air and carbon dioxide is about 0.006 m^3/s. The reason why the volume flow rate of these gas saturation points is different is that among these gases, helium has the smallest solubility in water and the smallest influence on the formation of microbubbles in the boundary layer. Therefore, the saturation point of helium corresponds to a smaller gas injection flow rate. Air is more soluble than helium, and argon is slightly more soluble than air. The solubility of carbon dioxide is the largest, which also has the largest influence on the formation of microbubbles in the boundary layer, so the gas saturation point of carbon dioxide corresponds to a larger gas injection flow rate;

(3) As can be seen from Figures 7–10, where the gas saturation point is passed, if the volume flow rate of gas injection continues to increase, the numerical simulation results of the drag reduction ratio of all gases are basically consistent with the experimental data. This is because the gas injection speed and dissolution in the boundary layer no longer affect the diameters of microbubbles in the boundary layer, and the drag reduction ratio completely depends on the volume flow rate of the gas injection. Under the condition that the volume flow rate is the same, the numerical results are basically the same as the experimental data;

(4) As can be seen from Figures 11–13, the comparison between the simulation results and the experimental data of MBDR of different types of gases after the water tunnel pressure increases is consistent with Figures 7–10. The volume flow rate of different types of gas injection still has a gas saturation point, but the volume flow rate corresponding to the gas saturation point increases after the water tunnel pressure increases. In addition, by comparing Figure 7 with Figure 11, Figure 8 with Figures 9 and 12 with Figure 13, it can be seen that the solubility of different types of gases in water is also greatly affected by the water tunnel pressure. Carbon dioxide has the largest solubility, so its gas saturation point corresponds to the largest change in volume flow rate, followed by air, with helium being the smallest. The comparison between the simulation results and the experimental data is in accordance with the law of gas solubility variation with water pressure, which proves the correctness of the numerical model.

5. Conclusions

In this study, a numerical method for MBDR considering gas solubility is presented. A UDF is written to define the mass transfer velocity between the gas and liquid phase during microbubble injection of different types of gases, and the numerical models for MBDR of different types of gases are established. According to the experimental conditions, the numerical studies on MBDR of air, carbon dioxide, helium and argon are carried out, and the numerical simulation results and experimental data are compared and analyzed. Finally, the following conclusions are reached:

(1) Gas solubility cannot be ignored in the process of MBDR. The drag reduction ratio of gas with greater solubility decreases more slowly, and the drag reduction efficiency of gas with smaller solubility is higher;

(2) When the volume flow rate of injected gas is small, gas dissolution has a great influence on the drag reduction ratio of different types of gases. The larger the solubility of gas, the larger the drag reduction ratio and the lower the drag reduction efficiency. When the volume flow rate of injected gas is large, the influence of gas dissolution on drag reduction ratio of different types of gases is small;

(3) When the volume flow rate of the injected gas is small, for the same type of gas, if the volume flow rate of the injected gas is the same, but the injection speed is different, the drag reduction ratio is also different, and the greater the solubility of the gas, the greater the difference in the drag reduction ratio.

By comparing the numerical simulation results of the drag reduction ratio with the experimental data, it can be found that the volume flow rate of different types of gases injected has a gas saturation point, which is the dividing point between a small volume flow rate and the large volume flow rate of injected gas. Moreover, due to the difference in gas solubility, the volume flow rate of different types of gases at the gas saturation point is different. The existence of the gas saturation point only reflects the influence of the gas injection speed on the MBDR efficiency, and this point is also the critical point of the transition from MBDR state to the gas-layer drag-reduction state. In addition, in order to improve the calculation accuracy of the proposed model, further research can be carried out from the following aspects: (1) According to the study condition of the microbubble injection flow field, the appropriate turbulence model can be selected. (2) In order to improve the simulation accuracy of the population balance model and the interphase mass transfer coefficient model, the population distribution of the microbubble diameter generated during gas injection should be studied; and (3) the interphase mass transfer rate during microbubble injection is investigated, and the internal relationship between microbubble drag reduction and interphase mass transfer can be analyzed.

Author Contributions: Conceptualization, H.A.; methodology, H.A.; software, P.Y. and H.Z.; validation, P.Y. and H.Z.; formal analysis, X.L.; investigation, H.A. and P.Y.; resources, H.A.; data curation, P.Y. and H.Z.; writing—original draft preparation, H.A., P.Y., H.Z. and X.L.; writing—review and editing, H.A. and P.Y. All authors have read and agreed to the published version of the manuscript.

Funding: This research received no external funding.

Data Availability Statement: Data are contained within the article.

Conflicts of Interest: The authors declare no conflicts of interest.

Nomenclature

a	Area of the gas–liquid interface
$b(v', v)$	Breakup rate at which the bubbles of volume v' break into the bubbles of volume v
$c(v, v')$	Coalescence rate of bubbles with volumes v and v'
$c\left(v_i, v_j\right)$	Bubble coalescence rate
C_d	Drag coefficient
C_l	Lift coefficient
C_{vm}	Virtual mass force coefficient
d_p	Bubble diameter
D_L	Liquid phase diffusion coefficient
D_q	Diffusion coefficient of the qth component in the fluid
E	Henry coefficient
$\vec{F}_{d,q}$	Drag force
$\vec{F}_{lift,q}$	Lift
$\vec{F}_{vm,q}$	Virtual mass force
F_{vol}	Surface tension
$g(V')$	Bubble breakage rate
G_b	Turbulent kinetic energy caused by buoyancy
G_k	Turbulent kinetic energy caused by mean velocity gradient
$\vec{J}_q$	Diffusion flux of the qth component in the fluid
K_L	Gas–liquid interface mass transfer coefficient
$\dot{m}_{pq}$	Mass transfer from the pth phase to the qth phase
M_q	Molar mass of the qth phase
$n(v, \vec{x}, t)$	Number density of bubbles
p_i^*	Equilibrium pressure of the solute in the gas phase
$P_{ag}\left(v_i, v_j\right)$	Probability that a collision will result in a convergence

Re_g	Bubble Reynolds number
$\vec{R}_{pq}$	Interaction force between phases
$S(v, \vec{x}, t)$	Source term of the coalescence and breakup of bubble groups
Sc	Turbulence Schmidt number
S_q	Mass transfer rate generated by the qth phase from any source
$\vec{u}_b(v, \vec{x}, t)$	Representative bubble velocity
$\overline{u}_{ij}$	Collision characteristic velocity of two bubbles with diameters d_i and d_j and densities n_i and n_j
$\vec{v}_{pq}$	Inter-phase velocity
$\vec{v}_q$	Velocity of the qth phase
v_S	Bubble slip velocity
x_i	Actual molar fraction of the solute in the liquid phase
x_i^*	Molar fraction of the solute at equilibrium in the liquid phase
Y_m	Influence of turbulent pulsating flow on the total dissipation rate
Y_q	Concentration of the qth component in the fluid
α_q	Gas phase volume fraction of the qth phase
$\beta(v, v')$	Probability density function of the bubble of volume v' breaking into the bubble of volume v
$\gamma(v')$	Number of sub-bubbles of volume v'
ε	Vortex dissipation in liquid phase
κ_q	Surface curvature
λ_q	Bulk viscosity of the qth phase
μ	Turbulent viscosity
μ_L	Represents the liquid viscosity
μ_q	Shear viscosity of the qth phase
μ_t	Turbulence viscosity coefficient
ρ	Average volume density
ρ_q	Density of the qth phase
σ_k	Turbulent Prandtl numbers of the turbulent kinetic energy
σ_ε	Turbulent Prandtl numbers the dissipation rate
σ_{qp}	Tension coefficient between the qth phase and the pth phase
$\overline{\overline{\tau}}_q$	Stress tensor of the qth phase
ϕ_G	Gas content
$\omega\left(v_i, v_j\right)$	Collision frequency

References

1. Pavlov, G.A.; Yun, L.; Bliault, A.; He, S.L. *Air Lubricated and Air Cavity Ships: Development, Design, and Application*; Springer: New York, NY, USA, 2020; p. 28.
2. Elbing, B.R.; Winkel, E.S.; Lay, K.A.; Ceccio, S.L.; Dowling, D.R.; Perlin, M. Bubble-induced skin-friction drag reduction and the abrupt transition to air-layer drag reduction. *J. Fluid Mech.* **2008**, *612*, 201–236. [CrossRef]
3. An, H.; Pan, H.; Yang, P. Research Progress of Air Lubrication Drag Reduction Technology for Ships. *Fluids* **2022**, *7*, 319. [CrossRef]
4. McCormick, M.E.; Bhattacharyya, R. Drag Reduction of a Submersible Hull by Electrolysis. *Nav. Eng. J.* **1973**, *85*, 11–16. [CrossRef]
5. Pal, S.; Deutsch, S.; Merkle, C.L. A comparison of shear stress fluctuation statistics between microbubble modified and polymer modified turbulent boundary layers. *Phys. Fluids A* **1989**, *1*, 1360–1362. [CrossRef]
6. Deutsch, S.; Castano, J. Microbubble skin friction reduction on an axisymmetric body. *Phys. Fluids* **1986**, *29*, 3590–3597. [CrossRef]
7. Fontaine, A.A.; Deutsch, S. The influence of the type of gas on the reduction of skin friction drag by microbubble injection. *Exp. Fluids* **1992**, *13*, 128–136. [CrossRef]
8. Deutsch, S.; Money, M.; Fontaine, A.; Petrie, H. Microbubble Drag Reduction in Rough Walled Turbulent Boundary Layers. In Proceedings of the ASME FEDSM'03 4th ASME/JSME Joint Fluids Engineering Conference, Honolulu, HI, USA, 6–10 July 2003; pp. 665–673.
9. Zhu, R.; Zhang, H.; Wen, W.; He, X.; Zhao, C.; Liu, Y.; Zhuang, Q.; Liu, Z. Flow-drag reduction performance of a resident electrolytic microbubble array and its mechanisms. *Ocean Eng.* **2023**, *268*, 113496. [CrossRef]
10. Skudarnov, P.V.; Lin, C.X. Drag reduction by gas injection into turbulent boundary layer: Density ratio effect. *J. Heat Fluid Flow* **2006**, *27*, 436–444. [CrossRef]
11. Mattson, M.; Mahesh, K. Simulation of bubble migration in a turbulent boundary layer. *Phys. Fluids* **2011**, *23*, 045107. [CrossRef]
12. Pang, M.J.; Wei, J.J.; Yu, B. Numerical study on modulation of microbubbles on turbulence frictional drag in a horizontal channel. *Ocean Eng.* **2014**, *81*, 58–68. [CrossRef]

13. Rawat, S.; Chouippe, A.; Zamansky, R.; Legendre, D.; Climent, E. Drag modulation in turbulent boundary layers subject to different bubble injection strategies. *Comput. Fluids* **2019**, *178*, 73–87. [CrossRef]
14. Velasco, L.J.; Venturi, D.N.; Fontes, D.H.; de Souza, F.J. Numerical simulation of drag reduction by microbubbles in a vertical channel. *Eur. J. Mech. B-Fluid* **2022**, *92*, 215–225. [CrossRef]
15. Mohanarangam, K.; Cheung, S.C.P.; Tu, J.Y.; Chen, L. Numerical simulation of micro-bubble drag reduction using population balance model. *Ocean Eng.* **2009**, *36*, 863–872. [CrossRef]
16. Yan, W. Numerical Simulation of Microbubble Drag Reduction and Mechanism Analysis. Master's Thesis, Harbin Engineering University, Harbin, China, 2013. (In Chinese)
17. Pang, M.; Zhang, Z. Numerical Investigation on Turbulence Drag Reduction by Small Bubbles in Horizontal Channel with Mixture Model Combined with Population Balance Model. *Ocean Eng.* **2018**, *162*, 80–97. [CrossRef]
18. Qin, S.; Chu, N.; Yao, Y.; Liu, J.; Huang, B.; Wu, D. Stream-wise distribution of skin-friction drag reduction on a flat plate with bubble injection. *Phys. Fluids* **2017**, *29*, 037103. [CrossRef]
19. Zhang, X.; Wang, J.; Wan, D. Euler–Lagrange study of bubble breakup and coalescence in a turbulent boundary layer for bubble drag reduction. *Phys. Fluids* **2021**, *33*, 037105. [CrossRef]
20. Lyu, X.; Tang, H.; Sun, J.; Wu, X.; Chen, X. Simulation of microbubble resistance reduction on a suboff model. *Brodogradnja* **2014**, *65*, 23–32.
21. Wang, T.; Sun, T.; Wang, C.; Xu, C.; Wei, Y. Large Eddy Simulation of Microbubble Drag Reduction in Fully Developed Turbulent Boundary Layers. *J. Mar. Sci. Eng.* **2020**, *8*, 524. [CrossRef]
22. Zhao, X.-J.; Zong, Z.; Jiang, Y.-C.; Pan, Y. Numerical simulation of micro-bubble drag reduction of an axisymmetric body using OpenFOAM. *J. Hydrodyn.* **2019**, *31*, 900–910. [CrossRef]
23. Wang, B. Numerical Simulation and Mechanism Research on Drag Reduction of Ship by Microbubbles. Master's Thesis, Harbin Engineering University, Harbin, China, 2012. (In Chinese)
24. Shih, T.-H.; Liou, W.W.; Shabbir, A.; Yang, Z.; Zhu, J. A new k-ε eddy viscosity model for high reynolds number turbulent flows. *Comput. Fluids* **1995**, *24*, 227–238. [CrossRef]
25. Schiller, L.; Naumann, A. A drag coefficient correlation. *Z. Ver. Deutsch. Ing.* **1935**, *77*, 318–320.
26. Drew, D.A.; Lahey, R.T. Application of general constitutive principles to the derivation of multidimensional two-phase flow equations. *Int. J. Multiph. Flow* **1979**, *5*, 243–264. [CrossRef]
27. Legendre, D.; Magnaudet, J. The lift force on a spherical bubble in a viscous linear shear flow. *J. Fluid Mech.* **1998**, *368*, 81–126. [CrossRef]
28. Magnaudet, J.J. The forces acting on bubbles and rigid particles. In Proceedings of the ASME Fluids Engineering Division Summer Meeting, FEDSM, Vancouver, BC, Canada, 22–26 June 1997; pp. 22–26.
29. Yeoh, G.H.; Tu, J. *Computational Techniques for Multi-Phase Flows*; Elsevier Butterworth Heinemann; Elsevier Ltd.: London, UK, 2010; pp. 351–456.
30. Luo, H. Coalescence, Breakup and Liquid Circulation in Bubble Column Reactors. Ph.D. Thesis, Norwegian Institute of Technology, Trondheim, Norway, 1993.
31. Laakkonen, M.; Alopaeus, V.; Aittamaa, J. Validation of bubble breakage, coalescence and mass transfer models for gas–liquid dispersion in agitated vessel. *Chem. Sci.* **2006**, *61*, 218–228. [CrossRef]
32. Sander, R. Compilation of Henry's law constants (version 5.0.0) for water as solvent. *Atmos. Chem. Phys.* **2023**, *23*, 10901–12440. [CrossRef]
33. Resnick, W.; Gal-Or, B. Gas-liquid dispersions. *Adv. Chem. Eng.* **1968**, *7*, 295–395.
34. Higbie, R. The rate of absorption of a pure gas into a still liquid during short periods of exposure. *Trans. Am. Inst. Chem. Eng.* **1935**, *31*, 365–389.
35. Danckwerts, P.V. Significance of Liquid-Film Coefficients in Gas Absorption. *Ind. Eng. Chem. Res.* **1951**, *43*, 1460–1467. [CrossRef]
36. Balcázar-Arciniega, N.; Antepara, O.; Rigola, J.; Oliva, A. A level-set model for mass transfer in bubbly flows. *Int. J. Heat Mass Transf.* **2019**, *138*, 335–356. [CrossRef]
37. Macfarlan, L.H.; Phan, M.T.; Bruce Eldridge, R. A volume-of-fluid methodology for interfacial mass transfer. *Chem. Eng. Sci.* **2023**, *275*, 118720. [CrossRef]
38. Li, W.-L.; Wang, J.-H.; Lu, Y.-C.; Shao, L.; Chu, G.-W.; Xiang, Y. CFD analysis of CO_2 absorption in a microporous tube-in-tube microchannel reactor with a novel gas-liquid mass transfer model. *Int. J. Heat Mass Transf.* **2020**, *150*, 119389. [CrossRef]
39. The Engineering ToolBox. Gases Solved in Water—Diffusion Coefficients. 2008. Available online: https://www.engineeringtoolbox.com/diffusion-coefficients-d_1404.html (accessed on 13 December 2023).
40. Hashim, A.; Yaakob, O.B.; Koh, K.K.; Ismail, N.; Ahmed, Y.M. Review of micro-bubble ship resistance reduction methods and the mechanisms that affect the skin friction on drag reduction from 1999 to2015. *J. Teknol.* **2015**, *74*, 105–114.

Disclaimer/Publisher's Note: The statements, opinions and data contained in all publications are solely those of the individual author(s) and contributor(s) and not of MDPI and/or the editor(s). MDPI and/or the editor(s) disclaim responsibility for any injury to people or property resulting from any ideas, methods, instructions or products referred to in the content.

inventions

MDPI

Article

Evaluation of a Serrated Edge to Mitigate the Adverse Effects of a Backward-Facing Step on an Airfoil

Real J. KC [1], Trevor C. Wilson [1], Aaron S. Alexander [2], Jamey D. Jacob [1], Nicholas A. Lucido [3] and Brian R. Elbing [1,*]

[1] Mechanical and Aerospace Engineering, Oklahoma State University, Stillwater, OK 74078, USA; realk@okstate.edu (R.J.K.); trevor.wilson@okstate.edu (T.C.W.); jdjacob@okstate.edu (J.D.J.)
[2] Mechanical Engineering Technology, Oklahoma State University, Stillwater, OK 74078, USA; aaral@okstate.edu
[3] Mechanical Engineering, University of Michigan, Ann Arbor, MI 48109, USA; nalucido@umich.edu
* Correspondence: elbing@okstate.edu

Abstract: Backward-facing steps are commonly formed on wings and blades due to misalignment between segments or the addition of protective films. A backward-facing step (BFS) is known to degrade the airfoil performance. To mitigate these adverse effects, a three-dimensional low-profile serrated pattern (termed sBFS) was applied downstream of a BFS on an LA203A profile airfoil. The model drag was determined from wake surveys using a traversing Pitot-static probe within a subsonic wind tunnel operating at a chord-based Reynolds number of 300,000. The airfoil spanned the wind tunnel width (914 mm) and had a 197 mm chord length. Four different sBFS configurations were tested, each formed by applying a 1 mm thick film around the model leading edge. In addition, a BFS at various chord locations and a clean wing (i.e., no film applied) were tested for reference. The sBFS was able to reduce the drag relative the BFS by up to 8–10%, though not outperforming the clean wing configuration. In addition, the wake surveys showed the sBFS produced strong coherent structures that persist into the far-wake region (five chord length downstream of the model) with a scale that was much larger than the step height. Additionally, a computational study was carried out to further examine the flow behavior on the airfoil that produced the coherent structures. This showed that fluid near the surface gets entrained towards the sBFS downstream tip of the sBFS, which creates the initial rotation of these coherent structures that persist into the far-wake region.

Keywords: flow control; backward-facing step; passive; coherent structures; airfoil; drag

1. Introduction

A portion of the parasitic drag on an aircraft is due to irregularities and deviations from a smooth (clean) external surface. This contribution is commonly termed excrescence drag. The percentage of the total drag due to excrescence drag varies significantly based on the plane design, size, and operation. The study of surface imperfections dates back to the 1930s (e.g., [1]) and a review of early studies is provided in Young and Paterson [2]. More recently, studies have been performed to better understand excrescence effects on transition and the use of flow-control techniques to mitigate their impact [3–6]. A common source of excrescence drag is the creation of a step due to a mismatch in height between two surfaces. Steps are frequently formed at skin joints, around windows, and control surfaces. In addition, a backward-facing step (BFS) is frequently created when protective films are added to the leading edge of airfoils for various applications including wind turbine and helicopter blades. While these protective films do protect the integrity of the leading edge, the backward-facing step created by the film is detrimental to the performance [7–9]. The issue of a backward-facing step on airfoils is not new and has been studied extensively [10–13]. The current study is a preliminary examination of a serrated (i.e., saw-tooth) pattern being

added to the downstream edge of a BFS as a means of mitigating its adverse effects on airfoil aerodynamic performance.

Before the previous study on the sBFS is presented, low-profile flow-control methods will be discussed. A common passive flow-control device is a vortex generator (VG), which is commonly used on aircraft to control the wing aerodynamic boundary layer. It does so by re-energizing the boundary layer to delay flow separation and aerodynamic stalling [14]. Some VGs are designed for specific flow regimes. For example, Yao et al. show that low-profile vortex generators outperform traditional VGs at high angles of attack [15]. The Gurney flap can significantly increase lift at low angles of attack without any penalty in terms of drag [16]. While the advantages of VGs are plenty, passive flow-control methods such as these require tuning of the geometry with the flow conditions, typically resulting in a relatively narrow range where they are beneficial, which is why they are generally designed for specific flow regimes. An extensive review of low-profile VGs is presented by Lin [17]. Additionally, the micro vortex generators that are used in supersonic regimes improve shockwave-induced boundary layer separation [18], or to eliminate the flap separation of take-off and landing configurations of aircrafts and increase the lift-to-drag ratio at various angles of attack [19]. Since these micro VGs are mostly used in supersonic regimes, the literature on subsonic regimes is scarce.

There is evidence that the addition of various patterns to the trailing edge of a BFS is an effective passive flow-control technique for mitigating the adverse effects (e.g., [20]) and even reduction in noise [21]. Serration (i.e., making a saw-tooth pattern) in the BFS is a pattern that has shown potential for mitigating the BFS impact. For the current study, a serrated BFS (sBFS) was created by applying a thin film around the leading edge of an airfoil and then cutting triangular shapes into the downstream edge that would form the BFS. This mimics the use of protective leading edge tapes or coatings used for helicopter and wind turbine blades. Protective tapes without the serration have previously been studied and shown to protect the rotor blades while significantly increasing the profile drag [22]. Qualitative investigations adding the serration suggested that it could mitigate the added drag. The National Renewable Energy Laboratory (NREL) performed a comparative study of the performance of wind turbines with a serrated protective film relative to a non-serrated protective film [23]. The turbine was a two-bladed Westinghouse WWG-0600 with a nominal rotor diameter of 44 m. Preliminary data from that study show the KWH power production increased with the sBFS relative to the BFS by 6% and 7.4% at wind speeds of 7 m/s and 11 m/s, respectively. However, this study only looked at the bulk performance (i.e., turbine efficiency) and no information was provided about the impact of the aerodynamic performance due to the sBFS. Consequently, there is little insight into the relationship between the sBFS shape and flow parameters, which is required to develop an optimized design for a given application.

Most reported aerodynamic work on sBFS has been related to their application on airplane wings. Commercial flight testing with sBFS (termed a conformal vortex generator or CVG) on a Boeing 737 was performed by Safair, which reportedly showed a 1% reduction in fuel consumption [24]. The first assessment of the aerodynamic impact of the sBFS on the Boeing 737 suggested that shock stabilization on the wing could be a cause for the reduced fuel consumption [25]. However, flight tests on a subsonic aircraft (Piper Cherokee) that provided wall shear distribution on the wings indicated that sBFS redistributes the near-wall momentum. This was apparent as a low-shear diamond pattern formed downstream of the sBFS valleys (i.e., the furthest upstream step location) [26]. A computational model was developed to further investigate the induced flow pattern observed on the subsonic aircraft [24]. The model confirmed the low-shear diamond pattern from the subsonic flight tests. Further evaluation computationally [10] and experimentally [26] showed that these diamonds were created by the sBFS peak (i.e., furthest downstream step location), inducing the laminar-to-turbulent transition while delaying the transition downstream of the valley. In addition, these studies showed that low-profile (i.e., step height was approximately 5%

of the boundary layer height) sBFS could produce strong coherent structures that persisted downstream with a height that was comparable to the boundary layer thickness.

The first part of the current study experimentally investigates the sBFS applied to an airfoil (LA203A) mounted in a wind tunnel and operated at subsonic conditions. The aim was to quantify the aerodynamic impact of the sBFS relative to a BFS as well as a clean (i.e., no BFS) wing. The total drag was quantified from wake surveys in the far-wake region. We present evidence that the sBFS-induced coherent structures that persisted into the far-wake region led to further examination of the induced vorticity and its dependence on sBFS size (length and width) for a subset of conditions. All results are compared relative to the BFS and clean conditions. Then, a computational model was created and validated against the available experimental results to further examine the flow behavior on the airfoil that produced the coherent structures. The remainder of the article describes the experimental and computational methods used in Section 2; Section 3 presents drag coefficient and vorticity results from both the experiment and computations; Section 4 provides a qualitative and quantitative discussion of the sBFS's performance; and Section 5 provides a brief summary and concluding remarks.

2. Methods

2.1. Experimental Methods

2.1.1. Test Facility and Model

The experiments were conducted in the custom built Flexible-use Wind Tunnel (Diehl Aero-Nautical) located at Oklahoma State University [27–29]. It was an open loop, draw down tunnel powered with a 125 hp centrifugal fan, which can achieve speeds of up to 30.5 m/s (100 ft/s). The tunnel test section can be varied, and, for the current study, it was 2.44 m (8 ft) long with a 0.91 m (3 ft) square cross section. The freestream turbulent intensity within the test section was measured to be below 1.4% [28]. A schematic of the wind tunnel test section is provided in Figure 1 with the test model located 0.762 m downstream from the test section inlet and vertically centered. The test model was an airfoil with an LA203A profile and a chord length (c) of 0.197 m (7.75 in). The model airfoil angle of attack (defined in Figure 2a) was then varied for a given test speed.

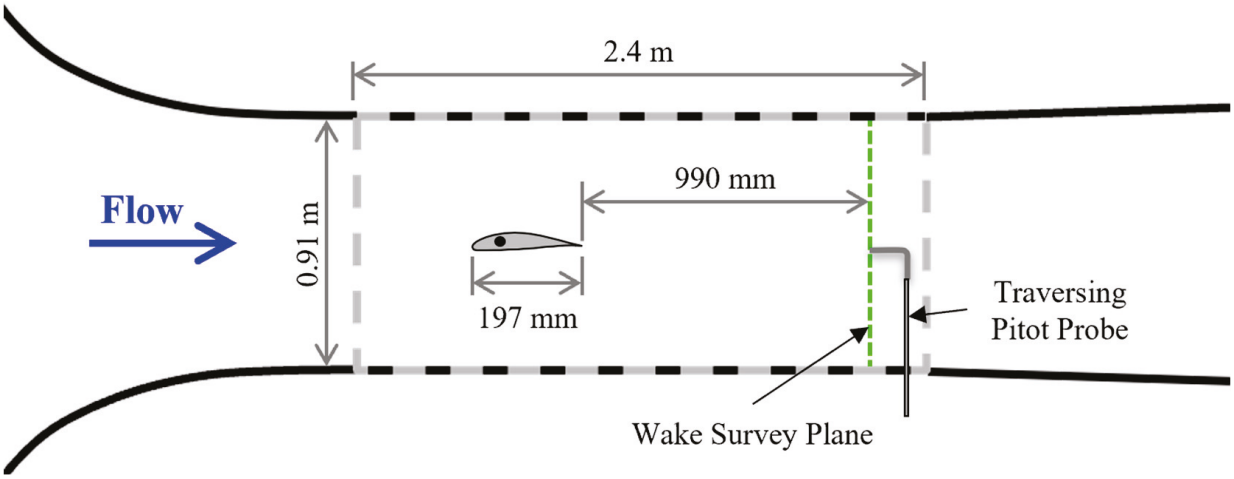


Figure 1. Side view schematic of the wind tunnel test section (dashed rectangle) with the airfoil and probe locations and their relative positions shown.

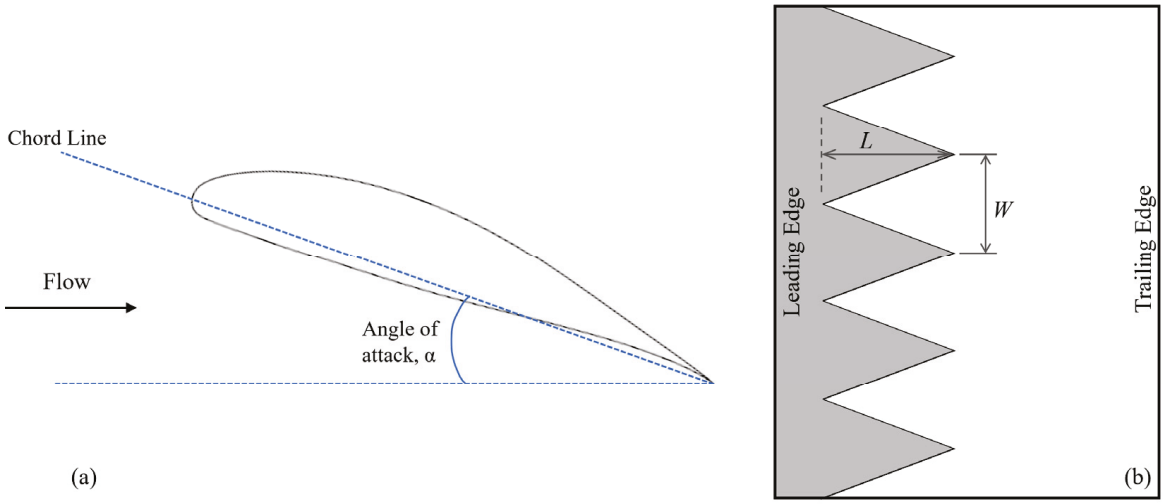


Figure 2. (**a**) The LA203A airfoil profile with the definition of angle of attack (α). (**b**) Schematic of the top view of an sBFS configuration on the airfoil.

2.1.2. Backward-Facing Steps

A film (i.e., thin tape) was applied around the leading edge of the airfoil model and extended downstream to the desired chord location. If a BFS was being tested, the end of the film sheet was cut straight, while for sBFS, a serrated pattern, as illustrated in Figure 2b, would be cut into the film. As previously mentioned, the upstream point and downstream point of the sBFS are referred to as the valley and peak locations, respectively. The height of the BFS and sBFS was fixed at 1.02 mm. The foil thickness varied with a maximum thickness of 15.6% of the chord length (30.7 mm). The step height was selected to correspond to that of a Boeing 737 aircraft following the scaling proposed in Lucido et al. [26], though the current study was subsonic. Four different sBFS configurations were tested, termed sBFS-V1, -V2, -V3, and -V4. The size and position of each sBFS and BFS, as well as their position on the airfoil, are listed in Table 1.

Table 1. Summary of test configurations with the sizes, geometric ratios, and the relative chord positions. NA indicates that the measure is "not applicable."

							Location [%*c*]	
Model	***L* [mm]**	***W* [mm]**	***H* [mm]**	***L*/*W***	***L*/*H***	***W*/*H***	**Valley**	**Peak**
Clean Wing	NA	NA	NA	NA	NA	NA	NA	NA
BFS1	NA	NA	1.02	NA	NA	NA	10	NA
BFS2	NA	NA	1.02	NA	NA	NA	27.3	NA
BFS3	NA	NA	1.02	NA	NA	NA	44.5	NA
sBFS-V1	70	50	1.02	1.4	68.6	49	10	44.5
sBFS-V2	35	25	1.02	1.4	34.3	24.5	10	27.3
sBFS-V3	35	25	1.02	1.4	34.3	24.5	27.3	44.5
sBFS-V4	70	25	1.02	2.8	68.6	24.5	10	44.5

The sBFS-V1 length (L = 70 mm), width (W = 50 mm), and height (H = 1.02 mm) were three times those tested on the Boeing 737 aircraft, which was selected to scale to flight conditions at cruise altitude [13]. The sBFS-V1 valley was located at 10% chord length as the flight tested on the Boeing 737. To separate geometric and kinematic dependence, the length and width were halved for sBFS-V2, which produced the same L/W ratio without changing boundary thickness or step height. The sBFS-V2 valley location was matched with sBFS-V1 at 10% chord length, but the peak location was changed due to the decreased length. Consequently, sBFS-V3 had the same dimensions as sBFS-V2 but shifted downstream such that its peak location matched the downstream position of sBFS-V1. For

the final configuration (sBFS-V4), the length matched that of sBFS-V1, while the width was halved (i.e., matched sBFS-V2 and -V3) to assess the impact of the L/W ratio on the sBFS performance. Both sBFS-V3 and -V4 configurations were tested at the same time with half of the airfoil model span having one of the configurations, which was carried out since initial configurations showed minimal spanwise variation for scales larger than the sBFS width. In addition to the sBFS, the BFS was tested with the step height fixed at 1.02 mm and its location at 10%, 27%, or 44% chord lengths, which corresponds to peak and/or valley locations for the sBFS configurations. Pressure measurements at these locations were not recorded for the experiments; however, they could be tabulated using the simulations. The corresponding pressure gradients were as follows: -8 kPa/m at 10% chord length, 2.5 kPa/m at 27% chord length, and 5 kPa/m at 44% chord length.

2.1.3. Instrumentation and Data Analysis

The primary measurements for the current study were wake surveys via a Pitot-static tube mounted five chord lengths downstream of the airfoil model (see Figure 1). The Pitot-static probe was traversed through the test section cross-section on an automated traverse (Dantec) with each wake survey acquiring data at nominally 100 locations. For all conditions, the streamwise velocity component (u) was measured, and for a subset of conditions, a 5-hole probe was installed. The 5-hole probe measures the velocity magnitude (V), angle of attack (α), and the slip angle (β), which can be converted to the streamwise ($u = V\cos\alpha\ \cos\beta$), spanwise ($v = V\sin\beta$), and vertical ($w = V\sin\alpha\ \cos\beta$) velocity components.

In addition, another Pitot-static probe was located in the test section inlet to measure the free-stream velocity. The turbulent intensity at the test section inlet was also measured with a hot wire. Finally, the barometric pressure and temperature of the air at the test section inlet were recorded with a data-logger (SD700, Extech Instruments, Nashua, NH, USA), which was used to determine the fluid properties (e.g., density, kinematic viscosity). The signals were sampled at 1000 Hz via an analog data acquisition module (NI-9220, National Instruments, Austin, TX, USA) and chassis (cDAQ-9188, National Instruments, Austin, TX, USA). A commercial software package (LabView, National Instruments, Austin, TX, USA) created a Virtual Instrument (VI) that was used to handle the data with the mean voltage from every 100 samples recorded, which produced an effective sample rate of 10 Hz. The pressure and temperature data-logger did not have an external output, so that data was manually inputted into the VI.

The vertical spacing of the velocity profiles within the wake was 3.18 mm, which was half the diameter of the probe head. Integration of the streamwise velocity is a well-established method for obtaining the total drag on 2D objects that can be extended to 3D models [30]. Three-dimensional considerations were required due to some of the sBFS producing significant coherent structures that persisted into the far-wake region where the wake survey was acquired. A brief overview of the drag analysis is provided here for completeness as well as its relationship to the measurement uncertainty. Assuming a uniform inlet velocity and nearly horizontal streamlines sufficiently far from the model, integration of the streamwise component of velocity in the wake gives the drag coefficient $\left(C_d = D/0.5\rho U_\infty^2 A\right)$ as

$$C_d = \frac{2}{c}\int \frac{U}{U_\infty}\left(1 - \frac{U}{U_\infty}\right)dz.$$

Here, D is the total drag, A is the planform area, U_∞ is the freestream speed, ρ is the fluid density, c is the chord length, z is the vertical distance, and U is the mean streamwise velocity in the wake. The vertical wake velocity profiles were integrated using the trapezoidal rule to determine C_d. No correction for blockage was performed since the maximum solid body blockage was 7%, and for the majority of conditions tested it was below 5%. Corrections for measurements within the wake of a streamlined body are minimal prior to separation [31]. The uncertainty of C_d calculation was determined using standard propagation of uncertainty procedures. While the uncertainty for instruments and geometric measurements were readily available, the final uncertainty was heavily

dependent on the covariance between the mean velocity measurements and the free-stream speed. With a covariance of 0.395, the resulting uncertainty in C_d was 3.6% at the maximum test speed. Given the uncertainty of the covariance and weak variation between operation conditions, error bars on C_d plots have been fixed at 5% for reference.

Due to the observation of coherent structures in the far-wake region for a subset of conditions, the induced vorticity within the wake was computed as a measure of the strength of the coherent structures produced by the sBFS. Vorticity is defined as the curl of the flow velocity vector,

$$\vec{\omega} \equiv \nabla \times \vec{V} = \left(\frac{\partial w}{\partial y} - \frac{\partial v}{\partial z}\right)\hat{e}_x + \left(\frac{\partial u}{\partial z} - \frac{\partial w}{\partial x}\right)\hat{e}_y + \left(\frac{\partial v}{\partial x} - \frac{\partial u}{\partial y}\right)\hat{e}_z$$

Since the traverse system could not move in the streamwise direction, none of the streamwise gradients could be computed experimentally. Preliminary results from the computational study indicate that the streamwise component of vorticity (ω_x) is dominant [19]. This is also consistent with the expectation that a coherent structure persisting to the far-field would have significantly stronger gradients in the cross-stream directions relative to the streamwise. Note that since the vorticity is dependent on resolving the velocity vector, only the subset of conditions that used the 5-hole probe could analyze the vorticity. The streamwise vorticity was calculated at each measurement location and then averaged to create vorticity profiles of the wake deficit for each test configuration.

2.1.4. Test Conditions

The airfoil configurations were tested at free-stream speeds of 20 m/s and 26 m/s, which have a corresponding chord length-based Reynolds number $(Re = cU_\infty/\nu)$ of nominally 2.3×10^5 and 3.0×10^5, respectively. The current study focuses on the $Re = 3.0 \times 10^5$ results since no significant variation was observed between test speeds. This was expected due to the relatively narrow Reynolds number range but tested to confirm the insensitivity to Reynolds number over this range. For each test configuration, the angle of attack (α) was typically varied between 0 and 10 degrees in 2-degree increments. The test model configurations were clean wing (i.e., no film), three BFS, and four sBFS (see Table 1 for geometries and locations). For all configurations, the vertical increment (Δz) for the wake survey was 3.18 mm, which was half of the probe head diameter. For the clean wing and 7 BFS configurations, the spanwise increment (Δy) was increased to 25 mm since there was negligible spanwise variation. Conversely, the sBFS configurations produced coherent structures that created spanwise variations; the spanwise increment was reduced to 12.5 mm. In addition, the measurement locations with the sBFS were selected such that measurements were acquired directly downstream of peaks and valleys. The subset of conditions tested with the 5-hole probe were clean wing, BFS at 10% chord, BFS at 44% chord, and sBFS-V1.

2.2. Computational Methods

STAR-CCM+ v2022.1.1, a commercially available CFD software, was used for the computational study. The complex 3D models were created in SolidWorks and imported to STAR-CCM+, which has its own built in 3D-CAD, where the models were further edited to facilitate the simulation. STAR-CCM+ provides built-in automated mesh capabilities that include tetrahedral, trimmer, and polyhedral unstructured meshes. These mesh algorithms also have the capability of utilizing prism layers, which is essential in resolving the near-wall region of a boundary layer. STAR-CCM+ also has the capability to run a large range of physics- and flow-specific models that include RANS, DES, LES, and qDNS, with sub models for each. For the current study, RANS, or Reynolds-Averaged Navier–Stokes equations, which are often used to study the mean characteristics of the flow, were chosen.

The experimental setup was replicated in the computational model. A 3D rectangular domain was created for all simulations. The side walls were given periodic boundary conditions, while the top and bottom walls were subjected to slip conditions. The inlet was

a velocity inlet, while the outlet was treated as a pressure outlet. The side walls had periodic boundary conditions. The domain total length was 3.75 m, width 15.24 (width of 3 sBFS), and the height was 0.91 m to match the height of the wind tunnel in the experimental study. In this study, the span of the airfoil was reduced to 3 sBFS widths (152.4 mm). The sBFS-V1 configuration was chosen since it provided the most significant wake structures. The length, width, and thickness were 69.9 mm, 50.8 mm, and 1.1 mm, respectively, with the valley and peak locations at 10% and 45%, respectively. The turbulence model used for this study was k-omega turbulence and the turbulent intensity at the inlet was set to 1%. Surface, polyhedral and prism layer meshers were chosen for this study. The mesh was compared by studying 3 independent meshes comprising 2.5, 14, and 25 million cells. All 3 meshes produced similar results and the one with the highest number of cells was used for all of the analysis.

3. Results

3.1. Experimental Investigation

3.1.1. Reference Conditions

The clean wing (i.e., no step) and BFS configurations were tested as reference conditions for comparison with the sBFS results. The contour plot of the streamwise velocity scaled by the local free-stream speed (U_∞) for the clean wing is shown in Figure 3a with the abscissa the spanwise location (y) and the ordinate the vertical location (z) scaled by the wake half-deficit height $(z_{0.5})$. The wake half-deficit height is the distance from the wake center (i.e., maximum wake deficit) to the location where the wake deficit is half of the maximum deficit. For the current study, it was determined from the average half-deficit height from each spanwise location. This shows that there was a slight spanwise slope observed in the wake survey. Upon inspection, this was determined to be created by a slight misalignment between traverse coordinate system and the test section coordinate system, which, in the analysis, could be corrected by aligning the maximum wake deficit at a given spanwise location. Accounting for the slope, there was no significant spanwise variation in the wake deficit for the clean wing. In addition, this showed that the wake velocity at the maximum wake deficit was nominally 92% of the free-stream speed. This was consistent with wake deficits from streamlined bodies and supports the previous comment that wake corrections for streamlined bodies are minimal [31]. The coefficient of drag (C_d) was then calculated by integrating the wake profiles and averaging the results from individual spanwise locations. The clean wing results were compared with the XFOIL results [32] in Figure 3b. The current C_d results matched within the measurement uncertainty of the theoretical XFOIL results at lower angles of attack. At higher angles of attack, the experimental and XFOIL results appeared to deviate, but the discrepancy was close to the stall angle (10.25 degrees) for this airfoil shape.

The contour plots for the BFS configurations are not shown since there was no spanwise variation observed, but BFS contour plots are presented in the work of KC et al. [29] and KC [33]. The BFS wake structures were similar to that observed on the clean wing in Figure 3a. While the BFS structure was similar, the coefficient of drag was significantly increased relative to the clean wing. The BFS C_d at a chord length of 10%, 27%, and 45% are compared with the clean wing (CW) results in Figure 4. This illustrates the negative impact on the drag performance with the presence of BFS. This is consistent with the literature [34]. The BFS at 27% and 45% chord length produced similar curves to that of the clean wing with an average increase of 33% and 24% increase in C_d, respectively. The curve for BFS at 10% had a different trend, but the generally the C_d decreased with increased chord position. The BFS 10% chord produced the most amount of drag in comparison to BFS at 27 and 45% chord. This is due to the fact that the early step location caused the flow to separate earlier on the airfoil.

The streamwise vorticity (ω_x) was also computed for the clean wing and two of the BFS conditions (10% and 45% chord length), which were selected as reference conditions to align with the peak and valley locations of sBFS-V1. Figure 5 shows the maximum streamwise vorticity in the far-wake region for the clean wing and two BFS configurations.

The maximum vorticity was identified from the magnitude of the streamwise vorticity computed within the wake for each test configuration. The general trend for both the clean wing and the BFSs has the maximum vorticity decreased with an increasing angle of attack at small angles. Then, at higher angles of attack, the maximum vorticity begins to increase with increasing the angle of attack. This trend is comparable to that reported in the literature [35]. The clean wing and BFS at 45% have similar trends and magnitudes over the range of angles of attack tested, but BFS at 10% has significantly lower maximum vorticity and the change in trend occurs at a lower angle of attack. This is indicative of a structural change in the flow pattern at BFS of 10% relative to the other reference conditions, which is consistent with the C_d results.

3.1.2. sBFS Conditions

The coefficient of drag (C_d) for all four sBFS configurations is plotted in Figure 6 along with the clean wing and BFS at 10% chord length for reference. The coefficient of drag at zero angle of attack was within the measurement uncertainty for all four sBFS configurations. The sBFS at $\alpha = 0^\circ$ was higher than the clean wing but lower than the BFS at 10% chord, and, of note, sBFS-V1, -V2, and -V4 had the valley located at the 10% chord. At higher angles of attack, the C_d increases except for sBFS-V3, which is nearly constant over the range tested. Since sBFS-V3 was the only configuration with the valley location further downstream than the 10% chord length, this suggests that the drag performance at higher angles of attack might converge to the performance of a BFS at the valley location. The other three sBFS configurations (sBFS-V1, -V2, and -V4) steadily increased C_d with increasing α until 10°, when the value exceeds that of the BFS at 10% chord length. This is consistent with the literature (e.g., [34]), which shows that the location of the step has a significant impact on performance, with reduced impact as the step moves towards the trailing edge. For these cases, the flow separated early compared to when the valley was located further downstream as in the case of sBFS-V3. The early separation caused the drag of the three configurations to rise quickly relative to the sBFS-V3. A comparison between sBFS-V1 and -V2 (i.e., half the length and width of -V1 with same step height) showed that the variation was comparable to the measurement uncertainty until the highest angle of attack. Conversely, when the length-to-width ratio was increased for sBFS-V4, it shows a decrease in C_d for low angles of attack, but then converged to sBFS-V1 and -V2 at higher angles of attack.

Figure 7 compares the velocity contour plots of clean wing, BFS at 10% chord length, and sBFS-V1. Like Figure 3a, the ordinate in Figure 7 is the vertical distance (z) from the wake center scaled by the wake half-deficit ($z_{0.5}$), but the spanwise location (y) is scaled by the sBFS-V1 width (W). As expected, the clean wing and BFS distributions do not show any significant spanwise variation in the deficit. However, the sBFS profile shows a clear spanwise variation in the velocity distribution. This suggests that the sBFS promotes the formation of coherent structures. The streamwise velocity is scaled by the free-stream speed (U_∞), while the other velocity components (v and w) are normalized by their respective maximum magnitudes. The spanwise variation observed for the sBFS-V1 configuration is proportional to the width of the sBFS. This was unexpected since these measurements were acquired five chord lengths downstream of the model. The sBFS-V1 coherent structures are apparent in all three velocity components with a scale that is nominally twice the wake deficit's half height ($z_{0.5}$). This is because the coherent structures are turbulent, which will have a three-dimensional flow field. The cross-stream components indicate that the structures form in counter-rotating pairs.

The vorticity within the wake was computed to quantify the sBFS-V1's coherent structure production. The maximum streamwise vorticity of the sBFS-V1 configuration is compared with that of the clean wing and BFS at 10% chord length in Figure 8. As expected, the vorticity is consistently higher for sBFS-V1 relative to both the clean wing and the 10% chord BFS. This is especially true at zero angle of attack where the maximum streamwise vorticity was 2.7 and 3.5 times larger than the clean wing and 10% chord BFS, respectively. This

suggests that these low-profile shapes are imparting significant rotation that can redistribute the momentum on the airfoil surface, which is critical for passive flow control.

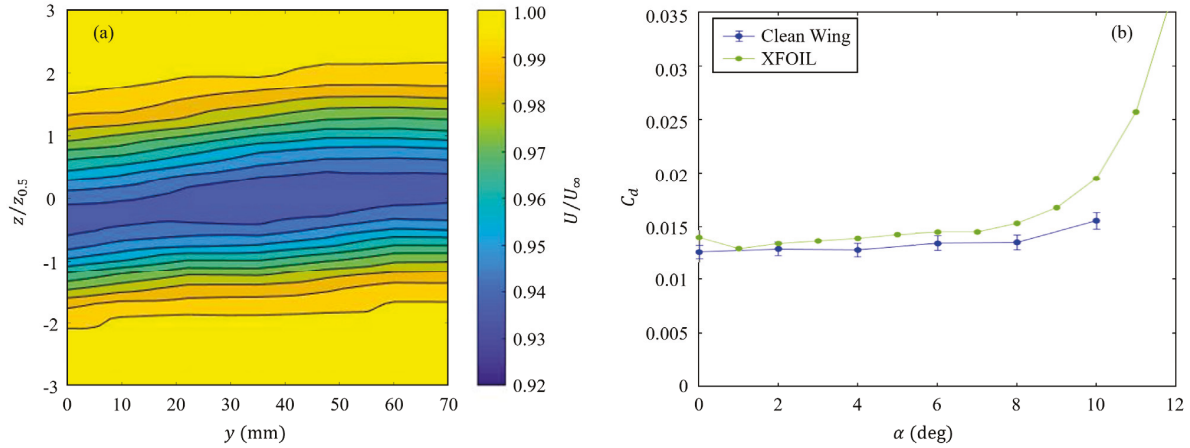


Figure 3. (**a**) Clean wing contour plot of wake at Reynolds number of 300,000. (**b**) Coefficient of drag (C_d) versus angle of attack for the clean wing compared with estimation using XFOIL.

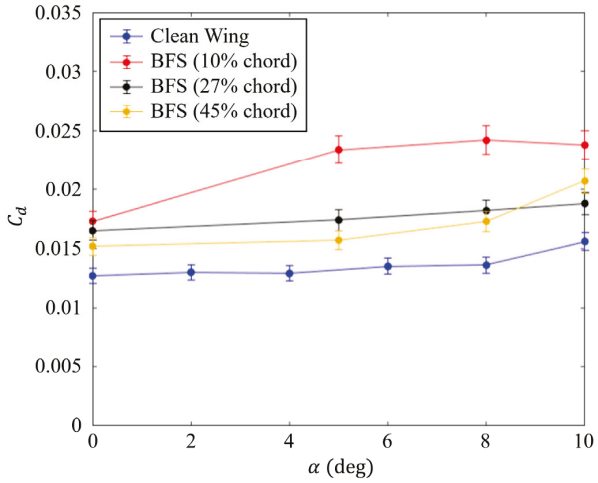


Figure 4. BFS coefficient of drag as function of angle of attack and chord position compared to the clean wing.

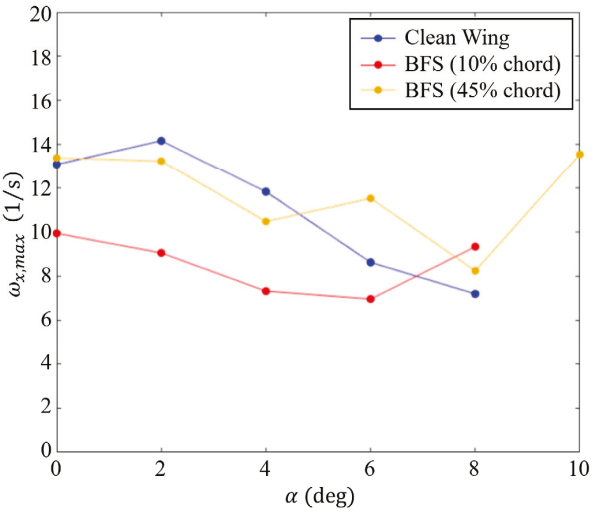


Figure 5. The maximum streamwise vorticity (ω_x) for the clean wing and BFS configurations tested with the five-hole probe.

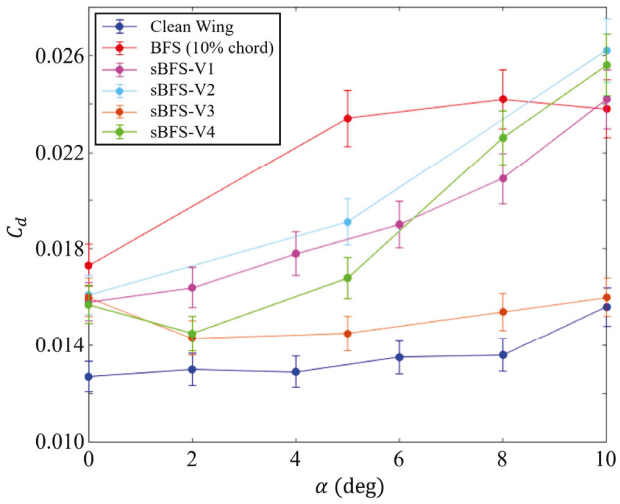


Figure 6. The coefficient of drag for all sBFS configurations tested as a function of the angle of attack. Curves for the clean wing and BFS at 10% chord are included for reference.

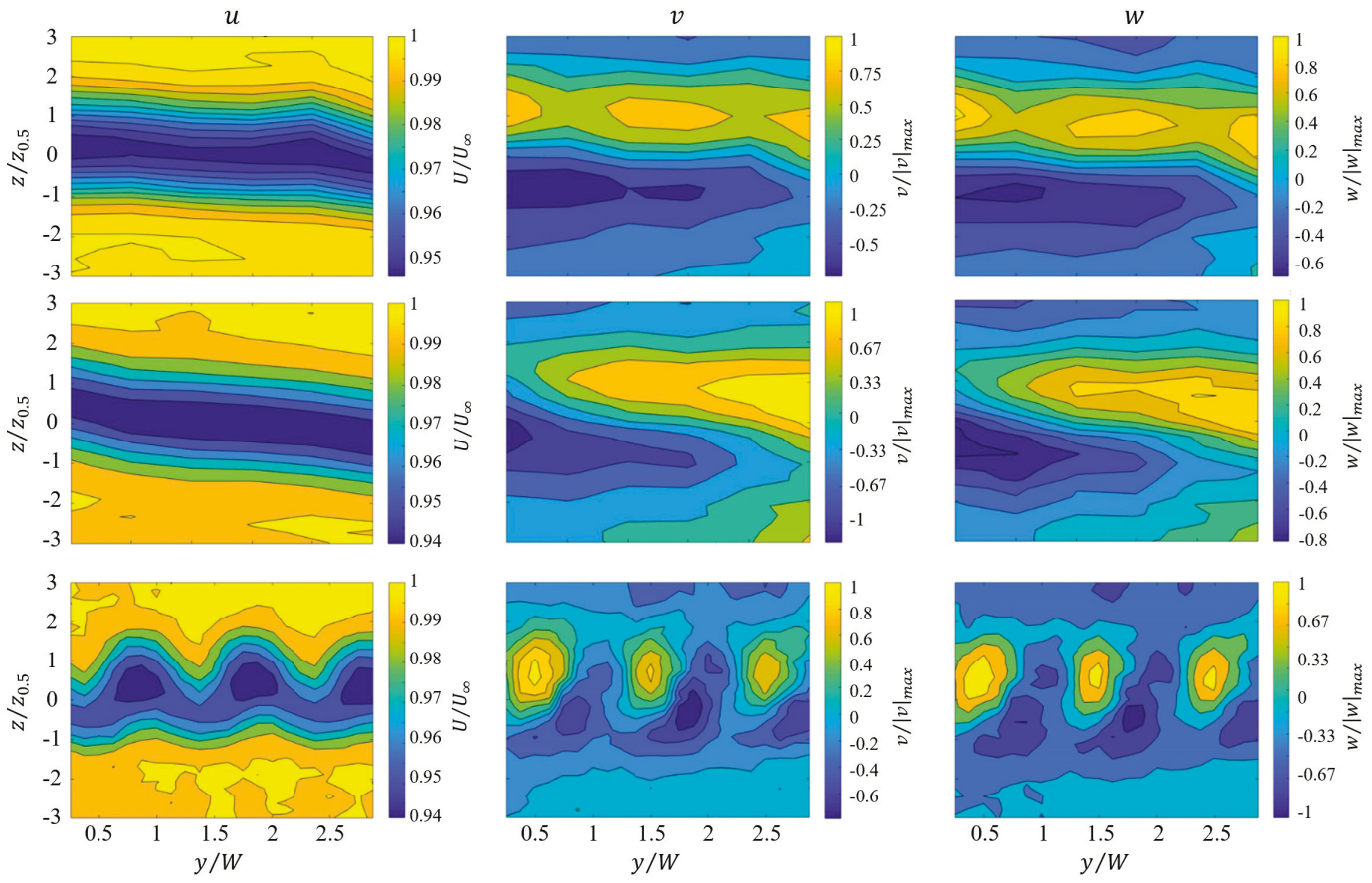


Figure 7. Contour plots of the (**left column**) streamwise, (**middle column**) spanwise, and (**right column**) vertical velocity components from the (**top row**) clean wing, (**middle row**) BFS at 10% chord length, and (**bottom row**) sBFS-V1.

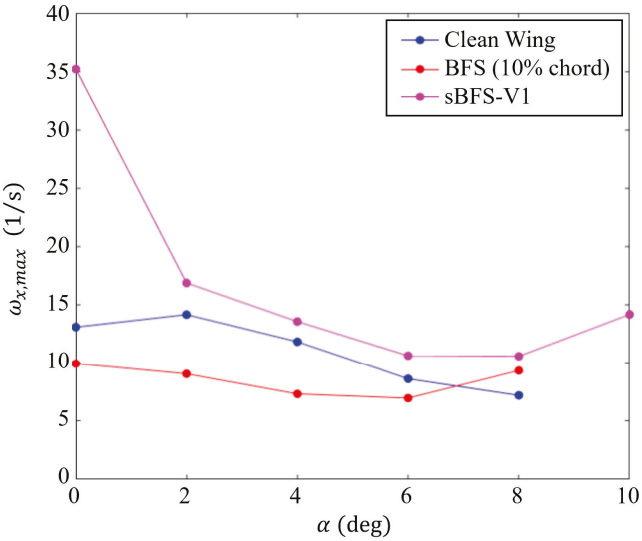


Figure 8. Maximum streamwise vorticity for the sBFS-V1 configuration compared with the clean wing and 10% chord BFS.

3.2. Computational Investigation

The experimental results provided insights into the overall impact on the airfoil's performance, but the specific flow modifications induced by the sBFS could not be examined. Consequently, a computational model was also developed and validated via direct comparison of the available experimental data with the computational results. The comparison between the experimental and computational wake results for the sBFS-V1 condition are shown in Figure 9. The experimental result is the streamwise component in the lower row of Figure 7. The peaks and the valleys of the sBFS are well aligned with the structures in the wake region, which is also observed in the computational results. The size and pattern of the structures are in excellent agreement. The velocity magnitudes, indicated by the color, are also in agreement with each other. Thus, giving confidence that the computational model is providing an accurate representation of the experimental flow field.

Now, the induced vorticity in the far-wake region can be explored with the full velocity gradient distribution available. The streamwise vorticity in the far-wake region from the computational simulation is shown in Figure 10. The resulting structures are consistent with the experimental results. This shows that the coherent structure in the far-wake region is counter-rotating pairs. This also shows that the counter-rotating vortices are not symmetric, with the red vortices showing a much tighter core (i.e., darker color) relative to the blue vortices. This is also consistent with the experimental observations.

Now, the computational model can be utilized to examine the flow field induced by the sBFS on the airfoil. Streamlines were used to explore the flow patterns induced by the sBFS. This revealed that streamlines originate from near the wall prior to the step rollup as they go over the step. Near-surface streamlines near the sBFS valley location are then redirected from the streamwise direction towards the sBFS peak. Conversely, the streamlines that originate in the far-wall region do not have any significant spanwise movement. These differences are illustrated in Figure 11, where half of the streamlines originate from near the surface and the other half in the far-wall region. In addition, Video S1 in the Supplemental Material shows the computational simulation streamlines from various views and their relationship to the resulting wake structure. In addition, Video S1 shows that the region directly downstream of the peak has flow reversal, which is indicative of flow separation. Conversely, the flow remains attached to the trailing edge in the region directly downstream of the valley. Thus, it was concluded that the near-surface flow becomes entrained in the direction towards the peak and this is responsible for producing the coherent structures that persist into the far-wake region. This finding is consistent with the work of Wang et al. [36]

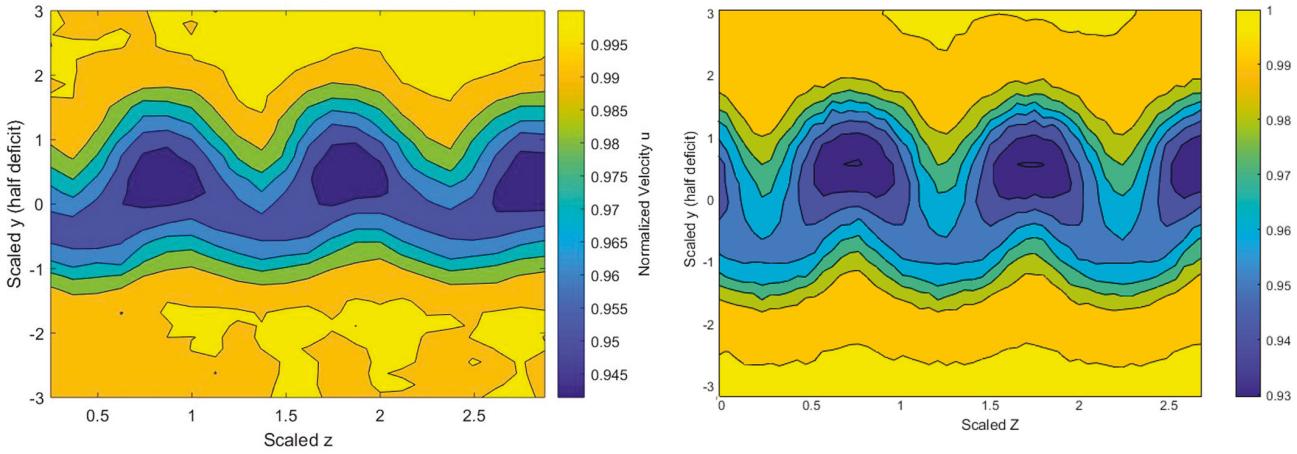


Figure 9. Comparison of the streamwise velocity contour plots produced by the (**left**) experimental measurements and (**right**) computational models.

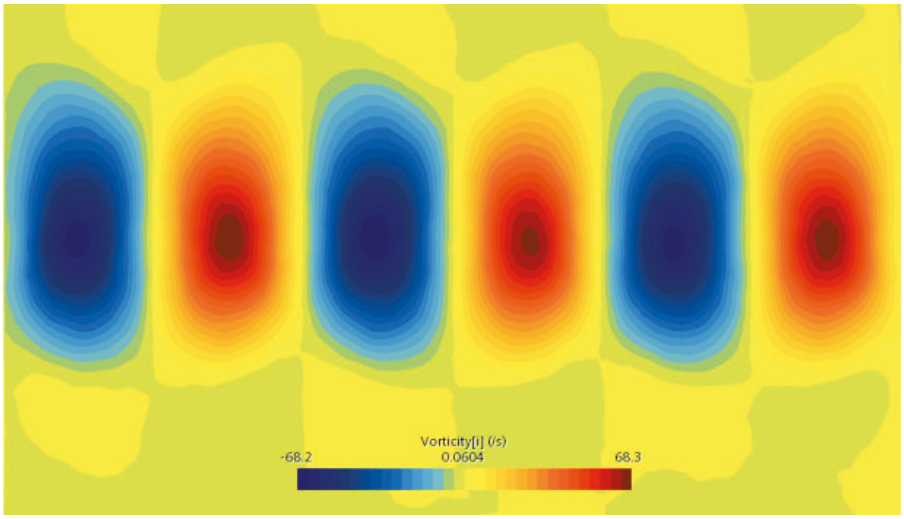


Figure 10. Computational simulation results of the streamwise vorticity in the far-wake region from the sBFS-V1 configuration.

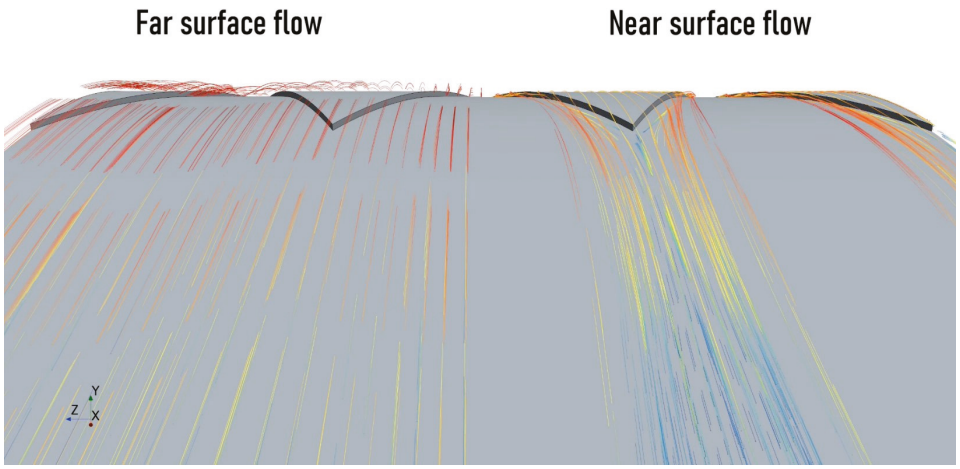


Figure 11. Flow entrainment over the sBFS visualized with streamlines colored based on the local relative speed (cool to warm colors indicate low to high speeds). Streamlines originate from either (**left**) the far-wall or (**right**) near-surface region upstream of the step.

4. Discussion

The lowest drag results for the BFS (i.e., 45% chord) and sBFS are compared along with the clean wing results in Figure 12. As expected, the sBFS did not reduce the drag relative to the clean wing, though at the highest angle of attack tested, the two configurations are within the measurement uncertainty. Conversely, sBFS-V3 had lower drag than BFS at 45% chord for nearly all angles of attack tested, and at zero angle of attack, the increase was comparable to the measurement uncertainty. This was in spite of the fact that sBFS-V3 had the valley location (27% chord) closer to the leading edge than the BFS at 45% chord. Note that the peak location of sBFS-V3 was at 45%, which matches the BFS location compared in Figure 12. As previously discussed, airfoils regularly have BFSs such as that created by the slat step on the wing on the Boeing 737, which is nominally located at the 10% chord length. These results indicate that the sBFS can mitigate the negative drag effect created by BFS. These findings are consistent with recent work studying microsteps, which have shown that they could have a significant impact on boundary layer flows at scales much larger than their step height [37,38]. It should also be noted that minimal effort has been dedicated to date on the sizing of the sBFS relative to the flow parameters, which is critical, as most passive flow-control methods require a tuning of the geometry given the flow parameters.

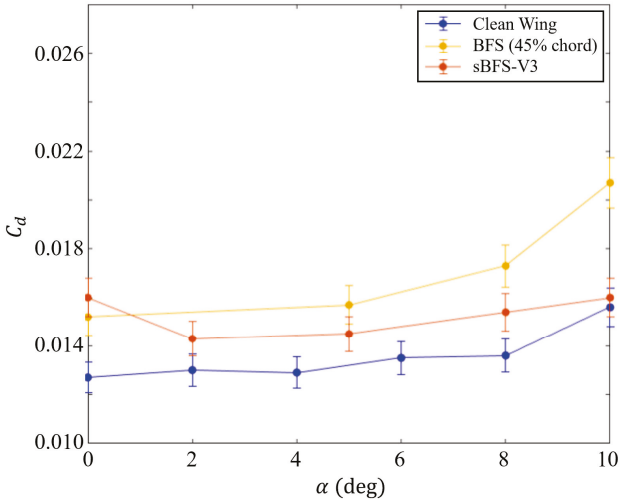


Figure 12. Comparison of the sBFS-V3 that produced the lowest C_d values with that of the clean wing and the BFS with the lowest drag (i.e., BFS at 45% chord length). The sBFS-V3 had the valley and peak at 27% and 45% chord length, respectively.

The computational study showed evidence that these coherent structures are formed by the sBFS redirecting the near-wall flow at the valley towards the peaks. Then, downstream of the valley, the flow remains attached even when the flow separates downstream of the sBFS peak. The pattern then persists downstream, forming the spanwise variation observed in the far-wake region. In addition, the streamwise vorticity in the computational study showed that the coherent structures in the wake are counter-rotating pairs.

5. Conclusions

Wake surveys in the far-wake region of a LA203A airfoil model were used to measure the drag associated with the application of a protective film around the model's leading edge. A BFS was created on the model with a thin film. The use of a serrated (i.e., saw-tooth) pattern on the trailing edge of the BFS was explored to investigate its potential for mitigating negative impacts. For reference, the clean wing (i.e., no film) and three standard BFSs were tested. These results showed that the BFS increased the drag relative to the clean wing, and that the drag increased the closer the BFS was to the leading edge. Four sBFS configurations, each with the same step height, were tested. In general, over most angles of

attack, the sBFS produced lower drag relative to the BFS located at the sBFS valley location. In addition, vorticity and contour plots showed that the sBFS produced strong coherent structures that could persist into the far-wake region.

Computational simulations showed that these structures were produced by the sBFS, with the flow near the surface of the airfoil being entrained in the direction of the sBFS peak. This induced motion modified the downstream flow structure, which, in the sBFS condition computationally examined, impacted separation at the trailing edge. This pattern at the trailing edge likely produced such a strong pattern in the far-wake region, though they were induced by the sBFS as evidenced by the structure alignment with the sBFS peak and valley geometry. The strength of the structures does appear to be dependent, in part, on the length-to-width ratio of the sBFS; however, the possible influence of the width itself was not studied and should be explored further in connection with the impact on the trailing edge separation.

Overall, there is evidence that sBFS could mitigate the adverse effects on drag associated with BFS on airfoils, which are frequently created due to the addition of protective leading edge films or mismatch in height between adjoining surfaces. Mitigating these effects could lead to improved performance across certain flight regimes, and improve the efficiency of wind turbines. The next steps are to develop an LES-based simulation to enable a study of the coherent structures on the airfoil and how they are modified by the sBFS; these insights will enable the tuning of the step geometry based on the operation condition.

Supplementary Materials: The following supporting information can be downloaded at: https://www.mdpi.com/article/10.3390/inventions8060160/s1, Video S1: Video of streamlines originating from either the near-wall or far-wall region upstream of the step.

Author Contributions: Conceptualization, R.J.K., B.R.E. and J.D.J.; methodology, R.J.K., N.A.L., B.R.E. and J.D.J.; software, R.J.K., T.C.W. and A.S.A.; validation, R.J.K., T.C.W., A.S.A., J.D.J., B.R.E. and N.A.L.; formal analysis, R.J.K., A.S.A., B.R.E. and N.A.L.; investigation, R.J.K., T.C.W., A.S.A., J.D.J., B.R.E. and N.A.L.; resources, B.R.E. and J.D.J.; data curation, R.J.K., A.S.A. and N.A.L.; writing—original draft preparation, R.J.K., T.C.W., A.S.A., J.D.J., B.R.E. and N.A.L.; writing—review and editing, R.J.K. and B.R.E.; visualization, R.J.K.; supervision, B.R.E. and J.D.J.; project administration, B.R.E. and J.D.J.; funding acquisition, B.R.E. and J.D.J. All authors have read and agreed to the published version of the manuscript.

Funding: This research was funded, in part, by B.R.E.'s John Brammer Professorship.

Data Availability Statement: The data presented in this study are available on request from the corresponding author.

Acknowledgments: The authors thank Kurt Rouser and his laboratory group for their assistance with wind tunnel operations and measurements.

Conflicts of Interest: The authors declare no conflict of interest.

References

1. Hood, M.J. *The Effects of Surface Waviness and of Rib Stitching on Wing Drag*; Technical Report NACA-TN-724; National Advisory Committee for Aeronautics: Washington, DC, USA, 1939.
2. Young, A.D.; Paterson, J.H. *Aircraft Excrescence Drag*; Technical Report AGARD-AG-264; North Atlantic Treaty Organization (NATO) Advisory Group for Aerospace Research and Development (AGARD): Bruxelles, Belgium, 1981.
3. Rizzetta, D.P.; Visbal, M.R. Numerical Simulation of Excrescence Generated Transition. *AIAA J.* **2014**, *52*, 385–397. [CrossRef]
4. Rizzetta, D.P.; Visbal, M.R. Plasma-Based Flow Control for Delay of Excrescence-Generated Transition. *AIAA J.* **2015**, *53*, 1455–1467. [CrossRef]
5. Rizzetta, D.P.; Visbal, M.R. Plasma-Based Control of Transition on a Wing with Leading-Edge Excrescence. *AIAA J.* **2016**, *54*, 129–140. [CrossRef]
6. Rizzetta, D.P.; Visbal, M.R. Plasma-Based Control of Excrescence-Generated Transition on a Swept Wing. *AIAA J.* **2017**, *55*, 1610–1621. [CrossRef]
7. Major, D.; Palacios, J.; Maughmer, M.; Schmitz, S. A numerical model for the analysis of leading-edge protection tapes for wind turbine blades. *J. Phys. Conf. Ser.* **2020**, *1452*, 012058. [CrossRef]

8. Major, D.; Palacios, J.; Maughmer, M.; Schmitz, S. Aerodynamics of leading-edge protection tapes for wind turbine blades. *Wind Eng.* **2021**, *45*, 1296–1316. [CrossRef]
9. Agrim, S.; Sapre, C.A.; Selig, M.S. Effects of leading-edge protection tape on wind turbine blade performance. *Wind Eng.* **2012**, *36*, 525–534.
10. Witherspoon, S.; Finaish, F. Experimental and Computational studies of flow developments around an airfoil with backward-facing steps. In Proceedings of the 14th Applied Aerodynamics Conference, New Orleans, LA, USA, 17–20 June 1996.
11. Kostas, J.; Soria, J.; Chong, M. Particle image velocimetry measurements of a backward-facing step flow. *Exp. Fluids* **2002**, *33*, 838–853. [CrossRef]
12. Barri, M.; Andersson, H.I. Turbulent flow over a backward-facing step. Part 1. Effects of anti-cyclonic system rotation. *J. Fluid Mech.* **2010**, *665*, 382–417. [CrossRef]
13. Hasan, M.A.Z. The flow over a backward-facing step under controlled perturbation: Laminar separation. *J. Fluid Mech.* **1992**, *238*, 73–96. [CrossRef]
14. Lin, J. Control of turbulent boundary-layer separation using micro-vortex generators. In Proceedings of the 30th Fluid Dynamics Conference, Norfolk, VA, USA, 28 June–1 July 1999.
15. Yao, C.; Lin, J.; Allen, B. Flowfield measurement of device-induced embedded streamwise vortex on a flat plate. In Proceedings of the 1st Flow Control Conference, St. Louis, MO, USA, 24–26 June 2002.
16. Storms, B.L.; Jang, C.S. Lift enhancement of an airfoil using a Gurney flap and vortex generators. *J. Aircr.* **1994**, *31*, 542–547. [CrossRef]
17. Lin, J.C. Review of research on low-profile vortex generators to control boundary-layer separation. *Prog. Aerosp. Sci.* **2002**, *38*, 389–420. [CrossRef]
18. Babinsky, H.; Li, Y.; Ford, C.W.P. Microramp control of supersonic oblique shock-wave/boundary-layer interactions. *AIAA J.* **2009**, *47*, 668–675. [CrossRef]
19. Chu, H.B.; Zhang, B.Q.; Chen, Y.C. Controlling flow separation of high lift transport aircraft with micro vortex generators. *J. Northwestern Polytech. Univ.* **2011**, *29*, 799–805.
20. Bolgar, I.; Scharnowski, S.; Kahler, C.J. Passive Flow Control for Reduced Load Dynamics Aft of a Backward-Facing Step. *AIAA J.* **2019**, *57*, 120–131. [CrossRef]
21. Paruchuri, C.; Joseph, P.; Ayton, L.J. On the superior performance of leading edge slits over serrations for the reduction of aerofoil interaction noise. In Proceedings of the 2018 AIAA/CEAS Aeroacoustics Conference, Atlanta, Georgia, 25–29 June 2018; p. 3121.
22. Calvert, M.; Wong, T.-C. Aerodynamic Impacts of Helicopter Blade Erosion Coatings. In Proceedings of the 30th AIAA Applied Aerodynamics Conference, New Orleans, LA, USA, 25–28 June 2012; p. 2914.
23. Scholbrock, A. *Power Performance Results UsingWind Turbine Blade Enhancing Devices Developed By Edge Aerodynamix*; Technical Report; National Renewable Energy Laboratory: Golden, CO, USA, 2017.
24. Wilson, T.C.; KC, R.; Lucido, N.A.; Elbing, B.R.; Alexander, A.S.; Jacob, J.D.; Ireland, P.; Black, J.A. Computational Investigation of the Conformal Vortex Generator. In Proceedings of the AIAA Scitech 2019 Forum, San Diego, CA, USA, 7–11 January 2019. [CrossRef]
25. Kibble, G.A. Experimental and Computational Investigation of the Conformal Vortex Generator. Master's Thesis, Oklahoma State University, Stillwater, OK, USA, 2017.
26. Lucido, N.A.; KC, R.; Wilson, T.C.; Jacob, J.D.; Alexander, A.S.; Elbing, B.R.; Ireland, P.; Black, J.A. Laminar Boundary Layer Scaling Over a Conformal Vortex Generator. In Proceedings of the AIAA Scitech 2019 Forum, San Diego, CA, USA, 7–11 January 2019. [CrossRef]
27. Lucido, N.A. Investigation of Low-Profile Vortex Generators on Low Reynolds Number Propellers for Small Unmanned Aircraft. Master's Thesis, Oklahoma State University, Stillwater, OK, USA, 2019.
28. Zimbelman, T. Plasma Flow Control for Distortion Tolerant Fans with Aircraft Boundary Layer Ingestion. Master's Thesis, Oklahoma State University, Stillwater, OK, USA, May 2018.
29. KC, R.; Lucido, N.A.; Wilson, T.C.; Elbing, B.R.; Jacob, J.D.; Alexander, A.S.; Ireland, P.; Black, J.A. Investigation of Wake Survey over a Wing with Conformal Vortex Generators. In Proceedings of the AIAA Scitech 2019 Forum, San Diego, CA, USA, 7–11 January 2019. [CrossRef]
30. Brune, G.W. Quantitative Low-Speed Wake Surveys. *AIAA J. Aircr.* **1994**, *31*, 249–255. [CrossRef]
31. Maskell, E.C. *A Theory of the Blockage Effects on Bluff Bodes and Stalled Wings in a Closed Wind Tunnel*; Technical Report ARC Reports and Memoranda R&M 3400; Aeronautical Research Council: London, UK, 1963.
32. Drela, M. XFOIL: An Analysis and Design System for Low Reynolds Number Airfoils. In *Low Reynolds Number Aerodynamics*; Mueller, T.J., Ed.; Springer: Berlin/Heidelberg, Germany, 1989; pp. 1–12. [CrossRef]
33. KC, R.J. Investigation of Low-Profile Vortex Generators via Experimental Methods. Master's Thesis, Oklahoma State University, Stillwater, OK, USA, July 2019.
34. Mishriky, F.; Walsh, P. Effect of the backward-facing step location on the aerodynamics of a morphing wing. *Aerospace* **2016**, *3*, 25. [CrossRef]

35. Wendt, B.J. Parametric study of vortices shed from airfoil vortex generators. *AIAA J.* **2004**, *42*, 2185–2195. [CrossRef]
36. Wang, B.; Liu, W.D.; Sun, M.B.; Zhao, Y.X. Fluid redistribution in the turbulent boundary layer under the microramp control. *AIAA J.* **2015**, *53*, 3777–3787. [CrossRef]
37. Falco, R. Drag Reduction Method and Surface. US Patent 5,133,519, 28 July 1992.
38. Al-Jaburi, K.; Feszty, D. Passive Flow Control of Dynamic Stall via Surface-Based Trapped Vortex Generators. *J. Am. Helicopter Soc.* **2018**, *63*, 1–14. [CrossRef]

Disclaimer/Publisher's Note: The statements, opinions and data contained in all publications are solely those of the individual author(s) and contributor(s) and not of MDPI and/or the editor(s). MDPI and/or the editor(s) disclaim responsibility for any injury to people or property resulting from any ideas, methods, instructions or products referred to in the content.

inventions

MDPI

Article

Applications of the Order Reduction Optimization of the H-Infinity Controller in Smart Structures

Amalia Moutsopoulou [1], Markos Petousis [1,*], Nectarios Vidakis [1], Georgios E. Stavroulakis [2] and Anastasios Pouliezos [2]

[1] Department of Mechanical Engineering, Hellenic Mediterranean University, 71410 Heraklion, Greece; amalia@hmu.gr (A.M.); vidakis@hmu.gr (N.V.)
[2] Department of Production Engineering and Management, Technical University of Crete, 73100 Chania, Greece; gestavr@dpem.tuc.gr (G.E.S.); tasos@dpem.tuc.gr (A.P.)
* Correspondence: markospetousis@hmu.gr; Tel.: +30-2810379227

Abstract: In this paper, our strategy is to look for locally optimum answers to a non-smooth optimization problem that has been constructed to include minimization goals and restrictions for smart structures' vibration suppression. In both theoretical analysis and practical implementation, it is widely recognized that designing multi-objective control systems poses a considerable challenge. In this study, we assess the effectiveness of this method by employing the open-source Matlab toolbox Hifoo 2.0 and juxtapose our findings with established industry standards. We start by framing the control problem as a mathematical optimization issue and proceed to identify the controller that effectively addresses this optimization. This approach introduces the potential application of intelligent structures in tackling the challenge of vibration suppression. This study makes use of the most recent version of the freely available application Hifoo which tries to study vibration suppression with the limits outlined above in the context of multi-objective controller design. A controller directive is initially set, allowing for a lower order.

Keywords: optimization problem; H-infinity controller; Hifoo control; smart structures

1. Introduction

In recent years, there has been a lot of interest in piezoelectrically activated smart structures that have robust vibration control. For systems that must maintain stability or performance in the face of several sources of uncertainty, such control rules are ideal [1–4]. The later robust controller leads to an appropriate design of smart structures by accounting for the uncertainties of the dynamical system and the incompleteness of the measured data. The numerical simulation demonstrates that the general methods proposed can effectively suppress vibration in the case of a piezoelectric smart structure, serving as a tutorial. The ultimate goal of this approach is to provide a comprehensive and unique methodology for the design and validation of robust H-infinity controllers for active structures [5–9].

The implementation of active control technologies in intelligent structures has been the focus of the current effort. In addition to vibration reduction, low steady-state error, fast recovery, and little-to-no maximum uplift are also desired; nevertheless, control energy cannot go beyond operational bounds. H-infinity control has the benefit of allowing the computation to account for the worst-case scenario of unpredictable disturbances and system noise. Furthermore, a wide frequency spectrum may be created as the H-infinity controller can effectively handle more input. The findings are noteworthy; vibration reduction is demonstrated even for actual wind loads when the voltage of the piezoelectric component is regulated within tolerance. Utilizing the Hifoo controller in conjunction with non-parametric and non-convex optimization methods. The results are good; we completely reject disturbances utilizing reduced-order control and H-infinity control [10–15]. The aforementioned discusses the many control techniques used to reduce noise and vibration

in structures. This study contributes to the use of control to reduce intelligent structures' oscillations. The main advancement is the use of a reduced-order controller to achieve total oscillation suppression.

In this research, we first make use of the H-infinity control implementations in smart structures. A controller based on H-infinity is intended to inhibit the smart piezoelectric structure's vibration under dynamic loading. It is demonstrated that the H-infinity controller is resilient to parametric uncertainty in vibration suppression situations. The advantages of active vibration suppression and robust control in smart structure dynamics are clearly described in this paper. Robust control theory is needed to develop smart structure controllers that deliver stability with guaranteed performance [1–3]. A disadvantage of controller H infinity is the large computational demands, especially when the number of finite elements increases. By using the controller, we can get just as good results as a reduced-order controller. Second, the most current version of the publicly accessible program, Hifoo [4–7], which aims to overcome the limitations mentioned above in the context of multi-objective controller design, is used in this study. Compared to traditional control approaches, Hifoo methods offer the benefit of being immediately adaptable to difficulties with multivariate systems. It is challenging to optimize both great performance and stability at the same time [7–13]. The behavior of a pair of piezoelectric patches applied symmetrically to the top and bottom surfaces of each beam element will be studied in an intelligent cantilever smart construction. No lifting or Lyapunov variables are used to address the requirements' incompatibilities. This leads to an optimization issue that is often short-dimensional, non-smooth, and nonconvex, and does not need the solution of any significant convex subproblems [4–7]. It is usually simple to locate an appropriate controller rather than an efficient robust control in reality, even though the behavior of this technique cannot be guaranteed [8–10]. Hifoo methods have the advantage of being quickly adaptive to problems involving multivariate systems in comparison to typical control approaches. Optimizing strong stability and performance at the same time is difficult [11–13]. A method known as Hifoo loop-shaping allows the control designer to use typical loop-shaping techniques to the multivariable frequency response in order to achieve beneficial robust performance, before optimizing the response near the system bandwidth to meet good robust criteria. In this article [12,14,15], the benefits of strong control in intelligent companies are discussed.

Very high-order controllers are often produced by most of the techniques or heuristics currently used to address these issues. The control behavior of the beam matches predictions, and the results show the effectiveness of the provided model and method. The beam's control behavior is in line with expectations, and the outcomes demonstrate the effectiveness of the suggested model and procedure. In this work, a beam with piezoelectric patches is controlled and oscillations caused under dynamic load are reduced. In recent years, there has been a lot of interest in piezoelectrically activated smart structures that have robust vibration control. The Hifoo robust controller leads to an appropriate design of smart structures by accounting for the uncertainties of the dynamical system and the incompleteness of the measured data. The numerical simulation demonstrates that the general methods proposed can effectively suppress vibration in the case of a piezoelectric smart structure, serving as a tutorial. The ultimate goal of this approach is to provide a comprehensive and unique methodology for the design and validation of robust Hifoo controllers for active structures [16–20]. The findings are remarkable; even for actual wind loads, vibration reduction is shown when the piezoelectric component voltage is adjusted tolerably. In order to reduce the model's processing requirements, the controller rank was dropped by combining non-parametric and nonconvex optimization approaches with the Hifoo controller. Both the local bundle technique and the gradient sampling method cannot be employed if the MATLAB route lacks the quadratic programming tool "quadprog". These three optimization techniques each make use of the gradients that Hifoo dynamically produces. Finding the odd locations where gradients do not exist is not attempted. The positions of the gradient discontinuities do not cause the procedures to fail. The latter

phases of the bundle and gradient sampling look for a place where a convex combination of gradients at neighboring points has a small norm. Even with a substantially lower system degree, the controller functioned flawlessly. Strong stabilization, in which a robust controller must stabilize a plant, and simultaneous stabilization, in which a single controller must be discovered to stabilize many plants, are characteristic instances of multi-objective robust control issues [7,16,17]. We evaluate the system's flexibility and durability after doing a system analysis. The beneficial aspects of this work are as follows: reduced-order optimization of the H-infinity controller in intelligent structures, control of oscillation suppression by simulating intelligent entities, results in the time–space domain and the frequency domain, application of measurement noise of beam state, complete suppression of oscillations, reduction of controller order, input of white noise as disturbance input, taking it as a percentage of the disturbances, and application of measurement noise. The results are excellent. We achieved complete disturbance rejections with H-infinity control and with reduced-order control. The following are alternative control techniques used to reduce structural noise and vibration. This work contributes to the application of control to reduce the oscillations of smart structures. The innovation is that full suppression of oscillations is achieved with a reduced-order controller. In other words, the optimal result is achieved with much smaller computational requirements and without compromising the accuracy of the model. The first focus of future studies will be on how to apply these certain command techniques to real intelligent structures in an experimental context. This article presents innovations in the application of the demanding theory of control to smart materials and computational mechanics. The innovation is that full suppression of oscillations is achieved with a reduced-order controller. In other words, the optimal result is achieved with much smaller computational requirements and without compromising the accuracy of the model.

2. Methodology

2.1. Controller Synthesis H-Infinity

The aforementioned provides ways for comparing and assessing controller performance as well as answers to analytical difficulties. Nonetheless, it is feasible to approximately synthesize a controller that delivers a specific performance in terms of the structured single -μ- value. In this procedure known as (D, G-K) iteration [17–22], i.e., the difficulty in identifying a μ-optimal controller K so that μ(F(jω), K(jω)) ≤ β, ∀ω, is converted into the problem of identifying finding transfer function matrices D(ω)∈ and G(ω)∈ ∞, such that,

$$\sup_{\omega}\overline{\sigma}\left[\left(\frac{D(\omega)\left(F_u(F(j\omega),K(j\omega))D^{-1}(\omega)\right.}{\gamma}-jG(\omega)\right)\left(I+G^2(\omega)\right)^{-\frac{1}{2}}\right]\leq 1,\forall\omega \quad (1)$$

Unfortunately, this approach fails to provide any guarantee of identifying local maxima. However, a method referred to as D-K iteration is available for complicated perturbations (additionally implemented in MATLAB). It connects H-infinity synthesis and μ-analysis generally, producing positive outcomes. The initial reference is a limit on μ expressed in relation to the adjusted singular value [22,23],

$$\mu(N)\leq\min_{D\in D}\overline{\sigma}\left(DND^{-1}\right) \quad (2)$$

The concept aims to identify a controller that minimizes the maximum value over the frequency of its upper bound, namely,

$$\min_{K}\left(\min_{D\in D}\left\|DN(K)D^{-1}\right\|_{\infty}\right) \quad (3)$$

by taking turns in the process of minimizing $\left\|DN(K)D^{-1}\right\|_{\infty}$ with respect to either K or D (while maintaining the other fixed) [21,23–26].

The challenge is the process of selecting a single controller using state-space equations, K = (A_K, B_K, C_K, D_K). The maximum 2-norm perturbation to a stable closed loop system that may be accepted whilst still ensuring that the perturbed system stays stable is the H-infinity norm, which is not specified. The biggest real component of a closed loop system's poles (eigenvalues) is called the spectral abscissa.

To exhibit P in state space, the natural partitioning must be generated,

$$P(s) = \begin{bmatrix} A & B_1 & B_2 \\ C_1 & D_{11} & D_{12} \\ C_2 & D_{21} & D_{22} \end{bmatrix} = \begin{bmatrix} P_{zw}(s) & P_{zu}(s) \\ P_{yw}(s) & P_{yu}(s) \end{bmatrix} \tag{4}$$

where the packed form has been used, while the equivalent type for K is,

$$K(s) = \begin{bmatrix} A_K & B_K \\ C_K & D_K \end{bmatrix} \tag{5}$$

Equation (4) specifies the equations,

$$\begin{gathered} \dot{x}(t) = Ax(t) + \begin{bmatrix} B_1 & B_2 \end{bmatrix} \begin{bmatrix} w(t) \\ u(t) \end{bmatrix} \\ \begin{bmatrix} z(t) \\ y(t) \end{bmatrix} = \begin{bmatrix} C_1 \\ C_2 \end{bmatrix} x(t) + \begin{bmatrix} D_{11} & D_{12} \\ D_{21} & D_{22} \end{bmatrix} \begin{bmatrix} w(t) \\ u(t) \end{bmatrix} \end{gathered} \tag{6}$$

and,

$$\begin{gathered} \ddot{x}_\kappa(t) = A_\kappa x_\kappa(t) + B_\kappa y(t) \\ u(t) = C_\kappa x_\kappa(t) + D_\kappa y(t) \end{gathered} \tag{7}$$

To find the matrices involved, we break the feedback loop and use the relevant equations, in order to receive the structure in state space form, and align the inputs, outputs, states, and input/output to the controller:

$$\begin{gathered} \dot{x}_F = Ax_F + (Gd + Bu),\ x = Ix_F \\ \dot{x}_u = A_u x_u + B_u u,\ u_w = C_u x_u + D_u u \\ \dot{x}_e = A_e x_e + B_e Jx,\ e_w = C_e x_e + D_e Jx \\ \dot{x}_{nw} = A_{nw} x_{nw} + B_{nw} n_w,\ n = C_{nw} x_{nw} + D_{nw} n_w \\ \dot{x}_{dw} = A_{dw} x_{dw} + B_{dw} d_w,\ d = C_{dw} x_{dw} + D_{dw} d_w \\ y = Cx + n \end{gathered} \tag{8}$$

Let,

$$x = \begin{bmatrix} x_F \\ x_u \\ x_e \\ x_{nw} \\ x_{dw} \end{bmatrix},\ y = y,\ w = \begin{bmatrix} d_w \\ n_w \end{bmatrix},\ z = \begin{bmatrix} u_w \\ e_w \end{bmatrix},\ u = u \tag{9}$$

The internal signals d, n, and e x are substituted into Equation (8) to produce,

$$\begin{bmatrix} \dot{x}_F \\ \dot{x}_u \\ \dot{x}_e \\ \dot{x}_{nw} \\ \dot{x}_{dw} \end{bmatrix} = \begin{bmatrix} A & 0 & 0 & 0 & GC_{dw} \\ 0 & A_u & 0 & 0 & 0 \\ B_e J & 0 & A_e & 0 & 0 \\ 0 & 0 & 0 & A_{nw} & 0 \\ 0 & 0 & 0 & 0 & A_{dw} \end{bmatrix} \begin{bmatrix} x_F \\ x_u \\ x_e \\ x_{nw} \\ x_{dw} \end{bmatrix} + \begin{bmatrix} GD_{dw} & 0 \\ 0 & 0 \\ 0 & 0 \\ 0 & B_{nw} \\ B_{dw} & 0 \end{bmatrix} \begin{bmatrix} d_w \\ n_w \end{bmatrix} + \begin{bmatrix} B \\ B_u \\ 0 \\ 0 \\ 0 \end{bmatrix} u \tag{10}$$

$$\begin{bmatrix} u_w \\ e_w \end{bmatrix} = \begin{bmatrix} 0 & C_u & 0 & 0 & 0 \\ D_e J & 0 & C_e & 0 & 0 \end{bmatrix} \begin{bmatrix} x_F \\ x_u \\ x_e \\ x_{nw} \\ x_{dw} \end{bmatrix} + 0 \begin{bmatrix} d_w \\ n_w \end{bmatrix} + \begin{bmatrix} D_u \\ 0 \end{bmatrix} u \tag{11}$$

$$y = \begin{bmatrix} C & 0 & 0 & C_{nw} & 0 \end{bmatrix} \begin{bmatrix} x_F \\ x_u \\ x_e \\ x_{nw} \\ x_{dw} \end{bmatrix} + \begin{bmatrix} 0 & D_{nw} \end{bmatrix} \begin{bmatrix} d_w \\ n_w \end{bmatrix} + 0u \tag{12}$$

Therefore, the matrices are:

$$\begin{gathered} = \begin{bmatrix} A & 0 & 0 & 0 & GC_{dw} \\ 0 & A_u & 0 & 0 & 0 \\ B_eJ & 0 & A_e & 0 & 0 \\ 0 & 0 & 0 & A_{nw} & 0 \\ 0 & 0 & 0 & 0 & A_{dw} \end{bmatrix}, B_1 = \begin{bmatrix} GD_{dw} & 0 \\ 0 & 0 \\ 0 & 0 \\ 0 & B_{nw} \\ B_{dw} & 0 \end{bmatrix}, B_2 = \begin{bmatrix} B \\ B_u \\ 0 \\ 0 \\ 0 \end{bmatrix} \\ C_1 = \begin{bmatrix} 0 & C_u & 0 & 0 & 0 \\ D_eJ & 0 & C_e & 0 & 0 \end{bmatrix}, D_{11} = 0, D_{12} = \begin{bmatrix} D_u \\ 0 \end{bmatrix} \\ C_2 = \begin{bmatrix} C & 0 & 0 & C_{nw} & 0 \end{bmatrix}, D_{21} = \begin{bmatrix} 0 & D_{nw} \end{bmatrix}, D_{22} = 0 \end{gathered} \tag{13}$$

As can be seen, the state vector in this design has a size of 16 + 4 + 4 + 4 + 8 = 36. Modeling the controller K(s)'s size is additionally determined by this. In cases where any weight matrices are constant, this number will be reduced by the appropriate order [20,27,28].

The challenge is to select a single controller K = (A_K, B_K, C_K, D_K) that has state-space equations $A_K \in R^{nK \times nK}$, with B_K, C_K, and D_K that have compatible dimensions with AK and the generalized plant matrices. The designer can specify the controller order K since it is fixed [29–32]. For a stable closed-loop system, the complex stability radius is the largest 2-norm perturbation that is tolerable whilst still ensuring that the disrupted mechanism continues to be stable when the w and z performance channels are not specified, and the H-infinity norm is not defined [32–35]. A closed loop system's spectral abscissa is the biggest real component of its poles (eigenvalues).

2.2. Optimization Method Hifoo

A two-phase algorithm is used. The quasi-Newton approach (BFGS optimization algorithm), which is effective for nonconvex, non-smooth optimization, is the main driving force behind each phase [4–7]. If the user does not provide a first estimate for the desired controller, Hifoo produces the first controllers at random. Even if the user does make an initial guess, Hifoo nonetheless generates more initial controllers at random just in case they give better results. Lowering the closed loop plants' maximum spectral abscissa using BFGS is the first step in stabilizing. Once one is discovered that stabilizes these plants, the procedure concludes and a starting point for the second phase with a finite controller is attained. Increasing the penalty factor, while optimization is repeated as necessary if BFGS is unable to find a site where the constraint violations are zero (unless F is identically zero, in which case all j are finite). Although this method is frequently quick and extremely successful, there are no guarantees. By default, Hifoo follows BFGS using the more time-consuming Burke et al.'s [7] gradient sampling strategy; however, this may be altered.

2.3. Problem Formulation and Optimization Method

More information is provided in the equations of a generalized plant G's state-space.

$$\begin{gathered} \dot{x}(t) = Ax(t) + B_1w(t) + B_2u(t), \\ z(t) = C_1x(t) + D_{11}w(t) + D_{12}u(t), \\ y(t) = C_2x(t) + D_{21}w(t) + D_{22}u(t) \end{gathered} \tag{14}$$

and the controller K(s)'s state-space realization is

$$\begin{gathered} \dot{x}_K(t) = A_K\, x_K(t) + B_Ky(t), \\ u(t) = C_K\, x_K(t) + D_Ky(t), \end{gathered} \tag{15}$$

where $A \in R^{n\times n}$, $D_{12} \in R^{p1\times m2}$, $D_{21} \in R^{p2\times m1}$, with additional matrices that share equal dimensions, and $A_K \in R^{nK\times nK}$, with B_K, C_K, D_K A_K and the generalized plant matrices comparable in terms of dimensions. Because the order of the control is fixed, the designer is able to specify it.

The signals (z, w, y, u) stand in for the controlled outputs, exogenous inputs (such as disturbances and directives), measured inputs (or sensor inputs), and control inputs, in that order. T_{zw} stands for the transfer function from the input w to the output z; for further information, see [14]. The closed loop H∞ typical function can be minimized to represent the ideal H-infinity controller architecture.

$$\underset{K\ stabilizing}{\text{Inf}} \quad \|T_{zw}\|_\infty,$$

in which K(s) internally stabilize the closed-loop system according to the restriction.

We apply the extra requirement that the controller be stable in this study because we want to decrease

$$\underset{K\ stabilizing\ and\ K\ stable}{\text{Inf}} \quad \|T_{zw}\|_\infty,$$

Let us use a(X) to represent the biggest real part of the eigenvalues, or the spectral abscissa of matrix X. As a result, we need both that $\alpha(A_{CL}) < 0$ and that $\alpha(A_K) < 0$ where A_{CL} is the closed-loop system matrix. The set of stable matrices, which is the feasible set for A_K, is not convex and has a rough boundary. It has received substantial research; for examples, see [5–7].

The two processes used by Hifoo are stability and performance optimization, just like in earlier versions [7,33]. As the closed-loop system is being stabilized, Hifoo 2 keeps minimizing $\max(\alpha(A_{CL}, \varrho\alpha(A_K))$, which is a positive parameter that will result in detaining more details subsequently, until it discovers a controller K for which this number is negative, indicating that the controller is stable. If Hifoo is unable to discover a suitable controller, it will return with an output to that effect.

Hifoo 2 searches for a local minimizer during the performance optimization phase of

$$f(K) = \begin{cases} \infty \text{ if } \max(\alpha(ACL),\ \alpha(AK)) \ \geq\ 0 \\ \max(\|T_{zw}\|_\infty \infty, \in \|K\|_\infty) \ \text{ otherwise} \end{cases} \tag{16}$$

where,

$$\|K\|_\infty = \sup_{\mathcal{R}f=0} \left\| C_K(sI - A_K)^{-1}B_K + D_K \right\|_2.$$

The primary design objective aims to minimize the transfer function Tzw and stabilize the closed-loop system, so the introduction is justified. However, the K term restrains the H-infinity norm of the controller from growing too large, a condition that the stability constraint alone cannot ensure. The performance phase of optimization starts with f (K), obtaining a bounded value because of the stabilization phase. The rejection occurs during the line search process, which demands a decrease in the objective function at each iteration. The optimization algorithm that Hifoo [36] calls at each level employs the non-smooth, nonconvex optimization technique known as HANSO. These components make up its composition: if a local bundle approach fails to identify local optimality for the best point determined by BFGS, gradient sampling [2,4] tries to enhance the local minimizer's estimate and returns a rough optimality value. To approximate a local minimizer faster, we use a quasi-Newton algorithm (BFGS). If the MATLAB route does not contain the quadratic programming tool "quadprog", neither the local bundle approach nor the gradient sampling method is used [34,36–38]. Each of these three methods of optimization takes advantage of the gradients that Hifoo dynamically generates. Identifying the peculiar places where the gradients do not exist is not attempted. The methods do not fail as a result of the gradient discontinuities at unusual locations. The last stages of the bundle and gradient sampling search parameter space for a location where a convex combination of gradients at nearby points has a small norm. The algorithm is two-phase. Each phase is mainly driven by the

quasi-Newton technique (BFGS optimization algorithm), which is efficient for nonconvex, non-smooth optimization [4–7]. Hifoo generates the initial controllers at random if the user does not supply a first estimate for the desired controller. Hifoo produces more initial controllers at random even if the user does make an initial estimate, just in case they produce better results. The first step in stabilizing is lowering the maximum spectral abscissa of the closed loop plants using BFGS. The process is complete and a starting point for the second phase with a finite controller is reached once one is found that stabilizes these plants. Increasing the penalty factor and repeating optimization, as necessary. A very poorly conditioned Hessian approximation matrix is produced during the BFGS phase. There is further information in [4–7,39].

3. Results

3.1. Application in Smart Structures

The following part will analyze the behavior of an eight-element cantilever smart structure with symmetrical bonds between four pairs of piezoelectric patches at each beam element's top and bottom surfaces (Figures 1 and 2). The different components of this construction have the dimensions presented below.

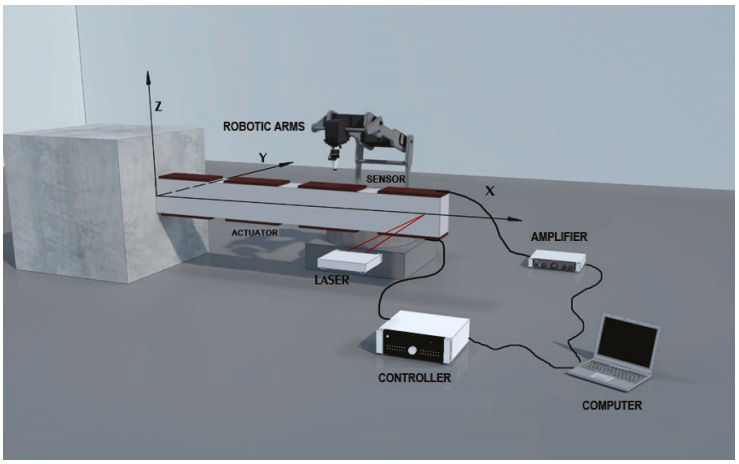


Figure 1. Intelligent structure.

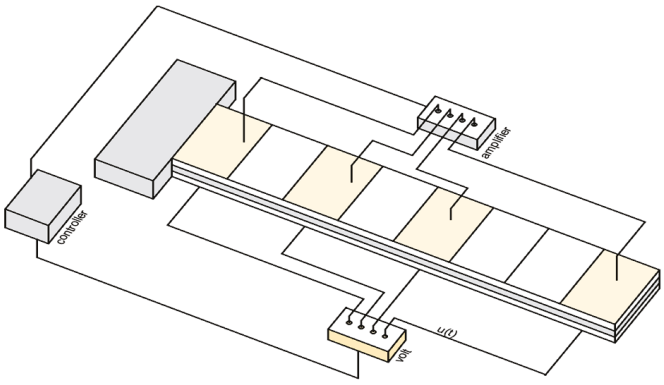


Figure 2. Piezoelectric smart beam.

The dynamical description of the system is provided by

$$M\ddot{q}(t) + C\dot{q} + Dq(t) = f_m(t) + f_e(t) \quad (17)$$

where M is the global mass matrix, C is the viscous damping matrix, D represents the global stiffness matrix, f_m represents the global external loading vector, and f_e is the global control

force vector produced by electromechanical coupling effects. The independent variable q(t) is composed of transversal deflections w_i and rotations ψ_i, i.e.,

$$q(t) = \begin{bmatrix} w_1 \\ \psi_1 \\ \vdots \\ w_n \\ \psi_n \end{bmatrix} additionally \tag{18}$$

in which n is the number of finite elements that the analysis is using. Vectors w and $\mathbf{f}_m$ is positive upwards.

In order to convert to state-space control representation, allow (in the usual manner)

$$x(t) = \begin{bmatrix} q(t) \\ \dot{q}(t) \end{bmatrix} \tag{19}$$

Additionally, to define $f_e(t)$ as Bu(t), we express it as $F_e^* u$, where F_e^* (of size $2n \times n$) is the piezoelectric force for a unit applied on the corresponding actuator, and u stands for the voltages on the actuators [40–42]. Lastly, $d(t) = f_m(t)$ is the disturbance vector. Then,

$$\begin{aligned} \dot{x}(t) = \begin{bmatrix} 0_{2n\times 2n} & I_{2n\times 2n} \\ -M^{-1}K & -M^{-1}D \end{bmatrix} x(t) + \begin{bmatrix} 0_{2n\times n} \\ M^{-1}F_e^* \end{bmatrix} u(t) + \begin{bmatrix} 0_{2n\times 2n} \\ M^{-1} \end{bmatrix} d(t) \\ = Ax(t) + Bu(t) + Gd(t) \\ = Ax(t) + \begin{bmatrix} B & G \end{bmatrix} \begin{bmatrix} u(t) \\ d(t) \end{bmatrix} \\ = Ax(t) + B\widetilde{u}(t) \end{aligned} \tag{20}$$

This can be enhanced using the output equation (displacements only measured),

$$y(t) = [x_1(t)\, x_3(t) \ldots x_{n-1}(t)]^T = Lx(t) \tag{21}$$

In this formulation u is $n \times 1$ (at most, but can be smaller), while d is $2n \times 1$, (n is the number of nodes). The units used are m, rad, sec, and N. The parameters of the smart beam are in Table 1. Our system remains stable in the field of time-space, but stability is presented in more detail in the field of frequency domain.

Table 1. Parameters of the smart beam.

Parameters	Values
L, for beam length	1.00 m
W, for Beam Width	0.002 m
Wp, PZT Width	0.002 m
h, for Beam thickness	0.096 m
hp, piezoelectric thickness	0.0002 m
ρ, for Beam density	1600 kg/m^3
E, for Young's modulus of the beam Ep, Young modulus of pzt 6.3×10^{10} N/m^2	1.5×10^{11} N/m^2
bs, ba, for PZT thickness	0.002 m
d_{31} the Piezoelectric constant	230×10^{-12} m/V

3.2. Results for H-Infinity Control

The Matlab routine for H-infinity control is: [Kinf] = h_{inf}syn(sysic, nmeas, ncont),

Where nmeas = 4 is the number of sensors, ncont = 4 is the number of the controller, and sysic is the formulation of the block diagram. In Figure 3 for this formulation, we use the Matlab code:

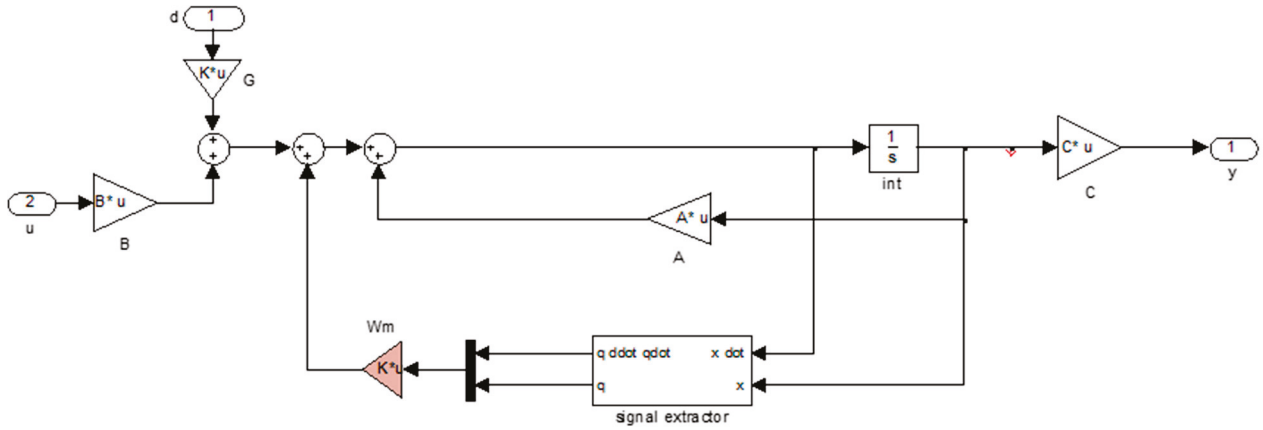


Figure 3. Block diagram in Simulink for the smart beam (* is × in the diagram).

```
beam0 = ss(A0, eye(2+nd), eye(2+nd), 0);
y = C0;
systemnames = ' beam0 y ad su se We Wu Wn ';
inputvar = '[ n(4); d(8); u(4)]';
input_to_sd = '[Wd]';
input_to_su = '[u]';
input_to_se = '[beam0]';
input_to_beam0 = '[ sd+su ]';
input_to_y = '[ beam0 ]';
input_to_Wu = '[u]';
input_to_Wn = '[n]';
input_to_Wd = '[d]';
input_to_We = '[se]';
```

The whetted matrix for noise, control, error, and disturbance are for control u:

$$W_u = \begin{bmatrix} \frac{5.556\times10^{-6}s+0.005556}{s+100} & 0 & 0 & 0 \\ 0 & \frac{5.556\times10^{-6}s+0.005556}{s+100} & 0 & 0 \\ 0 & 0 & \frac{5.556\times10^{-6}s+0.005556}{s+100} & 0 \\ 0 & 0 & 0 & \frac{5.556\times10^{-6}s+0.005556}{s+100} \end{bmatrix} \quad (22)$$

For error e:

$$W_e = \begin{bmatrix} \frac{2513}{s+31.42} & 0 & 0 & 0 \\ 0 & \frac{2513}{s+31.42} & 0 & 0 \\ 0 & 0 & \frac{2513}{s+31.42} & 0 \\ 0 & 0 & 0 & \frac{2513}{s+31.42} \end{bmatrix} \quad (23)$$

For disturbances d:

$$W_d = \begin{bmatrix} 40 & 0 & 0 & 0 & 0 & 0 & 0 & 0 \\ 0 & 40 & 0 & 0 & 0 & 0 & 0 & 0 \\ 0 & 0 & 40 & 0 & 0 & 0 & 0 & 0 \\ 0 & 0 & 0 & 40 & 0 & 0 & 0 & 0 \\ 0 & 0 & 0 & 0 & 40 & 0 & 0 & 0 \\ 0 & 0 & 0 & 0 & 0 & 40 & 0 & 0 \\ 0 & 0 & 0 & 0 & 0 & 0 & 40 & 0 \\ 0 & 0 & 0 & 0 & 0 & 0 & 0 & 40 \end{bmatrix} \quad (24)$$

For noise n:

$$W_{n=}\begin{bmatrix} 10^{-6} & 0 & 0 & 0 \\ 0 & 10^{-6} & 0 & 0 \\ 0 & 0 & 10^{-6} & 0 \\ 0 & 0 & 0 & 10^{-6} \end{bmatrix} \quad (25)$$

In all simulations the input is also white noise as the disturbance input, taking it as a percentage of the measurement (in Matlab Simulink) Figure 4. In all the simulations that have been done in Matlab, noise has been obtained in the measurements +, − one percent as a percentage of the signal input. This was done to take into account uncertain disturbances of the system, for example, unpredictable disturbances of the air force. The system was tested in the Simulink Matlab, and the model used is shown in Figure 4.

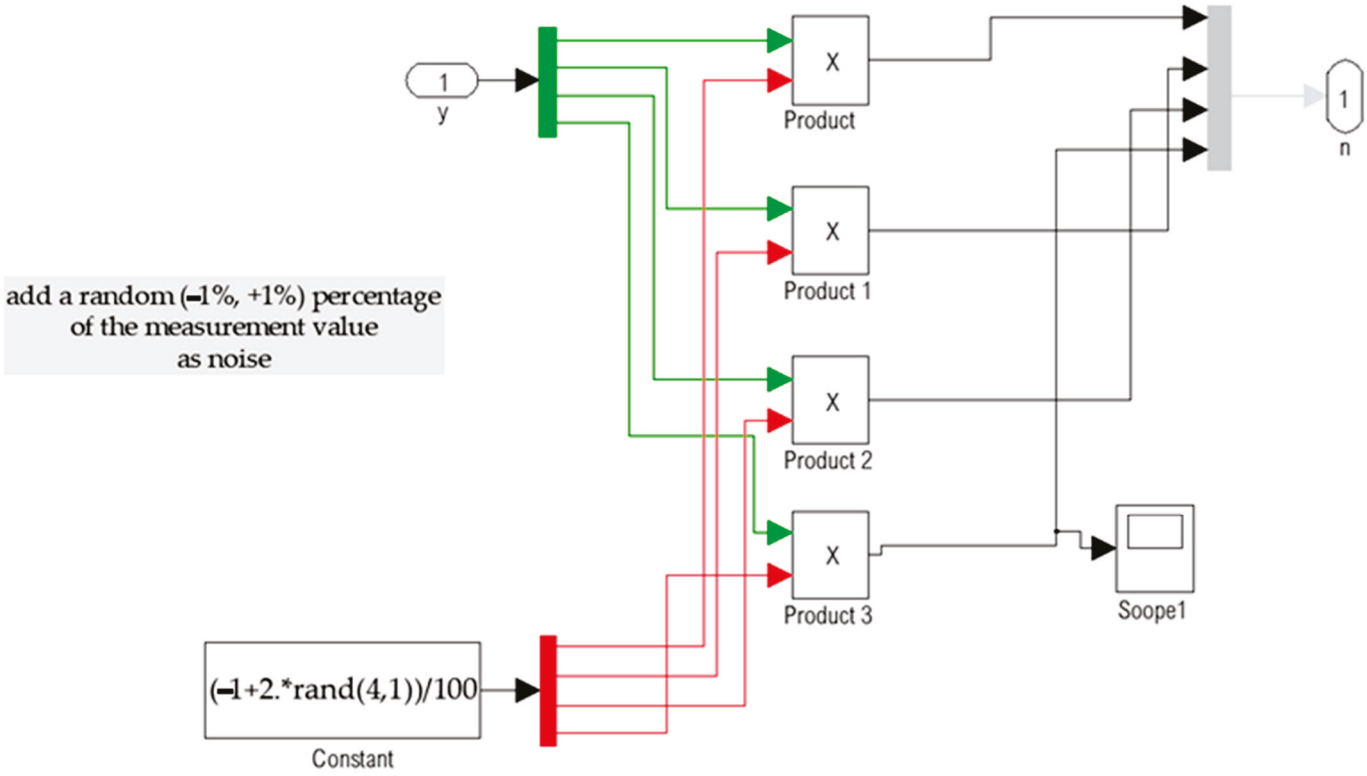


Figure 4. The block diagram in Simulink for the noise as a percentage of the measurement (* is × in the diagram).

All the simulations are in the Matlab program using the toolbox Simulink (Figure 5). The simulation has been done and the output of the result of the voltages (in volts) of the actuators can be seen. In all simulations, measurement noise has been taken as a percentage of the inputs as shown in Figures 4 and 5.

Figure 6 shows the beam's displacement over time as a result. In comparison to when there is no control, the displacement is almost zero. We were able to minimize vibrations by 95% by employing a unique control technique called H-infinity control. The green line is with H-infinity control (closed loop), and the red line is without control (open loop). Suppression of oscillations is achieved in all actuators and displacements are almost zero. This is very important in all mechanical constructions and a real innovation. At the same time, as shown in Figure 7, a relatively low voltage is achieved in the actuators since the suppression is done with approximately 50 Volts while the actuators withstand 500 Volts. As shown in Figure 7, the voltage generated by the control system to operate the control is within the 500 Volt safe limit for the material being utilized. The blue line shows the voltages of the last node, the green of the previous one, the red of the second, and the pale blue of the first node.

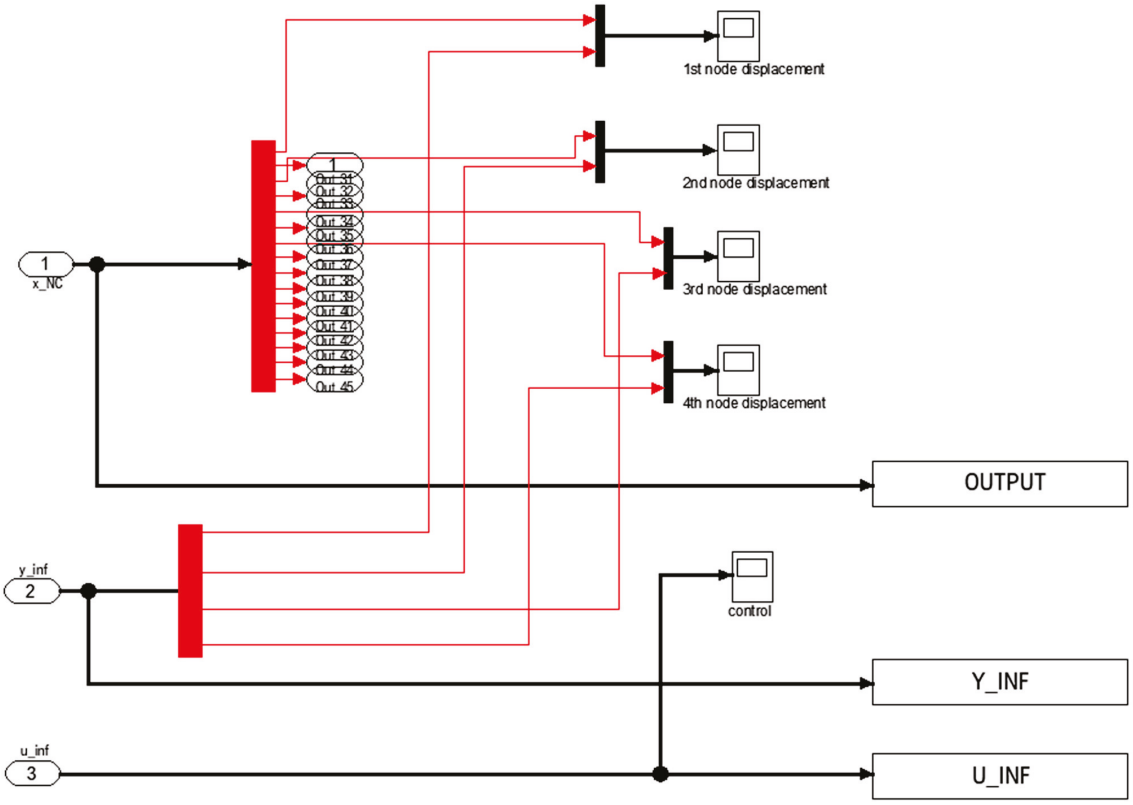


Figure 5. Simulation diagram for results in Matlab Simulink. The output is presented and explained in Figure 7 below.

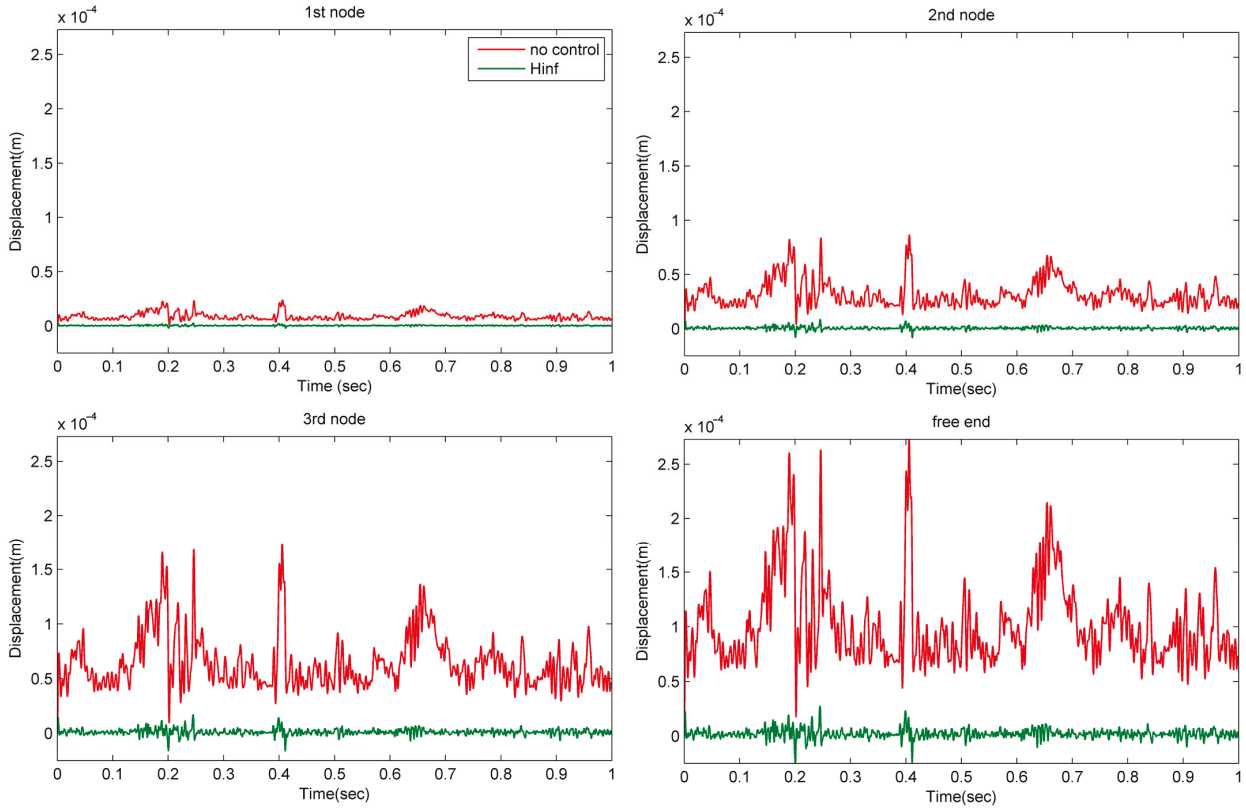


Figure 6. Displacements for the four nodes with actuators. The green line is with H-infinity control (closed loop), and the red line is without control (open loop).

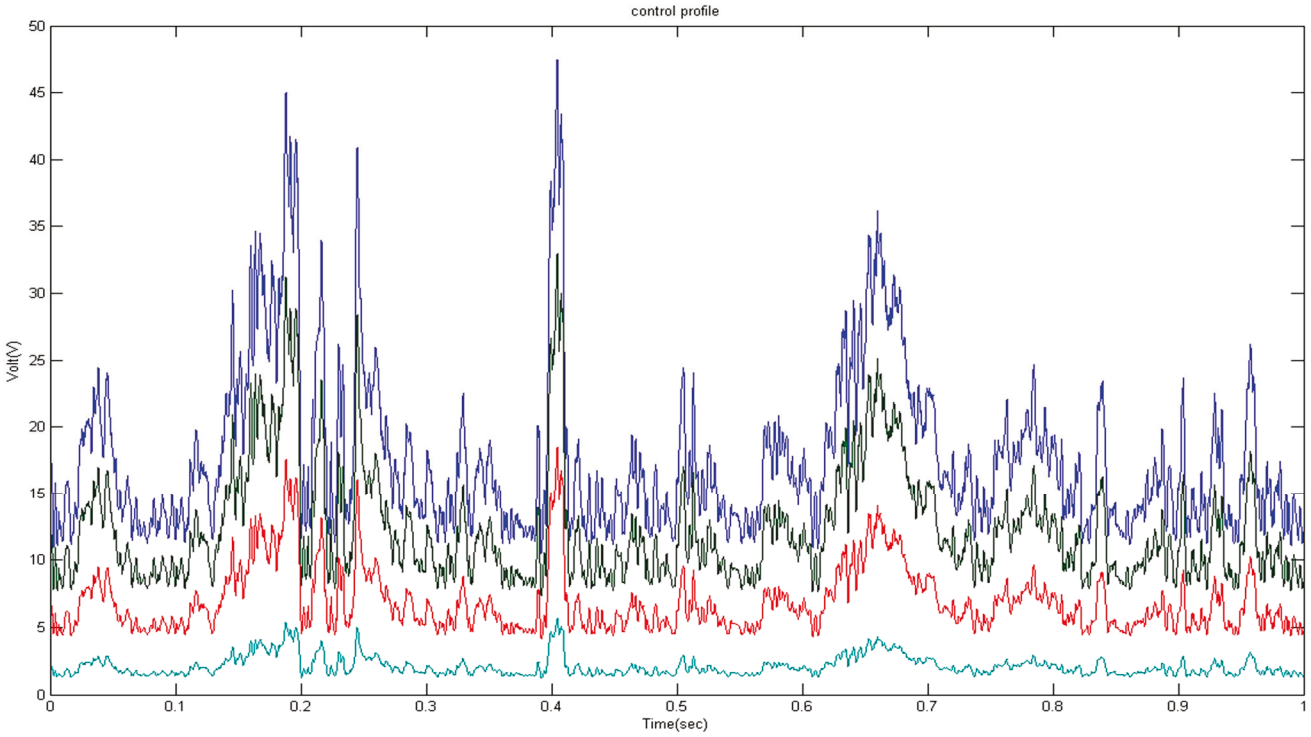


Figure 7. Control voltages for the four pairs of actuators of the beam. With the blue line is the control voltages for the free end of the smart beam, with green line the control voltages for the 3rd node of the smart beam, with red line the control voltages for the previous node of the smart beam and with the light blue line the first node of the smart beam.

In the frequency domain, Figure 8 shows graphs that represent the weight matrices. The results are obtained across the frequency range because oscillations must be classified at a specific value. The main advantage of H-infinite control is that we can work both in the time domain and the frequency domain. These matrices were made by doing a lot of tests to make sure we could find a controller. The controller that is made using H-infinity control has an order of 36. The value of γ for this controller is 0.074. The 36th order H-infinity controller was discovered. Because the order of the controller, which is equal to the order of the system, is typically higher than the order of conventional controllers like PI and LQR, researchers have developed order reduction techniques. The next method makes use of the Hifoo algorithm, which has been applied in the Matlab platform and is the most common of these algorithms.

The ultimate goal of the aforementioned system is to determine a controller of decreased rank/order n (36) while preserving the performance of the H-infinity criterion and a full-order controller's behavior [24,25,36,43,44]. The following are some advantages of this work: decline in order, complete suppression of oscillations, reduction of controller order, application of measurement noise of beam state, optimization of the H-infinity controller in intelligent structures, control of oscillation suppression through the simulation of intelligent entities, results in the time–space domain and the frequency domain, and input of white noise as disturbance input, taking it as a percentage of the disturbances. The outcomes are outstanding. With H-infinity control, we were able to obtain total rejections of disturbances.

3.3. Results for Hifoo Control

The Matlab routine for Hifoo control is:

Kfoo = hifoo (plant, 2)

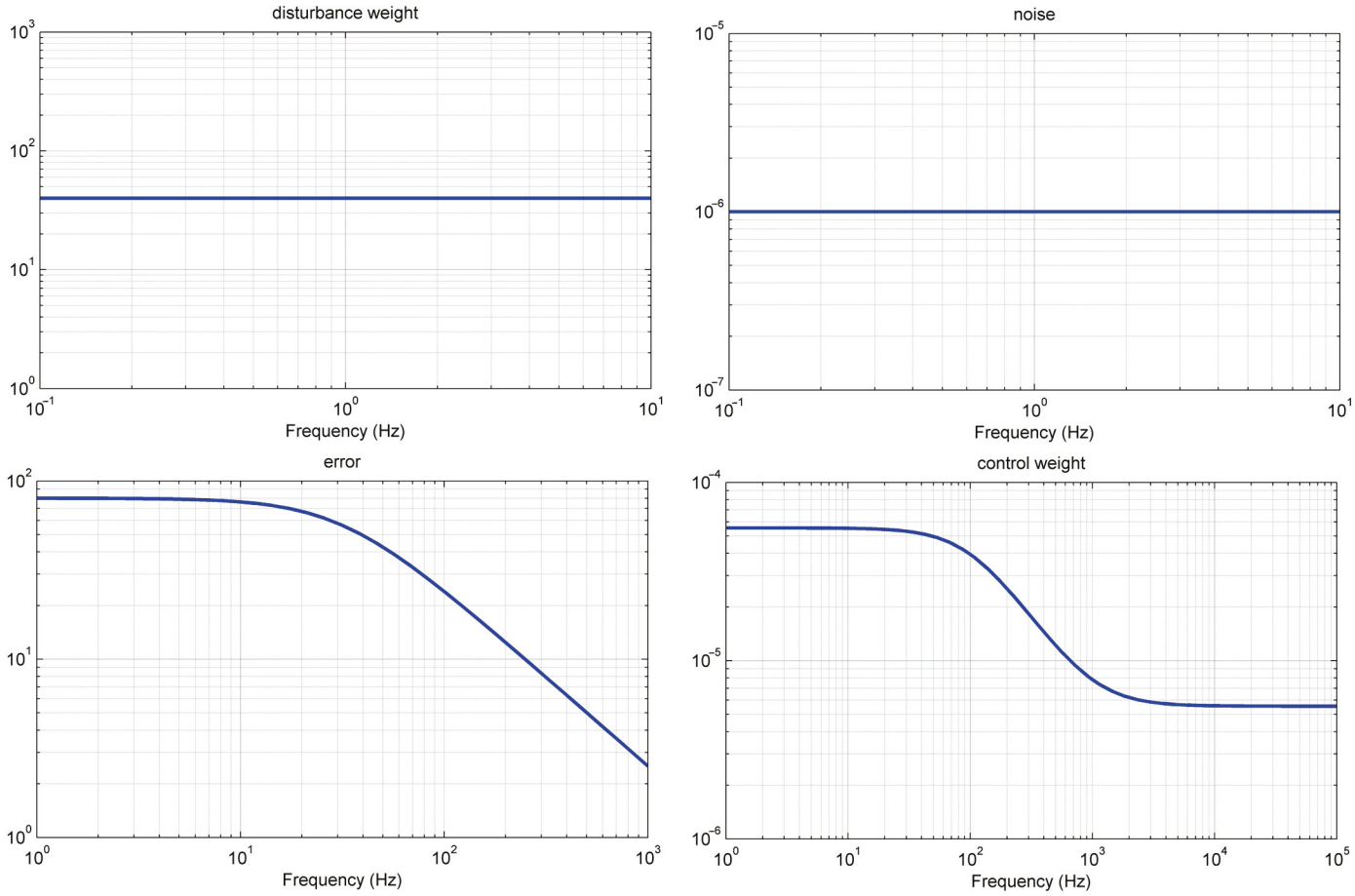


Figure 8. The Bode diagram in the frequency domain.

We employ a quasi-Newton technique (BFGS) to quickly estimate a local minimizer. Both the local bundle technique and the gradient sampling method are not employed if the MATLAB route does not include the quadratic programming tool "quadprog".

Where plants are the Equations (26) and (2) is the order of the controller, the matrices of the equation are:

$$\begin{aligned} \dot{x}_K(t) &= A_K\, x_K(t) + B_K y(t), \\ u(t) &= C_K\, x_K(t) + D_K y(t), \end{aligned} \tag{26}$$

$$\begin{aligned} A_{K=} &\begin{bmatrix} 828.1 & -5044 \\ 208.0 & -2408 \end{bmatrix} \\ B_{K=} &\begin{bmatrix} 412.8 & 911.6 & 1716 & 2810 \\ -164.9 & -637.2 & -1348 & -3207 \end{bmatrix} \\ C_{K=} &\begin{bmatrix} 1557 & -916.7 \\ 3013 & -592.3 \\ 627 & -297.9 \\ 144.3 & -92.59 \end{bmatrix} \\ D_{K=} &\begin{bmatrix} 76.1 & 6.6 & 287.1 & 468.3 \\ 23.5 & 87.69 & 186.5 & 303 \\ 12.12 & 44.12 & 93.39 & 154.3 \\ 4.204 & 12.53 & 26.92 & 783.51 \end{bmatrix} \end{aligned} \tag{27}$$

The control of beam position is achieved by displacing nodes on the order of 10^{-5} m, with the same output voltage, using the Hifoo controller for real wind loading. Therefore, even with a lower-order controller, we preserve H-infinity criteria performance. The Hifoo controller's maximum output voltage is 45 V, which is also true for the H_∞ controller. In other words, a lower-order controller that needs less voltage may adjust the beam to its

equilibrium point, as shown in Figure 9. The resultant displacement of the beam over time is seen in Figure 9 right. The displacement is nearly null as compared to when there is no control. By using a special control method known as H-infinity control, we were able to reduce vibrations by 95%. The red line is an open loop, whereas the green line has Hifoo control (closed loop). All actuators successfully suppress oscillations, and displacements are close to zero. In all mechanical structures, this is crucial and truly innovative. In addition, since the actuators can resist 500 Volts while the suppression is done with about 50 Volts, as illustrated in Figure 9 left, a reasonably low voltage is reached in the actuators. Figure 9 on the left displays the voltage produced. Even with the decreased order controller, the beam maintains balance. The blue line shows the voltages of the last node, the green of the previous one, the red of the second, and the pale blue of the first node. The control voltages fall below the 500 Volt piezoelectric limit [44–48].

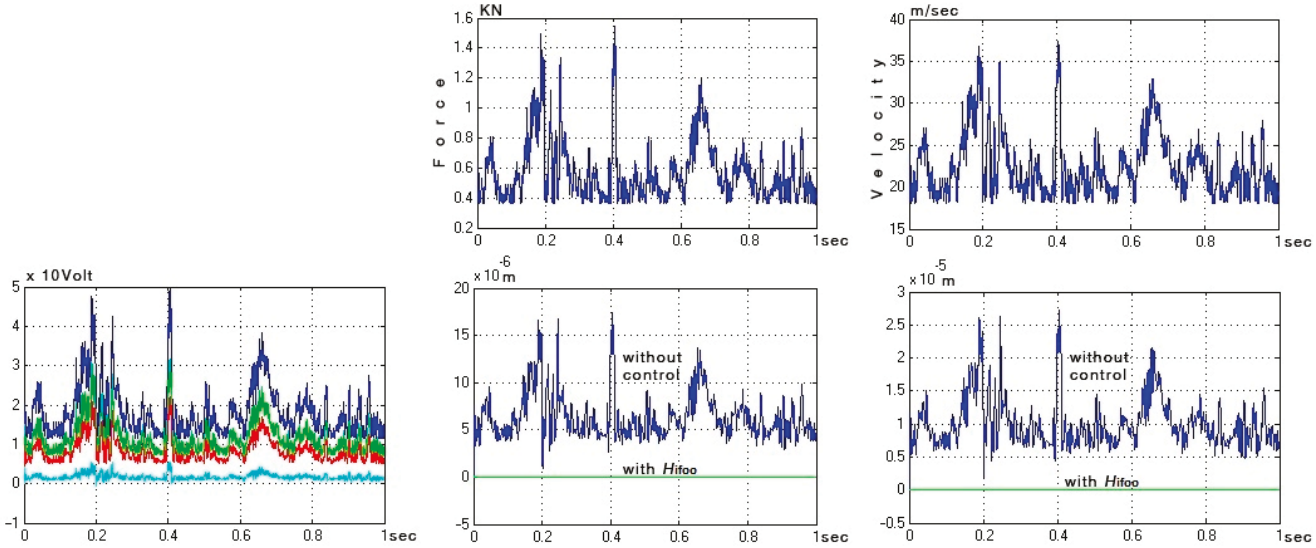


Figure 9. Control voltages and displacement response, of the middle and the free end of the beam with reduced-order control: Top two diagrams with the blue line is presented the wind force (top left diagram) and the wind velocity (top right diagram). Bottom three diagrams: For the bottom left diagram with the blue line is the control voltages for the free end of the smart beam, with green line the control voltages for the 3rd node of the smart beam, with red line the control voltages for the previous node of the smart beam and with the light blue line the first node of the smart beam. For the bottom right and middle diagram with blue line is the response without control and with green with Hifoo control.

The maximum singular values in the frequency domain, with and without the lowered order control are shown in Figure 10. The outcomes without control are shown by the blue line, and the green line is the results with control. For the above simulations, we apply a quasi-Newton technique (BFGS) for a quicker approximation of a local minimizer. Neither the local bundle technique nor the gradient sampling method is employed if the MATLAB route does not include the quadratic programming tool "quadprog". The gradients that Hifoo dynamically develops are utilized by each of these three optimization techniques. It is not attempted to locate the odd locations where gradients do not exist. The gradient discontinuities in unexpected locations do not cause the approaches to fail. A place where a convex combination of gradients at neighboring points has a small norm is sought in the last phases of the bundle and gradient sampling search parameter space. During the BFGS stage, an extremely ill-conditioned Hessian approximation matrix is generated. The local bundle technique or the gradient sampling method is not employed if the MATLAB route does not include the quadratic programming tool "quadprog". The gradients that Hifoo dynamically develops are utilized by each of these three optimization techniques. It is not attempted to locate the odd locations where gradients do not exist. The gradient

discontinuities in unexpected locations do not cause the approaches to fail. A place where a convex combination of gradients at neighboring points has a small norm is sought in the last phases of the bundle and gradient sampling search parameter space. During the BFGS stage, an extremely ill-conditioned Hessian approximation matrix is generated.

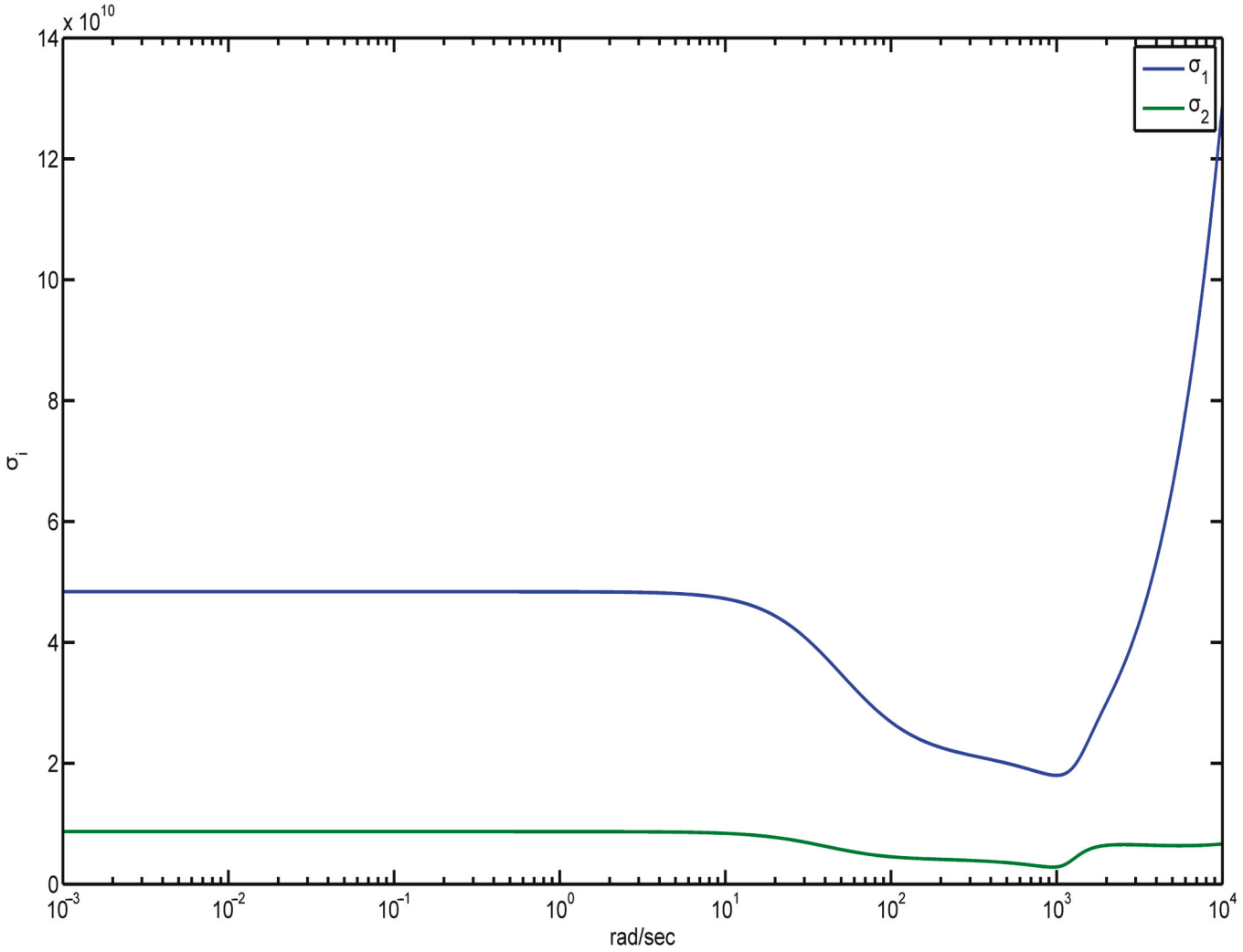


Figure 10. Structural singular values for reduced-order control.

4. Discussion

The current work has addressed the utilization of active control technologies in intelligent structures. Low steady-state error, quick recovery, and little-to-no maximum uplift are all desirable along with vibration reduction; nevertheless, control energy must not exceed operational limits [21,45,46]. The advantage of H-infinity control is that it enables the computation to take into consideration the worst-case scenario of disturbances with uncertainty and system noise [32,33,39,47]. Additionally, the H-infinity controller can efficiently handle greater input, allowing for the creation of a broad frequency spectrum. The results are significant; with piezoelectric component voltage controlled within tolerance, vibration reduction is shown even for genuine wind loads. By applying non-parametric and non-convex optimization techniques with the H_{IFOO} controller [5]. The model's processing requirements were reduced by lowering the controller rank. The controller worked properly even with a significantly lower system degree. Strong stabilization, which requires a controller that is self-stabilizing to stabilize a plant, and simultaneous stabilization, in which finding a single controller is required. To stabilize many plants, there are specific instances of multi-objective robust control issues [10,24,48]. Many important researchers

such as Crawley and de Louis [49] have dealt with smart materials and their inventions in construction. In this research, these materials are applied with advanced control techniques in the suppression of oscillations. Control and optimization on manufacturing processes and structures was also applied by various researchers afterward [50–53]. Most of the methods or heuristics that are currently used to address these issues usually lead to very high-order controllers as well. The outcomes demonstrate the utility of the suggested model and methodology, and the beam's control behavior conforms to expectations. The acknowledgment of new scientific issues that can serve as the foundation for study outside the purview of this work is a logical outcome of the suggested research advances. The maximum frequency of vibration for the system belongs to the high frequencies up to 10,000 Hz. Here, very good results are achieved in both high and low frequencies. The following are the outcomes of this work: a lowered order, the complete suppression of oscillations, reduction of controller order, optimization of the H-infinity controller in intelligent structures, and control of oscillation suppression by simulating intelligent entities, resulting in the time–space domain and the frequency domain, application of measurement noise of beam state, the input of white noise as disturbance input, taking it as a percentage of the disturbances, and application of measurement noise [25,36,44]. The outcomes are acceptable; using H-infinity control and reduced-order control, we completely reject disturbances. The different control methods used to lessen structural vibration and noise are referred to above. This investigation helps to apply controls to lessen the oscillations of intelligent structures. The major development is that complete oscillation suppression is accomplished with a reduced-order controller. In other words, the best outcome is obtained with significantly lower computing costs and without sacrificing any of the model's accuracy. In particular, experimental verification of the excellent results gained in the study of control might be a future research area.

5. Conclusions

Specific examples of multi-objective robust control problems are simultaneous stabilization, where a single controller must be created to stabilize a number of plants, and robust stabilization entails the requirement that a controller, in order to stabilize a plant, must also be inherently stable itself. In addition, the majority of the present methods or heuristics for resolving these problems frequently result in controllers of exceptionally high order. The beam's control behavior matches predictions, and the results show how useful the recommended model and methods are. Following a system analysis, we assess the system's usability and robustness.

The research investigates the positive aspects of robust control in intelligent systems by showing the use of H-infinity regulation and Hifoo optimization in both the state space and the frequency domain. These are the benefits of this work: order reduction optimization of the H-infinity controller in smart structures, control in oscillation suppression by modeling of intelligent entities, results in the time–space domain and the frequency domain, application of the measurement noise of the state of the beam, complete suppression of oscillations, reduction of the order of the controller, and the input of white noise as the disturbance input taking it as a percentage of the disturbances, to achieve the results programming has been done in Matlab. We employ a quasi-Newton technique (BFGS) to estimate a local minimizer more quickly. If the MATLAB route does not include the quadratic programming tool "quadprog", neither the local bundle technique nor the gradient sampling method is employed. These three optimization techniques each make use of the gradients that Hifoo dynamically produces. Finding the odd locations where gradients do not exist is not attempted. The positions of the gradient discontinuities do not cause the procedures to fail. The latter phases of the bundle and gradient sampling look for a place where a convex combination of gradients at neighboring points has a small norm. This technique helps to decrease the oscillations of intelligent structures by applying control. The breakthrough is the use of a reduced-order controller to completely suppress oscillations. In other words, the ideal outcome can be achieved with highly reduced processing needs and without

compromising the model's accuracy in any way. The focus of future studies will be on two areas; first, on how to apply these control mechanisms to real intelligent structures in an experimental scenario, and second, using alternative control strategies to suppress structural noise and vibration.

Author Contributions: G.E.S.: methodology; A.M. and M.P.: software, writing-review, and editing; N.V.: validation; M.P.: formal analysis; A.P.: investigation, software. All authors have read and agreed to the published version of the manuscript.

Funding: This research received no external funding.

Data Availability Statement: The data will be made available upon request to the corresponding author.

Acknowledgments: The authors are grateful for the support from Hellenic Mediterranean University and the Technical University of Crete.

Conflicts of Interest: The authors declare no conflict of interest.

References

1. Benjeddou, A.; Trindade, M.A.; Ohayon, R. New Shear Actuated Smart Structure Beam Finite Element. *AIAA J.* **1999**, *37*, 378–383. [CrossRef]
2. Bona, B.; Indri, M.; Tornambe, A. Flexible Piezoelectric Structures-Approximate Motion Equations and Control Algorithms. *IEEE Trans. Autom. Control* **1997**, *42*, 94–101. [CrossRef]
3. Okko, B.; Kwakernaak, H.; Gjerrit, M. *Design Methods for Control Systems*; Course Notes; Dutch Institute for Systems and Control: Delft, The Netherlands, 2001; Volume 67.
4. Burke, J.V.; Henrion, D.; Lewis, A.S.; Overton, M.L. HIFOO—A matlab package for fixed-order controller design and H∞ optimization. *IFAC Proc. Vol.* **2006**, *39*, 339–344. [CrossRef]
5. Burke, J.V.; Henrion, D.; Lewis, A.S.; Overton, M.L. Stabilization via Nonsmooth, Nonconvex Optimization. *IEEE Trans. Autom. Control* **2006**, *51*, 1760–1769. [CrossRef]
6. Burke, J.V.; Lewis, A.S.; Overton, M.L. A Robust Gradient Sampling Algorithm for Nonsmooth, Nonconvex Optimization. *SIAM J. Optim.* **2005**, *15*, 751–779. [CrossRef]
7. Burke, J.V.; Overton, M.L. Variational Analysis of Non-Lipschitz Spectral Functions. *Math. Program.* **2001**, *90*, 317–351. [CrossRef]
8. Choi, S.-B.; Cheong, C.-C.; Lee, C.-H. Position Tracking Control of a Smart Flexible Structure Featuring a Piezofilm Actuator. *J. Guid. Control Dyn.* **1996**, *19*, 1364–1369. [CrossRef]
9. Culshaw, B. Smart Structures—A Concept or a Reality? *Proc. Inst. Mech. Eng. Part I J. Syst. Control Eng.* **1992**, *206*, 1–8. [CrossRef]
10. Doyle, J.; Glover, K.; Khargonekar, P.; Francis, B. State-Space Solutions to Standard H2 and H∞ Control Problems. In Proceedings of the 1988 American Control Conference, Atlanta, GA, USA, 15–17 June 1988; pp. 1691–1696.
11. Tzou, H.S.; Gabbert, U. Structronics—A New Discipline and Its Challenging Issues. *Fortschr.-Ber. VDI Smart Mech. Syst.—Adapt. Reihe* **1997**, *11*, 245–250.
12. Tzou, H.S.; Anderson, G.L. *Intelligent Structural Systems*; Springer: Dordrecht, The Netherlands; Boston, MA, USA; London, UK, 1992; ISBN 978-94-017-1903-2.
13. Guran, A.; Tzou, H.-S.; Anderson, G.L.; Natori, M.; Gabbert, U.; Tani, J.; Breitbach, E. *Structronic Systems: Smart Structures, Devices and Systems*; World Scientific: Singapore, 1998; Volume 4, ISBN 978-981-02-2652-7.
14. Gabbert, U.; Tzou, H.S. IUTAM Symposium on Smart Structures and Structronic Systems. In Proceedings of the IUTAM Symposium, Magdeburg, Germany, 26–29 September 2000; Kluwer: Dordrecht, The Netherlands; Boston, MA, USA; London, UK, 2001.
15. Tzou, H.S.; Natori, M.C. *Piezoelectric Materials and Continua*; Braun, S., The Encyclopedia of Vibration, Eds.; Elsevier: Oxford, UK, 2001; pp. 1011–1018, ISBN 978-0-12-227085-7.
16. Cady, W.G. *Piezoelectricity: An Introduction to the Theory and Applications of Electromechanical Phenomena in Crystals*; Dover Publication: New York, NY, USA, 1964.
17. Tzou, H.S.; Bao, Y. A Theory on Anisotropic Piezothermoelastic Shell Laminates with Sensor/Actuator Applications. *J. Sound Vib.* **1995**, *184*, 453–473. [CrossRef]
18. David, C.; Sagris, D.; Petousis, M.; Nasikas, N.K.; Moutsopoulou, A.; Sfakiotakis, E.; Mountakis, N.; Charou, C.; Vidakis, N. Operational Performance and Energy Efficiency of MEX 3D Printing with Polyamide 6 (PA6): Multi-Objective Optimization of Seven Control Settings Supported by L27 Robust Design. *Appl. Sci.* **2023**, *13*, 8819. [CrossRef]
19. Moutsopoulou, A.; Stavroulakis, G.E.; Petousis, M.; Vidakis, N.; Pouliezos, A. Smart Structures Innovations Using Robust Control Methods. *Appl. Mech.* **2023**, *4*, 856–869. [CrossRef]
20. Cen, S.; Soh, A.-K.; Long, Y.-Q.; Yao, Z.-H. A New 4-Node Quadrilateral FE Model with Variable Electrical Degrees of Freedom for the Analysis of Piezoelectric Laminated Composite Plates. *Compos. Struct.* **2002**, *58*, 583–599. [CrossRef]

21. Packard, A.; Doyle, J.; Balas, G. Linear, Multivariable Robust Control With a μ Perspective. *J. Dyn. Syst. Meas. Control* **1993**, *115*, 426–438. [CrossRef]
22. Kim, S.-W.; Boo, C.-J.; Kim, S.; Kim, H.-C. Stable Controller Design of MIMO Systems in Real Grassmann Space. *Int. J. Control Autom. Syst.* **2012**, *10*, 213–226. [CrossRef]
23. Feng, Z.; Allen, R. Reduced Order H∞ Control of an Autonomous Underwater Vehicle. *IFAC Proc. Vol.* **2003**, *36*, 121–126. [CrossRef]
24. Chandrashekhara, K.; Varadarajan, S. Adaptive Shape Control of Composite Beams with Piezoelectric Actuators. *J. Intell. Mater. Syst. Struct.* **1997**, *8*, 112–124. [CrossRef]
25. Ackermann, J. *Robust Control, The Parameter Space Approach*; Springer: London, UK, 2002; ISBN 978-1-85233-514-4.
26. Gao, H.; Lam, J.; Wang, C. Controller Reduction with Error Performance: Continuous- and Discrete-Time Cases. *Int. J. Control* **2006**, *79*, 604–616. [CrossRef]
27. Yang, S.M.; Lee, Y.J. Optimization of Noncollocated Sensor/Actuator Location and Feedback Gain in Control Systems. *Smart Mater. Struct.* **1993**, *2*, 96. [CrossRef]
28. Ramesh Kumar, K.; Narayanan, S. Active Vibration Control of Beams with Optimal Placement of Piezoelectric Sensor/Actuator Pairs. *Smart Mater. Struct.* **2008**, *17*, 55008. [CrossRef]
29. Hanagud, S.; Obal, M.W.; Calise, A.J. Optimal Vibration Control by the Use of Piezoceramic Sensors and Actuators. *J. Guid. Control Dyn.* **1992**, *15*, 1199–1206. [CrossRef]
30. Song, G.; Sethi, V.; Li, H.-N. Vibration Control of Civil Structures Using Piezoceramic Smart Materials: A Review. *Eng. Struct.* **2006**, *28*, 1513–1524. [CrossRef]
31. Karatzas, I.; Lehoczky, J.P.; Shreve, S.E.; Xu, G.-L. Modeling, Control and Implementation of Smart Structures: A FEM-State Space Approach. Springer: London, UK, 1990; ISBN 9783540483939.
32. Miara, B.; Stavroulakis, G.E.; Valente, V. Topics on Mathematics for Smart Systems. In Proceedings of the European Conference, Rome, Italy, 26–28 October 2006; World Scientific Publishing: Singapore, 2006.
33. Moutsopoulou, A.; Stavroulakis, G.E.; Pouliezos, A.; Petousis, M.; Vidakis, N. Robust Control and Active Vibration Suppression in Dynamics of Smart Systems. *Inventions* **2023**, *8*, 47. [CrossRef]
34. Leibfritz, F. *COMPl e Ib: COnstrained Matrix-Optimization Problem Library—A Collection of Test Examples for Nonlinear Semidefinite Programs, Control System Design and Related Problems*; Universität Trier: Trier, Germany, 2001; pp. 1–23.
35. Wie, B.; Bernstein, D.S. Benchmark Problems for Robust Control Design. *J. Guid. Control Dyn.* **1992**, *15*, 1057–1059. [CrossRef]
36. Burke, J.V.; Lewis, A.S.; Overton, M.L. A Nonsmooth, Nonconvex Optimization Approach to Robust Stabilization by Static Output Feedback and Low-Order Controllers. *IFAC Proc. Vol.* **2003**, *36*, 175–181. [CrossRef]
37. Henrion, D.; Overton, M.L. Maximizing the Closed Loop Asymptotic Decay Rate for the Two-Mass-Spring Control Problem. *arXiv* **2006**, arXiv:math/0603681.
38. Henrion, D.; Sebek, M. Overcoming Non-Convexity in Polynomial Robust Control Design. In Proceedings of the Symposium on Mathematical Theory of Networks and Systems, Leuven, Belgium, 1 January 2004.
39. Zhang, N.; Kirpitchenko, I. Modelling Dynamics of A Continuous Structure with a Piezoelectric Sensoractuator for Passive Structural Control. *J. Sound Vib.* **2002**, *249*, 251–261. [CrossRef]
40. Vidakis, N.; Petousis, M.; Mountakis, N.; Moutsopoulou, A.; Karapidakis, E. Energy Consumption vs. Tensile Strength of Poly [Methyl Methacrylate] in Material Extrusion 3D Printing: The Impact of Six Control Settings. *Polymers* **2023**, *15*, 845. [CrossRef]
41. Vidakis, N.; Petousis, M.; Mountakis, N.; Papadakis, V.; Moutsopoulou, A. Mechanical Strength Predictability of Full Factorial, Taguchi, and Box Behnken Designs: Optimization of Thermal Settings and Cellulose Nanofibers Content in PA12 for MEX AM. *J. Mech. Behav. Biomed. Mater.* **2023**, *142*, 105846. [CrossRef]
42. Petousis, M.; Vidakis, N.; Mountakis, N.; Karapidakis, E.; Moutsopoulou, A. Functionality Versus Sustainability for PLA in MEX 3D Printing: The Impact of Generic Process Control Factors on Flexural Response and Energy Efficiency. *Polymers* **2023**, *15*, 1232. [CrossRef] [PubMed]
43. Kwakernaak, H. Robust Control and H∞-Optimization—Tutorial Paper. *Automatica* **1993**, *29*, 255–273. [CrossRef]
44. Blondel, V.D.; Tsitsiklis, J.N. A Survey of Computational Complexity Results in Systems and Control. *Automatica* **2000**, *36*, 1249–1274. [CrossRef]
45. Zhang, X.; Shao, C.; Li, S.; Xu, D.; Erdman, A.G. Robust H∞ Vibration Control for Flexible Linkage Mechanism Systems With Piezoelectric Sensors And Actuators. *J. Sound Vib.* **2001**, *243*, 145–155. [CrossRef]
46. Stavroulakis, G.E.; Foutsitzi, G.; Hadjigeorgiou, E.; Marinova, D.; Baniotopoulos, C.C. Design and Robust Optimal Control of Smart Beams with Application on Vibrations Suppression. *Adv. Eng. Softw.* **2005**, *36*, 806–813. [CrossRef]
47. Kimura, H. Robust Stabilizability for a Class of Transfer Functions. *IEEE Trans. Autom. Control* **1984**, *29*, 788–793. [CrossRef]
48. Francis, B.A. *A Course in H∞ Control Theory*; Springer: Berlin/Heidelberg, Germany, 1987; ISBN 978-3-540-17069-3.
49. Crawley, E.F.; de Luis, J. Use of piezoelectric actuators as elements of intelligent structures. *AIAA J.* **1987**, *25*, 1373–1385. [CrossRef]
50. Stavropoulos, P.; Chantzis, D.; Doukas, C.; Papacharalampopoulos, A.; Chryssolouris, G. Monitoring and Control of Manufacturing Processes: A Review. *Procedia CIRP* **2013**, *8*, 421–425. [CrossRef]
51. Turchenko, V.A.; Trukhanov, S.V.; Kostishin, V.G.; Damay, F.; Porcher, F.; Klygach, D.S.; Vakhitov, M.G.; Lyakhov, D.; Michels, D.; Bozzo, B.; et al. Features of Structure, Magnetic State and Electrodynamic Performance of $SrFe_{12-x}In_xO_{19}$. *Sci. Rep.* **2021**, *11*, 18342. [CrossRef]

52. Almessiere, M.A.; Slimani, Y.; Algarou, N.A.; Vakhitov, M.G.; Klygach, D.S.; Baykal, A.; Zubar, T.I.; Trukhanov, S.V.; Trukhanov, A.V.; Attia, H.; et al. Tuning the Structure, Magnetic, and High Frequency Properties of Sc-Doped $Sr_{0.5}Ba_{0.5}Sc_xFe_{12-X}O_{19}/NiFe_2O_4$ Hard/Soft Nanocomposites. *Adv. Electron. Mater.* **2022**, *8*, 2101124. [CrossRef]
53. Zaszczyńska, A.; Gradys, A.; Sajkiewicz, P. Progress in the applications of smart piezoelectric materials for medical devices. *Polymers* **2020**, *12*, 2754. [CrossRef]

Disclaimer/Publisher's Note: The statements, opinions and data contained in all publications are solely those of the individual author(s) and contributor(s) and not of MDPI and/or the editor(s). MDPI and/or the editor(s) disclaim responsibility for any injury to people or property resulting from any ideas, methods, instructions or products referred to in the content.

inventions

MDPI

Article

Flow Instability Control in a Model Swirl-Stabilized Combustor with Central Jet Injection

Alexey Savitskii [1,2], Dmitriy Sharaborin [1,2], Leonid Chikishev [1,2] and Vladimir Dulin [1,2,*]

[1] Kutateladze Institute of Thermophysics, 1 Lavrentyev Avenue, 630090 Novosibirsk, Russia; a.savitskii@alumni.nsu.ru (A.S.); sharaborin.d@gmail.com (D.S.); chlm@itp.nsc.ru (L.C.)
[2] Department of Physics, Novosibirsk State University, 1 Pirogov Street, 630090 Novosibirsk, Russia
* Correspondence: vmd@itp.nsc.ru

Abstract: Swirling flows often occur in nature and industrial applications. With an increase in swirl intensity, such rotating flows are known to become unstable and undergo a sudden breakdown of the vortex core, resulting in unsteady flow dynamics with intensive pressure fluctuations. In particular, swirling flows are organized in combustion chambers to stabilize the flame around the central recirculation zone, formed due to the vortex core breakdown. However, the impact of large-scale vortex structures, including the precessing vortex core and secondary helical vortices, on unsteady combustion regimes is still unclear. The present paper demonstrates experimentally that for the swirling flow of a model swirl combustor, the injection of a central jet may be used to alter the configuration of coherent flow structures, including helical vortices. In particular, the asymmetric hydrodynamics mode, associated with the precessing vortex core, is suppressed, whereas the symmetrical one becomes dominant. This effect demonstrates the importance of central jet injection to control the dominant mode of flow instability for the design of swirl combustors.

Keywords: precessing vortex core; swirling flow; flow control; proper orthogonal decomposition

1. Introduction

Rotating or swirling flows are generally realized in combustion chambers of gas turbines for the stabilization of flames. When the rotating flow enters the combustion chamber and expands, the flow at the vortex core decelerates and forms a wake/recirculation zone at the centerline, enclosed by a swirling annular jet. This effect is known as the breakdown of the vortex core [1,2]. A number of large-scale secondary vortex structures are formed in the shear layer between the main annular flow and the central wake zone and are accompanied by smaller-scale eddies and broadband turbulence. The configuration and dynamics of such secondary and primary (the core of the swirling flow) vortices are known to play a key role in turbulent transport and mixing in the near-wake zone. In particular, the vortex core dynamics are often related to slow or strong precession with intensive velocity and pressure fluctuations. In the latter case, the effect is referred to as the precessing vortex core (PVC) [3]. The PVC is known to play an important role in the steady or unsteady operation of gas turbine combustion chambers [4–7], hydro-turbines [8] and other devices with flow rotation.

The configurations and geometry of real gas turbine combustors are very different. However, in fundamental studies of the features of flow dynamics, mixing and combustion, they are commonly modeled using single (e.g., TURBOMECA design [9,10], PRECCINSTA burner [11]), double (e.g., dual DLR burner [11,12], BIMER device [13]) or even triple [14,15] radial swirlers. Fuel is commonly injected as the central jet/spray, jets between the vanes of a swirler or through a special pre-filmer between two swirlers to organize air-blast atomization [16,17]. The single-swirl models are usually designed to supply fuel gas between the swirler vanes to provide a well-premixed fuel–air mixture at the nozzle of

the swirler in order to organize lean-premixed combustion [18]. However, such flames are prone to external perturbation and flow instabilities, thus resulting in thermoacoustic pulsations inside the combustion chamber [11,19–21]. Hence, part of the fuel may be supplied as a central jet to organize the pilot flame and stabilize combustion.

However, the central jet also appears to affect the development of hydrodynamic instabilities in the swirling flow. It is well-known that the strong flow pulsations incidental to the PVC in swirling flows are associated with the domination of a global helical instability mode, arising due to the formation of central reverse flow, providing a feedback mechanism. In particular, Midgley and others [9,22] reported that the central jet results in a double-helix vortex structure instead of a spiral PVC for the single-swirler burner based on the Turbomeca design. Later, a similar conclusion was made by Mullyadzhanov et al. [23] for such a burner with combustion based on a large eddy simulation. The present paper reports on a further demonstration of control over the dominant flow instability mode for this burner by injecting a central jet. Turbulent swirling flow is investigated using a combination of stereoscopic particle image velocimetry (PIV) and planar laser-induced fluorescence (PLIF) systems. The measured velocity fluctuation fields are processed using the snapshot proper orthogonal decomposition (POD) method to extract coherent flow structures and analyze the associated vortex structures. Studies of non-reacting flows in combustors are important for better understanding the impact of hydrodynamic instability modes, such as PVC, on momentum and mass transport and to develop strategies for flow control. Moreover, the features of hydrodynamics structure and dynamics of non-reacting flow are important for efficient ignition organization. Numerical simulation of flow and combustion in swirl burners requires adequate modeling of turbulent transport and mixing in the rotating flow, reproduction of emerging large-scale vortex structures and relevant chemical kinetics approximation, accounting for the acoustic modes of the chamber. Therefore, detailed experimental data for non-reacting flows in swirl-stabilized combustors are needed for the first-step validation purposes.

2. Materials and Methods

The measurements are performed for a model gas turbine combustor with a flow swirler and fuel injector based on the Turbomeca design [10]. Detailed information on the configuration of the combustor rig, equipment and data processing routines may be found in a previous study of fuel mixing characteristics [24]. This paper presents only the main parameters of the experimental setup. The flow is organized in an enclosed combustion rig, equipped with flowmeters (Bronkhorst High-Tech) and temperature and pressure transducers, and connected to fuel and air tanks and an exhaust shaft. The rig consists of a plenum section, combustion chamber and cooled exhaust pipe. The swirler is installed inside the plenum section upstream of the combustion chamber. The swirler represents a centerbody with 12 radial vanes with an inclination angle of 30° (see the design in [9]). Fuel is supplied through the holes between the vanes. In addition, fuel can be injected as a central jet from the hole at the tip of the centerbody. The diameter of such a central nozzle is 5.8 mm. The effect of the central jet density on the flow properties was studied in the previous paper [24]. The diameter of the swirler nozzle exit is 37 mm. The Reynolds number of the air flow without a fuel supply corresponds to 3×10^4 with a bulk velocity U_0 of 12.8 m/s. This is calculated based on the volume flowrate through the exit of the swirler nozzle.

The measurements of the velocity field in the central longitudinal plane are performed using a stereoscopic PIV system. A sketch of the equipment arrangement relative to the model combustor is shown in Figure 1. The PIV system consists of a pair of 4 Mpix CCD cameras (ImperX Bobcat IGV-B2020, Boca Raton, FL USA), equipped with 105 mm optical lenses (Sigma DG MACRO, Hyogo, Japan) and band-pass optical filters (532 ± 5 nm). Flow tracers, viz., 0.5 μm TiO_2 particles, are introduced into the air flow with a fluidized-bed feeder and illuminated in the measurement plane with two light pulses from a double-head Nd:YAG laser (Quantel Ever Green 200, Les Ulis Cedex, France). The duration of the

200 mJ pulses is 6 ns. The laser wavelength is 532 nm. The PIV and PLIF measurements are conducted simultaneously. PLIF is applied for the vapor of acetone admixed to the air flow in the fuel supply line. Acetone is added as a tracer to quantify the turbulent transport and mixing inside the model combustion chamber.

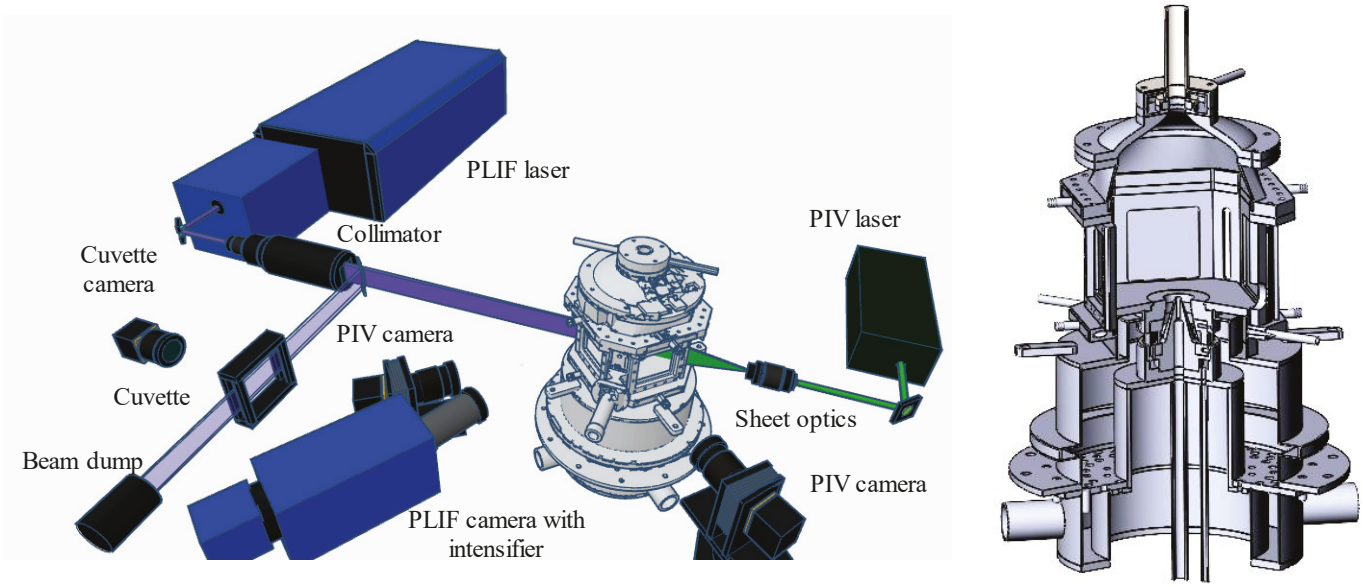


Figure 1. Sketch of the experimental setup and combustion chamber design.

The PLIF system consists of a tunable dye laser (Sirah Precision Scan, Sirah Lasertechnik, Grevenbroich, Germany), which is pumped with a pulsed Nd:YAG laser (QuantaRay) and intensified 5 Mpix sCMOS camera (LaVision, Göttingen, Germany), equipped with a UV-sensitive image intensifier (LaVision IRO Göttingen, Germany), a 100 mm UV lens and an optical band-pass filter (415–455 nm). The pulses of the tunable laser correspond to a wavelength of approximately 283 nm, an energy of 12 mJ, and a duration of about 12 ns. The tunable laser is used to excite the acetone fluorescence in the same cross-section where the PIV measurements are conducted. For this purpose, the PLIF laser beam is converted to a collimated laser sheet with a system of cylindrical and spherical UV lenses. Using photo-bleaching paper, the width and thickness of the laser sheet in the measurement plane are evaluated to be approximately 50 mm and 800 μm, respectively. Each PLIF image is captured within 200 ns between the pair of PIV laser pulses, which are separated by 20 μs.

The PIV and PLIF images are processed using in-house "ActualFlow v.1.18" software. The PIV velocity fields are evaluated using an adaptive cross-correlation algorithm with iterative continuous window shift and refinement (see description in [25]). Examples of the PIV images for two cameras are shown in Figure 2. Both the main annular flow and the central jet are seeded with the tracer particles. The maximal particle shift in the images is approximately 8 pixels. Therefore, the final size of the interrogation area during the interactive cross-correlation of the image pairs for each camera is 32 × 32 pixels. A 50% spatial overlap rate between the interrogation areas is used. A reconstruction of the three-component velocity field in the measurement plane based on two two-component projections to the PIV cameras is performed using the corresponding mapping functions [26] obtained from images of the calibration target, captured prior to the experiments. The mapping function corresponds to a third-order polynomial. The grid spacing of the stereo PIV data is 0.53 mm. For the in-plane velocity components, the accuracy of PIV data is generally accepted as 0.1-pixel (i.e., approximately 1.5% of maximum velocity) accuracy. The accuracy of the normal-to-plane component is expected to be about 3%.

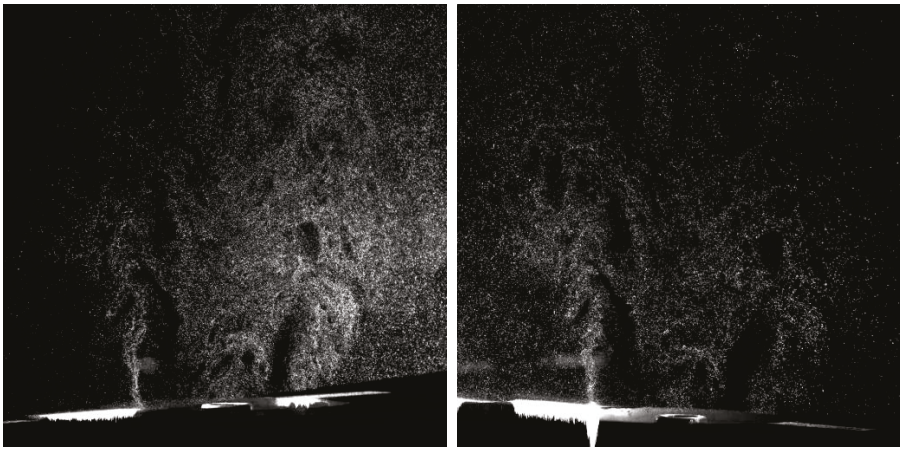


Figure 2. Examples of stereoscopic PIV images captured with two separate cameras.

The PLIF images are processed by removing the background signal and correcting the non-uniformity of the laser sheet intensity. In the latter case, an additional CCD camera monitors the light sheet intensity inside a cuvette, filled with a rhodamine 6G solution (see examples in Figure 3). In addition, the attenuation of the PLIF laser sheet in the measurement plane due to absorption is corrected. The PLIF data are back-projected into the measurement plane using the mapping function of the PLIF camera. The obtained data correspond to a regular square grid with a step of approximately 0.5 mm and an actual optical resolution of 1 mm. In total, 1500 snapshots of the PIV and PLIF data are captured simultaneously with an acquisition rate of 5 Hz and used for statistics calculation.

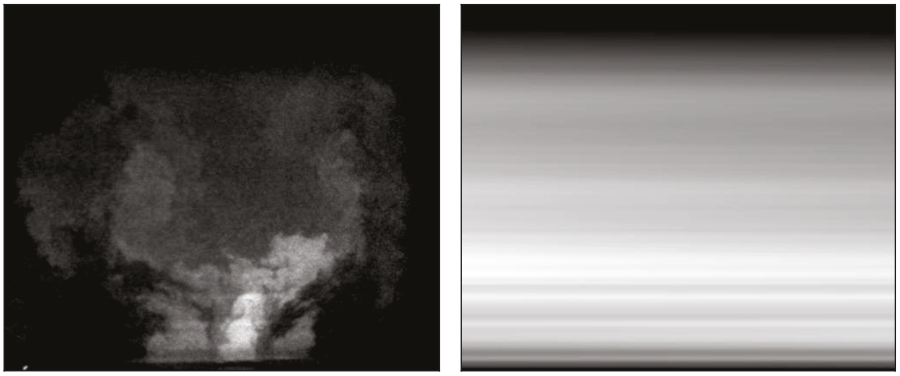


Figure 3. Examples of PLIF images captured in the measurement area (**left**) and in the calibration cuvette (**right**).

The sets of the measured velocity fluctuation fields $\mathbf{u}'(\mathbf{x}, t)$ are decomposed into the series (1) of orthonormal spatial functions $\boldsymbol{\phi}(\mathbf{x})$ (POD modes) and temporal coefficients $\alpha(t)$ based on a singular value decomposition (SVD) procedure (2). In Equation (2), $\mathbf{U} = [\mathbf{u}'(\mathbf{x}, t_1) \ldots \mathbf{u}'(\mathbf{x}, t_N)]$, $\boldsymbol{\Sigma} = \mathrm{diag}[\sigma_1 \ldots \sigma_N]$ and $\mathbf{W} = [\boldsymbol{\phi}_1(\mathbf{x}) \ldots \boldsymbol{\phi}_N(\mathbf{x})]$ are the initial data matrix, matrix of singular values and that of left-singular vectors, respectively. The left-singular vectors in $\mathbf{W}$ correspond to the POD modes. $\mathbf{V}$ is the matrix of right-singular vectors, where $\mathbf{V}^T$ consists of the normalized temporal coefficients α_q.

$$\mathbf{u}'(\mathbf{x}, t_k) = \sum_{q=1}^{N} \alpha_q(t_k)\sigma_q\boldsymbol{\varphi}_q(\mathbf{x}),\ \sum_{k=1}^{M} \boldsymbol{\varphi}_i(\mathbf{x}_k)\boldsymbol{\varphi}_j(\mathbf{x}_k) = \delta_{ij},\ \sum_{k=1}^{N} \alpha_i(t_k)\alpha_j(t_k) = \delta_{ij}; \quad (1)$$

$$\mathbf{U} = \mathbf{W}\boldsymbol{\Sigma}\mathbf{V}^T,\ \mathbf{W}^T\mathbf{W} = \mathbf{I}_M,\ \mathbf{V}^T\mathbf{V} = \mathbf{I}_N. \quad (2)$$

In the equations, δ_{ij} is the Kronecker symbol and $\mathbf{I}$ is the identity matrix. M and N are the numbers of the spatial points and temporal snapshots, respectively. In matrix

Σ, the singular values are in descending order according to their values, related to the contribution σ^2 of each POD mode to the total kinetic energy of the velocity fluctuations in the considered spatial domain. In particular, when flow dynamics are dominated by strong flow pulsations, a low-order model of the phase-averaged flow dynamics can be obtained using the first pair of the most energetic POD modes (3). φ is the phase of the flow pulsations. According to the linear dependence between the matrixes of the POD modes and velocity fluctuation snapshots (4), the PLIF data can be phase-averaged (5) to reveal coherent concentration pulsations. The weight coefficients a_{qk} are the elements of the right-singular vector matrix **V**. The normalization coefficient in (4) is related to the number of the used snapshots N and appears due to the condition (2). In the present study, 500 snapshots are used for the POD.

$$\mathbf{u}^{\mathrm{L.O.}}(\mathbf{x},\phi) = \mathbf{U}(\mathbf{x}) + \left(\sigma_1/\sqrt{N}\right)\sin(\phi)\boldsymbol{\varphi}_1(\mathbf{x}) + \left(\sigma_2/\sqrt{N}\right)\cos(\phi)\boldsymbol{\varphi}_2(\mathbf{x}) \tag{3}$$

$$\boldsymbol{\varphi}_q(\mathbf{x}) = \sum_{k=1}^{N} a_{qk}\mathbf{u}'(\mathbf{x},t_k)\sigma_q^{-1} \text{ or } \mathbf{W} = \mathbf{U}\mathbf{V}\boldsymbol{\Sigma}^{-1} \tag{4}$$

$$\hat{c}(\mathbf{x}) = \left(1/\sqrt{N}\right)\sum_{k=1}^{N} a_{qk}c'(\mathbf{x},t_k) \tag{5}$$

3. Results and Discussion

Table 1 presents the flowrates for the considered flows (ln/min according to the normal temperature and pressure standard of NIST). Instead of fuel, a mixture of acetone (with a concentration of 3% by volume) and air is supplied through the central orifice at the tip of the swirler centerbody (as a pilot jet) and through the orifices between the swirler vanes (see Figure 4). The ratio between the mass flowrates of the acetone–air mixture, modeling the gaseous fuel, and air, supplied through the plenum chamber and swirler, corresponds to an equivalence ratio of 0.7 for the case of methane. Three flow cases are considered, where different portions of the acetone–air mixture are injected as the pilot jet, viz., 0%, 10% and 50%.

3.1. Instantenous Snapshots

Figure 5 provides examples of an instantaneous velocity field and a normalized spatial distribution of the local concentration of acetone for the case without pilot jet injection. The velocity components in the measurement plane are shown by (small) arrows, whereas the concentration is indicated with color. Large arrows indicate the approximate locations of large-scale vortex structures, which are present in the inner shear layer between the annular swirling jet and the recirculation zone. The vortex structures are extracted by regions with positive values of a modified Q-criterion [27]. The burner is designed to produce a well-premixed fuel–air mixture at the exit of the swirler nozzle when fuel is injected between the vanes. However, even in the case when 100% acetone is supplied between the vanes, the acetone concentration is not uniform at the entrance of the combustion chamber. Obviously, large-scale vortex structures affect the mixing of acetone inside the chamber, viz., large-scale vortex structures in the inner mixing layer (indicated by the arrows with solid line) are close to observed zones with high acetone concentration.

Table 1. Flow parameters.

Flowrate through Swirler (ln/min)	Flowrate between Vanes (ln/min)	Flowrate through Central Jet (ln/min)	Ratio through Central Jet
799	58.3	0	0%
799	52.5	5.8	10%
799	29.15	29.15	50%

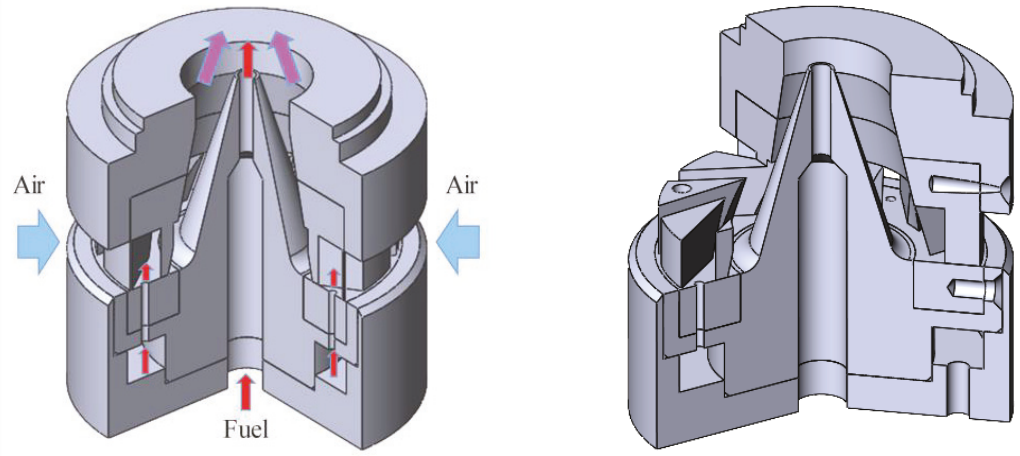


Figure 4. Design of the swirler with changeable radial vanes.

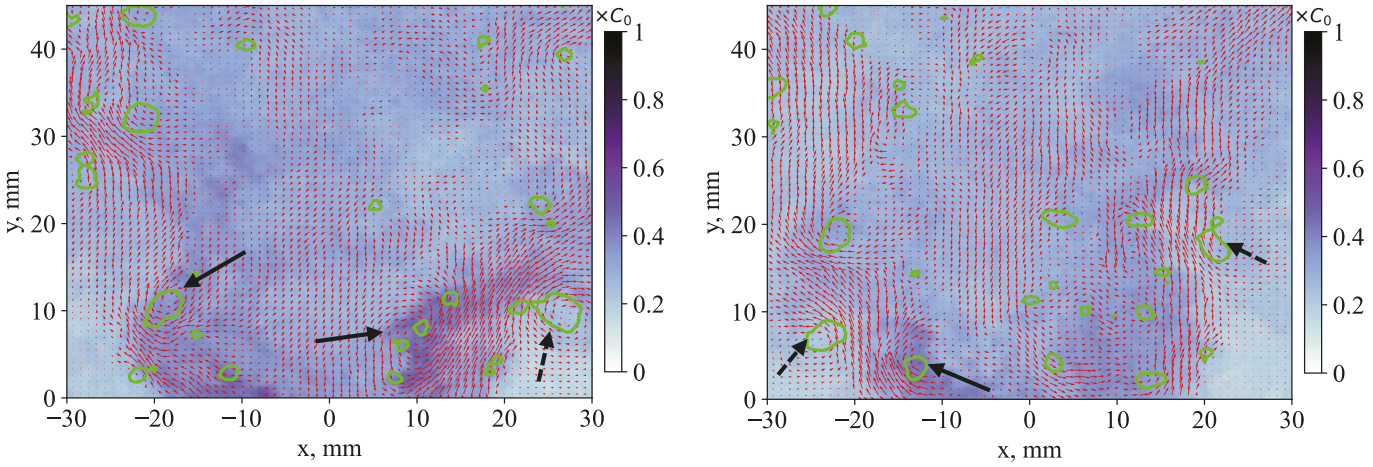


Figure 5. Examples of the instantaneous flow velocity and model fuel concentration for the case without central jet injection. The snapshots are captured in the central x0y plane.

Figure 6 shows similar examples for the case of a 10% injection. The main difference from the previous case is the high acetone concentration at the exit of the central jet near (x = 0, y = 0). The central jet is directed against the central reverse flow and does not have a potential core due to weak momentum. Thus, the central jet impinges the opposite reverse flow and quickly mixes with it. Figure 7 shows snapshots for the case of a 50% central injection. The arrangement of large-scale vortex structures in the distributions appears to be more symmetrical, and the main flow is associated with the variation in jet opening angle during the propagation of the pairs of large-scale vortex structures in the inner and outer shear layers (marked by solid and dashed arrows, respectively). The central jet also penetrates further into the recirculation zone due to a greater momentum than that for the 10% case. The large-scale vortex structures in the inner and outer mixing layers emerge in pairs, suggesting that they correspond to toroidal vortices or double-helical structures, as predicted by Mullyadzhanov [21].

3.2. Time-Averaged Data

The time-averaged velocity and concentration fields are given in Figure 8. The opening angle of the main annular swirling jet is not sufficiently affected by the central jet (the case of 50% injection is shown), which penetrates into the recirculation zone. The acetone concentration is expectedly high inside the central jet. Figure 9 compares the distributions of the longitudinal and transverse components of the mean velocity near the nozzle exit of the swirler (at y = 3.7 mm) for three considered flow cases. The figure demonstrates

that the fuel injection between the vanes has no sufficient impact on the axial velocity distribution at the exit of the annular nozzle of the swirler. The injection of 10% of the acetone–air mixture as the central jet seems to produce a minor effect on the axial flow momentum. However, when 50% of the acetone–air mixture is injected as the central jet, its velocity magnitude is close to that of the annular jet. In addition, the radial velocity profile near x = 0 for the present cross-section suggests that the central jet expands in the radial direction and partially entrains the air inside the reverse flow (see the region near 6 mm < |x| < 10 mm). Thus, the central jet momentum is sufficient to affect the time-averaged flow structure near the exit of the swirler nozzle.

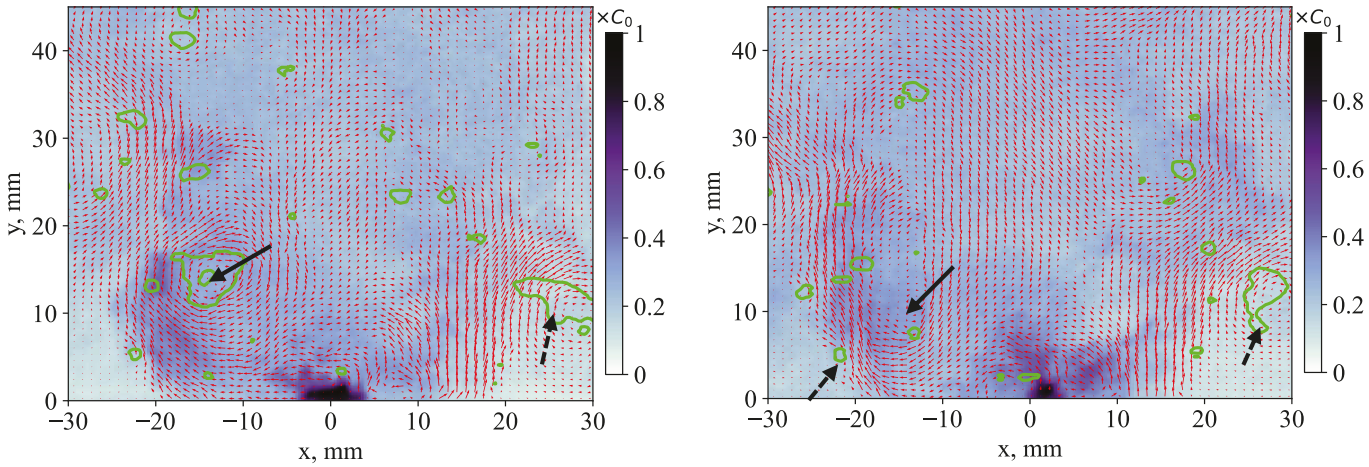


Figure 6. Examples of the instantaneous flow velocity and model fuel concentration in x0y plane for the case of a 10% central jet injection.

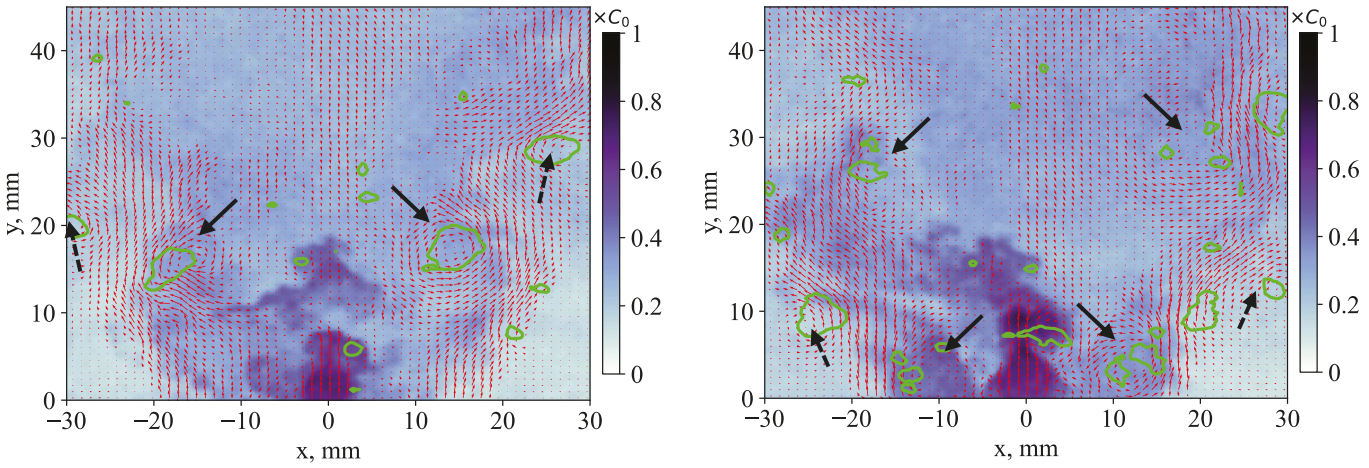


Figure 7. Examples of the instantaneous flow velocity and model fuel concentration in x0y plane for the case of a 50% central jet injection.

The difference is more pronounced for the Reynolds stresses. Figures 10 and 11 show the mean square deviations of the radial and axial velocity fluctuations $<u_x'^2>$ and $<u_y'^2>$, respectively. Only the kinetic energy of the longitudinal and transverse components of turbulent velocity fluctuations is considered. For the flow region under examination, the shape of the distribution of $<u_z'^2>$ and the central jet effect are found to be similar to those for $<u_x'^2>$. For example, the profiles at y = 3.7 mm are compared in Figure 12. The main observation is that the transverse velocity fluctuations near the center of the nozzle exit (x = 0, y = 0) are suppressed by the central jet. Without this, they reach values of up to 80% of the square of the mean bulk velocity U_0. In general, the intensity of the axial velocity fluctuations in the inner shear layer around the reverse flow is also dramatically reduced

by the central jet, which forms another conical mixing layer at the jet axis. Thus, whereas the central jet does not strongly affect the mean flow properties, it has a pronounced effect on the anisotropy of velocity fluctuations near the exit of the swirler nozzle. The patterns of large-scale vortex arrangements in the instantaneous snapshots (cf. Figures 5 and 7) also suggest that the properties of the dominant hydrodynamic instability mode are affected by the central jet.

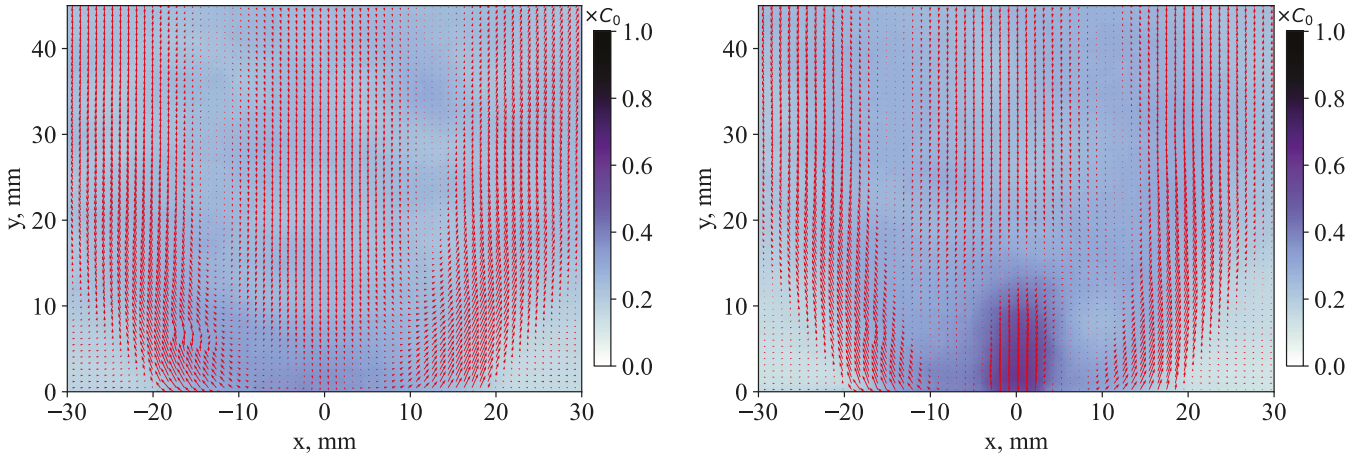


Figure 8. Time-averaged velocity field and concentration fields for the cases: (**a**) without and (**b**) with a 50% central jet injection.

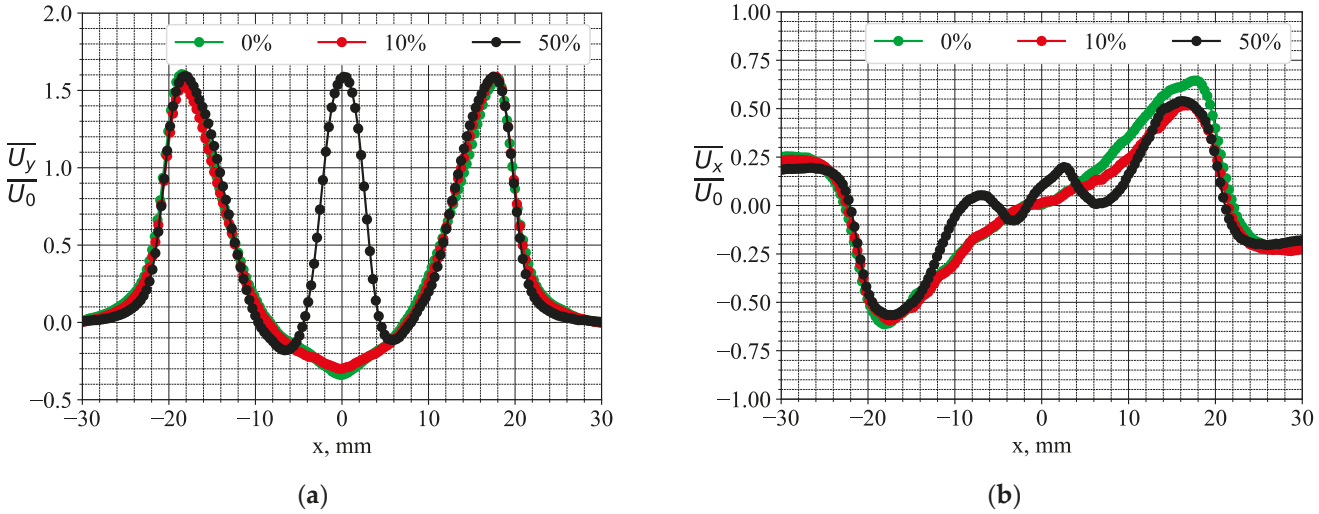


Figure 9. Profiles of the time-averaged velocity components for the flow cross-section with y = 3.7 mm without and with a 10% and 50% central jet injection. (**a**) Longitudinal and (**b**) transversal components.

Figures 10 and 11 show the distribution of local axial and radial velocity fluctuations in the swirling annular jet (x = 8.5 mm, y = 3.7 mm) and near the centerline (x ≈ 1.1 mm, y = 3.7 mm). If the influence of the central jet is insufficient for the region of the main swirling flow, the distributions of the velocity fluctuations become very different for the centerline region. In all cases, the local distributions of velocity fluctuations are far from a Gaussian shape, which is typical for normally distributed random variables. As demonstrated in the next subsection, this is due to intensive coherent velocity fluctuations in the flow, produced by the motion of large-scale vortex structures. For the near-axis region, the effect of the central jet is very strong, which results in narrow bell-shaped distributions. For the axial velocity component, the distribution is accompanied by less-probable small

values of axial velocity, indicating that the central jet is sometimes suppressed by reverse flow at the centerline.

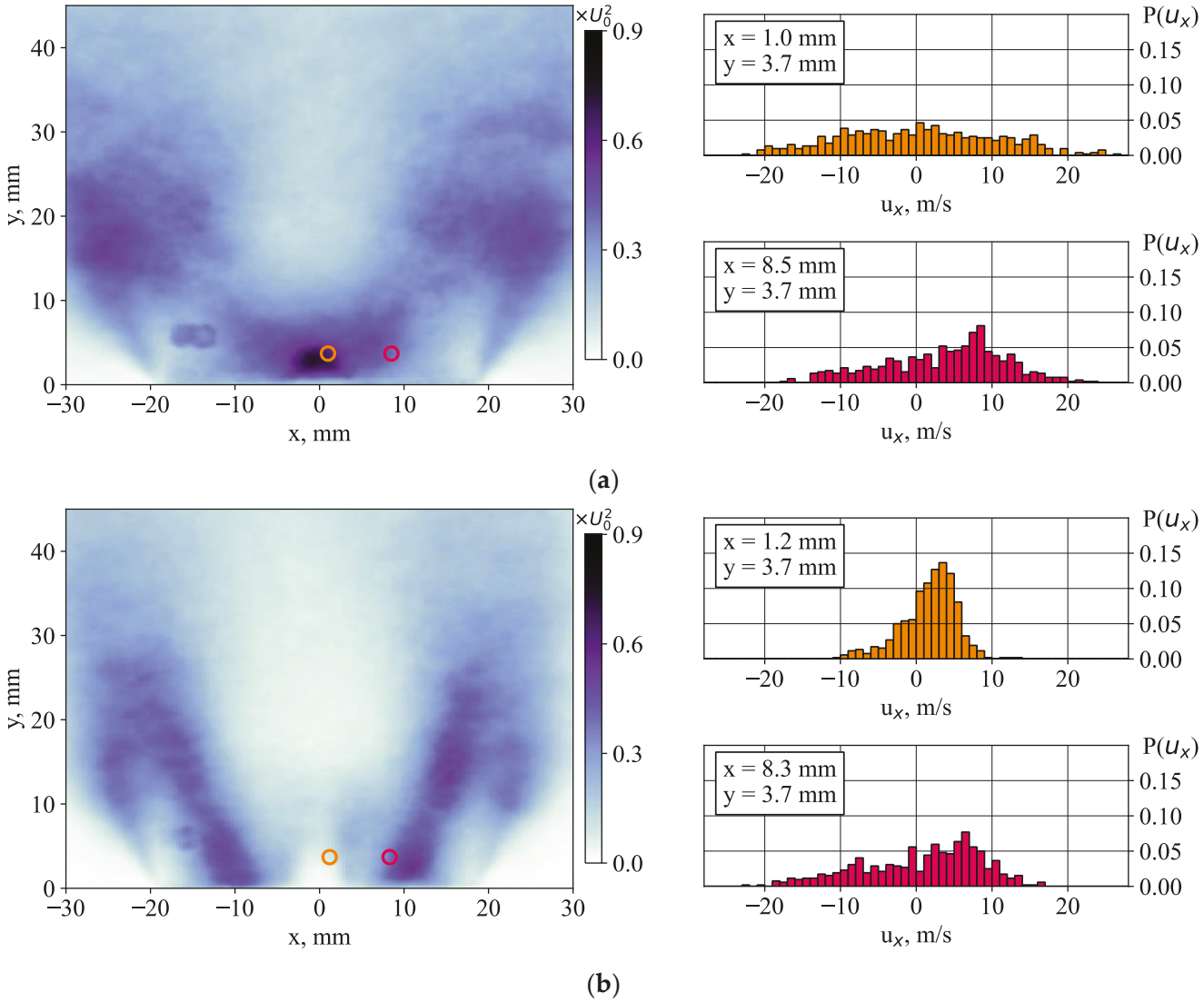


Figure 10. Mean square deviation $<u_x'^2>$ of the radial velocity fluctuations and the examples of local values for the cases: (**a**) without and (**b**) with a 50% central jet injection.

Figure 13 shows the effect of the central jet on the intensity of acetone concentration fluctuations. The local fluctuation probabilities are also analyzed near the centerline and in the region of the annular swirling jet. The concentration values are normalized by the maximal observed concentration values at the exit of the central jet. In the region of the main annular flow, the effect of the central jet injection (the 50% case is shown) is minor. It is noteworthy, that without the central jet, the distribution of acetone concentration fluctuations in the shown locations are quite similar. This is in agreement with the previous observation that the fuel injection between the swirler vanes does not provide complete mixing. The injection of 50% acetone through the central jet results in a greater average concentration and also in a greater width of the distribution. Thus, the central jet injection does not strongly affect the mean velocity distribution in the flow and has only a local effect on the fuel concentration fluctuations in the region close to the jet core. However, the intensities of the longitudinal and transverse velocity fluctuations are affected dramatically in the considered flow region.

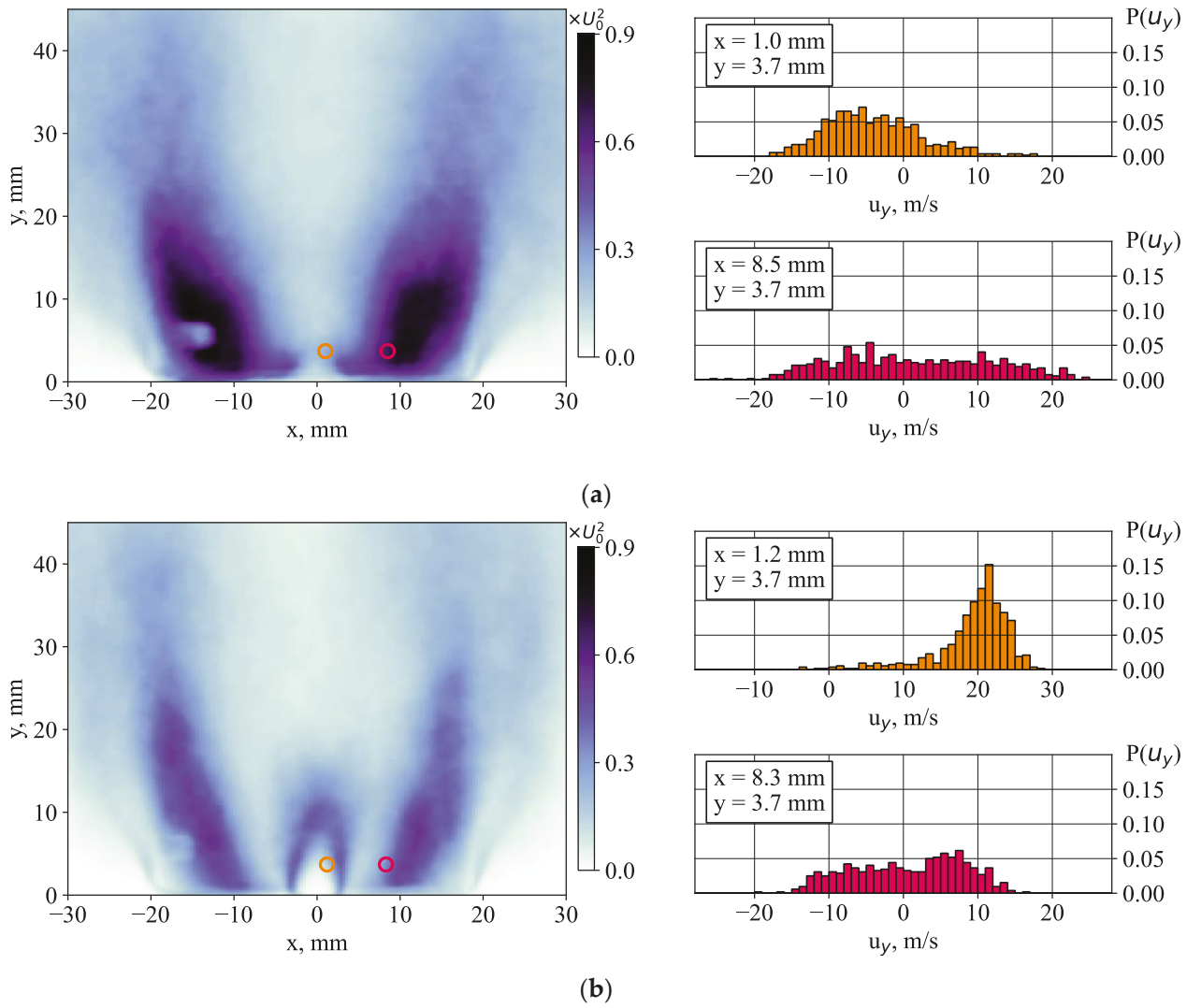


Figure 11. Mean square deviation <$u_y{}'^2$> of the axial velocity fluctuations and the examples of local values for the cases: (**a**) without and (**b**) with a 50% central jet injection.

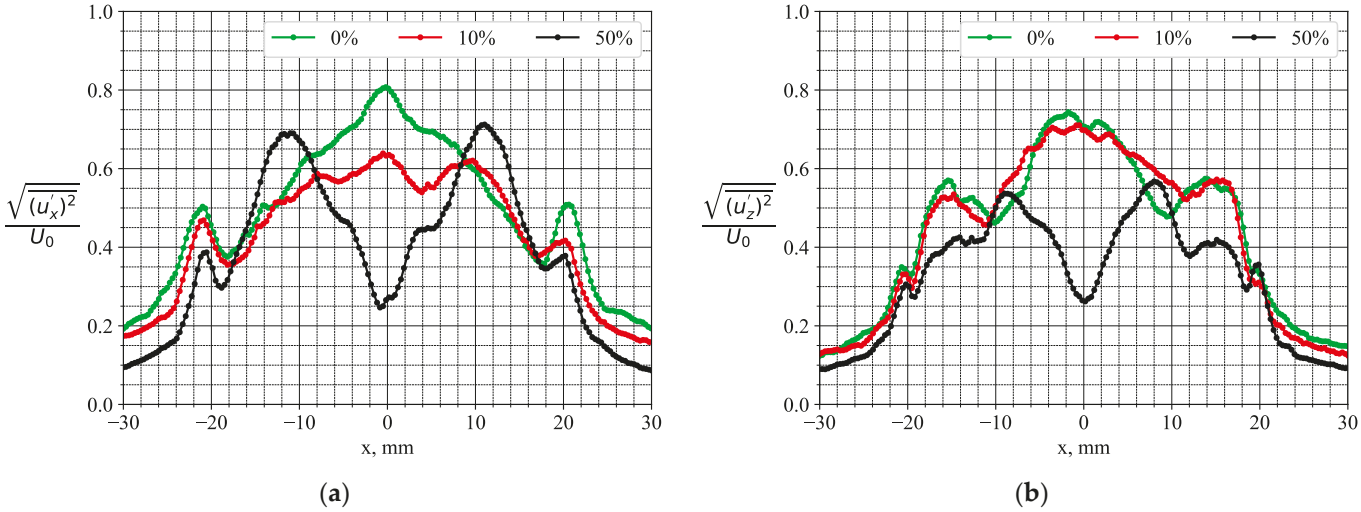


Figure 12. Profiles of the intensities of velocity fluctuations for the flow cross-section with y = 3.7 mm without and with a 10% and 50% central jet injection. (**a**) Radial and (**b**) azimuthal velocity components.

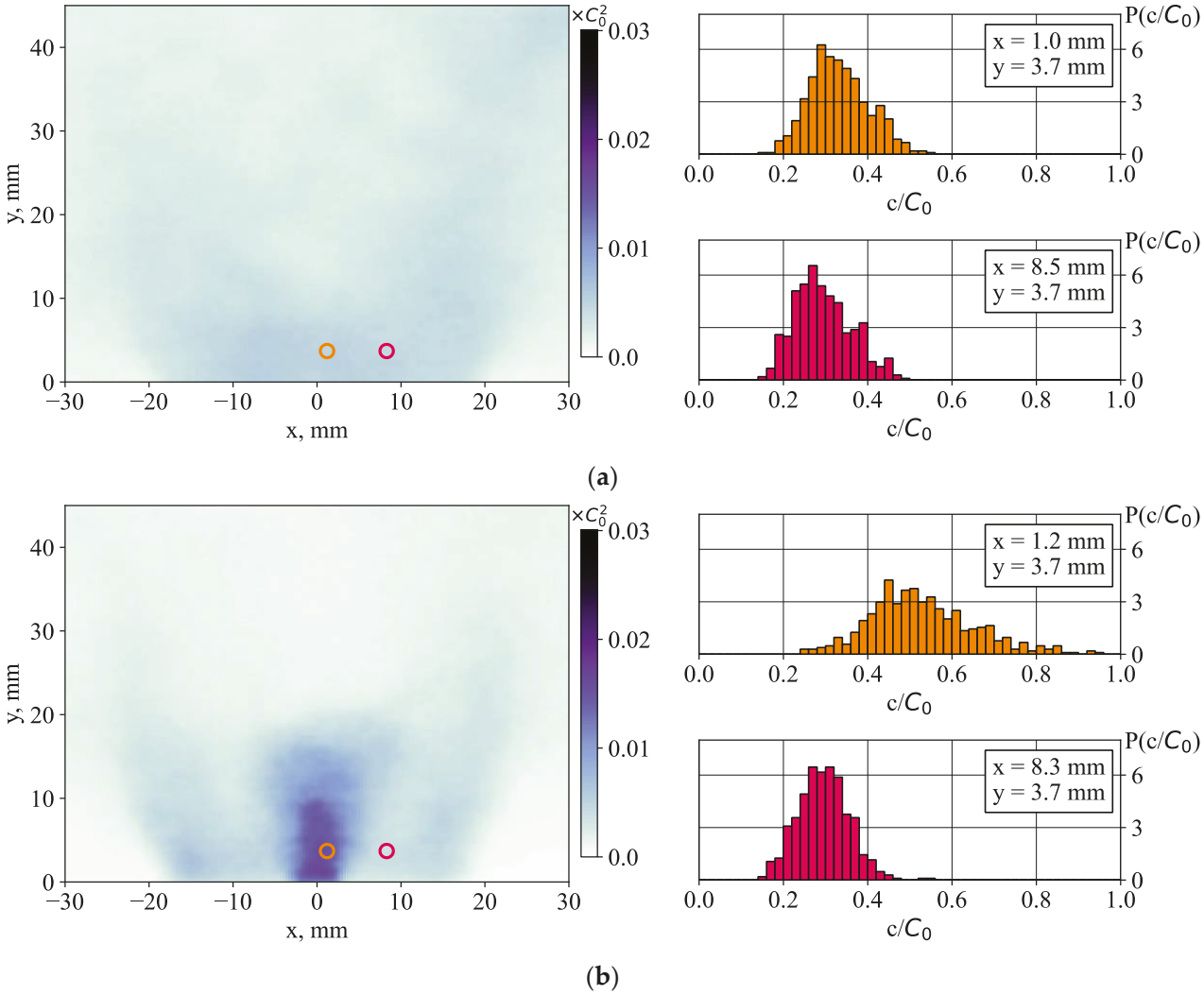


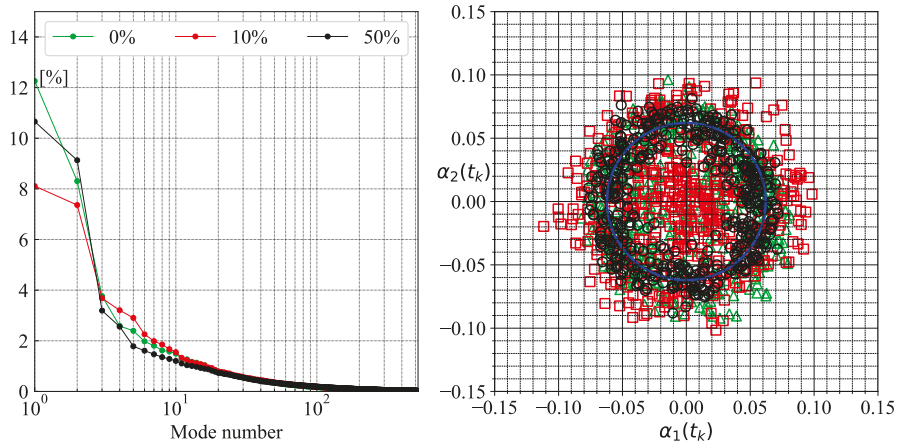
Figure 13. Mean square deviation <c'^2> of the acetone concentration and examples of local values for the cases: (**a**) without and (**b**) with a 50% central jet injection.

3.3. Coherent Fluctuations

To reveal coherent flow structures, the velocity snapshots are processed using the POD method. Figure 14 provides the distribution of the kinetic energy of velocity fluctuations related to different modes for the considered three flow cases. The energy is evaluated as $\sigma_k{}^2$. As can be seen, in all cases, there are two dominant modes that are typical for the flow. The cases without and with a 50% injection are associated with approximately 20% of the turbulent kinetic energy for the considered spatial domain. For the case of 10%, the content is insignificant, viz., 15%. The inset in Figure 12 contains the values of the temporal coefficients of the first two POD modes $\alpha_1(t)$ and $\alpha_2(t)$. Apparently, for the case without injection and the case of a 50% injection, the values are scattered around a Lissajous figure circle, indicating that these two modes are statistically correlated. In these cases, the flow dynamics can be represented by the low-order model (3). For the case of a 10% injection, the scattering is considerably greater.

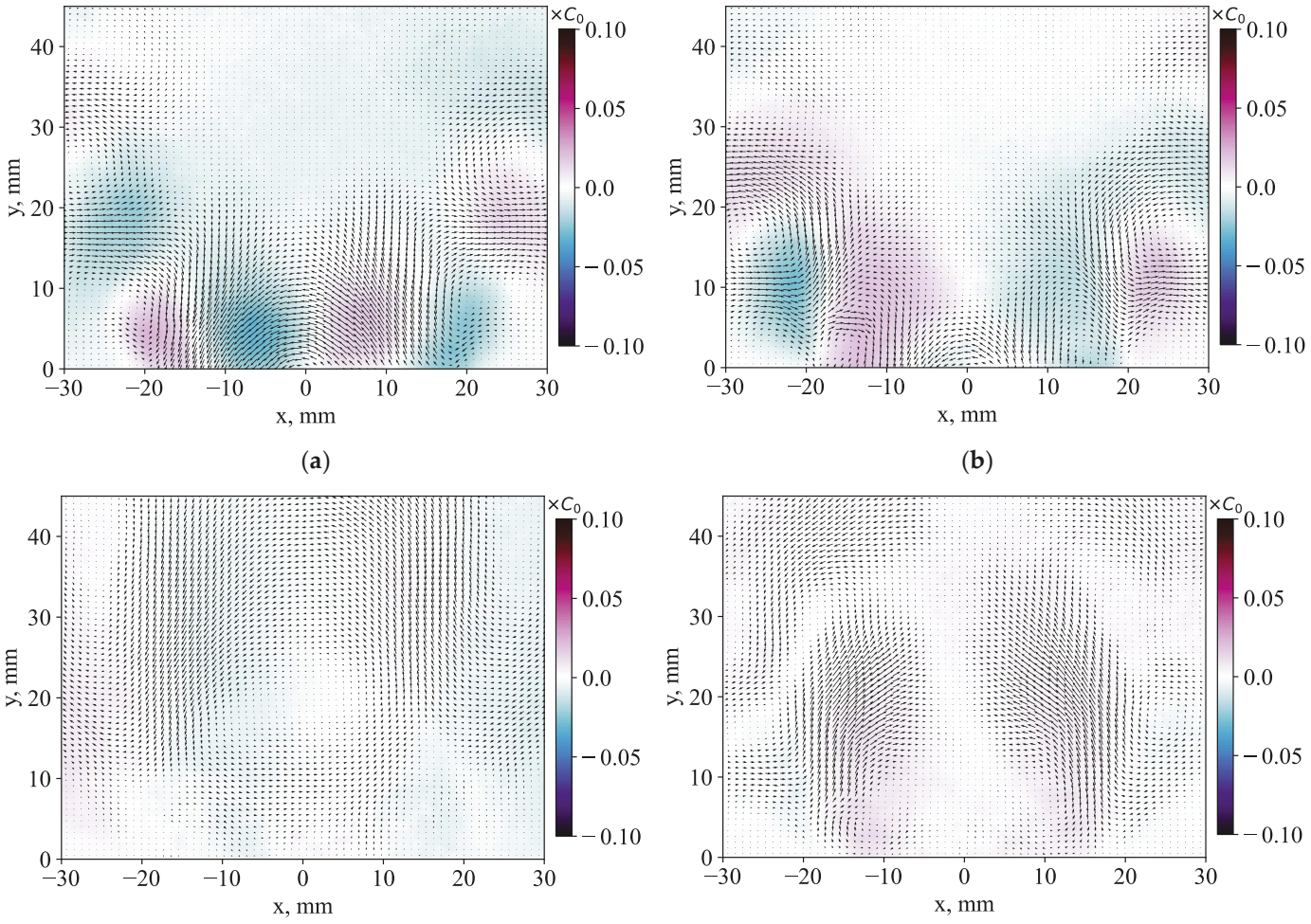
Figure 15 shows distributions of the first four POD modes for the case without injection. Two in-plane components of the POD modes are shown by vectors, whereas the color corresponds to the phase-averaged fluctuations in acetone concentration. These fluctuation amplitudes reach up to 4% of C_0. The first two POD modes are related to intensive velocity and concentration fluctuations in the inner and outer mixing layers. The distributions appear to be almost anti-symmetric relative to the centerline. Therefore, they are suggested

to correspond to the PVC mode with intensive flow fluctuations. The third and fourth modes are associated with larger but less intensive velocity and concentration fluctuations.



(**a**) (**b**)

Figure 14. (**a**) Distribution of kinetic energy of the velocity fluctuations associated with different POD modes and (**b**) temporal coefficients $\alpha_1(t)$ and $\alpha_2(t)$ for the cases of a 0%, 10% and 50% central jet injection.



(**a**) (**b**)

(**c**) (**d**)

Figure 15. Examples of (**a**) the first, (**b**) second, (**c**) third and (**d**) fourth POD modes and phase-averaged concentration fluctuations for the case without a central jet injection.

Figure 16 shows the distribution of the first four POD modes for the case of a 10% central jet injection. The first two modes also manifest antisymmetric properties of velocity and concentration fluctuations even in the region of the central jet. Therefore, it is concluded that the PVC still determines the flow dynamics and the turbulent transport of acetone near the nozzle exit. However, the third and fourth POD modes also exhibit quite a high magnitude of velocity and concentration fluctuations. There, the turbulent kinetic energy content is about 7% in comparison with 15% for the first two modes. In addition, the fourth POD mode clearly demonstrates the nearly symmetric mode of velocity and concentration fluctuations. Thus, the injection of a weak central jet promotes another hydrodynamic instability mode, corresponding to an even azimuthal mode.

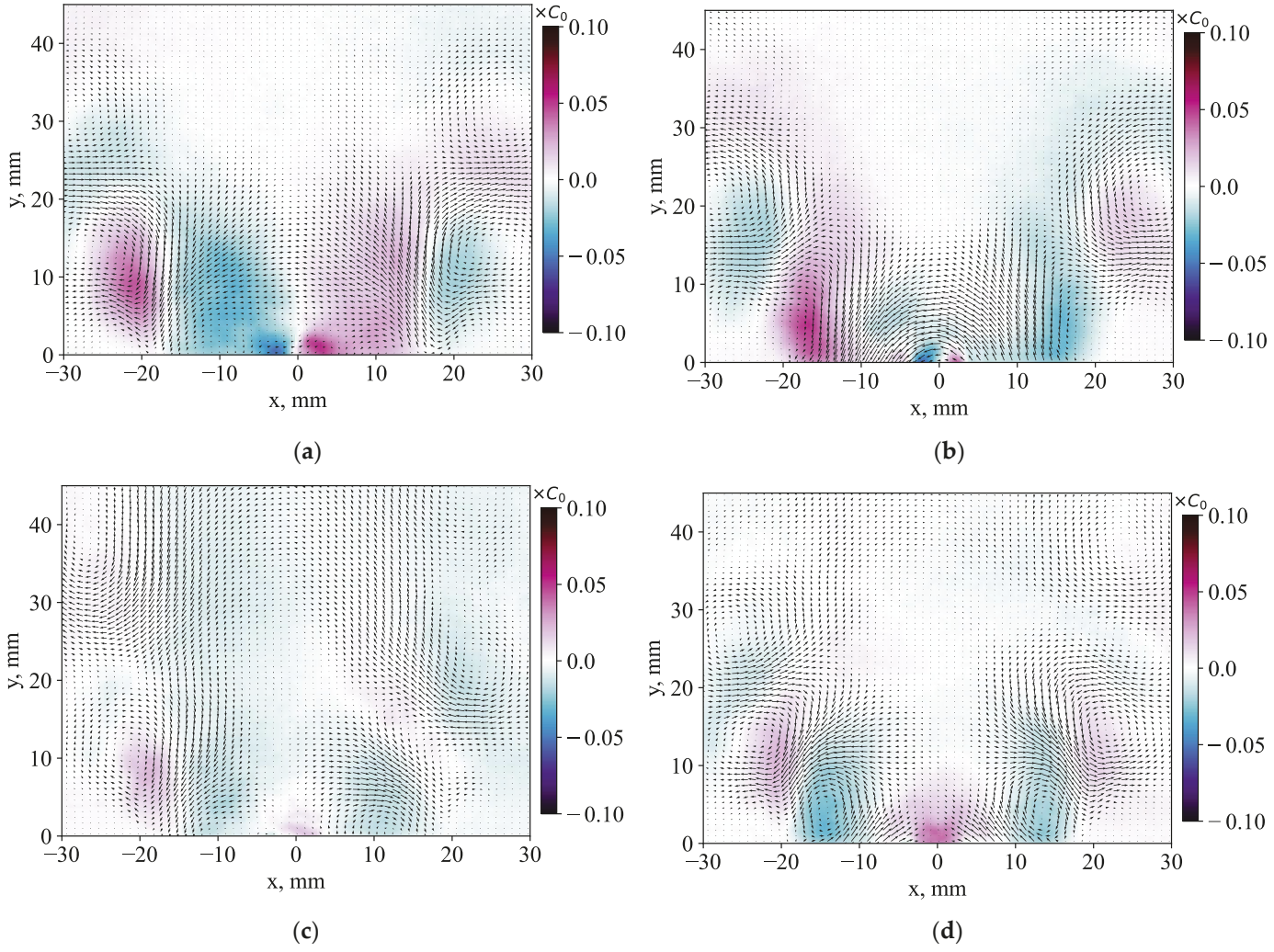


Figure 16. Examples of (**a**) the first, (**b**) second, (**c**) third and (**d**) fourth POD modes and phase-averaged concentration fluctuations for the case of a 10% central jet injection.

Figure 17 shows the first four POD modes for the case of a 50% injection. It is clear that in this case, the symmetrical mode is dominant and corresponds to the first most energetic POD modes. Antisymmetric coherent velocity and concentration fluctuations are visible in the third POD mode, but the energy content is much smaller for this mode (3.2%). Currently, there is evidence of PVC for this case. Thus, the injection of the central jet allows altering the properties of the dominant instability mode and, in particular, replacing an antisymmetric (odd) mode with one having reflective symmetry relative to the centerline (even azimuthal mode). This approach may be used to suppress thermoacoustic pulsations in combustion chambers.

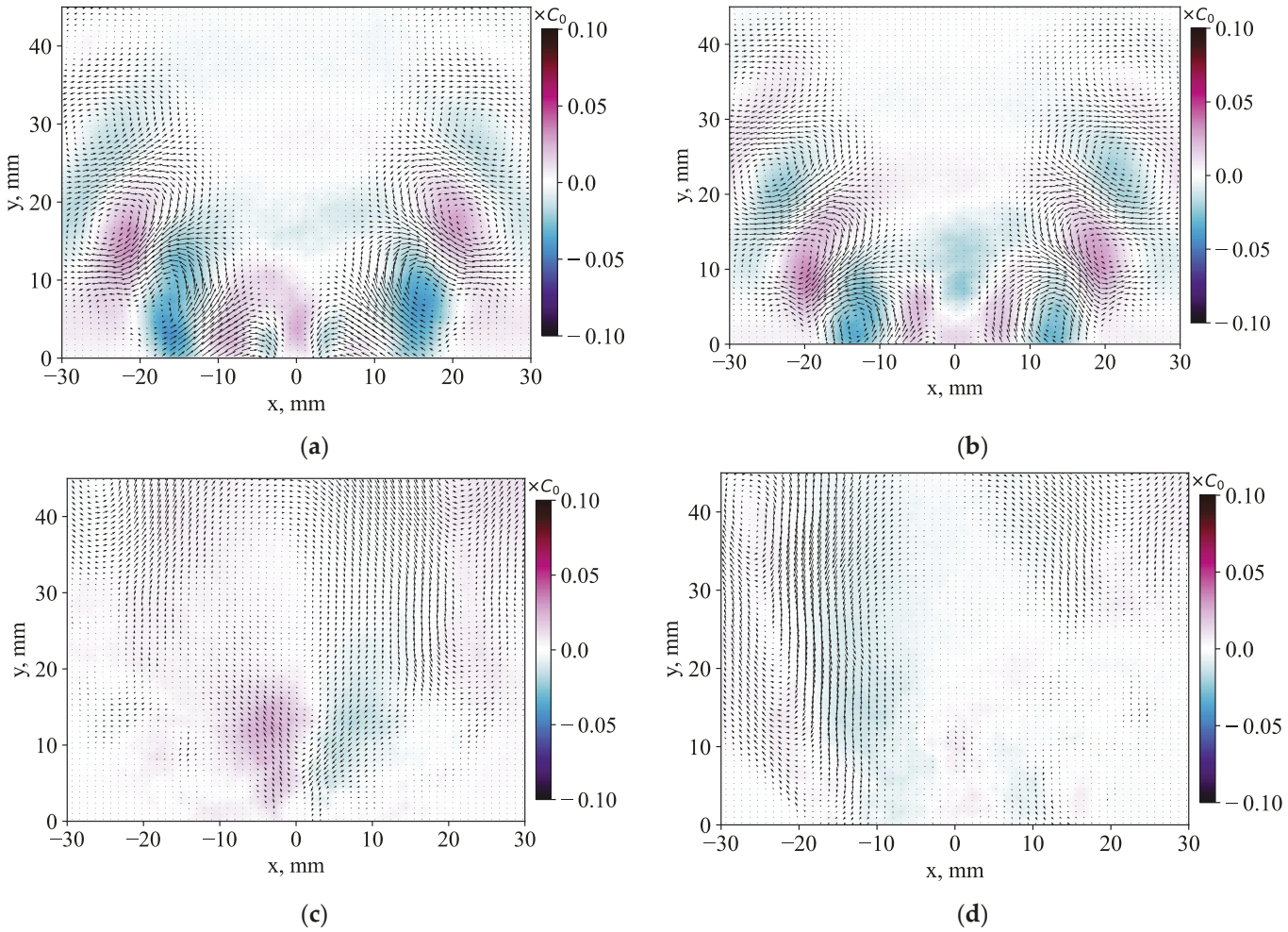


Figure 17. Examples of (**a**) the first, (**b**) second, (**c**) third and (**d**) fourth POD modes and phase-averaged concentration fluctuations for the case of a 50% central jet injection.

3.4. Stochastic Fluctuations

When the flow dynamics are dominated by coherent flow pulsations, the velocity fluctuations can be decomposed into coherent and stochastic parts $\mathbf{u}' = \hat{\mathbf{u}}+\mathbf{u}''$ [28]. The use of POD allows for separating the contribution of the stochastic and coherent velocity fluctuations to the total Reynolds stresses and Reynolds fluxes:

$$\left\langle u_i' u_j' \right\rangle = \left\langle \hat{u}_i \hat{u}_j \right\rangle + \left\langle u_i'' u_j'' \right\rangle \text{ and } \left\langle u_i' c' \right\rangle = \left\langle \hat{u}_i \hat{c} \right\rangle + \left\langle u_i'' c'' \right\rangle, \tag{6}$$

$$\text{where } \left\langle \hat{u}_i \hat{u}_j \right\rangle = \sigma_1^2 \varphi_{1i} \varphi_{1j} + \sigma_2^2 \varphi_{2i} \varphi_{2j} \text{ and } \left\langle \hat{u}_i \hat{c} \right\rangle = \sigma_1 \varphi_{1i} \hat{c}_1 + \sigma_2 \varphi_{2i} \hat{c}_2. \tag{7}$$

Figure 18 compares the intensity of stochastic velocity fluctuations for the radial and axial velocity components. The difference between the distributions and magnitude is not as substantial as for the total fluctuations, as shown in Figures 10 and 11. The effect of the central jet injection on the entire flow is also rather minor, except for the region around the central jet. Thus, the central jet affects mainly the properties of coherent velocity fluctuations, which manifest strong anisotropy of the velocity fluctuations. Figures 19 and 20 also compare the effect of the central jet on the Reynolds stress and flux, respectively, for the total fluctuations and the stochastic part. The central jet strongly affects the entire distribution of the total Reynolds shear stress, whereas, for the stochastic part, the effect is mainly near the central jet. The contribution of the coherent part to the total turbulent shear stress is found to be above 65% near the exit of the swirler nozzle for the cases without and with the central jet injection. The contribution is found to be even stronger in the case

of the radial turbulent flux plotted in Figure 20. Only near the core of the central jet (for the case of 50% supply) do stochastic fluctuations provide sufficient turbulent transport of the admixture. Thus, it is concluded that for all considered flow cases, coherent velocity fluctuations play a dominant role in the turbulent mass and momentum transport in the inner mixing layer around the central recirculation zone. The central jet strongly affects the turbulent transport in the inner mixing layer by altering the properties of large-scale coherent structures, whereas its effect inside the recirculation zone is minor.

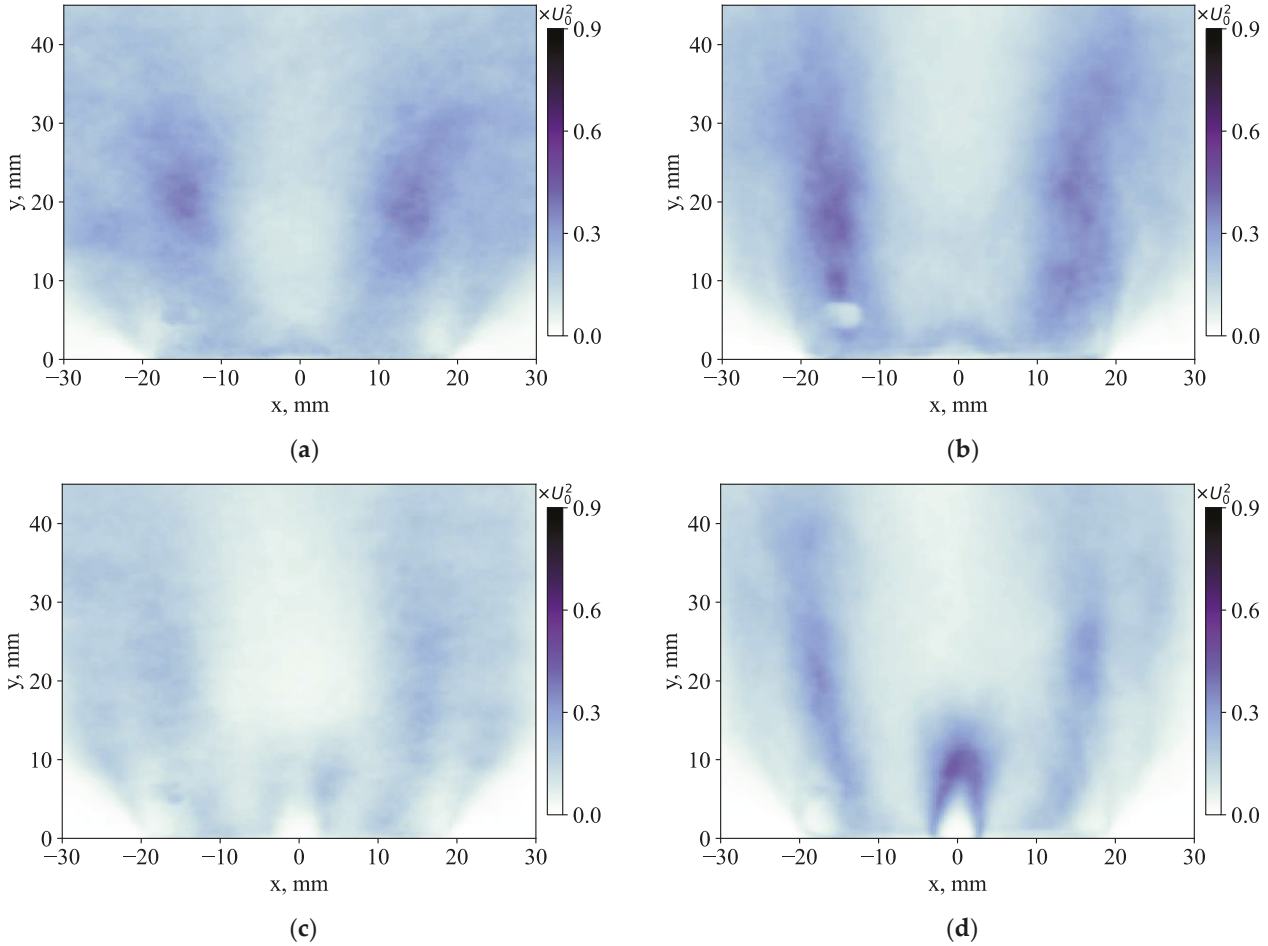


Figure 18. Mean square deviation of the radial (**a**,**c**) $<u_x''^2>$ and axial (**b**,**d**) $<u_y''^2>$ components the stochastic velocity fluctuations for the cases: (**a**,**b**) without and (**c**,**d**) with a 50% central jet injection.

Figure 21 compares linearized anisotropy invariant maps of the velocity fluctuations in the inner mixing layer around the central recirculation zone (x = 8.5 mm, y = 3.7 mm) and near the flow axis (x ≈ 1.1 mm, y = 3.7 mm). The maps correspond to the local values of modified invariants η and ξ defined by (8), where *II* and *III* are the invariants (9) of the characteristic equation for the anisotropy tensor b_{ij} (10) for the Reynolds shear stress [29]. The data are shown for the total or stochastic velocity fluctuations. In the latter case (square symbols), the effect of the central jet is minor, whereas, for the total fluctuations, the effect is clearly visible. With and without the central jet, the stochastic fluctuations near the flow axis and in the inner shear layer manifest properties of axisymmetric turbulence, with one component being considerably higher and lower in comparison to the other two, respectively. For the total velocity fluctuations, the injection of the central jet leads to the switching between the properties of the axial symmetry near the flow axis and the inner mixing layer.

$$\eta^2 = -II/3 \text{ and } \xi^3 = III/2, \quad (8)$$

$$II = -\frac{1}{2}b_{ij}b_{ji} \text{ and } III = \frac{1}{3}b_{ij}b_{jk}b_{ki}. \tag{9}$$

$$b_{ij} = \frac{\left\langle u_i' u_j' \right\rangle}{\left\langle u_k' u_k' \right\rangle} - \frac{1}{3}\delta_{ij} \text{ or } b_{ij} = \frac{\left\langle u_i'' u_j'' \right\rangle}{\left\langle u_k'' u_k'' \right\rangle} - \frac{1}{3}\delta_{ij}. \tag{10}$$

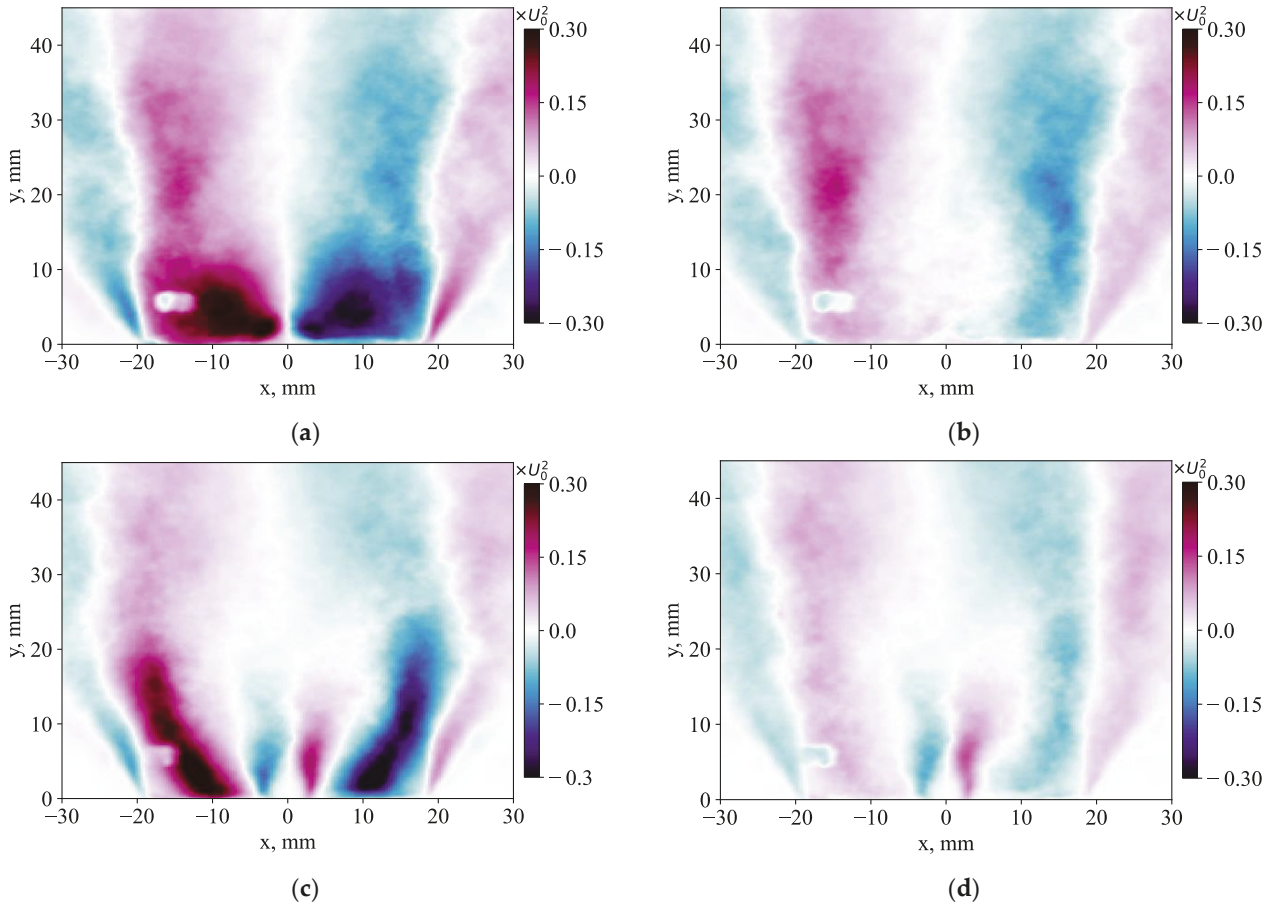


Figure 19. Total (**a**,**c**) <$u_x{}'u_y{}'$> and stochastic (**b**,**d**) <$u_x{}''u_y{}''$> turbulent shear stress for the cases: (**a**,**b**) without and (**c**,**d**) with a 50% central jet injection.

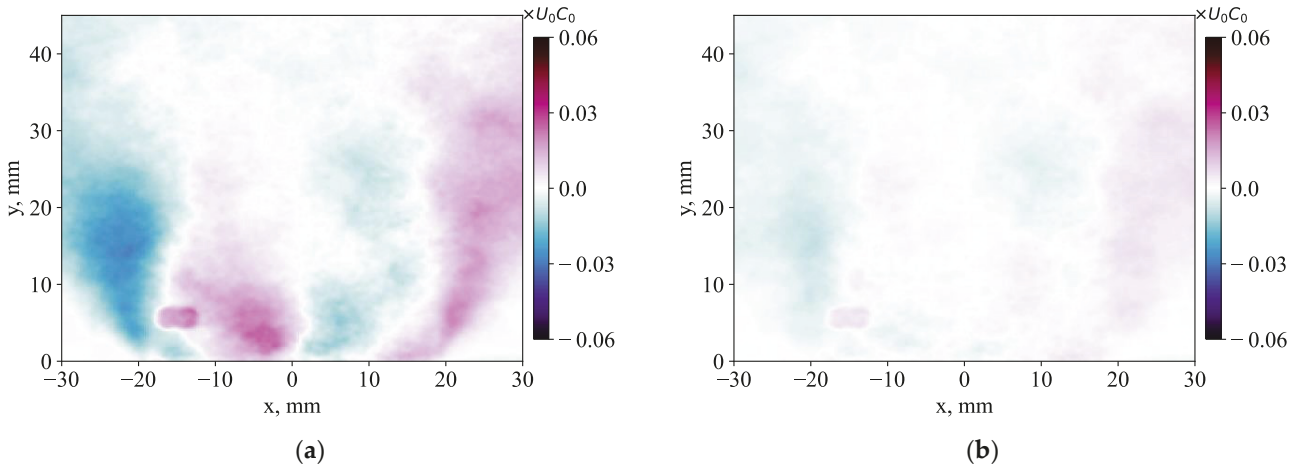


Figure 20. *Cont.*

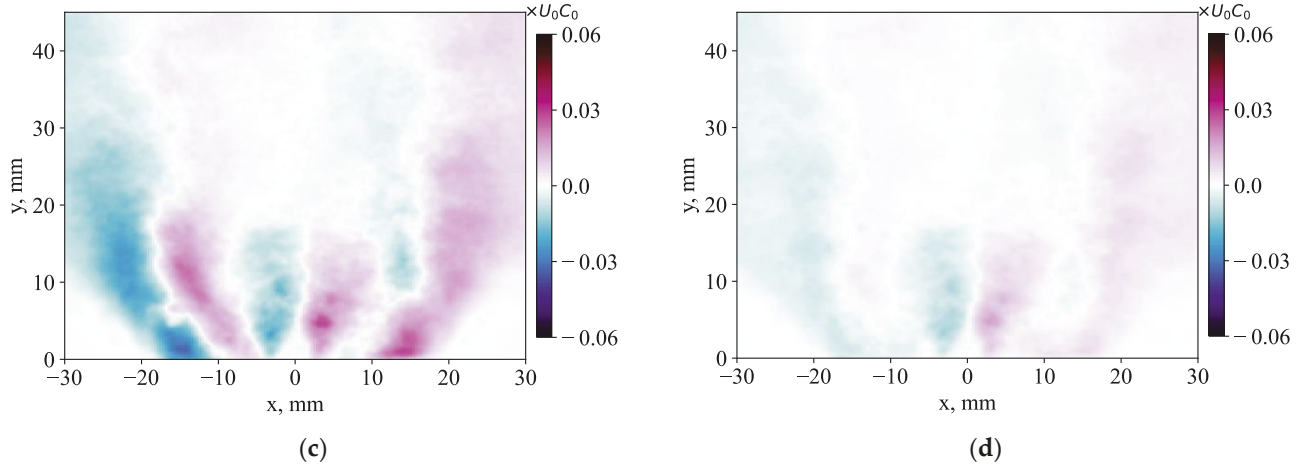


Figure 20. Total (**a**,**c**) <$u_x'c'$> and stochastic (**b**,**d**) <$u_x''c''$> turbulent fluxes for the cases: (**a**,**b**) without and (**c**,**d**) with a 50% central jet injection.

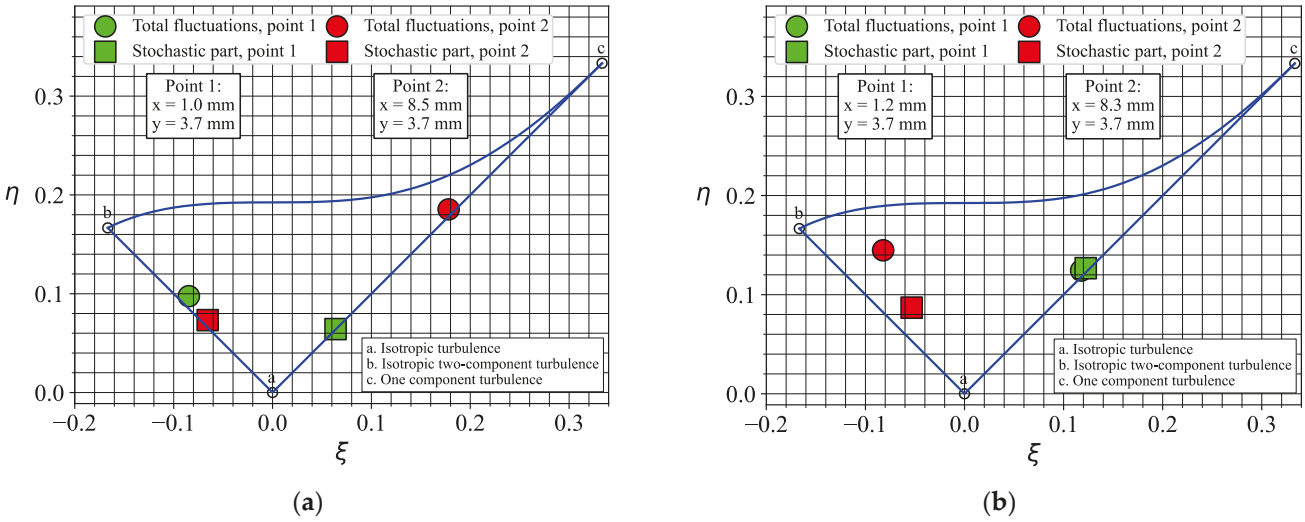


Figure 21. The linearized anisotropy invariant maps for the cases: (**a**) without and (**b**) with a 50% central jet injection.

4. Conclusions

The present paper reports on the PIV and PLIF measurements of flow structure and turbulent fluctuations in a model swirl-stabilized combustor with a two-zone swirl burner based on Turbomeca geometry. The swirler provides fuel injection in the form of a central jet to organize a pilot flame, and upstream the exit of the nozzle between the swirler vanes, to ensure the supply of a well-premixed fuel. PIV and PLIF measurements demonstrate that when gas is supplied between the vanes, its concentration at the entrance to the combustion chamber is still considerably nonuniform and fluctuates inside the chamber due to the presence of a large-scale vortex structure. The analysis of the coherent velocity fluctuations with POD suggests that the vortex structure in the inner mixing layer corresponds to the spiral PVC. Injecting part (10%) of the fuel gas as a central control jet contributes to another instability mode that exhibits reflection symmetry relative to the geometric axis. When half of the fuel is supplied through the central jet, the PVC mode appears to be suppressed, and the flow dynamics are driven by a symmetrical mode, related to either toroidal or double-helix vortex structures. Thus, the central jet injection does not have a strong influence on the mean velocity distribution in the flow, only locally affecting the fuel concentration fluctuation in the region close to the jet core. However, the intensities of the longitudinal and transverse velocity fluctuations and the properties of the dominant hydrodynamic

instability mode are affected dramatically in the near-nozzle flow region. Moreover, for all considered flow cases, it is found that the coherent velocity fluctuations play a dominant role in the turbulent mass and momentum transport in the inner mixing layer around the central recirculation zone. Thus, the central jet strongly affects turbulent transport in the inner mixing layer by altering the properties of large-scale coherent structures, whereas its effect inside the recirculation zone is minor. Therefore, the central jet injection may be used to control the dominant mode of flow instability and, in particular, to suppress thermo-acoustic instabilities during combustion.

Author Contributions: Conceptualization, V.D. and L.C.; methodology, D.S.; data processing, D.S. and A.S.; data acquisition, D.S. and A.S.; writing—original draft preparation, V.D. and L.C.; writing—review and editing, V.D.; visualization, A.S.; supervision, V.D.; project administration, L.C.; funding acquisition, L.C. All authors have read and agreed to the published version of the manuscript.

Funding: This research was supported by the Ministry of Science and Higher Education of the Russian Federation, agreement No. 075-15-2020-806.

Data Availability Statement: The data that support the findings of this study are available from the corresponding author upon reasonable request.

Acknowledgments: The authors are grateful to Roman Tolstoguzov for assistance during the experiments.

Conflicts of Interest: The authors declare no conflict of interest.

References

1. Billant, P.; Chomaz, J.M.; Huerre, P. Experimental study of vortex breakdown in swirling jets. *J. Fluid Mech.* **1998**, *376*, 183–219. [CrossRef]
2. Lucca-Negro, O.; O'doherty, T. Vortex breakdown: A review. *Prog. Energy Combust. Sci.* **2001**, *27*, 431–481. [CrossRef]
3. Syred, N. A review of oscillation mechanisms and the role of the precessing vortex core (PVC) in swirl combustion systems. *Prog. Energy Combust. Sci.* **2006**, *32*, 93–161. [CrossRef]
4. Stöhr, M.; Arndt, C.M.; Meier, W. Transient effects of fuel–air mixing in a partially-premixed turbulent swirl flame. *Proc. Combust. Inst.* **2015**, *35*, 3327–3335. [CrossRef]
5. Stöhr, M.; Sadanandan, R.; Meier, W. Experimental study of unsteady flame structures of an oscillating swirl flame in a gas turbine model combustor. *Proc. Combust. Inst.* **2009**, *32*, 2925–2932. [CrossRef]
6. Boxx, I.; Stöhr, M.; Carter, C.; Meier, W. Temporally resolved planar measurements of transient phenomena in a partially pre-mixed swirl flame in a gas turbine model combustor. *Combust. Flame* **2010**, *157*, 1510–1525. [CrossRef]
7. Oberleithner, K.; Paschereit, C.O.; Seele, R.; Wygnanski, I. Formation of turbulent vortex breakdown: Intermittency, criticality, and global instability. *AIAA J.* **2012**, *50*, 1437–1452. [CrossRef]
8. Shtork, S.; Suslov, D.; Skripkin, S.; Litvinov, I.; Gorelikov, E. An Overview of Active Control Techniques for Vortex Rope Mitigation in Hydraulic Turbines. *Energies* **2023**, *16*, 5131. [CrossRef]
9. Midgley, K.; Spencer, A.; McGuirk, J.J. Unsteady Flow Structures in Radial Swirler Fed Fuel Injectors. *ASME J. Eng. Gas Turbines Power* **2005**, *127*, 755–764. [CrossRef]
10. Janus, B.; Dreizler, A.; Janicka, J. Experimental study on stabilization of lifted swirl flames in a model GT combustor. *Flow Turbul. Combust.* **2005**, *75*, 293–315. [CrossRef]
11. Meier, W.; Weigand, P.; Duan, X.R.; Giezendanner-Thoben, R. Detailed characterization of the dynamics of thermoacoustic pulsations in a lean premixed swirl flame. *Combust. Flame* **2007**, *150*, 2–26. [CrossRef]
12. Meier, W.; Duan, X.R.; Weigand, P. Investigation of swirl flames in a gas turbine model combustor II. Turbulence-chemistry interactions. *Combust. Flame* **2006**, *144*, 225–236. [CrossRef]
13. Renaud, A.; Ducruix, S.; Scouflaire, P.; Zimmer, L. Flame shape transition in a swirl stabilised liquid fueled burner. *Proc. Combust. Inst.* **2015**, *35*, 3365–3372. [CrossRef]
14. Li, G.; Gutmark, E.J. Geometry effects on the flow field and spectral characteristics of a triple annular swirler. In Proceedings of the ASME Turbo Expo, Power for Land, See and Air, Atlanta, GA, USA, 16–19 June 2003; 2003. [CrossRef]
15. Vashahi, F.; Lee, J. Effects of the Interaction Point of Adjacent Swirlers on Swirling Flow Using POD Analysis in a Triple Swirler Configuration. *J. Eng. Gas Turbines Power* **2019**, *141*, 0610113. [CrossRef]
16. Wehr, L.; Meier, W.; Kutne, P.; Hassa, C. Single-pulse 1D laser Raman scattering applied in a gas turbine model combustor at elevated pressure. *Proc. Combust. Inst.* **2007**, *31*, 3099–3106. [CrossRef]
17. Stöhr, M.; Sadanandan, R.; Meier, W. Phase-resolved characterization of vortex–flame interaction in a turbulent swirl flame. *Exp. Fluids* **2011**, *51*, 1153–1167. [CrossRef]
18. Dunn-Rankin, D. *Lean Combustion. Technology and Control*; Elsevier: Oxford, UK, 2008.

19. Lieuwen, T.; Torres, H.; Johnson, C.; Zinn, B.T. A mechanism of combustion instability in lean premixed gas turbine combustors. *J. Eng. Gas Turbines Power* **2001**, *123*, 182–189. [CrossRef]
20. Candel, S.; Durox, D.; Schuller, T.; Bourgouin, J.-F.; Moeck, J.P. Dynamics of swirling flames. *Ann. Rev. Fluid Mech.* **2014**, *46*, 147–173. [CrossRef]
21. Lieuwen, T.C. *Unsteady Combustor Physics*; Cambridge University Press: Cambridge, UK, 2021.
22. Spencer, A.; McGuirk, J.; Midgley, K. Vortex breakdown in swirling fuel injector flows. *J. Eng. Gas Turbines Power* **2008**, *130*, 021503. [CrossRef]
23. Palkin, E.V.; Hrebtov, M.Y.; Slastnaya, D.A.; Mullyadzhanov, R.I.; Vervisch, L.; Sharaborin, D.K.; Lobasov, A.S.; Dulin, V.M. Influence of a Central Jet on Isothermal and Reacting Swirling Flow in a Model Combustion Chamber. *Energies* **2022**, *15*, 1615. [CrossRef]
24. Sharaborin, D.K.; Savitskii, A.G.; Bakharev, G.Y.; Lobasov, A.S.; Chikishev, L.M.; Dulin, V.M. PIV/PLIF investigation of unsteady turbulent flow and mixing behind a model gas turbine combustor. *Exp. Fluids* **2021**, *62*, 96. [CrossRef]
25. Scarano, F. Iterative image deformation methods in PIV. *Meas. Sci. Technol.* **2001**, *13*, R1–R19. [CrossRef]
26. Soloff, S.M.; Adrian, R.J.; Liu, Z.-C. Distortion compensation for generalized stereoscopic particle image velocimetry. *Meas. Sci. Technol.* **1997**, *8*, 1441–1454. [CrossRef]
27. Lobasov, A.S.; Alekseenko, S.V.; Markovich, D.M.; Dulin, V.M. Mass and momentum transport in the near field of swirling turbulent jets. Effect of swirl rate. *Int. J. Heat Fluid Flow* **2020**, *83*, 108539. [CrossRef]
28. Hussain, A.K.M.F.; Reynolds, W.C. The mechanics of an organized wave in turbulent shear flow. *J. Fluid Mech.* **1970**, *41*, 241–258. [CrossRef]
29. Choi, K.-S.; Lumley, J.L. The return to isotropy of homogeneous turbulence. *J. Fluid Mech.* **2001**, *436*, 59–84. [CrossRef]

Disclaimer/Publisher's Note: The statements, opinions and data contained in all publications are solely those of the individual author(s) and contributor(s) and not of MDPI and/or the editor(s). MDPI and/or the editor(s) disclaim responsibility for any injury to people or property resulting from any ideas, methods, instructions or products referred to in the content.

inventions

MDPI

Article

A Hydro-Powered Climate-Neutral Pump: Full Cycle Simulation and Performance Evaluation

Mansour Al Qubeissi *,† and Scott Daniel Beard

School of Mechanical Engineering, Coventry University, Coventry CV1 5FB, UK; beards2@uni.coventry.ac.uk
* Correspondence: mansour.alqubeissi@udst.edu.qa or ac1028@coventry.ac.uk
† Current address: College of Engineering Technology, University of Doha for Science and Technology, Doha 24449, Qatar.

Abstract: This paper presents a parametric study of the multistorey hydro-powered pump, known as 'Bunyip', which has demonstrated significant potential in contributing to rural regions. The study is aimed at understanding the underlying physics of the system and ways to enhance its hydraulic performance. A transient three-dimensional model using the commercial Computational Fluid Dynamics (CFD) tool Ansys-Fluent is utilized to gain insights into its fundamental flow mechanics, operational efficiency, standard capacity, and relative delivery. The investigation involves an initial assessment of performance for three Bunyip devices based on manufacturing data. A parametric analysis is conducted for the dataset generated through meticulous application and numerical modelling. The CFD results are validated against experimental data. Three main design configurations are considered, and 58 sets of varied input parameters are examined. The best design configuration is evaluated against five cases of conventional hydro-power pump systems. The results indicate that a smaller diameter of the pressure chamber and a higher supply head lead to higher pressure, achieving a target head of 3 m with 15% efficiency and a flowrate of 11.82 L/min.

Keywords: clean energy; hydraulic pump; modelling; renewable energy; sustainable propulsion

1. Introduction

The escalating climate crisis and the need for sustainable energy solutions have prompted a global push towards renewable energy adoption [1]. As fossil fuel prices continue to rise due to inflation and geopolitical conflicts, the finite nature of these resources poses challenges to their accessibility [2]. In response to these concerns, significant investments have been made in transitioning towards cleaner energy sources, reaching a staggering USD 1.3 trillion in 2022 [3].

Developing regions, often facing economic vulnerability, bear the brunt of the increasing pressure to afford and access reliable power sources. These regions heavily rely on stable access to power for sustaining growth, productivity, and overall well-being. Among the crucial resources required for development, access to water stands as an indispensable necessity [4]. Whether it is for safe drinking, personal hygiene, agriculture, livestock rearing, or other developmental needs, a stable water supply plays a pivotal role. Traditionally, fossil-fuel or electrically powered systems have been the primary mechanisms used for lifting and transporting water in these regions. However, the detrimental impact of fossil fuels, including rising prices and environmental concerns, is now driving the need to shift towards alternative renewable mechanisms that can capture and harness the natural energy systems present in the local environment.

The hydraulic ram pump (HRP) is a simple yet effective device that utilizes a paired check-valve mechanism to harness hydro-kinetic energy from a drive volume and convert a fraction of the incoming flow into an elevated head potential. By tapping into the 'free' gravitational energy present in natural rivers, springs, or flowing water bodies, the HRP offers a sustainable solution for micro-hydro-power needs [5]. Due to its potential

and versatility, the HRP has been actively researched and recognized as a prominent hydro-powered system in current technology reviews [6]. Despite its success, much of the existing research on the HRP, like other pumping technologies, tends to focus on marginal improvements rather than exploring more significant enhancements. This raises questions regarding the feasibility and benefits of introducing additional hydraulic complexity to the system in pursuit of enhanced water head potential.

Over the past decade, research on internal flows has significantly advanced, enabling a more detailed and focused analysis of individual components within hydraulic pumping systems. This progress has led to the discovery of additional capabilities, offering opportunities to enhance the previously established analytical relationships [7]. To serve as a valuable resource to observe best practices and methodologies used in HRP systems, we have utilized the development of an advanced multi-storey hydraulic pumping system known as 'Bunyip [8].' Several studies have been conducted, providing valuable insights into the modelling procedures, validation processes, and overall success of hydraulic pumping systems but with limited application to Bunyip systems. Among these studies, two groups of researchers have made notable contributions:

In [9,10], a detailed study on the adopted CFD setup and validation for ramp pump is given. This includes an RNG k-ε Turbulence model suitable for high shear rate flow and separation, the PISO pressure–velocity coupling, and the coarse mixed mesh, designed within a 5–20 mm size range and 1 million cells. The wall treatment exploits four inflation layers for y+ between 17.78–442.79, utilising standard wall functions and a roughness of 0.15 mm. Nonetheless, the settings attained an average relative error of 1.9% for head loss and drag coefficients when corroborated with their physical equipment. Thus, despite the criticisms made, the model performed well in application and remains to be one of the most successful validations and hybrid studies published.

In [11,12], a detailed simulation of a ram pump is made, including the traditional spring waste valve mechanism, to conclude three optimal designs. The best numerically analysed design reduced the waste valve loss by 30%. The latter finding is less extensive than the previous two pieces of research but still nontrivial, using the realizable k-ε turbulence model and second-order spatial, kinetic, and turbulence dissipation. However, the latter finding provides little insight into the validation and description, particularly surrounding the mesh and the justification for the model's accuracy.

Yet, the Bunyip system has only been recognised within the grey, non-scientific literature. The first detailed review of the HRP and Bunyip systems was presented in [6], reinforcing the wealth and depth of research available for conventional systems. Despite the lack of research, the commercial momentum indicates great promise for the system and its capacity to outperform the conventional system. Thus, the door opens for the current piece of research to conduct a comparative appraisal of performance based on manufacturer-provided data, develop an advanced numerical model to investigate the current operational capacity, and examine the internal flow features and characteristics before delivering the first report of its kind within the scientific research field to evaluate and appraise the potential threshold for the next steps of research within the field.

A critical gap in the literature is in addressing the motion definition in six degrees of freedom (6DOF). Such a set-up requires a time-based user-defined function (UDF) to establish the relative motion within the domain, which is favourable for computational speed and control [13]. In Ansys-Fluent [14], the excellent capacity of the 6DOF solver enables direct calculation of the motion observed. However, this is computationally expensive and notably difficult to validate. Therefore, it requires significant input to attain suitable validation [15]. This study is aimed at providing parametric optimisation to provide potential hydraulic system advancement. The simulation of a multi-story hydraulic pump (Bunyip) is conducted, accounting for the 3D and 6DOF effects. The latter underlying physics of this system have not been addressed elsewhere in the literature to the best of our knowledge. In what follows, the system is described in Section 2. The numerical set-ups and modelling are

presented in Section 3. In Section 4, we present the results. The key findings are concluded in Section 5.

2. System Description

2.1. Conventional Hydraulic Ram Pump

The conventional hydraulic ram pump (HRP) system operates through a series of well-defined phases, each contributing to its efficient and continuous operation. Figure 1 illustrates the fundamental components and arrangement of the conventional HRP system, showcasing the three operational phases: 'acceleration', 'delivery', and 'recoil'.

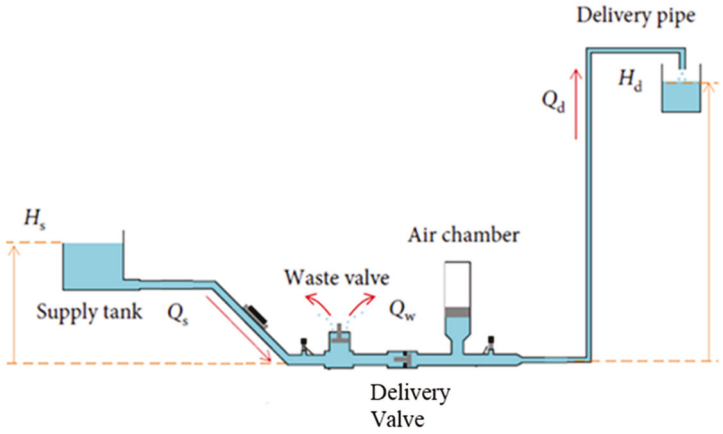


Figure 1. Conventional hydraulic ramp pump and associated system diagram, inferred from [8,16] with permission.

The system includes the supply pipe, installed at a known height and measured relative to the delivery valve. Water from higher source flows through the supply pipe and undergoes 'acceleration' as it enters the drive pipe. During this phase, the potential energy of the water is marginally elevated, transforming it into hydro-kinetic energy. Subsequently, the water rapidly discharges through the waste valve. As the water continues to flow, it passes the waste valve at a critical velocity, resulting in a drag force that overcomes the spring mechanism, leading to the abrupt closure of the waste valve. This action traps the high dynamic pressure flow, generating a sharp peak in static pressure known as a water hammer. The water hammer phenomenon allows the internal pressure to overcome the elevated head, pre-loading the delivery valve. Consequently, a fraction of the initial flow is rapidly passed through to enter the delivery system. The subsequent drop in internal pressure following the peak re-opens the initial waste valve, enabling the flow to recommence its initial flow regime, known as the 'recoil'. The drive flow begins to accelerate once again, initiating a perpetual cycle. The pair of check valves in the system play a crucial role in regulating the flow direction during the operational phases. These check valves ensure that water flows in the desired direction and prevent backflow, contributing to the pump's efficiency.

Over time, auxiliary components have been developed to improve the conventional HRP system's performance [17]. One such component is the air chamber, which dampens the sharp peaks in pressure and results in a more gradual delivery stroke, leading to a more consistent flow [7,18].

2.2. HRP Limitations

When discussing the perpetual operation and regulation of the system, it can be recognised that the start of the HRP cycle requires an external physical input to prime the system. This initially opens the waste valve to initiate the 'acceleration' phase. The supplied partially elevated flow enters the body and at the critical velocity closes the waste valve, inducing a peak in the static water hammer as the flow is abruptly brought to 'rest'. In

principle, under consistent flow conditions, the pump can be observed and acknowledged to operate independently, though in application, it could be that naturally occurring flow variation has impact on the timing of the pair of valves and result in stalled cycles. This is further escalated by the pump's inability to self-start, as discussed. In remote regions, where these systems tend to thrive, it is both time-consuming to restart and potentially could go unrecognised for some time, compromising system supplies within the likes of storage vessels [7,19]. One of the greatest distinguishing features for the Bunyip system is its 'automated' ability to self-regulate dependent on the incident flow from the drive supply [8]. In no-flow conditions, the pump remains dormant. Once the supply returns with sufficient dynamic pressure, the tyre will begin to inflate and commence the cycle. The ability to manage the complexities of operation is critical for the productivity of the pumping system. Thus, although the output will vary subject to the water available to the system, the Bunyip would likely provide an enhanced degree of flexibility and consistency.

Due to the simple operational principle, manipulated by two isolated components, previous research is used to highlight the limitations of the arrangement and the risks associated with dependency on the sprung mechanisms. Harith et al. [11,12] and Li et al. [10] both identified the waste valve as the primary contributor to the improved performance of the HRP. It is acknowledged to dictate the associated critical velocities, cycle rate sustained, volume wasted during the acceleration phase, and capacity to overcome or deliver greater quantity to the elevated supply. The process of 'tuning' the valve, typically using a threaded travel mechanism, could be described as temperamental and, by nature, directly tailoring the operation to a singular case, whereby actual flow parameters will change. In the subsequent research of [11,12], multiple adapted arrangements are considered to realise height regulation with a more developed sprung mechanism to increase the associated model operational efficiency by up to 20%. The Bunyip system also utilises a pair of check valves; however, they operate in a significantly different manner. The pair operates across a larger cycle period and does not dictate the critical velocity and the volume of water wasted directly; it is instead managed by the simple tyre seal mechanism. The mechanism utilises a blend of components, including the body mass, internal spring tyre stiffness, and the dynamic water pressure, for example, for a more reliable operation [16].

The conventional HRP principle operates through a rapid and relatively forceful motion to generate a sufficient hammer pressure to breach the delivery valve. This could be researched and identified to account for multiple considerations. In [9], the full losses are considered, and they are attributed to abrupt changes in velocity, turbulent flow conditions, geometry, and internal pressure gradients. One can conclude that features should be designed to implement diffuser entry regions and a more efficient entry geometry. This was aimed at reducing the head loss coefficients and improving the velocity distribution, described as producing enhanced efficiencies of 50–70% for their designs.

2.3. System Design

The co-founders of the Bunyip system (Porta and Trew [8]) provided the requirement for higher-quality rubber seal materials. In the same vein as accessibility, the exerted hammer forces induced within the HRP throughout rapid operation place greater stress on the system and consumable parts, thus increasing its maintenance requirements and the likelihood of failure. The advanced model's core components may last up to 50 years; conversely, the likely capacity of a design made in remote regions could be as little as 10 years using weaker materials and limited facilities [4]. The Bunyip's low velocity requires a less complex features and manufacturing procedure and lighter-weight components, resulting in the maintenance of the consumable rod and piston seals lasting up to three years without significantly compromising their performance and with limited replacements [16].

This paper begins to investigate and explore an alternative design, known as the Bunyip, shown in Figure 2. The research was inspired by its developed commercial momentum yet extremely limited presence within academic research. The following study

aims to investigate the operational characteristics and performance capacity of the adapted mechanism. This will utilise a combined methodology of secondary performance data and a dedicated numerical model constructed in Ansys-Fluent 2021 R2 [14]. The work facilitates a critical analysis of its internal physics and performance potential using the model's constrained discretization capacity and appropriately simplified domain. The design will implement verified methods where possible to quantify and evaluate the domain to support discussion alongside manufacturer-provided data and the conventional HRP system.

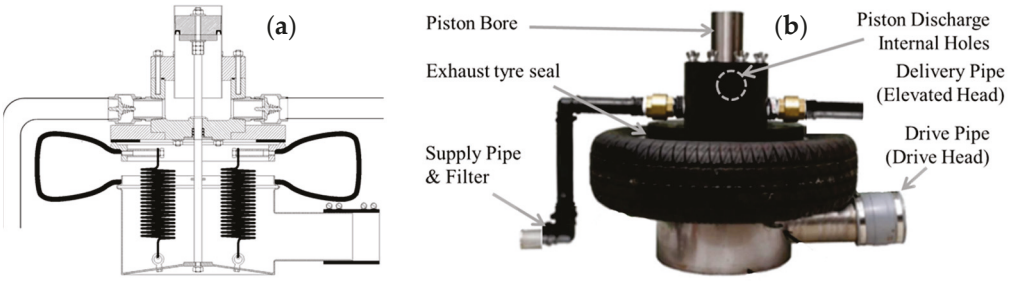


Figure 2. Alternative Bunyip system: (**a**) in-house sketching and (**b**) annotated photograph—inferred from [8] with permission from [16].

The introduced Bunyip pump was very much inspired by the HRP previously described, whereby the inventors (Brett Porta and Ralph Glockemann [16]) recognised that for their specific application, the conventional design failed to manage the fluctuating operating conditions. They realised that a chain of new systems and designs could be developed at a domestic level, incrementally surpassing and growing in capacity. Focused on enhancing the pump's resilience in varied operation conditions and minimising the disruptive hammer noise and forces in the HRP for a local installation at their residence, several designs were produced, namely, the Oasis, Water Dragon and the Glockemann Pump [20,21]. The last of these was awarded a gold medal at the Geneva 2002 International Exhibition [16], setting a high standard for its successor in the form of the Bunyip, invented in 2006 by Bunyip Water Pumps, formally Porta's Affordable Pumps [8]. The previously introduced Bunyip system operates using a vastly different principle and cycle, as depicted in Figure 3.

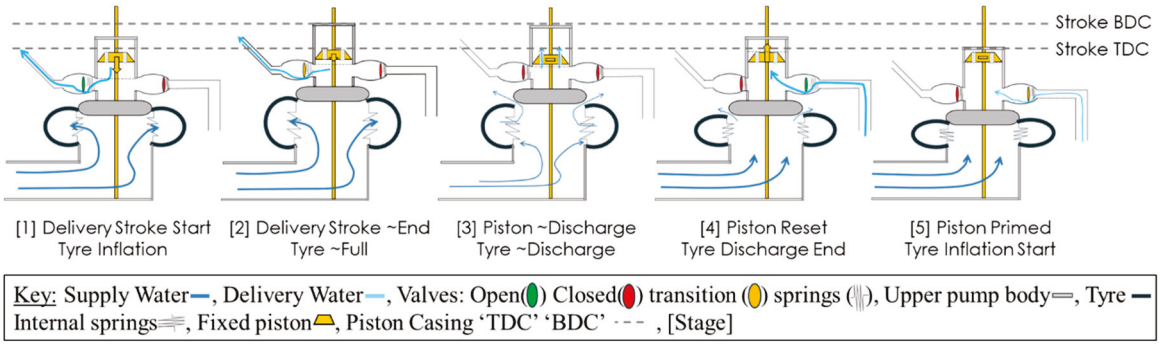


Figure 3. Bunyip operational process diagram, inferred from [8] with permission from [16].

As can be seen in Figure 3, the system utilises a positive displacement piston arrangement with two separate upper and lower flow volume chambers to transfer and amplify the dynamic tyre pressure into the elevated head pressure. Then, a series of relative strokes are generated using a fixed length piston to deliver a secondary supply of water against the elevated head, which is understood through five operational phases (1–5), as follows [8]:

(1) The incident drive supply inflates the tyre, increasing its static pressure and resulting in a smooth relative piston stroke. The stroke is resisted by the elevated pressures in the upper system, and internal tyre and spring stiffnesses, resulting in delivery

through sufficient pressure to breach the delivery line and overcome the elevated head for a stroke of delivery.

(2) As the upper body approaches TDC, the delivery stroke output reduces and transitions to close the delivery check valve as the tyre inflation approaches the limit of its travel.

(3) At TDC, the piston travels beyond a series of discharge holes in the walls of the piston housing, resulting in the 'unlock' and discharge of the Piston. Meanwhile, the incident internal tyre pressure is sufficient to overcome the tyre seals, detaching and expelling the trapped internal pressure from the domain.

(4) The reduced internal tyre pressure, internal stiffness of the tyre, and springs and mass of the upper portion result in the 'dump' phase collapse. The upper body and tyre fall, generating a relative suction stroke in the piston, priming the volume for the next cycle.

(5) The piston is now full, the tyre and upper body are connected, and the drive pipe is beginning to inflate as the cycle restarts.

2.4. Performance Indicators

Upon reviewing several studies in the field, the primary indicator adopted for performance is the operational efficiency, calculated as the ratio of power through the delivered volume (P_d) relative to the total input quantity supplied (P_s). The relationship is derived using the head (H) and flow rate (q) ratio [21,22]. Ultimately, this value quantifies the capacity of the pump to overcome the elevated head and provides an opportunity to compare the system model and data against alternative pumps. The operational efficiency (η) will change depending upon the supply and delivery head ratios, nominally in the range of 50–60%. For a typical HRP system under 30 m, this can be determined as [9]:

$$\eta = \frac{P_d}{P_s} = \frac{\rho g q_d H_d}{\rho g q_s H_s} = \frac{q_d}{q_s}\frac{H_d}{H_s} = QH. \quad (1)$$

A secondary method identified uses the standard capacity (S_c), a normalised method to standardise a flow rate capacity. This is calculated using the delivery flow rate (q_d) and inlet diameter for the pump squared (D^2) in mm^{-2}. Several studies utilise this measure to compare their novel designs against established models in the market, represented in a normalised form, independent of the system size [10], as shown in Figure 4. This is known as the standard capacity (S_c) and used as an indicator of the pure delivery capacity [23]:

$$S_c = \frac{q_d}{D^2}. \quad (2)$$

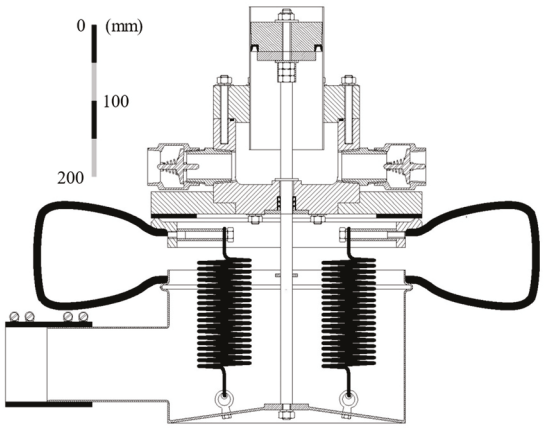


Figure 4. Bunyip PA-13 technical drawing, scalable using 100 mm drive pipe, inferred from private communication with the manufacturer [16].

The final measure has been considered in reference to the total percentage of water delivered [11]. This is crucial for remote applications where water scarcity is a challenge. In previous research, it has been recognised that the volume of water wasted could outweigh the magnitude of other performance indicators for a given Thai application in Ban Ha, Samoeng District, Thailand [19]. This can be facilitated with the Bunyip pump using multiple inlets/outlets through a total flow rate term (q_T). The delivery ratio is calculated as:

$$R_d = \frac{q_d}{q_T} \tag{3}$$

The identified performance criteria enabled manufacturer-published output data to be tabulated for comparison in Table 1. The table presents the relationship between the supply head and delivery head to assess the system's effectiveness for the traditional-style Blake's HRP [24], the recently adapted springless in-line HRP PaPa [25], and the Bunyip system. These are further illustrated in plots, as shown in Figure 5.

Table 1. Operational efficiency for common HPP systems in 58 cases of varied supply and delivery values found using manufacturer-published data of Bunyip pumps [8], Blake's Hydram [24], and PaPa Pumps [25].

Blake								
Delivery head (m)→ Supply head (m)↓	10	20	30	50	80	100	125	200
0.6	-	-	-	-	-	-	-	-
1.0	45	40	41				-	-
1.5	45	50	50	35			-	-
2.0	54	55	55	43	35		-	-
4.0		60	60	60	50	40	-	-
PaPa								
Delivery head (m)→ Supply head (m)↓	10	23	31	46	77	92	150	200
0.6	25	19	-	-	-	-	-	-
0.9	33	25	17	-	-	-	-	-
1.5	39	45	41	45	-	-	-	-
2.1	47	54	51	43	36	43	-	-
4.0	47	60	59	54	48	52	-	-
4.6	48	65	68	65	59	60	-	-
Bunyip								
Delivery head (m)→ Supply head (m)↓	10	20	35	50	75	100	150	200
0.6	45	45	45	45	45	-	-	-
1.0	45	45	45	45	45	45	-	-
1.5	39	55	55	55	55	55	55	55
2.0	29	55	55	55	55	55	55	55
4.0	14	29	51	55	55	55	55	55

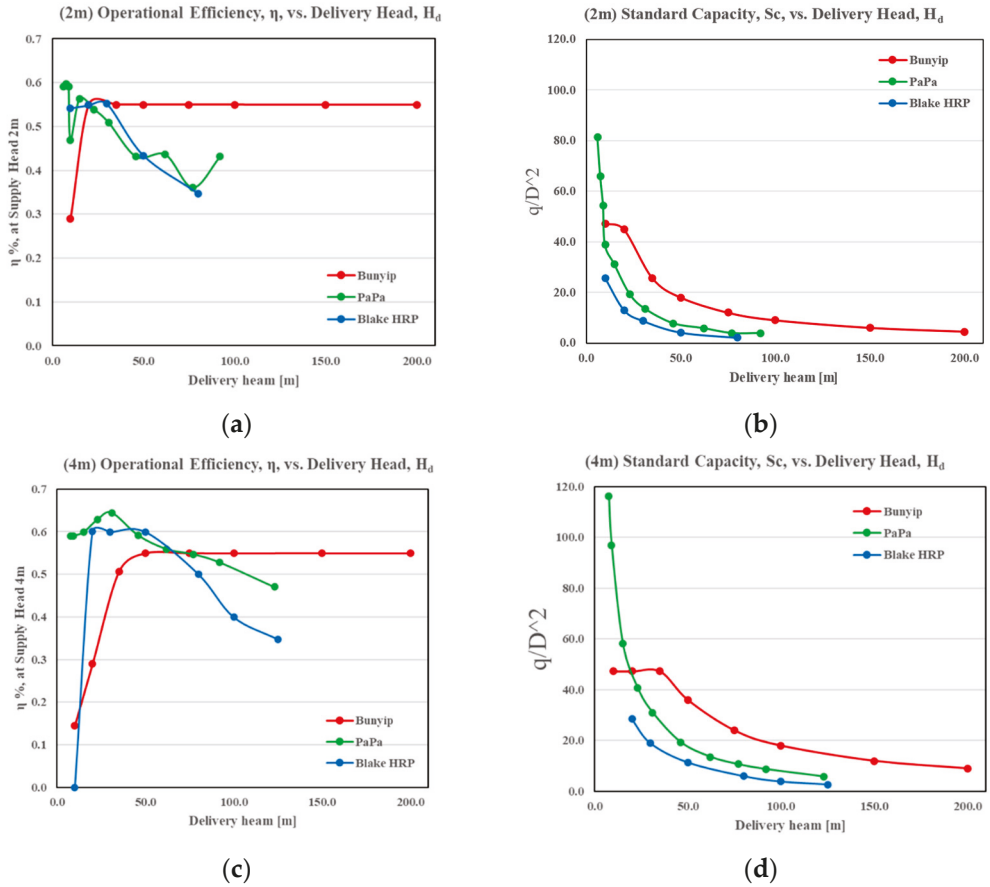


Figure 5. Graphical performance evaluation at 60 L/min and 2–4 m supply heads for the 3 pump systems (**a**) efficiency at 2 m supply head, (**b**) S_c at 2 m supply head, (**c**) efficiency at 4 m supply head, and (**d**) S_c at 4 m supply head.

The Bunyip pump can operate at a reduced supply head, as shown in Table 1 (note: a consultation has been made with the associated Bunyip team for application at or less than 1 m for the two HRP designs to verify this). Additionally, the figures given in Table 1 for the HRP demonstrate that it has better effectiveness than the HRP in the lower region of Figure 5a,c at approximately a 15 m delivery head. The Bunyip pump in principle provides a significantly greater capacity to deliver to greater ranges for the equivalent supply, illustrated by the extended line lengths in Figure 5, attainable through its pressure-amplified positive displacement design. Clearly, this establishes the Bunyip pump as the only system that can operate to greater heads than 100 m, and it is even reported to operate up to 432 m in an adapted reinforced cylinder model currently under development.

It is noticeable that when the Bunyip pump receives a relatively high supply head for delivery to a low elevation, the efficiency drops considerably in Figure 5a,c, indicating high waste in the cycle at the delivery elevation. This is likely due to the mechanism's extended positive displacement travel. In this region, the HRP will enable greater volumes to propagate per cycle, increasing its operational performance and standard capacity. The PaPa pump enables faster manipulation of the low-travel and springless valves to manage internal pressures more efficiently. At a low head ratio, the supply also has a greater ability to overcome a 'lighter' elevation head and deliver a greater portion of the flow provided [25]. As such, the Bunyip pump yields the greatest standard capacity, measured relative to the supply pipe diameter. Though the Bunyip supply is defined at Ø = 35 mm, this definition does not consider the drive pipe at a greater Ø (100 mm). Thus, it holds limited insight, and one can use an alternate pump volume to maximise its benefit.

3. Parameters

Numerical methods in recent years continue to drive innovation, routinely integrating advanced features and the identification of further applications that would benefit from the depth of analysis available. The research platform implemented utilises Ansys-Fluent [14], a market-leading suite of progressive modelling modules, to construct each stage of the model process with unique potential to utilise user-defined functions (UDF) to enhance the standard capacity and investigate an advanced multi-body physics 6DOF capacity. In what follows, the parametric set-ups are explained from the modelling perspectives, including the geometric design, meshing, transient set-up for motion, boundary set-ups, and pre-processing.

3.1. Geometry

To access the most accurate geometry possible, contact was made with the Bunyip pump's inventor [8,16,20] to receive a scalable technical drawing of their best-selling PA-13 model. This has been used in conjunction with available Bunyip content, including the operational calculation tool and charts, to describe the typical stroke length (y_{sl}) and piston bore, 90 mm and 98 mm, respectively [8]. The procedure followed when analysing the domain is made using a developed 3D CAD render based on a technical illustration and annotations provided in parallel, shown in Figures 6 and 7.

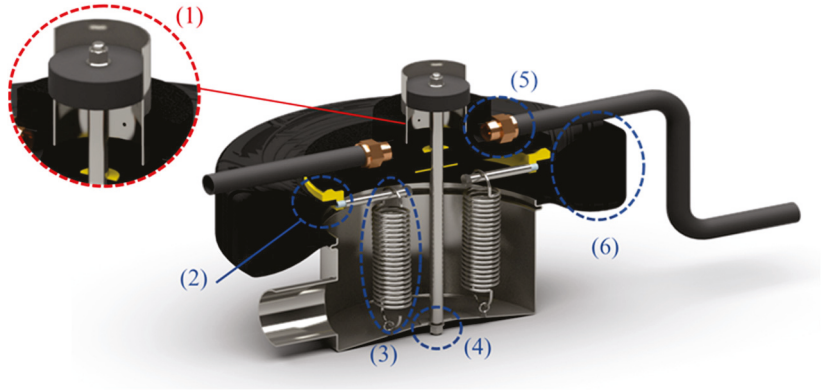


Figure 6. Bunyip 3D internal system render used in this analysis. Annotations are discussed following this figure.

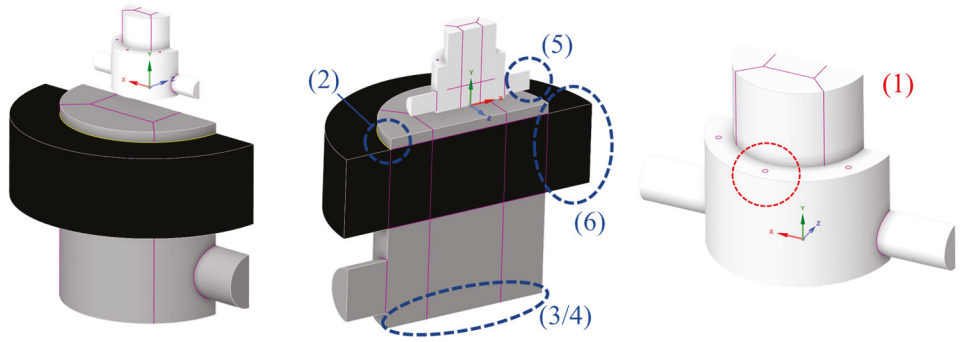


Figure 7. Volume of interest model, annotated with discussed features.

The illustration introduces the decisions made to translate the real-world system into a functional modelling form, considering the reduction in complexity, cell count, and computational requirements. The domain shared in Figure 7 illustrates shared faces that connect adjacent zones, illustrated in pink, enabling separate volumes to facilitate the structured meshing strategy to be discussed.

(1) Internal piston discharge holes: to prevent the requirement to place the feature upon a meshing interface and dynamic region, they could be relocated on the adjacent bore surface as indicated.
(2) Tyre body seals are indicated in yellow. This component could be treated as a raised region to reduce the requirement to model the confined mechanism due to licence limitations. This will also provide limited compromise through a relatively representative entry region and discharge path for internal flow.
(3/4) Internal spring/rod: These features were defeatured as they were assumed to have a limited influence on the outlet regions, with the flow primarily being driven by strong pressure gradients. Their induced losses were acknowledged but removed at this time.
(5) Check-valve mechanisms: the operation of these mechanisms is less significant for the study and is modelled as idealised changes in the boundary inlet-to-outlet.
(6) Tyre deformation: The multi-directional expansion, non-linear rubber material properties, and specific deformation pattern surrounding the tyre walls are complex to model. They are primarily act as a large piston. Thus, a vertical cylinder defined at an equivalent scaled size to deliver an equivalent stroke rate for the provided flow could be implemented.

3.2. Dynamic Meshing

The developed model is discretised using the integrated Ansys meshing module. This enables a suite of meshing tools to utilise the previously highlighted edges in fluid zones to assign meshing controls. Namely, the application of edge, face, and body sizing in conjunction with both structured sweep and couple compatibility regions of tetrahedral elements to maintain high mesh quality could facilitate the dynamics of the domain. For the study, a development mesh is utilised, opting for a nominal mesh size of 5 mm across the core areas and 10 mm in zones within dynamic regions, as shown in Figure 8. This is to compromise within the Ansys licence capacity and trade-off time step size across relatively extended transient simulations ~2–4 s at 0.005 s. The upper and lower regions of the system occupy separate volumes and utilise cylindrical structures comprising a square face surrounded by an anulus of sections. This can be recognised to maintain quality in central regions, particularly in the aspect ratio. A prospective mesh sensitivity test was conducted. To maintain layers' successful operation and avoid negative cell volumes due to the implicit layering approach, the time steps have also been adjusted.

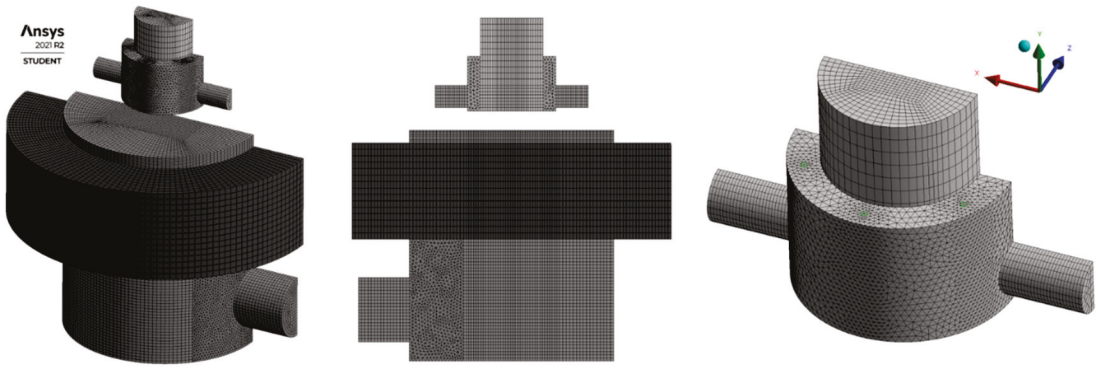


Figure 8. Illustration of the development mesh employed within the study at 5 mm nominal and 10 mm dynamic.

A grid independence check was conducted, but within a limited range that is not at the expense of quality. The internal motion of the domain could be facilitated using dynamic meshing. Ansys, as a platform, provides three available methods, including smoothing, layering, and remeshing. Upon careful review, the layering method was considered to provide the best functionality for application. The method operates through

the construction and destruction of individual layers of the domain using the user-defined relative height split and collapse factors defined at 0.4 and 0.2, respectively. This not only provides the advantage of only remeshing the direct group of cells influenced but more importantly ensures that the cell quality initially established is maintained. In the case that the other methods were used, it would be more difficult to maintain control, while the additional computation requirements are arguably only for multi-dimensional rotations and translations, which are not included within the model at this stage.

In Figure 9a,b, we illustrate the dynamic zones established to describe the operation in the upper chamber. In this case, the relative power and reset stroke of the piston could be defined by setting the piston as static, which is depicted in blue. The upper piston surface could be defined as static, and the foot could be set as a rigid body (RB) dynamic zone with established solution stabilization and meshing options set for the adjacent boundary, indicated in orange. This could be defined in parallel for the lower region on the lower 'roof' of the tyre. The orange and green regions could then be set in RB motion through the application of a designed UDF profile. This enables the internal tyre and piston region to extend and contract to represent the changes in the domain. This required the definition of over 60 dynamic zones, including interiors, boundaries, and volumes, as depicted in Figure 10.

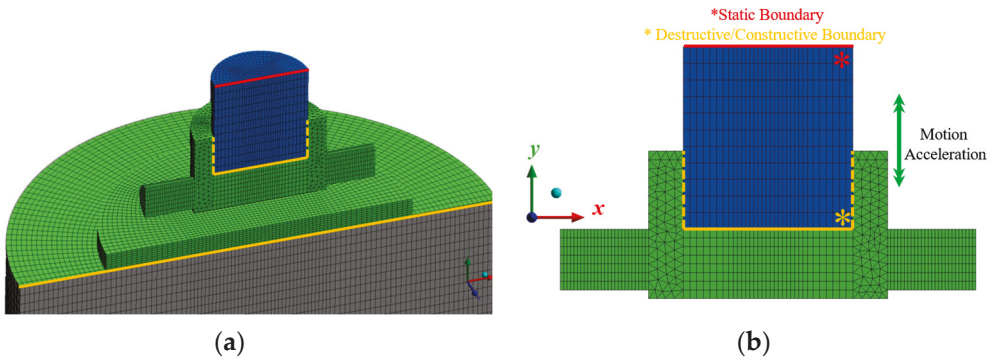


Figure 9. Dynamic mesh zone setup, showing (**a**) isometric and (**b**) front cross-sectional views. Green regions depict rigid body motion, blue depicts active dynamic layering in the upper piston, and grey depicts the interface between the static tyre/base.

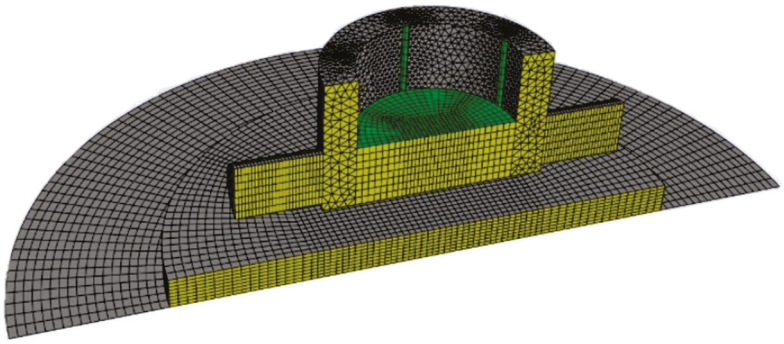


Figure 10. Ansys Fluent dynamic zone mesh preview using default colours. Yellow regions indicate some parts of critical dynamic meshing, and green region indicate an example of the consequence influence of the dynamic region.

3.3. Motion Methodology

To integrate motion within the domain, the system has two potential options: UDF profiles to determine positions based on time or the powerful 6DOF multibody physics solver. Naturally, both methods provide advantages and disadvantages. The UDF's functionality provides additional computational complexity and the ability for the user to develop bespoke features within the model to enhance its operation. For this application,

the 'DEFINE_CG_MOTION' function could be implemented to initialise a dynamically set cell velocity across the thread (face ID) defined using the C code shared in Appendix A.

The UDF methods provide an opportunity to utilise the available manufacturer data and video footage to investigate and setup an associated time- and position-based profile. The simpler of the two methods can then be compiled into machine code for definition at each time step. One primary advantage of this method is the simplification of the internal physics to avoid making specific assumptions in calculations, using data based on real-world characteristics that could be known and measured in real-world applications. Although, by definition, a more simplified approach, this has the potential to improve validation and significantly reduce the calculation required. Its limitation, however, is its capacity to directly isolate operational parameters, such as the stiffness or components of pressure, to directly investigate their influence. These will now be limited to a defined cycle rate, which can be expected to act as a function of flow rate, supply, delivery, and drive pressure. Thus, the boundaries will also be required to be fixed at the determined pressure, and then inlets/outlets will be used to act on domain changes as opposed to the external pressure driving the system.

The second method uses a multi-body physics solver with the capacity to define the internal physics through the individual definition of the mass and stiffness properties of the system. For the Bunyip application, a free-body diagram is illustrated, as shown in Figure 11, to introduce the primary forces considered within an operation. For the given case in study, the internal pressure in the piston is calculated as an equivalent hydrostatic pressure 'mass' and defined through the 6DOF properties in addition to the Bunyip body mass of 5.6 kg. This will be directly applied during the power stroke and removed using a UDF during the reset phase [14]. In addition, other properties can be defined; for example, the internal spring stiffness can be implemented at 700 N/m across a constrained stroke length of 90 mm. At this time, we ignore the tyre stiffness due to its non-linear properties and multi-dimensional characteristics as well as additional losses due to friction. The solver enables internal equilibrium equations incident on the internal flow forces at the base volume of the tyre to be calculated, referenced centrally to the upper tyre surface. The result, similarly to the UDF, mapped across the domain relative to the surrounding green cell zones, as illustrated in Figure 9 before.

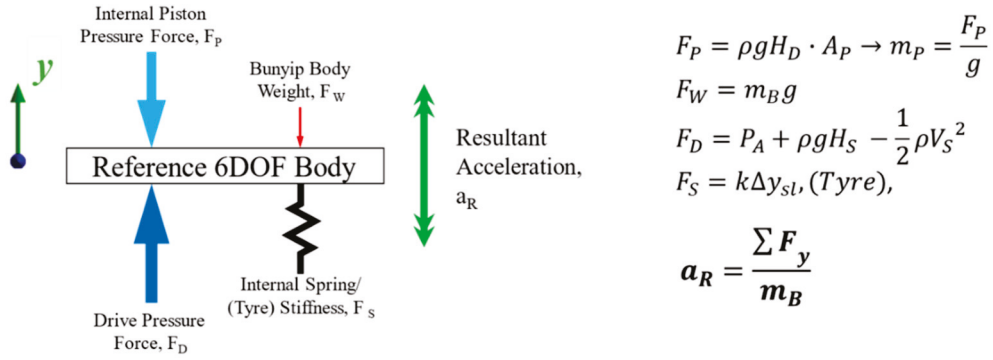


Figure 11. Free-body diagram and determination of 6DOF solver's properties.

A time-based velocity UDF has been adopted in this analysis. The 6DOF solver for the limited mesh is found to be unstable, accelerating rapidly, which is uncharacteristic of the pump. This can significantly influence the model's validation. In retrospect, with its very limited presence within research applications, it is quite likely the gap previously discussed for motion was primarily developed within the simplified UDF profile definition.

3.4. Boundary Method and Automation

The domain can now be informed with the appropriate boundary conditions across several inlets and outlets for the operational cycle, as shown in Figure 12. This includes the application of both traditional pressure inlet/outlets and vent types to provide potential

functionality to define losses across components such as check valves. The associated pressures could be calculated using the standard Bernoulli equation, assuming each source of water is static and at atmospheric pressure. Then, the hydrostatic head pressures can be calculated relative to the delivery valve, which is demonstrated for an example delivery pressure condition below.

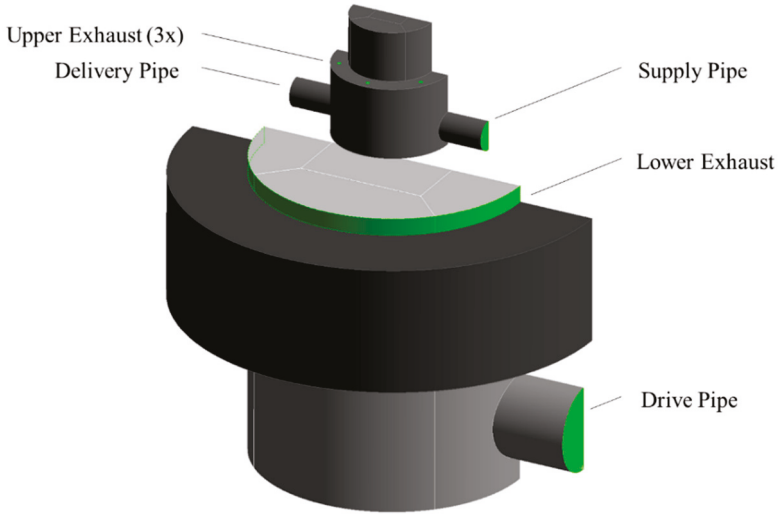


Figure 12. Annotated Bunyip pump for boundary condition definition.

The pressures and outlets for a typical example case are presented in Table 2 at a supply head of 4 m, a delivery up to 35 m, and the defined inlet/outlet conditions to observe cycle-time-dependent flow rates. The ideal representation of the energy balance is Bernolli's equation:

$$P_A + \frac{1}{2}\rho V^2 + \rho g h = \text{Constant} \tag{4}$$

$$P_{\text{Delivery}} = P_A + 1000 \cdot 9.81 \cdot 35 = P_A + 343.4 \ \ (in \text{ kPa}) \tag{5}$$

Table 2. Pressure boundary condition types and example case: 4 m supply and 35 m delivery.

Name	Type	Gauge Pressure (*k*Pa)
Drive pipe	Velocity inlet	39.2
Supply pipe	Pressure inlet vent	−2.9
Delivery pipe	Pressure outlet vent	343.4
Upper/lower exhaust	Pressure outlet vent	0

Due to the dynamic nature of the system and the incorporation of check valves and multiple exhausts, the domain is coupled to integrate the boundary conditions and synchronise the cycle in relation to the defined motion. Again, two options remain for its application.

Scheme file methods enable the time-based sequencing of model inputs using the integrated Text User Interface (TUI) commands. These definitions make use of conditional sequencing to determine the current phase of the cycle and adjust the boundaries accordingly, as depicted in an example script provided in Appendix B. The file can be constructed and read to define a new command in the '.scm' format, providing full access to edit and manipulate internal boundary types, values, and 6DOF properties. It could be recognised that their limitation appeared to be their dependency on 'RP-variables', such as standard global variables or constants, such as flowtime and '2', for example. Consequently, the desire to utilise user-defined reports to inform decisions using mesh velocity and co-ordinates did not appear to be possible with this method. As the 6DOF solver previously discussed was unsuited to having a stable operation on a limited mesh domain, the scheme file

application provides the desired flexibility for time-based UDF operation. Thus, it could be implemented directly within the model.

When investigating alternative methods for applications with time-independent solvers, such as the 6DOF solver, an alternative control script could be developed, again using the powerful UDF capacity. This could be facilitated utilising the DEFINE_ADJUST and DEFINE_PROFILE functions to directly access the solver to quantify the co-ordinates and velocity of the hooked tyre boundary. Each quantity could be calculated using a surface average for each face in the domain (grid) thread and used again in place with a sequence of conditional statements to define the pump phase and associated pressures at each boundary described in Appendix C.

3.5. Pre-Processing and Modelling

The pumping system is inherently turbulent, exhibiting flow mixing and chaotic motion due to sharp changes in pressure gradients and flow direction throughout its geometry. For this reason, the study will utilise an appropriate turbulence model. The transient 3D incompressible Navier–Stokes equations are used for the developed model to measure the continuity of various forms within the model, e.g., the conservation of momentum and turbulent kinetic energy and dissipation. There is no best fit for selecting the appropriate model, and this could be best informed through a review of the active researchers in the field (e.g., [15]), who have adopted the use of *k*-ε models, which have improved computational speed and mesh sensitivity relative to the default *k*-ω model. In the previously discussed literature, the realizable model could be recognised to provide strong validation in similar work [10,12]. The basic equations used in the computation stated are summarised below, but given in more detail in [15] and the ANSYS User Guide [14]:

The turbulent kinetic energy:

$$\frac{\partial}{\partial t}(\rho k) + \frac{\partial}{\partial x_j}(\rho k u_j) = \frac{\partial}{\partial x_j}\left(\left(\mu + \frac{\mu_t}{\sigma_k}\right)\frac{\partial k}{\partial x_j}\right) + G_k + G_b - \rho\varepsilon \tag{6}$$

The turbulent dissipation rate:

$$\frac{\partial}{\partial t}(\rho \varepsilon) + \frac{\partial}{\partial x_j}(\rho \varepsilon u_j) = \frac{\partial}{\partial x_j}\left(\left(\mu + \frac{\mu_t}{\sigma_\varepsilon}\right)\frac{\partial \varepsilon}{\partial x_j}\right) + \rho C_1 S\varepsilon - \rho C_2 \frac{\varepsilon^2}{k + \sqrt{\nu\varepsilon}} + C_{1\varepsilon}\frac{\varepsilon}{k}C_{3\varepsilon}G_b \tag{7}$$

where $C_1 = \max\left[0.43, \frac{\chi}{\chi+5}\right]$, $\chi = S\frac{k}{\varepsilon}$, $S = \sqrt{2S_{ij}^2}$, $S_{ij} = \frac{1}{2}\left(\frac{\partial u_j}{\partial x_i} + \frac{\partial u_i}{\partial x_j}\right)$, and $\mu_t = \rho C_\mu \frac{k^2}{\varepsilon}$. The default values for the model constants are set in Ansys-Fluent as: $C_{1\varepsilon} = 1.44$, $C_{3\varepsilon} = 1.92$, $C_\mu = 0.09$, $\sigma_\varepsilon = 1.3$, and $\sigma_k = 1$.

The model developed is constrained by the extended nature of a relatively long physical simulation time and short time steps of 0.005 s. To resolve the near-wall treatment, the model implements standard wall functions. As the model does not include any associated heat transfer or other models, for an initial development method, the default option could be considered sufficient, which is advised for a broad range of applications. The Ansys guidance indicates that it can be utilised when the first node cannot be placed within the viscous sub-layer developed [14].

The coupling scheme used for the pressure-based transient calculations, with the Pressure-Implicit with Splitting of Operators (PISO) algorithm, is typically advised for fully turbulent flow and described to maintain stability with larger time steps. The latter is relevant when simulating over an extended period of physical time associated with a complete cycle (see Ansys guide, Section 26.3.1 of [14]). The discretization method is set as Green–Gauss-node-based, calculating the scalar values and gradients using the arithmetic average of the element values surrounding each node. Additionally, it avoids the default least squares method which is observed to require additional calculation when implemented in parallel with PISO (See Ansys guide, Section 18.3.3 of [14]). To ensure a sufficiently small error, the convergence criterion was set to 10^{-5} for continuity equation.

4. Results

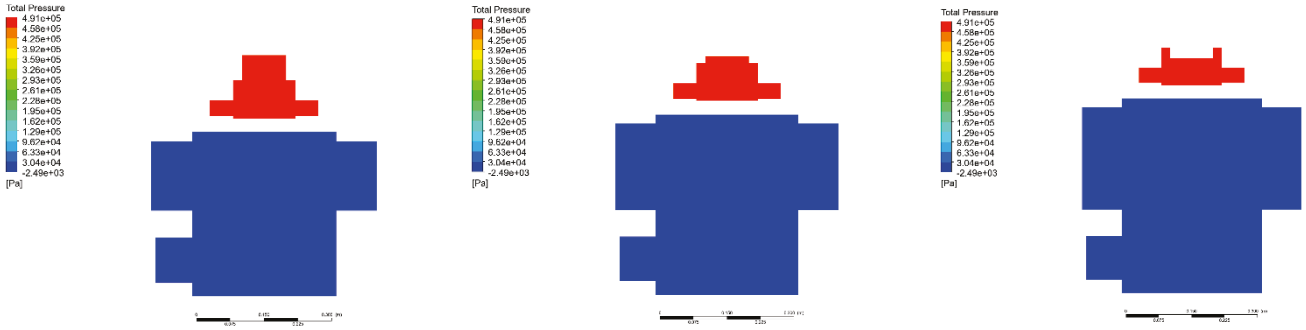
To investigate the model developed, a series of cases could be identified through an applied video analysis of physical testing (PT) models and installed Bunyip systems. The key operational parameter inputs are listed in Table 3. The delivery flow rate is set within 5 to 6 L/s to investigate varied head ratios' influence on the performance of the Bunyip system and to support its model validation. The associated sources are provided in Appendix D. The following figures illustrate the operational principle through total pressure and velocity graphics to be discussed in tandem with focused post-processed depictions to aid the analysis.

Table 3. Tabulation of physical testing (PT) cases, inferred from [8].

Features	Drive Flowrate (L/s)	Supply Head (m)	Delivery Head (m)	Daily Capacity (L/day)	Observed Cycle Period (s)
Case 1	5	1.2	22	8600	2.06
Case 2	5	2.0	50	8640	2.51
Case 3	5	2.0	60	5800	2.74
Case 4	6	2.2	36	14,400	1.39

Firstly, to illustrate the 'free' hydro-power cycle in principle, the propagation of the total internal pressure within the domain could be plotted globally to indicate the associated values relative to the total cycle. This additionally provides an opportunity to review the initial flow mechanics alongside a series of vector and magnitude illustrations, again using graphics to aid an internal investigation of the Bunyip mechanism. Figure 13 describes the process from motion initiation to upper piston compression and delivery. In Figure 13d,e, the discharge features release the upper piston to a reduced pressure for the motion to reset.

The above operational process visualisation can also be enhanced through the application of the definition of internal planes to enable enhanced visuals of the relative quantities and better illustrate the internal flow, set apart using local and global pressures and velocity scenes. In this case, the rotation and mixing induced by the abrupt changes in the inlet geometry in Figure 14a,b are better described. The plots illustrate the complex dynamic nature of the chamber and the turbulent incident flow.



(**a**) (**b**) (**c**)

Figure 13. *Cont.*

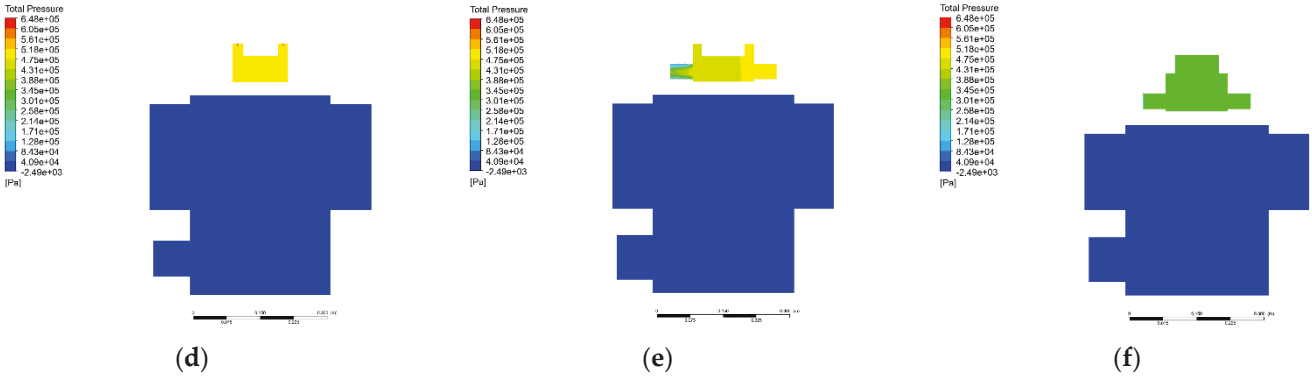


Figure 13. Illustration of Bunyip cycle's internal total pressure distribution. (**a**) At 0.1 s: delivery stroke start; (**b**) 1.0 s: mid-delivery stroke; (**c**) 1.875 s: piston approaches BDC; (**d**) 1.925 s: upper piston discharge 'Un-lock'; (**e**) 2.025 s: piston prime initiates using supply; (**f**) 2.4 s: operational cycle complete.

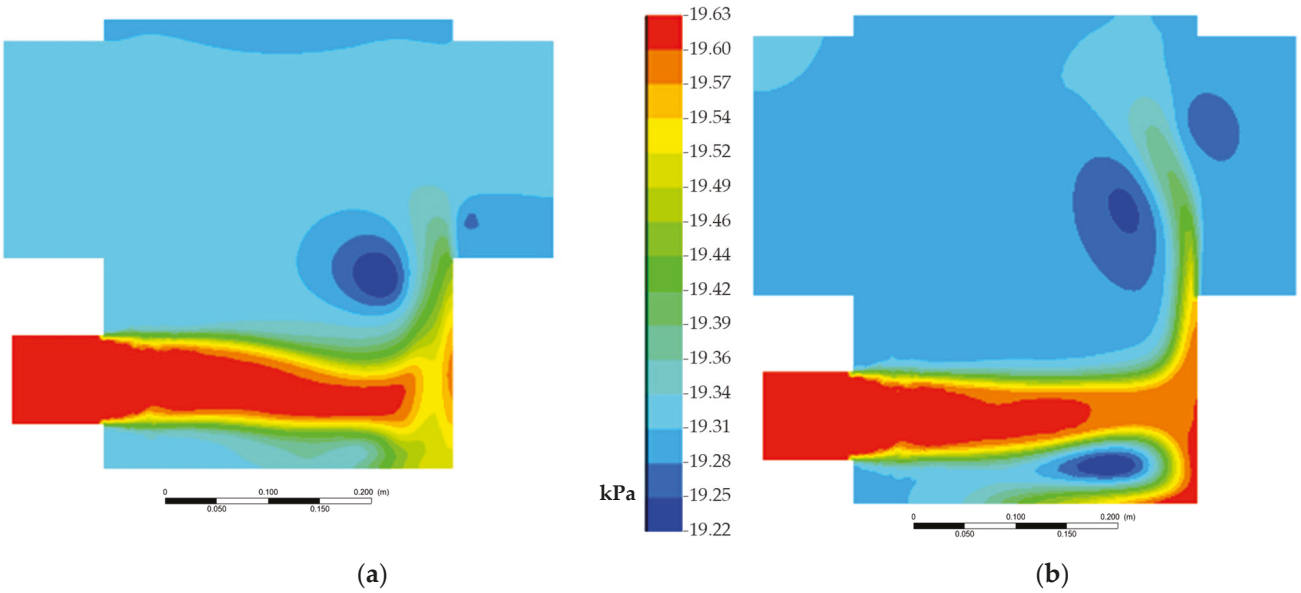


Figure 14. Tyre inflation flow intake total pressure (kPa), showing (**a**) initial recirculation at 1 s and (**b**) acceleration to the lower discharge region at 1.925 s.

In addition to the total pressure, the flow velocity could also be used to illustrate the advancement and properties of flow within the volume and construct an improved picture of where energy may be lost and routes for improvement. This could be closely evaluated for the operation of the lower tyre in Figure 15. It can be recognised that the inlet flow generates a catalogue of chained rotational regions that build from their entry in the base right up to the filling of the tyre and upper discharge domain. The figures illustrate the extended path taken by the flow, which is generally associated with greater losses. In this case, the drive flow is forced directly to the far side wall. This results in the rapid deceleration and re-direction of the flow and momentum to rotate away from the wall, either rolling under the delivery flow or around and over the drive flow, mixing layers and inducing the rotational effects observed, particularly in Figure 15e,f.

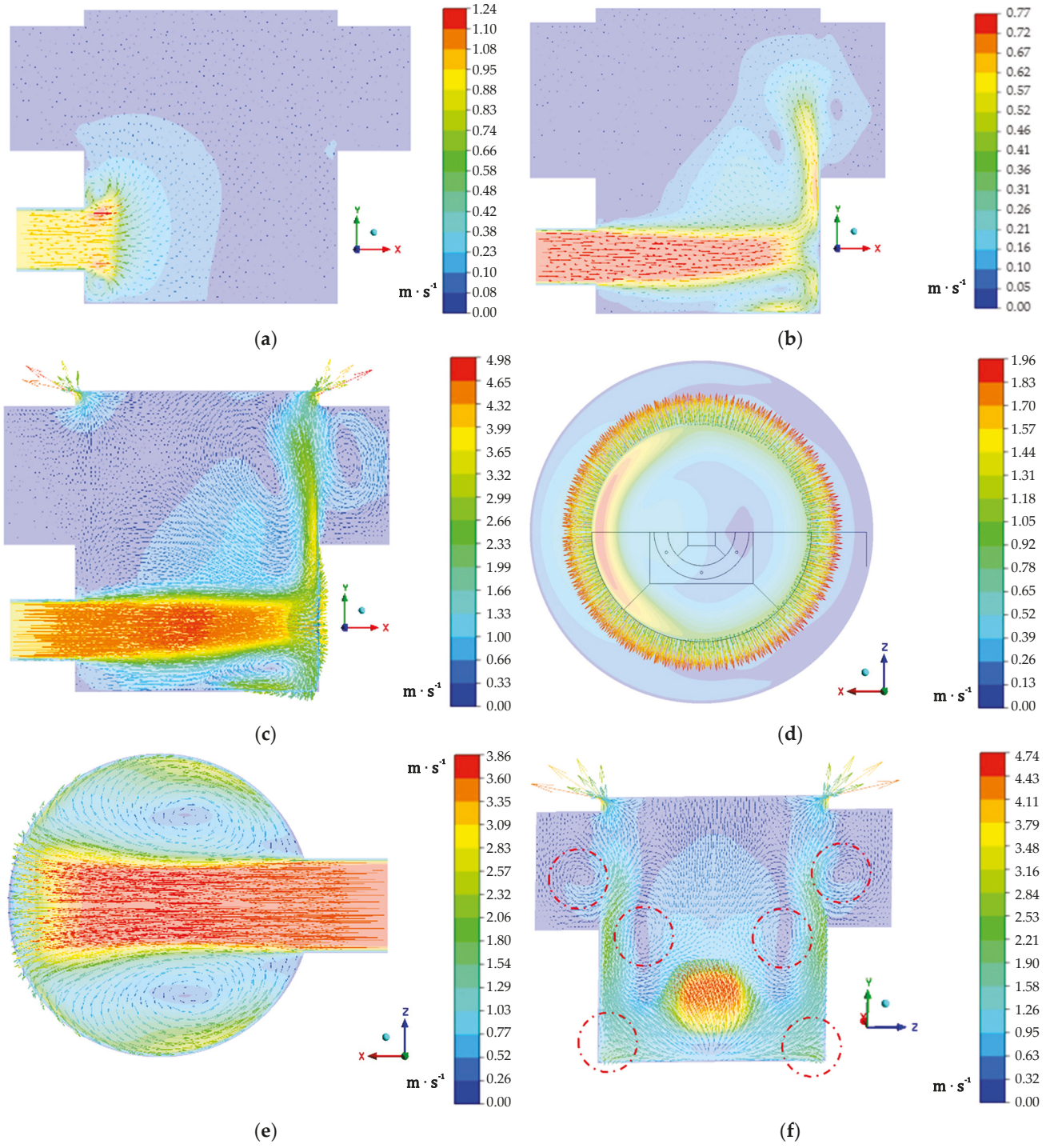


Figure 15. Bunyip lower system velocity contours (in $m \cdot s^{-1}$) at different instants, identified with vectors to show the internal mixing and energy loss/unfavourable flow characteristics during the 'dump' phases. The graphs indicate: (**a**) drive entry: immediately inducing rotation as flow enters the domain at 0.1 s; (**b**) flow and recirculation region encouraged to the far side as the tyre inflates through aggressive entry at 1.5 s; (**c**) flow taking an extended path to discharge relief, preventing a faster 'dump' phase at 2.35 s; (**d**) drive pipe forces flow to the far side of the system, leading to non-uniformity across the tyre discharge seals; (**e**) velocity of drive flow around the perimeter and rolling above/below the base section; and (**f**) 3D effects of the abrupt drive velocity and highlighted recirculation in the red dashed circles.

Similarly to the lower system, the upper piston can also be analysed using the velocity vector and contour plot. In this case, the flow of the piston is very predictable due to the dominant changes in static pressure in the drive flow. The upper piston compression and exhaust phase were also investigated and are presented below in the delivery pattern illustrations in Figure 16.

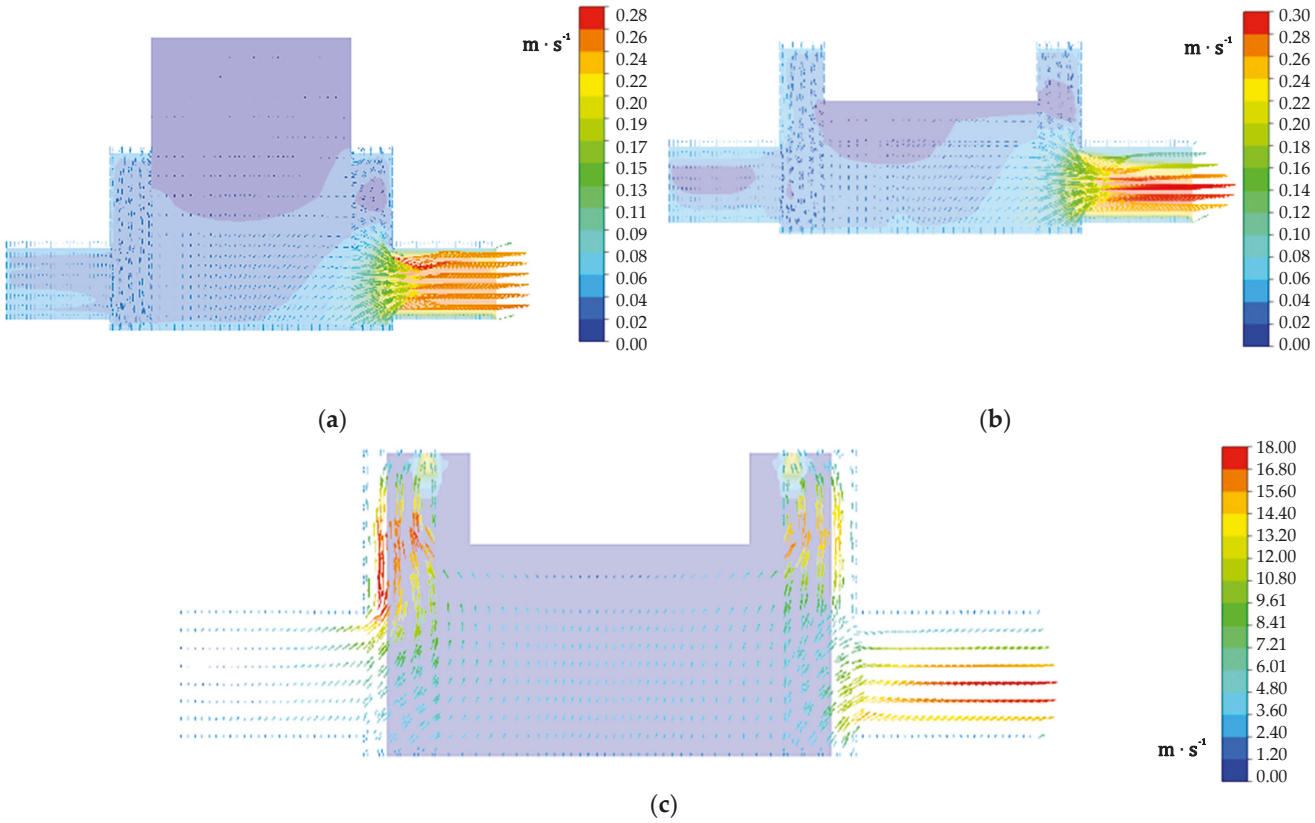


Figure 16. Velocity contours in the upper piston stroke and discharge regions, illustrating the transient motion vectors at different time instants for (**a**) delivery stroke at 0.1 s; (**b**) water delivery as piston approaches BDC of the power stroke at 1.875 s; and (**c**) waterflow accelerates from the domain to the three exhaust points at 1.91 s.

4.1. Operational Observations

The previously conducted analysis provided valuable insights into the flow mechanics of the system in demonstrating the complete operational cycle and enhanced detail on the dump and discharge of the upper piston. In principle, the 'free' hydro-kinetic energy principle utilised could be successfully demonstrated across the four cases, and the model could be validated against real-world operational data with moderate corroboration. The study can now use the numerical model and physical data to appreciate and discuss where the system excels and where it may need further development.

The created model could utilise the power of numerical tools to individually measure and monitor quantities throughout the domain. This would enable the associated flow rates at each boundary to be measured under the action of the initialized motion relative to the pump cycle period in practice. Of which, the model provided reasonable agreement with the advertised capacity using the modelling method comprehensively discussed. The efficiency maintains, as anticipated, a respectable value across the three cases, operating within the regions previously shown in the supply head values in Table 1. The initial appraisal indicated that the pumps do provide significant potential but can be somewhat limited by their mechanisms within certain flows. It is important to recognise that in this case, the primary driver for the Bunyip pump would be the significant jump in elevation

capacity relative to the HRP. Thus, as expected to be the case in the inspected regions, the HRP is potentially more efficient in the overall hydro-kinetic energy transfer at a moderate supply and delivery head. Though discussed at length, performance should also consider self-regulation amongst other factors as opposed to purely capacity.

As previously hypothesised, to manipulate the pressure amplifier and act on the large tyre system, the Bunyip pump would be expected to hold a greater portion of water. It yields a reduced relative delivery in contrast to a conventional HRP, delivering an extremely small 2% of the available water. For water-rich regions, this may still be deemed appropriate through the ability to unlock head potential in excess of, reportedly, 400 m in a recently developed steel piston chamber device for application in the Philippines [20]. The latter results are far better than the maximum excess described for the Blake HRP of 100 m and even the significantly improved design against conventional centrifugal fossil-fuel based pumps, but it is unable to match the potential delivery power of a piston mechanism. Although this naturally opens many doors for operation, the high portion of waste may impede the application of the Bunyip pump in some regions. Thus, an advised area of research would be to better utilise the supplied water, as discussed before briefly.

4.2. Data Validation

To verify the results, a series of four initial cases is used to assess the model's suitability, along with a data analysis with a simple calculation using Bernoulli's equation (Equations (4) and (5)). In parallel, four cases of Bunyip's results are inspected for the model validation, as presented in Table 4. The content focuses on the installations delivered, sharing an insight into operational parameters and achieved outputs, paired with the fundamental values to validate the modelling approach. The set of parameters is studied for a PA-13 Bunyip, operational with a 98 mm piston without water ballast devices. The device remains in the conventional position (no submerged tyre valves or out-of-water installations), sharing the same input flowrate to investigate the head ratio's influence on the associated performance metrics without impacting the flowrate. Each case could be modelled as per the video parameters and the bespoke UDF files developed for the time-based cycle to facilitate the motion relative to the observed cycle period and establish boundary pressures to enable the compilation of a complete summary, as given in Table 4.

In Table 4, several values are contrasted between the physical testing (PT) data inferred from [8] and the numerical modelling (NM) data. This enables the fundamental components to be corroborated, in addition to the enhanced break down of components in the NM case, to appraise the model's suitability for applications. The cases investigated operated within the bounds of a 5–6 L/s drive supply with a varied supply between 1.2 and 2.2 m. The system-maintained operation within an appropriate magnitude and demonstrated fluctuations both above and below the physical value, additionally feeding into the operational efficiency. Upon installation, certain parameters will be fixed; however, the model additionally enables the individual case stroke length to be tailored to the application, and each case is assumed to have a standard Ø = 98 mm design. Naturally, in practice, the spacers on the central rod can be used to adapt the system's stroke length for its application. This could be assumed at 90 mm from the scaled geometry; thus, the PT devices are expected to induce a degree of variation. Thus, a good indication of a suitable validation is the bi-directional variance for similar cases, as in cases 2 and 3. This indicates that the model values attained still provide a reasonable indicator for the anticipated output capacity. Although, it could be noted that there is potential for both under and overestimates. Due to the enhanced lifting capacity, even a small variance in the output can quickly develop into a notable variance in the efficiency, as emphasised further within the Bunyip pump. The variance in both the output and efficiency remains consistently above or below each PT result and should be considered when extracting data. The model is suitable for an initial analysis, and in future, further investigation into cases in which each system parameter is observed should be considered.

Table 4. Summary of the tested operational cases for validation of data.

Descriptions		Cycle Period (s)	Supply Head (m)	Delivery Head (m)	Flow Components (L/cycle)					Daily Capacity (L/day)	% Error (NM to PT)	% Efficiency	% Error (NM to PT)	Standard Capacity Sc (m/s)	Relative Delivery RD
					Delivery	Drive Flow	L-Exhaust	Supply	U-Exhaust						
case 1	PT [8]	2.06	1.2	22	0.205	10.30	-	0.21	-	8600	6	36	5	81.3	2.0
	NM				0.218	10.38	10.95	0.26	0.04	9125		38		86.2	2.1
case 2	PT [8]	2.51	2.0	50	0.251	12.55	-	0.25	-	8640	−14	50	−15	81.6	2.0
	NM				0.216	12.70	13.26	0.27	0.05	7443		43		70.3	1.7
case 3	PT [8]	2.74	2.0	60	0.184	13.70	-	0.18	-	5800	18	40	27	54.8	1.3
	NM				0.216	12.71	13.25	0.27	0.05	6821		51		64.4	1.7
case 4	PT [8]	1.39	2.2	36	0.232	12.51	-	0.23	-	14,400	−6	30	−11	136.1	1.9
	NM				0.219	13.28	14.05	0.25	0.03	13,594		27		128.4	1.6

4.3. Parametric Analysis

The previously discussed series of real-world systems provide the opportunity to observe the influence of supply and delivery performance. The data collected and calculated using the numerical model are used to produce a three-dimensional surface plot (see Figure 17). This visual representation uses the analysed cases to begin building an indication of how the supply and delivery heads in combination may influence the daily output and proportional operational performance of the pump. Importantly, note that the lower delivery head regions, we assign an average capacity of 8600 L/day to illustrate the surface floor average. In many of the cases away from our inspected data points, it is recommended to adopt a smaller Bunyip PA-8. Generally, such unique cases and data are not available in low-end performance systems either. At the given supply rate, the trend within the current dataset indicates that, as expected, with an increased supply head, the Bunyip pump can access improved daily output. Meanwhile, the ability to connect the two variables again indicates that for the typical 2 m average tested, the greatest accessible performance capacity would be at a ~32 m delivery.

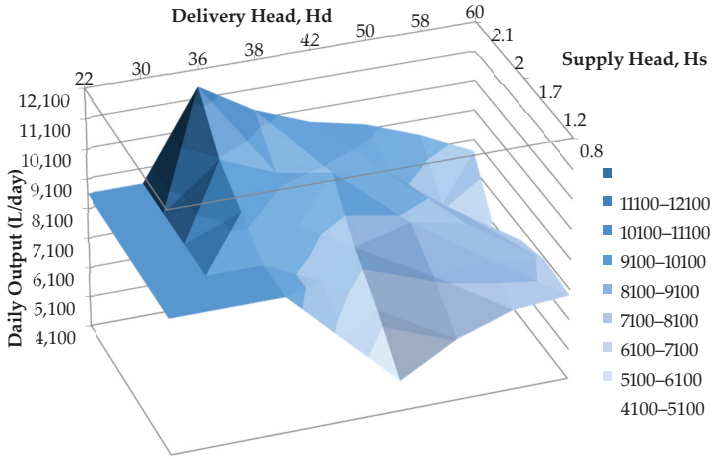


Figure 17. Parametric data graph showing the delivery head, Hd (m), and supply head, Hs (m), versus the predicted Bunyip daily output capacity (L/day).

It was also recognised that the elevated lifting capacity attained through the positive displacement pump can in fact impede performance at low delivery heads. In this region, the 'lighter' pressure on the conventional HRP delivery valve enables the rapid delivery of water in increased volumes. Conversely, the distance required for the piston mechanism and two stroke process spears to reach a terminal speed is extended, whereby the linear delivery cannot benefit from a similar operation. It should also be recognised that the cases available for the analysis did not operate at a head greater than 60 m. Thus, expanding the study to include additional data would enable Figure 17 to become a more powerful tool for parametric assessment. This could be achieved using the implementation of the current CFD data or further advanced simulation tools to strategically identify a clear performance 'surface' to inform installation and identify the optimal range for operation at varied supply rates available to end users.

5. Conclusions

The results highlight several key findings and potential areas for further research related to the Bunyip micro hydro-power system. The research began with a comprehensive literature review, which provided valuable insights into conventional hydro-ram pump (HRP) systems, their limitations, and micro hydro-power performance indicators. The project aimed to explore the potential of the Bunyip system as an innovative technology in the hydro-powered pumping field.

The research involved creating a detailed and advanced dynamic model, which required new modelling and programming skills to evolve the underlying physics of the flow. The use of software user-defined functions (UDFs) facilitated a good degree of verification for the initial analysis and provided a clear pathway for future research and model development. We conducted a further attempt to validate the data, but we could not reach a full validation. However, the data were comparable.

The study acknowledges that the Bunyip system cannot completely replace the HRP, as the latter remains more operationally efficient under a moderate supply and moderate delivery conditions. However, the Bunyip's enhanced delivery head capacity and operation under a reduced supply head make it a valuable alternative in the field, which is dominated by traditional HRPs. It is highlighted in this study that further research is needed to fully validate a 6DOF (six degrees of freedom) model capable of isolating each variable within the Bunyip system. The system shows promise in lifting water to significantly greater elevations, surpassing typical HRPs and fossil-fuel centrifugal systems. However, this increased capacity comes at the cost of reduced relative delivery, making it less suitable for water-scarce regions. The results indicate that a smaller diameter of the pressure chamber and a higher supply head lead to a higher pressure, achieving a target head of 3 m with a 15% efficiency and a flowrate of 11.82 L/min.

To better capture and utilize the lower portion of the exhaust flow during the dump phase, submerging this region can help dissipate the discharge energy more efficiently. Also, trapped energy in the wasted water could be captured by using a combined large diaphragm valve. This could chain the energy from the initial Bunyip pump cycle into another renewable system for delivering elevated pressure to a secondary location. The conclusion emphasizes that the Bunyip system has the potential to elevate micro hydro-powered systems and calls for further focused research to optimize its design and improve its water delivery capacity.

Author Contributions: Conceptualization, M.A.Q.; methodology, S.D.B. and M.A.Q.; software, S.D.B.; validation, S.D.B.; formal analysis, S.D.B.; resources, S.D.B. and M.A.Q.; data curation, M.A.Q. and S.D.B.; writing—original draft preparation, S.D.B. and M.A.Q.; writing—review and editing, M.A.Q.; visualization, M.A.Q.; supervision, M.A.Q.; project administration, M.A.Q. All authors have read and agreed to the published version of the manuscript.

Funding: This research received no external funding.

Data Availability Statement: Data are contained within the article.

Conflicts of Interest: The authors declare no conflict of interest.

Nomenclature

Notation	Description
g	Acceleration due to gravity $[\mathrm{m{\cdot}s^{-2}}]$
σ_ε	Constant for turbulent energy dissipation rate, 1.2
σ_k	Constant for turbulent kinetic energy, 1.0
C_1, C_2, C_3	Constants in realizable k- ε turbulence model
ρ	Density of the fluid $[\mathrm{kg{\cdot}s^{-3}}]$
$\mu,\ \mu_t$	Dynamic viscosity, turbulent $[\mathrm{Pa{\cdot}s^{-1}}]$
η_S	Operational efficiency [%]
G_b	Turbulence kinetic energy, generated due to buoyancy $[\mathrm{Pa{\cdot}s^{-1}}]$
G_k	Turbulence kinetic energy, generated due to mean velocity gradient $[\mathrm{Pa{\cdot}s^{-1}}]$
H	Height relative to delivery valve [m]
i, j	Tensor indices
t	Time [s]
ε	Turbulent energy dissipation rate per unit mass $[\mathrm{m^2{\cdot}s^{-3}}]$
k	Turbulent kinetic energy $[\mathrm{m^2{\cdot}s^{-2}}]$
K	Internal spring stiffness $[\mathrm{N{\cdot}s^{-1}}]$
$u,\ \nu$, V	Velocity : x, y, mean flow $[\mathrm{m{\cdot}s^{-1}}]$
p	Pressure [Pa]

Q	Volumetric flow rate $[\ell \cdot s^{-1}]$
S_c	Standard capacity $[m \cdot s^{-2}]$
R_d	Relative delivery
F	Force [N]
A	Area $[m^2]$
a_R	Resultant acceleration $[m \cdot s^{-2}]$
y_{sl}	Bunyip stroke length [m]
m	Mass [kg]

Appendix A. User Defined Function for Linear Rise-Fall Velocity Profile Definition

```
DEFINE_CG_MOTION(Bunyip_UDF, dt, vel, omega, time, dtime)
{
real y_up, y_down, curr_t; /*Gradient Variable Definition*/
y_up = 0.09;
y_down = -0.18;
curr_t = RP_Get_Real("flow-time");
if (curr_t<1) /*Time based conditional control*/
    {
        vel[1]=y_up;
    }
else if (curr_t>=1)
    {
        vel[1]=y_down;
    }
else
    {
        vel[1]=0;
        printf("Velocity UDF Error\n"); /*Error Report*/
    }
}
```

Appendix B. Boundary Manipulation Scheme Functions

```
(define (BunyipBCtype_v13)
 (define (time) (rpgetvar 'flow-time))

(if (and (>= (time) 0.945) (< (time) 1))
    (begin
    (ti-menu-load-string (format #f "define bou zone-type 111 out-vent"))
    (ti-menu-load-string (format #f "define bou set out-vent 111 () dir-spec no yes gauge-pressure no 0  ke-spec no no no yes turb-hydraulic-diam 0.004 prevent-reverse-flow yes quit"))
    (ti-menu-load-string (format #f "define bou zone-type 112 out-vent"))
    (ti-menu-load-string (format #f "define bou set out-vent 112 () dir-spec no yes gauge-pressure no 0  ke-spec no no no yes turb-hydraulic-diam 0.004 prevent-reverse-flow yes quit"))
    (ti-menu-load-string (format #f "define bou zone-type 113 out-vent"))
    (ti-menu-load-string (format #f "define bou set out-vent 113 () dir-spec no yes gauge-pressure no 0  ke-spec no no no yes turb-hydraulic-diam 0.004 prevent-reverse-flow yes quit"))
    )

(if (and (>= (time) 1) (< (time) 1.025))
    (begin
    (ti-menu-load-string (format #f "define bou zone-type 110 wall"))
    (ti-menu-load-string (format #f "define bou zone-type 109 out-vent"))
    (ti-menu-load-string (format #f "define bou set out-vent 109 () dir-spec no yes gauge-pressure no 0  ke-spec no no no yes turb-hydraulic-diam 0.035 quit"))
    (ti-menu-load-string (format #f "define bou zone-type 108 out-vent"))
    (ti-menu-load-string (format #f "define bou set out-vent 108 () dir-spec no yes gauge-pressure no 0  ke-spec no no no yes turb-hydraulic-diam 0.0323 prevent-reverse-flow yes quit"))
    (ti-menu-load-string (format #f "define bou zone-type 107 out-vent"))
    (ti-menu-load-string (format #f "define bou set out-vent 107 () dir-spec no yes gauge-pressure no 0  ke-spec no no no yes turb-hydraulic-diam 0.0323 prevent-reverse-flow yes quit"))
    (ti-menu-load-string (format #f "define bou zone-type 106 out-vent"))
    (ti-menu-load-string (format #f "define bou set out-vent 106 () dir-spec no yes gauge-pressure no 0  ke-spec no no no yes turb-hydraulic-diam 0.0357 prevent-reverse-flow yes quit"))
    )

(if (and (>= (time) 1.025) (< (time) 1.5))
    (begin
    (ti-menu-load-string (format #f "define bou zone-type 109 in-vent"))
    (ti-menu-load-string (format #f "define bou set in-vent 109 () dir-spec no yes ke-spec no no no yes turb-hydraulic-diam 0.035 prevent yes p0 no -2493 prevent-reverse-flow yes quit"))
    (ti-menu-load-string (format #f "define bou zone-type 113 wall"))
    (ti-menu-load-string (format #f "define bou zone-type 112 wall"))
    (ti-menu-load-string (format #f "define bou zone-type 111 wall"))
    )
    ))))
```

Appendix C. Bunyip Automation Script Monitoring Tyre Boundary ID to Set Inlet/Outlet Profiles

```
/*********************************************************************
UDF for autonomously updating the internal BC for the Bunyip Advanced Model
*********************************************************************/
# include "udf.h"
static int last_ts = -1; /*Global static variable to define Ts never<0...*/
static int phase = 0;

/*First function is active in the first iteration and establishes the
current phase to define subsequent BC's*/
DEFINE_ADJUST(First_Iter_PhaseCheck, domain)
{
    real area[ND_ND]; /*Dimesnion definition for variales*/
    real x[ND_ND];
    int ref_surface_ID = 102; /*Sets surface to observe motion of tyre @ID 102*/
    Thread *t= Lookup_Thread(domain,ref_surface_ID); /*Fetch thread ID data*/
    face_t f;
    int curr_ts;
    curr_ts = RP_Get_Integer("time-step");
    if (last_ts != curr_ts)
        {
            last_ts = curr_ts; /*Prevents repeated operation*/
            real sum_area, sum_flux_yvel;
            real check_y, check_yvel, check_time;
            begin_f_loop(f,t) /*for each thread face*/
                {
                F_CENTROID(x,f,t);
                check_y = x[1]; /*Check Valve fetches y (1) coordinate*/
                F_AREA(area,f,t); /*Calculates some of the face area*/
                sum_area += NV_MAG(area);
                sum_flux_yvel += NV_MAG(area)*F_V(f,t); /*face area average velocity*/
                }
            end_f_loop(f,t)

            check_yvel = sum_flux_yvel/sum_area; /*Check Valve 2*/
            check_time= RP_Get_Real("flow-time"); /*Check Valve 3*/
```

```
            /*Check phase 1*/
            if ((check_y<=0.13 && check_yvel>=0) || check_time<0.2)
            {
                int static phase = 1;
            }

            else if (check_y>0.13 && check_yvel>=0)
            {
                int static phase = 2;
            }

            else if (check_y>0.13 && check_yvel<0)
            {
                int static phase = 3;
            }

            else if ((check_y<=0.13 && check_y>0.02) && check_yvel<0)
            {
                int static phase = 4;
            }

            else if (check_y<=0.02 && check_yvel<0)
            {
                int static phase = 5;
            }

            else
            {
                printf("Failed Case Definition!\n");
            }
        }
}
```

```
DEFINE_PROFILE(Delivery_outlet,th,i)
{
    face_t f;
    begin_f_loop(f,th)
        {
            if (phase == 1 || phase == 2)
            {
                F_PROFILE(f,th,i) = 343350; /*Pa delivery pressure*/
            }
            else
            {
                F_PROFILE(f,th,i) = 1e10; /*Simulated Wall!*/
            }
        }
    end_f_loop(f,th);
}
```

```
DEFINE_PROFILE(Upper_Exhaust_outlet,th,i)
{
    face_t f;
    begin_f_loop(f,th)
        {
            if (phase == 2 || phase == 3)
            {
                F_PROFILE(f,th,i) = 0; /*Pa atmospheric gauge pressure*/
            }
            else
            {
                F_PROFILE(f,th,i) = 1e10; /*Simulated Wall!*/
            }
        }
    end_f_loop(f,th);
}
```

```
DEFINE_PROFILE(Lower_Exhaust_outlet,th,i)
{
    face_t f;
    begin_f_loop(f,th)
        {
            if (phase == 3 || phase == 4)
            {
                F_PROFILE(f,th,i) = 0; /*Pa atmospheric gauge pressure*/
            }
            else
            {
                F_PROFILE(f,th,i) = 1e10; /*Simulated Wall!*/
            }
        }
    end_f_loop(f,th);
}
```

```
DEFINE_PROFILE(Supply_inlet,th,i)
{
    face_t f;
    begin_f_loop(f,th)
        {
            if (phase == 3 || phase == 5)
            {
                F_PROFILE(f,th,i) = 0; /*Pa atmospheric gauge pressure*/
            }
            else
            {
                F_PROFILE(f,th,i) = 1e-10; /*Simulated Wall!*/
            }
        }
    end_f_loop(f,th);
}
```

Appendix D. Bunyip PA-13 Operational Case Information

The set of parameters is studied for a Bunyip pump operational with a 98 mm piston without water ballast devices or drive supply connections to the supply piston [26]. The device remains in the conventional position (no submerged tyre valves or out-of-water installations).

Case 1—Bunyip PA13 Pump at Misty Mountain Biggs road Nth QLD, Australia. Available at <Bunyip PA13 Pump at Misty Mountain Biggs road Nth QLD, Australia.—YouTube: https://www.youtube.com/watch?v=pFPmeESb0Ao&t=18s> [accessed on 14 April 2022].

Case 2/Case 3—Bunyip Pump(s) on Thiaki Creek, available at <Second Bunyip Pump on Thiaki Creek—YouTube: https://www.youtube.com/watch?v=MDb8Exrg-F0> [accessed on 14 April 2022].

Case 4—Tableland Bunyip, available at <Another Tableland happy Bunyip—YouTube: https://www.youtube.com/watch?v=a0FQfoPJMWk> [accessed on 14 April 2022].

References

1. United Nations. What Is Renewable Energy? Available online: https://www.un.org/en/climatechange/what-is-renewable-energy (accessed on 2 July 2023).
2. IEA. The Global Energy Crisis Pushed Fossil Fuel Consumption Subsidies to an All-Time High in 2022. Available online: https://www.iea.org/commentaries/the-global-energy-crisis-pushed-fossil-fuel-consumption-subsidies-to-an-all-time-high-in-2022 (accessed on 2 July 2023).
3. IRENA; CPI. Global Landscape of Renewable Energy Finance 2023; IRENA. ISBN: 978-92-9260-523-0. Available online: https://www.irena.org/ (accessed on 25 June 2023).
4. Karekezi, S.; Kimani, J.; Wambille, A.; Balla, P.; Magessa, F.; Kithyoma, W.; Ochieng, X. *The Potential Contribution of Non-Electrical Renewable Energy Technologies (RETs) to Poverty Reduction in East Africa*; AFREPREN/FWD: Nairobi, Kenya, 2005.
5. Roberts, A.; Thomas, B.; Sewell, P.; Hoare, E. Generating Renewable Power from Water Hammer Pressure Surges. *Renew. Energy* **2019**, *134*, 1392–1399. [CrossRef]
6. Intriago Zambrano, J.C.; Michavila, J.; Arenas Pinilla, E.; Diehl, J.C.; Ertsen, M.W. Water Lifting Water: A Comprehensive Spatiotemporal Review on the Hydro-Powered Water Pumping Technologies. *Water* **2019**, *11*, 1677. [CrossRef]
7. Young, B.W. Design of Hydraulic Ram Pump Systems. *Proc. Inst. Mech.Eng. Part A J. Power Energy* **1995**, *209*, 313–322. [CrossRef]
8. Porta's Engineering Home | Bunyip Water Pumps. Available online: https://www.bunyipwaterpumps.com/ (accessed on 16 July 2023).
9. Guo, X.; Li, J.; Yang, K.; Fu, H.; Wang, T.; Guo, Y.; Xia, Q.; Huang, W. Optimal Design and Performance Analysis of Hydraulic Ram Pump System. *Proc. Inst. Mech.Eng. Part A J. Power Energy* **2018**, *232*, 841–855. [CrossRef]
10. Li, J.; Yang, K.; Guo, X.; Huang, W.; Wang, T.; Guo, Y.; Fu, H. Structural Design and Parameter Optimization on a Waste Valve for Hydraulic Ram Pumps. *Proc. Inst. Mech. Eng. Part A J. Power Energy* **2021**, *235*, 747–765. [CrossRef]
11. Harith, M.N.; Bakar, R.A.; Ramasamy, D.; Quanjin, M. A Significant Effect on Flow Analysis & Simulation Study of Improve Design Hydraulic Pump. *IOP Conf. Ser. Mater. Sci. Eng.* **2017**, *257*, 012076. [CrossRef]
12. Harith, M.N.; Bakar, R.A.; Ramasamy, D.; Kardigama, K.; Quanjin, M. A Study of Waste and Delivery Valve Design Modification to the Pump Performance. *IOP Conf. Ser. Mater. Sci. Eng.* **2018**, *342*, 012090. [CrossRef]

13. Rybdylova, O.; Al Qubeissi, M.; Braun, M.; Crua, C.; Manin, J.; Pickett, L.M.; de Sercey, G.; Sazhina, E.M.; Sazhin, S.S.; Heikal, M. A Model for Droplet Heating and Its Implementation into ANSYS Fluent. *Int. Commun. Heat Mass Transf.* **2016**, *76*, 265–270. [CrossRef]
14. *Ansys*®; R2; ANSYS, Inc.: Canonsburg, PA, USA, 2022.
15. Tu, J.; Yeoh, G.H.; Liu, C. *Computational Fluid Dynamics—A Practical Approach*; Butterworth-Heinemann: Oxford, UK, 2008.
16. Porta, B.; (Porta's Engineering, Silkwood, Australia); Glockemann, R.; (Porta's Engineering, Wyndhan, Australia); Beard, S.; (Coventry University, Coventry, UK). Bunyip vs. RAM Comparison. Personal communication, 1 February 2021.
17. Maratos, D.F. Technical Feasibility of Wavepower for Seawater Desalination Using the Hydro-Ram (Hydram). *Desalination* **2003**, *153*, 287–293. [CrossRef]
18. Yussupov, Z.; Yakovlev, A.; Sarkynov, Y.; Zulpykharov, B.; Nietalieva, A. Results of the Study of the Hydraulic Ram Technology of Water Lifting from Watercourses. *Int. J. Eng. Sci.* **2022**, *177*, 103713. [CrossRef]
19. Inthachot, M.; Saehaeng, S.; Max, J.F.J.; Müller, J.; Spreer, W. Hydraulic Ram Pumps for Irrigation in Northern Thailand. *Agric. Agric. Sci. Procedia* **2015**, *5*, 107–114. [CrossRef]
20. Glockemann, R.; (Porta's Engineering, Wyndhan, Australia); Beard, S.; (Coventry University, Coventry, UK). Opportunities to Improve the Bunyip System 2022. Personal communication, 10 February 2022.
21. Asvapoositkul, W.; Nimitpaitoon, T.; Rattanasuwan, S.; Manakitsirisuthi, P. The Use of Hydraulic Ram Pump for Increasing Pump Head-technical Feasibility. *Eng. Rep.* **2021**, *3*, e12314. [CrossRef]
22. Asvapoositkul, W.; Juruta, J.; Tabtimhin, N.; Limpongsa, Y. Determination of Hydraulic Ram Pump Performance: Experimental Results. *Adv. Civ. Eng.* **2019**, *2019*, 970218. [CrossRef]
23. Fatahi-Alkouhi, R.; Lashkar-Ara, B. Experimental Evaluation of Effective Parameters on Characteristic Curves of Hydraulic Ram-Pumps. *Sci. Iran.* **2017**, *26*, 283–294. [CrossRef]
24. Blake's Hydram. The Blake Hydram Water Pump-Self Powered-No Fuel-None Polluting. Available online: https://blakeshydram.co.uk/ (accessed on 16 July 2023).
25. Papa Pump Papa Multi-Pump Systems 2017, White paper. Available online: https://waterpoweredtechnologies.com/case-studies/ (accessed on 2 July 2023).
26. Beard, S.D.; Al Qubeissi, M.; Khanal, B. Computational Analysis of Hydro-Powered Bunyip Pump. In *Energy and Sustainable Futures: Proceedings of the 3rd ICESF, 2022*; Nixon, J.D., Al-Habaibeh, A., Vukovic, V., Asthana, A., Eds.; Springer Proceedings in Energy; Springer Nature Switzerland: Cham, Switzerland, 2023; pp. 61–71, ISBN 978-3-031-30959-5.

Disclaimer/Publisher's Note: The statements, opinions and data contained in all publications are solely those of the individual author(s) and contributor(s) and not of MDPI and/or the editor(s). MDPI and/or the editor(s) disclaim responsibility for any injury to people or property resulting from any ideas, methods, instructions or products referred to in the content.

inventions

MDPI

Article

A Wide Operating Range Ejector with Part Nested Nozzles for PEMFC Hydrogen Recirculation System

Anning Yi [1,2], Chen Wang [1,2,*], Lei Wang [1,2,*] and Xinli Wang [1,2]

[1] School of Control Science and Engineering, Shandong University, Jinan 250061, China
[2] Center for Hydrogen Energy, Shandong University, Jinan 250061, China
* Correspondence: chenwangsdu@gmail.com (C.W.); leiwang@sdu.edu.cn (L.W.)

Abstract: The ejector drives unreacted hydrogen from the anode to improve fuel utilization ratio and discharges redundant water to prevent flooding and shutdown in the proton exchange membrane fuel cell (PEMFC). However, the traditional fixed structure ejector cannot meet the recycling requirements in the whole dynamic working condition of the fuel cell. In this article, a part nested four-nozzle (PNFN) ejector is proposed to enhance the hydrogen recycling efficiency under variable working conditions of the PEMFC by restricting the nozzle flow as 10%, 20%, 20%, and 50% of the fuel cell-rated power, respectively. Systematical analyses are performed on the experimentally verified 3D model to study inner flow characteristics and performance under different nozzle running modes. The results indicate that the PNFN ejector satisfies the recirculation ratio requirements in the power range of 34–220 kW within the 7–9 bar suitable supply pressure. By comparing with traditional ejectors, the PNFN ejector has a wider working range and especially outputs better performance in the low power range.

Keywords: ejector; hydrogen recirculation; four-nozzle; proportional nozzle; PEMFC

1. Introduction

Large fossil energy consumption brings a series of environmental issues, such as energy crisis, greenhouse effect, and so on [1–4]. A green and effective energy conversion technology is the proton exchange membrane fuel cell (PEMFC), which converts chemical energy directly into electric energy without burning and without being affected by heat engine efficiency [5–8].

The hydrogen recycle subsystem provides fuel for continuous electrochemical reactions and electric power generation of fuel cells. The advantages of the ejector for hydrogen recirculation systems include its small volume, lack of noise, inexpensive cost, straightforward construction, and no power consumption [9–11].

In recent years, research results show that the ejector driven PEMFC hydrogen recycle system can significantly increase fuel utilization efficiency [12,13]. Kim et al. [14] invented an ejector for the PEMFC of the submarine and experimental verification indicated that the ejector can meet the PEMFC anode hydrogen requirements. Dadvar et al. [15] proposed a design approach for the ejector based on the relationship between the ejector and the stack parameters (cell number, battery active area, etc.). Yin et al. [16] put forward a sequential procedure for optimizing the ejector geometry based on the ejector numerical model in three dimensions for PEMFC anode recycling. Maghsoodi et al. [17] investigated the impact of four crucial geometries (nozzle exit position (NXP), mixing chamber length, diffusion chamber length, and diffusion angle of diffusion chamber) on the ejector performance. Apart from the four geometries, Yang et al. [18] also investigated two other parameters (nozzle outlet diameter and mixing chamber diameter) that affect the performance of the ejector. Pei et al. [19] investigated how the area ratio (the ratio of the mixing chamber diameter to the nozzle diameter) and NXP affect ejector performance. The results show that

the ejector's ejection capability declines rapidly when the area ratio and NXP are too large or too small. Wang et al. [20] found that nozzle length and nozzle angle have an impact on the ejector performance. Amin et al. [21] designed a new type of ejector nozzle and studied the gas-liquid two-phase flow inside the ejector by computational fluid dynamics (CFD) technology. The results show that the two fluids mix more uniformly and the ejector has better ejection performance. The aforementioned studies are primarily concerned with ejector structural optimization and its effects on ejection performance in the PEMFC anode recycle system.

Some scholars have also conducted investigation on ejectors operation in variable working conditions. Brunner et al. [22] proposed a variable structure ejector, whose nozzle structure may be altered to enable the ejector to operate at a wide range with regard to a low-power PEMFC. The outcomes showed that the ejector performs well during cycles where the output power is between 7 and 17 kW. Jenssen et al. [23] created a model of the variable structure ejector for the cascade PEMFC system. One could draw the conclusion that the ejector in the PEMFC with low output power has a high recirculation ratio. He et al. [24] combined ejector and blower to increase the operating range of the PEMFC system. Nikiforow [25] built a control strategy for the three-way solenoid valve to change the ejector primary flow in the variable working condition of PEMFC. Hwang [9] installed the solenoid valve and proportional valve on the fuel delivery line of the ejector. This method can achieve stable hydrogen delivery for the PEMFC system and expand the ejector working range to a certain extent.

The above-mentioned research results mainly focus on the small power PEMFC under rated power of 80 kW, but the results cannot be directly generalized to high-power PEMFC applications for the nonlinear properties of fluids and electrochemistry. With the current rapid development towards high-power PEMFC, it is important to design an ejector that can meet the recycling requirements in the dynamic condition of the high-power PEMFC system. Therefore, this study proposes a part nested four-nozzle (PNFN) ejector for the high rated power fuel cell of 170 kW. The four nozzles are designed with 10%, 20%, 20%, and 50% of the fuel cell rated power. By altering the operation model of the nozzles, the four-nozzle ejector can enhance the hydrogen recirculation performance to satisfy the high-power fuel cell's recycling requirements under varying working conditions.

2. PNFN Ejector Design Method

2.1. Ejector in the PEMFC Operating Theory

The anode hydrogen recirculation system with a single nozzle ejector is depicted in Figure 1 Diagram of an anode hydrogen recirculation system with a single nozzle ejector. The ejector is made up of a nozzle, a suction chamber, a mixing chamber with constant pressure, constant area, and a diffusion chamber. The pressure-reducing valve lowers the high-pressure hydrogen coming from the hydrogen tank. Next, low-pressure hydrogen (primary flow (PF)) expands via the nozzle, transforming the hydrogen's pressure potential energy into kinetic energy. The secondary flow (unreacted hydrogen (SF)) from the PEMFC stack anode is sucked into the ejector's suction chamber. After that, the SF and the PF are then combined in the mixing chamber. The combined gas then enters the fuel cell anode after passing through the diffusion chamber.

In the recycling process, the ejector can increase fuel usage rate while also releasing fuel cell anode water. In the fuel cell system, the relationship between the different hydrogen mass flows about the ejector is expressed as follows:

$$m_{in} = m_r + m_c \tag{1}$$

where m_{in} is the mass of hydrogen entering the fuel cell, m_r and m_c are the hydrogen mass of the recirculated (unreacted) and consumed in the fuel cell, respectively.

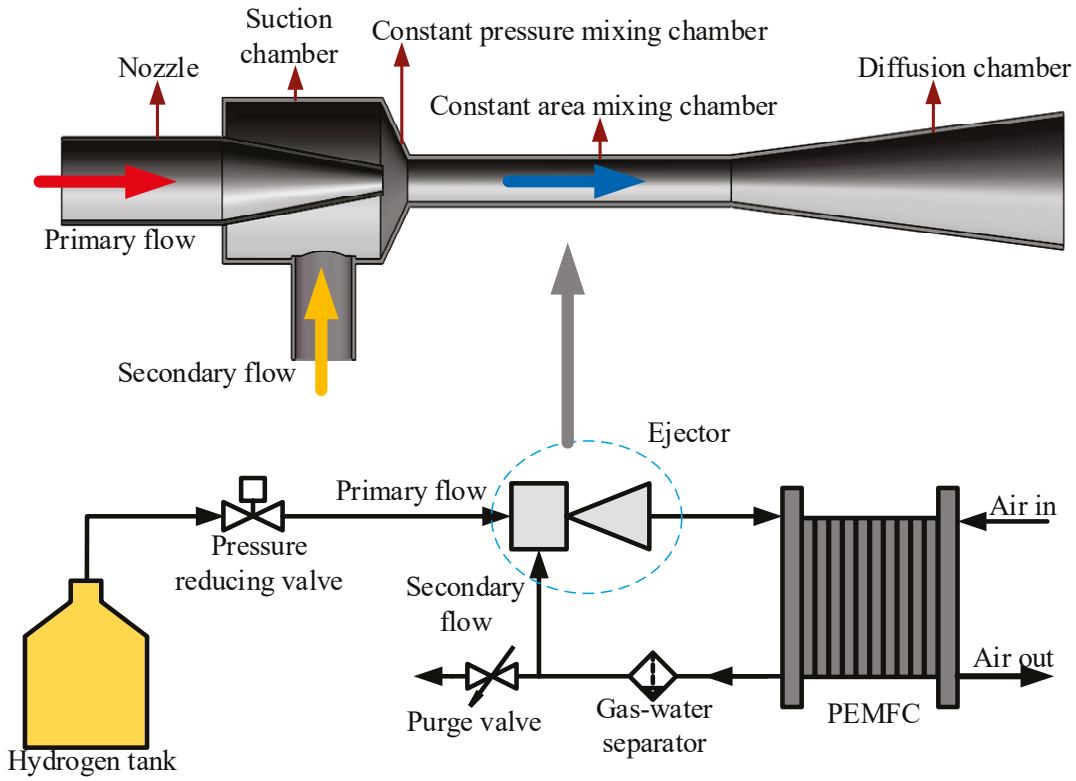


Figure 1. Diagram of an anode hydrogen recirculation system with a single nozzle ejector.

The hydrogen mass entering the fuel cell in the fuel cell system is greater than the hydrogen mass that should have theoretically responded. The following equation can be used to express the hydrogen excess coefficient λ_{H_2}, which represents the actual mass of hydrogen entering the fuel cell:

$$\lambda_{H_2} = \frac{m_{in}}{m_c} = \frac{m_r + m_c}{m_c} = \frac{m_r}{m_c} + 1 \tag{2}$$

2.2. Structural Design of the PNFN Ejector

It is important that PEMFC rated power, mass flow rate, cell voltage, and other geometric parameters for the ejector design.

According to fuel cell parameters, the hydrogen PF mass flow m_p is calculated as follows:

$$m_p = \frac{P_{stack} M_{H_2}}{2 V_c F} \tag{3}$$

where P_{stack} is the fuel cell's rated power of the, M_{H_2} is the hydrogen molar mass, V_c and F are the single cell voltage and Faraday constant, respectively.

Designing the nozzle structure is the key step for the ejector. The following formulas are used to compute the nozzle throat area A_{nt}:

$$A_{nt} = \frac{m_p v_{cr}}{k p_{cr} p_p} \tag{4}$$

$$p_{cr} = \frac{p_*}{p_p} = \left(\frac{2}{k+1}\right)^{\frac{k}{k-1}} \tag{5}$$

$$v_{cr} = \sqrt{2\frac{k}{k+1}}\sqrt{RT_{p^*}} \tag{6}$$

where v_{cr} is the critical velocity, k is the ratio of the specific heat of gas, p_{cr} is the relative pressure, p_p is the PF pressure, p_* is the gaseous critical pressure, R is the gas constant, and T_{p*} is the gaseous critical temperature.

Aiming at a 170 kW (Pe) high-power fuel cell, this study proposes a new type of four-nozzle ejector. The conventional single-nozzle ejector is designed under certain operating points of the fuel cell. When the fuel cell power changes in a large scale, the performance of the conventional single-nozzle ejector will sharply decrease and therefore, it cannot meet the flow requirements. So, we design the multi-nozzle ejector to improve the performance of the ejector under full operating range. We select four nozzles (10%, 20%, 20%, and 50% of the fuel cell rated power) because this type can meet the whole power requirements by combining nozzles with different working modes. If the number of nozzles is lower than four, the ejector cannot work at the whole power range of the fuel cell, and when the number of nozzles is greater than four, the ejector's structure will be too complicated.

The nozzle that meets 10% of rated power is called the first nozzle (N1). The second nozzle (N2) and the third nozzle (N3) are identical nozzle applied to 20% of rated power. The nozzle of 50% rated power is called the fourth nozzle (N4). Combined with the different power nozzles, the PNFN ejector can operate throughout the fuel cell's whole power range. The operation modes of ejector in different powers based on the number of nozzles working are shown in Table 1.

Table 1. The ejector operation mode.

Power	Operation Nozzle	Operation Mode
10% Pe	N1	1
20% Pe	N2 (or N3)	2
30% Pe	N1 and N2 (or N3)	3
40% Pe	N2 and N3	4
50% Pe	N4	5
60% Pe	N4 and N1	6
70% Pe	N4 and N2 (or N3)	7
80% Pe	N4, N2 (or N3) and N1	8
90% Pe	N4, N2 and N3	9
100% Pe	N1, N2, N3 and N4	10

In the four-nozzle ejector, the hydrogen supply flow of each nozzle is equal to the percentage of the hydrogen supply flow of the fuel cell at its rated operating condition, and the throat area of each nozzle is equal to the percentage of the total throat area. Combined with the above formula, the throat area of each nozzle is calculated as follows:

$$A_{nt1} = 10\%A_{nt} \tag{7}$$

$$A_{nt2} = A_{nt3} = 20\%A_{nt} \tag{8}$$

$$A_{nt4} = 50\%A_{nt} \tag{9}$$

$$A_{ntx} = \frac{1}{4}\pi {D_x}^2 \tag{10}$$

where D_x is the nozzle (x) diameter, x = 1, 2, 3, 4.

The ejector design process is illustrated in Figure 2.

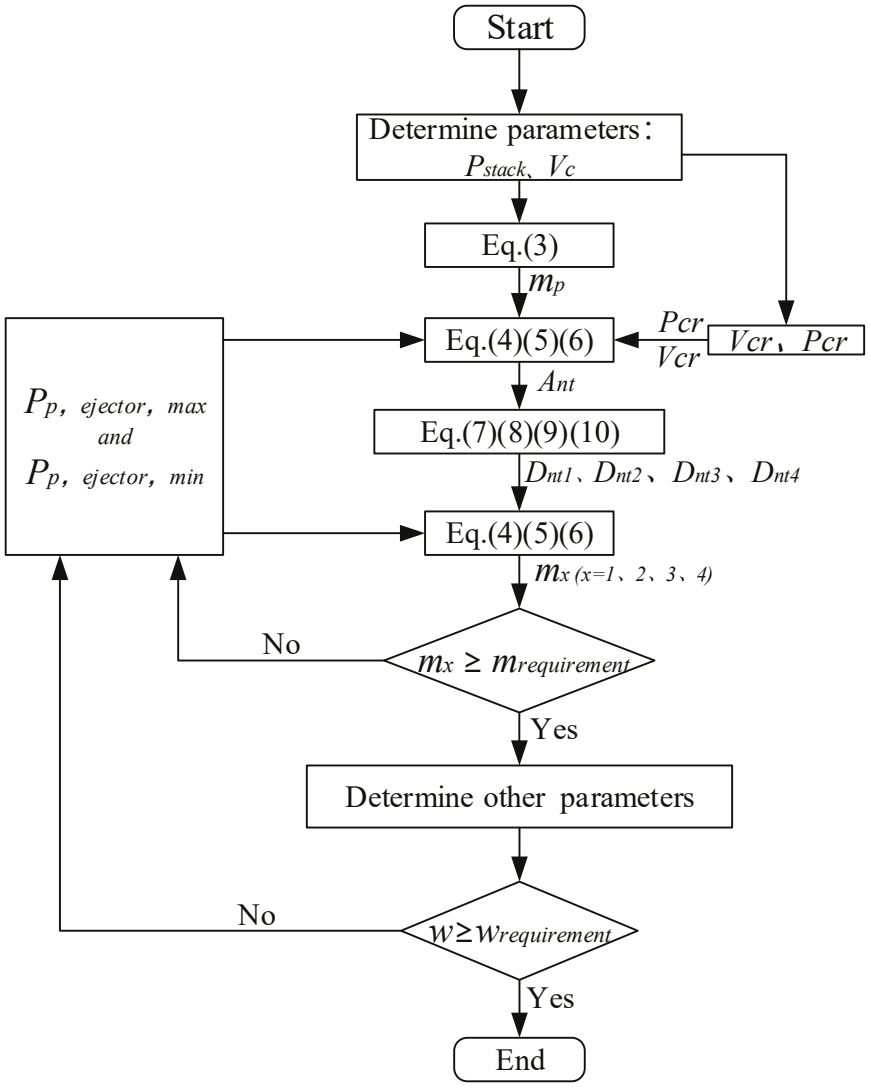


Figure 2. Design process of the PNFN ejector.

Table 2 shows the diameter of the four nozzles carried out with the above iterative calculation process.

Table 2. The diameter of the four nozzles.

Nozzles	Values
First nozzle diameter D_{nt1}	1 mm
Second nozzle diameter D_{nt2}	1.2 mm
Third nozzle diameter D_{nt3}	1.2 mm
Fourth nozzle diameter D_{nt4}	2.4 mm

The PEMFC system uses the recirculation ratio (ω) to assess the performance of the ejector, which is defined as:

$$\omega = \frac{m_s}{m_p} \tag{11}$$

here m_p is the PF mass flow rate, m_s is the SF mass flow rate.

The recirculation ratio (ω) for the PNFN ejector can be calculated using the formula below:

$$\omega = \frac{m_s}{m_p} = \frac{m_s}{m_{f1} + m_{f2} + m_{f3} + m_{f4}} \tag{12}$$

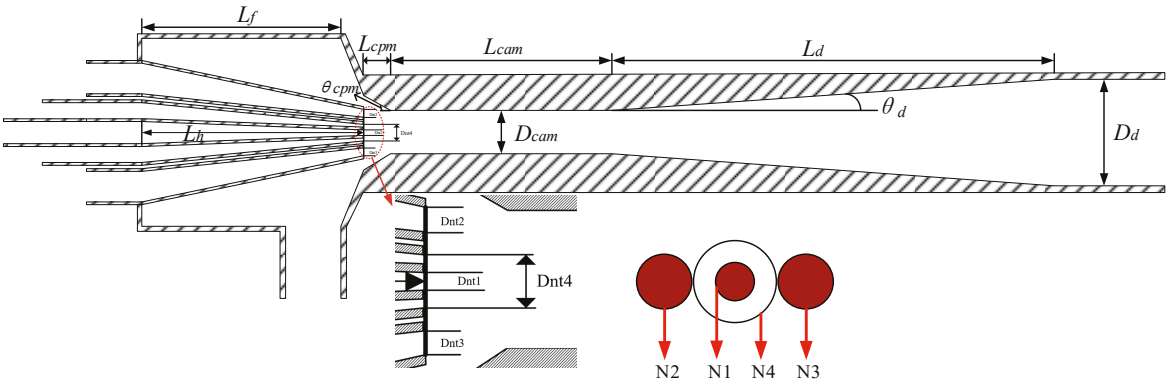
where, m_{f1}, m_{f2}, m_{f3} and m_{f4} are the mass flow rate of the N1, N2, N3 and N4, respectively.

In addition to the ejector nozzle, the performance and mass flow rate of the ejector are significantly influenced by other structural factors, such as NXP, mixing chamber diameter, diffusion chamber length, and others. These values are determined by multiple simulations. When the minimum recirculation ratio ω exceeds 0.50, the ejector design process is over, or else, redesign the ejector structure. Table 3 displays the values of the PNFN ejector's other geometric parameters.

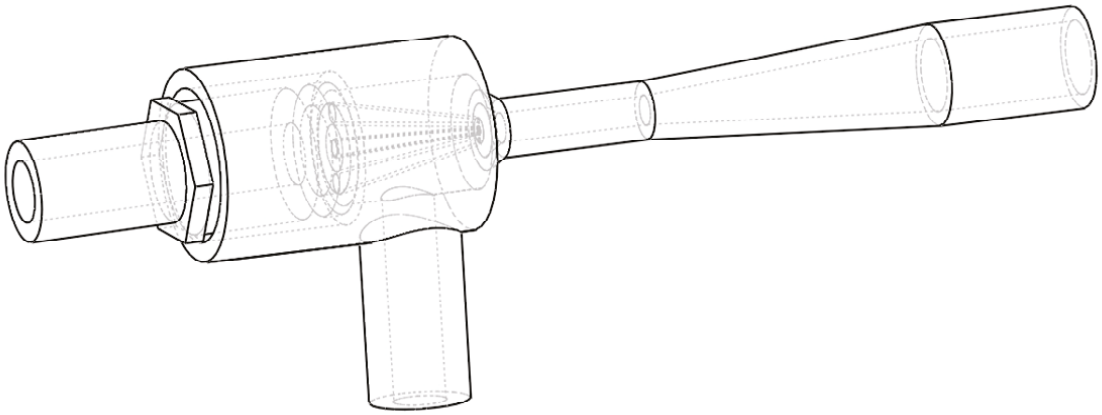
Table 3. The PNFN ejector geometric parameters value.

Parameters	Values
Suction chamber length L_f	37 mm
Nozzle length L_h	40 mm
Constant-pressure mixing chamber convergence angle θ_{cpm}	21°
Constant-pressure mixing chamber length L_{cpm}	5 mm
Constant-area mixing chamber diameter D_{cam}	8 mm
Constant-area mixing chamber length L_{cam}	40 mm
Diffusion chamber length L_d	80 mm
Diffusion chamber divergence angle θ_d	4°
Diffusion chamber outlet diameter D_d	19.2 mm

The PNFN ejector structure diagram and 3D model diagram are shown in Figures 3a and 3b, respectively.



(**a**)



(**b**)

Figure 3. (**a**)The PNFN ejector structure diagram; (**b**) 3D model diagram.

3. Numerical Model and Simulation

3.1. Governing Equation

To analyze performance and optimize the geometric structure of the ejector by using computational fluid dynamics (CFD) under various operating conditions. For the numerical simulation of the ejector, the following assumptions are made:

(1) The walls are considered adiabatic.
(2) The internal gas is considered an ideal gas.
(3) The inner fluid of the ejector is fully mixed.
(4) The inner fluid is regarded as compressible fluid.

The conservation equations governing the ejector can be stated as follows using the aforementioned presumptions:

Continuity equation:

$$\nabla \bullet \left(\rho \vec{v} \right) = 0 \tag{13}$$

Momentum equation:

$$\nabla \bullet \left(\rho \vec{v} \vec{v} \right) = -\nabla \mathrm{P} + \nabla \bullet \overline{\tau} + \rho \vec{g} \tag{14}$$

Energy equation:

$$\nabla \bullet \left[\vec{v} (\rho E + P) \right] = \nabla \bullet \left[\lambda \nabla T - \sum_{q} h_q \vec{J_q} + \overline{\tau} \vec{v} \right] \tag{15}$$

Species transport equation and the ideal gas relationship:

$$\nabla \bullet \left(\rho \vec{v} Y_q \right) = -\nabla \bullet \vec{J_q} \tag{16}$$

$$\rho = P/RT \tag{17}$$

$$\overline{\tau} = \mu \left[\left(\nabla \vec{v} + \nabla \vec{v}^{T} \right) - \frac{2}{3} \nabla \bullet \vec{v} I \right] \tag{18}$$

$$\vec{J_q} = -\left(\rho D_{q,m} + \frac{\mu_t}{S_{ct}} \right) \nabla Y_q - D_{T,q} \frac{\nabla T}{T} \tag{19}$$

The inner fluid of the ejector occurs in various flow phenomena including mixing, turbulence, backflow, etc. In this paper, the RNG $k-\varepsilon$ turbulence model is adopted, which can simulate jet impingement, SF, and whirlwind complex flow phenomena. Because previous studies [26,27] have accomplished many experiments to compare the SST $k-\omega$ turbulence model with the RNG $k-\varepsilon$ turbulence model for the PEMFC ejector. The results show that the RNG $k-\varepsilon$ turbulence model is appropriate for the full working condition PEMFC ejector model, it is represented as follows:

$$\frac{\partial}{\partial t}(\rho k) + \frac{\partial}{\partial x_i}(\rho k u_i) = \frac{\partial}{\partial x_j}\left(\alpha_k \mu_{eff} \frac{\partial k}{\partial x_j} \right) + G_k + G_b - \rho\varepsilon - Y_M + S_k \tag{20}$$

$$\frac{\partial}{\partial t}(\rho \varepsilon) + \frac{\partial}{\partial x_i}(\rho \varepsilon u_i) = \frac{\partial}{\partial x_j}\left(\alpha_\varepsilon \mu_{eff} \frac{\partial \varepsilon}{\partial x_j} \right) + C_{1\varepsilon} \frac{\varepsilon}{k}(G_k + C_{3\varepsilon} G_b) - C_{2\varepsilon} \rho \frac{\varepsilon^2}{k} - R_\varepsilon + S_\varepsilon \tag{21}$$

where, $C_{1\varepsilon} = 1.42$, $C_{2\varepsilon} = 1.68$, G_k represents the turbulent kinetic energy generated, G_b represents the turbulent kinetic energy generated, Y_M represents the fluctuating expansion to total dissipation ratio in compressible turbulent, α_k and α_ε are the reciprocal of an effective Prandtl number.

3.2. Grid Generation

Grid generation is one of the important components of CFD and the stability and precision of the numerical calculation are determined by the grid's quality. Ansys software

serves as grid generator and solver for governing equations. The grid numbers will affect simulation result. For the region with intensive gradient change, the grid density needs to be encrypted. In order to improve the accuracy of fluid flow simulation, the nozzle outlet grid needs a fine refinement treatment. Figure 4 shows the final grid results.

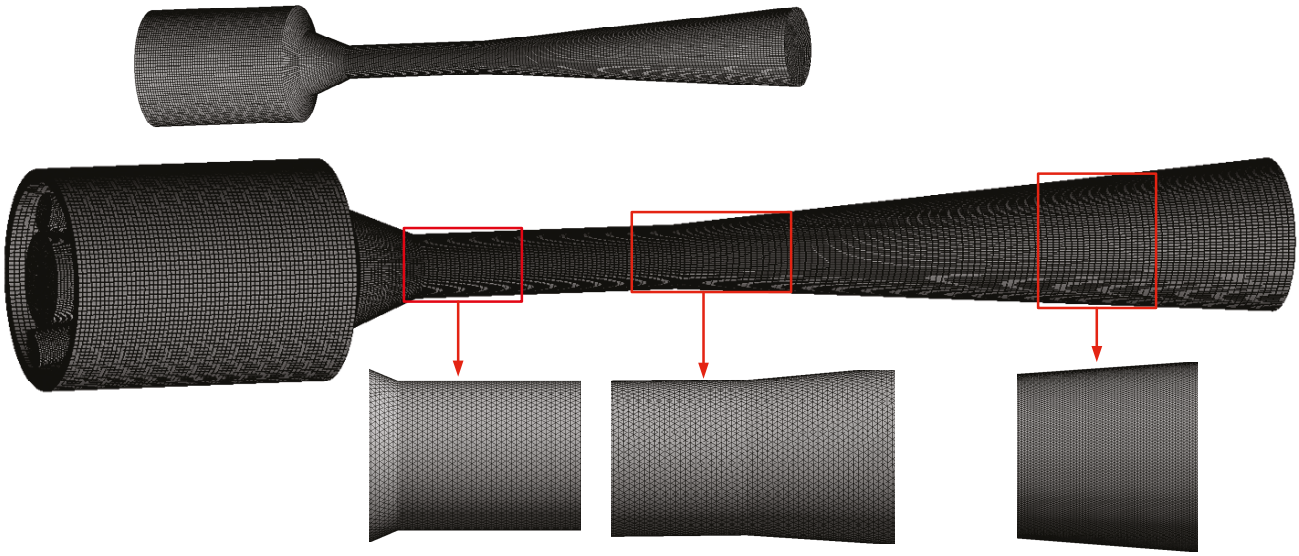


Figure 4. The grids of the PNFN ejector model.

3.3. Boundary Conditions

The simulated boundary conditions in this study are set in accordance with the PEMFC's real operational settings (Table 4).

Table 4. The actual operating conditions of the PEMFC.

Power (kW)	Current (A)	Mass Flow Rate of the Hydrogen (g s^{-1})	Fuel Cell Entry Pressure (kPa)
170	495	2.84	270
153	445	2.44	270
136	396	2.16	270
102	297	1.63	260
85	247	1.36	247
68	198	1.08	228
51	148	0.81	205
34	99	0.54	177

The PF inlet and the SF inlet are set to the pressure inlet and the outlet is set to the outlet pressure. In addition, the PF temperature is 293 K same as the environmental temperature, the SF temperature and the outlet temperature are both 338 K same as the fuel cell stack temperature. The fluid that flows near the wall takes the standard wall function method.

3.4. Grid Independence Verification

The grid independence verification of the models guarantees the accuracy and reliability of the results. Three grid models are studied including sparse grid with 785,242 elements, medium grid with 1,245,316 elements, and encrypted grid with 1,613,454 elements. The simulated working gas is dry hydrogen, and the results are compared with each other under the same conditions (the PF pressure, the SF pressure and the outlet pressure are 7.0 bar, 1.9 bar and 2.1 bar, respectively). Figure 5a shows the static pressure on the internal axis of the ejector under the three different grid numbers. With varying numbers of grids, the static pressure trend is the same, and the values for medium and encrypted

grids are quite close. Figure 5b shows the connection between the recirculation ratio and model gird number at different operation modes of the ejector. The results show that the simulation data are also quite close to each other.

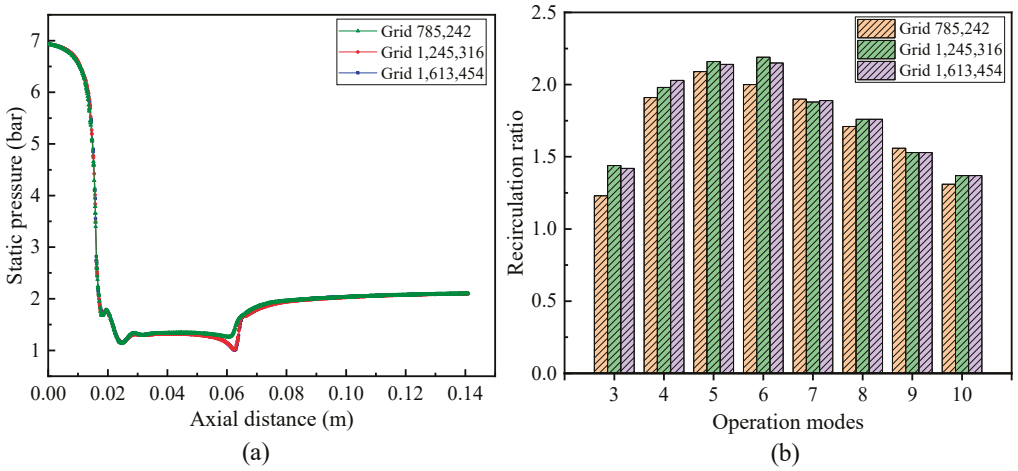


Figure 5. Grid independent validation. (**a**)The static pressure distribution on the axis under different grids (Mode 10). (**b**) The comparison of the recirculation ratio at different operation modes.

Two groups of ejector operation mode are selected to verify the deviation from PF, SF, and recirculation ratio as shown in Tables 5 and 6. The deviation can be expressed by the following equation:

$$\sigma = \frac{|x_{n+1} - x_n|}{x_n} \times 100\% \tag{22}$$

where x_n is the nth calculated value.

Table 5. Grid independence validation results (Mode 4).

Grid	$m_p(g \bullet s^{-1})$	$\sigma(\%)$	$m_s(g \bullet s^{-1})$	$\sigma(\%)$	ω	$\sigma(\%)$
785,242	1.195	-	2.312	-	1.935	-
1,245,316	1.229	2.81	2.441	5.54	1.986	2.64
1,613,454	1.221	0.65	2.482	1.64	2.033	2.36

Table 6. Grid independence validation results (Mode 6).

Grid	$m_p(g \bullet s^{-1})$	$\sigma(\%)$	$m_s(g \bullet s^{-1})$	$\sigma(\%)$	ω	$\sigma(\%)$
785,242	1.738	-	3.497	-	2.012	-
1,245,316	1.711	1.55	3.751	7.26	2.192	8.95
1,613,454	1.705	0.35	3.678	1.95	2.157	1.61

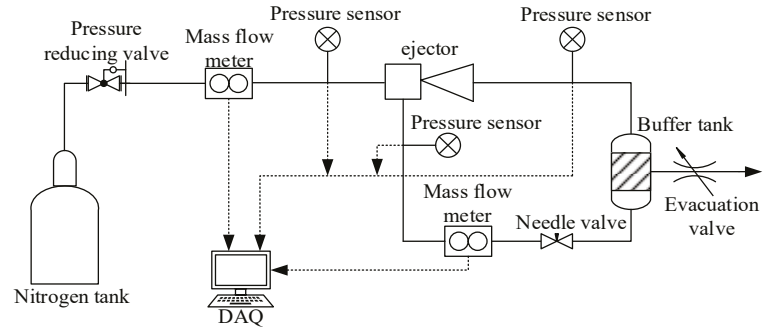
From the tables, the deviation becomes smaller when the grid number increases in the two modes. The deviations of the three factors of the mode 6 between medium and fine grid are decreased to 0.35%, 1.95%, and 1.61%, respectively. The deviations between the medium and fine grids are far less than that between the coarse and medium grids.

In CFD numerical simulation, the level of grid quality is related to calculation accuracy and calculation time. Although the higher of the model grid quality and more accurate results are, the calculation time is longer. Considering the calculation accuracy and the calculation time, the medium grid model is selected to accomplish the following numerical simulation.

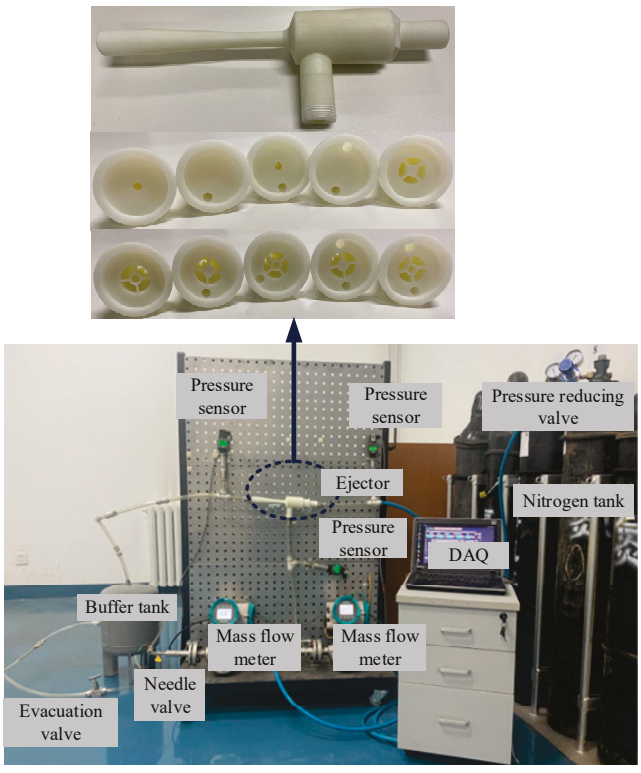
4. Experimental Facility and Model Verification

4.1. Experimental Facility

Figure 6a,b are the diagrammatic sketch and system schematic of the experimental facility. The experimental setup consists of an ejector, a buffer tank, pressure sensors, mass flow meters, a pressure-reducing valve, a needle valve, an evacuation valve, and a computer. A 3D printing technology is used to manufacture the ejector and nozzles. The nozzles need to be switched on in turn to evaluate the performance of each mode. Considering the safety of the experiment, nitrogen is substituted for hydrogen as the supply gas. In order to meet the experimental requirements, the gas pressure from the cylinder needs to be reduced by the pressure-reducing valve. The mass flow meter is used for measuring the PF mass flow rate and SF mass flow rate, and the pressure sensor is used for checking the pressure of the ejector inlet and outlet. To achieve simulation of the pressure drop in the fuel cell stack, evacuation valve, buffer tank, and needle valve are employed. In addition, the experimental temperature is 293 K, and the flow data and pressure data are collected and stored in the computer.



(a)



(b)

Figure 6. (**a**) Diagrammatic sketch of the experimental facility. (**b**) System schematic of the experimental facility.

4.2. Model Verification

Experimental data is used to validate the CFD model. In the experimental process, the PF pressure is set at 6.0 bar and 7.0 bar by changing the opening of the pressure-reducing valve. The SF pressure and outlet pressure are set at 1.9 bar and 2.1 bar by adjusting the opening of the needle valve and evacuation valve. The experimental conditions are the same as the simulation conditions. As given in Figure 7, the experimental data agree with the simulation data and relative errors are within 7%. The deviation perhaps results from the experimental instrumentation measurement errors and the machining errors of the ejector prototype. Hence, the simulation model can predict the performance of ejector accurately.

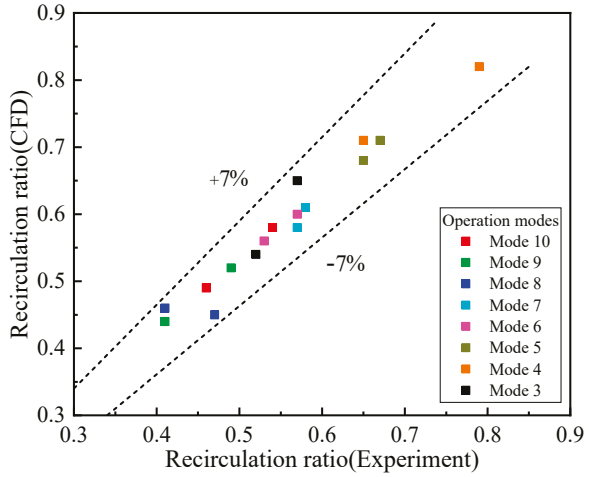


Figure 7. Comparison of experiment and simulation data.

5. Results and Analysis

This part investigates the interior flow field and ejector performance using 3D numerical simulation. The recirculation ratio of ejector is systematically studied under different power and PF pressure conditions.

5.1. Characteristics of the PNFN Ejector's Flow

Figure 8 shows two-dimensional velocity image and velocity streamlined diagram of the PNFN ejector under the different operation modes. The operating conditions are as follows: the dry hydrogen serves as the working fluid, the PF pressure is 7.0 bar, the SF pressure is 1.9 bar, the outlet pressure is 2.1 bar. The operation modes are shown on the left side of Figure 8a.

In the red frame of the two pictures, we can see that inner fluid of the ejector flow along the central axis and the ejector inner flow mechanism is more stable under three modes. From the perspective of flow mechanism, the ejector performance is best under these three modes. The ejector performance is best when the toroidal fourth nozzle and the circular first nozzle work at the same time in mode 6. The superposition of two flows stream in the same direction generates higher velocity, consequently, produces lower pressure which makes the SF be easily sucked. In operation mode 7, the fourth nozzle and the second nozzle work together. In this case, the vortex and backflow phenomena are not found in the ejector inner fluid although there is a certain angle between the fourth nozzle and the second nozzle that may cause partial energy loss. Therefore, the ejector performance is relatively good in this mode. When the fuel cell power changes, the ejector can work at these three modes to meet the recycling requirements by changing the PF pressure. In other modes, either fluid impacts the constant-area mixing chamber wall causing energy losses, or several streams of fluid crashes causing lots of energy lost, or constant-area mixing

chamber entrance appears choking phenomenon, resulting in ejector inner appears serious vortex and backflow phenomenon.

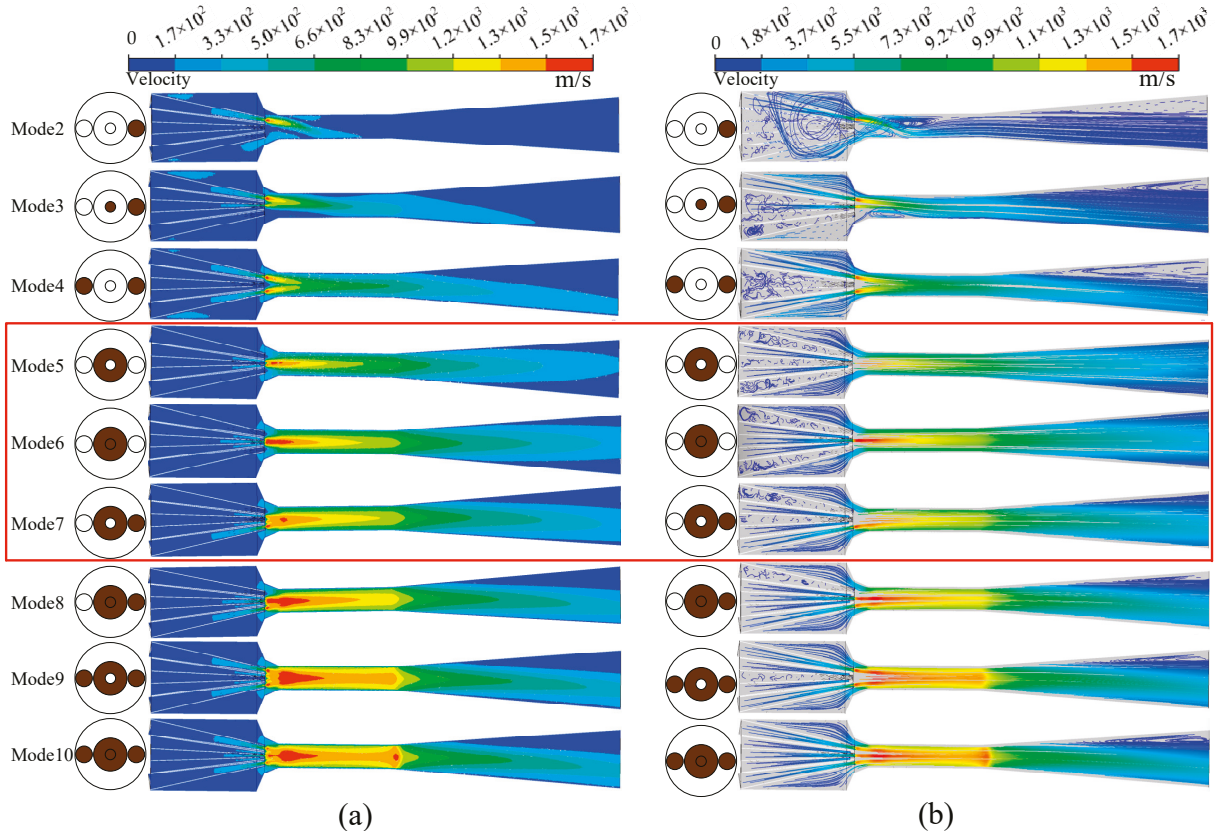


Figure 8. Velocity flow field diagram of the PNFN ejector. (**a**) Velocity image. (**b**) Velocity streamline.

5.2. Performance of the PNFN Ejector

Except structural parameters of the ejector, the PF pressure and outlet pressure significantly affects how well the ejector performs. Figure 9 demonstrates the effects of the PF pressure and the outlet pressure on the recirculation ratio and mass flow of the SF under the fixed SF pressure of 1.9 bar.

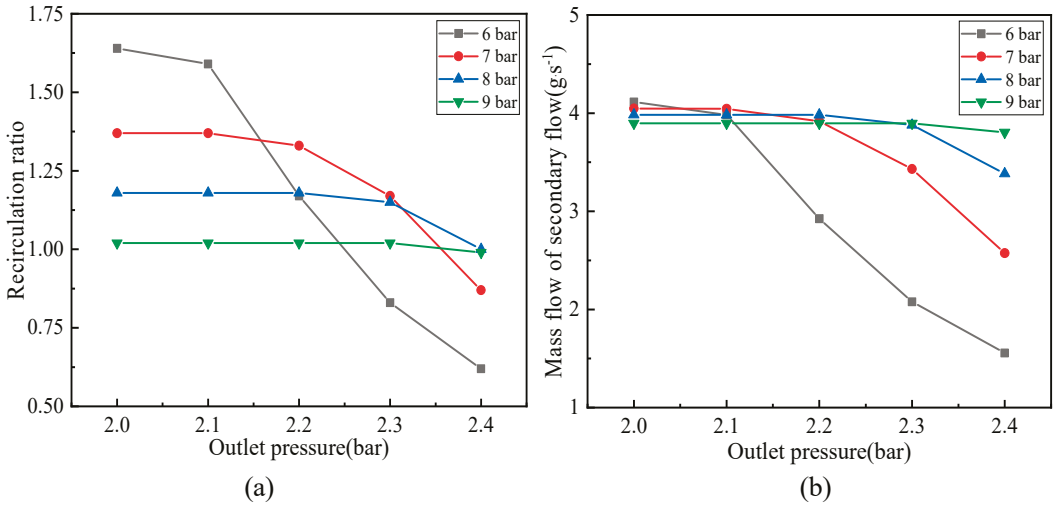


Figure 9. (**a**) PF pressure and outlet pressure's impact on recirculation ratio. (**b**) The impact of the PF pressure and outlet pressure on the mass flow of SF.

As can be seen from the pictures, when the PF pressure is lower than 9 bar, the recirculation ratio and mass flow of SF are easy to be influenced by the outlet pressure. When the PF pressure is fixed, the lower the outlet pressure is, the larger recirculation ratio is. When the outlet pressure is 2.0 bar, each recirculation ratio reaches its maximum value, in which the lower the PF pressure is, the larger the recirculation ratio can be.

The performance of the ejector is significantly impacted by PF pressure and output pressure. When the PF pressure is fixed, the ejector performance decreases with the outlet pressure increasing. The ejector performance is best when the PF pressure is 6.0 bar and outlet pressure is 2.0 bar.

5.3. Performance of the PEMFC System's PNFN Ejector in Terms of Recirculation

Figures 10 and 11 illustrate performances of the PNFN ejector under different operation modes.

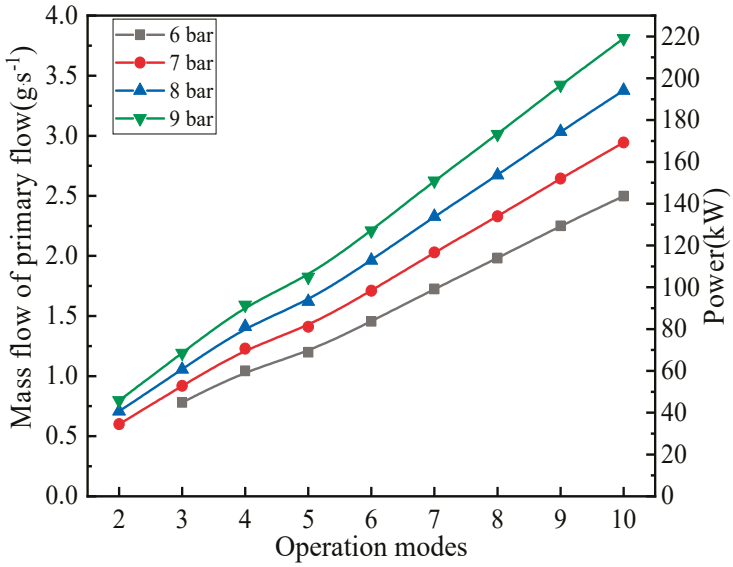


Figure 10. The mass flow of PF and power change at different operation modes.

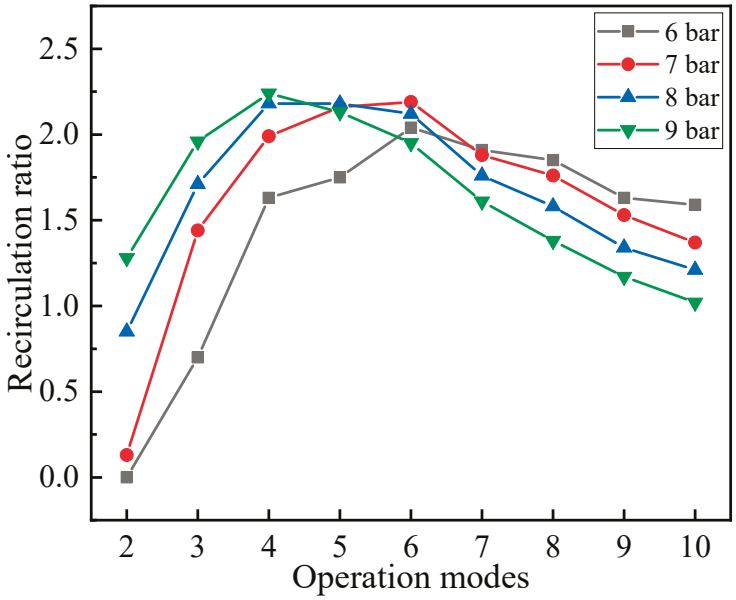


Figure 11. The PNFN ejector's recirculation performance.

The mass flow of PF and the power range of the PNFN ejector relate to the operation modes of the ejector. The working range of the ejector is determined by the mass flow of PF for meeting the power requirement of the PEMFC system. When all the nozzles are working, the ejector can only work at the power of 150 kW when the PF pressure is 6.0 bar and beyond the rated power 170 kW of the fuel cell with the PF pressure increases 7.0 bar. It can be seen in Figure 10 that higher PF pressure makes the rated power can be fulfilled more easily.

Figure 11 shows the change of recirculation ratio with the ejector operation modes at different PF pressures. The maximum recirculation ratio is 1.28 when the pressure is 9 bar and the ejector operates at mode 2. All recirculation ratios reach the maximum value of 2.24 under different PF pressures when the ejector operates in modes 4–6.

The ejector can operate in the 34–220 kW power range by switching operation mode when the PF pressure is in the range of 7.0 bar to 9.0 bar. In the lower power range, increasing the PF pressure can increase the ejector's performance. The PNFN ejector not only expands the PEMFC's operating range, but also adjusts the PF pressure to keep the recirculation ratio above 1.0 which meets the recycling requirement of the PEMFC.

5.4. Performance Comparison of the PNFN and Traditional Ejectors

The traditional ejector is usually designed at a certain operating point of the PEMFC. The performance of the traditional ejector sharply declines and therefore it is difficult meet the power requirements when the PEMFC deviates from the rated power. However, the PNFN ejector can solve the problem and work at a wide power range.

The PNFN ejector at each mode corresponds to a throat diameter of the traditional ejector that Equation (4) can be used to determine the throat diameter of the traditional ejector. Table 7 demonstrates the throat diameter of the traditional ejector while other structures keep fixed.

Table 7. Throat diameter of traditional ejector corresponds to PNFN ejector mode.

Fuel Cell Output Power (kW)	Four-Nozzle Ejector Operation Modes	PF ($g \bullet s^{-1}$)	Traditional Ejector Throat Diameter (mm)
20% Pe	2	0.56	1.4
30% Pe	3	0.81	1.7
40% Pe	4	1.10	1.9
50% Pe	5	1.38	2.0
60% Pe	6	1.66	2.2
70% Pe	7	1.93	2.4
80% Pe	8	2.25	2.5
90% Pe	9	2.49	2.7
100% Pe	10	2.78	2.8

The PNFN ejector and traditional ejector's recirculation ratios are displayed in Figure 12. The two types of ejectors are compared under the same conditions of the PF pressure of 7.0 bar, the SF pressure of 1.9 bar, and the outlet pressure is 2.1 bar.

The recirculation ratio of the PNFN ejector and the traditional ejector exhibit the similar trend, as can be shown in Figure 12. The recirculation ratio of the PNFN ejector is almost equal to that of the corresponding traditional ejector. When the PEMFC's output power is low, the PNFN ejector has a better recirculation ratio that is hard for the traditional ejector to achieve. The performance of the PNFN ejector is good more than the traditional single nozzle ejector. The PNFN ejector can contain working ranges of the many traditional ejectors and overcome the problem that the failure of traditional ejector in variable working conditions.

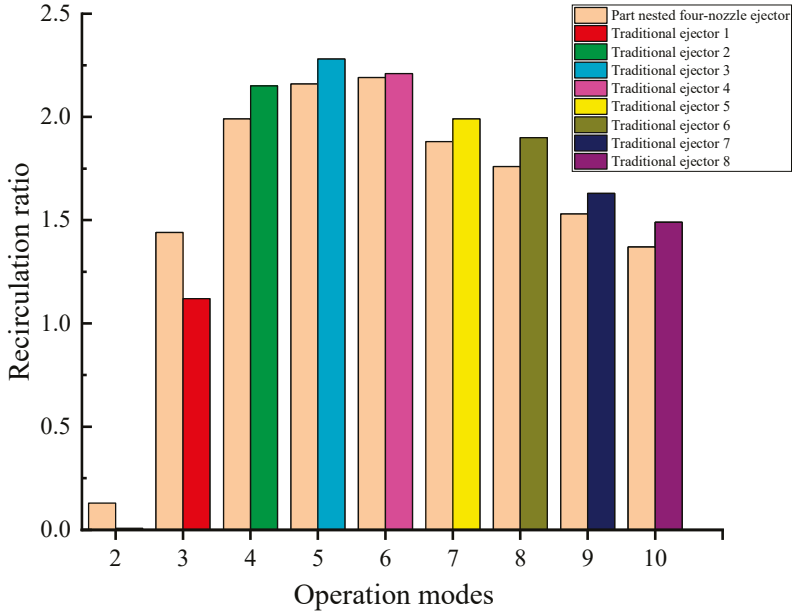


Figure 12. Comparison between two type of ejectors.

5.5. Performance Comparison of Different Configuration Four-Nozzle Ejector

The four nozzles have multiple layout styles with the equal mass flow rate. The ejector performance is largely affected by the ejector nozzle position. The typical nozzle combination types are compared.

Plan 1, the N4 comprises the N1 with the same central axis. The N2 and the N3 have axial symmetry that are distributed on both sides of the N4 at angle of 180°, as shown in Figure 13a.

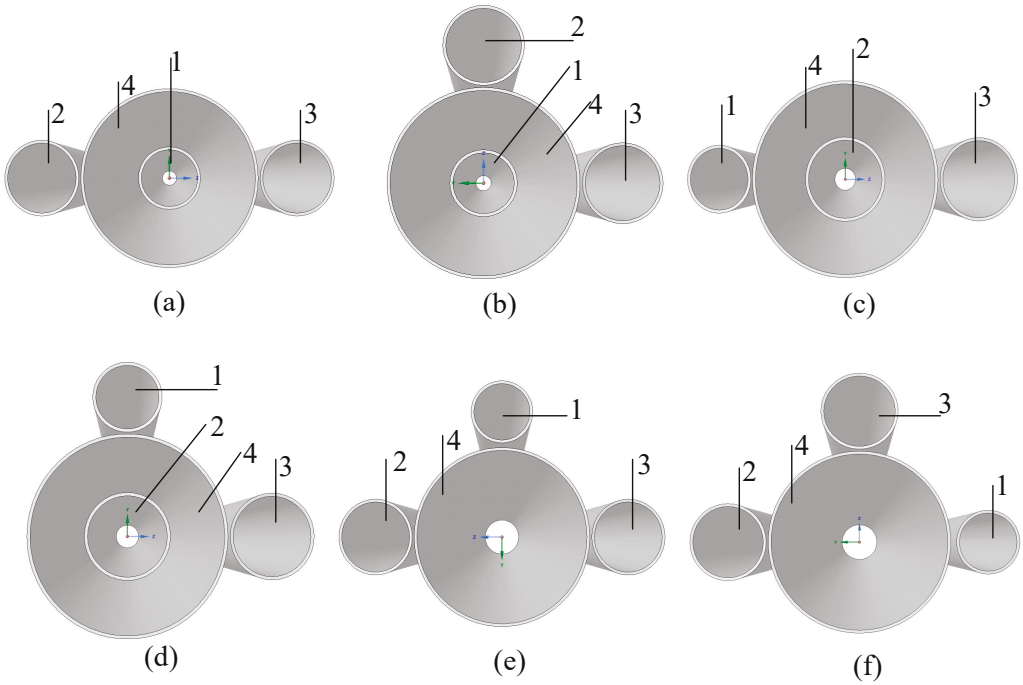


Figure 13. (**a**–**f**) Diagram of plans 1 to 6.

Plan 2, the N4 comprises the N1 with the same central axis. The N2 and the N3 are distributed on adjacent sides of the N4 at angle of 90°, as shown in Figure 13b.

Plan 3, the N4 comprises the N2 (or the N3) with the same central axis. The N3 (or the N2) and the N1 are distributed on opposite sides of the N4 at angle of 180°, as shown in Figure 13c.

Plan 4, the N4 comprises the N2 (or the N3) with the same central axis. The N3 (or the N2) and the N1 are distributed on adjacent sides of the N4 at angle of 180°, as shown in Figure 13d.

Plan 5, the N4 is on the central axis while the N2 and the N3 have axial symmetry distributed on both sides of the N4 at angle of 180°. The N1 locates at another orientation with the N2 and N3 at angle of 90°, as shown in Figure 13e.

Plan 6, the N4 is on the central axis. The N2 and the N3 are distributed on adjacent sides of the N4 at angle of 90°. The N1 is distributed on the other side of the N4 at angle of 90° with the N2 (or the N3), as shown in Figure 13f.

Plan 7, the N4 comprises the N1, the N2 and the N3. The N4 is divided into three regions with each region angle of 120°. The nozzle is drawn on the central plane of each region. The angle of the central axis of the adjacent two nozzles is 120°. The diameter of the N4 is enlarged accordingly in this plan to ensure the fluid flow mass same as in other plans, as shown in Figure 14.

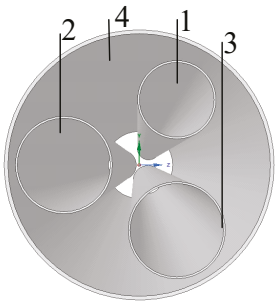


Figure 14. Diagram of Plan 7.

In Figures 13 and 14, the number 1, 2, 3, and 4 represents the N1, N2, N3, and N4, respectively, Blue and green arrows represent the x and y axis of the three-dimensional coordinate axis.

The ejector plans are compared under the same conditions. The dry hydrogen is selected as the working gas under the PF pressure of 7.0 bar, the SF pressure of 1.9 bar, and the outlet pressure of 2.1 bar. The recirculation ratio is used to assess the ejector's performance. Table 8 shows the recirculation ratio value of seven types of ejectors at different operation modes. Figure 15 is ejector curve of the recirculation ratio with different plans.

Table 8. The values of the recirculation ratio of different plans.

Modes \ Plans	Plan 1	Plan 2	Plan 3	Plan 4	Plan 5	Plan 6	Plan 7
3	1.44	1.25	1.24	1.22	1.24	1.28	2.59
4	1.99	1.72	1.74	1.68	2.09	1.57	2.54
5	2.16	2.02	0.96	0.96	1.98	1.97	1.62
6	2.19	2.1	1.63	1.63	1.76	1.78	1.52
7	1.88	1.83	1.68	1.67	1.56	1.53	1.34
8	1.76	1.7	1.76	1.76	1.37	1.37	1.21
9	1.53	1.53	1.83	1.8	1.2	1.2	1.07
10	1.37	1.36	1.67	1.61	1.07	1.07	0.96

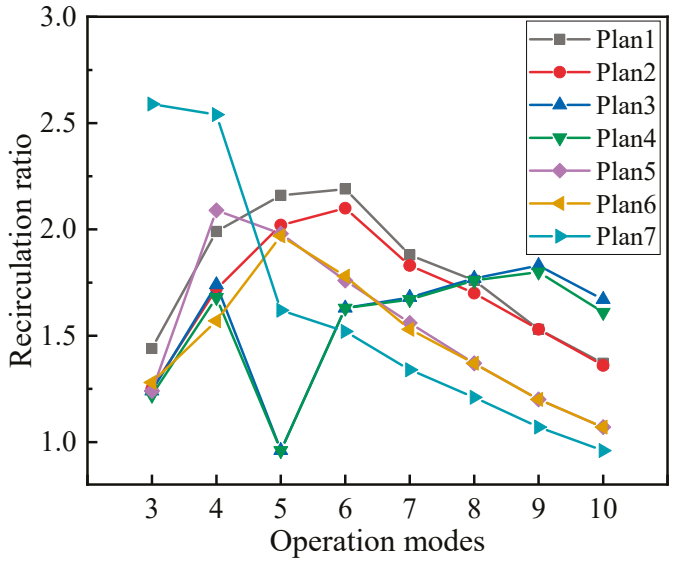


Figure 15. Recirculation ratio curve of the ejector.

It can be seen from the Figure 15 that the performance of Plan 1 is better than that of Plan 2, Plan 5, and Plan 6 in general. As for Plan 3 and Plan 4, their performance curves are very close. Their recirculation ratio values are equal to Plan 1 in operation mode 8. In operation mode 8, the recirculation ratio of Plan 3 and Plan 4 has the minimum value of 0.96. The performance of Plan 7 is better than Plan 1 in mode 3 and mode 4. The performance of Plan 1 is far higher than Plan 7 when the operation modes are 5–10. The performance curve of Plan 7 is descending with the minimum value of 0.96 in mode 10.

By comparing seven types of ejectors, the performance of Plan 3, Plan 4, and Plan 7 are better than that of Plan 1 in individual modes, but performance of Plan 1 is better than that of the other plans at most modes. In general, Plan 1 as previously mentioned has the best overall performance.

6. Conclusions

In this study, a new type of part nested four-nozzle (PNFN) ejector is proposed in order to substitute for the traditional ejector to meet the hydrogen recycle requirement in the high-power PEMFC system within the full power range. The four nozzles are designed at 10%, 20%, 20%, and 50% of the PEMFC rated power. The internal flow properties and recirculation performance of the PNFN ejector are studied using a 3D numerical model of the device. The PNFN ejector can meet the flow requirements in the high-power fuel cell full power range by switching the nozzle's working conditions. The main conclusions are as follows:

1. The ejector inner flow field is at the most stable state and ejector performance reach the best value point when the first nozzle and the fourth nozzle (mode 6) work together. By observing the velocity field image and velocity streamline map, the ejector inner flow mechanism becomes more complex with the increase of working nozzles.
2. The PNFN ejector with different operation modes can operate in the 34–220 kW power range with the recirculation ratio above 1.0 when the PF pressure range is between 7–9 bar.
3. The PNFN ejector performs better than the traditional single nozzle ejector in the whole power range. It's worth noting that the PNFN ejector has better performance compared to traditional ejectors in the low power zone.
4. The performance of the PNFN ejector (Plan 1) is better than other combined plans by comparing the typical combined plans of the four nozzles.

Author Contributions: Conceptualization, C.W., L.W. and X.W.; methodology, C.W., L.W. and X.W.; Investigation, A.Y.; Soft, A.Y.; Writing—original draft, A.Y.; Writing—review & editing, C.W., L.W. and X.W. All authors have read and agreed to the published version of the manuscript.

Funding: The work was funded by the National Key Research and Development Program of China (Grant No. 2019YFB1504700), the National Natural Science Foundation of China (Grant No. 52306256) and China Postdoctoral Science Foundation (Grant No. 2023M732048).

Data Availability Statement: Data are contained within the article.

Conflicts of Interest: The authors declare no conflict of interest.

Nomenclature

A	area (m^2)
D	diameter (m)
Dq,m	mass diffusion coefficient ($m^2\ s^{-1}$)
DT,q	Thermal diffusion coefficient ($m^2\ s^{-1}$)
E	total energy ($J\ kg^{-1}$)
F	Faraday's constant ($C\ mol^{-1}$)
$\vec{g}$	gravitational acceleration ($m\ s^{-2}$)
$G_b G_k$	turbulence kinetic energy generation ($J\ m^{-3}\ s^{-1}$)
h	enthalpy ($J\ kg^{-1}$)
$\vec{I\,J}$	unit tensordiffusion flux ($kg\ m^{-2}\ s^{-1}$)
k	turbulent kinetic energy ($m^2\ s^{-2}$)
L	length (m)
m	mass flow rate ($kg\ s^{-1}$)
M	molar weight ($kg\ mol^{-1}$)
P	pressure (Pa)
P_{stack}	power (W)
R	gas constant ($J\ mol^{-1}\ K^{-1}$)
S_{ct}	Schmidt number
T	temperature (K)
v_{cr}	critical velocity ($m\ s^{-1}$)
$\vec{v}$	velocity vector ($m\ s^{-1}$)
V_c	single cell voltage (V)
Y	mass fraction
Y_M	the fluctuating expansion to total dissipation ratio in compressible turbulent
Greek letters	
ε	turbulence kinetic energy dissipation rate ($m^2\ s^{-3}$)
θ	angle (°)
α_k	inverse effective Prandtl numbers
κ	specific heat ratio
λ	stoichiometric ratio/thermal conductivity ($W\ m^{-1}\ K^{-1}$)
μ	dynamic viscosity ($N\ s\ m^{-2}$)
ρ	density ($kg\ m^{-3}$)
ω	recirculation ratio
μ	dynamic viscosity ($N\ s\ m^{-2}$)
ρ	density ($kg\ m^{-3}$)
Subscript	
r	recirculated hydrogen
c	hydrogen consumption
cam	constant-area mixing chamber
cpm	constant-pressure mixing chamber
d	diffusion
H_2	hydrogen
i, j	direction
nt	nozzle throat
N1	first nozzle
N2	second nozzle
N3	
N4	fourth nozzle
Abbreviations	
CFD	computational fluid dynamics
NXP	nozzle exit position
PEMFC	polymer electrolyte membrane fuel cell
PNFN	part nested four-nozzle
PF	primary flow
SF	secondary flow

References

1. Liu, Z.; Chen, J.; Liu, H.; Yan, C.; Hou, Y.; He, Q.; Zhang, J.; Hissel, D. Anode purge management for hydrogen utilization and stack durability improvement of PEM fuel cell systems. *Appl. Energy* **2020**, *275*, 115110. [CrossRef]
2. Rodosik, S.; Poirot-Crouvezier, J.-P.; Bultel, Y. Simplified anode architecture for PEMFC systems based on alternative fuel feeding: Experimental characterization and optimization for automotive applications. *Int. J. Hydrogen Energy* **2020**, *45*, 19720–19732. [CrossRef]
3. Wang, X.; Zhong, W.; Xiao, B.; Liu, Q.; Yang, L.; Covaci, A.; Zhu, L. Bioavailability and biomagnification of organophosphate esters in the food web of Taihu Lake, China: Impacts of chemical properties and metabolism. *Environ. Int.* **2019**, *125*, 25–32. [CrossRef] [PubMed]
4. Zhu, Y.; Yousefi, N. Optimal parameter identification of PEMFC stacks using Adaptive Sparrow Search Algorithm. *Int. J. Hydrogen Energy* **2021**, *46*, 9541–9552. [CrossRef]

5. Chen, H.; Song, Z.; Zhao, X.; Zhang, T.; Pei, P.; Liang, C. A review of durability test protocols of the proton exchange membrane fuel cells for vehicle. *Appl. Energy* **2018**, *224*, 289–299. [CrossRef]
6. Kazim, A. Introduction of PEM fuel-cell vehicles in the transportation sector of the United Arab Emirates. *Appl. Energy* **2003**, *74*, 125–133. [CrossRef]
7. Pei, P.; Chen, H. Main factors affecting the lifetime of Proton Exchange Membrane fuel cells in vehicle applications: A review. *Appl. Energy* **2014**, *125*, 60–75. [CrossRef]
8. Li, W.; Wang, X.; Wang, L.; Jia, L.; Song, R.; Fu, Z.; Xu, W. An LSTM and ANN Fusion Dynamic Model of a Proton Exchange Membrane Fuel Cell. *IEEE Trans. Ind. Inform.* **2023**, *19*, 5743–5751. [CrossRef]
9. Hwang, J.-J. Passive hydrogen recovery schemes using a vacuum ejector in a proton exchange membrane fuel cell system. *J. Power Sources* **2014**, *247*, 256–263. [CrossRef]
10. Li, F.; Du, J.; Zhang, L.; Li, J.; Li, G.; Zhu, G.; Ouyang, M.; Chai, J.; Li, H. Experimental determination of the water vapor effect on subsonic ejector for proton exchange membrane fuel cell (PEMFC). *Int. J. Hydrogen Energy* **2017**, *42*, 29966–29970. [CrossRef]
11. Toghyani, S.; Afshari, E.; Baniasadi, E. A parametric comparison of three fuel recirculation system in the closed loop fuel supply system of PEM fuel cell. *Int. J. Hydrogen Energy* **2019**, *44*, 7518–7530. [CrossRef]
12. Liu, Y.; Luo, X.; Tu, Z.; Chan, S.H. Droplet Dynamics in a Proton Exchange Membrane Fuel Cell with Ejector-Based Recirculation. *Energy Fuels* **2021**, *35*, 11533–11544. [CrossRef]
13. Liu, Y.; Tu, Z.; Chan, S.H. Applications of ejectors in proton exchange membrane fuel cells: A review. *Fuel Process. Technol.* **2021**, *214*, 106683. [CrossRef]
14. Kim, M.; Sohn, Y.-J.; Cho, C.-W.; Lee, W.-Y.; Kim, C.-S. Customized design for the ejector to recirculate a humidified hydrogen fuel in a submarine PEMFC. *J. Power Sources* **2008**, *176*, 529–533. [CrossRef]
15. Dadvar, M.; Afshari, E. Analysis of design parameters in anodic recirculation system based on ejector technology for PEM fuel cells: A new approach in designing. *Int. J. Hydrogen Energy* **2014**, *39*, 12061–12073. [CrossRef]
16. Yin, Y.; Fan, M.; Jiao, K.; Du, Q.; Qin, Y. Numerical investigation of an ejector for anode recirculation in proton exchange membrane fuel cell system. *Energy Convers. Manag.* **2016**, *126*, 1106–1117. [CrossRef]
17. Maghsoodi, A.; Afshari, E.; Ahmadikia, H. Optimization of geometric parameters for design a high-performance ejector in the proton exchange membrane fuel cell system using artificial neural network and genetic algorithm. *Appl. Therm. Eng.* **2014**, *71*, 410–418. [CrossRef]
18. Yang, Y.; Du, W.; Ma, T.; Lin, W.; Cong, M.; Yang, H.; Yu, Z. Numerical studies on ejector structure optimization and performance prediction based on a novel pressure drop model for proton exchange membrane fuel cell anode. *Int. J. Hydrogen Energy* **2020**, *45*, 23343–23352. [CrossRef]
19. Pei, P.; Ren, P.; Li, Y.; Wu, Z.; Chen, D.; Huang, S.; Jia, X. Numerical studies on wide-operating-range ejector based on anodic pressure drop characteristics in proton exchange membrane fuel cell system. *Appl. Energy* **2019**, *235*, 729–738. [CrossRef]
20. Wang, L.; Yan, J.; Wang, C.; Li, X. Numerical study on optimization of ejector primary nozzle geometries. *Int. J. Refrig.* **2017**, *76*, 219–229. [CrossRef]
21. Amin, B.; Tavousi, E.; Noghrehabadi, A.; Behbahani-Nejad, M. Study of a novel inlet geometry for ejectors. *Int. J. Refrig.* **2022**, *139*, 113–127. [CrossRef]
22. Brunner, D.A.; Marcks, S.; Bajpai, M.; Prasad, A.K.; Advani, S.G. Design and characterization of an electronically controlled variable flow rate ejector for fuel cell applications. *Int. J. Hydrogen Energy* **2012**, *37*, 4457–4466. [CrossRef]
23. Jenssen, D.; Berger, O.; Krewer, U. Improved PEM fuel cell system operation with cascaded stack and ejector-based recirculation. *Appl. Energy* **2017**, *195*, 324–333. [CrossRef]
24. He, J.; Choe, S.-Y.; Hong, C.-O. Analysis and control of a hybrid fuel delivery system for a polymer electrolyte membrane fuel cell. *J. Power Sources* **2008**, *185*, 973–984. [CrossRef]
25. Nikiforow, K.; Koski, P.; Ihonen, J. Discrete ejector control solution design, characterization, and verification in a 5 kW PEMFC system. *Int. J. Hydrogen Energy* **2017**, *42*, 16760–16772. [CrossRef]
26. Xue, H.; Wang, L.; Zhang, H.; Jia, L.; Ren, J. Design and investigation of multi-nozzle ejector for PEMFC hydrogen recirculation. *Int. J. Hydrogen Energy* **2020**, *45*, 14500–14516. [CrossRef]
27. Wang, X.; Xu, S.; Xing, C. Numerical and experimental investigation on an ejector designed for an 80 kW polymer electrolyte membrane fuel cell stack. *J. Power Sources* **2019**, *415*, 25–32. [CrossRef]

Disclaimer/Publisher's Note: The statements, opinions and data contained in all publications are solely those of the individual author(s) and contributor(s) and not of MDPI and/or the editor(s). MDPI and/or the editor(s) disclaim responsibility for any injury to people or property resulting from any ideas, methods, instructions or products referred to in the content.

inventions

MDPI

Article

A Modified Phase-Transition Model for Multi-Oscillations of Spark-Generated Bubbles

Rui Han [1,*], Jiayi Chen [1,2] and Taikun Guo [1]

[1] College of Nuclear Science and Technology, Harbin Engineering University, Harbin 150001, China; 18846076791@163.com (J.C.); 17866603769@163.com (T.G.)
[2] China Nuclear Power Technology Research Institute Co., Ltd., Shenzhen 518000, China
* Correspondence: hanrui@hrbeu.edu.cn

Abstract: The main composition within a spark-generated bubble primarily consists of vapor, accompanied by a minor presence of noncondensable gases. The phase transition exerts a substantial influence on bubble dynamics throughout various stages, a facet that has been frequently overlooked in prior research. In this study, we introduce a modified theoretical model aimed at accurately predicting the multiple oscillations of spark-generated bubbles. Leveraging the Plesset equation, which integrates second-order corrections for compressibility and non-equilibrium evaporation, we further incorporate the thermal boundary layer approximation for bubbles, as proposed by Zhong et al. We employ an adjusted phase transition duration tailored to the unique characteristics of spark-generated bubbles. Furthermore, we meticulously ascertain initial conditions through repeated gas content measurements within the bubble. Our proposed theoretical model undergoes rigorous validation through quantitative comparisons with experimental data, yielding commendable agreement in modeling the dynamic behavior of bubbles across multiple cycles. Remarkably, we uncover that the condensation rate significantly governs the behavior of spark bubbles during their initial two cycles. Finally, we investigate the dependence of spark-generated bubble dynamics on the phase transition and the presence of air. Air content exhibits a minimal impact on bubble motion prior to the initial bubble collapse, but plays a role in the bubble's rebound thereafter.

Keywords: spark-generated bubble; bubble dynamics

1. Introduction

The cavitation phenomenon is the process of formation, development and collapse of vapor or gas holes inside the liquid or at the liquid–solid interface when the local pressure in the liquid drops below the saturated vapor pressure, which widely exists in nature and engineering applications [1–5]. In the cavitation process, cavitation bubble dynamics as an academic research topic is of great significance for many industrial applications. Due to the rapid generation, expansion and collapse of cavitation, shock waves and high-speed microjets are generated, and the impact of the metal material will accelerate the electrochemical corrosion process and cause material ablation. Additionally, because a large number of gas molecules gather inside the very small cavitation bubble within a very short collapse phase, it can even produce local high temperature of thousands of degrees and high pressure of thousands of standard atmospheric pressures. All of the above may cause severe damage to structures.

Researchers have conducted many experiments to explore cavitation bubbles dynamics. There are generally three methods to generate cavitation bubbles in the laboratory: ultrasound, pulsed laser, and electric discharge [5–7]. Underwater electric discharge is more commonly used because of its controllability and economy, and generated bubbles are often called spark-generated bubble. The content inside a spark-generated bubble is mainly vapor and some special non-condensable gas may also exists [8]. Luo and Xu [9]

used low voltage discharge method to produce cavitation bubbles, and the combination of high-speed photography and a pressure measurement system allowed for simultaneous observation and measurement of the evolution of the shock wave and the change in shock wave strength with the presence of the air bubble in the vicinity. The high-speed imaging revealed the predominant roles of the relative distance and relative size between the cavitation and air bubbles in the determination of the stratification effect that the air bubble exerted on the shock wave produced from the first collapse of the cavitation bubble.

The development of theoretical models is also an important part of studying the dynamic behavior of bubbles, and the current research on cavitation bubbles mainly focuses on the formation of bubbles, the influence of shock waves and boundary conditions on the collapse characteristics of bubbles [10–12]. Fujikawa and Akamastu [13] considered the compressibility, heat transfer, and non-equilibrium evaporation and condensation of vapors, and proposed an analytical model that showed that evaporation and condensation strongly affect the bubble dynamics. Han [14] experimentally, numerically and theoretically investigate the nonlinear interaction between a spark cavitation bubble and the interface of two immiscible fluids (oil and water) on multiple time scales, but she also only focused on the first cycle of bubble motion. Thereafter, Zhang [15] established a novel theory for the dynamics of oscillating bubbles that can simultaneously take into consideration the effects of boundaries, bubble interaction, ambient flow field, gravity, bubble migration, fluid compressibility, viscosity, and surface tension, but his theory still does not consider the effect of phase transitions in vapor.

With the development of bubble dynamics, people began to pay attention to the condensation of vapor in bubbles [16–24]. Phan [19] used the two-phase heterogeneous mixing model to simulate the bubble motion of spark-generated cavitation containing vapor, and by comparing with the experimental data, the results showed that the condensation phenomenon mainly occurs at the vapor–water interface with a thin boundary layer, the evaporation phenomenon mainly occurs in the bubble, and the temperature change of the flow field has little effect on the first two cycles of bubble motion. However, his model can only predict the first two cycles of bubble motion, and according to our results, the difference between the predicted radius and experimental data of different models mainly occurs after two cycles of motion, taking into account the condensation and evaporation of vapor. Zhong [20] established a laser cavitation bubble model, adopted the modified Rayleigh–Plesset equation, and established an interpolation function to try to obtain the optimal initial motion conditions of the bubble for many times, the numerical results were consistent with the evolution of laser cavitation bubble, and the influence of condensation coefficient on the bubble motion radius, the maximum temperature and pressure peak at collapse were discussed, but the model was only applicable to laser cavitation bubbles. Mustafin [22] presented a numerical technique for studying the collapse and rebound of a spherical cavitation bubble in an unbounded volume of water. The dynamics of the vapor in the bubble and the surrounding liquid is governed by the equations of gas dynamics with allowing for the heat conductivity of the fluids, the heat and mass exchange across the bubble surface. His theory focuses on verifying the reliability of computational methods for the new setting of non-reflecting boundary conditions.

As the non-condensable gas in the bubble has damping effects, which can weaken the pressure wave when the bubble collapses and enhance the bubble rebound, Trummler [25] used a uniform mixing model with the coupled equation of the state of all components to study this damping effect, and the numerical results proved that the free air in the vapor bubble will cause the bubble to bounce stronger and weaken the emitted shock wave strength. In addition, Sato [26] proved through experiments that hydrogen molecules will be generated when cavitation bubbles are induced by laser or electric sparks, and the hydrogen content of different types of cavitation bubbles is determined by monitoring the dissolved hydrogen concentration in water, and it was found that the mass of dissolved hydrogen is proportional to the potential energy of the rebound bubbles, indicating that different types of gas content may change the dynamic behavior of bubbles. Kerboua [27]

considered the heat loss caused by the chemical reaction during the bubble motion, and the results showed that considering the chemical reaction leads to a decrease in the temperature in the bubble and an increase in the pressure peak during collapse. However, none of them quantified the magnitude of the effect of these non-condensable gases on bubble motion.

In the present study, a modified theoretical model is proposed to accurately predict multi-oscillations of spark-generated bubbles. This paper is structured as follows. In Section 2, details about the modified theoretical model and experimental setup are given. In Section 3, the proposed theoretical model is validated by quantitative comparison with our experiments. And then the effects of phase transition duration and air content on the bubble motion are discussed in detail in Section 4. Finally, conclusions are made.

2. Methodology

2.1. A Modified Theoretical Model

First, we assume a spherical bubble with evenly distributed internal temperature and pressure. Regardless of the change in the density of the liquid medium caused by the propagation of sound in the liquid, gravity and the chemical reactions that may occur in the bubbles are ignored. Based on Yasui's theoretical results [28], it is assumed that there are two thin hot layers on the surface of the bubble, i.e., inner and outer hot layers, as shown in Figure 1. The thickness of the inner and outer hot layers are δ_1 and δ_2 , respectively. The heat conduction, evaporation and condensation between the gas inside the bubble and the flow field only occur in the inner hot layer, and the temperature changes linearly from T inside the bubble surface T to T_B at the bubble surface in the inner hot layer. We assume that the temperature T_l in the outer hot layer is the same as the flow field temperature at infinity T_∞, then there is a temperature difference between the two hot layers.

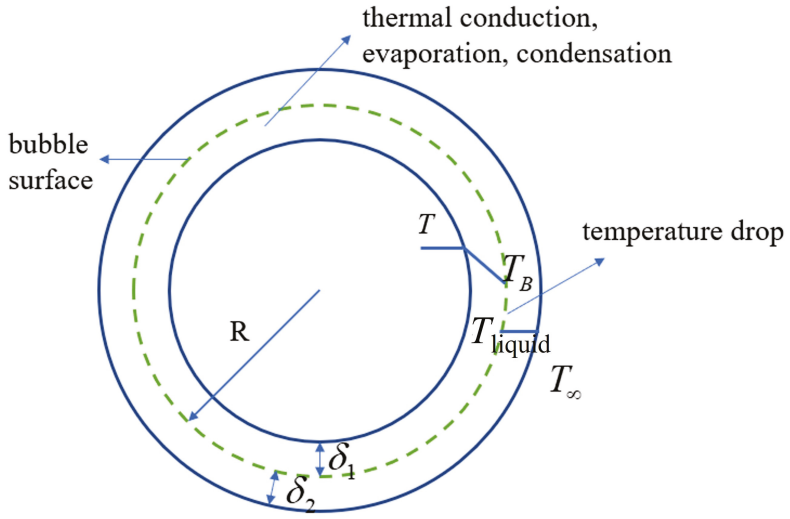


Figure 1. Two thermal boundary layers on the bubble surface.

A second-order modified Rayleigh–Plesset equation is used, with non-equilibrium evaporative condensation taken into consideration [29].

$$
\begin{aligned}
&R\left(\ddot{R}-\frac{\ddot{m}}{\rho_1}\right)\left[1-\frac{1}{c}\left(2\dot{R}-\frac{\dot{m}}{\rho_1}\right)+\frac{1}{c^2}\left(\frac{23\dot{R}^2}{10}-\frac{31\dot{m}\dot{R}}{10\rho_1}-\frac{\dot{m}^2}{5{\rho_1}^2}\right)\right]\\
&+\frac{3}{2}\left(\dot{R}-\frac{\dot{m}}{\rho_1}\right)\left[\dot{R}+\frac{\dot{m}}{3\rho_1}-\frac{4\dot{R}^2}{3c}+\frac{1}{c^2}\left(\frac{7\dot{R}^3}{5}-\frac{49\dot{m}\dot{R}^2}{30\rho_1}-\frac{14\dot{m}^2\dot{R}}{15\rho_1}-\frac{\ddot{m}^3}{6{\rho_1}^3}\right)\right]\\
&+\frac{1}{\rho_1}\left[p_\infty-p_{B,2}-\frac{R\dot{p}_{B,1}}{c}+\frac{1}{c^2}\left\{\left(2\dot{R}-\frac{\dot{m}}{\rho_1}\right)\frac{R\dot{p}_{B,1}}{c}+(p_\infty-p_{B,1})\left[\frac{\dot{R}^2}{2}-\frac{3\dot{m}\dot{R}}{2\rho_1}-\frac{\dot{m}^2}{{\rho_1}^2}+\frac{3(p_\infty-p_{B,1})}{2\rho_1}\right]\right\}\right]=0
\end{aligned}
\tag{1}
$$

in which

$$p_{B,1} = p - \frac{2\sigma}{R} - \frac{4\mu}{R}\left(\dot{R} - \frac{\dot{m}}{\rho_l}\right) - \dot{m}^2\left(\frac{1}{\rho_l} - \frac{1}{\rho_g}\right) \tag{2}$$

$$p_{B,2} = p_{B,1} + \frac{4\mu}{3c^2}\left[\frac{3\dot{m}}{2\rho_l R}\left(\dot{R} - \frac{\dot{m}}{\rho_l}\right)^2 - \frac{\dot{p}_{B,1}}{\rho_l} + \frac{\dot{m}(p_\infty - p_{B,1})}{{\rho_l}^2 R}\right] \tag{3}$$

Among them, R, c, ρ_l, σ, μ, p and p_∞ are bubble radius, sound velocity in water, water density, surface tension coefficient, viscosity, bubble internal pressure, and flow field pressure at infinity, respectively. $\dot{m}$ is the net rate of evaporation per unit area per unit time of bubbles. ρ_g is the average density of the gas in the bubble, satisfying

$$\rho_g = \frac{M_{vapor} n_{vapor} + M_{air} n_{air}}{V N_A} \tag{4}$$

In which, M_{vapor}, M_{air}, n_{vapor} and n_{air} are the molar mass of vapor in the bubble, the molar mass of air, the molecular number of vapor and the number of air molecules, respectively, and N_A is the Avogadro constant.

With the Van der Waals equation, the pressure inside the bubble can be calculated using the number of vapor molecules and the number of air molecules inside the bubble [28,29].

$$\left(p + \frac{a}{v^2}\right)(v - b) = R_g T \tag{5}$$

in which

$$a = a_{air}\left(\frac{n_{air}}{n_t}\right)^2 + 2\sqrt{a_{air} a_{vapor}}\left(\frac{n_{air}}{n_t}\right)\left(\frac{n_{vapor}}{n_t}\right) + a_{vapor}\left(\frac{n_{vapor}}{n_t}\right)^2 \tag{6}$$

$$b = b_{air}\left(\frac{n_{air}}{n_t}\right)^2 + 2\sqrt{b_{air} b_{vapor}}\left(\frac{n_{air}}{n_t}\right)\left(\frac{n_{vapor}}{n_t}\right) + b_{vapor}\left(\frac{n_{vapor}}{n_t}\right)^2 \tag{7}$$

R_g and T are the gas constant and the temperature inside the bubble. v is the molar volume $v = N_A V / n_t$, n_t is the total number of molecules in the bubble $n_t = n_{air} + n_{vapor}$, and V is the bubble volume. The non-equilibrium evaporation and condensation processes of vapor in the bubble are modeled by a modified Hertz–Knudsen–Langmuir relationship [23].

$$\dot{m} = \dot{m}_{eva} - \dot{m}_{con} \tag{8}$$

$$\dot{m}_{eva} = \frac{\alpha_M}{\sqrt{2\pi R_v}} \frac{p_v^*\left(T_{liquid}\right)}{\sqrt{T_{liquid}}} \tag{9}$$

$$\dot{m}_{con} = \frac{\alpha_M}{\sqrt{2\pi R_v}} \frac{\Gamma p_v}{\sqrt{T_B}} \tag{10}$$

$\dot{m}_{eva}$ and $\dot{m}_{con}$ are the evaporation rate and condensation rate per unit area of bubbles; respectively; α_M is the ratio of the number of vapor molecules penetrating the bubble wall to the number of vapor molecules hitting the bubble wall, and $\alpha_M = 0.04$ [30]. The saturated vapor pressure of water is obtained by $p_v^*\left(T_{liquid}\right) = \exp(77.345 + 0.0057 T_{liquid} - 7235/T_{liquid})/T_{liquid}$[8.2]. R_v is the vapor gas constant, and p_v is the actual vapor partial pressure in the bubble. Γ is the correction factor, which is set as 1.

The temperature change at the gas-liquid interface is expressed as

$$T_B - T_{liquid} = \Lambda \frac{\partial T_l}{\partial r}|_{r=R} \tag{11}$$

$$\Lambda = -\frac{1}{2kn'}\sqrt{\frac{\pi\bar{m}}{2kT_B}}\frac{2 - a'\alpha_e}{\alpha_e}\kappa \tag{12}$$

In which $a' = 0.827$. α_e, κ and k are the thermal containment coefficient, the thermal conductivity of vapor and the Boltzmann constant, respectively. $n' = n_t/V$ indicates the density of molecules within a bubble. $\bar{m} = \left(n_{vapor}M_{vapor} + n_{air}M_{air}\right)/\left(N_A n_t\right)$ indicates the average molecular mass inside the bubble. $\partial T_1/\partial r(r = R)$ represents the temperature gradient in the inner hot layer δ_1 on the surface of the bubble. Yasui assumes that the temperature in the thermosphere varies linearly and can therefore be simplified to [27,31,32]

$$\frac{\partial T_{liquid}}{\partial r}|_{r=R} \approx \frac{T_B - T}{\delta_1} \tag{13}$$

The thermal boundary layer δ_1 thickness is the molecular free path. Plesset and Prosperetti theorize that the thickness of the thermal boundary layer is related to the change of the radius during the violent collapse of the bubble, and $\partial T_1/\partial r(r = R)$ becomes larger only when the internal temperature of the bubble is high, and the radius of the bubble is small and about to collapse. In order to calculate the bubble motion period more completely, in the present study, it is assumed that the temperature of the second thermal layer is equal to the surrounding temperature, i.e., $T_{liquid} = T_\infty$. The main reason is that the specific heat capacity of water is large compared with the internal gas. Additionally, Jebali and Francois [33] demonstrated that the thermal resistance on the liquid side of the interface can be neglected. Therefore, $T_{liquid} - T_\infty$ is always equal to 0 during the bubble motion, taking the moment when the bubble radius reaches its maximum as the starting point, and the thickness of the hot layer δ_2 is inversely proportional to the square of the bubble radius, which is $\delta_2 \sim 1/R^2$, while assuming that the heat flux through the liquid–vapor interface is continuous, i.e., [20]

$$\kappa\frac{\partial T_{liquid}}{\partial r}|_{r=R} = k_l\frac{\partial T_2}{\partial r}|_{r=R} = 2k_l\frac{T_\infty - T_{liquid}}{\delta_2} \tag{14}$$

$$\frac{\partial T_1}{\partial r}|_{r=R} \approx \frac{(T_B - T)R^2}{{\delta_1}^{(0)}R_0^2} \tag{15}$$

which indicates the thickness of the thermal layer δ_1 at the initial moment. The temperature in the bubble is updated according to the energy change [18],

$$\dot{E} = -4\pi R^2\dot{R}P + 4\pi R^2\left[\dot{m}_{eva}e_{vapor}(T_l) - \dot{m}_{con}e_{vapor}(T_B)\right]\frac{N_A}{M_{vapor}} + 4\pi R^2\kappa\frac{\partial T_1}{\partial r}|_{r=R} + \sigma_r 4\pi R^2\left(T_B^4 - T^4\right) \tag{16}$$

On the right side of the equation, the first term represents the work carried out by the flow field on the bubble when it moves, the second term represents the energy reduced by vapor evaporation condensation, the third term represents the energy of the heat conduction change between the gas and the flow field in the bubble, and the fourth term represents the energy change caused by thermal radiation.

The formula for calculating the temperature change in the bubble is

$$\dot{T} = \frac{\dot{E}}{Mc'_v} \tag{17}$$

where $c'_v = \left(M_{air}c_{vair} + M_{vapor}c_{vvapor}\right)/\left(M_{air} + M_{vapor}\right)$ is the average specific heat capacity of the gas in the bubble.

Sato's [26] experiments found that due to the collision dissociation and electrolysis of the spark-generated bubble, the hydrogen mass of the spark-generated bubble is 2.7 times that of the laser bubble, and the rebound potential energy of the spark-generated bubble is significantly greater than that of the laser bubble because the potential energy of the rebound bubble is proportional to the mass of dissolved hydrogen. Therefore, the laser bubble model that always considers vapor condensation in the calculation process will overpredict the effect of condensation on the spark-generated bubble, so that the predicted bubble rebound radius is too small. In our model, when the bubble moves to the maximum

radius in the second cycle of the spark-generated bubble, that is, the corresponding condensation rate is the minimum. After that, the mass transfer between the bubble and the flow field is ignored, and the gas in the bubble is considered to be an ideal gas, satisfying the ideal gas equation of state, that is

$$P = \frac{M_{\text{total}} R_{\text{g}} T}{V} \tag{18}$$

where M_{total} is the total mass of the bubble, including air and vapor. Since it is believed that the vapor no longer condenses in the subsequent cycle, only considering the influence of liquid compressibility, the bubble dynamics equation is replaced with a spherical bubble dynamics equation that only considers compressibility [29,34–36]

$$\left(1 - \frac{1}{c}\dot{R}\right) R\ddot{R} + \frac{3}{2}\left(1 - \frac{1}{3c}\dot{R}\right)\dot{R}^2 = \left(1 + \frac{1}{c}\dot{R}\right)\frac{1}{\rho}(P - P_\infty) + \frac{R}{\rho c}\dot{P} \tag{19}$$

where $\dot{P}$ is the derivative of pressure in the bubble over time. At this time, the energy in the bubble changes to

$$\dot{E} = -4\pi R^2 \dot{R} P - \kappa_{\text{a}}(T - T_\infty) \tag{20}$$

The second term on the right side of the equation indicates the energy change caused by the heat conduction between the bubble and the flow field, κ_{a} is the heat transfer coefficient between the bubble and the water, which is generally 2000∼7000 $\text{W}/\left(\text{m}^2 \cdot \text{K}\right)$. The bubble temperature can still be updated according to Equation (17).

2.2. Experimental Set-Up

As shown in Figure 2, the present experimental devices include: a high-voltage discharge system, a high-speed camera, an adjustable structure positioning device and lighting source and a series of equipment [14,37]. We conducted experiments in a transparent water tank of $30 \times 30 \times 60$ $\left(\text{cm}^3\right)$, using a DC voltage discharge box. When the voltage reaches the set working conditions, electric discharge occurs and the liquid vaporized by short circuit of lapping 0.25 mm diameter thin copper wire. And thus a spark-generated bubbles is formed.

Under this discharge voltage condition, the maximum radius of the oscillating bubble is about 15∼20 mm, and the radius of the copper wire is about 1.25∼1.67% of the maximum bubble radius, indicating a minor effect on the bubble motion. The distance from the bubble center to the nearest tank wall is greater than 10 times of the maximum bubble radius, so the bubble can be considered to oscillate in a free field. A high-speed camera with a resolution of 1 million pixels (Phantom, TMX 6410, form AMETEX, Paoli, Madison, WI, USA) is used to capture the bubble motion, illuminated by a supplementary light source placed on the other side of the tank. Two frosted glasses are placed between the tank and the light source to provide uniform illumination.

We use a combination of a small funnel and a test tube in the water above the copper wire cross point to collect the air after the bubble collapses. Instead of data fitting to obtain the initial number of molecules, the initial conditions for spark-generated bubbles are determined by repeatedly measuring the air content inside a bubble, which is a key factor to accurately capture the dynamics of a spark-generated bubble during multi-oscillations. Air in ten same experiments is collected together, and then an average air volume is obtained, in order to reduce the experimental error. The molecular weight of air is determined by using the ideal gas equation of state. At the beginning, the pressure in the bubble is considered to be equal to atmospheric pressure, and the molecular weight of the vapor can be obtained by calculating the saturated vapor pressure at this time. In order to ensure the reliability of the experiment, we performed a series of experiments under the same working conditions. The multi-oscillations of a spark-generated bubble is given in Figure 3. Obviously, in the fourth cycle, the bubble shape is no longer regular and begins to break.

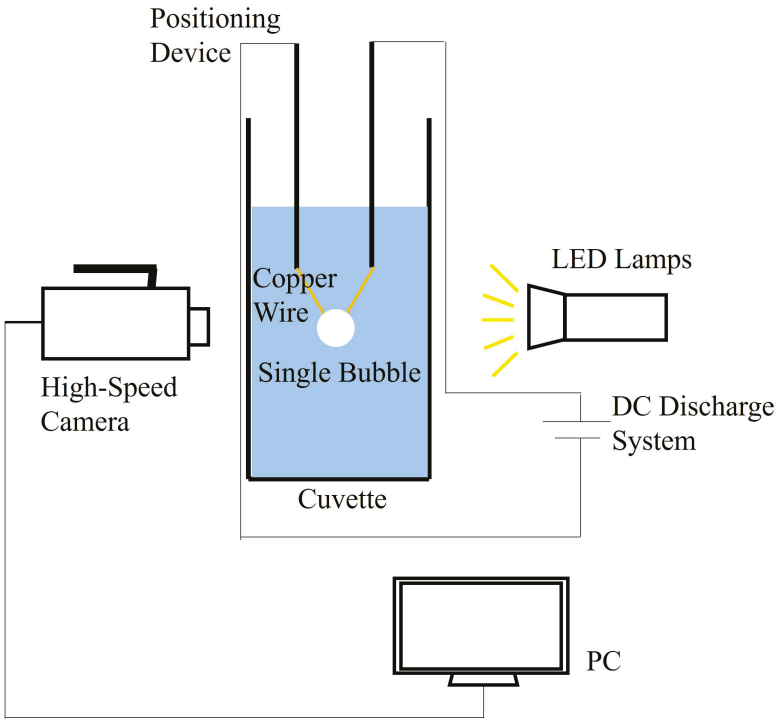


Figure 2. Schematic diagram of the experimental setup.

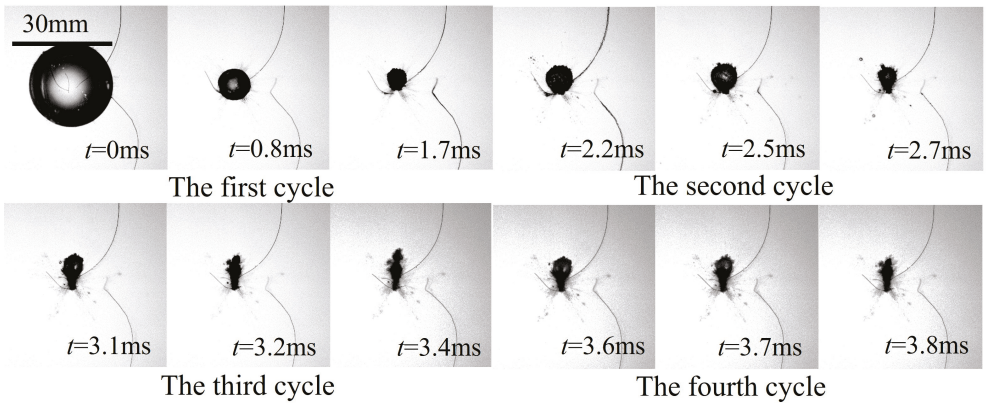


Figure 3. Growth and collapse of spark bubbles. Voltage = 450 V.

3. Validation

3.1. Comparison of Experiments and Theoretical Results

In the present study, equations are solved using the fourth-order Runge–Kutta method. In all cases considered in this paper, we take the moment when the bubble radius reaches maximum R_m as the start. The other required physical parameters in the model are listed in Table 1. It is supposed that both the bubble temperature and flow field temperature at this time are equal to the ambient temperature of 293 K. Because the specific heat capacity of water is much greater than that of vapor, it can be considered that during the entire bubble motion $T_{\text{liquid}} = T_\infty$. Since the thermal layer thickness cannot be measured experimentally, we assume that $\delta_1^{(0)}$ = 0.45 (μm) based on Zhong's hypothesis [20].

Figure 4 compares the experimental results with the Keller–Miksis equation, the Zhong model, and the present modified theoretical model. In the experiments, the uncertainty of the measurement is about one pixel (0.04 mm), which is much smaller than the maximum bubble radius. The Keller–Miksis equation takes fluid compressibility into account during bubble motion [34]. The bubble radius change in the first period is well predicted by the

three models, which indicates that the energy dissipation is mainly due to the compressibility. But in the subsequent motion, the prediction by Keller–Miksis equation significantly underestimates the energy dissipation, it suggests that mass and heat transfer becomes the dominant factor for the energy dissipation in the multi-oscillations of the spark-generated bubble. In the Zhong model, the compressibility, heat conduction and energy dissipation caused by equilibrium evaporation and condensation are considered at the same time, and the model matches well with the first two cycles of bubble motion in the experiment, but the results begins to deviate from the experimental data in the third cycle. It is believed that dissolved hydrogen content of spark-generated bubbles differs from that of laser-induced bubbles, leading to the difference in bubble rebound potential energy. Given this, liquid compressibility, heat conduction and non-equilibrium evaporation and condensation are considered in the first two cycles, while heat conduction and non-equilibrium evaporation and condensation are neglected in the subsequent motion. As shown in Figure 4, the predicted radius with the present modified model agrees well with the experimental data during the multi-oscillations of the spark-generated bubble, with a maximum error of 2%. It is believed that the modified theoretical model can better predict multi-oscillations of spark-generated bubbles. From the comparison above, it is noted that the effect of heat and mass transfer becomes weaker on the energy dissipation after two cycles of spark-generated bubble motion. It is believed to be caused by the reduction of vapor molecules in the bubble, which will be discussed in detail later.

Table 1. Physical properties at 1 (atm) and 20 (°C).

Physical Property	Symbol	Value	Unit
Sound speed in water	c	1483	$m \cdot s^{-1}$
Water density	ρ_l	1000	$kg \cdot m^{-3}$
Surface tension coefficient	σ	0.072	$N \cdot m^{-1}$
Water viscosity	μ	0.001	Pa·s
Molar weight of vapor	M_{vapor}	0.018	$kg \cdot mol^{-1}$
Molar weight of air	M_{air}	0.02897	$kg \cdot mol^{-1}$
Avogadro constant	N_A	6.02×10^{23}	mol^{-1}
Gas constant	R_g	8.314	$J \cdot mol^{-1} \cdot K^{-1}$
Intermolecular attraction of air	a_{air}	0.1402	$J \cdot m^3 \cdot mol^{-2}$
Intermolecular attraction of vapor	a_{vapor}	0.5536	$J \cdot m^3 \cdot mol^{-2}$
Volume occupied by air molecules	b_{air}	3.753×10^{-5}	$m^3 \cdot mol^{-1}$
Volume occupied by vapor molecules	b_{vapor}	3.049×10^{-5}	$m^3 \cdot mol^{-1}$
Gas constant of vapor	R_v	461.52	$J \cdot kg^{-1} \cdot K^{-1}$
Thermal accommodation coefficient	α_e	1	-
Thermal conductivity of vapor	κ	0.02	$W \cdot m^{-1} \cdot K^{-1}$
Thermal conductivity of water	k_l	0.55	$W \cdot m^{-1} \cdot K^{-1}$
Boltzmann constant	k	1.38×10^{-23}	$J \cdot K^{-1}$
Stefan-Boltzmann constant	σ_r	5.67×10^{-8}	$W \cdot m^{-2} \cdot K^{-4}$
Flow field temperature	T_{liquid}	293.15	K
Vapor specific heat capacity at constant volume	c_{vair}	1089	$J \cdot kg^{-1} \cdot K^{-1}$
Specific heat capacity of air at constant volume	c_{vvapor}	717	$J \cdot kg^{-1} \cdot K^{-1}$

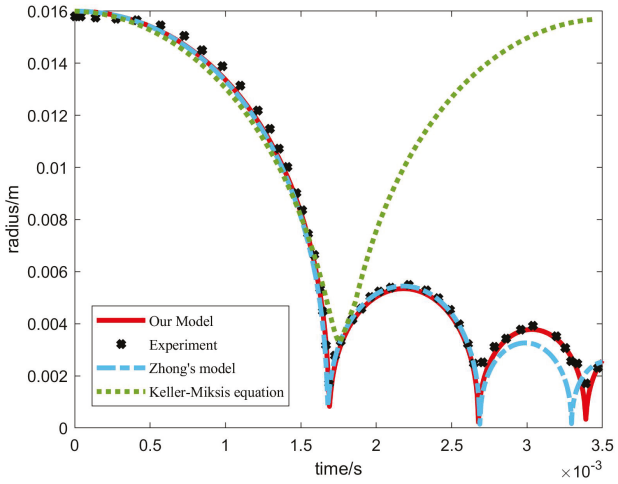


Figure 4. Comparison of bubble radii (Black dots: experimental data points. Green dotted line: Keller–Miksis equation result. Blue dot line: Zhong model results, where $n_t^{(0)} = 1.4 \times 10^{20}$, $n_{air}^{(0)} = 4 \times 10^{16}$, $\alpha_M = 0.04$. Red line: This paper model results, where $n_t^{(0)} = 1.4 \times 10^{20}$, $n_{air}^{(0)} = 4 \times 10^{16}$, $\alpha_M = 0.04$, $\delta_1^{(0)} = 0.45$ μm. In the Keller–Miksis equation, it is assumed that the bubble movement process is adiabatic and the initial gas pressure is 101,000 Pa. Zhong model parameters are obtained by best fitting the measured data of experimental bubble radius).

3.2. Further Discussions

Yasui [28] gives an equation for approximating the energy carried by each vapor molecule, and the energy carried by the non-equilibrium evaporation of the vapor molecule can be calculated by

$$e_{vapor}(T) \approx 6.272 \times 10^{-23} T - 5.247 \times 10^{21} (J) \tag{21}$$

Figure 5 shows time histories of the total energy taken away by the reduced vapor molecules if condensation is taken into account during the entire process. It is noted that the energy loss due to the reduction of vapor molecules in the first collapse is over 100 times that of the second collapse. In the second collapse, the work carried out by the flow field on the bubbles is not much different from the energy taken away by the vapor condensation, but if the vapor condensation is considered, the radius of rebound for the bubbles is too small.

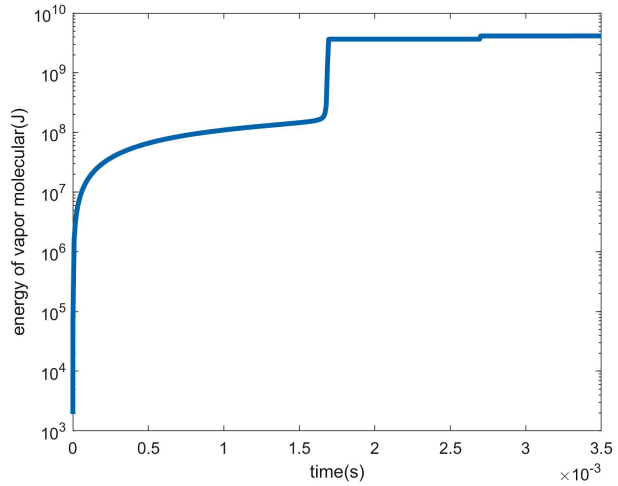


Figure 5. Total energy loss caused by condensation of vapor molecules.

Figure 6 compares the predicted time histories of bubble radius with the experimental results at different voltages, and the calculation method of air molecular number is determined in the same way as in Figure 4. The standard evaporation coefficient is $\alpha_M = 0.04 \pm 0.005$, and the thickness of the vapor thermal layer is $\delta_1^{(0)} = 0.45$ μm. It can be seen that the experimental results in the first three cycles are well reproduced using the present modified model.

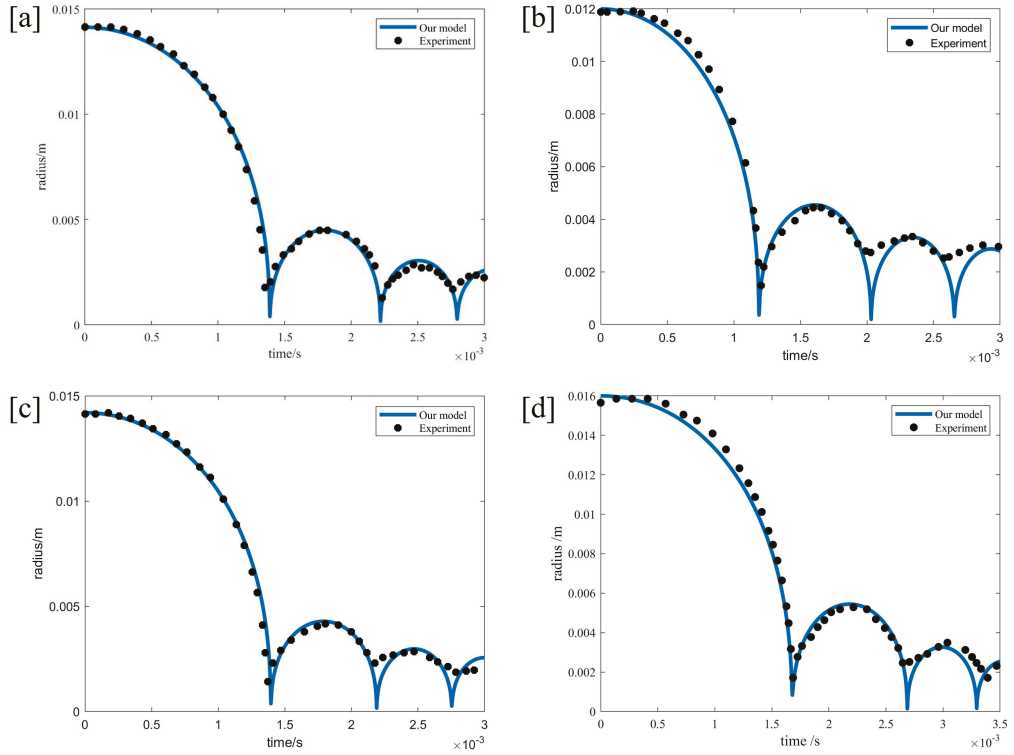


Figure 6. Comparison of experimental measurement radius and predicted radius (Black dots: experimental data points. Blue dot line: our model results, (**a**) voltage = 450 V, $R_{\max 1} = 14.2$ mm, $T_{collapse1} = 1.38$ ms, $R_{\max 2} = 4.96$ mm, $T_{collapse2} = 2.24$ ms, $R_{\max 3} = 4.96$ mm, $T_{collapse3} = 2.83$ ms; (**b**) voltage = 450 V, $R_{\max 1} = 12$ mm, $T_{collapse1} = 1.18$ ms, $R_{\max 2} = 4.12$ mm, $T_{collapse2} = 2.04$ ms, $R_{\max 3} = 3.24$ mm, $T_{collapse3} = 2.83$ ms; (**c**) voltage = 450 V, $R_{\max 1} = 14.4$ mm, $T_{collapse1} = 1.42$ ms, $R_{\max 2} = 3.86$ mm, $T_{collapse2} = 2.2$ ms, $R_{\max 3} = 2.46$ mm, $T_{collapse3} = 2.88$ ms; (**d**) voltage = 450 V, $R_{\max 1} = 16$ mm, $T_{collapse1} = 1.68$ ms, $R_{\max 2} = 4.82$ mm, $T_{collapse2} = 2.66$ ms, $R_{\max 3} = 3.16$ mm, $T_{collapse3} = 3.32$ ms).

4. Results and Discussion

4.1. Effect of Phase Transition Duration

We take the spark-generated bubble with an initial radius of $R_0 = 16$ mm induced by voltage 450 V DC as an example to study the motion of bubbles containing 0.25% air content in a free field. In the model prediction result plot, the maximum temperature and maximum pressure in the bubble reach their maximum at the second collapse moment. To meet the initial conditions for the application of the Rayleigh–Plesset equation, the phase transition process is taken into account after the bubble reaches the maximum radius for the first time [19]. According to the Hertz–Knudsen–Langmuir modified relationship, the evaporation process is mainly determined by the ambient temperature. The temperature change of flow field during the transient bubble motion can be ignored, and Phan's research [19] proves that the evaporation process has little effect on the bubble motion compared with the condensation process; therefore, it is assumed that the evaporation rate remains constant during the entire phase transition process, taking $\dot{m}_{\text{eva}} = 0.04\ \text{kg}/(\text{m}^2 \cdot \text{s})$.

The model assumes that the gas inside the bubble is composed only of condensable vapor and non-condensable air. But in practice, N_2, O_2 and H_2O in extreme cases, such as extremely high pressure and temperature conditions when bubbles collapse, chemical reactions and recombination processes will occur to generate NO_2, NO, etc., which may lead to a decrease in pressure peaks in the bubble movement cycle. These reaction products are soluble in water, and their presence may reduce the pressure peak when the bubble collapses, that is the occurrence of chemical reaction at the collapse moment can enhance the rebound potential energy of the bubble [25]. However, it is hard to quantitatively calculate the influence of chemical reactions on bubble motion, according to the work by Zhong and Phan et al. [19,20], the highest temperature and pressure is reached at the second bubble collapse. Presumably, it is considered that chemical reactions occur at the end of the second cycle, we consider this effect by ignoring vapor non-equilibrium evaporation and condensation after the bubble reaches the maximum radius of the second cycle, as is shown of the condensation rate curve in Figure 7.

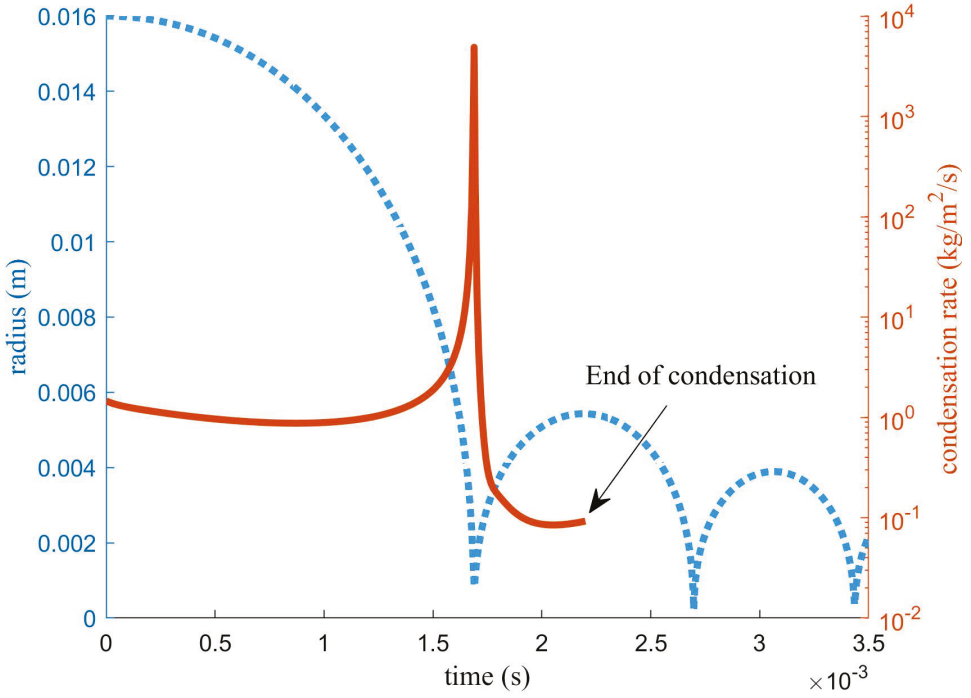


Figure 7. Prediction of mass transfer rate during bubble motion.

Effect of phase transition duration on radius, pressure and temperature of the bubble multi-cycles motion are given in Figure 8a–c. The pressure and temperature peaks inside the bubble are observed at the second collapse moment. If the phase transition is considered during the whole bubble motion, the pressure and temperature in the bubble can reach a maximum of 1237 MPa and 20,000 K, respectively. Because if the phase transition keeps happening, the number of vapor molecules undergoing phase transition at the bubble collapse moment will increase significantly, it causes a stronger energy change. The stronger energy change obviously may lead to a sharp increase in the pressure and temperature peaks, far greater than the pressure and temperature peaks of 358.5 MPa and 6200 K in the present model. It is believed that the pressure and temperature peaks predicted by the present model are more reasonable.

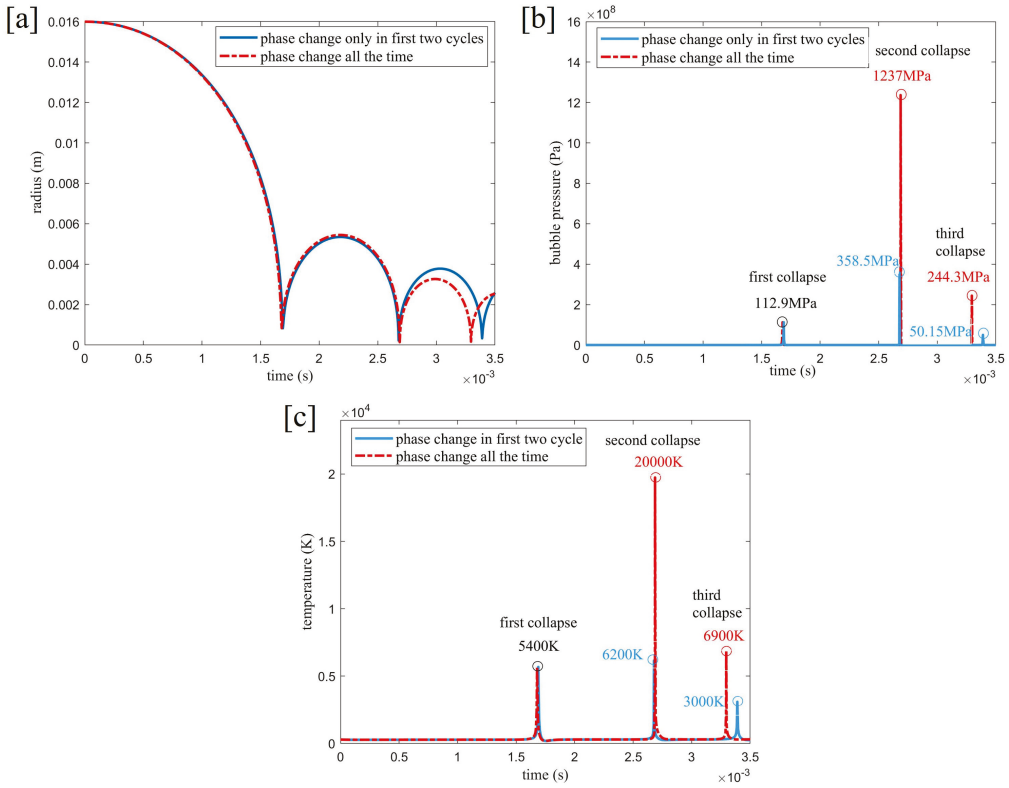


Figure 8. Effect of condensation duration on bubble motion (Initial conditions: $n_t^{(0)} = 1.4 \times 10^{20}$, $n_{air}^{(0)} = 4 \times 10^{16}$, $\alpha_M = 0.04$, $\delta_1^{(0)} = 0.45$ μm).

4.2. Effect of Air Content

Time histories of bubble radius, temperature and pressure with different air contents are given in Figure 9a–c. As the total number of gas molecules in all working conditions remains unchanged, the increase in air content indicates the decrease in the number of vapor molecules. As shown in Figure 9, the curves before the first collapse are basically coincident, indicating that air content has little effect on the bubble motion before the first collapse, and phase transition (the decrease in the number of vapor molecules) mainly occurs at the collapse moment.

As air content increases, the mix-gases bubble motion tends to be similar to an air bubble. The decrease in the vapor molecules leads to a slower energy dissipation, so a larger rebound bubble potential energy and increased rebound radius are expected. Since the maximum pressure and temperature at the collapse moment are mainly determined by the intensity of energy change, a larger air content (a decrease in the vapor molecules) leads to a decrease in the intensity of the energy change. Therefore, the pressure and temperature peaks at the first and second collapse moments decrease with the increase in the air content. It is also noted that the bubble oscillation period increases with the air content.

Since the mixture in the bubble is considered an ideal gas after the vapor condensation is stopped, the pressure and temperature of the bubble are updated using the ideal gas state formula. As air content increases, the mix-gases bubble motion tends to be similar to an air bubble. The decrease in the vapor molecules leads to a slower energy dissipation, so a larger rebound bubble potential energy and increased rebound radius are expected. Since the maximum pressure and temperature at the collapse moment are mainly determined by the intensity of the energy change, a larger air content (the decrease in the vapor molecules) leads to a decrease in the intensity of the energy change. Therefore, the pressure and temperature peaks at the first and second collapse moments decrease with the increase in the air content. It is also noted that the bubble oscillation period increases with the air content.

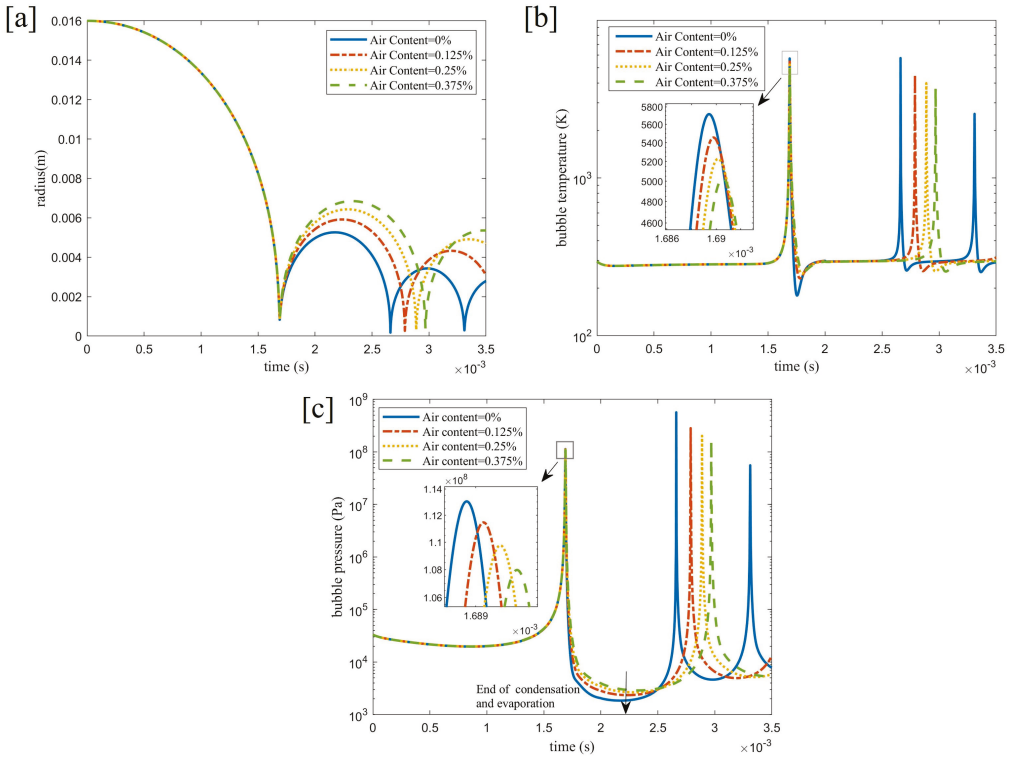


Figure 9. Effect of air content on bubble motion (Initial conditions: $n_t^{(0)} = 1.4 \times 10^{20}$, $\alpha_M = 0.04$, $\delta_1^{(0)} = 0.45$ μm.)

5. Conclusions

In this study, we have introduced a modified theoretical model designed to capture the multi-oscillation behavior of spark-generated bubbles. Tailoring our approach to the unique characteristics of these bubbles, we have incorporated a modified phase transition duration. Our model builds upon the Plesset bubble dynamics equation, which has been augmented by Fujikawa and Akamatsu, and also integrates the surface temperature gradient approximation proposed by Zhong et al. Additionally, we have diligently determined the initial conditions through repeated measurements of gas content within the bubble. Through rigorous validation involving quantitative comparisons with experimental data, our proposed theoretical model has demonstrated commendable accuracy in simulating the dynamic behavior of bubbles across multiple cycles.

Our calculations have revealed that when factoring in the phase change effect, bubble collapse becomes highly energetic, with rapid increases in internal pressure and temperature at the finally stage of the bubble. Notably, the vapor condensation rate experiences fluctuations during both the collapse and rebound stages of the bubble. As the concentration of air within the bubble increases, it fosters more pronounced rebound behavior. Starting from the second cycle, we observe a decrease in the rate of maximum radius decay. This phenomenon is attributed to the rising air content, diminishing vapor concentration, and a lower energy decay rate per bubble collapse compared to pure vapor bubbles. This, in turn, accounts for the decreasing peak pressure and temperature of the bubble with increasing air content.

It is important to acknowledge that our model employs a uniform thermal boundary layer thickness across different bubbles, chosen to optimize simulation results according to Zhong et al. However, this choice may not precisely mirror real-world conditions. In future work, we aim to refine our model, considering variations in thermal boundary layer thickness for different bubble scenarios, which could impact the heat conduction efficiency of bubbles and their flow dynamics.

Author Contributions: Conceptualization, J.C. and R.H.; methodology, J.C.; software, J.C.; validation, J.C., R.H. and T.G.; formal analysis, J.C.; investigation, J.C.; resources, J.C.; data curation, J.C.; writing—original draft preparation, J.C.; writing—review and editing, R.H.; visualization, J.C.; supervision, R.H.; project administration, R.H.; funding acquisition, R.H. All authors have read and agreed to the published version of the manuscript.

Funding: This work was funded by the National Natural Science Foundation of China (12072087) and the Heilongjiang Postdoctoral Fund (LBH-Q19094, LBH-Q20016).

Data Availability Statement: The results of the work are new, some of the known results are in the available sources, which are cited in the article.

Acknowledgments: This work was supported by the National Natural Science Foundation of China (12072087) and the Heilongjiang Postdoctoral Fund (LBH-Q19094, LBH-Q20016).

Conflicts of Interest: The authors declare no conflict of interest.

References

1. Johnsen, E.; Colonius, T. Numerical simulations of non-spherical bubble collapse. *J. Fluid Mech.* **2009**, *629*, 231–262. [CrossRef]
2. Philipp, A.; Lauterborn, W. Cavitation erosion by single laser-produced bubbles. *J. Fluid Mech.* **1998**, *361*, 75–116. [CrossRef]
3. Wang, S.P.; Zhang, A.M.; Liu, Y.L. Bubble dynamics and its applications. *J. Hydrodyn.* **2018**, *30*, 975–991. [CrossRef]
4. Melissaris, T.; Schenke, S.; Bulten, N.; Terwisga, T.J. On the accuracy of predicting cavitation impact loads on marine propellers. *Wear* **2020**, *456*, 203393. [CrossRef]
5. Han, B.; Kohler, K. Dynamics of laser-induced bubble pairs. *J. Fluid Mech* **2015**, *771*, 706–742. [CrossRef]
6. Zhang, Y.N.; Gao, Y.H.; Du, X.Z. Stability mechanisms of oscillating vapor bubbles in acoustic fields. *Ultrason. Sonochem.* **2018**, *40*, 808–814. [CrossRef]
7. Ma, X.J.; Huang, B.; Zhao, X. Comparisons of spark-charge bubble dynamics near the elastic and rigid boundaries. *Ultrason. Sonochem.* **2018**, *43*, 80–90. [CrossRef]
8. Shan, M.L.; Chen, B.Y.; Yao, C. Electric characteristic and cavitation bubble dynamics using underwater pulsed discharge. *Plasma Sci. Technol.* **2019**, *21*, 16–22. [CrossRef]
9. Luo, J.; Xu, W.L.; Khoo, B.C. Stratification effect of air bubble on the shock wave from the collapse of cavitation bubble. *J. Fluid Mech.* **2021**, *919*, A16. [CrossRef]
10. Huang, G.; Zhang, M.; Ma, X. Dynamic behavior of a single bubble between the free surface and rigid wall. *Ultrason. Sonochem.* **2020**, *67*, 105147. [CrossRef]
11. Xu, W.L. Interaction of a Cavitation Bubble and an Air Bubble with a Rigid Boundary. *J. Hydrodyn.* **2010**, *22*, 503–512. [CrossRef]
12. Zhang, A.M. Experiments on Bubble Dynamics between a Free Surface and a Rigid Wall. *Exp. Fluids* **2013**, *54*, 1602. [CrossRef]
13. Fujikawa, S.; Akamatsu, T. Effects of the non-equilibrium condensation of vapour on the pressure wave produced by the collapse of a bubble in a liquid. *J. Fluid Mech.* **1980**, *97*, 481–512. [CrossRef]
14. Han, R.; Zhang, A.M.; Tan, S.; Li, S. Interaction of cavitation bubbles with the interface of two immiscible fluids on multiple time scales. *J. Fluid Mech.* **2022**, *932*, A8. [CrossRef]
15. Zhang, A.M.; Li, S.M.; Cui, P.; Li, S.; Liu, Y.L. A unified theory for bubble dynamics. *Phys. Fluids* **2023**, *35*, 033323. [CrossRef]
16. Zein, A.; Hantke, M.; Warnecke, G. On the modeling and simulation of a laser-induced cavitation bubble. *Int. J. Numer. Methods Fluids* **2013**, *73*, 172–203. [CrossRef]
17. Lee, H.; Gojani, A.B.; Han, T.; Yoh, J.J. Dynamics of laser-induced bubble collapse visualized by time-resolved optical shadowgraph. *J. Vis.* **2011**, *14*, 331–337. [CrossRef]
18. Sagar, H.; Moctar, O. Numerical simulation of a laser-induced cavitation bubble near a solid boundary considering phase change. *Ship Technol. Res.* **2018**, *65*, 1–17. [CrossRef]
19. Phan, T.H.; Nguyen, V.T.; Duy, T.N. Influence of phase-change on the collapse and rebound stages of a single spark-generated cavitation bubble. *Int. J. Heat Mass Transf.* **2022**, *184*, 122270. [CrossRef]
20. Zhong, X.X.; Eshraghi, J.; Vlachos, P. A model for a laser-induced cavitation bubble. *Int. J. Multiph. Flow.* **2020**, *132*, 103433. [CrossRef]
21. Aganin, A.A.; Khismatullina, A.N. Influence of the phase interface mass transfer characteristics on the cavitation bubble collapse in water. *Ocean Eng.* **2023**, *283*, 115013. [CrossRef]
22. Mustafin, N.I. Numerical Simulation of Collapse and Rebound of a Cavitation Bubble in Water. *Lobachevskii J. Math.* **2023**, *44*, 1771–1777. [CrossRef]
23. Li, S.; Meer, D.V.d.; Zhang, A.M.; Prosperetti, A.; Lohse, D. Modelling large scale airgun-bubble dynamics with highly non-spherical features. International Journal of Multiphase Flow. *Int. J. Multiph. Flow.* **2020**, *122*, 103143. [CrossRef]
24. Li, S.; Zhang, A.M.; Han, R.; Ma, Q. 3D full coupling model for strong interaction between a pulsating bubble and a movable sphere. *J. Comput. Phys.* **2019**, *392*, 713–731. [CrossRef]
25. Trummler, T.; Schmidt, S.J.; Adams, N.A. Numerical investigation of non-condensable gas effect on vapor bubble collapse. *Phys. Fluids* **2021**, *33*, 096107. [CrossRef]

26. Sato, T.; Tinguely, M.; Oizumi, M.; Farhat, M. Evidence for hydrogen generation in laser- or spark-induced cavitation bubbles. *Appl. Phys. Lett.* **2013**, *102*, 074105. [CrossRef]
27. Kaouther, K.; Hamdaoui, O. Influence of reactions heats on variation of radius, temperature, pressure and chemical species amounts within a single acoustic cavitation bubble. *Ultrason. Sonochem.* **2018**, *41*, 449–457.
28. Yasui, K. Alternative model of single-bubble sonoluminescence. *Phys. Rev. E* **1997**, *56*, 6750. [CrossRef]
29. Plesset, M.S.; Pasadena, C. The dynamics of cavitation bubbles. *J. Appl. Mech.* **1949**, *48*, 277–282. [CrossRef]
30. Alty, T.; Mackay, C.A. The accommodation coefficient and the evaporation coefficient of water. *Proc. R. Soc.* **1935**, *149*, 104–116.
31. Yasui, K. Effects of thermal conduction on bubble dynamics near the sonolu- minescence threshold. *J. Acoust. Soc. Am.* **1995**, *98*, 2772–2782. [CrossRef]
32. Prosperetti, A.; Lezzi, A. Bubble dynamics in a compressible liquid. Part 1. First-order theory. *J. Fluid Mech.* **1986**, *168*, 457–478. [CrossRef]
33. Jebali, F.; Francois, M.X. Thermal resistance of a vapor-liquid He II interface. *Phy. B Condensed Matter* **1994**, *194*, 599–600. [CrossRef]
34. Grunt, K.; Lewkowicz, M.; Pietrowicz, S.; Takada, S.; Kimura, N.; Murakami, M. Dynamics of vapour bubbles induced during the boiling of superfluid helium under microgravity conditions. *Int. J. Heat Mass Trans.* **2019**, *134*, 1073–1083. [CrossRef]
35. Keller, J.; Miksis, M. Bubble oscillations of large amplitude. *J. Acoust. Soc. Am.* **1980**, *68*, 628–633. [CrossRef]
36. Cui, P.; Zhang, A.M.; Wang, S.; Khoo, B.C. Ice breaking by a collapsing bubble. *J. Fluid Mech.* **2018**, *841*, 287–309. [CrossRef]
37. Akhatov, L.; Lindau, O.; Topolnikov, A.; Vlachos, R. Collapse and rebound of a laser-induced cavitation bubble. *Phys. Fluids* **2001**, *13*, 2805–2819. [CrossRef]

Disclaimer/Publisher's Note: The statements, opinions and data contained in all publications are solely those of the individual author(s) and contributor(s) and not of MDPI and/or the editor(s). MDPI and/or the editor(s) disclaim responsibility for any injury to people or property resulting from any ideas, methods, instructions or products referred to in the content.

inventions

MDPI

Article

Obtaining Vortex Formation in Blood Flow by Particle Tracking: Echo-PV Methods and Computer Simulation

Ilya Starodumov [1,2,3], Sergey Sokolov [1,2,3], Ksenia Makhaeva [1,2], Pavel Mikushin [1,2,4], Olga Dinislamova [3] and Felix Blyakhman [1,2,3,*]

[1] Laboratory of Multiphase Physical and Biological Media Modelling, Department of Theoretical and Mathematical Physics, Ural Federal University, Ekaterinburg 620000, Russia; ilya.starodumov@urfu.ru (I.S.); sergey.sokolov@urfu.ru (S.S.); ksenia.makhaeva@urfu.ru (K.M.); mikushin.pv18@physics.msu.ru (P.M.)
[2] Laboratory of Multi-Scale Mathematical Modeling, Department of Theoretical and Mathematical Physics, Ural Federal University, Ekaterinburg 620000, Russia
[3] Department of Biomedical Physics and Engineering, Ural State Medical University, Ekaterinburg 620000, Russia; odinislamova@gmail.com
[4] Moscow Institute of Physics and Technology, Moscow 141701, Russia
* Correspondence: feliks.blyakhman@urfu.ru

Abstract: Micrometer-sized particles are widely introduced as fluid flow markers in experimental studies of convective flows. The tracks of such particles demonstrate a high contrast in the optical range and well illustrate the direction of fluid flow at local vortices. This study addresses the theoretical justification on the use of large particles for obtaining vortex phenomena and its characterization in stenotic arteries by the Echo Particle Velocimetry method. Calcite particles with an average diameter of 0.15 mm were chosen as a marker of streamlines using a medical ultrasound device. The Euler–Euler model of particle motion was applied to simulate the mechanical behavior of calcite particles and 20 µm aluminum particles. The accuracy of flow measurement at vortex regions was evaluated by computational fluid dynamics methods. The simulation results of vortex zone formation obtained by Azuma and Fukushima (1976) for aluminum particles with the use of the optical velocimetry method and calcite particles were compared. An error in determining the size of the vortex zone behind of stenosis does not exceed 5%. We concluded that the application of large-size particles for the needs of in vitro studies of local hemodynamics is possible.

Keywords: hemodynamics; computer modeling; particle velocimetry; stenotic vessel

1. Introduction

The high mortality rate in the world from cardiovascular diseases has lead to numerous studies of hemodynamic flows in coronary vessels. Distortions of the blood vessel lumen, including physiologic bifurcations and bends, can cause localized blood flow disturbances. The abnormal hemodynamic forces associated with these disturbances may play an important role in the pathogenesis of focal vascular lesions such as atherosclerosis, extrinsic thrombus, poststenotic dilatation, and aneurysm [1–5]. In particular, a number of studies have demonstrated the appearance of flow separation, vortices and turbulence, and flow recirculation in the post-stenotic region [6–9]. These findings are of great interest for studying the contribution of hemodynamic factors to the formation of stenosis.

In recent decades, the development of CFD (Computational Fluids Dynamic) methods has resulted in an increase in the number of works on the modeling of local hemodynamics, including ones with the use of patient-specific data [10–25]. To account for the rheology of blood and the interaction of liquid and solid with the walls of blood vessels, many complex multiphase and multiparametric models have been developed [26–29]. These models, based mainly on the numerical solution of the Navier–Stokes equations, allow the complete detailed reconstruction of the local hemodynamics in the area of stenosis.

One of the most interesting features of the local hemodynamics in damaged arteries is the formation of a low-velocity vortex behind the stenosis. Due to the non-Newtonian nature of blood, the vortex zone is associated with a local increase in viscosity and lower near-wall shear stresses [9,15,30–35]. The complex blood rheological effects result in the appearance of a cell-free layer (CFL) [19,36] with a lower viscosity compared to the core region. The thickness of CFL significantly affects the velocity profiles and dimensions of the vortex zone. The quantitative characterization of the vortex zone is important for the development of stenosis theory, diagnostics, and clinical applications. As the nature of the CFL is still not clear, the size of the vortex region is difficult to predict without in silico simulations.

In general, a reliable investigation on the effect of local hemodynamics in vessels with stenosis on the development of disease and its treatment methods requires an integrated approach combining in vivo, in vitro, and in silico studies (Figure 1).

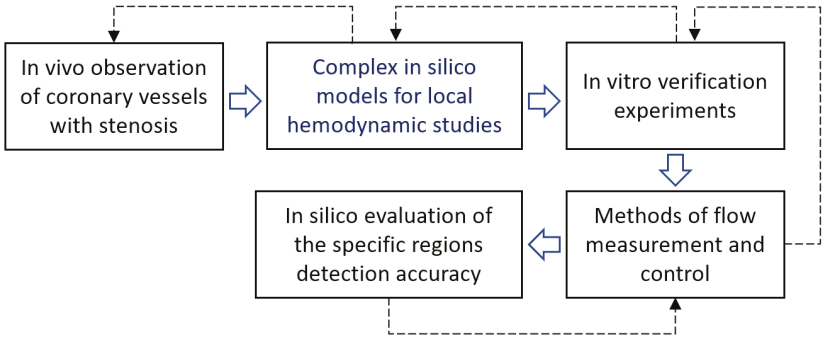


Figure 1. Algorithm for the study of specific local hemodynamic characteristics using a complex approach.

Since the complex models of local hemodynamics usually contain a number of empirical coefficients, in vitro experiments of model verification are necessary. For this purpose, optical particle velocimetry (PV) [37–42] and ultrasonic PV (Echo-PV) [43,44] technologies are widely used. The optical PV method operates with a fine contrast impurity (polystyrene, polyamide, or glass beads with size 0.2–100 µm). Such methods are highly accurate and informative for assessing local hemodynamics. The main disadvantage of optical methods is the requirement for optical transparency of the vessel wall and fluid. In contrast, the Echo-PV method allows measurements in optically opaque media, making it most suitable for flow studies in phantom vessels or in vivo.

At the same time, Echo-PV requires particles with a high reflectivity of ultrasonic waves. In particular, polystyrene beads of approximately 100 µm in diameter or air microbubbles of the same size are suitable for in vitro or in vivo studies, respectively [45]. Meanwhile, the accuracy of the optical PV method for assessing the peculiarities of vortex zone behind the stenosis has been confirmed experimentally [1], while the suitability of the Echo-PV method for this purpose is not yet determined. Therefore, the last stage in the methodological chain presented in Figure 1 is necessary to evaluate the accuracy of vortex zone formalization by Echo-PV using large echo contrast particles as stream markers.

This study addresses the theoretical justification on the use of large particles for obtaining vortex phenomena and its characterization in stenotic arteries by the Echo-PV method. First, we assessed the echogenicity of calcite particles with an average diameter of approximately 0.15 mm as a marker of streamlines. We show that such particles are well visualized by a medical ultrasound device and can be used to detect the vortex zone behind the stenosis. Then, we applied the Euler–Euler model of particle motion to simulate the mechanical behavior of calcite particles at the experimental conditions and compared the results of our simulations with the data of a classic in vitro study by Azuma and Fukushima [1] obtained with aluminum microparticles of 20 µm in diameter and their optical imaging. Finally, we show that large particles provide an error in the measured dimensions of the vortex zone within 5%.

2. Materials and Methods

2.1. Experimental Setup for Particle Echogenicity Testing in a Fluid Flow

To evaluate the ability of particle visualization in fluid flow through vessels of complex geometry by ultrasonography, an experimental setup of laboratory design was used. A piece of silicon tube with an inner diameter of 6 mm was inserted into a silicone tube with a higher inner diameter (8 mm) to simulate arterial stenosis. The silicon tube was connected to a reservoir filled with a suspension containing distilled water and calcite particles with a volume fraction of 0.1%. The calcite particles KoelgaCarb KM-200 (JSC «Koelgamramor», Chelyabinsk, Russia) were close to spherical shape, with a diameter 0.1–0.2 mm. The fluid flow rate of 500 mL/s was set by the height of the water column. The constant level of the water column in the reservoir was provided by the continuous addition of suspension into the reservoir from a buffer tank with the help of a peristaltic pump. For details of the hydrodynamic system, see [46].

A fragment of the silicon tube with a model stenosis was immersed in a polystyrene cuvette filled with 500 mL of water. A SIEMENS 7.5L45s Prima/Adara linear transducer of an ultrasonic medical device Sonoline Adara (Siemens, Munich, Germany) was immersed in the same cuvette at a distance of 40 mm from the silicone tube. The following hardware settings of the ultrasonic apparatus were used: dynamic range—66 dB, operating frequency—10 MHz, wavelength—0.15 mm, gain—19 dB, and power—50%. Two-dimensional images of the samples were recorded by video for several seconds at a rate of 25 frames per second and resolution of 720 × 480 pixels. The brightness was measured in gray scale in a range from 30 to 255 arbitrary units with the use of specially designed software. For details of the echolocation, see [47]. Calcite particles were captured and showed good echogenicity, so it was possible to capture the tracks of individual particles (Figure 2).

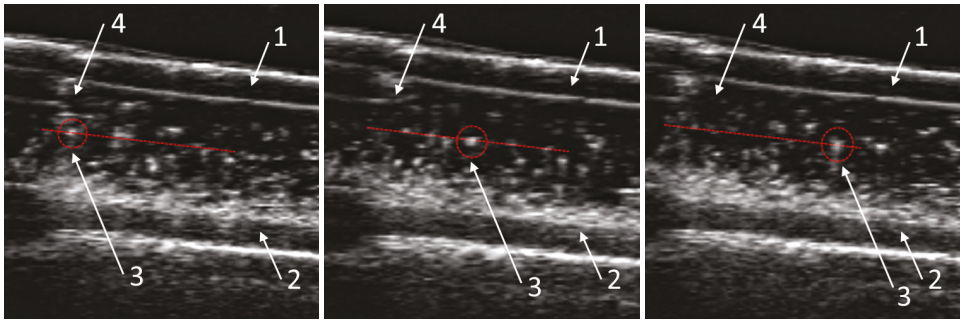


Figure 2. Tracking of a calcite particle in a vortex post-stenotic flow and reconstruction of the particle trajectory. 1,2—silicone tube walls, 3—calcite particle, 4—boundary for a silicone tube with an inner diameter of 6 mm and the beginning of the poststenotic area. Presented frames were sequentially taken with an interval of 1 ms.

2.2. Liquid–Particle Model: Equations Describing the Processes in the Dispersed and Liquid Phases

A model for the propagation of marker particles in fluid flow was developed using the the Euler–Euler concept. Due to the small impurity concentration, the influence of particles on the fluid flows can be neglected. The model takes into account the change of hydrodynamic force on the particles from the liquid side as its diameter increases through coefficient C_D (Equations (3) and (4)) in the drag force.

The advection equation for the dispersed phase can be written as

$$\frac{\partial n}{\partial t} + \nabla \cdot (\boldsymbol{V}_d n) = 0, \tag{1}$$

where $n\left[\mathrm{m}^{-3}\right]$ is the concentration of the dispersed phase (concentration of aluminum particles and calcite particles) and $\boldsymbol{V}_d$ $\left[\mathrm{m\ s}^{-1}\right]$ is the velocity of its motion.

The momentum transfer of the dispersed phase (aluminum particles, calcite particles) is expressed by the non-homogeneous convection equations for the conservative variable $\boldsymbol{V}_d n$:

$$\begin{aligned} m_d \frac{\partial(\boldsymbol{V}_d n)}{\partial t} + m_d(n\boldsymbol{V}_d \cdot \nabla)\boldsymbol{V}_d &= -n\frac{\pi d^3}{6}\nabla P + \boldsymbol{F}_D, \\ \boldsymbol{F}_D &= n\rho_c C_D \frac{\pi d^2}{8}|\boldsymbol{V}_c - \boldsymbol{V}_d|(\boldsymbol{V}_c - \boldsymbol{V}_d). \end{aligned} \tag{2}$$

In Equation (2), m_d[kg] is the local mass of particles, d[m] is the particle diameter, P [Pa] is the fluid pressure measured relative to the hydrostatic pressure, $\rho_c\left[\text{kg m}^{-3}\right]$ is the density of the continuous phase, $\boldsymbol{F}_D\left[\text{N m}^{-3}\right]$ is the drag force, C_D is the drag coefficient, and $V_c\left[\text{m s}^{-1}\right]$ is the velocity of continuous phase.

The movement of dispersed phase particles is primarily determined by the drag force, F_D, which prevents the movement. The drag coefficient in the equation for F_D shows the relationship between the drag force and the inertial forces of the supporting medium. C_D depends on many parameters, but it has been shown that, for particles of a particular shape, it is a function of only the Reynolds number (Re) [48]. The Reynolds number is the ratio of the inertial forces to the internal friction forces arising from the particle motion. In the range of small values of Re, the inertial forces make a negligibly small contribution to the drag force, which is completely determined by the viscosity of the fluid.

It has been found that the C_D coefficient is approximately constant when the inertial forces are much larger than the internal friction forces (large values of Re). However, as can be seen from Figure 3, C_D increases significantly as Re decreases.

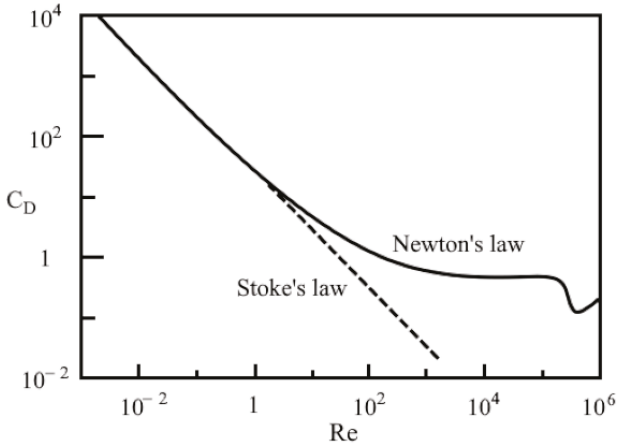


Figure 3. Dependence of hydrodynamic drag coefficient of particles as a function of Reynolds number [49].

Figure 3 is the result of numerous experiments with sphere-shaped particles and can be divided into three regions: (1) $Re > 500$, where $C_D \approx 0.44$ and approximately constant (Newton's law is fulfilled); (2) intermediate region $(0.2 < Re < 500)$, where C_d depends significantly on Re; (3) $Re < 0.2$, where $C_D = 24/Re$ (Stokes law).

In the range of small values of Re, the inertial forces make a negligibly small contribution to the drag force, which is completely determined by the viscosity of the fluid.

The applicability of Stokes law is limited by the velocity of particles in fluid: the motion must be so slow that the inertial forces are small compared to the drag forces. Large particles are capable of accelerated motion. The rapid movement of particles can lead to the development of local micro-turbulence, in which the Stokes law is no longer observed.

In this study, for each dispersed phase (aluminum particles, calcite particles), Re was calculated in order to select a model for the drag coefficient based on the calculations. For aluminum particles with a diameter of 20 µm, $Re = 0.19$, for calcium particles with a diameter of 200 µm, $Re = 1.9$. From the results, it can be seen that, for aluminum particles, Stokes law is satisfied and the drag coefficient can be calculated as Equation (3). For larger

calcite particles, the Stokes law is not fulfilled and the resistance coefficient, C_D, depends significantly on Re in the intermediate region (see Figure 3). For calcite particles, the drag coefficient was calculated using the empirical Formula (4) obtained by Klyachko [50] for the range $0.2 < Re < 500$.

For the drag coefficient of the aluminum particle cloud, the following expression [51] is used:

$$C_D = \frac{24}{Re_d} + 0.44. \tag{3}$$

The dependence of $C_D(Re)$ for the calcite particle cloud was described using the empirical Klyachko formula [50]:

$$C_D = \frac{24}{Re_d} + \frac{4}{Re_d^{1/3}}. \tag{4}$$

In Equations (3) and (4), Re is defined as

$$Re = \frac{\rho_c |\boldsymbol{V}_c - \boldsymbol{V}_d| d}{\mu_c}, \tag{5}$$

where μ_c is the molecular viscosity dynamic coefficient of the continuous phase, $\left[\mathrm{kg\ m^{-1}\ s^{-1}}\right]$.

For liquid fraction, the continuity equation can be written as

$$\frac{\partial(\varphi_c \rho_c)}{\partial t} + \nabla \cdot (\varphi_c \rho_c \boldsymbol{V}_c) = 0, \tag{6}$$

where φ_c is the relative volume of the liquid phase. The momentum equation takes the form of:

$$\begin{aligned} &\frac{\partial(\varphi_c \rho_c \boldsymbol{V}_c)}{\partial t} + (\varphi_c \rho_c (\boldsymbol{V}_c \cdot \nabla)\boldsymbol{V}_c) = -\varphi_c \nabla p + \nabla \cdot (\varphi_c \boldsymbol{\tau}) - \boldsymbol{F}_D, \\ &\boldsymbol{\tau} = \mu_c 2\boldsymbol{S}, \\ &\boldsymbol{S} = \frac{1}{2}\left(\frac{\partial V_i}{\partial x_j} + \frac{\partial V_j}{\partial x_i}\right). \end{aligned} \tag{7}$$

In Equation (7), $\boldsymbol{\tau}[Pa]$ is the viscous stress tensor, $\mu_c\left[\mathrm{kg\ m^{-1}\ s^{-1}}\right]$ is the dynamic coefficient of molecular viscosity of liquid phase, and $\boldsymbol{S}\left[\mathrm{s^{-1}}\right]$ is the absolute value of the generalized velocity gradient.

2.3. Design and Procedure of Simulations

Figure 4 represents a sketch of the computational domain used in simulations.

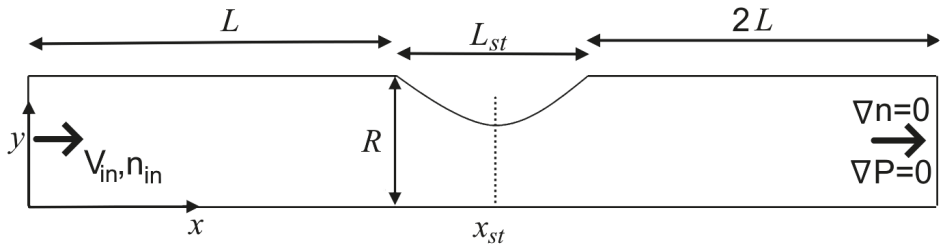


Figure 4. A sketch of the modeled pipe with stenosis. For reasons of symmetry of the solution, only a half of the pipe is considered below. In our simulations, we consider $R = 13.15$ mm, $L = 50$ mm , and $L_{st} = 2.63$ mm.

In this liquid–particle model, we consider four types of boundary conditions, which are presented in Table 1.

Table 1. Boundary conditions for numerical simulations.

Term	Method
Wall type boundary condition	No-slip condition
Symmetry type boundary condition	Impermeability condition
Inlet type boundary condition	Condition with a defined velocity field at the boundary
Free outlet type boundary condition	Condition with a zero static pressure gradient

The boundary condition on the left (see Figure 4) is normal for the boundary $V_{c,in} = V_{max}(1 - (y/R)^2)$ for the fluid, where V_{max} is the velocity at the center of the flow. The concentration of the dispersed phase, n, corresponds to a value of 0.074%. The boundary conditions on the right follows the zero gradient condition for static pressure, P, and dispersed phase concentration, n. We consider the upper boundary as a rigid wall with a no-slip velocity effect. The lower limit corresponds to a rigid wall without the no-slip effect. This approach is valid [15] and can be used for laminar flows in a straight axisymmetric channel. In this paper, the time step was calculated at each iteration based on the Courant–Friedrichs–Lewy condition (CFL) [52]. The shape of stenosis was determined by the proportion

$$y(x) = \begin{cases} R\left[1 - G\left\{L_{st}(x-L) - (x-L)^2\right\}\right], & L \le x < L + L_{st} \\ R, & x < L \text{ or } x > L + L_{st} \\ G = \frac{\left(R^2 - y^2(x_{st})\right)}{R^2}, \end{cases} \quad (8)$$

and corresponds to the stenosis with overlap of $G = 0.6$.

Parameters for the liquid–particle model are presented in Table 2.

Table 2. Parameters for the liquid–particle model.

Parameter	Value	Unit
ρ_c	1055	kg/m^3
μ_c	0.004	Pa s
d (Aluminum particles)	20	µm
d (Calcite particles)	200	µm
ρ (Aluminum particles)	2700	kg/m^3
ρ (Calcite particles)	2710	kg/m^3
m_d (Aluminum particles)	11.3×10^{-12}	kg
m_d (Calcite particles)	9.7×10^{-9}	kg

To solve Equations (2)–(7), we use the finite-volume numerical scheme for a hexagonal mesh implemented in the FlowVision © CFD software (version 3.13.02) [53]. This software uses the original stable implicit velocity-pressure split algorithm to solve the momentum and pressure equations. In describing the particle dynamics, we used an Eulerian approach in which the dispersed and continuous phase interacted as interpenetrating continuous media. All computer simulations were executed on an HPC server with 2 × 64-core processors AMD EPYC 7763 (3.2 GHz).

Test calculations were performed to investigate mesh convergence and number of hexogonal cells. The initial grid was constructed to be non-uniform, with thickening in the vortex formation area (Figure 5), which allowed a clearer representation of the flow dynamics in the poststenotic region. The size of the minimum computational cell in the vortex area was 0.1 mm. The calculations were performed for a model with aluminum particles and the parameter of vortex area and mean velocity of particles was investigated; the results are presented in Table 3 and show that the difference between the results for the 414,000 and 850,000 mesh was less than 10%. This indicates that the chosen grid is sufficiently acceptable for this model.

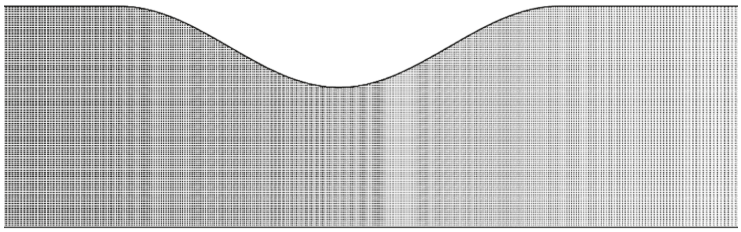


Figure 5. Non-uniform computational grid with condensation in the vortex formation region.

Table 3. Results of the mesh independence study.

Mesh Size (k)	Mean Velocity Particles (m/s)	Vortex Area (m^2)
117	0.00523	0.00016728
320	0.00542	0.0001616
414	0.00557	0.000162
850	0.00598	0.000162

3. Results and Discussion

3.1. Obtaining the Vortex Zone by Echo-PV Tracking of Calcite Particles

As was shown in Figure 2 (see Section 2.1), calcite particles are clearly visualized using medical ultrasound. The brightness of the particles by gray scale is 7–8 times greater than the brightness of the surrounding water (30–40 arbitrary units). In addition, the motion of particles in a fluid flow is also well determined. Figure 6 presents an example of the vortex zone visualization at the same experimental conditions. One can see the absence of particles in the upper part of the area behind the stenosis so that the shape and size of the zone are clearly visible.

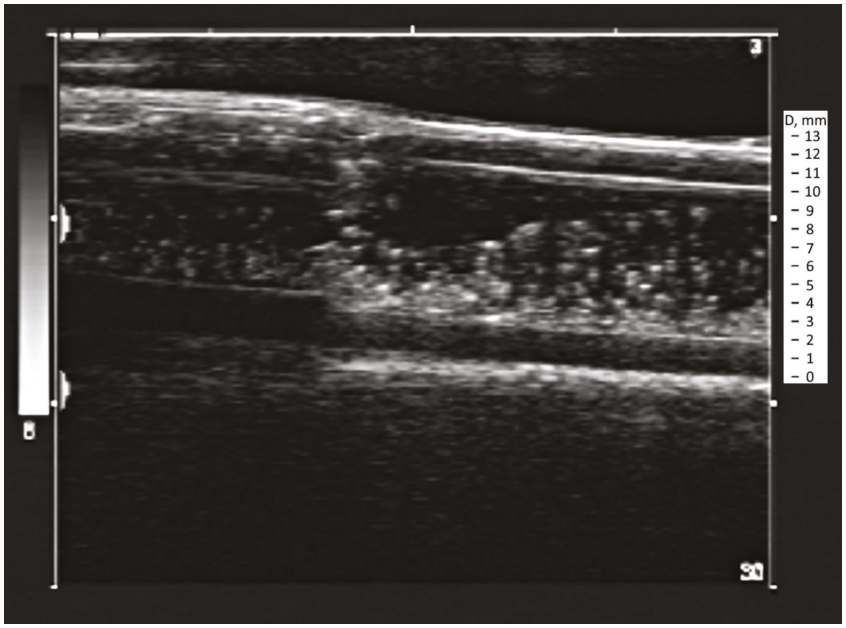


Figure 6. A typical example of vortex zone visualization by echolocation of calcite particles (0.1–0.2 mm in diameter) in the area of modeled arterial stenosis. On the left is the gray scale (B—brightness), on the right is the scale bar of dimension (D).

In general, calcite particles are a well-suited substance for Echo-PV technology to evaluate the vortex zone in stenotic arteries. The high echogenicity of particles is ensured due to the optimal density and size of the material. Additionally, the particle size is at least an order greater than the dimensions of blood cells (∼10 µm). This implies no significant effects of particle–cell interaction on the trajectory of particle motion.

Recently, modern Ultrasound Localization Microscopy (ULM) technology with higher spatial–temporal resolution was introduced for Echo-PV. ULM operates with the scattered ultrasonic vibrations reflected from microbubbles used as an echo contrast agent [54]. The size of a single microbubble is in the range of 3–10 µm. ULM uses high-speed recording of reflected echo signals (up to 20,000 frames/s). Specially developed visualization algorithms are applied to obtain the location of each microbubble and their motion from frame to frame. As a result, ULM provides the spatial resolution of 5–20 µm.

The ULM method is a promising tool for in vivo measurements, in particular for microvascular mapping [55–57]. However, the motion of microbubbles depends on their mechanical interaction with blood cells. Entry of bubbles into a region with vortices and high shear stresses may result in the coalescence, fission, or dissolution of microbubbles, which potentially affects the accuracy of streamline detection in the vortex zones. Thus, the verification of ULM accuracy for the determination of local hemodynamic peculiarities is necessary. Perhaps the development of more complex models than those for solid particles will be needed for this purpose.

It is noteworthy that the limitations of the medical ultrasound used in this work in relation to the advantages of the ULM method for in vitro Echo-PV for vessels can be overcome by scaling up the vessel size of the phantom, maintaining the dimensions of the post-stenotic vortex zone. Further in vitro studies to confirm the feasibility of such a large-scale transition are planned.

3.2. Computer Simulations and Accuracy Investigation

The results of the comparison of simulation and experiment are summarized below.

Figure 7 shows the result of field simulations of 20-µm aluminum particles (as used in the experiment) and 200-µm calcite particles. The modeling results are superimposed on the photo of particle motion during the Azuma experiment [1]. We note a good qualitative correspondence of the distribution of the volume fraction of model particles with the density and trajectories of real particles.

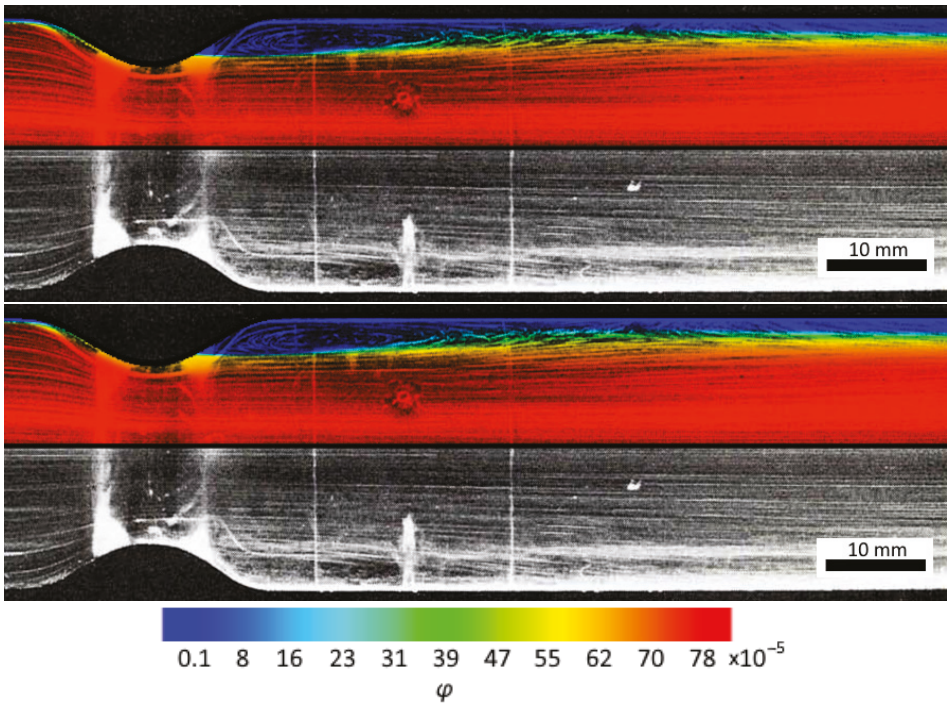


Figure 7. Distribution of particles volume fraction $\varphi = \frac{V_d}{V_d+V_c}$ near the area of stenosis, where V_d is the reduced volume of dispersed phase and V_c is the volume of continuous phase. Upper panel: model with aluminum particles; lower panel: model with calcite particles. The simulation results were compared with the experimental data [1].

However, the analysis of the velocities of model particles (Figure 8) shows that larger particles are not as well captured by the slow vortex behind the stenosis. The drag force grows slower than the inertia with increasing particle size. Therefore, the inertia of larger calcite particles begins to dominate and straightens the particle trajectory in the vortex zone. At the same time, the motion of small aluminum particles is to a greater extent determined by drag force, which entrains the particles following the streamlines inside the post-stenotic vortex zone. This leads to the circulation trajectories of the calcite particles in this region becoming indistinct. We can see this effect in Figure 6. At the same time, the small aluminum particles in the model give clear circulation streamlines, which agrees with the Azuma experiment.

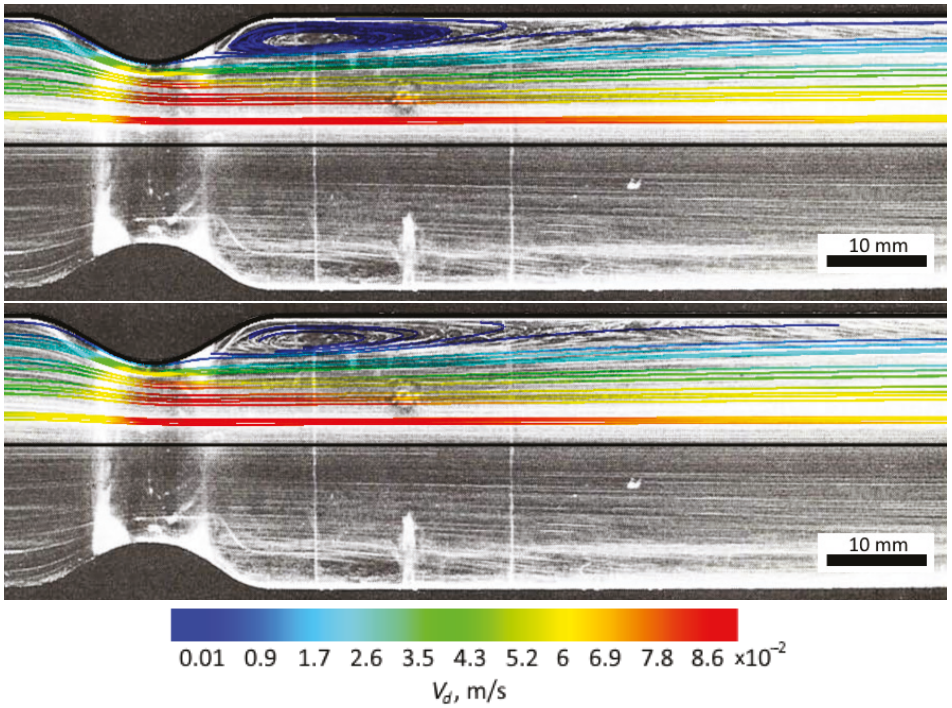


Figure 8. The streamlines represent the velocity of the dispersed phase, V_d. Upper panel: model with aluminum particles; lower panel: model with calcite particles. The simulation results were compared with the experimental data [1].

A comparison of the particle velocity absolute value (Figure 9) shows that, regardless of the size, the particles are captured by the flow equally well (differences do not exceed 0.1% of the fluid velocity). However, in the poststenotic region (highlighted in the red box and magnified), the circulating vortex contours determined by the gradient method are significantly different.

To evaluate the quantitative difference between the methods using calcite and aluminum particles, we prepared a template of the measured parameters of the poststenotic zone. Figure 10 schematically shows the contour for the circulating vortices, which was determined by the gradient method (Figure 9).

Using this template, the results of the simulations were processed and the results were summarized.

Table 4 quantifies the poststenotic circulation region. The largest deviation is observed for the parameters "Length" and "y_3". This is due to the fact that larger calcite particles have greater inertia and are not as well captured by the vortex. As can be seen, the use of large calcite particles for detection does not lead to a serious increase in the size of the vortex region (up to 5%), which is significant for the verification process. Note that the largest error is observed in determining the length of the vortex zone. This is explained by the effect of the greater inertia of large calcite particles, which, as was shown earlier, rarely

get into the vortex zone and envelope it. Thus, this zone is closed later than when using small aluminum particles.

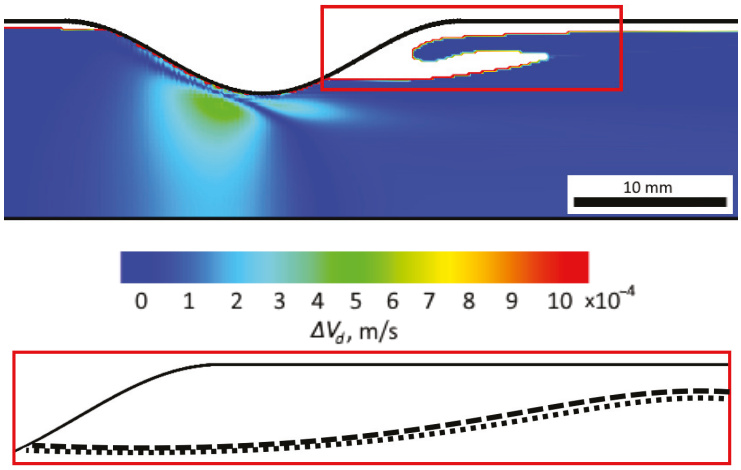


Figure 9. Difference between velocities of aluminum particles and calcite particles, ΔV_d, near the area of stenosis. The poststenotic region for which the isolines reflecting the volume fraction of particles $\varphi = 15 \times 10^{-5}$ were considered is included in the red box. Dashed line: model with aluminum particles; dotted line: model with calcite particles.

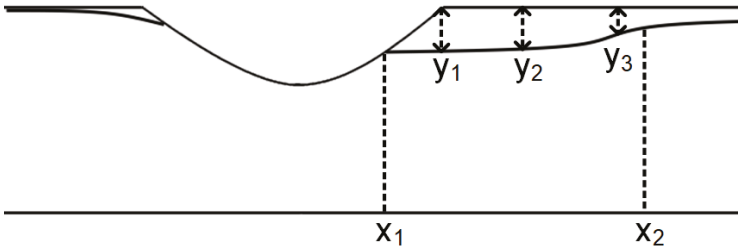


Figure 10. Schematic representation of the circulating vortex contour for the poststenotic region. Parameters x_1 and x_2 are coordinates along the symmetry axis of the vessel, which characterize the position of the separation point and the attachment point of the boundary layer. The parameters y_1, y_2, and y_3 characterize the vortex width that was measured at the beginning, middle, and end of the vortex area. The "Length" quantity defines the length of the vortex zone.

Table 4. Comparison of the model with aluminum particles and the model with calcite particles. Parameters for comparison are presented in the scheme (see Figure 10).

Parameter (m)	Aluminum Particles	Calcite Particles	Difference (%)
x_1	0.0673	0.0679	0.88
x_2	0.094	0.096	2.08
Length	0.0267	0.0281	4.98
y_1	0.0038	0.00379	0.26
y_2	0.00395	0.00389	1.51
y_3	0.0020	0.0019	5

Experimentation and modelling allows us to formulate a number of limitations for the Echo-PV technique under consideration.

The method has significant dependence on the characteristics of ultrasonic equipment (low resolution and noise make it difficult to restore particle tracks and smear the boundary of the vortex zone), the liquid environment must be pre-cleaned and degassed to reduce noise, and the fluid pump must provide an even flow of fluid in the area of occlusion. For phantom vessels, this condition is not a big problem, but in the case of in vivo it is much more difficult to provide them.

Particle (marker) size should significantly exceed the size of blood cells and aggregates. If the size of the marker is comparable to the size of an erythrocyte, the track of the marker will be largely determined, not by the fluid flow, but by interaction with blood cells. For this reason, the PV technique with large (>100 μm) particles is more relevant for detecting flows in vessels. On the other hand, the use of large particles leads to a nonlinear dependence of the hydrodynamic and rheological forces on the velocity. Therefore, the accuracy of in vivo detection will strongly depend on the shape of the vessel, the properties of the liquid, and the properties of the ultrasound machine.

For asymmetric vessels, the choice of projection and depth of acoustic focusing will play a key role. It is likely that several measurements in different projections will be required. Finally, it should be taken into account that, especially in low-velocity fluid flows, the role of gravity will increase.

For in vitro experiments in phantom vessels, any available particle materials with sufficient echogenicity can be used. However, in vivo experiments require confirmation of the safety of materials and their concentration. It is very difficult to select large solid particles with such properties. In in vivo practice, gas bubbles are commonly used as tracers [58,59]. However, gas bubbles have several disadvantages. Solid particles have stronger acoustic backscattering and higher echo intensity compared to gas bubbles. This enhanced acoustic response allows for more reliable and accurate detection of solids, even under difficult flow conditions or in the presence of background noise. Gas bubbles, on the other hand, can have weaker acoustic signals, resulting in lower detection sensitivity and possible measurement errors. Particulate matter allows for better control of particle characteristics such as size, shape, and density that directly affect the accuracy of velocity measurements. Gas bubbles, due to their inherent variability in size and shape, can introduce uncertainty and errors in velocity measurements. Thus, additional theoretical and clinical studies are needed to select a particle material that has a sufficiently strong acoustic response, has stable and controllable characteristics, and can provide high accuracy in measuring localized vortex flows.

4. Conclusions

This paper presents a theoretical study of the Echo-PTV method for tracing streamlines and segmentation of the low-velocity vortex zone in vessels with stenosis. A mathematical model of the particle motion in a liquid flow was developed, and computer simulations were carried out for two experimental conditions. The first is the formation of a vortex zone by means of large-size calcite particles (100–200 μm in diameter) and the second—small-size microparticles of aluminum (20 μm in diameter) [1]. The possibility of calcite particles detection using the echolocation method was confirmed experimentally. Despite the fundamental difference between particle visualization methods (optical or Echo-PV), an error in determining the size of the vortex zone does not exceed 5%. Thus, calcite particles meet the requirements of Echo-PV technology for the in vitro verification of complex hemodynamic models.

Finally, this study is a first step towards applying the proposed methodology in clinical practice. Further in vitro studies are needed. We plan to compare the simulation results mentioned in this study with in vitro experimental findings that can be obtained using the Echo-PV methodology. In particular, the effects of various experimental variables (stenosis size and shape, flow rate, fluid viscosity, particle nature, etc.) on local flow features will be the focus of our next investigations.

Author Contributions: Conceptualization, I.S. and F.B.; methodology, I.S., O.D. and K.M.; software, K.M. and S.S.; formal analysis, F.B. and I.S.; investigation, I.S., P.M., F.B., O.D. and K.M.; data curation, F.B. and S.S.; writing—original draft preparation, I.S., F.B., K.M., P.M. and S.S.; writing—review and editing, I.S., F.B., P.M. and S.S.; visualization, I.S. and K.M.; supervision, I.S. and F.B.; project administration, I.S. and F.B.; funding acquisition, I.S. and F.B. All authors have read and agreed to the published version of the manuscript.

Funding: This study was supported by the Russian Science Foundation (project No. 22-71-10071).

Data Availability Statement: All data are contained within the article.

Conflicts of Interest: The authors declare no conflict of interest.

References

1. Azuma, T.; Fukushima, T. Flow patterns in stenotic blood vessel models. *Biorheology* **1976**, *13*, 337–355. [CrossRef]
2. Kwak, B.R.; Bäck, M.; Bochaton-Piallat, M.L.; Caligiuri, G.; Daemen, M.J.; Davies, P.F.; Hoefer, I.E.; Holvoet, P.; Jo, H.; Krams, R.; et al. Biomechanical factors in atherosclerosis: Mechanisms and clinical implications. *Eur. Heart J.* **2014**, *35*, 3013–3020. [CrossRef]
3. Chatzizisis, Y.S.; Coskun, A.U.; Jonas, M.; Edelman, E.R.; Feldman, C.L.; Stone, P.H. Role of endothelial shear stress in the natural history of coronary atherosclerosis and vascular remodeling: Molecular, cellular, and vascular behavior. *J. Am. Coll. Cardiol.* **2007**, *49*, 2379–2393. [CrossRef]
4. Morbiducci, U.; Kok, A.M.; Kwak, B.R.; Stone, P.H.; Steinman, D.A.; Wentzel, J.J. Atherosclerosis at arterial bifurcations: Evidence for the role of haemodynamics and geometry. *Thromb. Haemost.* **2016**, *115*, 484–492. [CrossRef]
5. Gimbrone, M.A., Jr.; Topper, J.N.; Nagel, T.; Anderson, K.R.; Garcia-Cardeña, G. Endothelial dysfunction, hemodynamic forces, and atherogenesis a. *Ann. N. Y. Acad. Sci.* **2000**, *902*, 230–240. [CrossRef]
6. Chahed, N.; Peronneau, P.; Delouche, A.; Diebold, B. Velocity profiles and streamlines of a revolution post-stenotic flow. *Biorheology* **1991**, *28*, 383–400. [CrossRef]
7. Buchanan, J., Jr.; Kleinstreuer, C.; Comer, J. Rheological effects on pulsatile hemodynamics in a stenosed tube. *Comput. Fluids* **2000**, *29*, 695–724. [CrossRef]
8. Mallinger, F.; Drikakis, D. Instability in three-dimensional, unsteady, stenotic flows. *Int. J. Heat Fluid Flow* **2002**, *23*, 657–663. [CrossRef]
9. Neofytou, P.; Drikakis, D. Effects of blood models on flows through a stenosis. *Int. J. Numer. Methods Fluids* **2003**, *43*, 597–635. [CrossRef]
10. Cheng, L.; Robertson, J.; Clark, M. Numerical calculations of plane oscillatory non-uniform flow—II. Parametric study of pressure gradient and frequency with square wall obstacles. *J. Biomech.* **1973**, *6*, 521–538. [CrossRef]
11. Daly, B.J. A numerical study of pulsatile flow through stenosed canine femoral arteries. *J. Biomech.* **1976**, *9*, 465–475. [CrossRef] [PubMed]
12. Mandal, D.; Manna, N.; Chakrabarti, S. Influence of different bell-shaped stenoses on the progression of the disease, atherosclerosis. *J. Mech. Sci. Technol.* **2011**, *25*, 1933–1947. [CrossRef]
13. Paul, M.C.; Molla, M.M.; Roditi, G. Large–Eddy simulation of pulsatile blood flow. *Med. Eng. Phys.* **2009**, *31*, 153–159. [CrossRef] [PubMed]
14. Lee, T.; Liao, W.; Low, H. Numerical simulation of turbulent flow through series stenoses. *Int. J. Numer. Methods Fluids* **2003**, *42*, 717–740. [CrossRef]
15. Starodumov, I.O.; Blyakhman, F.A.; Sokolov, S.Y.; Bessonov, I.S.; Zubarev, A.Y.; Alexandrov, D.V. In-silico study of hemodynamic effects in a coronary artery with stenosis. *Eur. Phys. J. Spec. Top.* **2020**, *229*, 3009–3020. [CrossRef]
16. Starodumov, I.O.; Sokolov, S.Y.; Alexandrov, D.V.; Zubarev, A.Y.; Bessonov, I.S.; Chestukhin, V.V.; Blyakhman, F.A. Modelling of hemodynamics in bifurcation lesions of coronary arteries before and after myocardial revascularization. *Phil. Trans. R. Soc. A* **2022**, *380*, 20200303. [CrossRef]
17. Starodumov, I.; Alexandrov, D.; Zubarev, A.; Toropova, L.; Sokolov, S.; Blyakhman, F. Influence of near-wall layer hemodynamics on blood flow in a vessel with stenosis. *AIP Conf. Proc.* **2023**, *2803*, 040002.
18. Starodumov, I.O.; Sokolov, S.Y.; Blyakhman, F.A.; Zubarev, A.Y.; Fedotov, S.P.; Alexandrov, D.V. In silico study of magnetic nanoparticles transport in channels of various diameters in the presence of a constant magnetic field. *Eur. Phys. J. Spec. Top.* **2023**, *232*, 1207–1217. [CrossRef]
19. Starodumov, I.; Makhaeva, K.; Zubarev, A.; Bessonov, I.; Sokolov, S.; Mikushin, P.; Alexandrov, D.; Chestukhin, V.; Blyakhman, F. Modeling of Local Hematocrit for Blood Flow in Stenotic Coronary Vessels. *Fluids* **2023**, *8*, 230. [CrossRef]
20. Dirix, P.; Buoso, S.; Peper, E.; Kozerke, S. Synthesis of patient-specific multipoint 4D flow MRI data of turbulent aortic flow downstream of stenotic valves. *Sci. Rep.* **2022**, *12*, 16004. [CrossRef]
21. Jhun, C.S.; Newswanger, R.; Cysyk, J.; Ponnaluri, S.; Good, B.; Manning, K.; Rosenberg, G. Dynamics of Blood Flows in Aortic Stenosis: Mild, Moderate, and Severe. *ASAIO J. (Am. Soc. Artif. Intern. Organs 1992)* **2021**, *67*, 666–674. [CrossRef] [PubMed]
22. Gracka, M.; Lima, R.; Miranda, J.M.; Student, S.; Melka, B.; Ostrowski, Z. Red blood cells tracking and cell-free layer formation in a microchannel with hyperbolic contraction: A CFD model validation. *Comput. Methods Programs Biomed.* **2022**, *226*, 107117. [CrossRef]
23. Abbasian, M.; Shams, M.; Valizadeh, Z.; Moshfegh, A.; Javadzadegan, A.; Cheng, S. Effects of different non-Newtonian models on unsteady blood flow hemodynamics in patient-specific arterial models with in-vivo validation. *Comput. Methods Programs Biomed.* **2020**, *186*, 105185. [CrossRef] [PubMed]
24. Guerciotti, B.; Vergara, C. Computational comparison between Newtonian and non-Newtonian blood rheologies in stenotic vessels. In *Biomedical Technology: Modeling, Experiments and Simulation*; Springer: Berlin/Heidelberg, Germany, 2018; pp. 169–183.

25. Liu, B.; Tang, D. Influence of non-Newtonian properties of blood on the wall shear stress in human atherosclerotic right coronary arteries. *Mol. Cell. Biomech. MCB* **2011**, *8*, 73.
26. Hund, S.J.; Kameneva, M.V.; Antaki, J.F. A Quasi-Mechanistic Mathematical Representation for Blood Viscosity. *Fluids* **2017**, *2*, 10. [CrossRef]
27. Wajihah, S.A.; Sankar, D. A review on non-Newtonian fluid models for multi-layered blood rheology in constricted arteries. *Arch. Appl. Mech.* **2023**, *93*, 1771–1796. [CrossRef]
28. Ponalagusamy, R.; Manchi, R. A study on two-layered (K.L-Newtonian) model of blood flow in an artery with six types of mild stenoses. *Appl. Math. Comput.* **2020**, *367*, 124767. [CrossRef]
29. Beris, A.N.; Horner, J.S.; Jariwala, S.; Armstrong, M.J.; Wagner, N.J. Recent advances in blood rheology: A review. *Soft Matter* **2021**, *17*, 10591–10613. [CrossRef]
30. Rabby, M.G.; Shupti, S.P.; Molla, M.M. Pulsatile non-newtonian laminar blood flows through arterial double stenoses. *J. Fluids* **2014**, *2014*, 757902. [CrossRef]
31. Rosenfeld, M. Validation of numerical simulation of incompressible pulsatile flow in a constricted channel. *Comput. Fluids* **1993**, *22*, 139–156. [CrossRef]
32. Rosenfeld, M. A numerical study of pulsating flow behind a constriction. *J. Fluid Mech.* **1995**, *301*, 203–223. [CrossRef]
33. Tutty, O. Pulsatile Flow in a Constricted Channel. *J. Biomech. Eng.* **1992**, *114*, 50–54. [CrossRef] [PubMed]
34. Mucci, R. Compact, Low Cost Particle Image Velocimetry System for the In Vitro Analysis of Cardiovascular Flows. Ph.D. Thesis, Politecnico di Torino, Turin, Italy, 2021.
35. Katritsis, D.; Theodorakakos, A.; Pantos, I.; Andriotis, A.; Efstathopoulos, E.; Siontis, G.; Karcanias, N.; Redwood, S.; Gavaises, M. Vortex formation and recirculation zones in left anterior descending artery stenoses: Computational fluid dynamics analysis. *Phys. Med. Biol.* **2010**, *55*, 1395. [CrossRef] [PubMed]
36. Kim, S.; Ong, P.K.; Yalcin, O.; Intaglietta, M.; Johnson, P.C. The cell-free layer in microvascular blood flow. *Biorheology* **2009**, *46*, 181–189. [CrossRef] [PubMed]
37. Shakeri, M.; Khodarahmi, I.; Sharp, M.K.; Amini, A.A. Optical imaging of steady flow in a phantom model of iliac artery stenosis: Comparison of CFD simulations with PIV measurements. *SPIE Med. Imaging* **2010**, *7626*, 187–194.
38. Gülan, U.; Lüthi, B.; Holzner, M.; Liberzon, A.; Tsinober, A.; Kinzelbach, W. Experimental study of aortic flow in the ascending aorta via particle tracking velocimetry. *Exp. Fluids* **2012**, *53*, 1469–1485. [CrossRef]
39. Roloff, C.; Stucht, D.; Beuing, O.; Berg, P. Comparison of intracranial aneurysm flow quantification techniques: Standard PIV vs stereoscopic PIV vs tomographic PIV vs phase-contrast MRI vs CFD. *J. Neurointerv. Surg.* **2019**, *11*, 275–282. [CrossRef]
40. Buchmann, N.; Atkinson, C.; Jeremy, M.; Soria, J. Tomographic particle image velocimetry investigation of the flow in a modeled human carotid artery bifurcation. *Exp. Fluids* **2011**, *50*, 1131–1151. [CrossRef]
41. Wu, X.; Gürzing, S.; Schinkel, C.; Toussaint, M.; Perinajová, R.; van Ooij, P.; Kenjereš, S. Hemodynamic Study of a Patient-Specific Intracranial Aneurysm: Comparative Assessment of Tomographic PIV, Stereoscopic PIV, In Vivo MRI and Computational Fluid Dynamics. In *Cardiovascular Engineering and Technology*; Springer: Berlin/Heidelberg, Germany, 2021; pp. 1–15.
42. Fouras, A.; Kitchen, M.J.; Dubsky, S.; Lewis, R.; Hooper, S.B.; Hourigan, K. The past, present, and future of x-ray technology for in vivo imaging of function and form. *J. Appl. Phys.* **2009**, *105*, 102009. [CrossRef]
43. Brum, J.; Bernal, M.; Barrere, N.; Negreira, C.; Cabeza, C. Vortex dynamics and transport phenomena in stenotic aortic models using echo-PIV. *Phys. Med. Biol.* **2021**, *66*, 055026. [CrossRef]
44. Walker, A.M.; Scott, J.; Rival, D.E.; Johnston, C.R. In vitro post-stenotic flow quantification and validation using echo particle image velocimetry (Echo PIV). *Exp. Fluids* **2014**, *55*, 1–16. [CrossRef]
45. DeMarchi, N.; White, C. Echo particle image velocimetry. *JoVE J. Vis. Exp.* **2012**, *70*, 4265.
46. Blyakhman, F.; Safronov, A.; Starodumov, I.; Kuznetsova, D.; Kurlyandskaya, G. Remote Positioning of Spherical Alginate Ferrogels in a Fluid Flow by a Magnetic Field: Experimental and Computer Simulation. *Gels* **2023**, *9*, 711. [CrossRef] [PubMed]
47. Blyakhman, F.A.; Sokolov, S.Y.; Safronov, A.P.; Dinislamova, O.A.; Shklyar, T.F.; Zubarev, A.Y.; Kurlyandskaya, G.V. Ferrogels ultrasonography for biomedical applications. *Sensors* **2019**, *19*, 3959. [CrossRef]
48. Rayleigh, L. VIII. On the question of the stability of the flow of fluids. *Lond. Edinb. Dublin Philos. Mag. J. Sci.* **1892**, *34*, 59–70. [CrossRef]
49. Boothroyd, R.G. Flowing Gas-Solids Suspensions. *J. Fluid Mech.* **1971**, *53*, 591–592.
50. Klyachko, L. Equations of motion of dust particles in dust collectors. *Otop. Vent.* **1934**, *4*, 27–29.
51. James, P.; Hewitt, G.; Whalley, P. *Droplet Motion in Two-Phase Flow*; Technical Report; Nuclear Regulatory Commission: Washington, DC, USA, 1980; pp. 1484–1503.
52. Courant, R.; Friedrichs, K.; Lewy, H. Über die partiellen Differenzengleichungen der mathematischen Physik. *Math. Ann.* **1928**, *100*, 32–74. [CrossRef]
53. Aksenov, A.A. Flowvision: Industrial computational fluid dynamics. *Comput. Res. Model.* **2017**, *9*, 5–20. [CrossRef]
54. Couture, O.; Hingot, V.; Heiles, B.; Muleki-Seya, P.; Tanter, M. Ultrasound localization microscopy and super-resolution: A state of the art. *IEEE Trans. Ultrason. Ferroelectr. Freq. Control* **2018**, *65*, 1304–1320. [CrossRef]
55. Demeulenaere, O.; Mateo, P.; Ferrera, R.; Chiaroni, P.M.; Bizé, A.; Dai, J.; Sambin, L.; Gallet, R.; Tanter, M.; Papadacci, C.; et al. Assessment of coronary microcirculation alterations in a porcine model of no-reflow using ultrasound localization microscopy: A proof of concept study. *EBioMedicine* **2023**, *94*, 104727. [CrossRef]

56. Demeulenaere, O.; Sandoval, Z.; Mateo, P.; Dizeux, A.; Villemain, O.; Gallet, R.; Ghaleh, B.; Deffieux, T.; Deméné, C.; Tanter, M.; et al. Coronary flow assessment using 3-dimensional ultrafast ultrasound localization microscopy. *Cardiovasc. Imaging* **2022**, *15*, 1193–1208. [CrossRef] [PubMed]
57. Renaudin, N.; Demené, C.; Dizeux, A.; Ialy-Radio, N.; Pezet, S.; Tanter, M. Functional ultrasound localization microscopy reveals brain-wide neurovascular activity on a microscopic scale. *Nat. Methods* **2022**, *19*, 1004–1012. [CrossRef] [PubMed]
58. Chong, W.K.; Papadopoulou, V.; Dayton, P.A. Imaging with ultrasound contrast agents: Current status and future. *Abdom. Radiol.* **2018**, *43*, 762–772. [CrossRef] [PubMed]
59. Frinking, P.; Segers, T.; Luan, Y.; Tranquart, F. Three decades of ultrasound contrast agents: A review of the past, present and future improvements. *Ultrasound Med. Biol.* **2020**, *46*, 892–908. [CrossRef]

Disclaimer/Publisher's Note: The statements, opinions and data contained in all publications are solely those of the individual author(s) and contributor(s) and not of MDPI and/or the editor(s). MDPI and/or the editor(s) disclaim responsibility for any injury to people or property resulting from any ideas, methods, instructions or products referred to in the content.

inventions

MDPI

Article

Effect of Support Stiffness Nonlinearity on the Low-Frequency Vibro-Acoustic Characteristics for a Mechanical Equipment—Floating Raft—Underwater Cylindrical Shell Coupled System

Likang Wang [1,2] and Rui Huo [1,2,*]

[1] School of Mechanical Engineering, Shandong University, Jinan 250061, China; 202134363@mail.sdu.edu.cn
[2] Key Laboratory of High Efficiency and Clean Mechanical Manufacture, Shandong University, Ministry of Education, Jinan 250061, China
* Correspondence: huorui@sdu.edu.cn

Abstract: The low-frequency vibro-acoustic characteristics of a mechanical equipment—floating raft—cylindrical shell—underwater acoustic field coupled system with nonlinear supports are studied in this paper. Firstly, the state space equations were established by a modal superposition theory for the coupled system, and a modal parameter identification method was deduced and verified for the cylindrical shell—underwater acoustic field coupled subsystem. On this basis, the formulas were derived for transmitted power flow in the coupled system, and the nonlinear stiffness constitutive relation of the vibration isolation supports was expressed by softening and hardening characteristics. Finally, dynamic simulations were carried out by the Runge—Kutta method to analyze the effect of nonlinear stiffness characteristic parameters on the low-frequency vibration modes and vibro-acoustic transfer characteristics in the coupled system. The research shows that a superharmonic phenomenon is common in the steady vibration mode of the coupled system with a nonlinear softening (or hardening) stiffness characteristic under harmonic excitation. The stronger the softening (or hardening) stiffness characteristic is, the more complex the vibration form is, and the smaller (or larger) the low-frequency vibro-acoustic transfer level in resonance regions is.

Keywords: support stiffness nonlinearity; cylindrical shell; modal parameter identification; low-frequency vibration; transmitted power flow; vibro-acoustic transfer characteristics

1. Introduction

Nonlinear vibration mode is an important factor to be considered in the study of low-frequency vibration isolation for underwater cylindrical shell systems. Due to relatively high vibration energy at low frequencies, the elastic support, which presents linear stiffness in an original micro-amplitude vibration mode, will show nonlinear characteristics. Strictly speaking, stiffness characteristics of various elastic vibration isolation elements are nonlinear. In a micro-amplitude vibration mode, a vibration isolator has a certain linear stiffness working interval. Stiffness characteristics are nonlinear if amplitude is sufficiently large.

In recent years, many scholars have studied the vibration characteristics of nonlinear vibration isolation systems. Smirnov et al. [1] studied and compared the efficiency of linear and nonlinear vibration isolation systems. Santhosh [2] studied the dynamic performance of an asymmetric nonlinear vibration isolation mechanism under harmonic excitation. Dutta et al. [3] analyzed a nonlinear vibration isolator with magnetorheological fluid dampers and cubic nonlinear springs to determine the effectiveness of isolation during force or displacement excitation. Suman et al. [4] proposed a nonlinear vibration control device based on a negative stiffness mechanism, which can improve the isolation ability of the vibration suspension system in the low-frequency range. Araki et al. [5] proposed a

vertical quasi-zero stiffness (QZS) vibration isolator with adjustable restoring force. Zhao et al. [6,7] successively designed QZS vibration isolators with two and three pairs of inclined springs. Ye et al. [8] proposed a QZS system based on a cam—roller mechanism. Chang et al. [9] proposed a QZS dynamic shock absorber. Bouna et al. [10] studied the vibration control of multi-span girder bridges under the excitation of pier foundation vibration by using nonlinear QZS isolators. Drezet et al. [11] proposed a nonlinear vibration energy harvester based on the concept of high static and low dynamic stiffness (HSLDS). Lu et al. [12–14] studied an orthogonal six-degree-of-freedom vibration isolation system with HSLDS and an electromagnetic Stewart platform to suppress the low-frequency vibration of high-precision instruments, provided modal coefficients by improved Fourier series and the Rayleigh—Ritz method, and studied the nonlinear energy transfer of flexible plates with arbitrary boundaries coupled to HSLDS isolators. Sun et al. [15] proposed a method for designing HSLDS mounts based on target force curves, which are obtained by placing negative stiffness structures in parallel with positive stiffness linear springs. Yao et al. [16] proposed an HSLDS isolator with a cam—roller—spring mechanism, in which the cam profile can be specially designed to suit different operating requirements. Chong et al. [17] designed a nonlinear X-combined structure with HSLDS in a large displacement range, which avoided negative stiffness and instability factors and improved its vibration isolation characteristics.

Chaos is a unique dynamical behavior of nonlinear systems. Leutcho et al. [18] systematically studied a new type of chaotic system with single parametric nonlinearity. Yan et al. [19] proposed a novel bi-state nonlinear vibration isolator, whose motion can be either periodic or chaotic. Rahman et al. [20] proposed a new fractional-order chaotic system containing multiple nonlinear terms, which can excite hidden chaotic attractors or self-excited chaotic attractors depending on the chosen system parameters or the value of its fractional-order derivative. Li et al. [21] proposed an SRN feature extraction method combining maximum relevance minimum redundancy, which can effectively classify different chaotic signals. Karimov et al. [22] proposed a novel implementation of the chaotic Duffing oscillator as a simple mechanical system with a translational movement. Dreau et al. [23] introduced a stochastic modeling method for nonlinear systems with response surface discontinuity, which improved the efficiency of multi-variate polynomial chaos expansion.

The power flow characteristic is an important index to study nonlinear vibration isolation. Cassidy et al. [24] proposed a general nonlinear control synthesis method for power flow constrained energy harvesters, which is analytically guaranteed to be superior to the optimal static admittance in the steady state random response. Silva et al. [25] proposed a technique for evaluating and optimizing vibrational power flow involving beam-and-plate coupling. Varghese et al. [26] applied the combined transient power flow balancing and acceleration matching techniques to detect and quantify the crack damage of beam structures at different positions. Yang et al. [27,28] successively studied the power flow and force transmissibility characteristics of a two-degree-of-freedom nonlinear vibration isolation system and a coupled nonlinear oscillator. Ren et al. [29] compared the power transmission between rigid, single-stage isolation and double-stage isolation gearbox installation configurations with the vibration power flow of the system as the evaluation index. Zhang et al. [30] proposed a power flow analysis method for quantitatively evaluating the dynamic performance of a nonlinear energy sink in the frequency domain. Xu et al. [31] analyzed the bending vibration and power flow of axially loaded beams with arbitrary boundaries and nonuniform elastic foundations via energy principle in conjunction with the Rayleigh—Ritz procedure. Mahapatra et al. [32] studied the influence of general coupling conditions on the vibration and power flow characteristics of a two-plate composite plate structure.

There has been a lot of literature on the dynamics of nonlinear vibration isolation systems at home and abroad and, especially, the application of quasi-zero stiffness or high static and low dynamic stiffness nonlinear vibration isolators for low-frequency vibration control has become a research hotspot in the last decade. However, compared with the

wide application of nonlinear vibration isolators, the mechanism of vibro-acoustic transfer in nonlinear vibration isolation systems, especially the influence of nonlinear factors in low-frequency vibration modes, has not been fully studied. In this paper, the low-frequency vibro-acoustic characteristics of a mechanical equipment—floating raft—underwater cylindrical shell coupled system with nonlinear stiffness supports are studied. It can not only provide theoretical guidance for low-frequency vibration analysis, diagnosis, and design of dynamics of underwater nonlinear coupled systems but also provide reference for the design of nonlinear vibration isolators.

The rest of this paper is organized as follows. In Section 2, based on the parametric modeling of an admittance method of a mechanical equipment—floating raft—cylindrical shell—underwater acoustic field coupled system, the state space equations of the subsystems are established by using modal identification and modal superposition theories; and then the nonlinear stiffness constitutive relation of the vibration isolation supports is expressed by softening and hardening characteristics, and the calculation method of transmitted power flow is derived. In Section 3, the influence of nonlinear stiffness characteristic parameters on the vibro-acoustic characteristics of the coupled system is studied by using MATLAB numerical simulation. Finally, some conclusions are presented in Section 4.

2. Materials and Methods

2.1. Model of a Mechanical Equipment—Floating Raft—Cylindrical Shell—Underwater Acoustic Field Coupled System

Figure 1 describes the model of a mechanical equipment—floating raft—cylindrical shell—underwater acoustic field coupled system.

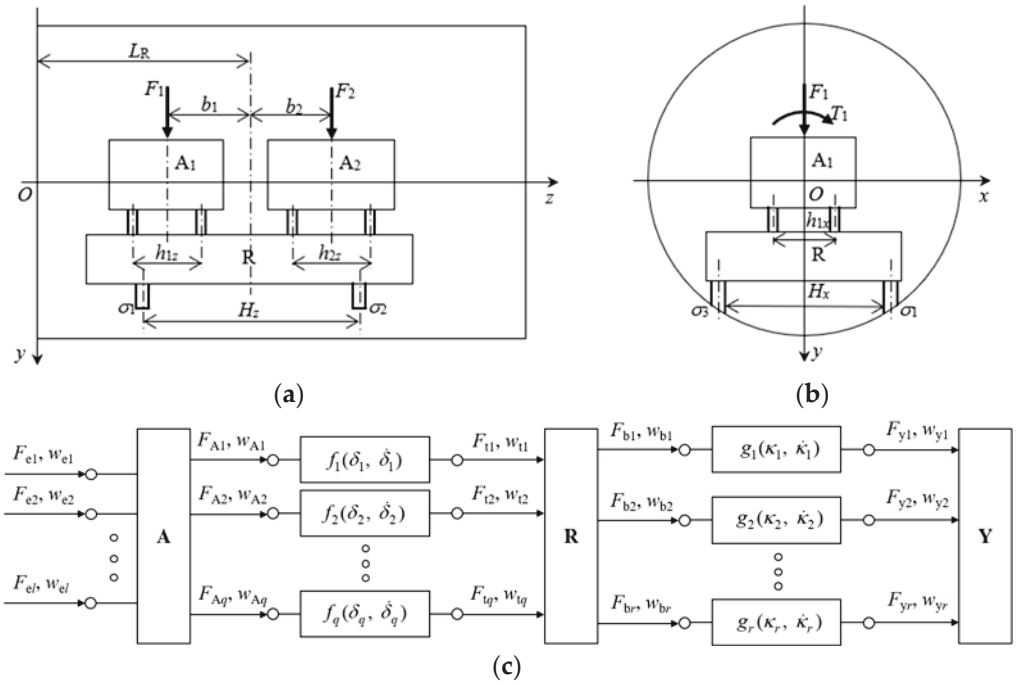


Figure 1. The model of a mechanical equipment—floating raft—cylindrical shell—underwater acoustic field coupled system: (**a**) $-x$ direction; (**b**) z direction; (**c**) complex coupled system with nonlinear connecting elements.

As shown in Figure 1a,b, vibration source mechanical equipment A_1 and A_2 (simulating multiple units) are installed on a floating raft R. Each unit is connected to the raft frame through four elastic supports, and the raft frame is connected to a cylindrical shell through four elastic supports. A rectangular coordinate system *Oxyz* is established, where the *Oz* axis is the center line of the cylinder and *Oy* is the vertical direction. To simplify analysis, only the vertical translational vibration and the rotational vibration around the

Oz and Ox axes of the system are considered. Therefore, vertical excitation forces F_1, F_2 and excitation torques T_1, T_2 around the Oz axis are applied at the center of mass of each unit. The units A_1, A_2 and the floating raft R are all rigid bodies symmetrical about the yOz plane. In Figure 1a,b, b_1, b_2, h_{1z}, h_{2z}, h_{1x}, h_{2x}, H_z, H_x, and L_R are the installation size parameters of the system, and σ_1, σ_2, σ_3, and σ_4 are the connection points of the lower vibration isolation supports with the cylindrical shell.

Figure 1c abstracts the complex coupled system with nonlinear connecting elements. **A** (the vibration source subsystem) is subjected to l excitations F_{en} (n = 1, 2, …, l) and has displacement responses w_{en} at the excitations. **A** is connected to **R** (the raft frame) by q elastic connecting elements. At the connection points of the elastic elements with **A** and **R**, there are excitation forces F_{Ai} and F_{ti} (i = 1, 2, …, q), as well as displacement responses w_{Ai} and w_{ti}. The elastic elements have constitutive relation $f_i(\delta_i, \dot{\delta}_i)$, where $\delta_i = w_{Ai} - w_{ti}$. Similarly, **R** is connected to **Y** (the cylindrical shell–underwater acoustic field coupled subsystem) by r elastic connecting elements. At the connection points of the elastic elements with **R** and **Y**, there are excitation forces F_{bj} and F_{yj} (j = 1, 2, …, r), as well as displacement responses w_{bj} and w_{yj}. The elastic elements have constitutive relation $g_j(\kappa_j, \dot{\kappa}_j)$, where $\kappa_j = w_{bj} - w_{yj}$. For specific practical problems, the number of elastic coupled elements in series in Figure 1c can be increased or decreased according to different modeling needs.

2.2. State Space Model of the Coupled System

For the unit A_1 in Figure 1, its vertical vibration displacement is represented by y_1; its angular displacement around the Ox axis is represented by θ_{1x}; and its angular displacement around the Oy axis is represented by θ_{1y}. Define a state variable $\boldsymbol{u}_{A1} = [u_1, u_2, u_3, u_4, u_5, u_6]^T = [y_1, \theta_{1x}, \theta_{1z}, \dot{y}_1, \dot{\theta}_{1x}, \dot{\theta}_{1z}]^T$, then the state space of the unit A_1 equation is

$$\dot{\boldsymbol{u}}_{A1} = \begin{bmatrix} \dot{u}_1 \\ \dot{u}_2 \\ \dot{u}_3 \\ \dot{u}_4 \\ \dot{u}_5 \\ \dot{u}_6 \end{bmatrix} = \begin{bmatrix} 0 & 0 & 0 & 1 & 0 & 0 \\ 0 & 0 & 0 & 0 & 1 & 0 \\ 0 & 0 & 0 & 0 & 0 & 1 \\ 0 & 0 & 0 & 0 & 0 & 0 \\ 0 & 0 & 0 & 0 & 0 & 0 \\ 0 & 0 & 0 & 0 & 0 & 0 \end{bmatrix} \begin{bmatrix} u_1 \\ u_2 \\ u_3 \\ u_4 \\ u_5 \\ u_6 \end{bmatrix} + \begin{bmatrix} 0 \\ 0 \\ 0 \\ -\boldsymbol{I}_{1\times4}\cdot\boldsymbol{F}_1/m_1 \\ \boldsymbol{Z}_1\cdot\boldsymbol{F}_1/J_{1x} \\ -\boldsymbol{X}_1\cdot\boldsymbol{F}_1/J_{1z} \end{bmatrix} + \begin{bmatrix} 0 \\ 0 \\ 0 \\ F_1/m_1 \\ 0 \\ T_1/J_{1z} \end{bmatrix} = \boldsymbol{\Lambda}_0\cdot\boldsymbol{u}_{A1} + \boldsymbol{f}_{A1}(\boldsymbol{F}_1) + \boldsymbol{f}_{in1}(t) \quad (1)$$

where $\boldsymbol{F}_1 = [F_{A1}, F_{A2}, F_{A3}, F_{A4}]^T$ is an excitation force column vector of the unit A_1 to its four supports; m_1, J_{1x}, and J_{1z} are the mass of the unit A_1 and the moment of inertia that bypasses its centroid and is parallel to the axis of Ox and Oz, respectively; $\boldsymbol{X}_1 = [0.5h_{1x}, 0.5h_{1x}, -0.5h_{1x}, -0.5h_{1x}]$; $\boldsymbol{Z}_1 = [-0.5h_{1z}, 0.5h_{1z}, -0.5h_{1z}, 0.5h_{1z}]$; $\boldsymbol{I}_{1\times4}$ denotes a 4-dimensional row vector with all elements 1; $\boldsymbol{f}_{A1}(\boldsymbol{F}_1)$ denotes a vector function with respect to $\boldsymbol{F}_1$; $\boldsymbol{f}_{in1}$ is a known external input vector function; $\boldsymbol{\Lambda}_0$ is a constant matrix.

Similarly, for the unit A_2, its vertical vibration displacement is represented by y_2; its angular displacement around the Ox axis is represented by θ_{2x}; and its angular displacement around the Oy axis is represented by θ_{2y}. Define a state variable $\boldsymbol{u}_{A2} = [u_7, u_8, u_9, u_{10}, u_{11}, u_{12}]^T = [y_2, \theta_{2x}, \theta_{2z}, \dot{y}_2, \dot{\theta}_{2x}, \dot{\theta}_{2z}]^T$, then the state space equation of the unit A_2 is

$$\dot{\boldsymbol{u}}_{A2} = \boldsymbol{\Lambda}_0\cdot\boldsymbol{u}_{A2} + \boldsymbol{f}_{A2}(\boldsymbol{F}_2) + \boldsymbol{f}_{in2}(t) \quad (2)$$

where $\boldsymbol{F}_2 = [F_{A5}, F_{A6}, F_{A7}, F_{A8}]^T$ is an excitation force column vector of the unit A_2 to its four supports; $\boldsymbol{f}_{A2}(\boldsymbol{F}_2) = [0, 0, 0, -\boldsymbol{I}_{1\times4}\cdot\boldsymbol{F}_2/m_2, \boldsymbol{Z}_2\cdot\boldsymbol{F}_2/J_{2x}, -\boldsymbol{X}_2\cdot\boldsymbol{F}_2/J_{2z}]^T$ denotes a vector function with respect to $\boldsymbol{F}_2$; $\boldsymbol{f}_{in2} = [0, 0, 0, F_2/m_2, 0, T_2/J_{2z}]^T$ is a known external input vector function; m_2, J_{2x}, and J_{2z} are the mass of the unit A_2 and the moment of inertia that bypasses its centroid and is parallel to the axis of Ox and Oz, respectively; $\boldsymbol{X}_2 = [0.5h_{2x}, 0.5h_{2x}, -0.5h_{2x}, -0.5h_{2x}]$; $\boldsymbol{Z}_2 = [-0.5h_{2z}, 0.5h_{2z}, -0.5h_{2z}, 0.5h_{2z}]$.

Combining the units A_1 and A_2 into the vibration source equipment subsystem, Equations (1) and (2) are merged into the following state space equation:

$$\dot{\boldsymbol{u}}_{\mathrm{A}} = \begin{bmatrix} \dot{\boldsymbol{u}}_{\mathrm{A1}} \\ \dot{\boldsymbol{u}}_{\mathrm{A2}} \end{bmatrix} = \begin{bmatrix} \boldsymbol{\Lambda}_0 & \boldsymbol{O}_{6\times6} \\ \boldsymbol{O}_{6\times6} & \boldsymbol{\Lambda}_0 \end{bmatrix} \begin{bmatrix} \boldsymbol{u}_{\mathrm{A1}} \\ \boldsymbol{u}_{\mathrm{A2}} \end{bmatrix} + \begin{bmatrix} \boldsymbol{f}_{\mathrm{A1}}(\boldsymbol{F}_1) \\ \boldsymbol{f}_{\mathrm{A2}}(\boldsymbol{F}_2) \end{bmatrix} + \begin{bmatrix} \boldsymbol{f}_{\mathrm{in1}}(t) \\ \boldsymbol{f}_{\mathrm{in2}}(t) \end{bmatrix} = \boldsymbol{\Lambda}\cdot\boldsymbol{u}_{\mathrm{A}} + \boldsymbol{f}_{\mathrm{A}}(\boldsymbol{F}_1, \boldsymbol{F}_2) + \boldsymbol{f}_{\mathrm{in}}(t) \tag{3}$$

For the raft frame **R**, its vertical vibration displacement is represented by y_{R}; its angular displacement around the Ox axis is represented by $\theta_{\mathrm{R}x}$; and its angular displacement around the Oy axis is represented by $\theta_{\mathrm{R}y}$. Define a state variable $\boldsymbol{u}_{\mathrm{R}} = [u_{\mathrm{R1}}, u_{\mathrm{R2}}, u_{\mathrm{R3}}, u_{\mathrm{R4}}, u_{\mathrm{R5}}, u_{\mathrm{R6}}]^{\mathrm{T}} = [y_{\mathrm{R}}, \theta_{\mathrm{R}x}, \theta_{\mathrm{R}z}, \dot{y}_{\mathrm{R}}, \dot{\theta}_{\mathrm{R}x}, \dot{\theta}_{\mathrm{R}z}]^{\mathrm{T}}$, then the state space equation of the raft frame **R** is

$$\dot{\boldsymbol{u}}_{\mathrm{R}} = \begin{bmatrix} \dot{u}_{\mathrm{R1}} \\ \dot{u}_{\mathrm{R2}} \\ \dot{u}_{\mathrm{R3}} \\ \dot{u}_{\mathrm{R4}} \\ \dot{u}_{\mathrm{R5}} \\ \dot{u}_{\mathrm{R6}} \end{bmatrix} = \begin{bmatrix} 0 & 0 & 0 & 1 & 0 & 0 \\ 0 & 0 & 0 & 0 & 1 & 0 \\ 0 & 0 & 0 & 0 & 0 & 1 \\ 0 & 0 & 0 & 0 & 0 & 0 \\ 0 & 0 & 0 & 0 & 0 & 0 \\ 0 & 0 & 0 & 0 & 0 & 0 \end{bmatrix} \begin{bmatrix} u_{\mathrm{R1}} \\ u_{\mathrm{R2}} \\ u_{\mathrm{R3}} \\ u_{\mathrm{R4}} \\ u_{\mathrm{R5}} \\ u_{\mathrm{R6}} \end{bmatrix} + \begin{bmatrix} 0 \\ 0 \\ 0 \\ \boldsymbol{I}_{1\times8}\cdot(\boldsymbol{F}_{\mathrm{t}} - \boldsymbol{F}_{\mathrm{b}})/m_{\mathrm{R}} \\ (\boldsymbol{Z}_{\mathrm{R2}}\cdot\boldsymbol{F}_{\mathrm{b}} - \boldsymbol{Z}_{\mathrm{R1}}\cdot\boldsymbol{F}_{\mathrm{t}})/J_{\mathrm{R}x} \\ (\boldsymbol{X}_{\mathrm{R1}}\cdot\boldsymbol{F}_{\mathrm{t}} - \boldsymbol{X}_{\mathrm{R2}}\cdot\boldsymbol{F}_{\mathrm{b}})/J_{\mathrm{R}z} \end{bmatrix} = \boldsymbol{\Lambda}_0\cdot\boldsymbol{u}_{\mathrm{R}} + \boldsymbol{f}_{\mathrm{R}}(\boldsymbol{F}_{\mathrm{t}}, \boldsymbol{F}_{\mathrm{b}}) \tag{4}$$

where $\boldsymbol{F}_{\mathrm{t}} = [F_{\mathrm{t1}}, F_{\mathrm{t2}}, F_{\mathrm{t3}}, F_{\mathrm{t4}}, F_{\mathrm{t5}}, F_{\mathrm{t6}}, F_{\mathrm{t7}}, F_{\mathrm{t8}}]^{\mathrm{T}}$ and $\boldsymbol{F}_{\mathrm{b}} = [F_{\mathrm{b1}}, F_{\mathrm{b2}}, F_{\mathrm{b3}}, F_{\mathrm{b4}}]^{\mathrm{T}}$ are excitation force column vectors of the upper supports to the raft frame and the raft frame to the lower supports, respectively; m_{R}, $J_{\mathrm{R}x}$, and $J_{\mathrm{R}z}$ are the mass of the raft frame and the moment of inertia that bypasses its centroid and is parallel to the axis of Ox and Oz, respectively; $\boldsymbol{X}_{\mathrm{R1}} = [0.5h_{1x}, 0.5h_{1x}, -0.5h_{1x}, -0.5h_{1x}, 0.5h_{2x}, 0.5h_{2x}, -0.5h_{2x}, -0.5h_{2x}]$; $\boldsymbol{X}_{\mathrm{R2}} = [0.5H_x, 0.5H_x, -0.5H_x, -0.5H_x]$; $\boldsymbol{Z}_{\mathrm{R1}} = [-b_1 - 0.5h_{1z}, -b_1 + 0.5h_{1z}, -b_1 - 0.5h_{1z}, -b_1 + 0.5h_{1z}, b_2 - 0.5h_{2z}, b_2 + 0.5h_{2z}, b_2 - 0.5h_{2z}, b_2 + 0.5h_{2z}]$; $\boldsymbol{Z}_{\mathrm{R2}} = [-0.5H_z, 0.5H_z, -0.5H_z, 0.5H_z]$; $\boldsymbol{f}_{\mathrm{R}}(\boldsymbol{F}_{\mathrm{t}}, \boldsymbol{F}_{\mathrm{b}})$ denotes a vector function about $\boldsymbol{F}_{\mathrm{t}}$, $\boldsymbol{F}_{\mathrm{b}}$.

For the connection supports between the vibration source equipment and the raft frame, ignoring the effect of their mass, the power/response transfer relation is

$$F_{\mathrm{t}i} = F_{\mathrm{A}i} = f_i(\delta_i, \dot{\delta}_i),\ (i = 1, 2, \ldots, 8) \tag{5}$$

where $\delta_i = w_{\mathrm{A}i} - w_{\mathrm{t}i}$, and there are linear relationships between $w_{\mathrm{A}i}$, $w_{\mathrm{t}i}$ and the state variables $\boldsymbol{u}_{\mathrm{A}}$ and $\boldsymbol{u}_{\mathrm{R}}$:

$$\begin{cases} \boldsymbol{w}_{\mathrm{A1}} = u_1\boldsymbol{I}_{4\times1} - u_2\boldsymbol{Z}_1^{\mathrm{T}} + u_3\boldsymbol{X}_1^{\mathrm{T}}, & \dot{\boldsymbol{w}}_{\mathrm{A1}} = u_4\boldsymbol{I}_{4\times1} - u_5\boldsymbol{Z}_1^{\mathrm{T}} + u_6\boldsymbol{X}_1^{\mathrm{T}} \\ \boldsymbol{w}_{\mathrm{A2}} = u_7\boldsymbol{I}_{4\times1} - u_8\boldsymbol{Z}_2^{\mathrm{T}} + u_9\boldsymbol{X}_2^{\mathrm{T}}, & \dot{\boldsymbol{w}}_{\mathrm{A2}} = u_{10}\boldsymbol{I}_{4\times1} - u_{11}\boldsymbol{Z}_2^{\mathrm{T}} + u_{12}\boldsymbol{X}_2^{\mathrm{T}} \\ \boldsymbol{w}_{\mathrm{t}} = u_{\mathrm{R1}}\boldsymbol{I}_{8\times1} - u_{\mathrm{R2}}\boldsymbol{Z}_{\mathrm{R1}}^{\mathrm{T}} + u_{\mathrm{R3}}\boldsymbol{X}_{\mathrm{R1}}^{\mathrm{T}}, & \dot{\boldsymbol{w}}_{\mathrm{t}} = u_{\mathrm{R4}}\boldsymbol{I}_{8\times1} - u_{\mathrm{R5}}\boldsymbol{Z}_{\mathrm{R1}}^{\mathrm{T}} + u_{\mathrm{R6}}\boldsymbol{X}_{\mathrm{R1}}^{\mathrm{T}} \end{cases} \tag{6}$$

where $\boldsymbol{w}_{\mathrm{A1}} = [w_{\mathrm{A1}}, w_{\mathrm{A2}}, w_{\mathrm{A3}}, w_{\mathrm{A4}}]^{\mathrm{T}}$; $\boldsymbol{w}_{\mathrm{A2}} = [w_{\mathrm{A5}}, w_{\mathrm{A6}}, w_{\mathrm{A7}}, w_{\mathrm{A8}}]^{\mathrm{T}}$; $\boldsymbol{w}_{\mathrm{t}} = [w_{\mathrm{t1}}, w_{\mathrm{t2}}, w_{\mathrm{t3}}, w_{\mathrm{t4}}, w_{\mathrm{t5}}, w_{\mathrm{t6}}, w_{\mathrm{t7}}, w_{\mathrm{t8}}]^{\mathrm{T}}$.

Let $\boldsymbol{w}_{\mathrm{A}} = [\boldsymbol{w}_{\mathrm{A1}}{}^{\mathrm{T}}, \boldsymbol{w}_{\mathrm{A2}}{}^{\mathrm{T}}]^{\mathrm{T}}$, then Equation (5) is expressed as:

$$\boldsymbol{F}_{\mathrm{A}} = \begin{bmatrix} \boldsymbol{F}_1 \\ \boldsymbol{F}_2 \end{bmatrix} = \boldsymbol{F}_{\mathrm{t}} = \boldsymbol{f}\big(\boldsymbol{w}_{\mathrm{A}}(\boldsymbol{u}_{\mathrm{A}}) - \boldsymbol{w}_{\mathrm{t}}(\boldsymbol{u}_{\mathrm{R}}), \dot{\boldsymbol{w}}_{\mathrm{A}}(\boldsymbol{u}_{\mathrm{A}}) - \dot{\boldsymbol{w}}_{\mathrm{t}}(\boldsymbol{u}_{\mathrm{R}})\big) = \bar{\boldsymbol{f}}(\boldsymbol{u}_{\mathrm{A}}, \boldsymbol{u}_{\mathrm{R}}) \tag{7}$$

Similarly, for the connection supports between the raft frame and the cylindrical shell, ignoring the effect of their mass, the power/response transfer relation is

$$F_{\mathrm{b}j} = F_{\mathrm{y}j} = g_j(\kappa_j, \dot{\kappa}_j),\ (j = 1, 2, 3, 4) \tag{8}$$

where $\kappa_j = w_{\mathrm{b}j} - w_{\mathrm{y}j}$ and there is a linear relationship between $w_{\mathrm{b}j}$ and the state variable $\boldsymbol{u}_{\mathrm{R}}$:

$$\boldsymbol{w}_{\mathrm{b}} = u_{\mathrm{R1}}\boldsymbol{I}_{4\times1} - u_{\mathrm{R2}}\boldsymbol{Z}_{\mathrm{R2}}^{T} + u_{\mathrm{R3}}\boldsymbol{X}_{\mathrm{R2}}^{\mathrm{T}}, \quad \dot{\boldsymbol{w}}_{\mathrm{b}} = u_{\mathrm{R4}}\boldsymbol{I}_{4\times1} - u_{\mathrm{R5}}\boldsymbol{Z}_{\mathrm{R2}}^{T} + u_{\mathrm{R6}}\boldsymbol{X}_{\mathrm{R2}}^{\mathrm{T}} \tag{9}$$

where $\boldsymbol{w}_{\mathrm{b}} = [w_{\mathrm{b1}}, w_{\mathrm{b2}}, w_{\mathrm{b3}}, w_{\mathrm{b4}}]^{\mathrm{T}}$.

The cylindrical shell is a continuum, and its modal parameters of all orders can be solved analytically. Further, a state space equation is established by using the modal param-

eters. The above is a common method for dealing with continuum problems. However, the cylindrical shell coupled with the external underwater acoustic field becomes a dissipative system, so it is difficult to obtain an analytical expression of the modal parameters through theoretical deduction. In view of the above problem, a discrete numerical solution of displacement admittance functions is first calculated for the cylindrical shell—underwater acoustic field coupled subsystem by referring to Equations (11)–(18) in the literature [33]. Then, analytical expressions are fitted according to the admittance functions data, and then system modal parameters are identified from the expressions. Finally, a state space equation is established by using these modal parameters.

For the modal parameter identification method and modeling process mentioned above, please refer to Appendix A. Here, the state space equation after modeling is directly given for the cylindrical shell—underwater acoustic field coupled subsystem:

$$\dot{\boldsymbol{u}}_{\mathrm{C}} = \boldsymbol{S}_{\mathrm{C}}\boldsymbol{u}_{\mathrm{C}} + \overline{\boldsymbol{\Phi}}_{\mathrm{C}}\boldsymbol{F}_{\mathrm{y}} \tag{10}$$

where $\boldsymbol{u}_{\mathrm{C}} = [u_{\mathrm{C}1}, u_{\mathrm{C}2}, u_{\mathrm{C}3}, \ldots, u_{\mathrm{C}f}]^{\mathrm{T}}$ is a state variable (f is first f-order modes intercepted for the low-frequency vibration problem); $\boldsymbol{F}_{\mathrm{y}} = [F_{\mathrm{y}1}, F_{\mathrm{y}2}, F_{\mathrm{y}3}, F_{\mathrm{y}4}]^{\mathrm{T}}$ is an excitation force column vector of the connection supports to the cylindrical shell; $\boldsymbol{S}_{\mathrm{C}} = \mathrm{diag}[s_{\mathrm{C}1}, s_{\mathrm{C}2}, s_{\mathrm{C}3}, \ldots, s_{\mathrm{C}f}]$ is a diagonal matrix composed of poles $s_{\mathrm{C}i}$ obtained by modal parameter identification ($s_{\mathrm{C}i}$ sorted by $|s_{\mathrm{C}1}| < |s_{\mathrm{C}2}| < |s_{\mathrm{C}3}| < \ldots < |s_{\mathrm{C}f}|$); $\overline{\boldsymbol{\Phi}}_{\mathrm{C}}$ is a matrix composed of identified modal parameter $\overline{\varphi}_{ij}$ (i = 1, 2, …, f is modal order; j = 1, 2, 3, 4 is the position of the connection point between the lower support and the cylindrical shell), and

$$\overline{\boldsymbol{\Phi}}_{\mathrm{C}} = \begin{bmatrix} \overline{\varphi}_{11} & \overline{\varphi}_{12} & \overline{\varphi}_{13} & \overline{\varphi}_{14} \\ \overline{\varphi}_{21} & \overline{\varphi}_{22} & \overline{\varphi}_{23} & \overline{\varphi}_{24} \\ \overline{\varphi}_{31} & \overline{\varphi}_{32} & \overline{\varphi}_{33} & \overline{\varphi}_{34} \\ \vdots & \vdots & \vdots & \vdots \\ \overline{\varphi}_{f1} & \overline{\varphi}_{f2} & \overline{\varphi}_{f3} & \overline{\varphi}_{f4} \end{bmatrix} \tag{11}$$

The functional relation between $w_{\mathrm{y}j}$ and the state space variable $\boldsymbol{u}_{\mathrm{C}}$ is

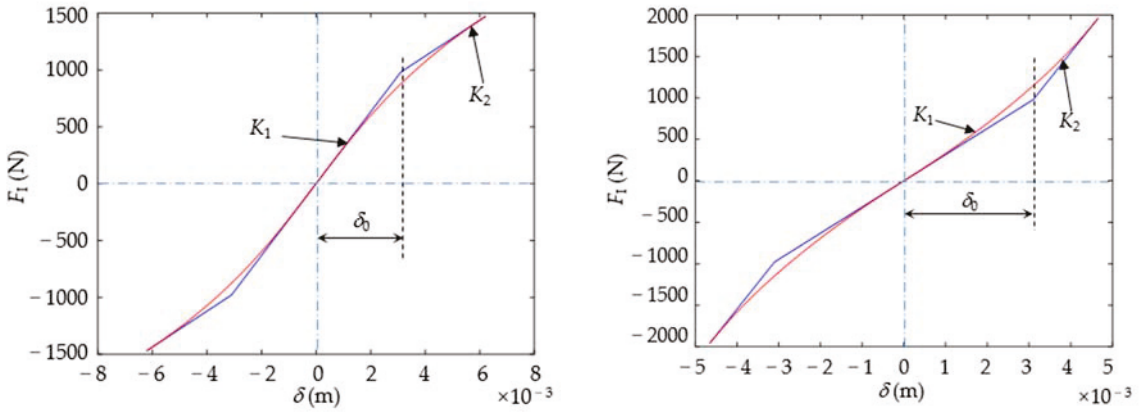
$$\boldsymbol{w}_{\mathrm{y}} = 2\mathrm{Re}\left\{\overline{\boldsymbol{\Phi}}_{\mathrm{C}}^{\mathrm{T}}\boldsymbol{u}_{\mathrm{C}}\right\} = 2\left(\mathrm{Re}\left\{\overline{\boldsymbol{\Phi}}_{\mathrm{C}}^{T}\right\}\cdot\mathrm{Re}\{\boldsymbol{u}_{\mathrm{C}}\} - \mathrm{Im}\left\{\overline{\boldsymbol{\Phi}}_{\mathrm{C}}^{T}\right\}\cdot\mathrm{Im}\{\boldsymbol{u}_{\mathrm{C}}\}\right) \tag{12}$$

where $\boldsymbol{w}_{\mathrm{y}} = [w_{\mathrm{y}1}, w_{\mathrm{y}2}, w_{\mathrm{y}3}, w_{\mathrm{y}4}]^{\mathrm{T}}$.

By combining the state space equations (Equations (3), (4), and (10)) of the vibration source equipment, raft frame, and cylindrical shell into one, the total state space equation of the system is formed. Then, through the constitutive equation of the elastic elements (Equations (5) and (8)), the subsystems can be connected into a whole.

2.3. Expression of Nonlinear Stiffness for Vibration Isolation Supports

In Equations (5) and (8), the constitutive relation of the elastic supports is only expressed in general terms, which can be a linear or nonlinear function. For the nonlinear stiffness characteristics of vibration isolation supports, they are generally classified qualitatively into two categories: softening and hardening characteristics, as shown in Figure 2a,b. The blue curve in Figure 2 indicates the nonlinear stiffness characteristics expressed by a piecewise linear method, where δ_0 is an approximate linear stiffness working interval control parameter, and K_1 and K_2 are approximate stiffness control parameters inside and outside the linear working interval, respectively. In practical problems, the transition from linear to nonlinear generally has a gradual process, rather than a sudden change, and the piecewise curve is not easy to deal with in numerical calculation because of its unsmoothness. So, the piecewise turning function is modified to a smooth transition function, as shown by the red curve in Figure 2.



(**a**) (**b**)

Figure 2. Nonlinear stiffness characteristics and their control parameters: (**a**) softening characteristic; (**b**) hardening characteristic.

The softening and hardening characteristics are expressed in this paper as Equations (13) and (14), respectively:

$$\begin{cases} \delta = \dfrac{|\tau| + K_1 c_1 \left[\sqrt[3]{1+(\tau/c_2)^3} - 1\right]}{\sqrt{1+K_1^2}} \mathrm{sgn}(\tau), \quad F_I = \dfrac{K_1|\tau| - c_1 \left[\sqrt[3]{1+(\tau/c_2)^3} - 1\right]}{\sqrt{1+K_1^2}} \mathrm{sgn}(\tau) \\ c_1 = \frac{K_1 - K_2}{1+K_1 K_2} c_2, c_2 = \sqrt{1+K_1^2}\delta_0, \quad \tau = |\tau|\mathrm{sgn}(\delta) \\ \left[(K_1 c_1/c_2)^3 + 1\right]|\tau|^3 - 3\left(\sqrt{1+K_1^2}|\delta| + K_1 c_1\right)|\tau|^2 + 3\left(\sqrt{1+K_1^2}|\delta| + K_1 c_1\right)^2|\tau| - \left(\sqrt{1+K_1^2}|\delta| + K_1 c_1\right)^3 + (K_1 c_1)^3 = 0 \end{cases} \tag{13}$$

where $\mathrm{sgn}(\tau)$ is the sign function; c_1 and c_2 are shape control parameters determined by K_1, K_2, and δ_0; τ is a parameter variable related to the positive real root $|\tau|$ of the polynomial equation.

$$\begin{cases} \delta = \dfrac{|\tau| - K_1 c_1 \left[\sqrt[3]{1+(\tau/c_2)^3} - 1\right]}{\sqrt{1+K_1^2}} \mathrm{sgn}(\tau), \quad F_I = \dfrac{K_1|\tau| + c_1 \left[\sqrt[3]{1+(\tau/c_2)^3} - 1\right]}{\sqrt{1+K_1^2}} \mathrm{sgn}(\tau) \\ c_1 = \frac{K_2 - K_1}{1+K_1 K_2} c_2, c_2 = \sqrt{1+K_1^2}\delta_0, \quad \tau = |\tau|\mathrm{sgn}(\delta) \\ \left[(K_1 c_1/c_2)^3 - 1\right]|\tau|^3 + 3\left(\sqrt{1+K_1^2}|\delta| - K_1 c_1\right)|\tau|^2 - 3\left(\sqrt{1+K_1^2}|\delta| - K_1 c_1\right)^2|\tau| + \left(\sqrt{1+K_1^2}|\delta| - K_1 c_1\right)^3 + (K_1 c_1)^3 = 0 \end{cases} \tag{14}$$

It is assumed that the three groups of vibration isolation supports have the same constitutive relation under the unit A_1, the unit A_2, and the floating raft R. The K_1 of the three groups of vibration isolators are denoted as $K_{A11} = \mathrm{Re}\{k_1\}$, $K_{A21} = \mathrm{Re}\{k_2\}$, and $K_{R1} = \mathrm{Re}\{k_R\}$, respectively, where k_1, k_2, and k_R are the linear complex stiffness. The K_2 of the three groups of isolators (denoted as K_{A12}, K_{A22}, and K_{R2}, respectively) is set as α (stiffness ratio) times K_1, that is, $K_{A12} = \alpha K_{A11}$, $K_{A22} = \alpha K_{A21}$, and $K_{R2} = \alpha K_{R1}$, where $\alpha \in [0.1, 3.0]$ (softening characteristic when $\alpha < 1.0$ and hardening characteristic when $\alpha > 1.0$). The δ_0 (denoted as δ_{10}, δ_{20}, and δ_{R0}, respectively) of the three groups of isolators is estimated to be β times their respective static settlement after installation of the units, that is, $\delta_{10} = \beta m_1 g/\mathrm{Re}\{4k_1\}$, $\delta_{20} = \beta m_2 g/\mathrm{Re}\{4k_2\}$, and $\delta_{R0} = \beta(m_1 + m_2 + m_R)g/\mathrm{Re}\{4k_R\}$, where $\beta \in [0.2, 5.0]$. In addition, the structural damping coefficients of the vibration isolators are approximately converted to the equivalent viscous damping coefficients by $c_1 = \mathrm{Im}\{k_1\}/\omega_1$, $c_2 = \mathrm{Im}\{k_2\}/\omega_1$, and $c_R = \mathrm{Im}\{k_R\}/\omega_1$ (where ω_1 is the fundamental frequency of the system).

2.4. Evaluation Index of Vibro-Acoustic Transfer Characteristics for the Nonlinear Coupled System

The transmitted power flow (which refers to the vibrational power flow transferred to the cylindrical shell through the supports under the floating raft in this paper) can reflect the process of vibration energy transfer and conversion into underwater acoustic radiation

of the coupled system [34], which can be regarded as a comprehensive reflection of the vibro-acoustic transfer characteristics.

For the coupled system shown in Figure 1, the instantaneous power of the excitation $\boldsymbol{F}_{\mathrm{y}}$ acting on the cylindrical shell by the vibration isolation support is

$$I(t) = \boldsymbol{F}_{\mathrm{y}}^{T} \cdot \dot{\boldsymbol{w}}_{\mathrm{y}} \tag{15}$$

The vibrational power flow is the average power of the excitation over a period $T = 2\pi/\omega$:

$$P_T = \frac{1}{T}\int_0^T I(t)dt \tag{16}$$

Similar to this, the time average power is introduced:

$$\overline{I}(t) = \frac{1}{t}\int_0^t I(\tau)d\tau \tag{17}$$

The initial value $\overline{I}(t)$ can be obtained by the above equation.

$$\overline{I}(0) = \lim_{t\to 0}\frac{1}{t}\int_0^t I(\tau)d\tau = \lim_{t\to 0} I(t) = I(0) = 0 \tag{18}$$

The derivative of time t on both sides of Equation (17) is calculated:

$$\dot{\overline{I}}(t) = -\frac{1}{t^2}\int_0^t I(\tau)d\tau + \frac{I(t)}{t} = \frac{-\overline{I}(t) + I(t)}{t} \tag{19}$$

From the above equation, combined with Equations (3), (4), (10), and (15), the initial value $\dot{\overline{I}}(t)$ can be obtained:

$$\dot{\overline{I}}(0) = \frac{1}{2}\lim_{t\to 0}\left(\dot{\boldsymbol{F}}_{\mathrm{y}}^{T}\cdot\dot{\boldsymbol{w}}_{\mathrm{y}} + \boldsymbol{F}_{\mathrm{y}}^{T}\cdot\ddot{\boldsymbol{w}}_{\mathrm{y}}\right) = \frac{1}{2}\lim_{t\to 0}\left(\dot{\boldsymbol{F}}_{\mathrm{y}}^{T}\cdot 2\mathrm{Re}\left\{\boldsymbol{\Phi}_{\mathrm{C}}^{-\mathrm{T}}\boldsymbol{S}_{\mathrm{C}}\boldsymbol{u}_{\mathrm{C}}\right\} + \boldsymbol{g}^{T}\left(\boldsymbol{w}_{\mathrm{y}} - \boldsymbol{w}_{\mathrm{b}}, \dot{\boldsymbol{w}}_{\mathrm{y}} - \dot{\boldsymbol{w}}_{\mathrm{b}}\right)\cdot\ddot{\boldsymbol{w}}_{\mathrm{y}}\right) = 0 \tag{20}$$

where the initial values of the system state variables $\boldsymbol{u}_{\mathrm{A}}$, $\boldsymbol{u}_{\mathrm{R}}$, and $\boldsymbol{u}_{\mathrm{C}}$ have been set to be $\boldsymbol{0}$ (the system is in a static state).

On the other hand, assuming that the vibration enters the steady state after a certain time t_0 and has a period T, it can be seen from Equation (17) that for any natural number N, the following equation holds:

$$(t_0 + NT)\overline{I}(t_0 + NT) - t_0\overline{I}(t_0) = \int_{t_0}^{t_0+NT} I(\tau)d\tau = \int_0^{NT} I(\tau)d\tau = NTP_T \tag{21}$$

Therefore, the vibration power flow can be calculated by the time average power:

$$P_T = \overline{I}(t_0 + T) + \frac{t_0}{T}\left[\overline{I}(t_0 + T) - \overline{I}(t_0)\right] \tag{22}$$

If t_0 is large enough, the system still does not exhibit perfect periodic oscillation. But as long as there is a mathematical expectation in Equation (16), then Equation (22) still holds. At this time, T can be understood as some kind of virtual value related to the excitation period, and P_T still represents the average power level of the excitation. Then, Equation (22) is rewritten as:

$$P_{\mathrm{T}} = \left[(T + t_0)\overline{I}(t_0 + T) - t_0\overline{I}(t_0)\right]/T \tag{23}$$

3. Results and Discussion

Based on the theories in Section 2, the effect of the nonlinear stiffness control parameters of the vibration isolation supports on the low-frequency vibration modes and

vibro-acoustic transfer characteristics of the coupled system are analyzed by numerical simulation methods in the following.

To obtain sufficient amplitude for the system to fully demonstrate its nonlinear vibration characteristics, the amplitude of the excitation force applied to the units A_1 and A_2 is set to 500 N. The values of the variable stiffness isolators and system structural parameters involved in the numerical simulations are set as shown in Tables 1 and 2, and other control parameters are shown in Appendix B.

Table 1. Control parameter settings of variable stiffness vibration isolator.

Control Parameters	Symbols	Units	Values	Remarks
Stiffness control parameters in the approximate linear working interval	K_{A11}	N/m	2.0×10^5	
	K_{A21}	N/m	2.7×10^5	
	K_{R1}	N/m	8.6×10^5	
Stiffness control parameters outside the linear working interval	K_{A12}	N/m	$\alpha \cdot 2.0 \times 10^5$	$\alpha \in [0.1, 3.0]$
	K_{A22}	N/m	$\alpha \cdot 2.7 \times 10^5$	$\alpha < 1$, softening characteristic
	K_{R2}	N/m	$\alpha \cdot 8.6 \times 10^5$	$\alpha > 1$, hardening characteristic
Linear working interval length control parameters	δ_{10}	m	$\beta \cdot 6.125 \times 10^{-4}$	$\beta \in [0.2, 5.0]$
	δ_{20}	m	$\beta \cdot 6.352 \times 10^{-4}$	
	δ_{R0}	m	$\beta \cdot 6.267 \times 10^{-4}$	
Damping coefficients	c_1	kg/s	159.155	
	c_2	kg/s	214.859	
	c_R	kg/s	684.366	

Table 2. System structure parameter settings.

System Structure Parameters		Symbols	Units	Values
Characteristic parameters of the cylindrical shell	Elastic modulus	E	N/m^2	2.1×10^{11}
	Density	ρ	kg/m^3	7.8×10^3
	Poisson's ratio	μ		0.28
	Dissipation factor	ξ		0.01
	Length, radius, thickness	L, a, d	m	2, 0.4, 0.02
Structure parameters of the units and the raft frame	Mass of the unit A_1	m_1	kg	50
	Mass of the unit A_2	m_2	kg	70
	Mass of the raft frame R	m_R	kg	100
	Moment of inertia of the unit A_1	J_{1x}, J_{1z}	$Kg \cdot m^2$	1, 0.5
	Moment of inertia of the unit A_2	J_{2x}, J_{2z}	$Kg \cdot m^2$	1.5, 1
	Moment of inertia of the raft frame R	J_{Rx}, J_{Rz}	$Kg \cdot m^2$	8.5, 2.5
Linear complex stiffness of the vibration isolation supports	Support stiffness of the unit A_1	k_1	N/m	$2.0 \times 10^5 \times (1 + 0.1\,j)$
	Support stiffness of the unit A_2	k_2	N/m	$2.7 \times 10^5 \times (1 + 0.1\,j)$
	Support stiffness of the raft frame R	k_R	N/m	$8.6 \times 10^5 \times (1 + 0.1\,j)$
Installation position parameters	Centroid positioning of the unit A_1	b_1	m	0.25
	Centroid positioning of the unit A_2	b_2	m	0.25
	Centroid positioning of the raft frame R	L_R	m	0.8
	Support spacing of the unit A_1	h_{1x}, h_{1z}	m	0.2, 0.3
	Support spacing of the unit A_2	h_{2x}, h_{2z}	m	0.2, 0.3
	Support spacing of the raft frame R	H_x, H_z	m	0.35, 0.7

3.1. Modal Parameter Identification for the Cylindrical Shell—Underwater Acoustic Field Coupled Subsystem

Taking the displacement derivative functions H_{11}, H_{12}, and H_{14} as examples, their fitting spectra obtained from the modal parameter identification method are compared with the numerical spectra obtained by the calculation method in the literature [33], as shown in Figure 3. It can be seen that the fitting results can match well with the original

data, and the difference between the two is mainly related to the modal truncation (residual admittance) and the computational error of the original data.

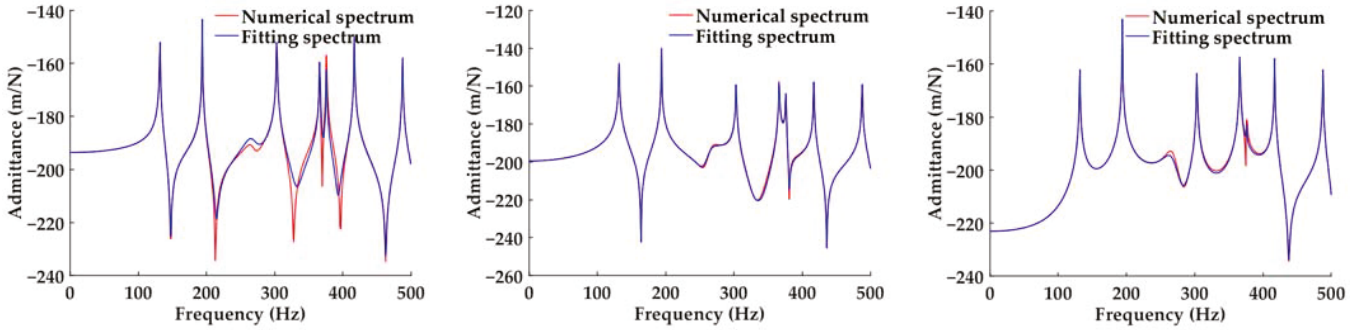


Figure 3. Comparison of the fitting spectra and the numerical spectra: (**a**) H_{11}; (**b**) H_{12}; (**c**) H_{14}.

The first 10 orders of poles identified for the cylindrical shell—underwater acoustic field coupled subsystem and their corresponding modal frequencies are listed in Table 3. The values of the modal parameters $\overline{\phi}_{ij}$ at the support connection points are listed in Table 4.

Table 3. The first 10 orders of poles and modal frequencies of the cylindrical shell—underwater acoustic field coupled subsystem.

Orders i	Poles s_{Ci}, $s_{Ci}{}^{*}$ *	Modal Frequencies f_{Ci} (Hz)
1	$-0.366 \pm 8.277 \times 10^2$ j	131.73
2	$-0.574 \pm 1.219 \times 10^3$ j	194.95
3	$-0.660 \pm 1.672 \times 10^3$ j	266.24
4	$-0.924 \pm 1.906 \times 10^3$ j	303.33
5	$-1.246 \pm 2.302 \times 10^3$ j	366.30
6	$-1.753 \pm 2.364 \times 10^3$ j	376.21
7	$-1.307 \pm 2.621 \times 10^3$ j	417.11
8	$-1.586 \pm 3.065 \times 10^3$ j	487.86
9	$-3.624 \pm 3.304 \times 10^3$ j	525.88
10	$-2.863 \times 10^3 \pm 1.973 \times 10^3$ j	553.34

* The poles s_{Ci} and $s_{Ci}{}^{*}$ are a pair of conjugate complex numbers.

Table 4. The values of the modal parameters $\overline{\phi}_{ij}$ at the support connection points.

Orders i	$j = 1$	$j = 2$	$j = 3$	$j = 4$
$i = 1$	0.475 − 4.630 j	0.686 − 0.703 j	0.104 − 0.117 j	0.163 − 0.172 j
$i = 2$	0.462 − 0.429 j	0.601 − 0.647 j	−0.317 + 0.312 j	−0.448 + 0.469 j
$i = 3$	0.436 − 0.208 j	0.271 − 0.328 j	0.068 − 0.226 j	0.214 − 0.335 j
$i = 4$	0.510 − 0.529 j	−0.274 + 0.240 j	−0.398 + 0.384 j	0.170 − 0.169 j
$i = 5$	0.367 − 0.352 j	0.402 − 0.441 j	−0.347 + 0.339 j	−0.453 + 0.479 j
$i = 6$	0.159 − 0.407 j	−0.342 + 0.117 j	0.412 − 0.031 j	0.006 + 0.032 j
$i = 7$	0.473 − 0.475 j	−0.218 + 0.218 j	−0.464 + 0.464 j	0.215 − 0.215 j
$i = 8$	0.357 − 0.356 j	−0.317 + 0.318 j	−0.261 + 0.261 j	0.233 − 0.234 j
$i = 9$	0.470 − 0.434 j	−0.254 + 0.271 j	−0.361 + 0.357 j	0.248 − 0.270 j
$i = 10$	0.716 − 0.762 j	0.082 − 0.105 j	−0.244 + 0.233 j	−0.053 + 0.012 j

3.2. Effect of Nonlinear Stiffness with Softening Characteristic on the Low-Frequency Vibro-Acoustic Characteristics for the Coupled System

3.2.1. Effect of Stiffness Ratio α

Figure 4 shows the bifurcation diagrams of the average vibration displacement and velocity for the coupled system when β is 1.0 and α is 1.0, 0.9, 0.7, 0.5, 0.3, and 0.1, respectively. Taking $\alpha = 0.1$ as an example, the discontinuity points near 6.75 Hz in the figure are

caused by the system resonating at the natural frequency, while the other discontinuity points are caused by the simulation program setting different steps in different frequency bands to improve the calculation efficiency. The discontinuity points in Figure 4 and in the bifurcation diagram below are the same and will not be explained one by one. It can be seen from Figure 4 that the steady vibration of the coupled system with nonlinear softening stiffness supports is single-periodic motion.

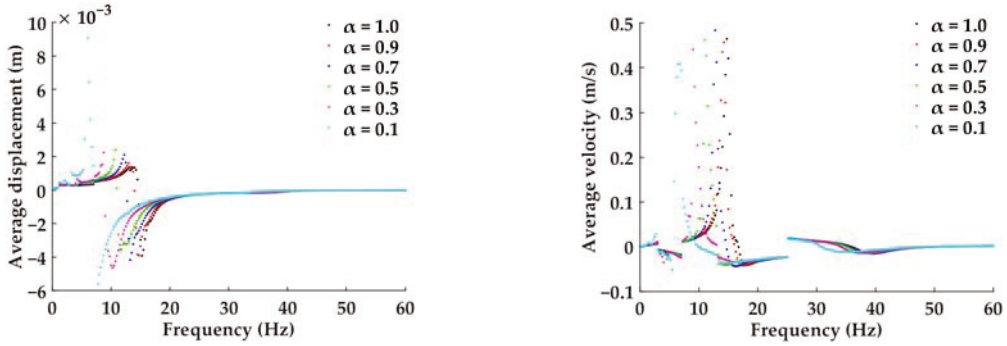


Figure 4. Effect of the strength variation of the nonlinear softening stiffness characteristic on the periodic bifurcation properties for the coupled system (β = 1.0): (**a**) bifurcation diagram of the average vibration displacement; (**b**) bifurcation diagram of the average vibration velocity.

Figure 5 shows the motion phase diagrams of the coupled system corresponding to the resonance frequencies of Figure 4. According to Figure 5a–d, when the softening characteristic is weak (α = 0.9), the units A_1, A_2 and the raft frame all are presented as approximate harmonic vibration modes. As the stiffness ratio decreases, the motion phase diagrams gradually show irregular closed graphics, indicating that the motions of the units A_1, A_2 and the raft frame are still single-periodic, but there are superharmonic components. According to Figure 5e, the vibration form at the connection points of the lower vibration isolators with the cylindrical shell is much more complex than that of the units A_1, A_2 and the raft frame, and the smaller the α, the more complex the vibration form. When α is equal to 0.1, the motion phase diagrams have become disordered or even chaotic. It can also be seen from Figure 5 that in a certain range of stiffness ratio $\alpha < 1.0$, the resonance displacement amplitudes of the units A_1, A_2 and the raft frame are larger than those of α = 1.0 (linear stiffness), and the smaller the α, the larger the amplitudes. The resonance velocity amplitudes show the opposite trend. In contrast, at the connection points of the lower vibration isolators with the cylindrical shell, the amplitudes of both the resonance displacement and resonance velocity decrease with the decrease in α. But the above law no longer holds when α decreases to a certain extent, as shown in Figure 5e, which is broken when α is equal to 0.1.

In addition, it can be found from Figure 5 that, when the vibration isolation supports have softening stiffness characteristics, the motion laws at the connection points of the upper vibration isolators with units A_1 and A_2 are basically the same, and the motion laws at the connection points of the upper and lower vibration isolators with the raft frame are also basically similar. In fact, through the simulation analysis, it can be seen that the above laws are also established when the vibration isolation supports have hardening stiffness characteristics. Therefore, in the following, only the motion phase diagrams are shown and analyzed at the connection points of the upper vibration isolators with the unit A_1, the lower vibration isolators with the raft frame, and the lower vibration isolators with the cylindrical shell.

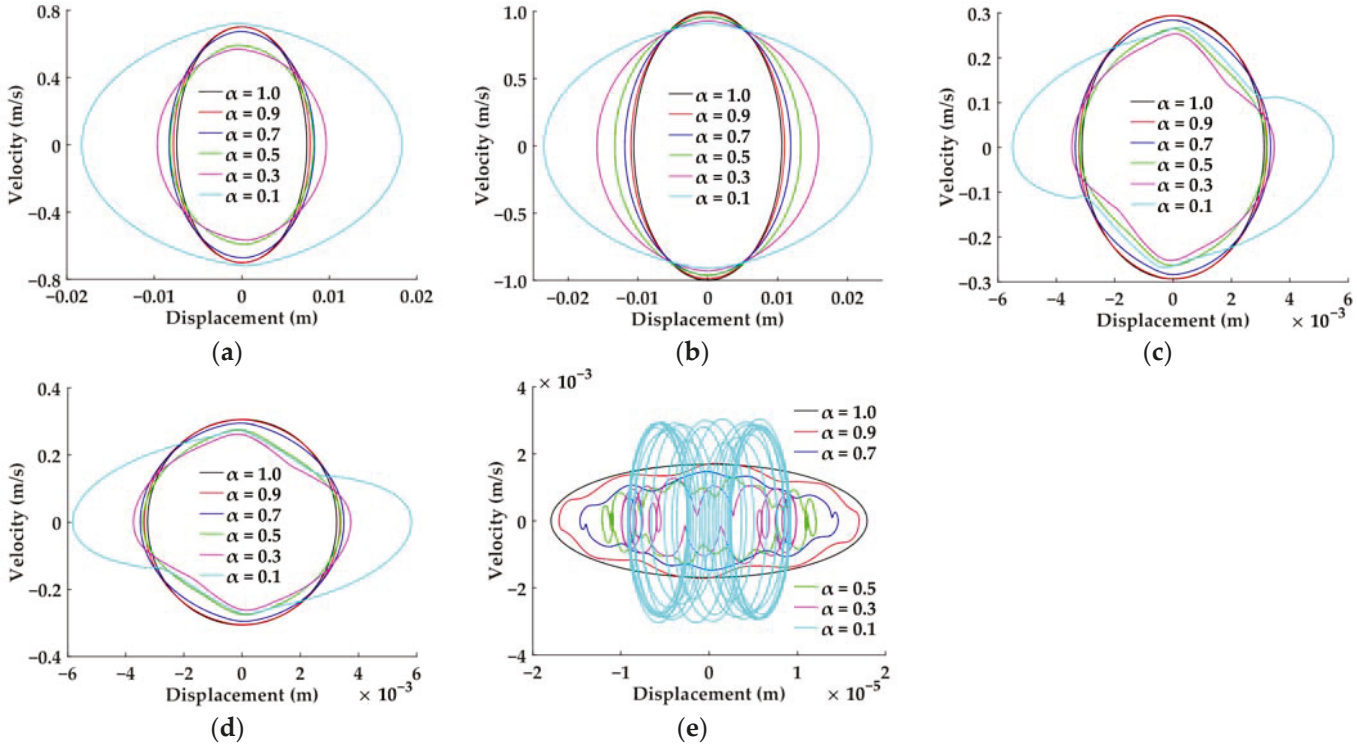


Figure 5. Effect of the strength variation of the nonlinear softening stiffness characteristic on the low-frequency vibration modes for the coupled system (β = 1.0): (**a**) motion phase diagram at the connection points of the upper vibration isolators with the unit A_1; (**b**) motion phase diagram at the connection points of the upper vibration isolators with the unit A_2; (**c**) motion phase diagram at the connection points of the upper vibration isolators with the raft frame; (**d**) motion phase diagram at the connection points of the lower vibration isolators with the raft frame; (**e**) motion phase diagram at the connection points of the lower vibration isolators with the cylindrical shell.

Figure 6 shows the transmitted power flow spectrum through the lower vibration isolators input to the cylindrical shell in the coupled system when β is 1.0 and α is 1.0, 0.9, 0.7, 0.5, 0.3, and 0.1, respectively. As can be seen from Figure 6, compared to the linear stiffness, the softening nonlinear characteristic of the support stiffness makes the resonance region of the system shift to lower frequencies, and the resonance peak and the second peak decrease. The smaller α is, the more significant the above effect is.

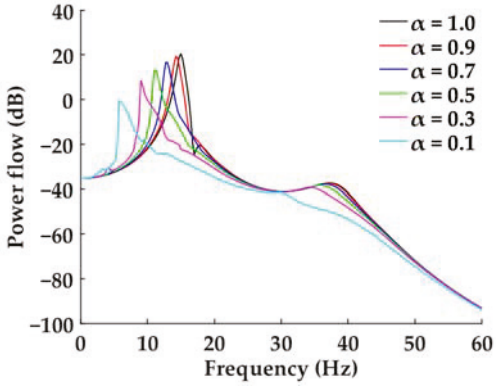


Figure 6. Effect of the strength variation of the nonlinear softening stiffness characteristic on the vibro-acoustic transfer characteristics for the coupled system (β = 1.0).

3.2.2. Effect of Approximate Linear Working Interval Length Control Parameter β

Figure 7 shows the bifurcation diagrams of the average vibration displacement and velocity for the coupled system when α is 0.5 and β is 5.0, 3.0, 2.0, 1.0, and 0.2, respectively. Comparing Figure 7 with Figure 4, it can be seen that the two are quite similar, and the steady state vibration of the coupled system is still single-periodic motion.

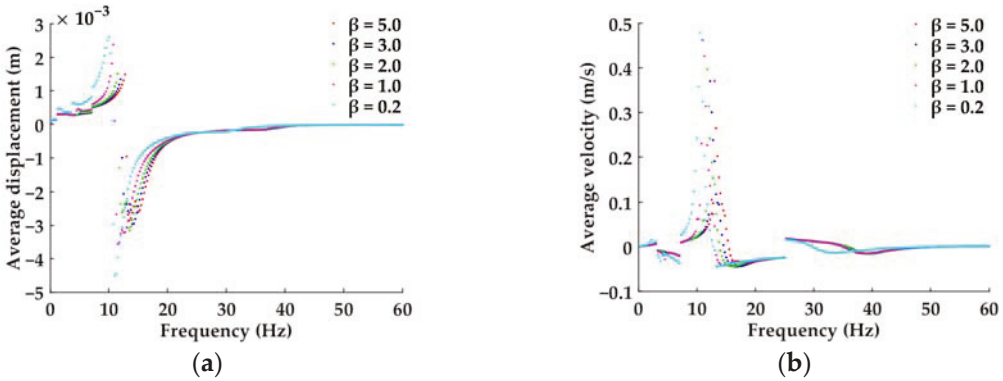


Figure 7. Effect of the length variation of the approximate linear working interval on the periodic bifurcation properties for the coupled system (α = 0.5): (**a**) bifurcation diagram of the average vibration displacement; (**b**) bifurcation diagram of the average vibration velocity.

Figure 8 shows the motion phase diagrams of the coupled system corresponding to the resonance frequencies of Figure 7. Since the stiffness ratio α = 0.5 here has determined that the vibration isolation supports have softening stiffness characteristics, reducing the approximate linear working interval will further strengthen their nonlinear stiffness characteristics. The results are that the amplitudes of the resonance displacement and resonance velocity of the unit, the raft frame, and the connection points of the lower vibration isolators with the cylindrical shell generally tend to increase with the decrease in β. From the perspective of motion form, the motion phase diagram of the unit is approximately a closed ellipse, that is, it is approximately a harmonic vibration. The motion phase diagram of the raft frame is irregular and closed, indicating that it contains strong superharmonic components. The motion phase diagram at the connection points of the lower vibration isolators with the cylindrical shell is relatively complex, indicating that the superharmonic components are complex and strong, and the phase diagram trajectory tends to be messy or even chaotic due to the enhancement of the nonlinear softening characteristic.

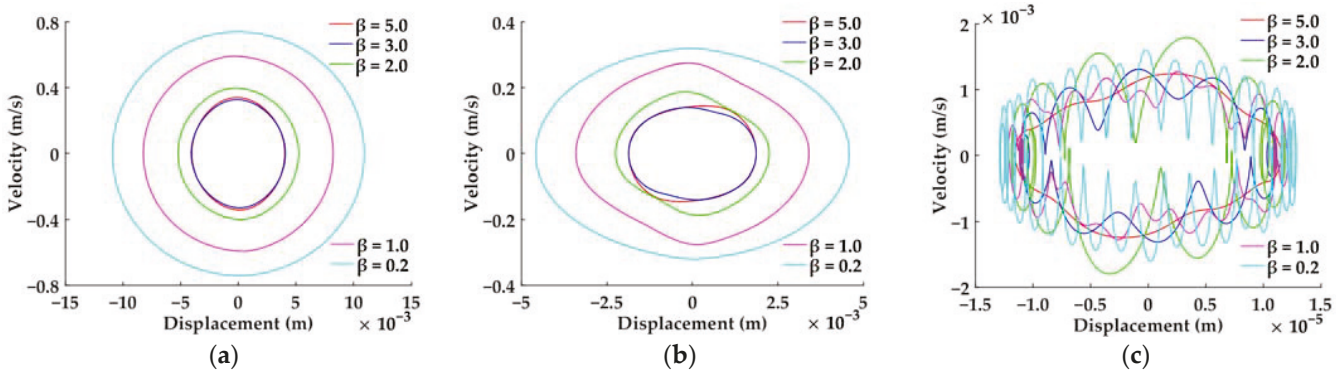


Figure 8. Effect of the length variation of the approximate linear working interval on the low-frequency vibration modes for the coupled system (α = 0.5): (**a**) motion phase diagram at the connection points of the upper vibration isolators with the unit A_1; (**b**) motion phase diagram at the connection points of the lower vibration isolators with the raft frame; (**c**) motion phase diagram at the connection points of the lower vibration isolators with the cylindrical shell.

Figure 9 shows the transmitted power flow spectrum in the coupled system when α is 0.5 and β is 5.0, 3.0, 2.0, 1.0, and 0.2, respectively. Comparing Figure 9 with Figure 6, it can be seen that the effect of reducing β is similar to that of reducing α. Both of them enhance the nonlinear softening stiffness effect and make the resonance region move to the lower frequency for the coupled system. Reducing α has a more obvious effect on reducing the fundamental frequency of the system and also weakens the resonance sharpness. But reducing β is more effective for reducing the transmitted power flow at higher frequencies after the fundamental frequency. For example, when α is equal to 0.5 and β is equal to 0.2 in Figure 9, the transmitted power flow level is significantly reduced on the band after the fundamental frequency and, especially, the second peak tends to disappear.

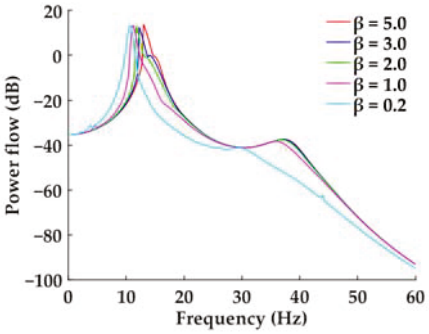
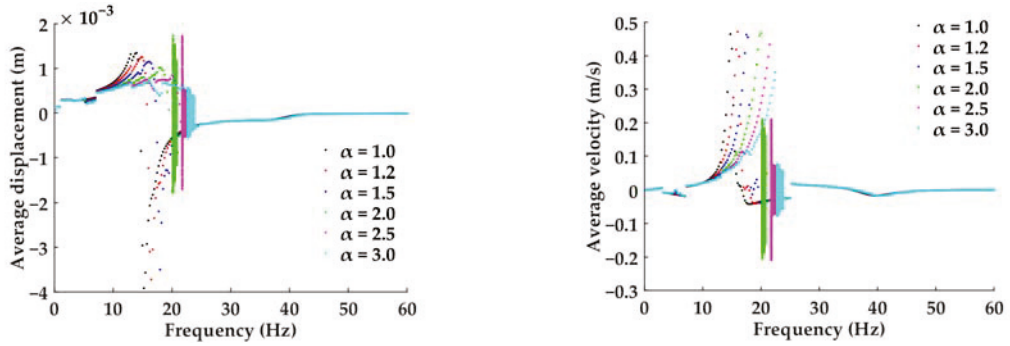


Figure 9. Effect of the length variation of the approximate linear working interval on the vibro-acoustic transfer characteristics for the coupled system (α = 0.5).

3.3. Effect of Nonlinear Stiffness with Hardening Characteristic on the Low-Frequency Vibro-Acoustic Characteristics for the Coupled System

3.3.1. Effect of Stiffness Ratio α

Figure 10 shows the bifurcation diagrams of the average vibration displacement and velocity for the coupled system when β is 1 and α is 1.0, 1.2, 1.5, 2.0, 2.5, and 3.0, respectively. It can be seen that the steady vibration of the coupled system with nonlinear hardening stiffness supports is dominated by single-periodic motion, but when the nonlinear hardening characteristic is enhanced (α = 2.0, 2.5, 3.0), aperiodic motion (quasi-periodic or chaotic) appears in a frequency band after the fundamental frequency resonance region.



(**a**) (**b**)

Figure 10. Effect of the strength variation of the nonlinear hardening stiffness characteristic on the periodic bifurcation properties for the coupled system (β = 1.0): (**a**) bifurcation diagram of the average vibration displacement; (**b**) bifurcation diagram of the average vibration velocity.

Figure 11 shows the motion phase diagrams of the coupled system corresponding to the resonance frequencies of Figure 10. According to Figure 11a, when the hardening characteristic is weak (α = 1.2, 1.5, 2.0), the unit is presented as an approximate harmonic vibration mode. But as the stiffness ratio further increases (α = 2.5, 3.0), the motion phase diagrams gradually become nonelliptical closed graphics, indicating that the motion of

the unit is still single-periodic, but there are superharmonic components. According to Figure 5b,c, the motion phase diagrams of the raft and the connection points of the lower vibration isolators with the cylindrical shell are all irregular closed graphics, indicating that their vibration modes are all single-period motion with superharmonics, and the vibration form at the connection points of the lower vibration isolators with the cylindrical shell is particularly complex. Through the calculation and analysis at different frequencies, it can be found that the above vibration modes and laws are universal in the coupled system with hardening characteristic stiffness supports. It can also be seen from Figure 11 that, when stiffness ratio $\alpha > 1.0$, the resonance displacement amplitudes of the unit and the raft frame are smaller than those of $\alpha = 1.0$ (linear stiffness), and the larger the α, the smaller the amplitudes. The resonance velocity amplitudes have no consistent change rule. In contrast, at the connection points of the lower vibration isolators with the cylindrical shell, the amplitudes of both the resonance displacement and resonance velocity increase with the increase in α. But they do not conform when α is equal to 3.0, indicating that the above law only holds in a certain range of $\alpha > 1.0$.

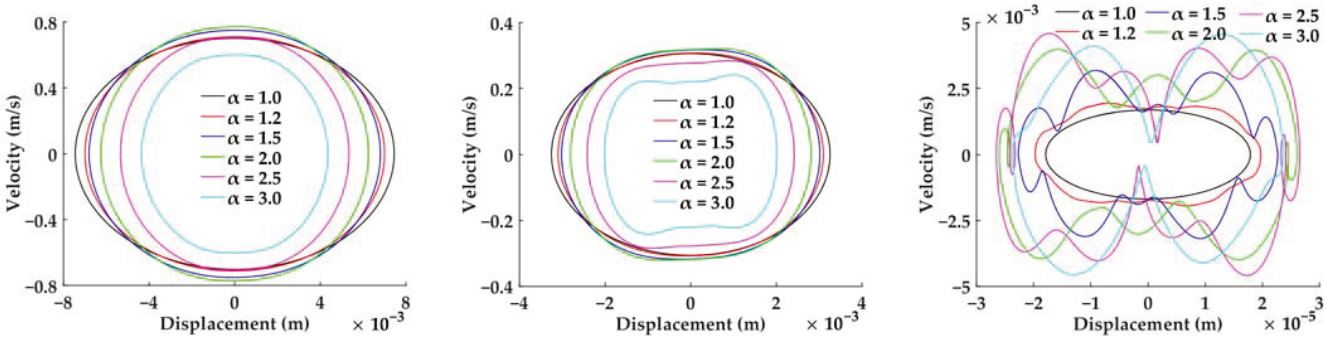


Figure 11. Effect of the strength variation of the nonlinear hardening stiffness characteristic on the low-frequency vibration modes for the coupled system ($\beta = 1.0$): (**a**) motion phase diagram at the connection points of the upper vibration isolators with the unit A_1; (**b**) motion phase diagram at the connection points of the lower vibration isolators with the raft frame; (**c**) motion phase diagram at the connection points of the lower vibration isolators with the cylindrical shell.

Figure 12 shows the transmitted power flow spectrum in the coupled system when β is 1.0 and α is 1.0, 1.2, 1.5, 2.0, 2.5, and 3.0, respectively. Comparing Figure 12 with Figure 6, it can be seen that the hardening and softening characteristics of the support stiffness have a significantly opposite effect on the transmitted power flow of the coupled system. The hardening nonlinear characteristic of the support stiffness makes the resonance region of the system shift to higher frequencies, and the resonance peak and the second peak increase slightly. The larger α is, the more significant the above effect is.

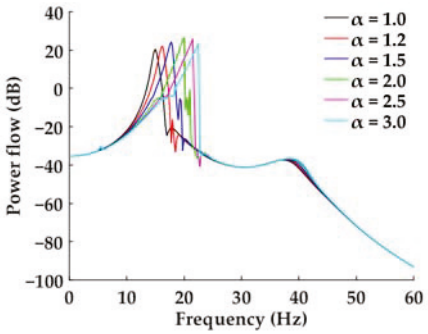
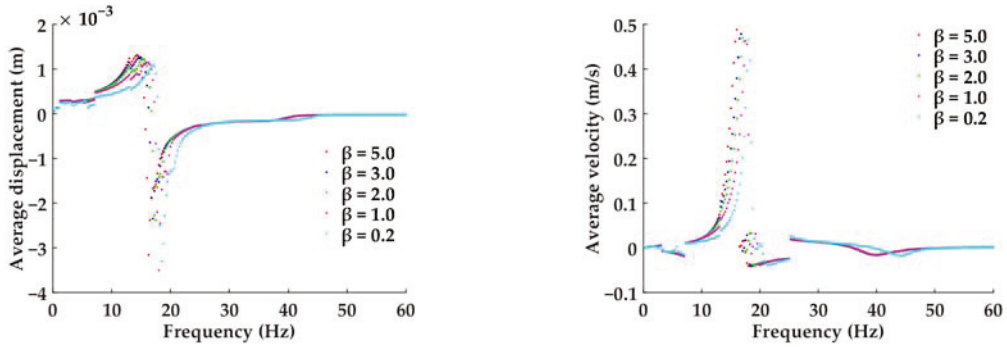


Figure 12. Effect of the strength variation of the nonlinear hardening stiffness characteristic on the vibro-acoustic transfer characteristics for the coupled system ($\beta = 1.0$).

3.3.2. Effect of Approximate Linear Working Interval Length Control Parameter β

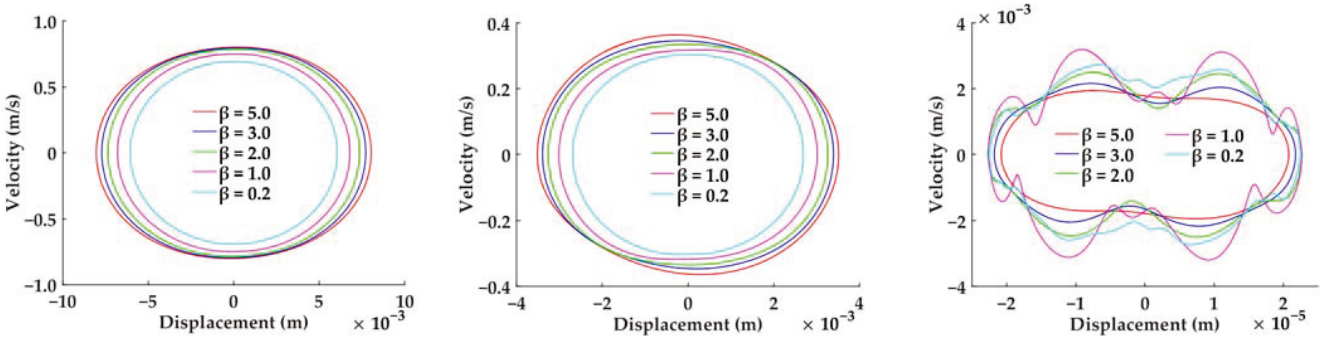
Figure 13 shows the bifurcation diagrams of the average vibration displacement and velocity for the coupled system when α is 1.5 and β is 5.0, 3.0, 2.0, 1.0, and 0.2, respectively. Comparing Figure 13 with Figure 10, it can be seen that the two are quite similar, and the steady state vibration of the coupled system is always single-periodic motion when α is equal to 1.5.



(**a**) (**b**)

Figure 13. Effect of the length variation of the approximate linear working interval on the periodic bifurcation properties for the coupled system (α = 1.5): (**a**) bifurcation diagram of the average vibration displacement; (**b**) bifurcation diagram of the average vibration velocity.

Figure 14 shows the motion phase diagrams of the coupled system corresponding to the resonance frequencies of Figure 13. In the case of a given α, the amplitudes of the resonance displacement and resonance velocity of the unit and the raft frame generally tend to decrease with the decrease in β. From the perspective of motion form, the motion phase diagram of the unit is approximately a closed ellipse, that is, it is approximately a harmonic vibration. The motion phase diagram of the raft frame has obvious irregularity, indicating that it contains strong superharmonic components. The motion phase diagram at the connection points of the lower vibration isolators with the cylindrical shell is the most complex, and with the decrease in β, the stability of the phase diagram orbits deteriorates and tends to be messy or even chaotic.



(**a**) (**b**) (**c**)

Figure 14. Effect of the length variation of the approximate linear working interval on the low-frequency vibration modes for the coupled system (α = 1.5): (**a**) motion phase diagram at the connection points of the upper vibration isolators with the unit A_1; (**b**) motion phase diagram at the connection points of the lower vibration isolators with the raft frame; (**c**) motion phase diagram at the connection points of the lower vibration isolators with the cylindrical shell.

Figure 15 shows the transmitted power flow spectrum in the coupled system when α is 1.5 and β is 5.0, 3.0, 2.0, 1.0, and 0.2, respectively. Comparing Figure 15 with Figure 12, it can be seen that the effect of reducing β is similar to that of increasing α. Both of them enhance the nonlinear hardening stiffness effect and make the resonance region move to the higher

frequency for the coupled system. Increasing α leads to a larger range of fundamental frequency variation of the system. But decreasing β extends the effect of nonlinear stiffness characteristics to higher frequencies. For example, when α is equal to 1.5 and β is equal to 0.2 in Figure 15, the effect of the nonlinear hardening characteristics of the vibration isolators extends significantly to higher frequency bands, increasing the transmitted power flow level on the band after the fundamental frequency for the coupled system.

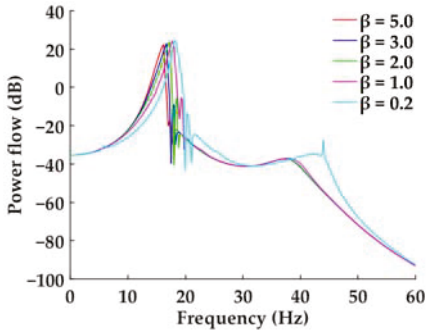


Figure 15. Effect of the length variation of the approximate linear working interval on the vibro-acoustic transfer characteristics for the coupled system (α = 1.5).

4. Conclusions

The present study was designed to study the effect of support stiffness nonlinearity on the low-frequency vibro-acoustic characteristics for the mechanical equipment—floating raft–cylindrical shell—underwater acoustic field coupled system. Firstly, the state space equations were established for the coupled system containing the vibration isolation supports with nonlinear stiffness characteristics, and in this process, the modal parameter identification method was deduced theoretically and verified by numerical simulation for the cylindrical shell—underwater acoustic field coupled subsystem. Then, the nonlinear stiffness constitutive relation was expressed in general by the softening and hardening characteristics for the vibration isolation supports, and the calculation formulas of the transmitted power flow in the nonlinear vibration isolation system were deduced. Finally, applying the Runge—Kutta method for the dynamics simulation, the effect of the variation of the nonlinear stiffness characteristics parameters on the low-frequency vibration modes and vibro-acoustic transfer characteristics was analyzed and discussed for the coupled system. The main findings are as follows:

1. For the coupled system with a nonlinear softening stiffness characteristic of the vibration isolation supports, the steady state vibration mode under harmonic excitation is single-periodic motion, but the superharmonic phenomenon is common. And the smaller the stiffness ratio is, the more superharmonic components are and the more complex the vibration form is. Compared with the linear stiffness case, the softening nonlinear stiffness can reduce the fundamental frequency and decrease the low-frequency vibro-acoustic transmission level within and after the resonance region for the vibration isolation system. And the stronger the softening characteristic is, the more significant the above effect is;
2. For the coupled system with a nonlinear hardening stiffness characteristic of the vibration isolation supports, the vibration mode under harmonic excitation is single-periodic motion at most frequencies, and the existence of superharmonics is its main vibration feature. And the larger the stiffness ratio is, the more superharmonic components are and the more complex the vibration form is. In a frequency band slightly higher than the fundamental frequency, it may show a nonperiodic motion mode (quasi-periodic or chaotic). Compared with the linear stiffness case, the hardening nonlinear stiffness can increase the fundamental frequency, broaden the resonance band and slightly raise the low-frequency vibro-acoustic transmission level within

and after the resonance region for the vibration isolation system. And the stronger the hardening characteristic is, the more significant the above effect is;

3. For the determined nonlinear stiffness ratio, the variation of the length of the approximate linear working interval has no effect on the periodicity of the vibration of the coupled system. For the coupled system with a nonlinear softening stiffness characteristic of the vibration isolation supports, the smaller the length of the approximately linear working interval is, the lower the low-frequency vibro-acoustic transfer level after the fundamental frequency resonance region is; while for the coupled system with a nonlinear hardening stiffness characteristic of the vibration isolation supports, the smaller the length of the approximately linear working interval is, the higher the low-frequency vibro-acoustic transfer level after the fundamental frequency resonance region is.

Author Contributions: Conceptualization, L.W. and R.H.; methodology, L.W. and R.H.; software, L.W. and R.H.; validation, L.W.; formal analysis, L.W. and R.H.; investigation, L.W.; resources, R.H.; data curation, L.W. and R.H.; writing—original draft preparation, L.W.; writing—review and editing, L.W. and R.H.; visualization, L.W.; supervision, R.H.; project administration, R.H.; funding acquisition, R.H. All authors have read and agreed to the published version of the manuscript.

Funding: This research received no external funding.

Data Availability Statement: The data used to support the findings of this study are available from the corresponding author upon request.

Conflicts of Interest: The authors declare no conflict of interest.

Appendix A. State Space Model of the Cylindrical Shell—Underwater Acoustic Field Coupled Subsystem

Appendix A.1. Solutions of the Admittance Functions for the Coupled Subsystem

A cylindrical coordinate system $Or\phi z$ is established on the middle surface of the cylindrical shell. Let the coordinate origin be located at the center of the left end face of the cylindrical shell, r and z be the distance from the spatial point $\sigma(r, \phi, z)$ to the central axis of the cylindrical shell and the left end face, respectively, and ϕ be the angle of $\sigma(r, \phi, z)$ deviating from the vertical direction. The transformation relationship between the cylindrical coordinates and the rectangular coordinates: $x = r\cos\phi$, $y = r\sin\phi$, $z = z$.

Let the length, thickness, and central radius of the cylindrical shell be L, d, and a, respectively, and the density, elastic modulus, and Poisson's ratio of the material of the cylindrical shell be ρ, E, and μ, respectively. A harmonic excitation force $F_z \cdot e^{j\omega t}$along the Oz axis direction is applied to the inside of the cylindrical shell at $\sigma_e(\varphi_e, z_e)$. Let $u(z, \phi, t) = U(z, \phi) \cdot e^{j\omega t}$, $v(z, \phi, t) = V(z, \phi) \cdot e^{j\omega t}$, and $w(z, \phi, t) = W(z, \phi) \cdot e^{j\omega t}$ denote the vibration displacement of the point $\sigma(\phi, z)$ on the cylindrical shell in z, ϕ, and r coordinate directions, respectively. Then, u, v, and w satisfy the following differential equations of motion:

$$\begin{cases} S_1(u,v,w) + \rho d \cdot \partial^2 u/\partial t^2 = F_z \cdot \delta(\varphi - \varphi_e) \cdot \delta(z - z_e) \cdot e^{j\omega t} \\ S_2(u,v,w) + \rho d \cdot \partial^2 v/\partial t^2 = 0 \\ S_3(u,v,w) + \rho d \cdot \partial^2 w/\partial t^2 = -p(r,\varphi,z)|_{r=a} \end{cases} \tag{A1}$$

where p is the radiated underwater acoustic pressure generated outside the cylindrical shell due to its vibration; S_1, S_2, and S_3 are differential operators, and

$$\begin{cases} S_1(U,V,W) = -\frac{Ed}{1-\mu^2}\left[\left(\frac{\partial^2}{\partial z^2} + \frac{1-\mu}{2a^2}\frac{\partial^2}{\partial \varphi^2}\right)U + \frac{1+\mu}{2a}\frac{\partial^2 V}{\partial z \partial \varphi} + \frac{\mu}{a}\frac{\partial W}{\partial z}\right] \\ S_2(U,V,W) = -\frac{Ed}{1-\mu^2}\left[\frac{1+\mu}{2a}\frac{\partial^2 U}{\partial z \partial \varphi} + \left(\frac{1-\mu}{2}\frac{\partial^2}{\partial z^2} + \frac{1}{a^2}\frac{\partial^2}{\partial \varphi^2}\right)V + \frac{1}{a^2}\frac{\partial}{\partial \varphi}\left(1 - \frac{d^2}{12}\nabla^2\right)W\right] \\ S_3(U,V,W) = \frac{Ed}{1-\mu^2}\left[\frac{\mu}{a}\frac{\partial U}{\partial z} + \frac{1}{a^2}\frac{\partial}{\partial \varphi}\left(1 - \frac{d^2}{12}\nabla^2\right)V + \left(\frac{1}{a^2} + \frac{d^2}{12}\nabla^4\right)W\right] \end{cases} \tag{A2}$$

where $\nabla^2 = \frac{\partial^2}{\partial z^2} + \frac{1}{a^2}\frac{\partial^2}{\partial \varphi^2}$, $\nabla^4 = \frac{\partial^4}{\partial z^4} + \frac{2}{a^2}\frac{\partial^4}{\partial z^2 \partial \varphi^2} + \frac{1}{a^4}\frac{\partial^4}{\partial \varphi^4}$.

The pressure $p = P(r, \phi, z)\cdot e^{j\omega t}$ of the underwater acoustic field outside the cylindrical shell satisfies the Helmholtz equation:

$$\nabla^2 P + k^2 P = 0 \tag{A3}$$

There are boundary conditions on the interface between the cylindrical shell and the external underwater acoustic field:

$$\left.\frac{\partial P}{\partial r}\right|_{r=a} = \begin{cases} \rho_0 \omega^2 \sum\limits_{j=0,k=1}^{\infty} \sum\limits_{l=1}^{3} q_{jkl} H_{jkl}^{w} \cos[j(\varphi - \varphi_e)] \sin\left(\frac{k\pi z}{L}\right) \ (0 \le z \le L) \\ 0 \ (z < 0 \text{ or } z > L) \end{cases} \tag{A4}$$

where ρ_0 is the density of the acoustic field medium; H_{jk} (j, k = 1, 2, 3, 4) denotes a displacement admittance function, which means that when a unit excitation is applied along the direction of the support force at the connection point σ_k of the support and the cylindrical shell, the displacement response is generated at the connection point σ_j.

The displacement admittance matrix of the cylindrical shell—underwater acoustic field coupled subsystem is denoted by:

$$H(j\omega) = \left[H_{jk}\right]_{4\times 4} \tag{A5}$$

For the calculation of the admittance functions of the cylindrical shell—underwater acoustic field coupled subsystem, see also Equations (11)–(18) in [33]. It can be seen from these equations that, due to the complexity of the calculation formulas, only discrete numerical solutions of the admittance functions can be given. Figure A1 shows examples of calculated results for the admittance functions of the cylindrical shell along the support direction (taking H_{11}, H_{12}, and H_{14} as examples).

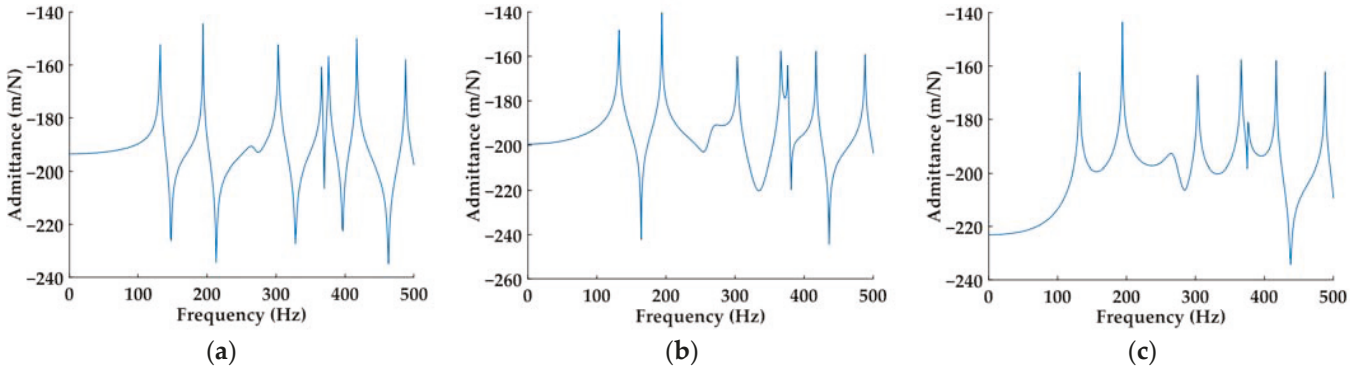


Figure A1. Examples of the calculation results for the admittance along the support direction: (**a**) H_{11}; (**b**) H_{12}; (**c**) H_{14}.

Appendix A.2. Modal Parameter Identification of the Coupled Subsystem

Since the main focus is on low-frequency vibration problems in this paper, only the first f-order modes are intercepted. Also, the admittance function is expressed as a ratio of two polynomial functions:

$$H_{jk}(j\omega) \approx \frac{a_m(j\omega)^{m-1} + a_{m-1}(j\omega)^{m-2} + \cdots + a_2(j\omega) + a_1}{(j\omega)^{n-1} + b_{n-1}(j\omega)^{n-2} + \cdots + b_2(j\omega) + b_1} \tag{A6}$$

where j, k = 1, 2, 3, 4; $n = 2f + 1$, $m = 2f - 1$.

Let $\hat{H}_{jk}(j\omega)$ be the discrete numerical spectrum of $H_{jk}(j\omega)$ obtained by theoretical calculation, and for a number of frequencies $\omega_1, \omega_2, \omega_3, \ldots, \omega_N$, there are $\hat{H}_{jk,i} = \hat{H}_{jk}(j\omega_i)$, ($i$ = 1, 2, …, N). Noting that $\boldsymbol{a} = [a_1, a_2, \ldots, a_m]^T$, $\boldsymbol{b} = [b_1, b_2, \ldots, b_{n-1}]^T$, $\boldsymbol{p}_i = [1, j\omega_i, \ldots,$

$(j\omega_i)^{m-1}]$, $\boldsymbol{q}_i = \hat{H}_{jk,i}\,[1, j\omega_i, \ldots, (j\omega_i)^{n-2}]$, $h_i = (j\omega_i)^{n-1}\,\hat{H}_{jk,i}$, $\boldsymbol{e}_i = \boldsymbol{p}_i\boldsymbol{a} - \boldsymbol{q}_i\boldsymbol{b} - h_i$, $\boldsymbol{P} = [\boldsymbol{p}_1, \boldsymbol{p}_2, \ldots, \boldsymbol{p}_s]^{\mathrm{T}}$, $\boldsymbol{Q} = [\boldsymbol{q}_1, \boldsymbol{q}_2, \ldots, \boldsymbol{q}_s]^{\mathrm{T}}$, and $\boldsymbol{h} = [h_1, h_2, \ldots, h_s]^{\mathrm{T}}$, the matrix expression and the total mean squared error can be obtained:

$$\boldsymbol{e} = \boldsymbol{P}\boldsymbol{a} - \boldsymbol{Q}\boldsymbol{b} - \boldsymbol{h} \tag{A7}$$

$$J = \boldsymbol{e}^{\mathrm{T}}\boldsymbol{e}^{*} = \boldsymbol{x}^{\mathrm{T}}\boldsymbol{A}_{\mathrm{R}}\boldsymbol{x} - 2\boldsymbol{B}\boldsymbol{x} + |\boldsymbol{h}|^2 \tag{A8}$$

where the superscript '*' represents conjugation relation; $\boldsymbol{x} = \begin{bmatrix}\boldsymbol{a}\\ \boldsymbol{b}\end{bmatrix}$, $\boldsymbol{A} = \begin{bmatrix}\boldsymbol{P}^{\mathrm{T}}\boldsymbol{P}^{*} & -\boldsymbol{P}^{\mathrm{T}}\boldsymbol{Q}^{*}\\ -\boldsymbol{Q}^{\mathrm{T}}\boldsymbol{P}^{*} & \boldsymbol{Q}^{\mathrm{T}}\boldsymbol{Q}^{*}\end{bmatrix}$, $\boldsymbol{B} = \left[\boldsymbol{h}_{\mathrm{R}}^{\mathrm{T}}\boldsymbol{P}_{\mathrm{R}} + \boldsymbol{h}_{\mathrm{I}}^{\mathrm{T}}\boldsymbol{P}_{I} - \left(\boldsymbol{h}_{\mathrm{R}}^{\mathrm{T}}\boldsymbol{Q}_{R} + \boldsymbol{h}_{\mathrm{I}}^{\mathrm{T}}\boldsymbol{Q}_{I}\right)\right]$, $\boldsymbol{P}_{\mathrm{R}}$ and $\boldsymbol{P}_{\mathrm{I}}$ are the real and imaginary parts of $\boldsymbol{P}$, respectively; $\boldsymbol{Q}_{\mathrm{R}}$ and $\boldsymbol{Q}_{\mathrm{I}}$ are the real and imaginary parts of $\boldsymbol{Q}$, respectively; $\boldsymbol{h}_{\mathrm{R}}$ and $\boldsymbol{h}_{\mathrm{I}}$ are the real and imaginary parts of $\boldsymbol{h}$, respectively; $\boldsymbol{A}_{\mathrm{R}}$ is the real part of $\boldsymbol{A}$.

Consider the total mean squared error $\boldsymbol{J}$ as a function of $\boldsymbol{x}$. To obtain a minimum of $\boldsymbol{J}$, let the gradient of Equation (A8) to $\boldsymbol{x}$ be 0:

$$\nabla\boldsymbol{J} = \boldsymbol{A}_{\mathrm{R}}\boldsymbol{x} - \boldsymbol{B}^{\mathrm{T}} = \boldsymbol{0} \Rightarrow \boldsymbol{x} = \boldsymbol{A}_{\mathrm{R}}^{-1}\boldsymbol{B}^{\mathrm{T}} \tag{A9}$$

The polynomial coefficients of the admittance function numerator and denominator can be fitted using the above equation.

Appendix A.3. Establishment of State Space Equation for the Coupled Subsystem

For a continuous structure, its vibration displacement response $w(\sigma, t)$ can be expressed in the form of vibration model superposition:

$$w(\sigma, t) = \sum_{i=1}^{\infty}\psi_i(\sigma)q_i(t) \tag{A10}$$

where $\psi_i(\sigma)$ is the ith-order vibration mode function and $q_i(t)$ is the ith-order modal coordinate.

A modal damping ratio ξ_i is introduced, and the modal coordinate equation is obtained by using the orthogonality of the vibration mode function:

$$\ddot{q}_i + 2\xi_i\omega_i\dot{q}_i + \omega_i^2 q_i = \sum_{j=1}^{4}F_j(t)\overline{\psi}_i(\sigma_j),\ (i = 1, 2, \ldots) \tag{A11}$$

where ω_i is the i-th order modal frequency; $F_j(t)$ is the concentrated excitation force of the cylindrical shell subjected to the support at point σ_j (j = 1, 2, 3, 4); $\overline{\psi}_i = \psi_i/\sqrt{M_i}$ is the regular vibration mode function; $M_i = \int_{\Sigma} m_{\Sigma}\psi_i^2(\sigma)\mathrm{d}\sigma$ is the i-th order modal mass, m_{Σ} is the areal density.

According to Equations (A10) and (A11), the admittance function can be expressed as:

$$H_{jk}(j\omega) \approx \sum_{i=1}^{f}\frac{\overline{\psi}_i(\sigma_j)\overline{\psi}_i(\sigma_k)}{j2\sqrt{1-\xi_i^2}\omega_i}\left(\frac{1}{j\omega + \xi_i\omega_i - j\sqrt{1-\xi_i^2}\omega_i} - \frac{1}{j\omega + \xi_i\omega_i + j\sqrt{1-\xi_i^2}\omega_i}\right) \tag{A12}$$

According to the above relation, if $\boldsymbol{H}(j\omega)$ is known, each $H_{jk}(j\omega)$ has the same poles $s_i = -\xi_i\omega_i + j\sqrt{1-\xi_i^2}\omega_i$, ($i$ = 1, 2, …, f). Since $|s_i| = \omega_i$, the poles are sorted by $|s_1| < |s_2| < |s_3| < \ldots$, and the modal parameters are determined as follows:

$$\omega_i = |s_i|,\ \xi_i = -\mathrm{Re}\{s_i\}/|s_i| \tag{A13}$$

$$\overline{\psi}_i(\sigma_1) = \sqrt{j2\mathrm{Im}\{s_i\}\cdot[H_{11}\cdot(j\omega - s_i)]_{j\omega=s_i}} \tag{A14}$$

$$\overline{\psi}_i(\sigma_j) = \frac{\mathrm{j2Im}\{s_i\}\cdot\left[H_{j1}\cdot(\mathrm{j}\omega - s_i)\right]_{\mathrm{j}\omega=s_i}}{\overline{\psi}_i(\sigma_1)} = \sqrt{\frac{\mathrm{j2Im}\{s_i\}}{\left[H_{11}\cdot(\mathrm{j}\omega - s_i)\right]_{\mathrm{j}\omega=s_i}}}\left[H_{j1}\cdot(\mathrm{j}\omega - s_i)\right]_{\mathrm{j}\omega=s_i} \tag{A15}$$

Substituting the above relations into Equations (A11) and (A10), the modal coordinate equation and the modal superposition formula of vibration displacement expressed in terms of the admittance functions are obtained:

$$\ddot{q}_i - 2\mathrm{Re}\{s_i\}\dot{q}_i + |s_i|^2 q_i = \sqrt{\mathrm{j2Im}\{s_i\}}\sum_{j=1}^{4} F_j(t)\frac{\left[H_{j1}\cdot(j\omega - s_i)\right]_{\mathrm{j}\omega=s_i}}{\sqrt{\left[H_{11}\cdot(\mathrm{j}\omega - s_i)\right]_{\mathrm{j}\omega=s_i}}},\ (i = 1, 2, \ldots, f) \tag{A16}$$

$$w(\sigma_j, t) = \sum_{i=1}^{f} q_i(t)\sqrt{\frac{\mathrm{j2Im}\{s_i\}}{\left[H_{11}\cdot(\mathrm{j}\omega - s_i)\right]_{\mathrm{j}\omega=s_i}}}\left[H_{j1}\cdot(\mathrm{j}\omega - s_i)\right]_{\mathrm{j}\omega=s_i},\ (j = 1, 2, 3, 4) \tag{A17}$$

The above theories are based on proportional damping assumption, and the vibration mode function is a real function by default. But applying Equation (A14) in practical analysis mostly yields complex numbers, that is, complex modes appear. If the complex modes are substituted into Equations (A11) or (A16), the modal coordinate equation will be made to have complex terms, and ultimately the displacement response obtained from Equation (A17) will also become a complex number, which is inconsistent with its physical meaning. Considering the universality of complex modes in this kind of problem, Equations (A11), (A12), and (A17) are modified as:

$$H_{jk}(\mathrm{j}\omega) \approx \sum_{i=1}^{f}\frac{\overline{\phi}_{ij}\overline{\phi}_{ik}}{\mathrm{j}\omega - s_i} + \sum_{i=1}^{f}\frac{\overline{\phi}^*_{ij}\overline{\phi}^*_{ik}}{\mathrm{j}\omega - s^*_i} \tag{A18}$$

$$\begin{bmatrix}\dot{v}_1\\ \vdots\\ \dot{v}_f\\ \dot{v}^*_1\\ \vdots\\ \dot{v}^*_f\end{bmatrix} - \begin{bmatrix}s_1 & & & & & \\ & \ddots & & & & \\ & & s_f & & & \\ & & & s^*_1 & & \\ & & & & \ddots & \\ & & & & & s^*_f\end{bmatrix}\begin{bmatrix}v_1\\ \vdots\\ v_f\\ v^*_1\\ \vdots\\ v^*_f\end{bmatrix} = \begin{bmatrix}\sum_{j=1}^{4}\overline{\phi}_{1j}F_j(t)\\ \vdots\\ \sum_{j=1}^{4}\overline{\phi}_{fj}F_j(t)\\ \sum_{j=1}^{4}\overline{\phi}^*_{1j}F_j(t)\\ \vdots\\ \sum_{j=1}^{4}\overline{\phi}^*_{fj}F_j(t)\end{bmatrix} \tag{A19}$$

$$w(\sigma_j, t) = \sum_{i=1}^{f} 2\left[\mathrm{Re}\{v_i(t)\}\cdot\mathrm{Re}\left\{\overline{\phi}_{ij}\right\} - \mathrm{Im}\{v_i(t)\}\cdot\mathrm{Im}\left\{\overline{\phi}_{ij}\right\}\right],\ (j = 1, 2, 3, 4) \tag{A20}$$

where the poles s_i and s_i^* (i = 1, 2, …, f) are the f pairs of conjugate latent roots obtained in solving the eigenvalue problem for the state space equation; v_i is obtained by variable substitution $\boldsymbol{q} = \boldsymbol{\Phi v}$;$\boldsymbol{\Phi}$ is a complex modal matrix consisting of $\boldsymbol{\Phi}_i$ and $\boldsymbol{\Phi}_i^*$; $\boldsymbol{\Phi}_i$ and $\boldsymbol{\Phi}_i^*$ are complex eigenvectors corresponding to s_i and s_i^*; $\overline{\phi}_{ij}$ is obtained by using the residue method, $\overline{\phi}_{ij} = \frac{H_{j1}\cdot(\mathrm{j}\omega - s_i)\big|_{\mathrm{j}\omega=s_i}}{\sqrt{H_{11}\cdot(\mathrm{j}\omega - s_i)\big|_{\mathrm{j}\omega=s_i}}}$ and $\overline{\phi}^*_{ij} = \frac{H_{j1}\cdot(\mathrm{j}\omega - s_i^*)\big|_{\mathrm{j}\omega=s_i^*}}{\sqrt{H_{11}\cdot(\mathrm{j}\omega - s_i^*)\big|_{\mathrm{j}\omega=s_i^*}}}$.

The upper part and the lower part of Equation (A19) are repeated (conjugate relation), so only the upper part is abbreviated to a state space equation:

$$\dot{\boldsymbol{u}}_{\mathrm{C}} = \boldsymbol{S}_{\mathrm{C}}\boldsymbol{u}_{\mathrm{C}} + \overline{\boldsymbol{\Phi}}_{\mathrm{C}}\boldsymbol{F}_{\mathrm{y}} \tag{A21}$$

where $\boldsymbol{u}_C = [u_{C1}, u_{C2}, u_{C3}, \ldots, u_{Cf}]^T$ is a state variable; $\boldsymbol{F}_y = [F_{y1}, F_{y2}, F_{y3}, F_{y4}]^T$ is an excitation force column vector of the connection supports to the cylindrical shell; $\boldsymbol{S}_C = \mathrm{diag}[s_{C1}, s_{C2}, s_{C3}, \ldots, s_{Cf}]$ is a diagonal matrix composed of poles (sorted by $|s_{C1}| < |s_{C2}| < |s_{C3}| < \ldots < |s_{Cf}|$); $\overline{\boldsymbol{\Phi}}_C$ is a matrix consisting of the modal parameter $\overline{\phi}_{ij}$, and

$$\overline{\boldsymbol{\Phi}}_C = \begin{bmatrix} \overline{\phi}_{11} & \overline{\phi}_{12} & \overline{\phi}_{13} & \overline{\phi}_{14} \\ \overline{\phi}_{21} & \overline{\phi}_{22} & \overline{\phi}_{23} & \overline{\phi}_{24} \\ \overline{\phi}_{31} & \overline{\phi}_{32} & \overline{\phi}_{33} & \overline{\phi}_{34} \\ \vdots & \vdots & \vdots & \vdots \\ \overline{\phi}_{f1} & \overline{\phi}_{f2} & \overline{\phi}_{f3} & \overline{\phi}_{f4} \end{bmatrix} \tag{A22}$$

The functional relation between $\boldsymbol{w}_{yj}$ and the state space variable $\boldsymbol{u}_C$ is

$$\boldsymbol{w}_y = 2\mathrm{Re}\left\{\overline{\boldsymbol{\Phi}}_C^T \boldsymbol{u}_C\right\} = 2\left(\mathrm{Re}\left\{\overline{\boldsymbol{\Phi}}_C^T\right\} \cdot \mathrm{Re}\{\boldsymbol{u}_C\} - \mathrm{Im}\left\{\overline{\boldsymbol{\Phi}}_C^T\right\} \cdot \mathrm{Im}\{\boldsymbol{u}_C\}\right) \tag{A23}$$

where $\boldsymbol{w}_y = [w_{y1}, w_{y2}, w_{y3}, w_{y4}]^T$.

Appendix B. Control Parameters in Simulation Calculation

MATLAB is used in the simulation calculation in this paper. The specific theory of mathematical operations has been described in detail in Section 2 and Appendix A. Here, some control parameters related to computational convergence are supplemented.

As mentioned above, the displacement response of the coupled system at any time t_1 is $\boldsymbol{w}_{A1} = [w_{A1}, w_{A2}, w_{A3}, w_{A4}]^T$, $\boldsymbol{w}_{A2} = [w_{A5}, w_{A6}, w_{A7}, w_{A8}]^T$, $\boldsymbol{w}_t = [\, w_{t1}, w_{t2}, w_{t3}, w_{t4}, w_{t5}, w_{t6}, w_{t7}, w_{t8}]^T$, $\boldsymbol{w}_b = [w_{b1}, w_{b2}, w_{b3}, w_{b4}]^T$, and $\boldsymbol{w}_y = [w_{y1}, w_{y2}, w_{y3}, w_{y4}]^T$. The above displacement responses are assembled into a total displacement vector $\boldsymbol{w} = \left[\boldsymbol{w}_{A1}^T, \boldsymbol{w}_{A2}^T, \boldsymbol{w}_t^T, \boldsymbol{w}_b^T, \boldsymbol{w}_y^T\right]^T$, whose corresponding velocity vector is $\dot{\boldsymbol{w}}$. Suppose there is a time $t_2 = t_1 + T$, the displacement response is $\boldsymbol{w}'$, and the velocity response is $\dot{\boldsymbol{w}}'$. Considering $\boldsymbol{w}'$ and $\dot{\boldsymbol{w}}'$ as two points in phase space, according to Poincaré mapping theory, if these two points can coincide, then the system has a period T. However, due to the error caused by the precision of numerical calculation, it is difficult to strictly meet this condition. Therefore, a tolerance criterion ε is set so that:

$$\frac{\left\|\boldsymbol{w}' - \boldsymbol{w}\right\|_2}{\left\|\boldsymbol{w}'\right\|_2} < \varepsilon \tag{A24}$$

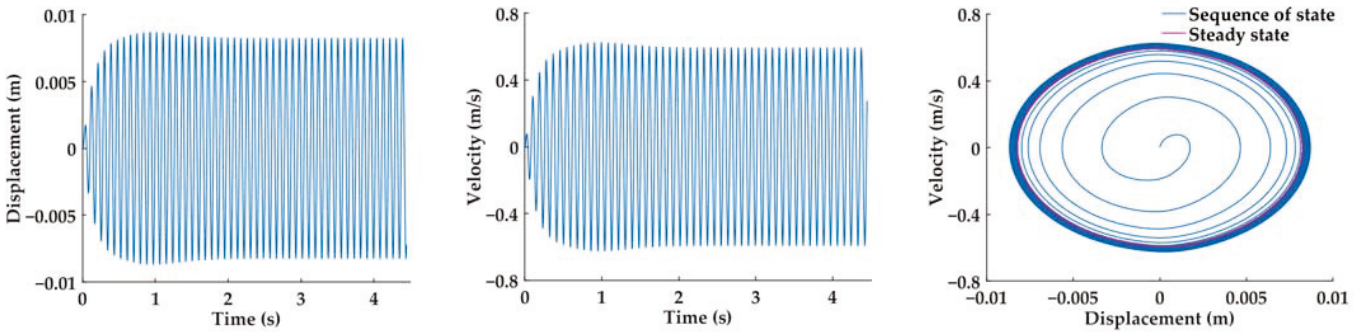
If the displacement responses w and $\boldsymbol{w}'$ satisfy the above condition, the calculation is considered to be convergent, that is, the motion of the system is periodic (T is a period). Otherwise, it is divergent, that is, the motion of the system is nonperiodic (quasi-periodic or chaotic).

Similarly, the velocity responses $\dot{\boldsymbol{w}}$ and $\dot{\boldsymbol{w}}'$ should also satisfy the condition, that is:

$$\frac{\left\|\dot{\boldsymbol{w}}' - \dot{\boldsymbol{w}}\right\|_2}{\left\|\dot{\boldsymbol{w}}'\right\|_2} < \varepsilon \tag{A25}$$

The above tolerance criterion ε is set to 1.0×10^{-5} in the simulation example of this paper.

Figure A2 shows the convergence process of simulation calculation under $\alpha = 0.5$ and $\beta = 1.0$ as an example of the connection points of the upper vibration isolators with unit A_1. It can be seen from Figure A2a,b that convergence is obtained when $t = 1.7$ s. Figure A2c shows a sequence of state as it move to the attractor.



(**a**) (**b**) (**c**)

Figure A2. The convergence process of the calculation at the connection points of the upper vibration isolators with the unit A_1 ($\alpha = 0.5$, $\beta = 1.0$): (**a**) time that the displacement response calculation took to obtain convergence; (**b**) time that the velocity response calculation took to obtain convergence; (**c**) the sequence of state as it moves to the attractor.

Similarly, at the connection points of the upper vibration isolators with the unit A_2, the upper vibration isolators with the raft frame, the lower vibration isolators with the raft frame, and the lower vibration isolators with the cylindrical shell, and under other nonlinear stiffness conditions, simulation calculation of the periodic motion has similar convergence properties, which will not be shown here one by one.

References

1. Smirnov, V.; Mondrus, V. Comparison of linear and nonlinear vibration isolation system under random excitation. *Procedia Eng.* **2016**, *153*, 673–678. [CrossRef]
2. Santhosh, B. Dynamics and performance evaluation of an asymmetric nonlinear vibration isolation mechanism. *J. Braz. Soc. Mech. Sci. Eng.* **2018**, *40*, 169. [CrossRef]
3. Dutta, S.; Chakraborty, G. Performance analysis of nonlinear vibration isolator with magneto-rheological damper. *J. Sound Vib.* **2014**, *333*, 5097–5114. [CrossRef]
4. Suman, S.; Balaji, P.S.; Selvakumar, K.; Kumaraswamidhas, L.A. Nonlinear vibration control device for a vehicle suspension using negative stiffness mechanism. *J. Vib. Eng. Technol.* **2021**, *9*, 957–966. [CrossRef]
5. Araki, Y.; Asai, T.; Kimura, K.; Maezawa, K.; Masui, T. Nonlinear vibration isolator with adjustable restoring force. *J. Sound Vib.* **2013**, *332*, 6063–6077. [CrossRef]
6. Zhao, F.; Ji, J.C.; Ye, K.; Luo, Q. Increase of quasi-zero stiffness region using two pairs of oblique springs. *Mech. Syst. Signal Process.* **2020**, *144*, 106975. [CrossRef]
7. Zhao, F.; Ji, J.C.; Ye, K.; Luo, Q. An innovative quasi-zero stiffness isolator with three pairs of oblique springs. *Int. J. Mech. Sci.* **2021**, *192*, 106093. [CrossRef]
8. Ye, K.; Ji, J.C.; Brown, T. Design of a quasi-zero stiffness isolation system for supporting different loads. *J. Sound Vib.* **2020**, *471*, 115198. [CrossRef]
9. Chang, Y.; Zhou, J.; Wang, K.; Xu, D. A quasi-zero-stiffness dynamic vibration absorber. *J. Sound Vib.* **2021**, *494*, 115859. [CrossRef]
10. Bouna, H.S.; Nbendjo, B.R.N.; Woafo, P. Isolation performance of a quasi-zero stiffness isolator in vibration isolation of a multi-span continuous beam bridge under pier base vibrating excitation. *Nonlinear Dyn.* **2020**, *100*, 1125–1141. [CrossRef]
11. Drezet, C.; Kacem, N.; Bouhaddi, N. Design of a nonlinear energy harvester based on high static low dynamic stiffness for low frequency random vibrations. *Sens. Actuators A Phys.* **2018**, *283*, 54–64. [CrossRef]
12. Lu, Z.; Wu, D.; Ding, H.; Chen, L. Vibration isolation and energy harvesting integrated in a Stewart platform with high static and low dynamic stiffness. *Appl. Math. Model.* **2021**, *89*, 249–267. [CrossRef]
13. Hao, R.; Lu, Z.; Ding, H.; Chen, L. Orthogonal six-DOFs vibration isolation with tunable high-static-low-dynamic stiffness: Experiment and analysis. *Int. J. Mech. Sci.* **2022**, *222*, 107237. [CrossRef]
14. Hao, R.; Lu, Z.; Ding, H.; Chen, L. A nonlinear vibration isolator supported on a flexible plate: Analysis and experiment. *Nonlinear Dyn.* **2022**, *108*, 941–958. [CrossRef]
15. Sun, Y.; Zhou, J.; Thompson, D.; Yuan, T.; Gong, D.; You, T. Design, analysis and experimental validation of high static and low dynamic stiffness mounts based on target force curves. *Int. J. Non-Linear Mech.* **2020**, *126*, 103559. [CrossRef]
16. Yao, Y.; Li, H.; Li, Y.; Wang, X. Analytical and experimental investigation of a high-static-low-dynamic stiffness isolator with cam-roller-spring mechanism. *Int. J. Mech. Sci.* **2020**, *186*, 105888. [CrossRef]
17. Chong, X.; Wu, Z.; Li, F. Vibration isolation properties of the nonlinear X-combined structure with a high-static and low-dynamic stiffness: Theory and experiment. *Mech. Syst. Signal Process.* **2022**, *179*, 109352. [CrossRef]

18. Leutcho, G.D.; Kengne, J. A unique chaotic snap system with a smoothly adjustable symmetry and nonlinearity: Chaos, offset-boosting, antimonotonicity, and coexisting multiple attractors. *Chaos Solitons Fractals* **2018**, *113*, 275–293. [CrossRef]
19. Yan, B.; Ma, H.; Jian, B.; Wang, K.; Wu, C. Nonlinear dynamics analysis of a bi-state nonlinear vibration isolator with symmetric permanent magnets. *Nonlinear Dyn.* **2019**, *97*, 2499–2519. [CrossRef]
20. Rahman, Z.A.S.A.; Jasim, B.H. Hidden Dynamics Investigation, Fast Adaptive Synchronization, and Chaos-Based Secure Communication Scheme of a New 3D Fractional-Order Chaotic System. *Inventions* **2022**, *7*, 108. [CrossRef]
21. Li, Y.; Yi, Y.; Wu, J.; Gu, Y. A novel feature extraction method for ship-radiated noise based on hierarchical refined composite multi-scale dispersion entropy-based Lempel-Ziv complexity. *Deep Sea Res. Part I Oceanogr. Res. Pap.* **2023**, *199*, 104111. [CrossRef]
22. Karimov, A.; Rybin, V.; Dautov, A.; Karimov, T.; Bobrova, Y.; Butusov, D. Mechanical Chaotic Duffing System with Magnetic Springs. *Inventions* **2023**, *8*, 19. [CrossRef]
23. Dreau, J.; Magnain, B.; Batailly, A. Multi-element polynomial chaos expansion based on automatic discontinuity detection for nonlinear systems. *J. Sound Vib.* **2023**, *567*, 117920. [CrossRef]
24. Cassidy, I.L.; Scruggs, J.T. Nonlinear stochastic controllers for power-flow-constrained vibratory energy harvesters. *J. Sound Vib.* **2013**, *332*, 3134–3147. [CrossRef]
25. Silva, O.M.; Neves, M.M.; Jordan, R.; Lenzi, A. An FEM-based method to evaluate and optimize vibration power flow through a beam-to-plate connection. *J. Braz. Soc. Mech. Sci. Eng.* **2017**, *39*, 413–426. [CrossRef]
26. Varghese, C.K.; Shankar, K.K. Damage identification using combined transient power flow balance and acceleration matching technique. *Struct. Control. Health Monit.* **2014**, *21*, 135–155. [CrossRef]
27. Yang, J.; Xiong, Y.; Xing, J. Vibration power flow and force transmission behaviour of a nonlinear isolator mounted on a nonlinear base. *Int. J. Mech. Sci.* **2016**, *115*, 238–252. [CrossRef]
28. Shi, B.; Yang, J. Quantification of vibration force and power flow transmission between coupled nonlinear oscillators. *Int. J. Dyn. Control.* **2020**, *8*, 418–435. [CrossRef]
29. Ren, Y.; Chang, S.; Liu, G.; Wu, L.; Wang, H. Vibratory power flow analysis of a gear-housing-foundation coupled system. *Shock. Vib.* **2018**, *2018*, 5974759. [CrossRef]
30. Zhang, Y.; Zhou, L.; Wang, S.; Yang, T.; Chen, L. Vibration power flow characteristics of the whole-spacecraft with a nonlinear energy sink. *J. Low Freq. Noise Vib. Act. Control* **2019**, *38*, 341–351. [CrossRef]
31. Xu, D.; Du, J.; Zhao, Y. Flexural vibration and power flow analyses of axially loaded beams with general boundary and non-uniform elastic foundations. *Adv. Mech. Eng.* **2020**, *12*, 1687814020921719. [CrossRef]
32. Mahapatra, K.; Panigrahi, S.K. Effect of general coupling conditions on the vibration and power flow characteristics of a two-plate built-up plate structure. *Mech. Based Des. Struct. Mach.* **2021**, *49*, 841–861. [CrossRef]
33. Liu, S.; Huo, R.; Wang, L. Vibroacoustic Transfer Characteristics of Underwater Cylindrical Shells Containing Complex Internal Elastic Coupled Systems. *Appl. Sci.* **2023**, *13*, 3994. [CrossRef]
34. More, S.; Padmanabhan, C. Power flow based analysis of a floating raft vibration isolation system. *Am. Phys. Soc.* **2014**, *72*, 691–708.

Disclaimer/Publisher's Note: The statements, opinions and data contained in all publications are solely those of the individual author(s) and contributor(s) and not of MDPI and/or the editor(s). MDPI and/or the editor(s) disclaim responsibility for any injury to people or property resulting from any ideas, methods, instructions or products referred to in the content.

inventions

MDPI

Article

Mathematical Model of the Working Processes of the Gas Cap of a Piston Pump Installed in the Discharge Line

Victor Shcherba [1,*] and Irina Bulgakova [2]

[1] Hydromechanics and Machines Department, Omsk State Technical University, 644050 Omsk, Russia
[2] Foreign Languages Department, Omsk State Technical University, 644050 Omsk, Russia; bulgakova-i@mail.ru
* Correspondence: scherba_v_e@list.ru or vesherba@omgtu.ru; Tel.: +7-3812-65-31-77

Abstract: A mathematical model of the working processes occurring in the gas cap has been developed on the basic fundamental laws of conservation of energy, mass and motion, and the equation of state, both taking into account the change in the mass of the gas due to phase transitions and the solubility of the gas in the liquid, and without taking them into account with a dividing element. In addition, there was developed a mathematical model of the liquid flow from the gas cap through a pipeline of constant cross section. It was found from the results of a numerical experiment that to reduce the feed irregularity, it is necessary to increase the length of the pipeline and the crankshaft revolutions, in addition to the known ratio of the volume of gas in the cap to the working volume of the pump; an increase in discharge pressure and an increase in the diameter of the connecting pipeline increases the feed irregularity.

Keywords: piston pump; gas cap; discharge pressure; connecting hydraulic lines; irregularity

1. Introduction

For many centuries, piston pumps have been widely used in industry and in everyday life, but one of their most important characteristics is the irregularity of pump flow. The regularity of the pump flow largely determines the regularity of the movement of the working element of the hydraulic motor, and, consequently, its reliability and efficiency.

The analysis of the scientific literature showed that most of them aimed at reducing flow, and pressure fluctuations caused by positive displacement pumps are associated with the geometric optimization of the machine itself. The researchers paid attention to the design of the inlet of axial piston pumps to ensure a smooth transition of fluid pressure between the suction and discharge phases, and vice versa [1–3]. In gear pumps, engineers have used special grooves in the side sleeves to improve machine performance and reduce pressure pulsations [4–9].

Another way to reduce intake and pressure pulsations is to use external devices in addition to the pump and hydraulic system [10–12]. These solutions can be divided into two groups: active damping systems and passive damping systems, which this article is devoted to.

Active methods involve the use of externally powered, controlled mechanisms. The method presented in [13,14] consists of high-frequency action on the angle of an oscillating plate in an axial piston pump through a switching valve, to soften the liquid intake. Various research efforts are investigating the application of piezoelectric actuators to control pistons, thereby neutralizing reverse flow by generating an anti-phase flow signal [14–16].

Their advantage is that they give effective results regardless of pressure and RPM (revolution per minute) settings, but they tend to be complex and expensive.

Passive methods are simpler and cheaper, because they do not require external control or power and do not need sensors for measurements. Mostly, passive methods dampen flow pulsations using elastic components that interact with the flow. However, they are

often designed to provide maximum performance within a certain operating range, beyond which their efficiency decreases.

Shan's study [17] demonstrates the above, and it stated where a spring accumulator is used to reduce the fundamental harmonic of the flow pulsation generated by an axial piston pump. The mechanism additionally uses the phase characteristics of suction and discharge flow pulsations, as well as pressure pulsations to improve performance. As an alternative, there was proposed a separate approach [16] in which the length and stiffness of elastic pipes are optimized in a hydraulic circuit to reduce pulsations.

This article investigates the potential of gas-filled bladder accumulators as a passive device to reduce flow and pressure pulsations. The practice of introducing accumulators into hydraulic systems to reduce noise and irregularities carried by the fluid is widespread [18,19]. By acting as a low-pass filter in a liquid-filled line, the accumulator can compensate for peaks, both negative and positive, occurring in the flow, by accumulating or intaking an excess or deficiency of liquid.

Many works devoted to the study of the operation of gas caps are performed on the calculation and analysis of the operation of air caps and they can be divided into three groups. The first group implements a mechanical approach; its fundamental work on the calculation of the gas cap is [4,20]. As the research was carried out when there were no computers and no development of the version of numerical methods of mathematical analysis, the author had to use assumptions to obtain analytical solutions. These studies were reduced to the study of the dynamics of the liquid level in the gas cap under the assumption that the water column is a material point.

It should be noted that gas caps are also used to dampen oscillatory processes in connecting hydraulic and pneumatic pipelines. These works include the study and damping of hydraulic shock [21–23]; the study and damping of oscillatory pressure processes in pipelines of reciprocating and compressor units [24–26]. An oscillatory approach is implemented in these works with consideration of resonance phenomena. In most cases, the solution of these issues was carried out using an analogy with electrical systems [27].

It should be noted that in a real gas cap there are processes of heat and mass transfer between the gas and the working fluid, and heat exchange processes between the gas and the cap surface at variable values of the heat transfer coefficient. Moreover, there is unsteady movement of a viscous fluid in the connecting pipelines, including the turbulent flow mode. To solve such a complex problem, it is necessary to use an approach based on the basic laws of thermodynamics, mass transfer, fluid and gas mechanics. This approach is the third main approach and it brings the mathematical model closer to reality and obtains the results closest to reality. It is proposed to place a gas cap directly in the pump cylinder, which will increase the efficiency of its operation while increasing the uniformity of the pump flow and reducing the weight and size indicators of the pumping unit [28]. Thus, in this paper, the task is to develop a mathematical model of the working processes of a gas cap installed on the discharge of a piston pump, based on the general laws of fluid and gas mechanics, and the theory of heat and mass transfer, to conduct a numerical experiment on its basis, in order to analyze the influence of the main geometric dimensions (relative volume of the gas cap, diameter and length of the connecting pipeline), as well as the number of revolutions and its discharge pressure on the pump flow irregularity.

2. Materials and Methods

In general, when developing a mathematical model of the working processes in the gas cap of a piston pump, four main objects can be distinguished: the piston pump (1), the connecting pipeline (2) between the pump and gas cap, the gas cap (3) and the connecting pipeline from the gas cap (4) (see Figure 1).

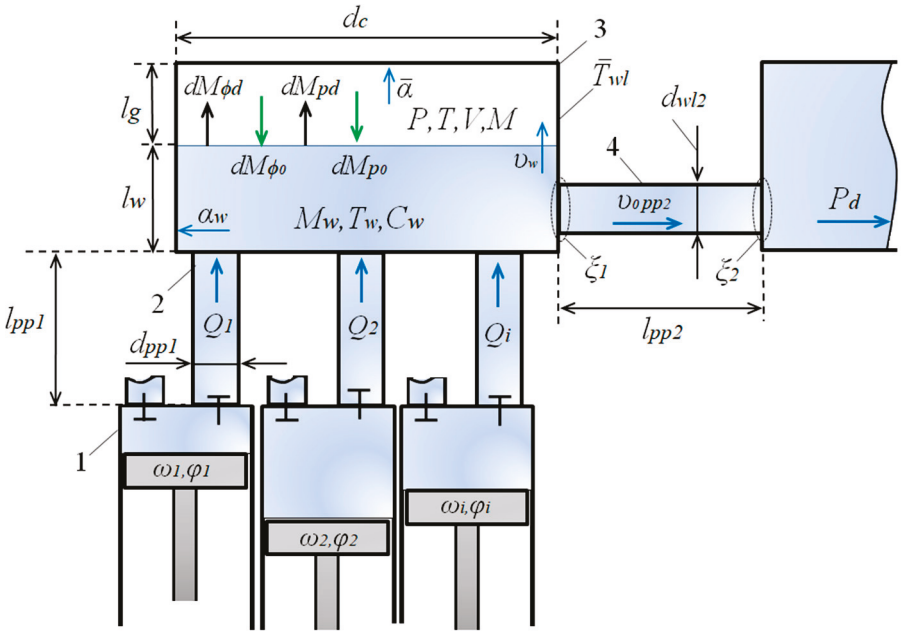


Figure 1. Design scheme of the gas cap of the piston pump.

The piston pump provides liquid supply from the working chamber to the gas cap through connecting pipeline 2. When performing calculations, we assume that the decrease in the volume of the delivered liquid due to leaks, underfilling of the working chambers and compressibility is negligible. Then, the liquid delivered to the cap can be determined as:

From working chamber 1

$$Q_1 = v_{n1} f_{n1} = \frac{S_{h1}}{2} \omega_1 \left(sin\varphi_1 + \frac{\lambda_1}{2} sin2\varphi_1 \right) \frac{\pi d_1^2}{4} \quad (1)$$

From working chamber 2

$$Q_2 = v_{n2} f_{n2} = \frac{S_{h2}}{2} \omega_2 \left(sin\varphi_2 + \frac{\lambda_2}{2} sin2\varphi_2 \right) \frac{\pi d_2^2}{4} \quad (2)$$

From *i*-th working chamber

$$Q_i = v_{ni} f_{ni} = \frac{S_{hi}}{2} \omega_i \left(sin\varphi_i + \frac{\lambda_i}{2} sin2\varphi_i \right) \frac{\pi d_i^2}{4} \quad (3)$$

In most practical cases, $S_{h1} = S_{h2} = S_{hi}$, $\lambda_1 = \lambda_2 = \lambda_i$, $\varphi_2 = f(\varphi_1)$; $\varphi_i = f(\varphi_1)$.

2.1. Mathematical Model of Working Processes in the Gas Cap

We consider the most general case, when there is no dividing element between the gas phase and the liquid phase in the gas cap.

The calculation of thermodynamic parameters in the gas phase of the air cap is similar to the calculation of the change in thermodynamic parameters in the processes of compression and expansion in a reciprocating compressor with a liquid piston.

Currently, three main approaches are used to calculate the working processes in reciprocating compressors: polytropic approximation, mathematical models with lumped parameters and mathematical models with distributed parameters [29].

The gas cap is a stage of a reciprocating compressor with a liquid piston. Mathematical models with distributed parameters determine the main thermodynamic parameters at any point in the volume of compressible gas. However, their application is limited by changing the computational grid at each moment of time, which requires time to implement this

approach and efforts to compile this program. Due to the low speed of the liquid piston compared to the speed of sound, with which pressure surges propagate, the resulting uneven distribution of thermodynamic parameters quickly disappears and, accordingly, its value tends to zero. For this reason, when calculating the working processes of reciprocating compressors, mathematical models with lumped parameters are used [29]. The developed mathematical model of working processes in a gas cap is based on the fundamental equations of conservation of energy, mass and motion, and considers many factors that are not taken into account in other models, namely: first-order phase transitions (condensation–evaporation), change in the heat transfer coefficient between gas and the walls of the gas cap in time, and change in the heat transfer coefficient between the liquid and the walls of the gas cap.

The main assumptions made are considered and their detailed analysis is given in [29]. Among the assumptions made, the following can be distinguished: the working processes are balanced and reversible, the compressible gas is homogeneous and there is no uneven distribution of temperatures and pressures in the compressible gas. The mathematical model with lumped parameters is based on the general equations of conservation of energy, mass, volume and the equation of state.

Taking into account that the kinetic energy of added and separated masses is insignificant, the energy conservation equation is transformed into the first law of thermodynamics of a body of variable mass for an open thermodynamic system in the presence of first-order phase transitions and gas solubility. Then,

$$\mathrm{dU} = \mathrm{dQ} - \mathrm{dL} + i_{phad}\mathrm{dM}_{phad} - i_{pho}\mathrm{dM}_{pho} + i_{gr}\mathrm{dM}_{gr} - i_{o}\mathrm{dM}_{go} \tag{4}$$

The elementary external heat transfer is determined in accordance with the Newton–Rahman law, as

$$\mathrm{dQ} = \alpha F_1\left(\overline{\mathrm{T}}_{\mathrm{wl}} - \mathrm{T}\right)\mathrm{d}\tau + \alpha F_2(\mathrm{T}_{\mathrm{w}} - \mathrm{T})\mathrm{d}\tau \tag{5}$$

where $F_1 = \frac{\pi d_c^2}{4} + \pi d_c l_r$, ($F_2 = \frac{\pi d_c^2}{4}$); $\overline{T}_{wl} = \frac{\int_{F_1} \mathrm{T}_{wl}(F)dF}{F_1}$ is temperature averaged over the surface of the walls in the cap (T_{wl} is determined experimentally [29]).

The determination of the heat transfer coefficient in the cylinders of reciprocating compressors is carried out experimentally for single-acting reciprocating compressors with a diameter of (0.1 ÷ 0.22) m; number of revolutions (1000 ÷ 1500) rpm, the Prilutsky–Fotin formula is widely used in the form [30]:

$$\mathrm{Nu}(\varphi) = \mathrm{ARe}^{\mathrm{x}}(\varphi) + \mathrm{B} \tag{6}$$

where $\mathrm{Nu} = \frac{\alpha \mathrm{d_c}}{\lambda}$ is Nusselt number; $\mathrm{Re} = \frac{v_w \mathrm{d_c}}{\mu/\rho}$ is Reynolds number.

The free surface velocity in the gas cap can be determined using the continuity equation for the liquid phase.

$$\mathrm{dM_w} = \sum \mathrm{dM_{ew}}i - \mathrm{dM_{ow}} - \mathrm{dM_{phad}} + \mathrm{dM_{pho}} - \mathrm{dM_{gr}} + \mathrm{dM_{go}} \tag{7}$$

where $\sum \mathrm{dM_{ew}}i = \rho_{\mathrm{w}} \cdot \mathrm{d}\tau \cdot \sum \mathrm{Q}_i$ is the mass of liquid entering the gas cap from the pump cylinders.

Considering (7), v_w is determined as

$$v_w = \frac{\mathrm{dM_w}}{F_2 \mathrm{d}\tau \cdot \rho_{\mathrm{w}}} \tag{8}$$

The deformation work dL is determined as

$$\mathrm{dL} = \mathrm{pdV} \tag{9}$$

The elementary change in the volume of the gas phase in the cap over $d\tau$ time can be determined as

$$dV = -v_w F_2 d\tau \tag{10}$$

The mass of the gas phase in the cap: The change in the mass of the gas phase in the cap without external leaks through the leaks of the cap is due to condensation or evaporation of the working fluid (phase transitions of the first order). In this case, mass transfer is carried out by concentration diffusion, thermal and barodiffusion. Taking into account the accepted assumption of constant pressure and temperature throughout all of the gas cap, there will be no thermal nor barodiffusion.

Taking into account that the mutual motion of the phases in the gas cap is negligibly small, then to calculate the mass flows during concentration diffusion, we use Fick's first law:

$$dM_{ph} = \beta_{ph} F_2 (C_w - C_2) d\tau \tag{11}$$

Values C_w and C_2 can be determined as

$$C_w = p_{elst} / (R_s T_w) \tag{12}$$

$$C_2 = p_s / (R_s T) \tag{13}$$

where p_{elst} is steam elasticity pressure at the surface of a liquid (is a function of the temperature of the liquid and the curvature of the interface and is determined by the Clausius–Claiperon equation [31]).

The mass transfer coefficient β_{ph} is determined based on [32]

$$\beta_{ph} = \frac{\alpha}{C_p \rho a_T / D} \tag{14}$$

It should be noted that the solubility of gas in liquid is generally described by the Henry equation and increases with increasing pressure.

Thus, taking into account the above, the equation for the conservation of the mass of the gas phase in the cap can be written:

$$dM = dM_{phad} - dM_{pho} + dM_{gr} - dM_{go} \tag{15}$$

State equation: It is well known that air follows the equation of state of an ideal gas up to 10 MPa and temperature up to 600 K. In this case, we have

$$pV = MRT \tag{16}$$

and also, taking into account that the specific internal energy and specific enthalpy for an ideal gas depend only on temperature, we have

$$dU = d(MC_v T) = C_v T dM + C_v T dM \tag{17}$$

$$i = C_p T \tag{18}$$

$$p = (k - 1)\frac{U}{V} \tag{19}$$

If the pressure in the gas cap is more than 10 MPa, it is necessary to introduce the compressibility factor into the equation of state and use one of the existing equations of state for an ideal gas: van der Waals, Berthelot, Dupre, Clausius or Vukalovich–Kirillin. It must be remembered that for a real gas, $u = f(v, T)$ and $i = f(p, T)$, where $v = \frac{1}{\rho}$ is specific volume.

If there is a dividing element, there will be no mass transfer processes and the system of equations to calculate changes in thermodynamic parameters will be written as

$$\begin{cases} \mathrm{dU} = \mathrm{dQ} - \mathrm{pdV} \\ dV = -(\Sigma \mathrm{dM_{nw}}i - \mathrm{dM_{sw}})/\rho_{\mathrm{w}} \\ \mathrm{p} = (\mathrm{k}-1)\mathrm{U}/\mathrm{V} \\ \mathrm{T} = \mathrm{pV}/(\mathrm{MR}) \end{cases} \quad (20)$$

Liquid phase: the pressure in the liquid phase is defined as

$$\mathrm{p_w} = \mathrm{p} + \Delta p \quad (21)$$

Overpressure Δp is due to the elastic force of the dividing element:

$$\Delta p = \frac{\mathrm{W_{els}}}{\mathrm{F_2}} = \frac{\mathrm{C_{stf}}(l_{\mathrm{w}} - l_{\mathrm{w0}})}{\mathrm{F_2}} \quad (22)$$

If there is no dividing element then $\mathrm{p_w} = \mathrm{p}$.

To determine the temperature of the liquid in the cap, we use the energy conservation equation, if there is no dividing element.

The studies carried out prove that the pressure fluctuations do not exceed 5% in the cap [10] from the average pressure in the cap. The liquid enters the gas cap being compressed in the pump. We calculate the relative change in the volume of a liquid due to its compressibility. We assume that the nominal pressure at the outlet of the piston pump is 40 MPa. Accordingly, the increase in pressure in the gas cap will be 2 MPa. Then, the relative change in volume will be equal to $\frac{\Delta V}{V} = \frac{\Delta p}{E} = \frac{2 \cdot 10^6}{2 \cdot 10^9}$ = 0.1%, i.e., the relative change in volume is much less than one percent and can be neglected without loss of accuracy in the results.

$$\mathrm{dU_w} = \mathrm{dQ_w} - \mathrm{pdV_{wc}} + \sum i_{adwi}\mathrm{dM_{wi}} - i_{ow}\mathrm{dM_{0w}} + i_{phad}\mathrm{dM_{phad}} - i_{pho}\mathrm{dM_{pho}} + i_{gr}\mathrm{dM_{gr}} - i_{\mathrm{o}}\mathrm{dM_{go}} \quad (23)$$

Taking into account that the liquid compression in the gas cap is negligibly small, then $\mathrm{dV_{wc}} = 0$ and the deformation work is equal to 0. The total internal energy can be determined as

$$\mathrm{U_w} = \mathrm{u_w} \cdot \mathrm{M_w} \quad (24)$$

Consequently,

$$\mathrm{dU_w} = \mathrm{d}(\mathrm{u_w} \cdot \mathrm{M_w}) = \mathrm{M_w du_w} + \mathrm{u_w dM_w} \quad (25)$$

du_w is written as

$$\mathrm{du_w} = \left(\frac{\partial \mathrm{u_w}}{\partial v_{\mathrm{w}}}\right)_{\mathrm{T}} \mathrm{d}v_{\mathrm{w}} + \left(\frac{\partial \mathrm{u_w}}{\partial T_{\mathrm{w}}}\right)_{\mathrm{v_w}} \mathrm{d}T_{\mathrm{w}} \quad (26)$$

Considering that the fluid is incompressible and $\mathrm{d}v_w = 0$, Equation (25) is converted to:

$$\mathrm{dU_w} = \mathrm{C_w M_w dT_w} + \mathrm{C_w T_w dM_w} \quad (27)$$

where $\left(\frac{\partial \mathrm{u_w}}{\partial \mathrm{T_w}}\right)_{\mathrm{v_w}} = \mathrm{C}_w$—specific heat capacity of a liquid.

Taking into account (27), the equation for determining the change in liquid temperature can be written as:

$$\mathrm{dT_w} = \frac{1}{\mathrm{C_w M_w}}\left[\mathrm{dQ_w} + \sum i_{\mathrm{adw}i}\mathrm{dM_{wi}} - i_{0w}\mathrm{dM_{0w}} + i_{\mathrm{phad}}\mathrm{dM_{phad}} - i_{ph0}\mathrm{dM_{ph0}} + i_{gr}\mathrm{dM_{gr}} - i_0\mathrm{dM_{p0}}\right] \quad (28)$$

For a gas cap with a dividing element, Equation (28) is converted to:

$$\mathrm{dT_w} = \frac{1}{\mathrm{C_w M_w}}\left(\mathrm{dQ_w} + \sum i_{\mathrm{adw}i}\mathrm{dM_{wi}} - i_{0w}\mathrm{dM_{0w}}\right) \quad (29)$$

In Equations (28) and (29), the specific enthalpies are determined as

$$i_{adwi} = \mathrm{C}_w T_{adi};\ i_{0w} = \mathrm{C}_w T_w \tag{30}$$

The elementary external heat transfer $\mathrm{dQ_w}$ is determined as

$$\mathrm{dQ_w} = \overline{\alpha}_w F_w \left(\overline{T}_{wl} - T_w\right) d\tau \tag{31}$$

The heat transfer coefficient α_w for convective heat transfer depends on the flow mode for a round pipe and is defined as [33] for laminar fluid flow:

$$\overline{\alpha}_w = \frac{\alpha_w}{d_c}\left[0.33 Re_w^{0.3} Pr_w^{0.43} \left(Pr_w / Pr_{wl}\right)^{0.25}\right] \tag{32}$$

and for turbulent flow mode:

$$\overline{\alpha}_w = \frac{\alpha_w}{d_c}\left[0.021 Re_w^{0.8} Pr_w^{0.43} \left(Pr_w / Pr_{wl}\right)^{0.25}\right] \tag{33}$$

where $Re_w = \frac{v_w d_\mathrm{K}}{\mu_w / \rho_w}$ is the Reynolds number; $Pr_w = \frac{\mu_w C_w}{\alpha_w}$ is the Prandtl number; and Pr_{wl} is the Prandtl number at wall temperature.

The heat exchange surface with a cylindrical shape of the cap is determined as

$$F_w = l_w \pi d_c + \frac{\pi d_c^2}{2} \tag{34}$$

Mass Conservation Equation: if there is no dividing element in the cap, it is determined by Equation (7); in another case we have

$$\mathrm{dM_w} = \sum \mathrm{dM_{adw}}i - \mathrm{dM}_{ow} \tag{35}$$

2.2. Mathematical Model of Liquid Flow in the Pipeline from the Gas Cap

Currently, various models are used to describe the flow of liquid in a pipeline, ranging from the simplest ones based on the energy conservation equation (Bernoulli), both without taking into account inertial pressure losses and taking them into account, to complex ones using two-parameter turbulence models: k-ε, k-ω, SST and others.

When developing a mathematical model of fluid flow in a connecting pipeline, we use the principle of hierarchy and consider the calculation of the flow based on the Bernoulli equation and the unsteady one-dimensional flow of a viscous incompressible fluid.

In accordance with [4,20], the integral of the Bernoulli equation can be written as

$$\int_{l_{pp2}} \frac{\partial}{\partial l}\left(z + \frac{p}{j} + \frac{v_{pp2}^2}{2g}\right) dl + \frac{1}{y}\int_{l_{pp2}} \frac{\partial v_{pp2}}{\partial \tau} dl + \Sigma \Delta h_i = 0 \tag{36}$$

where $\Sigma \Delta h_i = \left(\Sigma \xi_i + \lambda_{pp2} \frac{l_{pp2}}{d_{pp2}}\right) \frac{v_{pp2}^2}{2g}$—head losses due to local and hydraulic resistance along the length.

The solution of this equation was carried out in [34].

Without taking into account the forces of inertia, the equation for determining the velocity of the liquid in the pipeline is written as:

$$v_{pp2} = \sqrt{\frac{2g\left[\left(z_{1pp2} + \frac{p}{\rho_w g}\right) - \left(z_{2pp2} + \frac{P_d}{\rho_w g}\right)\right]}{\left(\lambda_{pp2} \frac{l_{pp2}}{d_{pp2}} + \Sigma \xi_i\right)}} \tag{37}$$

The coefficient of friction along the length λ_{pp2} is a function of the Reynolds number [35] and, accordingly, v_{pp2}. As a result, Equation (37) must be solved at each time step by the successive approximations method.

The system of differential equations for describing an unsteady one-dimensional flow of a viscous incompressible liquid can be written as a system of equations of motion and continuity [36–38]:

$$\rho_w \frac{\partial Q_{wpp2}}{\partial \tau} + f_{pp2} \frac{\partial p}{\partial x} + \frac{\lambda_{pp2} \rho_w}{2 d_{pp} f_{pp2}} Q_{wpp\mathrm{TP}2} |Q_{w\mathrm{TP}2}| = 0 \tag{38}$$

$$\frac{\rho_w a^2}{f_{pp2}} \frac{\partial p}{\partial x} + \frac{\partial p}{\partial \tau} = 0 \tag{39}$$

We recommend to solve this system by the method of "characteristics".

Boundary conditions at the ends of the pipeline are adjacent, on the one hand, to the gas cap, and on the other side to the consumer of the liquid in the form of pressures: in the gas cap—p_w; at the consumer of the liquid—p_d.

Having defined v_{pp2} or Q_{wpp2}, the value of $\mathrm{dM_{ow}}$ is determined as

$$\mathrm{dM_{ow}} = \rho_w v_{pp2} f_{pp2} d\tau = \mathrm{Q}_{wpp2} \rho_w d\tau \tag{40}$$

2.3. Verification of the Developed Model

Currently, there are two research methods: experimental and theoretical. Both research methods have an error in determining the true results. Until now, the experimental method is believed to correspond to reality most accurately, and the developed models have been verified on the results of experimental studies. In general, we also consider such an approach proper if a comprehensive assessment of the error in the determination of results in the experiment has been carried out. In some cases, the error in experimental studies exceeds the error in the mathematical models based on the known laws of conservation of energy, mass and motion. If experimental verification is not available, then the developed mathematical mode can be verified by the following methods:

1 Compare it with the results of experimental studies of other authors.
2 Compare it with the results of theoretical studies of other authors.

Both approaches are not available in this work. There are no complete results of experimental studies on the influence of the main design and operational parameters of the gas cap in the literature, and those that exist are theoretical and experimental results that correspond to the results obtained in this article (see Bashta, T. M. Displacement pumps and hydraulic engines of hydraulic systems: textbook for universities/T. M. Bashta.—Moscow: Mashinostroenie, 1974.—606 p.) [10]. When using the results obtained on other mathematical models, there is a question of how much the existing developed mathematical models are closer to real results than the data. In our opinion, they are further from reality, because mainly they use the theory of oscillatory processes, which do not consider many physical phenomena (heat and mass transfer, etc.).

3. Results and Discussion

We conducted a numerical experiment to analyze the influence of the main operational and design parameters on the irregular pump flow and the ongoing work processes in the gas cap. As a study object we took a single-acting piston pump with the following main dimensions: piston stroke—0.1 m; piston diameter—0.1 m; the ratio of the piston stroke to twice the length of the connecting rod—0.2. The piston pump was connected to a gas cap by a pipeline with a diameter of 0.03 m and a length of 0.5 m. The gas cap had a dividing element with an infinitesimal rigidity. We chose water and air as the working fluid. The gas cap was made in the form of a cylinder 0.6 m long. When the volume of the gas cap was changed, its diameter was changed. The initial height of the liquid level was chosen equal

to 1/3 of the total height of the tank. To simplify the calculations and due to the smallness of its change, the temperature of the liquid in the cap was assumed to be 293 K, and the average surface temperature of the cap walls was assumed to be 300 K. The gas cap helped to maintain a constant pressure over time (p_d) by a pipeline, the inner diameter and length of which varied, and the value of the roughness of the inner walls remained constant and equal to 0.000005 m. The preliminary analysis of the impact on the working processes in the cap and the irregular pump flow established that the crankshaft revolutions of the pump and the discharge pressure can be taken as independent operational parameters. We chose as the main geometric parameters: the volume of the gas cap due to a change in its diameter, and the diameter and length of the connecting pipeline. Thus, we obtained five independent variables: p_d, n_{rev}, d_{pp2}, l_{pp2},V_g/V_h.

V_g/V_h is the ratio of the initial gas volume to the working volume V_h of the pump.

As response functions, we chose: feed irregularity ($\Delta = \frac{Q_{max}-Q_{min}}{Q_{av}}$), maximum fluid flow ($Q_{max}$), minimum flow rate ($Q_{min}$), the average pressure in the cap ($p_{av} = \frac{\int_0^{2\pi} p(\varphi)d\varphi}{2\pi}$) and the average gas temperature in the cap ($T_{av} = \frac{\int_0^{2\pi} T(\varphi)d\varphi}{2\pi}$).

The classical plan with fractional replicas was chosen for the numerical experiment.

3.1. Features of the Implementation of the Mathematical Model

In general, the developed mathematical model is a set of first-order differential equations of total derivatives. This system does not have an analytical solution and well-known numerical methods can be used to solve it; for example, Euler, Runge–Kutta (of different orders of accuracy), Adamson, Monte Carlo, etc. In this article, the Euler method was used when solving differential equations.

As a base point, we take a point with the following independent variables: V_g/V_h = 64; l_{pp2} = 2 m; d_{pp2} = 0.03 m; n_{rev} = 300 rpm. The calculation starts from the crankshaft rotation angle $\varphi = \pi$; in this case, the pressure and temperature in the gas cap were set arbitrarily, while the pressure in the gas cap was set not much higher than the discharge pressure (p_d), and the temperature was set equal to the temperature of the liquid. The instantaneous supply of liquid from the pump cylinder through pipeline 2 to gas cap 3 was calculated. Then the gas cap and pipeline 4 were calculated. When calculating the pipeline, an equation was used to determine the fluid flow rate without taking into account inertial losses. The calculation was carried out with a step according to the crankshaft rotation angle $\Delta\varphi = 2\pi/7200$. After the calculation for one rotation of the crankshaft, the initial and final pressure values in the gas cap were compared. If the difference in the obtained pressures was less than 1 kPa, the calculation was stopped; if not, the calculation was started anew, while the obtained final thermodynamic parameters of the gas and liquid in the cap became the initial ones. In most of the calculation options performed, the number of iterations did not exceed 25.

When determining the fluid flow rate in pipeline 4, the number of iterations was limited to 50, while the discrepancy in determining the rate was set to less than 1%. During the calculation, at each iteration, the value of the maximum flow rate in pipeline 4 during the crankshaft rotation from 0 to 2π was determined—Q_{max}, the minimum value of the liquid flow rate—Q_{min}, and the average integral value of the liquid flow rate—Q_{av}.

3.2. Analysis of the Influence of the Ratio of the Initial Volume of the Gas Phase to the Working Volume of the Pump (V_g/V_h)

In accordance with the previously obtained results in [1,4], an increase in the ratio V_g/V_h leads to a decrease in the irregularity of the pump flow (see Figure 2). The resulting dependence is hyperbolic in nature. From the presented results, we can conclude that an acceptable feed irregularity (less than 10%) is achieved at V_g/V_h more than 70%.

The dependences of the minimum and maximum values of the liquid flow in pipeline 4 presented in Figure 3 established that these dependences are parabolic in nature and

their change decreases significantly, starting from $V_g/V_h > 50$. Increasing V_g/V_h leads to a decrease in the average pressure (p_{av}) and average gas temperature in the cap.

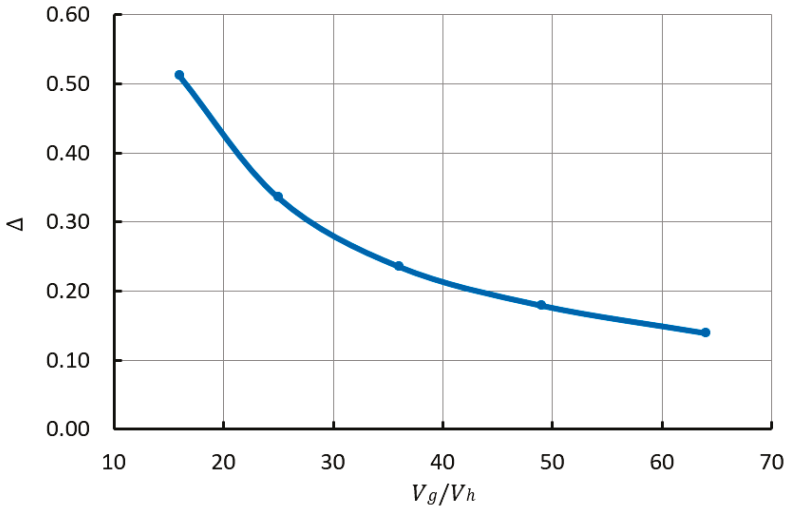


Figure 2. The dependence of the irregularity of the liquid supply on the ratio of the initial value of the volume of the gas phase to the working volume.

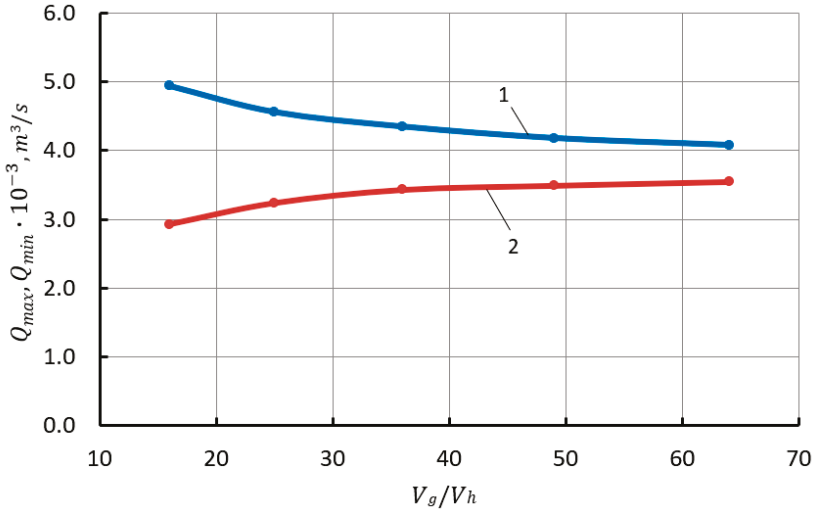


Figure 3. Dependence of the maximum and minimum liquid flow rate from the gas cap on the ratio of the initial value of the gas phase volume to the working volume (1—Q_{max}; 2—Q_{min}).

Figure 4 presents $\Delta p = p_{av} - p_d$ and T_{av} depending on the ratio V_g/V_h. The obtained dependences are close to linear. Values $p_{av}(\Delta p)$ and T_{av} change insignificantly and are about 5 kPa and about 0.6 K with the increasing V_g/V_h from 16 to 64.

3.3. Analysis of the Influence of the Crankshaft Revolutions

Increasing the crankshaft revolutions increases the amount of liquid entering the gas cap per unit time. This leads to a decrease in feed irregularity (see Figure 5). The presented dependence has a clearly non-linear nature, close to parabolic. At a speed greater than 350 rpm, Δ becomes less than 10%. With the increase in n_{rev} values, Q_{max} and Q_{min} increase almost linearly, and the difference between them decreases. As the number of revolutions increases, $p_{av}(\Delta p)$ and T_{av} increase almost linearly (see Figure 6). Increasing Δp with an increase in the number of revolutions from 200 rpm to 400 rpm is 70 kPa, the value of T_{av} is even more significant and is about 5 K. An increase in T_{av} is due to an increase in the frequency of fluctuations in the liquid level in the gas cap. Thus, increasing n_{rev} leads to a significant increase in p_{av} and T_{av} with a decrease in feed irregularity.

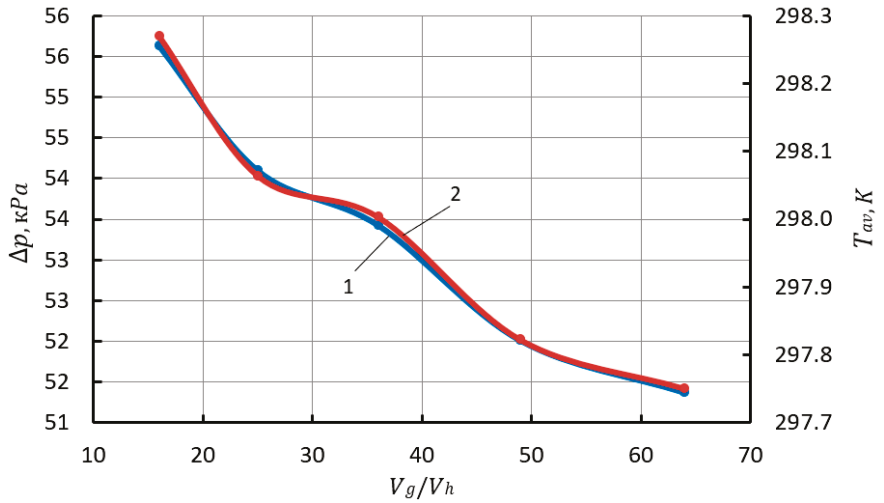


Figure 4. Dependence of the difference between the average pressure and the pressure in the cap (Δp), the average temperature of the gas in the cap from the ratio of the initial value of the volume of the gas phase to the working volume (1—Δp; 2—T_{av}).

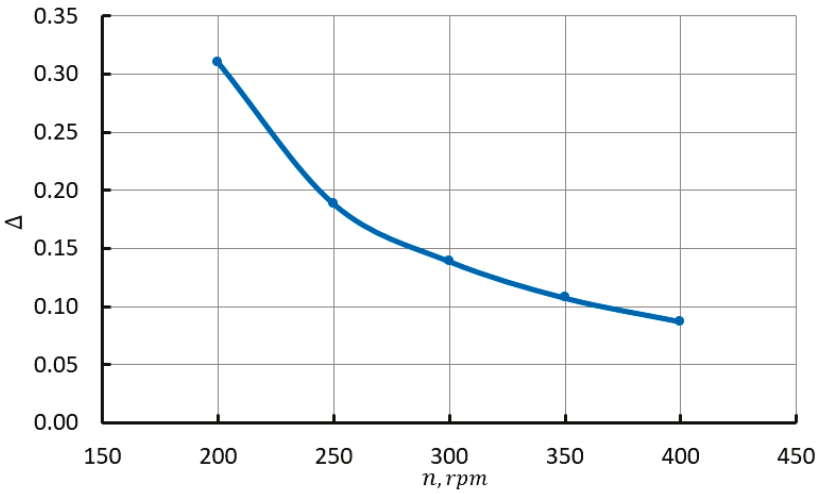


Figure 5. The dependence of the irregularity of liquid supply on the crankshaft revolutions.

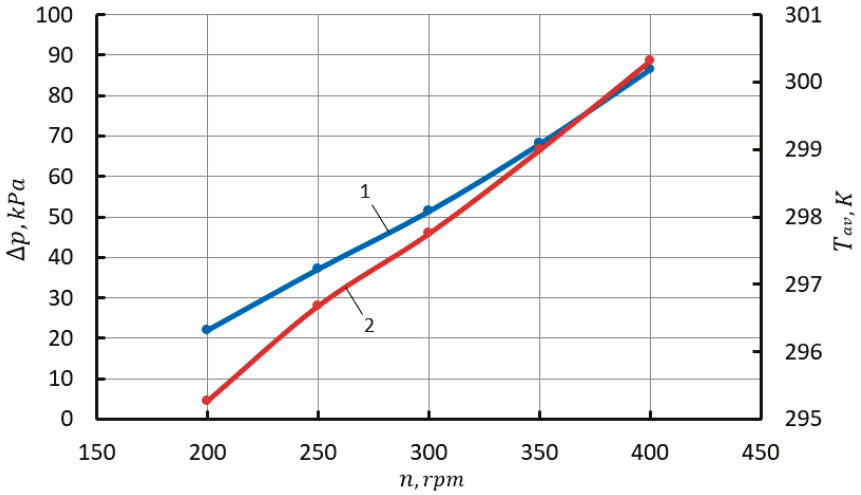


Figure 6. Dependence of the difference between the average pressure and the pressure in the cap (Δp), average gas temperature in the cap from the crankshaft revolutions (1—Δp; 2—T_{av}).

3.4. Discharge Pressure Analysis

With an increase in discharge pressure, the feed irregularity increases linearly (see Figure 7). This dependence is very significant. So, with an increase in discharge pressure from 1 MPa to 3 MPa, an increase in the feed irregularity occurs from 13.9% to 36.57%, i.e., also almost by 3 times.

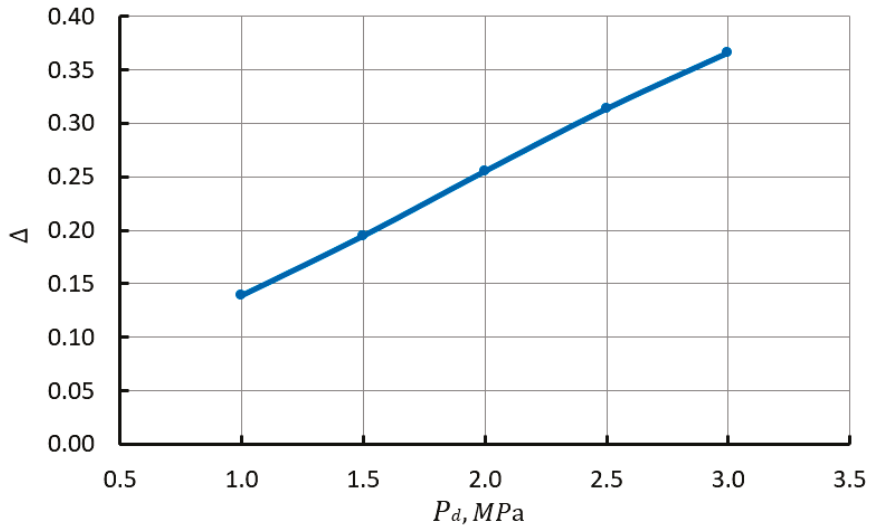


Figure 7. The dependence of the feed irregularity on the discharge pressure.

An increase in pressure in the gas cap is equivalent to a decrease in the volume of gas in it, and this, in turn, leads to an increase in the feed irregularity.

With an increase in discharge pressure, Q_{max} and Q_{min} also change almost linearly: Q_{max} increases, but Q_{min} decreases. With an increase in discharge pressure, Δp increases very slightly from 51.3 kPa to 54.83 kPa. The average temperature T_{av} in a gas cap with increasing p_d decreases. This is due to an increase in the gas density, which leads to an increase in the Re number and an increase in the heat transfer coefficient.

3.5. Analysis of the Influence of the Geometric Dimensions of Connecting Pipeline 4

Increasing the diameter of the pipeline increases the liquid flow rate from the gas cap, which increases pressure fluctuations in the cap and fluid flow fluctuations from the gas cap. Q_{max} with an increase in d_{pp2} increases parabolically and Q_{min} also decreases parabolically (see Figure 8). There is also a parabolic increase in feed irregularity with the d_{pp2} increase. It should be noted that the size of the pipeline diameter has a very significant effect on the feed irregularity (see Figure 9). An increase in the diameter of the pipeline leads to a decrease in the average pressure in the cap and the average temperature. We observe a significant decrease p_{av} by almost 100 kPa and temperature by 7.5 (see Figure 10).

An increase in the length of pipeline 4 leads to a decrease in the feed irregularity (see Figure 11). An increase in the length of the pipeline increases the hydraulic resistance, which leads to a decrease in the fluid velocity and its flow rate. Thus, an increase in the length of a pipeline is similar to a decrease in its diameter. The presented results allow us to conclude that the increase in length does not have a significant effect on the feed irregularity.

The decrease in feed irregularity is due to a decrease in Q_{max} and increase in Q_{min} (see Figure 12). An increase in the length of the pipeline leads to a linear increase in the average pressure p_{av} and temperature T_{av} (see Figure 13). It should be noted that the increase in p_{av} and T_{av} is insignificant.

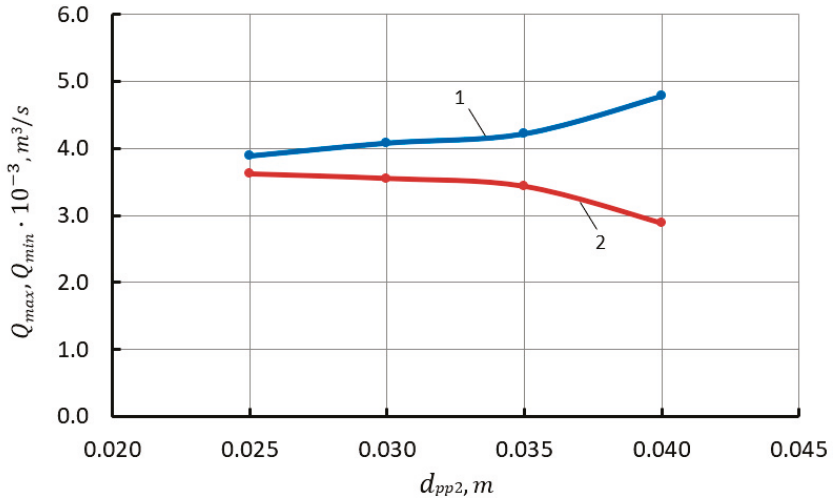


Figure 8. Dependence of the maximum and minimum liquid flow rate from the gas cap on the diameter of connecting pipeline 4 (1—Q_{max}; 2—Q_{min}).

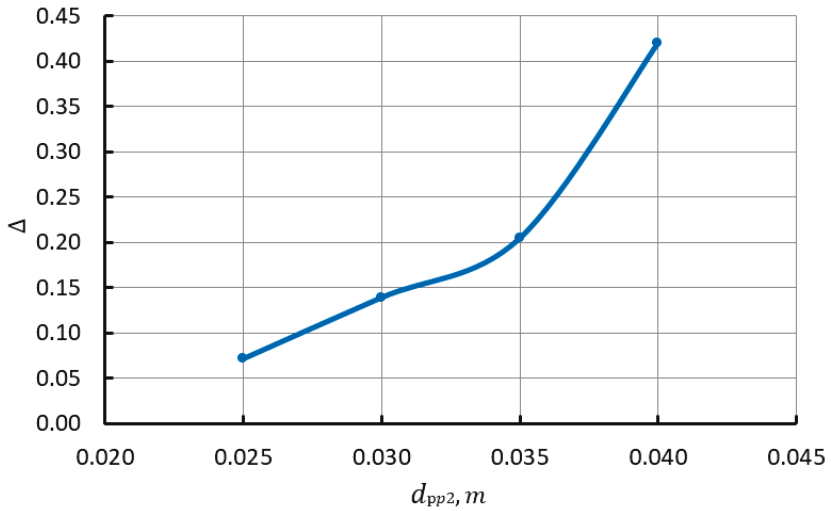


Figure 9. The dependence of the feed irregularity on the diameter of connecting pipeline 4.

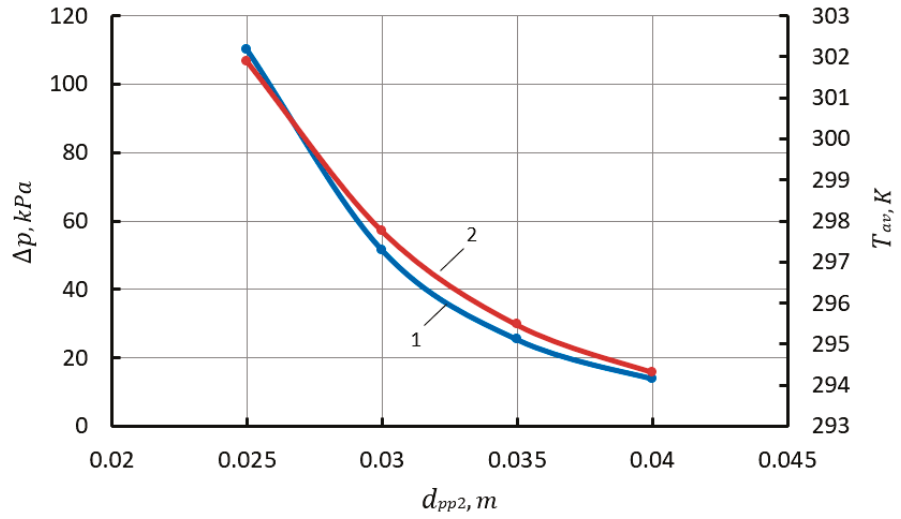


Figure 10. Dependence of the difference between the average pressure and the pressure in the cap (Δp), average gas temperature in the cap from the diameter of connecting pipeline 4 (1—Δp; 2—T_{av}).

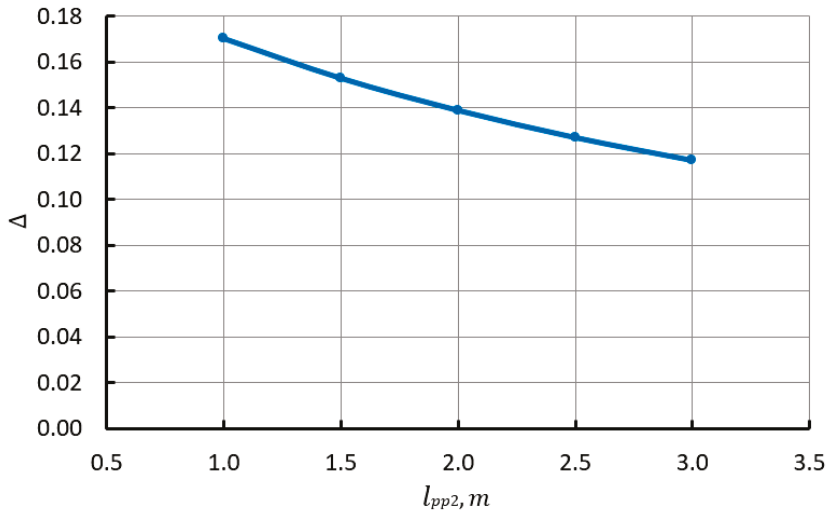


Figure 11. The dependence of the feed irregularity on the length of connecting pipeline 4.

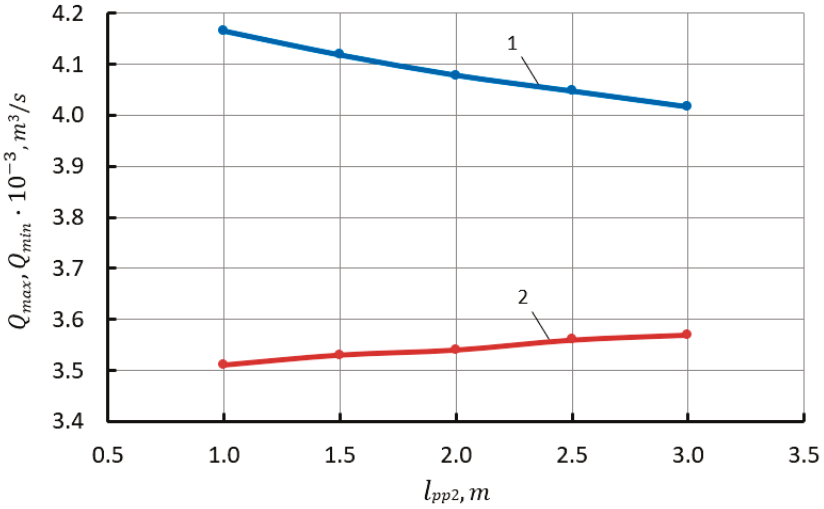


Figure 12. Dependence of the maximum and minimum liquid flow rate from the gas cap on the length of connecting pipeline 4 (1—Q_{max}; 2—Q_{min}).

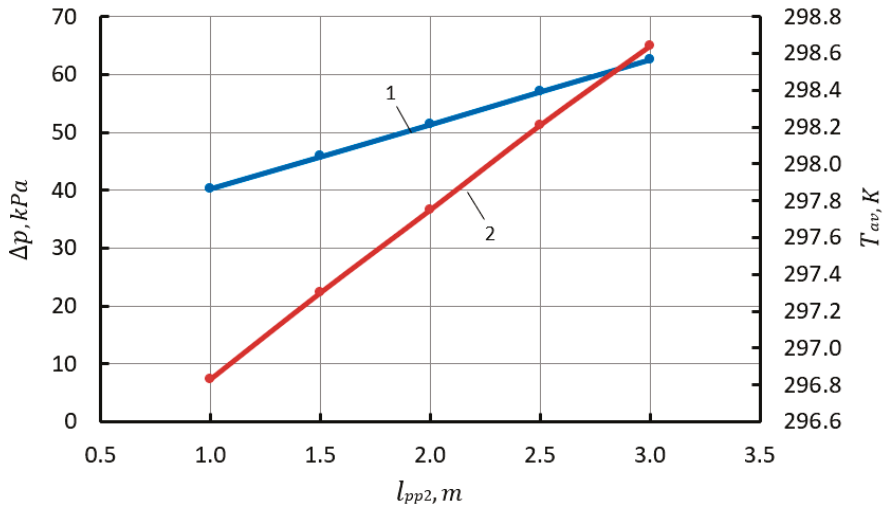


Figure 13. Dependence of the difference between the average pressure and the pressure in the cap (Δp), average gas temperature in the cap from the length of connecting pipeline 4 (1—Δp; 2—T_{av}).

3.6. Ranking the Influence of Independent Variables on Feed Irregularity

It is important for constructors and designers of positive displacement pumps with gas caps to know which independent variables to pay attention to in order to obtain the minimum non-uniformity of the pumping unit. As a result, it is necessary to rank the influence of independent variables on the feed irregularity of the pumping unit.

The ranking will be carried out in relation to the relative feed irregularity to the relative independent argument $\frac{\Delta\overline{\delta}}{\Delta\overline{x}}$, where $\Delta\overline{\delta} = \frac{\delta_{max}-\delta_{min}}{\delta_{av}}$; $\Delta\overline{x} = \frac{x_{max}-x_{min}}{x_{av}}$. The results of the ranking are presented in Table 1.

Table 1. The results of the ranking.

x	d_{pp}	V_g/V_h	n_{rev}	p_d	l_{pp}
$\Delta\overline{\delta}/\Delta\overline{x}$	3.073	0.955	0.94	0.899	0.371

The presented results allow us to draw the following conclusions:

- The diameter of pipeline 4 has the greatest influence on the feed irregularity;
- The relative initial gas volume V_g/V_h is only the second value, although it is considered as the main in existing works;
- The crankshaft revolutions and the discharge pressure have approximately the same effect;
- Pipeline 4 length has the least effect;
- Thus, it is important for developers, designers and those involved in the operation of pumping units with gas caps to determine the diameter of the supply pipe (this recommendation is not available in the existing literature), and to determine the ratio of the initial gas volume in the cap to the working volume of the pump chamber (this recommendation is in the technical literature).

4. Conclusions

1. We developed a mathematical model based on a thermodynamic approach which allowed detailed consideration of work processes occurring in the gas cap on the basic fundamental laws of conservation of energy, mass and motion, and the equation of state, both taking into account the change in the mass of the gas due to phase transitions and the solubility of the gas in the liquid, and without taking them into account (if there is a separating element). To close the developed mathematical model of working processes in the gas cap and to determine the maximum and minimum fluid flows from the pump, a mathematical model of the fluid flow from the gas cap through a pipeline of constant cross section has been developed;
2. It was found on the numerical experiment that to reduce the feed irregularity, it is necessary to increase the length of the pipeline and the crankshaft revolutions, in addition to the known ratio of the initial gas volume in the cap to the pump displacement; an increase in discharge pressure and an increase in the diameter of the connecting pipeline increases the feed irregularity;
3. The ranking of the influence of the analyzed independent variables on the feed irregularity proved that the diameter of the connecting pipeline has the greatest influence, then the ratio of the initial volume of gas in the cap to the volume of the working chamber of the pump. Regarding operating parameters, the crankshaft revolutions of the pump and the discharge pressure have approximately the same influence, and the length of the connecting pipeline has the least influence. The crankshaft revolutions of the pump and the discharge pressure of the pump have approximately the same effect on the feed irregularity of the pump. The length of the connecting pipeline between the gas cap has the least impact.

Author Contributions: Conceptualization, V.S.; methodology, V.S. and I.B.; software, V.S.; validation, V.S. and I.B.; formal analysis, V.S.; investigation, V.S.; data curation, V.S.; writing—original draft preparation, V.S. and I.B.; writing—review and editing, V.S. and I.B.; visualization, V.S. and I.B.; project administration, V.S. and I.B.; funding acquisition, V.S. and I.B. All authors have read and agreed to the published version of the manuscript.

Funding: The research was supported by the Russian Science Foundation Grant No. 22-29-00399, https://rscf.ru/project/22-29-00399/ (accessed on 10 June 2023).

Informed Consent Statement: Not applicable.

Data Availability Statement: The results of the work are new, some of the known results are in the available sources, which are cited in the article.

Conflicts of Interest: The authors declare no conflict of interest.

Nomenclature

The nomenclature of the paper is shown below:

v_{n1}, v_{n2}, v_{ni}	1, 2 and i-th piston speed
f_{n1}, f_{n2}, f_{ni}	areas of these pistons
$\omega_1, \omega_2, \omega_i$	angular velocities
S_{h1}, S_{h2}, S_{hi}	full piston strokes
d_1, d_2, d_i	piston diameters
$\varphi_1, \varphi_2, \varphi_i$	angles of crankshafts rotation
$\lambda_1, \lambda_2, \lambda_i$	ratio of piston strokes to crank lengths
dU	elementary change in the total internal energy of the gas phase in the cap
dQ	elementary external heat exchange
dL	elementary contour work
i_{phad}	specific enthalpy of the added steam due to liquid evaporation
i_{pho}	specific enthalpy of the separated steam during condensation
dM_{phad}	elementary mass added to the gas phase of the cap due to first-order phase transitions
dM_{pho}	elementary mass separated from the gas phase of the cap due to phase transitions of the first order
i_{gr}	specific enthalpy of a gas released from a liquid
i_o	specific enthalpy of a gas dissolved in a liquid
dM_{gr}	elementary mass of gas released from a liquid
dM_{Po}	elementary mass of gas dissolved in a liquid
F1	the heat exchange surface of the liquid
d_c	cap diameter
l_r	length of the generatrix of the cylinder of the gas cap in contact with the gas
F_2	free surface area of a liquid
T_w	liquid temperature
λ	gas thermal conductivity coefficient
A, x, B	constant coefficients (A = 0.2 ÷ 0.235, x = 0.8 ÷ 0.86, B = 500 ÷ 800)
μ	dynamic viscosity coefficient
ρ_w	liquid density
$d\tau$	elementary time
dM_{ow}	mass of liquid separated over time $d\tau$ from the gas cap
C_w	steam concentration on the liquid surface
C_2	average steam concentration in the gas phase
β_{pg}	mass transfer coefficient
R_s	steam gas constant
p_s	partial steam pressure
a_T	thermal diffusivity
C_P	specific isobaric heat capacity of gas
D	diffusion coefficient (is a function of pressure and temperature)
C_{stf}	dividing element stiffness
l_w	current position of the liquid level

l_{w0}	the initial position of the liquid level (in most practical cases, the liquid occupies 1/3 of the cap)
l_{pp2}	pipeline 4 length
z	center of gravity coordinate
$j = \rho_w g$	liquid specific gravity
g	acceleration of gravity
λ_{pp2}	coefficient of hydraulic friction along the length
d_{pp2}	pipeline 4 inner diameter
$\Sigma\xi_i$	sum of local coefficients (sudden expansion, sudden contraction, flow turn, etc.)
z_{1pp2}, z_{2pp2}	centers of gravity of control sections
p_d	fluid pressure
Q_{wpp2}	volume flow of liquid in pipeline 4
f_{pp2}	cross-sectional area of the connecting pipeline
a	sound speed

References

1. Harrison, A.M.; Edge, K. Reduction of axial piston pump pressure ripple. *Proc. Inst. Mech. Eng.* **2000**, *214*, 53–64. [CrossRef]
2. Manring, N. The Discharge Flow Ripple of an Axial-Piston Swash-Plate Type Hydrostatic Pump. *J. Dyn. Syst. Meas. Control.* **2000**, *122*, 263–268. [CrossRef]
3. Johansson, A.; Olvander, J.; Palmberg, J.-O. Experimental verification of cross-angle for noise reduction in hydraulic piston pumps. *Proc. Inst. Mech. Eng. Part I J. Syst. Control. Eng.* **2007**, *221*, 321. [CrossRef]
4. Borghi, M.; Zardin, B. Axial Balance of External Gear Pumps and Motors: Modelling and Discussing the Influence of Elastohydrodynamic Lubrication in the Axial Gap. In Proceedings of the ASME International Mechanical Engineering Congress and Exposition, Houston, TX, USA, 13–19 November 2015.
5. Zhao, X.; Vacca, A. Theoretical investigation into the ripple source of external gear pumps. *Energies* **2019**, *12*, 535. [CrossRef]
6. Zhao, X.; Vacca, A. Numerical analysis of theoretical flow in external gear machines. *Mech. Mach. Theory* **2017**, *108*, 41–56. [CrossRef]
7. Zhou, J.; Vacca, A.; Casoli, P. A Novel Approach for Predicting the Operation of External Gear Pumps Under Cavitating Conditions. In *Simulation Modelling Practice and Theory*; Elsevier: Amsterdam, The Netherlands, 2014; Volume 45, pp. 35–49.
8. Corvaglia, A.; Rundo, M.; Casoli, P.; Lettini, A. Evaluation of tooth space pressure and incomplete filling in external gear pumps by means of three-dimensional CFD simulations. *Energies* **2021**, *14*, 342. [CrossRef]
9. Corvaglia, A.; Ferrari, A.; Rundo, M.; Vento, O. Three-dimensional model of an external gear pump with an experimental evaluation of the flow ripple. *Proc. Inst. Mech. Eng. Part C J. Mech. Eng. Sci.* **2021**, *235*, 1097–1105. [CrossRef]
10. Bashta, T.M. *Displacement Pumps and Hydraulic Engines of Hydraulic Systems: Textbook for Universities*; Mashinostroenie: Moscow, Russia, 1974; 606p.
11. Shcherba, V.E.; Pavlyuchenko, E.A.; Kuzhbanov, A.K. Parametric analysis of the operation of the pump section of a piston pump-compressor with a gas damper. *Chem. Oil Gas Eng.* **2014**, *50*, 23–26.
12. Shcherba, V.E.; Bolshtyansky, A.P.; Kaigorodov, S.Y.; Kuzeeva, D.A. Study of the uneven theoretical supply of multi-cylinder piston pumps. *Bull. Mech. Eng.* **2016**, 33–36.
13. Casoli, P.; Pastori, M.; Scolari, F.; Rundo, M. Active pressure ripple control in axial piston pumps through high-frequency swash plate oscillations—A theoretical analysis. *Energies* **2019**, *12*, 1377. [CrossRef]
14. Hagstrom, N.; Harens, M.; Chatterjee, A.; Creswick, M. Piezoelectric actuation to reduce pump flow ripple. In Proceedings of the ASME/BATH 2019 Symposium on Fluid Power and Motion Control 2019 FPMC, Sarasota, FL, USA, 7–9 October 2019.
15. Casoli, P.; Vescovini, C.M.; Scolari, F.; Rundo, M. Theoretical Analysis of Active Flow Ripple Control in Positive Displacement Pumps. *Energies* **2022**, *15*, 4703. [CrossRef]
16. Pan, M.; Ding, B.; Yuan, C.; Zou, J.; Yang, H. Novel Integrated Control of Fluid-Borne Noise in Hydraulic Systems. In Proceedings of the BATH/ASME 2018 Symposium on Fluid Power and Motion Control FPMC 2018, Bath, UK, 12–14 September 2018.
17. Shang, Y.; Tang, H.; Sun, H.; Guan, C.; Wu, S.; Xu, Y.; Jiao, Z. A novel hydraulic pulsation reduction component based on discharge and suction self-oscillation: Principle, design and experiment. *Proc. Inst. Mech. Eng. Part I J. Syst. Control Eng.* **2020**, *234*, 433–445. [CrossRef]
18. Rabie, M.G. On the application of oleopneumatic accumulators for the protection of hydraulic transmission lines against water hammer—A theoretical study. *Int. J. Fluid Power* **2007**, *8*, 39–49. [CrossRef]
19. Yokota, S.; Somada, H.; Yamaguchi, H. Study on an active accumulator. *JSME Int. J.* **1996**, *39*, 119–124. [CrossRef]
20. Chinyaev, I.A. *Piston Pumps*; Mashinostroenie: Moscow, Russia, 1966; 188p.
21. Zhukovsky, N.E. On hydraulic shock in water pipes. In *Classics of Natural Science*; GITTL: Spring, TX, USA, 1949; 100p.
22. Khuzhaev, I.K.; Mamadaliev, K.A. Quasi-one-dimensional model and analytical solution of the problem of wave propagation in a pipeline with a pressure perturbation damper. *Probl. Comput. Appl. Math. Sci. J.* **2016**, 46–59.
23. Arbuzov, N.S. Comparative analysis of the use of a safety valve and a gas cap as protection systems against hydraulic shock of a marine oil terminal. *Territ. Neft.* **2014**, 56–61.

24. Pisarevsky, V.M. *Gas Vibration Dampers*; Nedra: Moscow, Russia, 1986; 120p.
25. Vladislavlev, A.P. *Pipelines of Reciprocating Compressor Machines*; Vladislavlev, A.P., Kozobkov, A.A., Malyshev, V.A., Messerman, A., Pisarevsky, V.M., Eds.; Mashinostroenie: Moscow, Russia, 1972; 287p.
26. Khachaturyan, S.A. *Wave Processes in Compressor Units*; Mashinostroenie: Moscow, Russia, 1983; 222p.
27. Zhou, H.Y.; Korolev, A.V. Algorithm for calculating a damping cap for a piston pump. *Refrig. Eng. Technol.* **2017**, *53*, 71–75.
28. Shcherba, V.E.; Shalay, V.V.; Tegzhanov, A.S.; Dorofeev, E.A.; Pavlyuchenko, E.A. On the issue of reducing the non-uniformity of supply in piston pumps. *News High. Educ. Inst. Eng.* **2018**, *6*, 68–77. [CrossRef]
29. Plastinin, P.I. Piston compressors. In *T. 1. Theory and Calculation: Textbook*; Plastinin, P.I., Ed.; Kolos: Moscow, Russia, 2006; 456p, ISBN 5-9532-0428-0.
30. Fotin, B.S.; Pirumov, I.B.; Prilutsky, I.K.; Plastinin, P.I.; Fotina, B.S. (Eds.) *Piston Compressors: Textbook Manual for University Students*; Mashinostroenie: Leningrad, Russia, 1987; 372p.
31. Kushnyrev, V.I. Technical Thermodynamics and Heat Transfer. In *Textbook for Universities*; Kushnyrev, V.I., Lebedev, V.I., Pavlenko, V.A., Eds.; Stroyizdat: Moscow, Russia, 1986; 464p.
32. Kast, V. *Convective Heat and Mass Transfer*; Kast, V., Krisher, O., Rainike, G., Wintermantel, K., Eds.; Energia: Moscow, Russia, 1980; 49p.
33. Isachenko, V.P. *Heat Transfer: Textbook for Universities*, 3rd ed.; Isachenko, V.P., Osipova, V.A., Sukomel, A.S., Eds.; Energy: Moscow, Russia, 1975; 488p.
34. Shcherba, V.E.; Zanin, A.V.; Khrapsky, S.F. Dynamics of Fluid Motion in a Two-Stage Piston Hybrid Power Machine. *Chem. Oil Gas Eng.* **2020**, *56*, 13–17. [CrossRef]
35. Idelchik, I.E. *Handbook of Hydraulic Resistance*; Book on Demand: Norderstedt, Germany, 2012; 466p.
36. Gimadiev, A.G.; Bystrov, N.D. *Dynamics and Regulation of Hydraulic and Pneumatic Systems*; Samara University Puublishing House: Samara, Russia, 2010; 178p.
37. Shcherba, V.E.; Shalai, V.V.; Pavlyuchenko, E.A. A generalized approach to the analysis of feed unevenness in displacement pumps. *Chem. Pet. Eng.* **2019**, *55*, 402–411. [CrossRef]
38. Shcherba, V.E.; Khait, A.; Pavlyuchenko, E.A.; Bulgakova, I.Y. Development and Research of a Promising Pumpless Liquid Cooling System for Reciprocating Compressors. *Energies* **2023**, *16*, 1191. [CrossRef]

Disclaimer/Publisher's Note: The statements, opinions and data contained in all publications are solely those of the individual author(s) and contributor(s) and not of MDPI and/or the editor(s). MDPI and/or the editor(s) disclaim responsibility for any injury to people or property resulting from any ideas, methods, instructions or products referred to in the content.

inventions

MDPI

Review

Mixer Design and Flow Rate as Critical Variables in Flow Chemistry Affecting the Outcome of a Chemical Reaction: A Review

Ilya V. Myachin and Leonid O. Kononov *

N.D. Zelinsky Institute of Organic Chemistry of the Russian Academy of Sciences, Leninsky Prosp., 47, Moscow 119991, Russia

* Correspondence: kononov@ioc.ac.ru or leonid.kononov@gmail.com

Abstract: Flow chemistry offers several advantages for performing chemical reactions and has become an important area of research. It may seem that sufficient knowledge has already been acquired on this topic to understand how to choose the design of microreactor/micromixer and flow rate in order to achieve the desired outcome of a reaction. However, some experimental data are difficult to explain based on commonly accepted concepts of chemical reactivity and performance of microfluidic systems. In this mini review, we attempt to identify such data and offer a rational explanation of unusual results based on the supramer approach. We demonstrate that variation in flow regime (determined by mixer design and flow rate) can either improve or worsen the reactivity and lead to completely different products, including stereoisomers. It is not necessary to mix the reagents with maximum efficiency. The real challenge is to mix reagents the *right way* since at a too high or too low flow rate (in the particular mixer), the molecules of reagents are incorrectly presented on the surface of supramers, leading to altered stereoselectivity, or form tight supramers, in which most of the molecules are located inside the supramer core and are inaccessible for attack, leading to low yields.

Keywords: microfluidics; flow chemistry; mixer design; flow rate; mixing efficiency; supramers; supramolecular chirality; chemical reactions; glycosylation; stereoselectivity

1. Introduction

Over the past decades, chemistry in flow became a powerful tool of modern organic and inorganic chemistry, and many publications devoted to the study of chemical reactions in flow appeared. Dozens of reviews have been published on flow chemistry. Here, we mentioned only some of them [1–20], in which a reader can find further references on specific topics. The most comprehensive coverage and critical analysis of the recent flow chemistry accounts can be found in an outstanding review [11], in which an in-depth analysis of almost every aspect of performing chemical experiments in flow accompanied by invaluable advice on how one can control the reaction parameters to achieve the desired result is presented.

Flow chemistry (aka microfluidics [2]) offers several advantages for performing chemical reactions such as minimizing of accident risks and cheaper production of chemicals to name a few [7,11,13,17–19]:

- Flow chemistry facilitates the optimization of reactions at a much faster rate, resulting in a reduction in costs and time. Reaction time, temperature, ratio of reagents, concentration, and reagents themselves can all be rapidly modified. One reaction can be followed by another, separated by solvent, increasing throughput. Automated flow chemistry allows for rapid variation of reaction conditions on a very small scale ($\leq$100 μL).

- Performing reactions in flow can be safer than in batch reactors, since only a small portion of reactive or hazardous material is transformed to product at any particular moment.
- The use of flow chemistry has the advantage of enhanced heat and mass transfer, which can result in faster reaction rates and higher yields.
- Flow reactors provide excellent reaction selectivity and allow for preparation of products that are not accessible under batch conditions.

Successful attempts to generalize the basic principles and fundamentals of flow chemistry [11] and to standardize the description of reactions in flow [14] have been advanced. Ten key issues in modern flow chemistry have been identified and discussed in detail [6]. Various designs of microreactors [3] and their classification [13] have been considered (for a more detailed discussion, *vide infra*). A state-of-the-art, future perspectives and challenges in creating reconfigurable microfluidic platforms, which would allow a user to easily tailor a microfluidic system for a specific application and "to tune a microscale experiment with the capacity to make real-time decisions", has been reviewed [16].

There are many examples of the successful use of flow reactors for conducting reactions of various classes [1,11,13,15,18], including those useful for production of active pharmaceutical ingredients [17]. Functional group interconversion reactions have been successfully performed in continuous flow reactors [15]. Flow technology was found to be unexpectedly efficient in supramolecular chemistry [12,20]. A new paradigm for synthesis of natural products including carbohydrates has been proposed [4,5,9,10], which is based on performing traditional organic reactions under microfluidic conditions.

Among many parameters [11] the design of the microreactor/micromixer [11,21–25] and flow rate used are considered as the key factors that determine the outcome of a reaction performed in flow. One may think that sufficient knowledge has already been acquired [11] on this topic to understand how to select appropriate experimental conditions to achieve the desired reaction result.

However, only few researchers publish the "negative" results that could demonstrate their "inability" to forecast the result of a particular experiment; many researchers tend to modify the initial objectives of research after obtaining the positive results ("much of good science is opportunistic and revisionist", as G. Whitesides put it [26]). For this understandable reason, reports of detailed studies of the influence of the design of the microreactor/micromixer and/or flow rate on the outcome of the real-life reactions (as opposed to the studies of "test reactions" in flow, *vide infra*), performed by practicing organic chemists (rather than by experts in chemical engineering), are rare. Conditions for successful practically important chemical transformations in flow are mostly reported.

This situation creates a "research gap" between reports on successes or failures of reactions, performed under specific conditions in flow, and understanding the reasons lying behind. Moreover, some experimental data are difficult to explain based on commonly accepted concepts of chemical reactivity (in general) and performance of microfluidic systems (in particular). In this mini review, we attempt to identify such data and offer a rational explanation of unusual results based on the supramer approach (*vide infra*) [27].

2. Mixing Performance

Typical microfluidic systems are featured by low Reynolds numbers (*Re*, [28]) ($Re \leq 1000$ [1,8,29]) that would generally suggest a laminar flow, even in reactors in which biphasic reactions proceed [30], and guarantee that there is no turbulence and therefore no back-mixing in the reactor [8]. This notion may create the wrong impression that mass transfer of reactants in microfluidic systems is controlled by diffusion only; in fact, convection/advection can also contribute significantly to the mass transfer in these systems (*vide infra*).

It is clear, even from general considerations, that the reagents need to be mixed well for the effective reaction to occur [29,31–37]. This review is limited to discussion of passive [29,35,36] mixing that does not rely on external energy input. This mixing is

realized within mixing devices (micromixers), which often serve also as microreactors (for this reason, hereinafter we denote them as "microreactors/micromixers").

Many studies [21,29,35–92] were dedicated to modeling various types of micromixers/microreactors and determining their mixing efficiency (mixing quality) theoretically and/or experimentally using a set of test reactions [39,57,63]. This widely used "chemical" approach for accessing the mixing efficiency, unlike purely physical approaches like flow imaging, is based on the *implicit supposition* that the dependence of outcome of a chemical reaction, performed in flow, on mixing conditions is determined by mixing efficiency of the micromixer/microreactor used. We emphasize that most experimental studies of mixing efficiency of different micromixers/microreactors are in fact providing information on chemical reactivity in the reactions performed under flow conditions using these micromixers/microreactors. This means that the observed dependence of conversion of the starting compound and product yield on mixing conditions may reflect not only the mixing issues (as usually believed) but also the influence of other (unknown) factors that are affected by changing the mixing mode. This opens the way for alternative views on chemical reactivity as exemplified by application of the supramer approach [27] to the flow chemistry (*vide infra*).

The mixing performance of different types of mixers has been previously compared [21, 35,36,43,53,57,69,70,72,79,93]. The main message for the practicing synthetic chemist from these studies is that the mixing quality is controlled by the flow regime in the mixing device. Importantly, the flow regimes may differ considerably for different mixers; for the same mixer flow regimes may also vary depending on the flow rate (an example is shown in Figure 1).

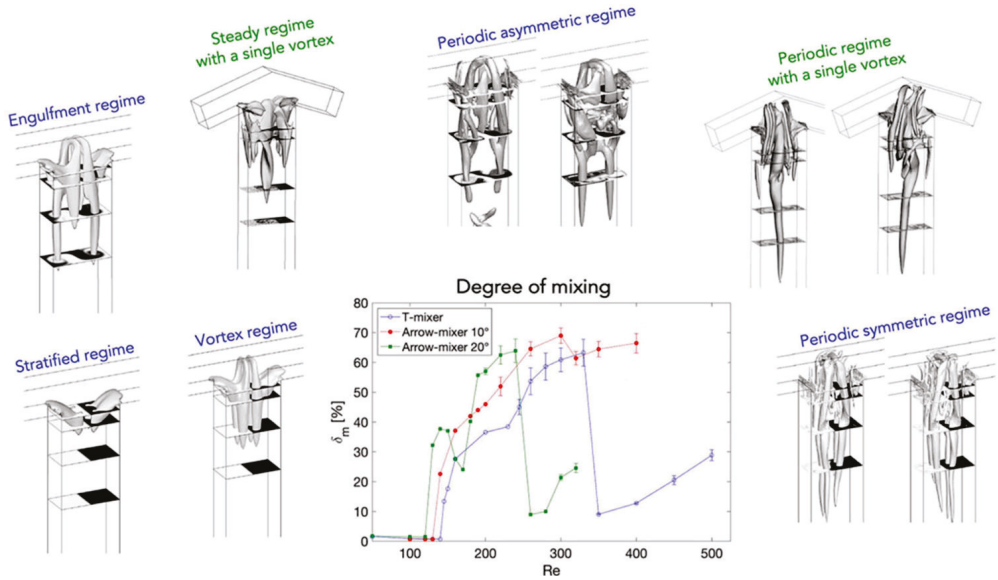


Figure 1. Summary of the steady flow regimes and mixing quality (δ) as a function of the Reynolds number (*Re*) in T-shaped and arrow-shaped micromixers. Adapted with permission from [79].

In most studies mainly the Reynolds number was used to describe the flow regime (but occasionally other numbers were used [94]). However, the Reynolds number alone is not necessarily always trustworthy for estimating mixing quality in micromixers/microreactors. It was demonstrated that mixing quality of a simple and widely used T-shaped micromixer sharply increases in the "engulfment flow regime", featured by the increased vorticity (Figure 2) hence mixing quality, which occurs at the high flow rates even in the low Reynolds number range (*Re* ~ 200) (Figure 3) [43]. It was concluded that the Reynolds number is not suitable for identification of the flow regime, since it varies a lot for different mixer geometries under similar flow regimes [43].

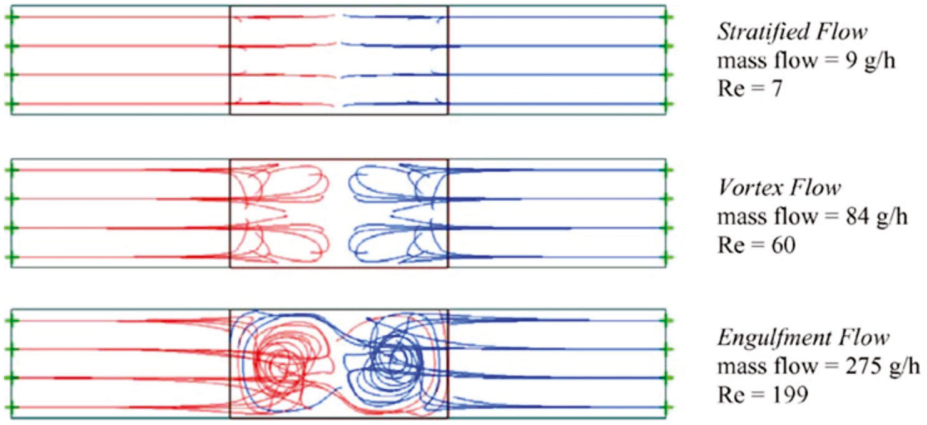


Figure 2. Streamlines inside a T-shaped micromixer (channel widths 300 and 600 μm) at different mass flows. View is into the mixing channel (left (red) and right (blue) are the inlet channels). Reproduced from [43] with permission from Elsevier.

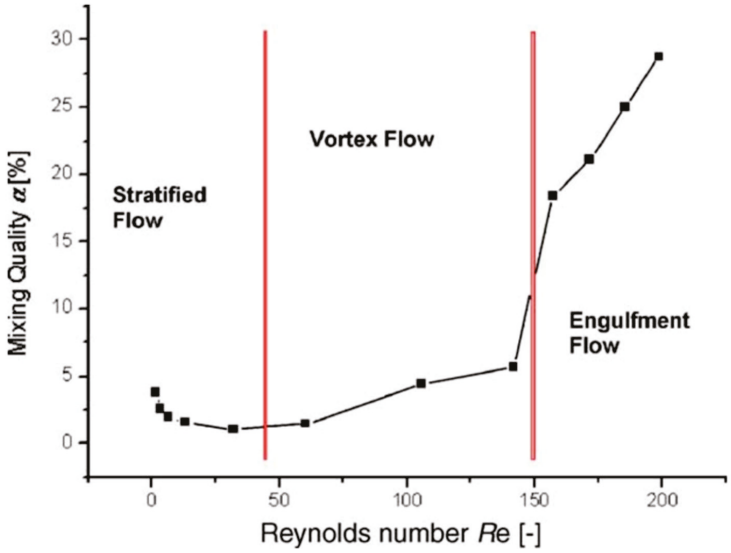


Figure 3. Mixing quality (α) over the Reynolds number (*Re*) for a T-shaped micromixer. Reproduced from [43] with permission from Elsevier.

Using examples of micromixers/microreactors of varying complexity (from the most studied simple T-shaped micromixers [35,43,44,46,48,49,53,58,60,69,70,72,74,76,79–85,88,91] to more sophisticated "split-and-recombine" microreactors [35–37,47,51,70,91,95,96]), it was shown that regardless of the value of the Reynolds number, mixing can be effective at least in some flow regimes. Especially effective is the so called "chaotic mixing/advection" [3,29,31,42,96]. Operation conditions of passive mixers based on chaotic advection can be distributed around the characteristic lines in the *Pe*–*Re* diagram for a wide range of Reynolds numbers (see Figure 4). Importantly, the passive micromixers work well either at low Reynolds numbers and low Peclet numbers (bottom left corner in Figure 4) or at high Reynolds numbers in the transition regime to turbulence (top right corner in Figure 4). Noteworthy, chaotic micromixers can be designed for use in a wide range of Reynolds numbers. Importantly, mixing with chaotic advection does not depend on the Péclet number [29].

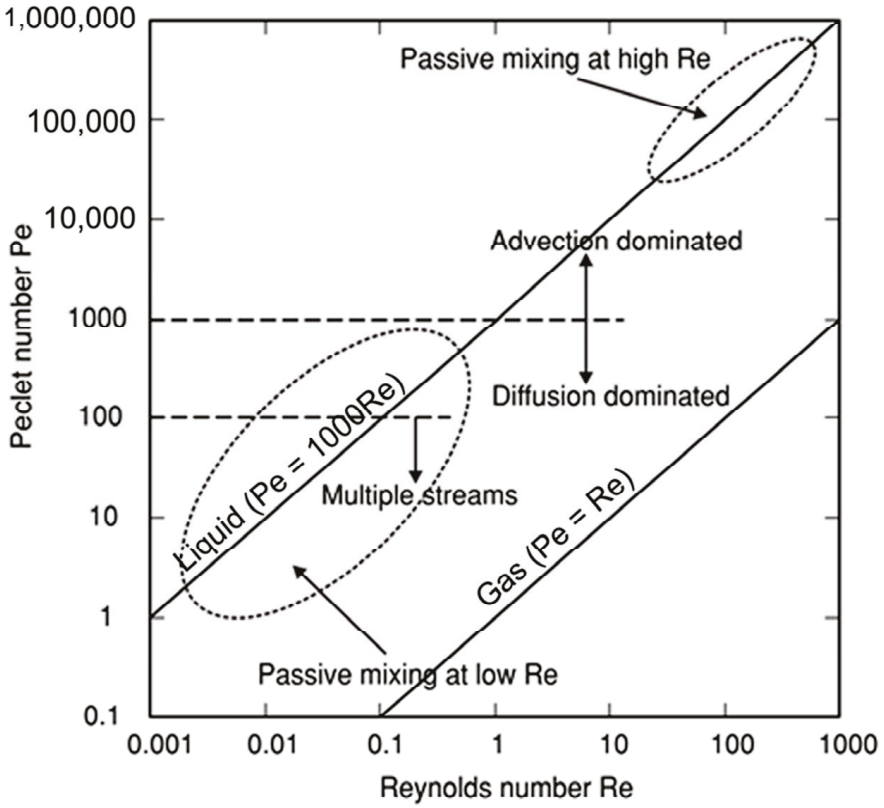


Figure 4. The *Pe*–*Re* diagram. The Reynolds number (*Re*) describes the flow regime in the mixing channel (*Re* is a convenient parameter for predicting whether a flow regime will be laminar or turbulent), while the Péclet number (*Pe*) represents the ratio between convection/advection and diffusion (when $Pe << 1$, then diffusive effects dominate over convective/advective transport, whilst the opposite is generally true for $Pe >> 1$). Adapted with permission from [29]. © IOP Publishing. All rights reserved.

Among many different micromixers designed for microflow systems, a Comet X-01 micromixer should be highlighted. This mixer has previously been used to perform and optimize various reactions [4,97–114]. Inside this mixer, the flow is split into three and merged back into one (repeated five times) (see Figure 5 and supporting information file for Ref. [113]) remotely resembling that in the previously mentioned "split-and-recombine" microreactor [35–37,47,51,70,91,95,96]) featured by "chaotic mixing" [3,29,31,42,96], which ensures efficient mixing regardless of the Reynolds number [3]. The unique design of the Comet X-01 micromixer made possible the discovery of unprecedented results described later in this review (*vide infra*).

Concluding this section, we must stress that current knowledge suggests the importance of mixing issues in chemical reactions to be related to the relative values of the mixing times as compared to the reaction times. For a detailed discussion and recommendations for choosing the design of the commercially available micromixers suitable for specific applications see [57].

The effects of mixing on the outcome of the sufficiently slow chemical reaction performed in flow can usually be neglected. If the reaction time is significantly longer than the mixing time, it can be considered that the reaction takes place under homogeneous environment ("homogeneous concentration field"). In such a situation, enhancing the mixing performance cannot increase the conversion rate [57].

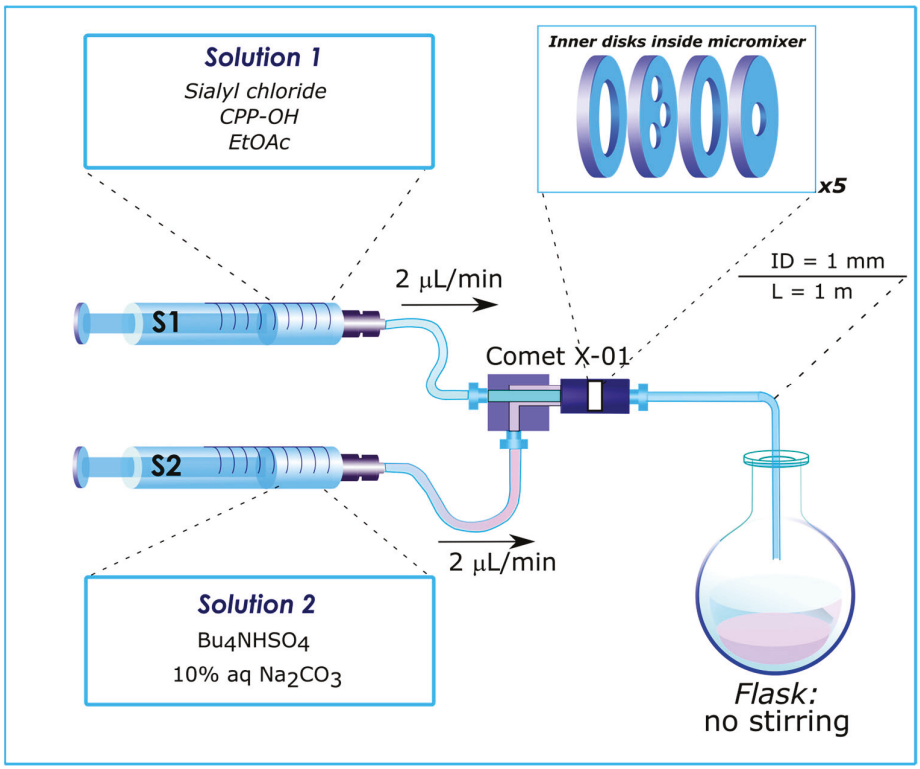


Figure 5. Flow reactor, based on Comet X-01 micromixer, used for glycosylation experiments. **S1**, **S2**—syringes. Internal volume of Comet X-01 micromixer—0.1 mL, that of outlet capillary—0.785 mL. Reproduced with permission from [114].

At the same time, fast and ultrafast reactions (as compared to mixing of reagents) should be extremely sensitive to changes in mixing efficiency which is determined by the flow regime realized in the mixer of specific design at the indicated flow rate. In this situation "the reaction takes place in a heterogeneous concentration field with multilamellae structures which are determined by the mixing process. The length scales of these structures as well as the time scale of their generation can have a strong influence on the conversion rate. In the case of a reaction system with competitive parallel or consecutive reactions, mixing time can also affect the selectivity of this system, especially if parallel reactions proceed at a different time scale" [57].

For this reason, many studies report the influence of both parameters (mixer design and the flow rate) on the reaction outcome, and they will be discussed together in the next section. Note that until recently, most of the reports on flow chemistry dealt with conversion of the starting material and product(s) yield as measures of the reaction progress. Issues of stereoselective formation of stereoisomers were mainly neglected; the rare examples will be mentioned below.

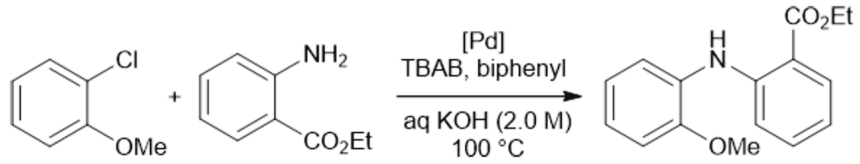
3. Influence of Mixer Design and Flow Rate on Reaction Outcome

The flow rate plays an important role in flow reactions. There is a lot of evidence that flow rate can influence the reaction yield. There are cases when the yield increases both with a decrease [110,115] and with an increase [116–119] in the flow rate.

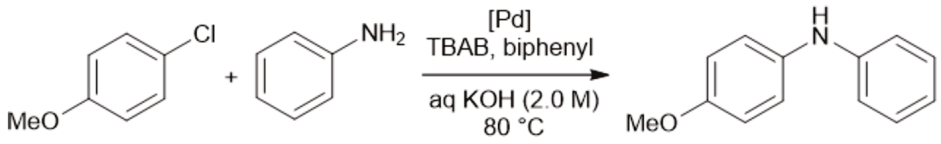
A change of flow rate with constant path length after mixing expectedly results in the change of reagents residence time (*vide infra*). A decrease in flow rate usually leads to an increase in product yield due to increase in residence time. However, in some cases due to increased residence time, the number of side processes leading to formation of undesirable products may also increase leading to a decrease in the yield of the target product. There are situations in which an increase in the flow rate (hence, the Reynolds number) leads to an increase in product yield [113]. However, increasing the flow rate is not a panacea: if the

flow rate is too high, then the reactants simply will not have enough time to react inside the reactor. It is generally accepted that for the optimal course of the reaction, it is necessary to find a golden mean between these extremes.

The crucial role of mixing efficiency, determined by the mixer design (*vide supra*), for chemical reactions performed under flow conditions was demonstrated for C–N cross-coupling reactions (Schemes 1 and 2) [120]. In one case, the capillary reactor contained grains around which the reaction solutions flow. In this case, in the thin films formed between the grains, mixing occurs efficiently, and the reaction is complete within 6 min. In another case, there was a free capillary in which conditions for effective mixing were not created. As a result, the yield after the same time was relatively small (Figure 6).



Scheme 1. Palladium-catalyzed C–N cross-coupling reaction performed in flow with packed bed and open tube reactor (see Figure 6) [120].



Scheme 2. C–N cross-coupling palladium-catalyzed reaction performed in flow with various packed bed volumes (see Figure 7) [120].

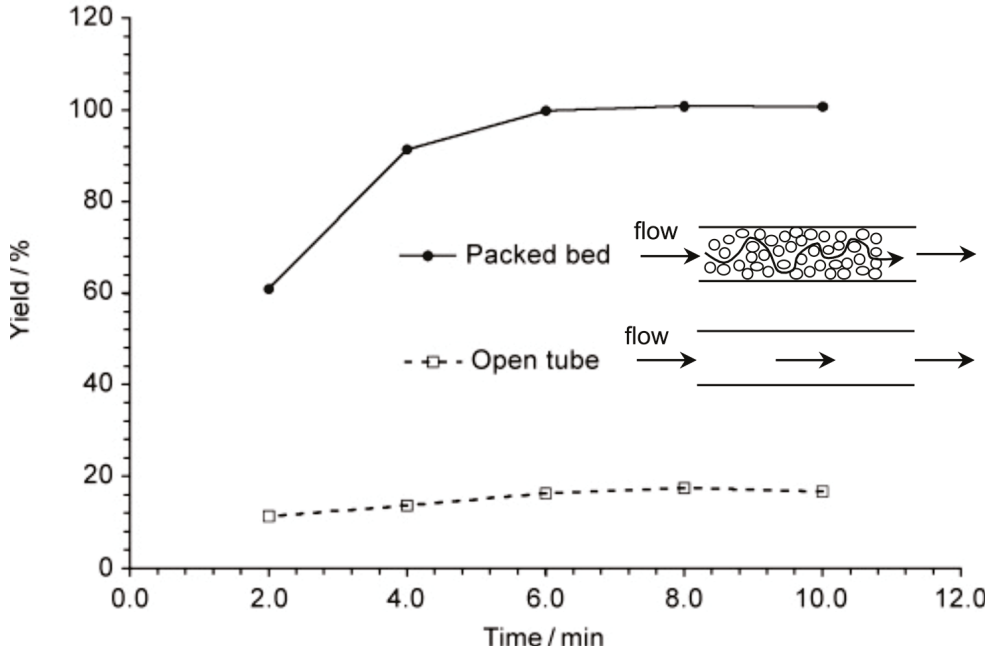


Figure 6. An example of the crucial role of mixing efficiency: the reaction (see Scheme 1) proceeds in high yield only when packed bed capillary is used for mixing reagents. Time indicated designates the residence time. Adapted with permission from [120]. Copyright © 2010 WILEY-VCH Verlag GmbH & Co. KGaA, Weinheim.

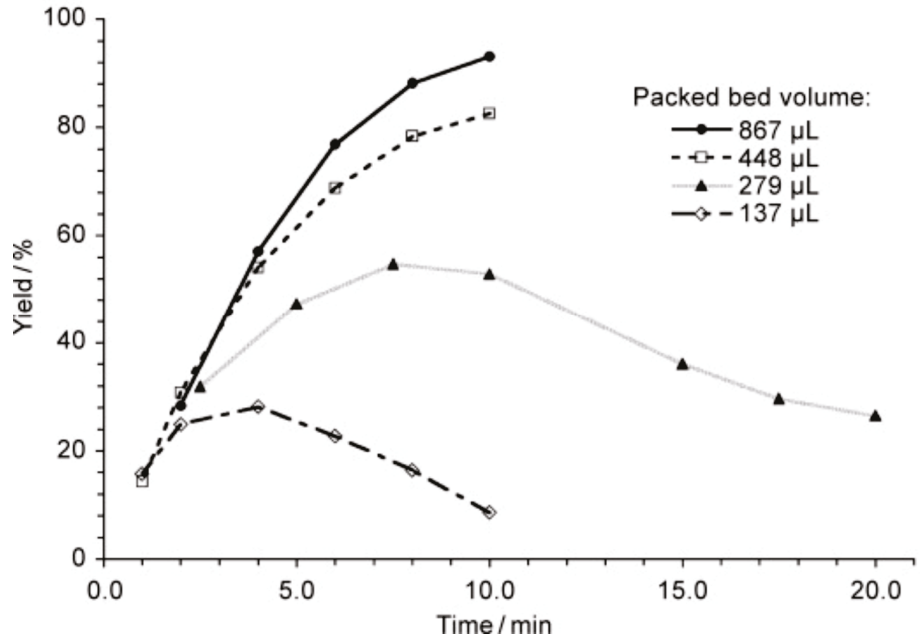
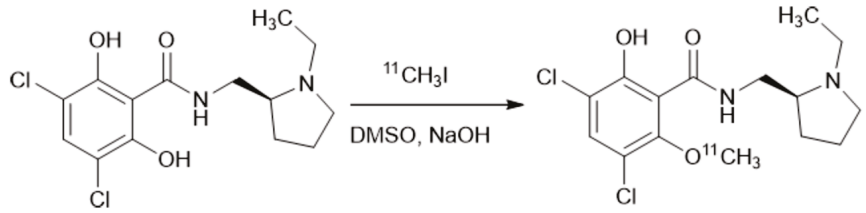


Figure 7. Comparison of the packed beds differing in size: the reaction (see Scheme 2) proceeds in high yield if the large packed bed capillary is used for the reaction proceeds (see also Figure 6). Time indicated designates the residence time. Adapted with permission from [120]. Copyright © 2010 WILEY-VCH Verlag GmbH & Co. KGaA, Weinheim.

More than that, a study of a similar reaction [120] showed that the yield depends on packed bed volume (Scheme 2, Figure 7). When the size of the packed bed was decreased, the yield of the reaction was decreased too. Note the maxima on the plots of the yield against the residence time. Since it was demonstrated that the product was not degrading over time the authors attributed the decrease in yield to changes in mixing performance at low flow rates (larger residence time).

An increase in the mixing efficiency often leads to an improvement of the reaction outcome. A remarkable example is the preparation of [^{11}C]raclopride under flow conditions by the methylation reaction (Scheme 3) [121]. During the study of the impact of the micromixer/microreactor design on this process, mixers with a consistently increasing number of additional loops (Figure 8a–c) were used, which were expected to increase the mixing efficiency and improve the reaction outcome. It was shown that reaction with non-radioactive CH_3I resulted in higher yields in the "abacus" micromixer than in the "no loop" micromixer (5.8% and 1.3% yields, respectively). At the stage of using radioactive $^{11}CH_3I$ as the methylation reagent it was also shown that the "full loop" microreactor is better than the "abacus" micromixer (relative radioactivity 25.6 and 16.0, respectively).



Scheme 3. Alkylation reaction performed in various types of flow reactors (see Figure 8) [121].

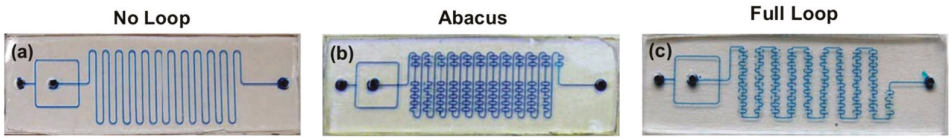


Figure 8. Three micromixers used for performing alkylation reaction (see Scheme 3) featured by different mixing efficiency. (**a**)—simple channel micromixer without additional loops ("no loop"); (**b**)—abacus-like micromixer with some additional loops ("abacus"); (**c**)—micromixer with maximum additional loops ("full loop"). Adapted with permission from [121].

The outcome of two-phase reactions carried out in flow may also depend strongly on the mixing method. This was shown using a Heck reaction where two modes of oxygen delivery to the reaction solution were compared (Figure 9) [122]. The main idea of this design is that the flows of liquid and gas occur not in one capillary, but in two parallel ones (Figure 9a). This can be achieved using the setup shown in Figure 9b: two parallel capillaries are separated by the PDMS membrane. This setup allows one to adjust the flow rate for each phase independently. Dual-channel design compared to slug flow showed higher convenience and higher yields: ≥75% in dual-channel and ≤65% in mono-channel modes (^{1}H NMR data).

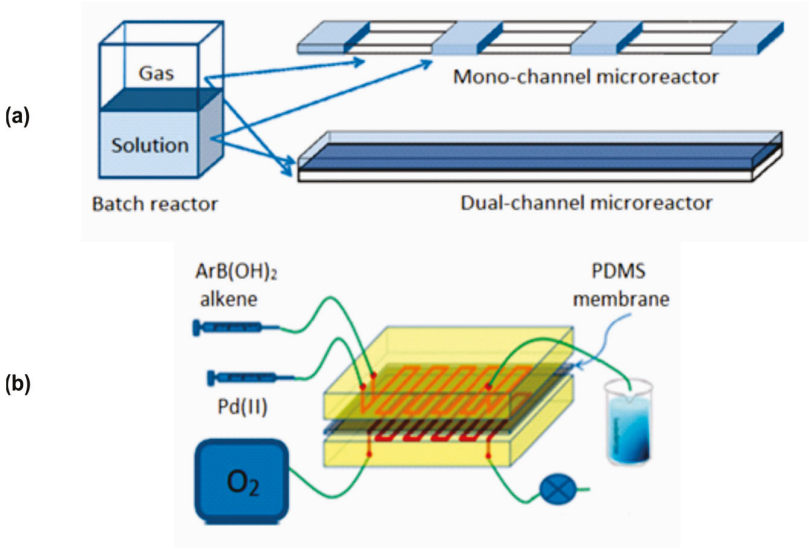


Figure 9. Mixer design for performing oxidation reaction under flow conditions. (**a**)—illustration of various modes of contact area between gas and liquid phases; (**b**)—schematic illustration of the dual-channel system. Adapted with permission from [122].

The mixing efficiency of a T-shaped micromixer is known to strongly depend on the flow rate [57]. When such mixer was used for a study of efficiency of metalation of substituted bromobenzenes with butyl lithium followed by quenching with methanol (Figure 10a) the inflection points on the plots of the yields of both electron-rich and electron-poor compounds were observed at 14 mL/min flow rate suggesting that the increased mixing efficiency within the T-shaped micromixer at a high flow rate, hence higher product yield, is due to a change in the flow regime [118] (Figure 10b; compare with Figure 3).

The design of the mixer plays an important role in the processes, during which further transformation of the product as a result of side reactions is possible. This is well illustrated by the Friedel–Crafts reaction (Scheme 4) [123]. In this example, sequential alkylation of the aromatic system occurs. The monosubstituted (main) and disubstituted (side) products were obtained in different ratios when different micromixers were used for mixing reagents. In a simple T-shaped micromixer the yields of the main and the side products were 36% and 31%, respectively. When the YM-1 mixer [45] was used the yields of the main and the

side products became 50% and 14%, respectively. The best result was achieved in the IMM mixer [21,35]: the yields of the main and the side products were 92% and 4%, respectively.

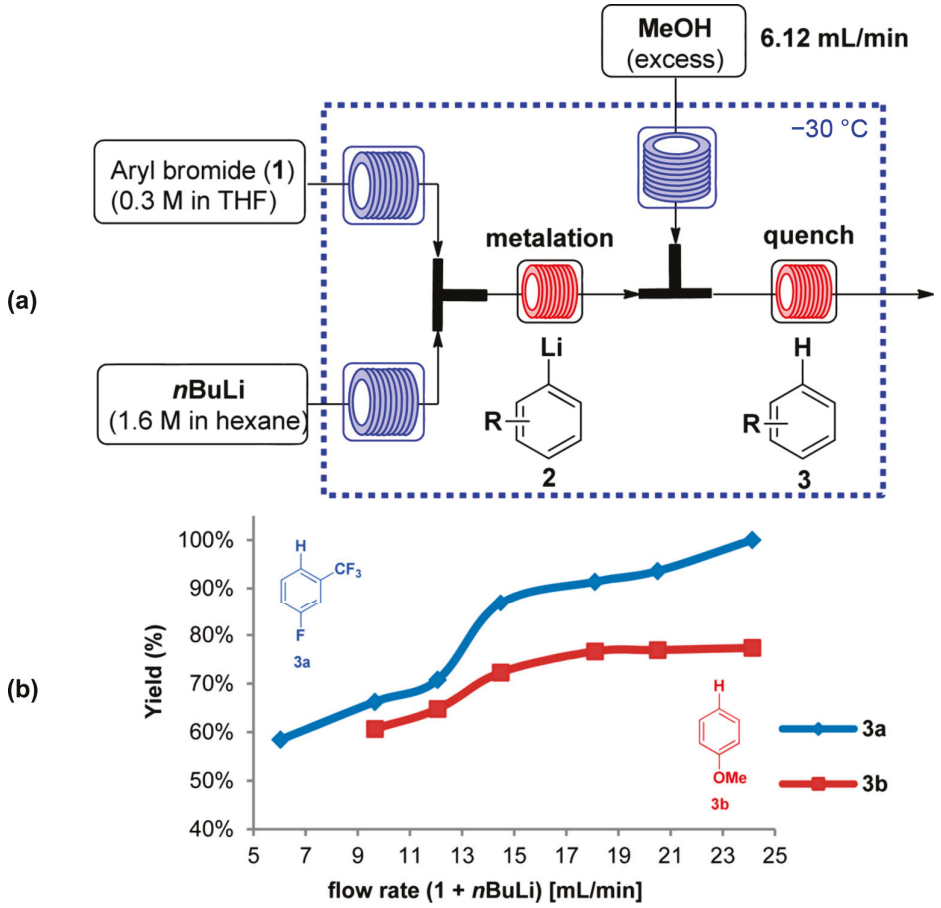
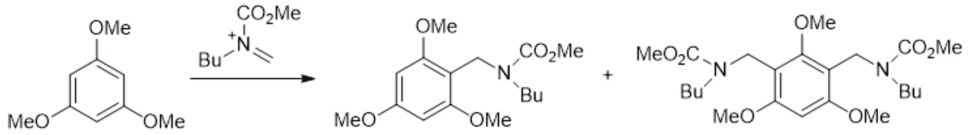


Figure 10. Investigation of mixing performance for the metalation step as a function of flow rate of aryl bromide (**1**) and *n*-BuLi: (**a**)—schematic illustration of the flow system. (**b**)—the yield of **3** as a function of the total flow rate. Adapted with permission from [118]. Copyright 2016 American Chemical Society.



Scheme 4. Friedel–Crafts reaction performed in flow using three types of micromixers: T-shaped, YM-1, and IMM [123].

Such a strong influence of the mixer design (hence the mixing efficiency) was explained [123] from the point of view of the model proposed by Rys [124] (see also a discussion in [57] on competitive consecutive reactions). This model can be used to describe multistep rapid reactions whose rate is limited by the diffusion of reagents (Figure 11). At the first time interval after mixing, regions with an increased concentration of reagent molecules (**B**) surrounded by a solution of another reagent (**A**) are formed. At the points of contact, the first product (**P1**) is formed, which, without effective mixing, does not have time to diffuse into the outer sphere and continues to react to give **P2** at the further time interval.

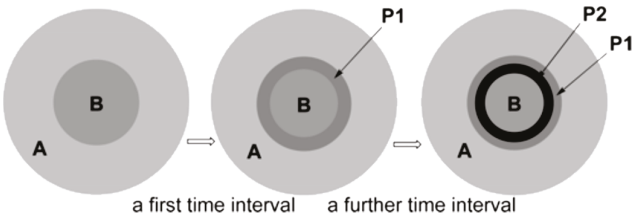
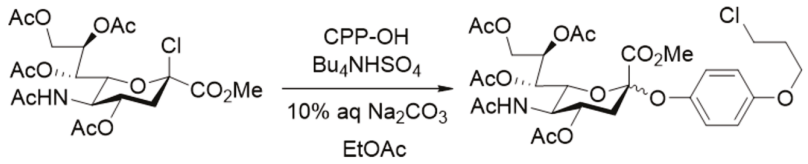


Figure 11. A model [124] of the course of a liquid two-step reaction (like in Scheme 4) where diffusion of reagents is main limitation of reaction rate. **A**, **B**—initial reagents, **P1**—monosubstituted product, **P2**—disubstituted product. Adapted with permission from [123].

During a study of Lewis acid (TMSOTf) promoted microfluidic glycosylation of a 4,6-galactose diol with a 5-azido-sialyl imidate in EtCN at −78 °C (bath temperature) a noticeable influence of the mixer design on the outcome of glycosylation was detected for the first time [100]. Both employed micromixers (IMM and Comet X-01) allowed highly efficient synthesis of the target disaccharide (yields were virtually quantitative in both cases). However, stereoselectivity was higher when the IMM micromixer was used (α/β = 95:5) as compared to stereoselectivity achieved in glycosylation with the Comet X-01 micromixer (α/β = 88:12). The authors explained this difference in selectivity by higher temperature in the second case, leading to lower stereoselectivity, "probably due to poorer heat removal of Comet X-01" (the reaction is exotermic) [100].

The influence of the mixer design on the result of glycosylation was also observed in the sialylation reaction of a substituted phenol (Scheme 5) performed at room temperature under conditions of phase transfer catalysis [113,114]. Here, two different micromixers were used: a Comet X-01 micromixer (*vide supra*), where flow splits into three and joins together several times (see Figure 5), and a simple T-shaped micromixer. At 2 μL/min flow rate the product yields in both cases turned out to be similar: 36% and 33%, respectively. However, the difference in stereoselectivity (α/β) was more significant: 6.2:1 and 13.3:1, respectively. Note that the same reaction performed in batch is stereospecific providing a kinetically controlled α-isomer as the only product of glycosylation [113].



Scheme 5. Sialylation reaction under phase transfer conditions performed in flow. CPP-OH—4-(3-chloropropoxy)phenol [113,114].

The effect of the flow rate on the yield and on the stereoselectivity of glycosylation was observed in this sialylation reaction (Scheme 5) [113]. In this case, with the increase of the flow rate from 2 to 250 μL/min, the yield and stereoselectivity decreased from 36% to 11% and from α/β = 6.2:1 to α/β = 1.9:1, respectively. However, after further increase of the flow rate to 1000 μL/min the yield and stereoselectivity increased to 37% and α/β = 3.8:1, respectively. Therefore, both high (1000 μL/min) and low (2 μL/min) flow rates result in similar yields and stereoselectivities, but intermediate flow rates give worse results. The influence of flow rate and mixer design on the product yield could be easily rationalized within the framework of the mixing-centered concept, discussed above, which emphasizes the importance of the adequate flow regime for efficient mixing of reagents.

However, the unexpected loss of stereoselectivity under microfluidic conditions and its dramatic dependence on mixing conditions (mixer design and flow rate), hence flow regime, does not fit the current knowledge [125–128] on the origin of stereoselectivity of glycosylation. It is unclear how flow rate or mixer design could affect the stereoselectivity of reactions that involve "isolated" molecules.

However, the found phenomenon can be rationally discussed within the framework of supramer hypothesis (supramer approach) [27], according to which the real reacting species in many cases are supramolecular aggregates (supramers) rather than single molecules of reacting substances (the "molecular species"). Recent studies revealed [129–137] that even macroscopically homogeneous aqueous and non-aqueous solutions of low-molecular-mass non-amphiphilic compounds can contain nano- and mesoscale heterogeneities (size from ca. 1 nm to 10^2–10^3 nm) that are kinetically stable, although very small interaction energy, which does not exceed k_BT [138], is involved. The most probable reason for their existence and omnipresence is the "solvophobicity-driven mesoscale" structuring [136] promoted by even minute amounts of "solvophobic admixtures" [27,136] that are present in most commercially available compounds [133] since "no truly pure chemicals exist" [136].

Considering the presence of such heterogeneities, supramers in our terminology [27], which belong to the realm of soft matter, we have been developing the supramer approach (*vide supra*) for the description of chemical reactions (see Refs. [27,139–141] and references cited therein). According to the supramer approach, the "presentation" (spatial orientation) of molecules on the surface of supramers of glycosyl donor (or glycosyl cation formed from it) may play an important role in determining reaction stereoselectivity (see Figure 12).

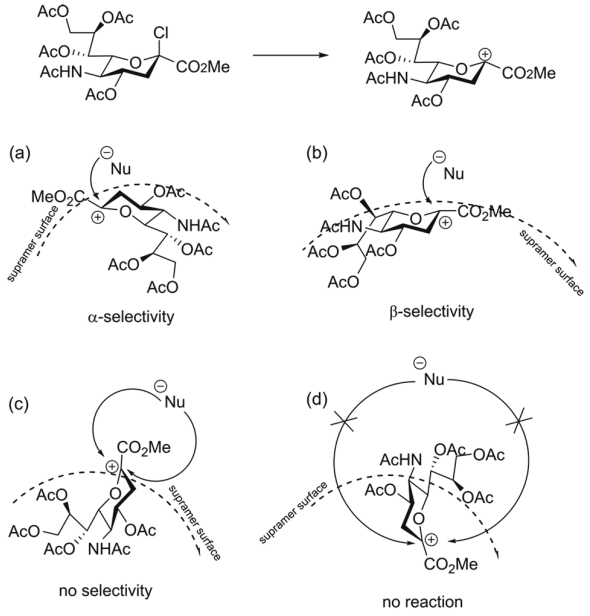


Figure 12. Presentation of glycosyl cation on supramer surface: (**a**,**b**)—α- and β-selective reactions, respectively, (**c**)—nonselective reaction, (**d**)—no reaction. Adapted with permission from [114].

The first stage of the reaction is formation of glycosyl cation which next reacts with nucleophile (Figure 12). Apparently, this stage is the most important one, since the presentation of the glycosyl cation on the surface of the supramer would determine the face of the glycosyl cation on which the nucleophile attack will occur leading to different stereoisomers of the product (Figure 12a–c). It is also possible that the cationic center is hidden inside the supramer (Figure 12d), which would prevent the attack of the nucleophile and lead to a decrease in reactivity of the starting compound (lowering conversion) and the product yield. Similar processes of orientation of molecules on a surface apparently occur during the formation of J-aggregates [142–147] for which the dependence of the resulting types of aggregates on the mixing method was established [148,149].

According to the explanation suggested [113], the efficiency of disaggregation/rearrangement (see Figure 13) of sialyl chloride supramers [27] varies under different mixing modes (in particular, at different flow rates). This makes the S_N1-like pathway within S_N1–S_N2-continuum of glycosylation mechanisms [150,151] possible under microfluidic conditions, leading to formation of both anomers of CPP sialoside (Scheme 5).

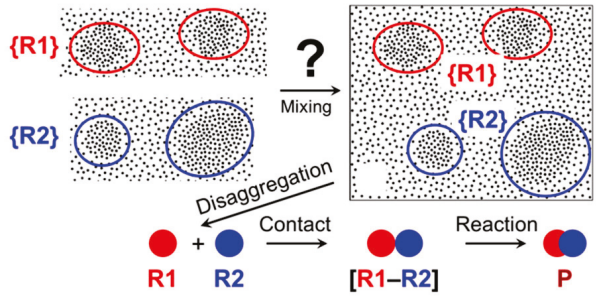


Figure 13. Reagent molecules inside solution domains (supramers) [**R1**] and [**R2**] cannot react with each other. Efficient destruction of domains is required for all molecules of reagents **R1** and **R2** to react—a clue for increasing reactivity of reagents and achieving high yield of product **P**. Supramers may react on their surfaces, in this case asymmetric environment of the surface molecules (presentation, see Figure 12) may lead to stereoselective reactions. Reproduced from [27] with permission from the Royal Society of Chemistry.

According to the authors [113,114], the β-anomer is formed only if sialyl chloride supramers undergo disaggregation (Figure 14), which seems to be more effective in Comet X-01 micromixer (apparently featured by "chaotic mixing" [3,29,31,42,96]) than in T-shaped micromixer. This result suggests that high efficiency of mixing is not a panacea for improving the reaction outcome.

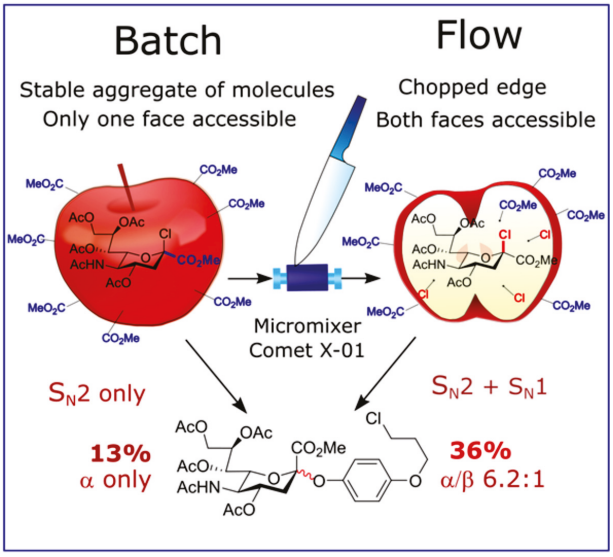


Figure 14. A model of supramers of sialyl chloride in the reaction mixture. In batch reactor the supramers are visualized as a whole intact "apple" (left panel). The spatial orientation of molecules of sialyl chloride in such supramers (presentation, see Figure 12) allows glycosylation from only one face within S$_N$2-like pathway leading to formation of only α-isomer. During "efficient mixing" of reaction mixture in Comet X-01 micromixer (**M**) the "apple" is chopped allowing the molecules of sialyl chloride to show *both* faces on the edge of the apple allowing S$_N$1-like mechanism which leads to formation of both α- and β-isomers (right panel). Reproduced with permission from [113]. Copyright © 2022 WILEY-VCH Verlag GmbH & Co. KGaA, Weinheim.

We must emphasize that this is the first documented example [113,114] of the influence of flow regime on stereoselectivity of a chemical reaction (that does not involve epimerization of the product), which has additionally been rationally explained.

An increase in the *syn*/*anti* ratio (from 8:1 to 18:1) of the product upon increase in the flow rate has been reported for organocatalyzed 1,4-addition of aldehydes to nitroolefins. The authors explained this by epimerization of the product by the catalyst, which be-

comes more profound at increased residence times that inevitably accompany lower flow rates [152].

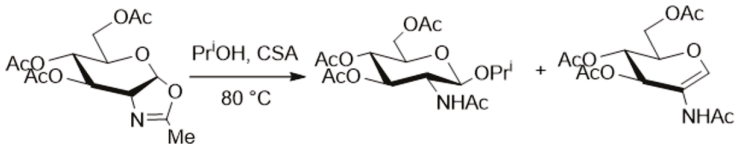
Continuous telescoped two-carbon homologation of esters to α,β-unsaturated esters was performed under microfluidic conditions, which incorporated an ester reduction, phosphonate deprotonation, and Horner–Wadsworth–Emmons olefination into a single, uninterrupted system. The authors are puzzled by the fact that the E/Z selectivity of the olefination in flow was noticeably higher than that under batch conditions using similar reagents [153].

All other previous studies of reactive mixing (see, e.g., [39,57,63]) were concerned with conversion of the starting compound and product yield as the measure of mixing quality. It is difficult to surmise from basic chemical principles [154] that flow regime could alter stereoselectivity of glycosylation, which is considered to be governed (for kinetically controlled reactions, to which glycosylation belongs) by relative rates of reagent attack on *Re*- and *Si*-faces of glycosyl cation, a real glycosylating agent in these systems [114]. One can speculate that the breakdown of symmetry (leading to inequality of these rates) could occur in the presence of an external chiral stimulus. Note that vortex-controlled generation of supramolecular chirality has been documented for batch systems [148,149,155–157].

The recently discovered [20] phenomenon of enhanced formation of non-covalent bonds under flow conditions, thus easing the self-assembly of new supramolecular structures, might also be related to rearrangements of supramers of reactants induced by shear stress in flow as discussed above (see Figure 14). Specifically, we hypothesize that supramers of reactants disaggregate (partially or completely) (see Figures 13 and 14) under flow conditions in a dynamical fashion creating the fragmented supramers (and, ultimately, the "molecular species") that are (1) more reactive compared to the parent supramers, present in the starting solutions, and (2) capable of forming supramolecular architectures different from those formed "passively" [20] in the flask from the parent supramers. In line with the discussion above, we propose that the ease of supramolecular assembly in flow would dramatically depend on the flow regime, hence on the mixer design and the flow rate used.

Similar reasoning might explain the well-known phenomenon of decreasing the reaction time in flow as compared to that of the same reaction performed in batch. From the supramer point of view, shear stress in flow might induce fragmentation of the parent supramers, which exist in solution before the reaction, leading to formation of more reactive species and making the reaction faster. Traditional explanation of this considerable decrease in reaction time (e.g., from 24 h in batch to 7 min in flow [152]) would involve listing beneficial features of the microfluidic technique such as improved mass transfer due to efficient mixing, fast heat transfer, and residence time control to name a few (see, e.g., [5,18,19]).

The design of the mixer and flow rate can strongly determine the reactivity of a substance. This phenomenon was demonstrated using glycosylation of isopropyl alcohol with oxazoline as the glycosyl donor (Scheme 6) carried out in a Comet X-01 micromixer (Figure 15) [110]. As expected, at high flow rates, the yields of both products were low—the reaction did not have enough time to occur. With a decrease in the flow rate, the yields expectedly increased. But at some point, at very low flow rates (flow rate $\leq$43 μL/h), the acid-labile oxazoline stopped reacting and the starting reagents were recovered. This apparent loss of reactivity was observed *only* when Comet X-01 micromixer was used. However, when a Comet X-01 micromixer was replaced with a T-shaped micromixer (at 30 μL/h flow rate), the expected reaction products, glycoside and glycal, appeared in the reaction mixture. Thus, the change in mixer design (from Comet X-01 micromixer to T-shaped micromixer) apparently altered the flow regime resulting in better mixing of reagents, if we follow the mixing-centered concept, discussed above.



Scheme 6. Glycosylation reaction of isopropyl alcohol by glyco-oxazoline. CSA—camphorsulfonic acid.

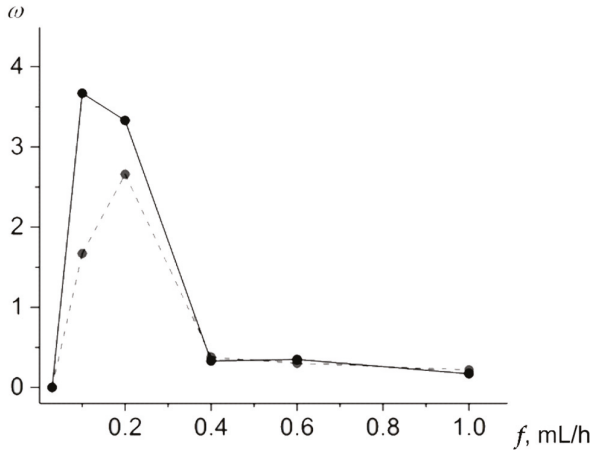


Figure 15. Formation of products in glycosylation reaction performed in flow at different flow rates (Scheme 6) using Comet X-01 micromixer. Relative amounts (ω) of products: dashed line—isopropyl glycoside, solid line—glycal (side product). *f*—flow rate, mL/h. No reaction was observed at low flow rates (≤43 μL/h). Adapted with permission from [110]. Copyright (2019), Springer Nature.

However, within the framework of the supramer approach [27] (*vide supra*), this result apparently suggests a higher disaggregation of the supramers of reagents under these conditions (using a T-shaped micromixer), which allows the chemical reaction between them to occur. Apparently, at very low flow rates (30 μL/h) in the Comet X-01 micromixer, the molecules of this glycosyl donor are located inside the core of tight supramers (similar to those discovered recently [113,114,139,158]) or presented on the surface of supramers in such a way that the anomeric position becomes inaccessible for attack (which is manifested as an enhanced stability of oxazoline under the action of acid), similarly to the situation shown in Figure 12 for glycosyl cation derived from sialyl chloride. Based on these facts, we conclude that the flow rate in combination with change in the mixer design in this case directly affects the *reactivity* of molecules probably by changing the flow regime which makes disaggregation (see Figures 13 and 14) of the supramers of reagents (im)possible thus altering the observed reactivity pattern.

Similar observations were made earlier for another reaction [159], where it has been proposed that the observed decrease in conversion at low flow rates is related to the change in the flow regime from "dispersed flow regime" (good mixing) to "stratified flow regime" (bad mixing) (Figure 16) supported by mixing experiments with non-reacting substances. Indeed, this phenomenon of "the dependence of mass transfer on the two-phase flow patterns" was studied in single- and two-phase flow systems [61,64]. However, as in the previous example, one can speculate that a change in the flow rate leads to a change in the flow regime, which modulates the efficiency of disaggregation of the supramers of reagents. As a result, at low flow rates, some of the molecules are located inside the core of tight supramers [113,114,139,158] and cannot react. As the flow rate increases, the efficiency of disaggregation increases, and the conversion rate increases accordingly. With a further increase in the flow rate, the conversion decreases, which may be due either to insufficient contact time of the reagents or to generation of supramers of different type formed during disaggregation of the parent supramers.

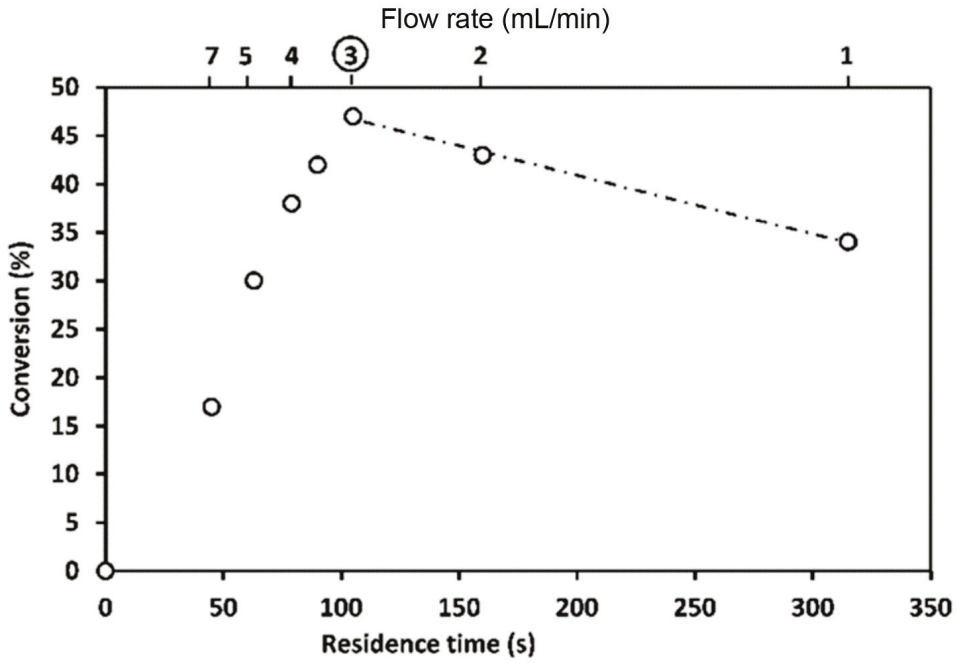


Figure 16. Observation of the change in flow regime during alkylation of benzoic acid by CH_3I in DMF in the presence of DBU in the Low Flow reactor. Reproduced with permission from [159].

An interesting example of dramatic reactivity enhancing upon increase in flow rate (from 0.3 mL/min to 5 mL/min) was reported for in-flow metalation of an acrylate ester containing thiophene moiety with 2,2,6,6-tetramethylpiperidinylmagnesium chloride lithium chloride complex at −25 °C. While at low flow rates only low conversions could be achieved with long residence times (5 or 15 min), at high flow rates almost full conversion was achieved within 1 min leading to isolation of the desired product in 72% yield [117].

4. Influence of Residence Time on the Reaction Outcome

The flow rate changes can affect the reaction outcome also by simply changing the residence time (time of contact = time of flowing reagents together without changing the flow rate) without apparent influence of the mixing efficiency. In fact, it may be difficult to separate these effects experimentally.

There are a number of examples when an increase in residence time of reagents leads to an increase in the reaction yield as expected for batch reactions [160]. However, with too long times, selectivity decreases [161] or by-products appear [119]. Special attention should be paid to examples when it is possible to obtain various products in high yields by varying the residence time. A striking example of such an approach is the Br-Li exchange reaction followed by the reaction of the lithiated species with electrophiles performed in flow (Figure 17) [162]. There, kinetically formed 5-substitued product is selectively formed at residence time 0.06 s (yield 84%). Increasing residence time to 63 s gives thermodynamically preferred 3-substitued product in yield 68%. In both cases only traces of another isomer were observed.

The value of the residence time, which is a powerful instrument for controlling reaction outcome, should be optimized as times that are too long may result in a decrease in the product yield probably due to reactants decomposition (Figure 18) [40].

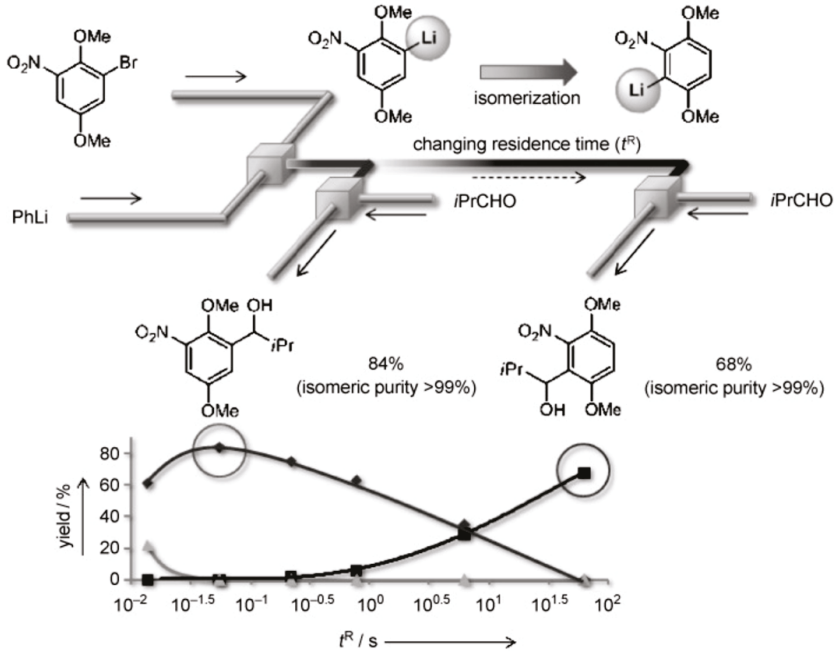


Figure 17. A switch between kinetic and thermodynamic control by changing the residence time of the Br-Li exchange reaction followed by the reaction of the lithiated species with Pr^iCHO as electrophile. ♦—5-substitued kinetically formed product, ■—3-substitued thermodynamically preferred product, ▲—initial aromatic reagent. Reproduced with permission from [162]. Copyright © 2009 WILEY-VCH Verlag GmbH & Co. KGaA, Weinheim.

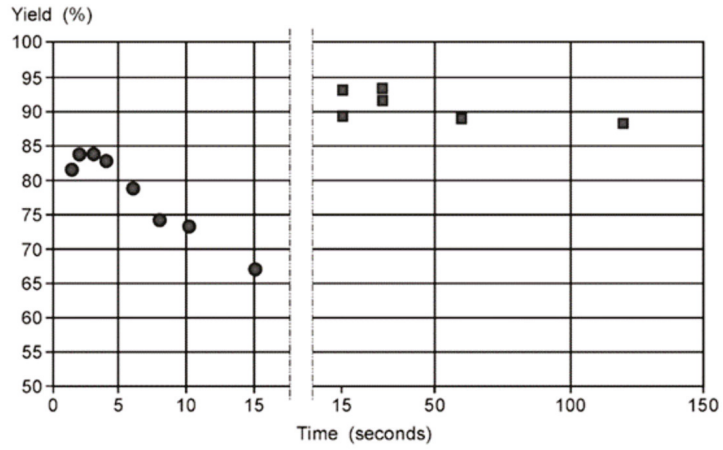


Figure 18. Dependence of the yield on the residence time of the liquid-liquid reaction at 50 °C (●) and 20 °C (■) in the microreactor. Reproduced with permission from [40]. Copyright © 2001 WILEY-VCH Verlag GmbH & Co. KGaA, Weinheim.

5. Conclusions

In conclusion, we demonstrated that variation in flow regime (determined by a combination of mixer design and flow rate) can either improve or worsen the reactivity and lead to completely different products, including stereoisomers. We would like to stress that it is not necessary to homogenize the reaction mixture as much as possible or to mix the reagents with maximum efficiency. The real challenge is to mix reagents the *right way*. To achieve this in a flow reactor one should combine the appropriate values of flow rate and the designs of microreactor.

In terms of the supramer approach [27], at too high or too low a flow rate (in the particular mixer), the molecules of reagents are incorrectly presented on the surface of supramers, leading to altered stereoselectivity, or form tight supramers (similar to those

discovered recently [113,114,139,158]), in which most of the molecules are located inside the supramer core and are inaccessible for attack, leading to low conversions and yields. The flow rate at which these problems do not exist can be considered optimal.

We can discuss the efficiency of mixing in a similar way. On the one hand, efficiently mixed reagents can react faster and with greater conversion, giving higher yields. On the other hand, the most efficiently mixed system loses the effect of the asymmetry of the supramer surface (since all supramers are disaggregated), which eliminates a possibility of controlling stereoselectivity of the reaction and allows all side processes to proceed.

Chemistry is definitely a statistical science. There are myriads of molecules in the reaction mixture, each of which can react (in one or many ways) or not. For each specific molecule, the reaction proceeds conditionally instantaneously, provided that the reaction partners (who have the fundamental ability to react) have approached the right faces. If it were possible to find a tool or a method of influencing molecules, in which only the approaches we need would be encountered, then product yields and stereoselectivities of any reactions would be high. Experimental data suggest that, for reactions conducted in flow, the flow rate and the design of the microreactor can serve as such tools.

Author Contributions: Conceptualization, I.V.M. and L.O.K.; methodology, I.V.M. and L.O.K.; investigation, I.V.M.; writing—original draft preparation, I.V.M.; writing—review and editing, L.O.K.; visualization, I.V.M. and L.O.K.; supervision, L.O.K.; project administration, L.O.K. All authors have read and agreed to the published version of the manuscript.

Funding: This research received no external funding.

Data Availability Statement: Not applicable.

Conflicts of Interest: The authors declare no conflict of interest.

References

1. Jahnisch, K.; Hessel, V.; Löwe, H.; Baerns, M. Chemistry in microstructured reactors. *Angew. Chem. Int. Ed.* **2004**, *43*, 406. [CrossRef] [PubMed]
2. Whitesides, G.M. The origins and the future of microfluidics. *Nature* **2006**, *442*, 368–373. [CrossRef] [PubMed]
3. deMello, A.J. Control and detection of chemical reactions in microfluidic systems. *Nature* **2006**, *442*, 394–402. [CrossRef] [PubMed]
4. Tanaka, K.; Fukase, K. Acid-mediated reactions under microfluidic conditions: A new strategy for practical synthesis of biofunctional natural products. *Beilstein J. Org. Chem.* **2009**, *5*, 40. [CrossRef] [PubMed]
5. Tanaka, K.; Fukase, K. Renaissance of Traditional Organic Reactions under Microfluidic Conditions: A New Paradigm for Natural Products Synthesis. *Org. Process Res. Dev.* **2009**, *13*, 983–990. [CrossRef]
6. Wegner, J.; Ceylan, S.; Kirschning, A. Ten key issues in modern flow chemistry. *Chem. Commun.* **2011**, *47*, 4583–4592. [CrossRef] [PubMed]
7. Hessel, V.; Kralisch, D.; Kockmann, N.; Noël, T.; Wang, Q. Novel Process Windows for Enabling, Accelerating, and Uplifting Flow Chemistry. *ChemSusChem* **2013**, *6*, 746–789. [CrossRef] [PubMed]
8. Elvira, K.S.; Casadevall i Solvas, X.; Wootton, R.C.R.; demello, A.J. The past, present and potential for microfluidic reactor technology in chemical synthesis. *Nat. Chem.* **2013**, *5*, 905–915. [CrossRef]
9. Fukase, K.; Shimoyama, A.; Manabe, Y. Effective Synthesis of Oligosaccharide under Microfiuidic Conditions. *J. Synth. Org. Chem. Jpn.* **2015**, *73*, 452–459. [CrossRef]
10. Fukase, K.; Tanaka, K.; Fujimoto, Y.; Shimoyama, A.; Manabe, Y. Sugar synthesis by microfluidic techniques. In *Glycochemical Synthesis*; Hung, S.-C., Zulueta, M.M.L., Eds.; Wiley Online Books; Wiley: Hoboken, NJ, USA, 2016; pp. 205–219. [CrossRef]
11. Plutschack, M.B.; Pieber, B.; Gilmore, K.; Seeberger, P.H. The Hitchhiker's Guide to Flow Chemistry. *Chem. Rev.* **2017**, *117*, 11796–11893. [CrossRef]
12. Sevim, S.; Sorrenti, A.; Franco, C.; Furukawa, S.; Pané, S.; deMello, A.J.; Puigmartí-Luis, J. Self-assembled materials and supramolecular chemistry within microfluidic environments: From common thermodynamic states to non-equilibrium structures. *Chem. Soc. Rev.* **2018**, *47*, 3788–3803. [CrossRef] [PubMed]
13. Guidi, M.; Seeberger, P.H.; Gilmore, K. How to approach flow chemistry. *Chem. Soc. Rev.* **2020**, *49*, 8910–8932. [CrossRef]
14. Hone, C.A.; Kappe, C.O. Towards the Standardization of Flow Chemistry Protocols for Organic Reactions. *Chem. Methods* **2021**, *1*, 454–467. [CrossRef]
15. Leslie, A.; Joseph, A.M.; Baumann, M. Functional Group Interconversion Reactions in Continuous Flow Reactors. *Curr. Org. Chem.* **2021**, *25*, 2217–2231. [CrossRef]
16. Paratore, F.; Bacheva, V.; Bercovici, M.; Kaigala, G.V. Reconfigurable microfluidics. *Nat. Rev. Chem.* **2021**, *6*, 70–80. [CrossRef] [PubMed]

17. Burange, A.S.; Osman, S.M.; Luque, R. Understanding flow chemistry for the production of active pharmaceutical ingredients. *iScience* **2022**, *25*, 103892. [CrossRef] [PubMed]
18. Capaldo, L.; Wen, Z.; Noel, T. A field guide to flow chemistry for synthetic organic chemists. *Chem. Sci.* **2023**, *14*, 4230–4247. [CrossRef] [PubMed]
19. Monbaliu, J.-C.M.; Legros, J. Will the next generation of chemical plants be in miniaturized flow reactors? *Lab Chip* **2023**, *23*, 1349–1357. [CrossRef]
20. Numata, M.; Kanzaki, C. Supramolecular Chemistry of a Moving Solution: Flow Drives New Non-covalent Bond Formation. *Chem. Lett.* **2023**, *52*, 602–610. [CrossRef]
21. Ehrfeld, W.; Hessel, V.; Löwe, H. (Eds.) Micromixers. In *Microreactors*; Wiley: Hoboken, NJ, USA, 2000; pp. 41–85. [CrossRef]
22. Suryawanshi, P.L.; Gumfekar, S.P.; Bhanvase, B.A.; Sonawane, S.H.; Pimplapure, M.S. A review on microreactors: Reactor fabrication, design, and cutting-edge applications. *Chem. Eng. Sci.* **2018**, *189*, 431–448. [CrossRef]
23. Bojang, A.A.; Wu, H.-S. Design, fundamental principles of fabrication and applications of microreactors. *Processes* **2020**, *8*, 891. [CrossRef]
24. Dong, Z.; Wen, Z.; Zhao, F.; Kuhn, S.; Noel, T. Scale-up of micro- and milli-reactors: An overview of strategies, design principles and applications. *Chem. Eng. Sci. X* **2021**, *10*, 100097. [CrossRef]
25. Kucherov, F.A.; Romashov, L.V.; Ananikov, V.P. Development of 3D + G printing for the design of customizable flow reactors. *Chem. Eng. J.* **2022**, *430*, 132670. [CrossRef]
26. Whitesides, G.M. Whitesides' Group: Writing a Paper. *Adv. Mater.* **2004**, *16*, 1375–1377. [CrossRef]
27. Kononov, L.O. Chemical reactivity and solution structure: On the way to a paradigm shift? *RSC Adv.* **2015**, *5*, 46718–46734. [CrossRef]
28. Reynolds, O. XXIX. An experimental investigation of the circumstances which determine whether the motion of water shall be direct or sinuous, and of the law of resistance in parallel channels. *Philos. Trans. R. Soc. Lond.* **1883**, *174*, 935–982. [CrossRef]
29. Nguyen, N.-T.; Wu, Z. Micromixers—A review. *J. Micromech. Microeng.* **2005**, *15*, R1–R16. [CrossRef]
30. Hisamoto, H.; Saito, T.; Tokeshi, M.; Hibara, A.; Kitamori, T. Fast and high conversion phase-transfer synthesis exploiting the liquid–liquid interface formed in a microchannel chip. *Chem. Commun.* **2001**, 2662–2663. [CrossRef]
31. Ottino, J.M. Mixing, Chaotic Advection, and Turbulence. *Annu. Rev. Fluid Mech.* **1990**, *22*, 207–254. [CrossRef]
32. Ottino, J.M. Mixing and chemical reactions a tutorial. *Chem. Eng. Sci.* **1994**, *49*, 4005–4027. [CrossRef]
33. Bałdyga, J.; Bourne, J.R. *Turbulent Mixing and Chemical Reactions*; Wiley: Chichester, UK, 1999; p. 896.
34. Bourne, J.R. Mixing and the Selectivity of Chemical Reactions. *Org. Process Res. Dev.* **2003**, *7*, 471–508. [CrossRef]
35. Hessel, V.; Löwe, H.; Schönfeld, F. Micromixers—A review on passive and active mixing principles. *Chem. Eng. Sci.* **2005**, *60*, 2479–2501. [CrossRef]
36. Lee, C.-Y.; Chang, C.-L.; Wang, Y.-N.; Fu, L.-M. Microfluidic Mixing: A Review. *Int. J. Mol. Sci.* **2011**, *12*, 3263–3287. [CrossRef] [PubMed]
37. Ghanem, A.; Lemenand, T.; Della Valle, D.; Peerhossaini, H. Static mixers: Mechanisms, applications, and characterization methods—A review. *Chem. Eng. Res. Des.* **2014**, *92*, 205–228. [CrossRef]
38. Arimond, J.; Erwin, L. A simulation of a motionless mixer. *Chem. Eng. Commun.* **1985**, *37*, 105–126. [CrossRef]
39. Ehrfeld, W.; Golbig, K.; Hessel, V.; Löwe, H.; Richter, T. Characterization of Mixing in Micromixers by a Test Reaction: Single Mixing Units and Mixer Arrays. *Ind. Eng. Chem. Res.* **1999**, *38*, 1075–1082. [CrossRef]
40. Wörz, O.; Jäckel, K.P.; Richter, T.; Wolf, A. Microreactors—A New Efficient Tool for Reactor Development. *Chem. Eng. Technol.* **2001**, *24*, 138–142. [CrossRef]
41. Johnson, T.J.; Ross, D.; Locascio, L.E. Rapid Microfluidic Mixing. *Anal. Chem.* **2002**, *74*, 45–51. [CrossRef]
42. Stroock, A.D.; Dertinger, S.K.W.; Ajdari, A.; Mezić, I.; Stone, H.A.; Whitesides, G.M. Chaotic Mixer for Microchannels. *Science* **2002**, *295*, 647–651. [CrossRef]
43. Engler, M.; Kockmann, N.; Kiefer, T.; Woias, P. Numerical and experimental investigations on liquid mixing in static micromixers. *Chem. Eng. J.* **2004**, *101*, 315–322. [CrossRef]
44. Kockmann, N.; Engler, M.; Woias, P. Theoretische und experimentelle Untersuchungen der Mischvorgänge in T-förmigen Mikroreaktoren—Teil 3: Konvektives Mischen und chemische Reaktionen. *Chem. Ing. Tech.* **2004**, *76*, 1777–1783. [CrossRef]
45. Mae, K.; Maki, T.; Hasegawa, I.; Eto, U.; Mizutani, Y.; Honda, N. Development of a new micromixer based on split/recombination for mass production and its application to soap free emulsifier. *Chem. Eng. J.* **2004**, *101*, 31–38. [CrossRef]
46. Bothe, D.; Stemich, C.; Warnecke, H.-J. Fluid mixing in a T-shaped micro-mixer. *Chem. Eng. Sci.* **2006**, *61*, 2950–2958. [CrossRef]
47. Hardt, S.; Pennemann, H.; Schönfeld, F. Theoretical and experimental characterization of a low-Reynolds number split-and-recombine mixer. *Microfluid. Nanofluid.* **2006**, *2*, 237–248. [CrossRef]
48. Kockmann, N.; Kiefer, T.; Engler, M.; Woias, P. Convective mixing and chemical reactions in microchannels with high flow rates. *Sens. Actuators B* **2006**, *117*, 495–508. [CrossRef]
49. Kockmann, N.; Dreher, S.; Woias, P. Unsteady Laminar Flow Regimes and Mixing in T-Shaped Micromixers. In Proceedings of the ASME 2007 5th International Conference on Nanochannels, Microchannels, and Minichannels, Puebla, Mexico, 18–20 June 2007; ASME: Puebla, Mexico, 2007; pp. 671–678. [CrossRef]
50. Kockmann, N. *Transport Phenomena in Micro Process Engineering*, 1st ed.; Springer: Berlin/Heidelberg, Germany, 2008; p. 365. [CrossRef]

51. Fang, W.-F.; Yang, J.-T. A novel microreactor with 3D rotating flow to boost fluid reaction and mixing of viscous fluids. *Sens. Actuators B* **2009**, *140*, 629–642. [CrossRef]
52. Singh, M.K.; Anderson, P.D.; Meijer, H.E.H. Understanding and Optimizing the SMX Static Mixer. *Macromol. Rapid Commun.* **2009**, *30*, 362–376. [CrossRef]
53. Dreher, S.; Engler, M.; Kockmann, N.; Woias, P. Theoretical and Experimental Investigations of Convective Micromixers and Microreactors for Chemical Reactions. In *Micro and Macro Mixing: Analysis, Simulation and Numerical Calculation*; Bockhorn, H., Mewes, D., Peukert, W., Warnecke, H.-J., Eds.; Springer: Berlin/Heidelberg, Germany, 2010; pp. 325–346. [CrossRef]
54. Suh, Y.K.; Kang, S. A Review on Mixing in Microfluidics. *Micromachines* **2010**, *1*, 82–111. [CrossRef]
55. Kockmann, N.; Roberge, D.M. Scale-up concept for modular microstructured reactors based on mixing, heat transfer, and reactor safety. *Chem. Eng. Process.* **2011**, *50*, 1017–1026. [CrossRef]
56. Zhdanov, V.; Chorny, A. Development of macro- and micromixing in confined flows of reactive fluids. *Int. J. Heat Mass Transf.* **2011**, *54*, 3245–3255. [CrossRef]
57. Schwolow, S.; Hollmann, J.; Schenkel, B.; Roeder, T. Application-Oriented Analysis of Mixing Performance in Microreactors. *Org. Process Res. Dev.* **2012**, *16*, 1513–1522. [CrossRef]
58. Orsi, G.; Roudgar, M.; Brunazzi, E.; Galletti, C.; Mauri, R. Water-ethanol mixing in T-shaped microdevices. *Chem. Eng. Sci.* **2013**, *95*, 174–183. [CrossRef]
59. Wunderlich, B.; Nettels, D.; Benke, S.; Clark, J.; Weidner, S.; Hofmann, H.; Pfeil, S.H.; Schuler, B. Microfluidic mixer designed for performing single-molecule kinetics with confocal detection on timescales from milliseconds to minutes. *Nat. Protoc.* **2013**, *8*, 1459–1474. [CrossRef] [PubMed]
60. Liu, Z.; Guo, L.; Huang, T.; Wen, L.; Chen, J. Experimental and CFD studies on the intensified micromixing performance of micro-impinging stream reactors built from commercial T-junctions. *Chem. Eng. Sci.* **2014**, *119*, 124–133. [CrossRef]
61. Woitalka, A.; Kuhn, S.; Jensen, K.F. Scalability of mass transfer in liquid–liquid flow. *Chem. Eng. Sci.* **2014**, *116*, 1–8. [CrossRef]
62. Ghotli, R.A.; Abdul Aziz, A.R.; Ibrahim, S. Liquid-liquid mass transfer studies in various stirred vessel designs. *Rev. Chem. Eng.* **2015**, *31*, 329–343. [CrossRef]
63. Jasińska, M. Test Reactions to Study Efficiency of Mixing. *Chem. Eng. Process.* **2015**, *36*, 171–208. [CrossRef]
64. Wu, K.-J.; Nappo, V.; Kuhn, S. Hydrodynamic Study of Single- and Two-Phase Flow in an Advanced-Flow Reactor. *Ind. Eng. Chem. Res.* **2015**, *54*, 7554–7564. [CrossRef]
65. Luo, J.-Z.; Luo, Y.; Chu, G.-W.; Arowo, M.; Xiang, Y.; Sun, B.-C.; Chen, J.-F. Micromixing efficiency of a novel helical tube reactor: CFD prediction and experimental characterization. *Chem. Eng. Sci.* **2016**, *155*, 386–396. [CrossRef]
66. Plouffe, P.; Bittel, M.; Sieber, J.; Roberge, D.M.; Macchi, A. On the scale-up of micro-reactors for liquid–liquid reactions. *Chem. Eng. Sci.* **2016**, *143*, 216–225. [CrossRef]
67. Gobert, S.R.L.; Kuhn, S.; Braeken, L.; Thomassen, L.C.J. Characterization of Milli- and Microflow Reactors: Mixing Efficiency and Residence Time Distribution. *Org. Process Res. Dev.* **2017**, *21*, 531–542. [CrossRef]
68. Kockmann, N. Transport Phenomena and Chemical Reactions in Modular Microstructured Devices. *Heat Transf. Eng.* **2017**, *38*, 1316–1330. [CrossRef]
69. Rahimi, M.; Azimi, N.; Parsamogadam, M.A.; Rahimi, A.; Masahy, M.M. Mixing performance of T, Y, and oriented Y-micromixers with spatially arranged outlet channel: Evaluation with Villermaux/Dushman test reaction. *Microsyst. Technol.* **2017**, *23*, 3117–3130. [CrossRef]
70. Reckamp, J.M.; Bindels, A.; Duffield, S.; Liu, Y.C.; Bradford, E.; Ricci, E.; Susanne, F.; Rutter, A. Mixing Performance Evaluation for Commercially Available Micromixers Using Villermaux-Dushman Reaction Scheme with the Interaction by Exchange with the Mean Model. *Org. Process Res. Dev.* **2017**, *21*, 816–820. [CrossRef]
71. Zhou, M.; Bai, D.; Zong, Y.; Zhao, L.; Thornock, J.N. Numerical investigation of turbulent reactive mixing in a novel coaxial jet static mixer. *Chem. Eng. Process.* **2017**, *122*, 190–203. [CrossRef]
72. Ansari, M.A.; Kim, K.-Y.; Kim, S.M. Numerical and Experimental Study on Mixing Performances of Simple and Vortex Micro T-Mixers. *Micromachines* **2018**, *9*, 204. [CrossRef]
73. Levesque, F.; Rogus, N.J.; Spencer, G.; Grigorov, P.; McMullen, J.P.; Thaisrivongs, D.A.; Davies, I.W.; Naber, J.R. Advancing Flow Chemistry Portability: A Simplified Approach to Scaling Up Flow Chemistry. *Org. Process Res. Dev.* **2018**, *22*, 1015–1021. [CrossRef]
74. Mariotti, A.; Galletti, C.; Mauri, R.; Salvetti, M.V.; Brunazzi, E. Steady and unsteady regimes in a T-shaped micro-mixer: Synergic experimental and numerical investigation. *Chem. Eng. J.* **2018**, *341*, 414–431. [CrossRef]
75. Rossetti, I. Continuous flow (micro-)reactors for heterogeneously catalyzed reactions: Main design and modelling issues. *Catal. Today* **2018**, *308*, 20–31. [CrossRef]
76. Su, Y.; Song, Y.; Xiang, L. Continuous-Flow Microreactors for Polymer Synthesis: Engineering Principles and Applications. *Top. Curr. Chem.* **2018**, *376*, 44. [CrossRef]
77. Li, W.; Xia, F.; Qin, H.; Zhang, M.; Li, W.; Zhang, J. Numerical and experimental investigations of micromixing performance and efficiency in a pore-array intensified tube-in-tube microchannel reactor. *Chem. Eng. J.* **2019**, *370*, 1350–1365. [CrossRef]
78. Wang, J.; Zhang, N.; Chen, J.; Rodgers, V.G.J.; Brisk, P.; Grover, W.H. Finding the optimal design of a passive microfluidic mixer. *Lab Chip* **2019**, *19*, 3618–3627. [CrossRef] [PubMed]

79. Camarri, S.; Mariotti, A.; Galletti, C.; Brunazzi, E.; Mauri, R.; Salvetti, M.V. An Overview of Flow Features and Mixing in Micro T and Arrow Mixers. *Ind. Eng. Chem. Res.* **2020**, *59*, 3669–3686. [CrossRef]
80. Cheng, D.; Chen, F.-E. Experimental and Numerical Studies of the Phase-Transfer-Catalyzed Wittig Reaction in Liquid-Liquid Slug-Flow Microchannels. *Ind. Eng. Chem. Res.* **2020**, *59*, 4397–4410. [CrossRef]
81. Desir, P.; Chen, T.-Y.; Bracconi, M.; Saha, B.; Maestri, M.; Vlachos, D.G. Experiments and computations of microfluidic liquid-liquid flow patterns. *React. Chem. Eng.* **2020**, *5*, 39–50. [CrossRef]
82. Hosseini, F.; Rahimi, M. Computational fluid dynamics and experimental investigations on liquid-liquid mass transfer in T-type microchannels with different mixing channel barrier shapes. *Sep. Sci. Technol.* **2020**, *55*, 3502–3516. [CrossRef]
83. Mariotti, A.; Antognoli, M.; Galletti, C.; Mauri, R.; Salvetti, M.V.; Brunazzi, E. The role of flow features and chemical kinetics on the reaction yield in a T-shaped micro-reactor. *Chem. Eng. J.* **2020**, *396*, 125223. [CrossRef]
84. Wang, X.; Wang, Y.; Li, F.; Li, L.; Ge, X.; Zhang, S.; Qiu, T. Scale-up of microreactor: Effects of hydrodynamic diameter on liquid-liquid flow and mass transfer. *Chem. Eng. Sci.* **2020**, *226*, 115838. [CrossRef]
85. Zhang, H.; Kopfmüller, T.; Achermann, R.; Zhang, J.; Teixeira, A.; Shen, Y.; Jensen, K.F. Accessing multidimensional mixing via 3D printing and showerhead micromixer design. *AIChE J.* **2020**, *66*, e16873. [CrossRef]
86. Gill, K.K.; Gibson, R.; Yiu, K.H.C.; Hester, P.; Reis, N.M. Microcapillary film reactor outperforms single-bore mesocapillary reactors in continuous flow chemical reactions. *Chem. Eng. J.* **2021**, *408*, 127860. [CrossRef]
87. Manzano Martínez, A.N.; Jansen, R.; Walker, K.; Assirelli, M.; van der Schaaf, J. Experimental and modeling study on meso- and micromixing in the rotor–stator spinning disk reactor. *Chem. Eng. Res. Des.* **2021**, *173*, 279–288. [CrossRef]
88. Kravtsova, A.Y.; Ianko, P.E.; Kashkarova, M.V.; Bilsky, A.V.; Kravtsov, Y.V.; Naumov, I.V. Conditions of the Effective Mixing in a T-Type Micromixer at Low Reynolds Numbers. In *Processes in GeoMedia—Volume V*; Chaplina, T., Ed.; Springer International Publishing: Cham, Switzerland, 2022; Volume 5, pp. 35–41. [CrossRef]
89. Trabzon, L.; Karimian, G.; Khosroshahi, A.R.; Gül, B.; Bakhshayesh, A.G.; Kocak, A.F.; Akyıldız, D.; Aldi, Y.E. High-throughput nanoscale liposome formation via electrohydrodynamic-based micromixer. *Phys. Fluids* **2022**, *34*, 102011. [CrossRef]
90. Jafarpour, A.M.; Khosroshahi, A.R.; Hanifi, M.; Moghanlou, F.S. Experimental study on the performance of a mini-scale Y-type mixer with two liquid metal-enabled pumps. *Phys. Fluids* **2022**, *34*, 112110. [CrossRef]
91. Chen, Q.; Zhang, M.; Zheng, C.; Li, H. Numerical Simulation of Mixing Characteristics in a Split-and-Recombine Microchannel. *Heat Transf. Eng.* **2023**, *44*, 1563–1577. [CrossRef]
92. Jiang, J.; Yang, N.; Liu, H.; Tang, J.; Wang, C.; Wang, R.; Yang, X. Modification of Meso-Micromixing Interaction Reaction Model in Continuous Reactors. *Processes* **2023**, *11*, 1576. [CrossRef]
93. Falk, L.; Commenge, J.M. Performance comparison of micromixers. *Chem. Eng. Sci.* **2010**, *65*, 405–411. [CrossRef]
94. Rehage, H.; Kind, M. The first Damköhler number and its importance for characterizing the influence of mixing on competitive chemical reactions. *Chem. Eng. Sci.* **2021**, *229*, 116007. [CrossRef]
95. Chen, Y.T.; Chen, K.H.; Fang, W.F.; Tsai, S.H.; Fang, J.M.; Yang, J.T. Flash synthesis of carbohydrate derivatives in chaotic microreactors. *Chem. Eng. J.* **2011**, *174*, 421–424. [CrossRef]
96. Chen, Y.-T.; Fang, W.-F.; Liu, Y.-C.; Yang, J.-T. Analysis of chaos and FRET reaction in split-and-recombine microreactors. *Microfluid. Nanofluid.* **2011**, *11*, 339–352. [CrossRef]
97. Tanaka, K.; Motomatsu, S.; Koyama, K.; Tanaka, S.I.; Fukase, K. Large-scale synthesis of immunoactivating natural product, pristane, by continuous microfluidic dehydration as the key step. *Org. Lett.* **2007**, *9*, 299–302. [CrossRef]
98. Tanaka, K.; Mori, Y.; Fukase, K. Practical Synthesis of a Manβ(1-4)GlcNTroc Fragment via Microfluidic β-Mannosylation. *J. Carbohydr. Chem.* **2009**, *28*, 1–11. [CrossRef]
99. Uchinashi, Y.; Nagasaki, M.; Zhou, J.; Tanaka, K.; Fukase, K. Reinvestigation of the C5-acetamide sialic acid donor for α-selective sialylation: Practical procedure under microfluidic conditions. *Org. Biomol. Chem.* **2011**, *9*, 7243–7248. [CrossRef] [PubMed]
100. Uchinashi, Y.; Tanaka, K.; Manabe, Y.; Fujimoto, Y.; Fukase, K. Practical and Efficient Method for α-Sialylation with an Azide Sialyl Donor Using a Microreactor. *J. Carbohydr. Chem.* **2014**, *33*, 55–67. [CrossRef]
101. Audiger, L.; Watts, K.; Elmore, S.C.; Robinson, R.I.; Wirth, T. Ritter Reactions in Flow. *ChemSusChem* **2012**, *5*, 257–260. [CrossRef] [PubMed]
102. Baker, A.; Graz, M.; Saunders, R.; Evans, G.J.S.; Kaul, S.; Wirth, T. Flow Synthesis of Symmetrical Di- and Trisulfides Using Phase-Transfer Catalysis. *J. Flow Chem.* **2013**, *3*, 118–121. [CrossRef]
103. Pradipta, A.R.; Tsutsui, A.; Ogura, A.; Hanashima, S.; Yamaguchi, Y.; Kurbangalieva, A.; Tanaka, K. Microfluidic Mixing of Polyamine with Acrolein Enables the Detection of the [4 + 4] Polymerization of Intermediary Unsaturated Imines: The Properties of a Cytotoxic 1,5-Diazacyclooctane Hydrogel. *Synlett* **2014**, *25*, 2442–2446. [CrossRef]
104. Umezu, S.; Yoshiiwa, T.; Tokeshi, M.; Shindo, M. Generation of ynolates via reductive lithiation using flow microreactors. *Tetrahedron Lett.* **2014**, *55*, 1822–1825. [CrossRef]
105. Matthew, H.; Thomas, W. Safe use of nitromethane for aldol reactions in flow. *J. Flow Chem.* **2016**, *6*, 202–205. [CrossRef]
106. Nagasaki, M.; Manabe, Y.; Minamoto, N.; Tanaka, K.; Silipo, A.; Molinaro, A.; Fukase, K. Chemical synthesis of a complex-type N-glycan containing a core fucose. *J. Org. Chem.* **2016**, *81*, 10600–10616. [CrossRef]
107. Ogasawara, S.; Hayashi, Y. Multistep Continuous-Flow Synthesis of (–)-Oseltamivir. *Synthesis* **2017**, *49*, 424–428. [CrossRef]
108. Ikawa, T.; Masuda, S.; Akai, S. Microflow Fluorinations of Benzynes: Efficient Synthesis of Fluoroaromatic Compounds. *Chem. Pharm. Bull.* **2018**, *66*, 1153–1164. [CrossRef] [PubMed]

109. Katayama, S.; Koge, T.; Katsuragi, S.; Akai, S.; Oishi, T. Flow Synthesis of (*R*)- and (*S*)-(*E*)-1-Iodohexa-1,5-dien-3-ol: Chiral Building Blocks for Natural Product Synthesis. *Chem. Lett.* **2018**, *47*, 1116–1118. [CrossRef]
110. Myachin, I.V.; Orlova, A.V.; Kononov, L.O. Glycosylation in flow: Effect of the flow rate and type of the mixer. *Russ. Chem. Bull.* **2019**, *68*, 2126–2129. [CrossRef]
111. Kondo, M.; Wathsala, H.D.P.; Sako, M.; Hanatani, Y.; Ishikawa, K.; Hara, S.; Takaai, T.; Washio, T.; Takizawa, S.; Sasai, H. Exploration of flow reaction conditions using machine-learning for enantioselective organocatalyzed Rauhut–Currier and [3 + 2] annulation sequence. *Chem. Commun.* **2020**, *56*, 1259–1262. [CrossRef] [PubMed]
112. Ota, K.; Fukumoto, S.; Iwase, T.; Mizota, I.; Shimizu, M.; Hachiya, I. Umpolung Reactions of α-Tosyloximino Esters in a Flow System. *Synlett* **2020**, *31*, 1930–1936. [CrossRef]
113. Myachin, I.V.; Mamirgova, Z.Z.; Stepanova, E.V.; Zinin, A.I.; Chizhov, A.O.; Kononov, L.O. Black swan in phase transfer catalysis: Influence of mixing mode on the stereoselectivity of glycosylation. *Eur. J. Org. Chem.* **2022**, *2022*, e202101377. [CrossRef]
114. Myachin, I.V.; Kononov, L.O. Phase-transfer catalyzed microfluidic glycosylation: A small change in concentration results in a dramatic increase in stereoselectivity. *Catalysts* **2023**, *13*, 313. [CrossRef]
115. Miller, P.W.; Long, N.J.; De Mello, A.J.; Vilar, R.; Passchier, J.; Gee, A. Rapid formation of amides *via* carbonylative coupling reactions using a microfluidic device. *Chem. Commun.* **2006**, 546–548. [CrossRef]
116. Webb, D.; Jamison, T.F. Diisobutylaluminum Hydride Reductions Revitalized: A Fast, Robust, and Selective Continuous Flow System for Aldehyde Synthesis. *Org. Lett.* **2012**, *14*, 568–571. [CrossRef]
117. Ganiek, M.A.; Becker, M.R.; Ketels, M.; Knochel, P. Continuous Flow Magnesiation or Zincation of Acrylonitriles, Acrylates, and Nitroolefins. Application to the Synthesis of Butenolides. *Org. Lett.* **2016**, *18*, 828–831. [CrossRef]
118. Hafner, A.; Meisenbach, M.; Sedelmeier, J. Flow Chemistry on Multigram Scale: Continuous Synthesis of Boronic Acids within 1 s. *Org. Lett.* **2016**, *18*, 3630–3633. [CrossRef] [PubMed]
119. Miyagawa, A.; Tomita, R.; Kurimoto, K.; Yamamura, H. Selective deprotection of trityl group on carbohydrate by microflow reaction inhibiting migration of acetyl group. *Synth. Commun.* **2016**, *46*, 556–562. [CrossRef]
120. Naber, J.R.; Buchwald, S.L. Packed-Bed Reactors for Continuous-Flow C–N Cross-Coupling. *Angew. Chem. Int. Ed.* **2010**, *49*, 9469–9474. [CrossRef] [PubMed]
121. Haroun, S.; Sanei, Z.; Jivan, S.; Schaffer, P.; Ruth, T.J.; Li, P.C.H. Continuous-flow synthesis of [^{11}C]raclopride, a positron emission tomography radiotracer, on a microfluidic chip. *Can. J. Chem.* **2013**, *91*, 326–332. [CrossRef]
122. Park, C.P.; Kim, D.-P. Dual-Channel Microreactor for Gas–Liquid Syntheses. *J. Am. Chem. Soc.* **2010**, *132*, 10102–10106. [CrossRef] [PubMed]
123. Nagaki, A.; Togai, M.; Suga, S.; Aoki, N.; Mae, K.; Yoshida, J.I. Control of extremely fast competitive consecutive reactions using micromixing. Selective Friedel-Crafts aminoalkylation. *J. Am. Chem. Soc.* **2005**, *127*, 11666–11675. [CrossRef] [PubMed]
124. Rys, P. Disguised chemical selectivities. *Acc. Chem. Res.* **1976**, *9*, 345–351. [CrossRef]
125. Roy, R.; Tropper, F.D.; Cao, S.; Kim, J.M. Anomeric Group Transformations Under Phase-Transfer Catalysis. In *Phase-Transfer Catalysis*; Halpern, M., Ed.; ACS Symposium Series; American Chemical Society: Washington, DC, USA, 1997; Volume 659, pp. 163–180. [CrossRef]
126. Boons, G.J.; Demchenko, A.V. Recent advances in *O*-sialylation. *Chem. Rev.* **2000**, *100*, 4539–4566. [CrossRef]
127. De Meo, C.; Jones, B.T. Chapter two—Chemical synthesis of glycosides of *N*-acetylneuraminic acid. *Adv. Carbohydr. Chem. Biochem.* **2018**, *75*, 215–316. [CrossRef]
128. De Meo, C.; Goeckner, N. 2.07—Synthesis of glycosides of sialic acid. In *Comprehensive Glycoscience*, 2nd ed.; Barchi, J.J., Vidal, S., Eds.; Elsevier: Amsterdam, The Netherlands, 2021; Volume 2, pp. 228–266. [CrossRef]
129. Sedlák, M. Large-scale supramolecular structure in solutions of low molar mass compounds and mixtures of liquids: I. Light scattering characterization. *J. Phys. Chem. B* **2006**, *110*, 4329–4338. [CrossRef]
130. Sedlák, M. Large-scale supramolecular structure in solutions of low molar mass compounds and mixtures of liquids: II. Kinetics of the formation and long-time stability. *J. Phys. Chem. B* **2006**, *110*, 4339–4345. [CrossRef] [PubMed]
131. Sedlák, M. Large-scale supramolecular structure in solutions of low molar mass compounds and mixtures of liquids. III. Correlation with molecular properties and interactions. *J. Phys. Chem. B* **2006**, *110*, 13976–13984. [CrossRef] [PubMed]
132. Sedlák, M.; Rak, D. Large-Scale Inhomogeneities in Solutions of Low Molar Mass Compounds and Mixtures of Liquids: Supramolecular Structures or Nanobubbles? *J. Phys. Chem. B* **2013**, *117*, 2495–2504. [CrossRef] [PubMed]
133. Sedlák, M.; Rak, D. On the origin of mesoscale structures in aqueous solutions of tertiary butyl alcohol: The mystery resolved. *J. Phys. Chem. B* **2014**, *118*, 2726–2737. [CrossRef] [PubMed]
134. Rak, D.; Ovadová, M.; Sedlák, M. (Non)existence of bulk nanobubbles: The role of ultrasonic cavitation and organic solutes in water. *J. Phys. Chem. Lett.* **2019**, *10*, 4215–4221. [CrossRef] [PubMed]
135. Rak, D.; Sedlák, M. On the mesoscale solubility in liquid solutions and mixtures. *J. Phys. Chem. B* **2019**, *123*, 1365–1374. [CrossRef] [PubMed]
136. Rak, D.; Sedlák, M. Solvophobicity-Driven Mesoscale Structures: Stabilizer-Free Nanodispersions. *Langmuir* **2023**, *39*, 1515–1528. [CrossRef] [PubMed]
137. Subramanian, D.; Anisimov, M.A. Phase behavior and mesoscale solubilization in aqueous solutions of hydrotropes. *Fluid Phase Equilib.* **2014**, *362*, 170–176. [CrossRef]

138. Zemb, T.; Kunz, W. Weak aggregation: State of the art, expectations and open questions. *Curr. Opin. Colloid Interface Sci.* **2016**, *22*, 113–119. [CrossRef]
139. Orlova, A.V.; Laptinskaya, T.V.; Malysheva, N.N.; Kononov, L.O. Light scattering in non-aqueous solutions of low-molecular-mass compounds: Application for supramer analysis of reaction solutions. *J. Solution Chem.* **2020**, *49*, 629–644. [CrossRef]
140. Orlova, A.V.; Kononov, L.O. Polarimetry as a method for studying the structure of aqueous carbohydrate solutions: Correlation with other methods. *RENSIT* **2020**, *12*, 95–106. [CrossRef]
141. Orlova, A.V.; Ahiadorme, D.A.; Laptinskaya, T.V.; Kononov, L.O. Supramer analysis of 2,3,5-tri-*O*-benzoyl-α-D-arabinofuranosyl bromide solutions in different solvents: Supramolecular aggregation of solute molecules in 1,2-dichloroethane mediated by halogen bonds. *Russ. Chem. Bull.* **2021**, *70*, 2214–2219. [CrossRef]
142. Jelley, E.E. Spectral Absorption and Fluorescence of Dyes in the Molecular State. *Nature* **1936**, *138*, 1009–1010. [CrossRef]
143. Jelley, E.E. Molecular, Nematic and Crystal States of I: I-Diethyl-Cyanine Chloride. *Nature* **1937**, *139*, 631. [CrossRef]
144. Scheibe, G. Über die Veränderlichkeit der Absorptionsspektren in Lösungen und die Nebenvalenzen als ihre Ursache. *Angew. Chem.* **1937**, *50*, 212–219. [CrossRef]
145. Mei, J.; Hong, Y.; Lam, J.W.Y.; Qin, A.; Tang, Y.; Tang, B.Z. Aggregation-Induced Emission: The Whole Is More Brilliant than the Parts. *Adv. Mater.* **2014**, *26*, 5429–5479. [CrossRef] [PubMed]
146. Dar, N.; Ankri, R. Theoretical Models, Preparation, Characterization and Applications of Cyanine J-Aggregates: A Minireview. *ChemistryOpen* **2022**, *11*, e202200103. [CrossRef] [PubMed]
147. Peng, Q.; Shuai, Z. Molecular mechanism of aggregation-induced emission. *Aggregate* **2021**, *2*, e91. [CrossRef]
148. Ribo, J.M.; El-Hachemi, Z.; Arteaga, O.; Canillas, A.; Crusats, J. Hydrodynamic Effects in Soft-matter Self-assembly: The Case of J-Aggregates of Amphiphilic Porphyrins. *Chem. Rec.* **2017**, *17*, 713–724. [CrossRef]
149. Maeda, T.; Mori, T.; Ikeshita, M.; Ma, S.C.; Muller, G.; Ariga, K.; Naota, T. Vortex Flow-controlled Circularly Polarized Luminescence of Achiral Pt(II) Complex Aggregates Assembled at the Air-Water Interface. *Small Methods* **2022**, *6*, 2200936. [CrossRef]
150. Adero, P.O.; Amarasekara, H.; Wen, P.; Bohé, L.; Crich, D. The experimental evidence in support of glycosylation mechanisms at the S_N1–S_N2 interface. *Chem. Rev.* **2018**, *118*, 8242–8284. [CrossRef] [PubMed]
151. Crich, D. En route to the transformation of glycoscience: A chemist's perspective on internal and external crossroads in glycochemistry. *J. Am. Chem. Soc.* **2021**, *143*, 17–34. [CrossRef] [PubMed]
152. Ötvös, S.B.; Mándity, I.M.; Fülöp, F. Highly efficient 1,4-addition of aldehydes to nitroolefins: Organocatalysis in continuous flow by solid-supported peptidic catalysts. *ChemSusChem* **2012**, *5*, 266–269. [CrossRef] [PubMed]
153. Webb, D.; Jamison, T.F. A Continuous Homologation of Esters: An Efficient Telescoped Reduction-Olefination Sequence. *Org. Lett.* **2012**, *14*, 2465–2467. [CrossRef] [PubMed]
154. Andreana, P.R.; Crich, D. Guidelines for *O*-glycoside formation from first principles. *ACS Cent. Sci.* **2021**, *7*, 1454–1462. [CrossRef] [PubMed]
155. Ribó, J.M.; Crusats, J.; Sagués, F.; Claret, J.; Rubires, R. Chiral Sign Induction by Vortices During the Formation of Mesophases in Stirred Solutions. *Science* **2001**, *292*, 2063–2066. [CrossRef] [PubMed]
156. Crusats, J.; El-Hachemi, Z.; Ribó, J.M. Hydrodynamic effects on chiral induction. *Chem. Soc. Rev.* **2010**, *39*, 569–577. [CrossRef] [PubMed]
157. Sang, Y.; Yang, D.; Duan, P.; Liu, M. Towards homochiral supramolecular entities from achiral molecules by vortex mixing-accompanied self-assembly. *Chem. Sci.* **2019**, *10*, 2718–2724. [CrossRef]
158. Nagornaya, M.O.; Orlova, A.V.; Stepanova, E.V.; Zinin, A.I.; Laptinskaya, T.V.; Kononov, L.O. The use of the novel glycosyl acceptor and supramer analysis in the synthesis of sialyl-α(2–3)-galactose building block. *Carbohydr. Res.* **2018**, *470*, 27–35. [CrossRef]
159. Penverne, C.; Hazard, B.; Rolando, C.; Penhoat, M. Scale-up Study of Benzoic Acid Alkylation in Flow: From Microflow Capillary Reactor to a Milliflow Reactor. *Org. Process Res. Dev.* **2017**, *21*, 1864–1868. [CrossRef]
160. Nagaki, A.; Kenmoku, A.; Moriwaki, Y.; Hayashi, A.; Yoshida, J.-i. Cross-Coupling in a Flow Microreactor: Space Integration of Lithiation and Murahashi Coupling. *Angew. Chem. Int. Ed.* **2010**, *49*, 7543–7547. [CrossRef]
161. Tomida, Y.; Nagaki, A.; Yoshida, J.-i. Asymmetric Carbolithiation of Conjugated Enynes: A Flow Microreactor Enables the Use of Configurationally Unstable Intermediates before They Epimerize. *J. Am. Chem. Soc.* **2011**, *133*, 3744–3747. [CrossRef]
162. Nagaki, A.; Kim, H.; Yoshida, J.-i. Nitro-Substituted Aryl Lithium Compounds in Microreactor Synthesis: Switch between Kinetic and Thermodynamic Control. *Angew. Chem. Int. Ed.* **2009**, *48*, 8063–8065. [CrossRef]

Disclaimer/Publisher's Note: The statements, opinions and data contained in all publications are solely those of the individual author(s) and contributor(s) and not of MDPI and/or the editor(s). MDPI and/or the editor(s) disclaim responsibility for any injury to people or property resulting from any ideas, methods, instructions or products referred to in the content.

MDPI AG
Grosspeteranlage 5
4052 Basel
Switzerland
Tel.: +41 61 683 77 34

Inventions Editorial Office
E-mail: inventions@mdpi.com
www.mdpi.com/journal/inventions



Disclaimer/Publisher's Note: The title and front matter of this reprint are at the discretion of the Guest Editors. The publisher is not responsible for their content or any associated concerns. The statements, opinions and data contained in all individual articles are solely those of the individual Editors and contributors and not of MDPI. MDPI disclaims responsibility for any injury to people or property resulting from any ideas, methods, instructions or products referred to in the content.





Academic Open
Access Publishing

mdpi.com

ISBN 978-3-7258-8794-1